

The hadron collider FCC-hh

Extended conceptual design report

Editor: Daniel Schulte, CERN



CERN Yellow Reports: Monographs
Published by CERN, CH-1211 Geneva 23, Switzerland

ISBN 978-92-9083-690-2 (paperback)
ISBN 978-92-9083-691-9 (PDF)
ISSN 2519-8068 (Print)
ISSN 2519-8076 (Online)
DOI <https://doi.org/10.23731/CYRM-2025-006>

Copyright © CERN, 2025
 Creative Commons Attribution 4.0

This volume should be cited as:

The hadron collider FCC-hh: Extended conceptual design report, Daniel Schulte (ed.)
CERN Yellow Reports: Monographs, CERN-2025-006 (CERN, Geneva, 2025)
<https://doi.org/10.23731/CYRM-2025-006>.

Corresponding editor: Daniel.Schulte@cern.ch.

Accepted in June 2025, by the [CERN Reports Editorial Board](#) (contact Carlos.Lourenco@cern.ch).

Published by the CERN Scientific Information Service (contact Jens.Vigen@cern.ch).

Indexed in the [CERN Document Server](#) and in [INSPIRE](#).

Published Open Access to permit its wide dissemination, as knowledge transfer is an integral part of the mission of CERN.

The hadron collider FCC-hh

Extended conceptual design report

A. Abada³³, M. Abbrescia^{118,258}, S.S. AbdusSalam²¹⁹, I. Abdyukhanov¹⁷, J. Abelleira Fernandez¹⁴³, A. Abramov²⁰⁵, M. Aburaia²⁸⁵, A.O. Acar²³⁹, P.R. Adzic²⁸⁸, P. Agrawal⁸⁰, J.A. Aguilar-Saavedra⁴⁷, J.J. Aguilera-Verdugo¹⁰⁷, M. Aiba¹⁹², I. Aichinger⁶⁵, G. Aielli^{135,273}, A. Akay²³⁹, A. Akhundov⁴⁶, H. Aksakal¹⁴⁶, J.L. Albacete⁴⁷, S. Albergio^{121,261}, A. Alekou³¹³, M. Aleksa⁶⁵, R. Aleksan⁴⁰, R.M. Alemany Fernandez⁶⁵, Y. Alexahin⁷¹, R.G. Alía⁶⁵, S. Alioli¹²⁷, N. Alipour Tehrani⁶⁵, B.C. Allanach²⁹⁹, P.P. Allport²⁹¹, M. Altunli^{63,113}, W. Altmannshofer²⁹⁸, G. Ambrosio⁷¹, D. Amorim⁶⁵, O. Amstutz¹⁶², L. Anderlini^{124,263}, A. Andreazza^{128,267}, M. Andreini⁶⁵, A. Andriatis¹⁶⁸, C. Andris¹⁶⁶, A. Andronic³⁴⁶, M. Angelucci¹¹⁶, F. Antinori^{130,268}, S.A. Antipov⁶⁵, M. Antonelli¹¹⁶, M. Antonello^{128,265}, P. Antoniolli¹¹⁹, S. Antusch²⁸⁷, F. Anulli^{134,272}, L. Apolinário¹⁵⁹, G. Apollinari⁷¹, A. Apollonio⁶⁵, D. Appelö³⁰², R.B. Appleby^{303,313}, A. Apyan⁷¹, A. Apyan¹, A. Arbey³³⁷, A. Arbutov¹⁸, G. Arduini⁶⁵, V. Ari¹⁰, S. Arias^{67,311}, N. Armesto¹⁰⁹, R. Arnaldi^{137,275}, S.A. Arsenyev⁶⁵, M. Arzoo⁶⁵, S. Asai²³⁷, E. Aslanides³², R.W. Aßmann⁵⁰, D. Astapovych²²⁹, M. Atanasov⁶⁵, S. Atieh⁶⁵, D. Attie⁴⁰, B. Auchmann⁶⁵, A. Audurier^{120,260}, S. Aull⁶⁵, S. Aumon⁶⁵, S. Aune⁴⁰, F. Avino⁶⁵, G. Avriilaud⁸⁴, G. Aydın¹⁷⁴, A. Azatov^{138,215}, G. Azuelos²⁴², P. Azzi^{130,268}, O. Azzolini¹¹⁷, P. Azzurri^{133,216}, N. Bacchetta^{130,268}, E. Bacchiocchi²⁶⁷, H. Bachacou⁴⁰, Y.W. Baek⁷⁵, V. Baglin⁶⁵, Y. Bai³³³, S. Baird⁶⁵, M.J. Baker³³⁵, M.J. Baldwin¹⁶⁸, A.H. Ball⁶⁵, A. Ballarino⁶⁵, S. Banerjee⁵⁵, D.P. Barber^{50,318}, D. Barducci^{138,215}, P. Barjhoux³, D. Barna¹⁷³, G.G. Barnaföldi¹⁷³, M.J. Barnes⁶⁵, A. Barr¹⁹¹, J. Barranco García⁵⁷, J. Barreiro Guimarães da Costa⁹⁸, W. Bartmann⁶⁵, V. Baryshevsky⁹⁶, E. Barzi⁷¹, S.A. Bass⁵⁴, A. Bastianin²⁶⁷, B. Baudouy⁴⁰, F. Bauer⁴⁰, M. Bauer⁵⁵, T. Baumgartner²³³, I. Bautista-Guzmán¹⁶, C. Bayindir^{20,83}, F. Beaudette³³, F. Bedeschi^{133,216}, M. Béguin⁶⁵, I. Bellafont⁷, L. Bellagamba^{119,259}, N. Bellegarde⁶⁵, E. Belli^{134,209,272}, E. Bellingeri⁴⁴, F. Bellini⁶⁵, G. Bellomo^{128,267}, S. Belomestnykh⁷¹, G. Bencivenni¹¹⁶, M. Benedikt⁶⁵, G. Bernardi³³, J. Bernardi²³³, C. Bernet^{33,337}, J.M. Bernhardt³, C. Bernini⁴⁴, C. Berriaud⁴⁰, A. Bertarelli⁶⁵, S. Bertolucci^{119,259}, M.I. Besana¹⁹², M. Besançon⁴⁰, O. Beznosov³¹⁸, P. Bhat⁷¹, C. Bhat⁷¹, M.E. Biagini¹¹⁶, J.-L. Biarrotte³³, A. Bibet Chevalier²⁸, E.R. Bielert³⁰⁶, M. Biglietti^{136,274}, G.M. Bilei^{132,271}, B. Bilki³⁰⁷, C. Biscari⁷, F. Bishara^{50,191}, O.R. Blanco-García¹¹⁶, F.R. Blázquez⁶⁵, F. Blekman³⁴², A. Blondel³⁰⁵, J. Blümlein⁵⁰, T. Boccali^{133,216}, R. Boels⁸⁵, S.A. Bogacz²³⁸, A. Bogomyagkov²⁴, O. Boine-Frankenheim²²⁹, M.J. Boland³²³, S. Bologna²⁹², O. Bolukbasi¹¹³, M. Bomben³³, S. Bondarenko¹⁸, M. Bonvini^{134,272}, E. Boos²²², B. Bordini⁶⁵, F. Bordry⁶⁵, G. Borghello^{65,276}, L. Borgonovi^{119,259}, S. Borowka⁶⁵, D. Bortoletto¹⁹¹, D. Boscherini^{119,259}, M. Boscolo¹¹⁶, S. Boselli^{131,270}, R.R. Bosley²⁹¹, F. Bossu³³, C. Botta⁶⁵, L. Bottura⁶⁵, R. Boughezal¹², D. Boutin⁴⁰, G. Bovone⁴⁴, I. Božović Jelisačić³⁴¹, A. Bozbey²³⁹, C. Bozzi^{123,262}, D. Bozzini⁶⁵, V. Braccini⁴⁴, S. Braibant-Giacomelli^{119,259}, J. Bramante^{194,201}, P. Braun-Munzinger⁷⁸, J.A. Briffa³¹², D. Britzger¹⁷⁰, S.J. Brodsky²²⁶, J.J. Brooke²⁹², R. Bruce⁶⁵, P. Brückman De Renstrom¹⁰⁰, E. Bruna^{137,275}, O. Brüning⁶⁵, O. Brunner⁶⁵, K. Brunner¹⁷³, P. Bruzzone⁵⁷, X. Buffat⁶⁵, E. Bulyak¹⁸², F. Burkart⁶⁵, H. Burkhardt⁶⁵, J.-P. Burnet⁶⁵, F. Butin⁶⁵, D. Buttazzo^{133,216}, A. Butterworth⁶⁵, M. Caccia^{128,265}, Y. Cai²²⁶, B. Caiffi^{125,264}, V. Cairo²²⁶, O. Cakir¹⁰, R. Calaga⁶⁵, S. Calatroni⁶⁵, G. Calderini³³, G. Calderola¹¹⁷, A. Caliskan⁷⁹, D. Calvet^{31,282}, M. Calviani⁶⁵, J.M. Camalich¹⁰³, P. Camarri^{135,273}, M. Campanelli²⁸⁴, T. Camporesi⁶⁵, A.C. Canbay¹⁰, A. Canepa⁷¹, E. Cantergiani⁸⁴, D. Cantore-Cavalli^{128,267}, M. Capeans⁶⁵, R. Cardarelli^{135,273}, U. Cardella¹⁶², A. Cardini¹²⁰, C.M. Carloni Calame^{131,270}, F. Carra⁶⁵, S. Carra^{128,267}, A. Carvalho¹⁵⁹, S. Casalbuoni¹⁴⁷, J. Casas⁷, M. Cascella²⁸⁴, P. Castelnovo²⁶⁷, G. Castorina^{134,272}, G. Catalano²⁶⁷, V. Cavasinni^{133,216}, E. Cazzato²⁸⁷, E. Cennini⁶⁵, A. Cerri³²⁹, F. Cerutti⁶⁵, J. Cervantes⁶⁵, I. Chaikovska³³, J. Chakraborty⁸⁸, M. Chala⁵⁵, M. Chamizo-Llatas²¹, H. Chanal³¹, D. Chanal²⁸, S. Chance³³, A. Chancé⁴⁰, P. Charitos⁶⁵, J. Charles⁵, T.K. Charles³¹⁶, S. Chattopadhyay¹⁸⁷, R. Chehab¹⁵⁴, S.V. Chekanov¹², N. Chen¹⁷⁵, A. Chernodod²²², V. Chetvertkova⁷⁸, L. Chevalier⁴⁰, G. Chiarelli^{133,216}, G. Chiarello^{134,209,272}, M. Chiesa¹⁴⁵, P. Chiggiato⁶⁵, J.T. Childers¹², A. Chmieleńska^{57,65}, A. Cholakian^{80,168}, P. Chomaz⁴⁰, M. Chorowski³⁴⁸, W. Chou⁹⁸, M. Chruszcz¹⁰⁰, E. Chyhyrynets¹¹⁷, G. Cibinetto^{123,262}, A.K. Ciftci¹⁴¹, R. Ciftci⁵⁹, R. Cimino¹¹⁶, M. Ciuchini^{136,274}, P.J. Clark³⁰³, Y. Coadou^{4,26,32}, M. Cobal^{138,276}, A. Cocco¹²⁵, J. Cogan^{32,33}, E. Cogneras³⁰, F. Collamati^{134,272}, C. Coldelram⁷, P. Collier⁶⁵, J. Collot^{33,283}, R. Contino²¹⁶, F. Conventi¹²⁹, C.T.A. Cook⁶⁵, L. Cooley^{11,178}, G. Corcella^{116,117}, A.S. Cornell³³⁰, G.H. Corral³⁶, H. Correia-Rodrigues⁶⁵, F. Costanza³³, P. Costa Pinto⁶⁵, F. Couderc⁴⁰, J. Coupard⁶⁵, N. Craig²⁹⁷, I. Crespo Garrido³³⁶, A. Crivellin¹⁹², J.F. Croteau⁸⁴, M. Crouch⁶⁵, E. Cruz Alaniz¹⁴³, B. Curé⁶⁵, J. Curti¹⁶⁸, D. Curtin³³¹, M. Czech⁶⁵, C. Dachauer¹⁶², R.T. D'Agnolo²²⁶, M. Daibo⁷⁴, A. Dainese^{130,268}, B. Dalena⁴⁰, A. Daljevec⁶⁵, W. Dallapiazza⁸⁶, L. D'Aloia Schwartzentruber²⁷, M. Dam¹⁸⁵, G. D'Ambrosio¹²⁹, S.P. Das²⁵⁰, S. DasBakshi⁸⁸, W. da Silva³³, G.G. da Silva²⁵², V. D'Auria⁵⁷, S. D'Auria²⁶⁷, A. David⁶⁵, T. Davidek⁶⁹, A. Deandrea^{33,337}, J. de Blas^{130,268}, C.J. Debono³¹², S. De Curtis^{124,263}, N. De Filippis^{118,258}, D. de Florian¹¹⁰, S. Deghaye⁶⁵, S.J. de Jong^{95,176}, C. Del Bo²⁶⁷, V. Del Duca^{137,275}, D. Delikaris⁶⁵, F. Deliot⁴⁰, A. Dell'Acqua⁶⁵, L. Delle Rose^{124,263}, M. Delmastro¹⁵³

E. De Lucia¹¹⁶, M. Demarteau¹², D. Denegri⁴⁰, L. Deniau⁶⁵, D. Denisov⁷¹, H. Denizli², A. Denner³³⁴, D. d'Enterria⁶⁵,
 G. de Rijk⁶⁵, A. De Roeck⁶⁵, F. Derue³³, O. Deschamps³³, S. Descotes-Genon³³, P.S.B. Dev³⁴³, J.B. de Vivie de
 Régie³³, R.K. Dewanjee¹⁷⁹, A. Di Ciaccio^{135,273}, A. Di Cicco¹¹⁶, B.M. Dillon¹⁰², B. Di Micco^{136,274},
 P. Di Nezza¹¹⁶, S. Di Vita^{128,267}, A. Doblhammer²³³, A. Dominjon¹⁵³, M. D'Onofrio³¹⁰, F. Dordei⁶⁵, A. Drago¹¹⁶,
 P. Draper³⁰⁶, Z. Drasal⁶⁹, M. Drewes¹⁴⁸, L. Duarte²⁴⁹, I. Dubovyk⁸⁵, P. Duda³⁴⁸, A. Dudarev⁶⁵, L. Dudko²²²,
 D. Duellmann⁶⁵, M. Dünser⁶⁵, T. du Pree¹⁷⁶, M. Durante⁴⁰, H. Duran Yildiz¹⁰, S. Dutta²²⁵, F. Duval⁶⁵, J.M. Duval^{41,283},
 Y. Dydyshka⁵⁶, B. Dziewit³²⁶, S. Eisenhardt³⁰³, M. Eisterer²³³, T. Ekelof³³⁸, D. El Khechen⁶⁵, S.A. Ellis²²⁶,
 J. Ellis¹⁵⁰, J.A. Ellison³¹⁸, K. Elsener⁶⁵, M. Elsing⁶⁵, Y. Enari²³⁷, C. Englert²¹¹, H. Eriksson¹⁶⁵, K.J. Eskola³⁰⁸,
 L.S. Esposito⁶⁵, O. Etisken¹⁰, E. Etzion²³⁴, P. Fabbriatore^{125,264}, A. Falkowski³³, A. Falou¹⁵⁴, J. Faltova⁶⁹,
 J. Fan²², L. Fanò^{132,271}, A. Farilla^{136,274}, R. Farinelli^{123,262}, S. Farinon^{125,264}, D.A. Faroughy¹⁰², S.D. Fartoukh⁶⁵,
 A. Faus-Golfe³³, W.J. Fawcett²⁹⁹, G. Felici¹¹⁶, L. Felsberger¹⁶⁴, C. Ferdeghini⁴³, A.M. Fernandez Navarro³⁵,
 A. Fernández-Téllez¹⁶, J. Ferradas Troitino^{65,305}, G. Ferrara^{128,267}, R. Ferrari^{131,270}, L. Ferreira⁶⁵, P. Ferreira da
 Silva⁶⁵, G. Ferrera^{127,267}, R. Ferrari^{131,270}, L. Ferreira⁶⁵, P. Ferreira da Silva⁶⁵, G. Ferrera^{127,267}, F. Ferro^{125,264},
 M. Fiascaris⁶⁵, S. Fiorendi¹²⁷, C. Fiorio²⁶⁷, O. Fischer^{147,287}, E. Fischer⁷⁸, W. Flieger³²⁶, M. Florio²⁶⁷, D. Fomesu⁶⁵,
 E. Fontanesi^{119,259}, N. Foppiani⁸⁰, K. Foraz⁶⁵, D. Forkel-Wirth⁶⁵, S. Forte²⁶⁷, M. Fouaidy⁹⁰, D. Fournier³³,
 T. Fowler⁶⁵, J. Fox²²⁷, P. Francavilla^{133,216}, R. Franceschini^{136,274}, S. Franchino²⁷⁸, E. Franco^{134,272}, A. Freitas¹⁹⁷,
 B. Fuks¹⁵⁷, K. Furukawa⁸², S.V. Furuseth⁵⁷, E. Gabrielli^{138,276}, A. Gaddi⁶⁵, M. Galanti³²¹, E. Gallo⁵⁰, S. Ganjour⁴⁰,
 J. Gao¹⁹², J. Gao⁹⁸, V. Garcia Diaz¹¹⁷, M. García Pérez⁶⁵, L. García Tabarés³⁵, C. Garion⁶⁵, M.V. Garzelli^{277,281},
 I. Garzia^{123,262}, S.M. Gascon-Shotkin^{33,337}, G. Gaudio^{131,270}, P. Gay^{31,33}, S.-F. Ge^{237,293}, T. Gehrmann³³⁵,
 M.H. Genest^{33,283}, R. Gerard⁶⁵, F. Gerigk⁶⁵, H. Gerwig⁶⁵, P. Giacomelli^{119,259}, S. Giagu^{134,272}, E. Gianfelice-
 Wendt⁷¹, F. Gianotti⁶⁵, F. Giffoni^{29,267}, S.S. Gilardoni⁶⁵, M. Gil Costa³⁵, M. Giovannetti¹¹⁶, M. Giovannozzi⁶⁵,
 P. Giubellino^{78,137}, G.F. Giudice⁶⁵, A. Giunta²⁵⁵, L.K. Gladilin²²², S. Glukhov²⁴, J. Gluza³²⁶, G. Gobbi⁶⁵,
 B. Goddard⁶⁵, F. Goertz¹⁶⁹, T. Golling³⁰⁵, V.P. Goncalves²⁵³, R. Gonçalo¹⁵⁹, L.A. Gonzalez Gomez¹¹⁶, S. Gorgi
 Zadeh³²², G. Gorine⁵⁷, E. Gorini^{126,257}, S.A. Gourlay¹⁶¹, L. Gouskos²⁹⁷, F. Grancagnolo^{126,266}, A. Grassellino⁷¹,
 A. Grau¹⁴⁷, E. Graverini³³⁵, H.M. Gray¹⁶¹, Ma. Greco^{136,274}, Mi. Greco^{136,274}, J.-L. Grenard⁶⁵, O. Grimm⁶⁰,
 C. Grojean⁵⁰, V.A. Gromov¹⁴⁴, J.F. Grosse-Oetringhaus⁶⁵, A. Grudiev⁶⁵, K. Grzanka³²⁶, J. Gu¹⁴², D. Guadagnoli¹⁵³,
 V. Guidi^{123,262}, S. Guiducci¹¹⁶, G. Guillermo Canton³⁶, Y.O. Günaydin¹⁴⁶, R. Gupta²¹, R.S. Gupta⁵⁵, J. Gutierrez⁸⁹,
 J. Gutleber⁶⁵, C. Guyot⁴⁰, V. Guzey¹⁹⁵, C. Gwenlan¹⁹¹, C. Haberstroh²³¹, B. Hacışahinoğlu¹¹³, B. Haerer⁶⁵,
 K. Hahn¹⁸⁸, T. Hahn³⁴⁵, A. Hammad²⁸⁷, C. Han²³⁷, M. Hance²⁹⁸, A. Hannah²¹², P.C. Harris¹⁶⁸, C. Hati^{31,282},
 S. Haug²⁹⁰, J. Hauptman¹¹¹, V. Haurylavets⁹⁶, H.-J. He²²⁰, A. Hegglin^{218,221}, B. Hegner²¹, K. Heinemann³¹⁸,
 S. Heinemeyer¹⁰⁶, C. Hensens⁶⁵, A. Henriques⁶⁵, A. Henriques⁶⁵, P. Hernandez¹⁰⁵, R.J. Hernández-Pinto²⁴⁶,
 J. Hernandez-Sanchez¹⁶, T. Herzig⁹⁹, I. Hiekkanen¹⁶⁵, W. Hillert²⁷⁷, T. Hoehn²³², M. Hofer²³³, W. Höfle⁶⁵,
 F. Holdener²²¹, S. Holleis²³³, B. Holzer⁶⁵, D.K. Hong²⁰⁰, C.G. Honorato¹⁶, S.C. Hopkins⁶⁵, J. Hrdinka⁶⁵, F. Hug¹⁴²,
 B. Humann²³³, H. Humer¹³, T. Hurth¹⁴², A. Hutton²³⁸, G. Iacobucci³⁰⁵, N. Ibarrola⁶⁵, L. Iconomidou-Fayard³³,
 K. Ilyina-Brunner⁶⁵, J. Incandela²⁹⁷, A. Infantino⁶⁵, V. Ippolito^{134,272}, M. Ishino²³⁷, R. Islam⁸⁷, H. Ita⁸, A. Ivanovs²⁰⁴,
 S. Iwamoto²⁶⁸, A. Iyer¹²⁹, S. Izquierdo Bermudez⁶⁵, S. Jadach¹⁰⁰, D.O. Jamin¹⁰¹, P. Janot⁶⁵, P. Jarry⁴⁰, A. Jeff^{37,65},
 P. Jenny¹⁶⁶, E. Jensen⁶⁵, M. Jensen⁶⁷, X. Jiang²⁸⁰, J.M. Jiménez⁶⁵, M.A. Jones⁶⁵, O.R. Jones⁶⁵, J.M. Jowett⁶⁵,
 S. Jung²¹⁷, W. Kaabi³³, M. Kado^{65,134,272}, K. Kahle⁶⁵, L. Kalinovskaya⁵⁶, J. Kalinowski³³², J.F. Kamenik¹⁰²,
 K. Kannike¹⁷⁹, S.O. Kara^{10,186}, H. Karadeniz⁷⁶, V. Karaventzas⁶⁵, I. Karpov⁶⁵, S. Kartal¹¹³, A. Karyukhin⁹⁴,
 V. Kashikhin⁷¹, J. Katharina Behr⁵⁰, U. Kaya^{10,239}, J. Keintzel²³³, P.A. Keinz³⁴⁰, K. Keppel¹¹⁷, R. Kersevan⁶⁵,
 K. Kershaw⁶⁵, H. Khanpour^{210,325}, S. Khatibi^{49,210}, M. Khatiri Yanehsari²¹⁰, V.V. Khoze⁵⁵, J. Kieseler⁶⁵, A. Kilic²⁴⁵,
 A. Kilpinen¹⁶⁵, Y.-K. Kim³⁰⁰, D.W. Kim⁷⁵, U. Klein³¹⁰, M. Klein³¹⁰, F. Kling²⁹⁵, N. Klinkenberg^{65,68}, S. Klöppel²³¹,
 M. Klute¹⁶⁸, V.I. Klyukhin²²², M. Knecht^{32,33}, B. Kniehl⁸⁵, F. Kocak²⁴⁵, C. Koeberl¹⁸⁴, A.M. Kolano⁶⁵, A. Kollegger²⁸⁵,
 K. Kołodziej³²⁶, A.A. Kolomiets¹⁴⁴, J. Komppula⁶⁵, I. Koop²⁴, P. Koppenburg¹⁷⁶, M. Koratzinos¹⁶⁸, M. Kordiaczyńska³²⁶,
 M. Korjik⁹⁶, O. Kortner³⁴⁵, P. Kostka³¹⁰, W. Kotlarski²³¹, C. Kotnig⁶⁵, T. Köttig⁶⁵, A.V. Kotwal⁵⁴, A.D. Kovalenko¹⁴⁴,
 S. Kowalski³²⁶, J. Kozaczuk³⁰⁶, G.A. Kozlov¹⁴⁴, S.S. Kozub¹⁴⁴, A.M. Krainer⁶⁵, T. Kramer⁶⁵, M. Kr"amer²⁰³,
 M. Krammer⁶⁵, A.A. Krasnov²⁴, F. Krauss⁵⁵, K. Kravalis²⁰⁴, L. Kretzschmar³⁴⁰, R.M. Kriske¹⁶⁸, H. Kritscher¹⁸⁴,
 P. Krkotic⁷, H. Kroha¹⁷⁰, M. Kucharczyk¹⁰⁰, S. Kuday¹¹², A. Kuendig¹⁶², G. Kuhlmann⁷², A. Kulesza³⁴⁶,
 M. Kumar⁵⁷, M. Kumar³³⁰, A. Kusina¹⁰⁰, S. Kuttimalai²²⁶, M. Kuze²⁴⁰, T. Kwon²¹⁷, F. Lackner⁶⁵, M. Lackner²⁸⁵,
 E. La Francesca^{116,272}, M. Laine²⁹⁰, G. Lamanna¹⁵³, S. La Mendola⁶⁵, E. Lançon²¹, G. Landsberg²², P. Langacker⁹¹,
 C. Lange⁶⁵, A. Langner⁶⁵, A.J. Lankford²⁹⁵, J.P. Lansberg³³, T. Lari¹²⁷, P.J. Laycock³¹⁰, P. Lebrun⁶⁶, A. Lechner⁶⁵,
 K. Lee²¹⁷, S. Lee^{25,152}, R. Lee²⁴, T. Lefevre⁶⁵, P. Le Guen⁶⁵, T. Lehtinen²⁰², S.B. Leith²⁸⁰, P. Lenzi^{124,263},
 E. Leogrande⁶⁵, C. Leonidopoulos²⁹⁹, I. Leon-Monzon²⁴⁶, G. Lerner⁶⁵, O. Leroy^{32,33}, T. Lesiak¹⁰⁰, P. Lévai¹⁷³,
 A. Leveratto⁴⁴, E. Levichev²⁴, G. Li⁹⁸, S. Li²²⁰, R. Li³⁵¹, D. Liberati⁴², M. Liepe⁴⁵, D.A. Lissauer²¹, Z. Liu³¹⁴,
 A. Lobko⁹⁶, E. Locci⁴⁰, E. Logothetis Agaliotis^{65,183}, M.P. Lombardo^{124,263}, A.J. Long³¹⁷, C. Lorin⁴⁰, R. Losito⁶⁵,
 A. Louzguiuti⁶⁵, I. Low¹², D. Lucchesi^{130,268}, M.T. Lucchini¹⁹⁸, A. Luciani⁶², M. Lueckhof²⁷⁷, A.J.G. Lunt⁶⁵,

M. Luzum²⁵¹, D.A. Lyubimsev¹⁴⁴, M. Maggiora^{137,275}, N. Magnin⁶⁵, M.A. Mahmoud⁷⁰, F. Mahmoudi^{33,337},
J. Maitre²⁸, V. Makarenko⁹⁶, A. Malagoli⁴⁴, J. Malclés⁴⁰, L. Malgeri⁶⁵, P.J. Mallon⁴⁰, F. Maltoni¹⁴⁸, S. Malvezzi¹²⁷,
O.B. Malyshev²¹², G. Mancinelli^{32,33}, P. Mandrik⁹⁴, P. Manfrinetti^{44,264}, M. Mangano⁶⁵, P. Manil⁴⁰, M. Mannelli⁶⁵,
G. Marchiori^{33,155}, F. Marhauser²³⁸, V. Mariani^{132,271}, V. Marinozzi^{128,267}, S. Mariotto^{128,267}, P. Marquard⁵¹,
C. Marquet³³, T. Marriott-Dodginton⁶⁵, R. Martin⁶⁵, O. Martin¹⁷¹, J. Martin Camalich^{103,248}, T. Martinez³⁵,
H. Martinez Bruzual^{131,270}, M.I. Martínez-Hernández¹⁶, D.E. Martins²⁵⁴, S. Marzani^{125,264}, D. Marzocca¹³⁸,
L. Marzola¹⁷⁹, S. Masciocchi^{78,278}, I. Masina^{123,262}, A. Massimiliano¹²⁸, A. Massironi⁶⁵, T. Masubuchi²³⁷,
V.A. Matveev¹⁴⁴, M.A. Mazzoni¹³⁴, M. McCullough⁶⁵, P.A. McIntosh²¹², P. Meade²²⁸, L. Medina²⁴⁷, A. Meier¹⁶²,
J. Maignan⁶⁵, B. Mele^{134,272}, J.G. Mendes Saraiva¹⁵⁹, F. Menez²⁸, M. Mentink⁶⁵, E. Meoni^{122,256},
P. Meridiani^{128,267}, M. Merk¹⁷⁶, P. Mermod³⁰⁵, V. Mertens⁶⁵, L. Mether⁵⁷, E. Métral⁶⁵, M. Migliorati^{134,272},
A. Milanese⁶⁵, C. Milardi¹¹⁶, G. Milhano¹⁵⁹, B.L. Militsyn²¹², F. Millet^{41,283}, I. Minashvili^{140,144}, J.V. Minervini¹⁶⁸,
L.S. Miralles⁶⁵, D. Mirarchi⁶⁵, S. Mishima⁸², D.P. Missiaen⁶⁵, G. Mitselmakher³⁰⁴, T. Mitshuhashi⁸², J. Mnich⁵⁰,
M. Mohammadi Najafabadi²¹⁰, R.N. Mohapatra³¹⁴, N. Mokhov⁷¹, J.G. Molson⁶⁵, R. Monge⁷, C. Montag²¹,
G. Montagna^{131,270}, S. Monteil^{31,33}, G. Montenero¹⁹², E. Montesinos⁶⁵, F. Moortgat⁶⁵, N. Morange¹⁵⁴,
G. Morello¹¹⁶, M. Moreno Llácer⁶⁵, M. Moretti^{123,262}, S. Moretti²¹³, A.K. Morley⁶⁵, A. Moros²³³, I. Morozov²⁴,
V. Morretta²⁶⁷, M. Morrone⁶⁵, A. Mostacci^{134,272}, S. Muanza^{32,33}, N. Muchnoi²⁴, M. Mühlegger¹⁶², M. Mulder¹⁷⁶,
M. Mulders⁶⁵, B. Müller^{21,54}, F. Müller⁹⁹, A.-S. Müller¹⁴⁷, J. Munilla³⁵, M.J. Murray³⁰⁹, Y. Muttoni⁶⁵, S. Myers⁶⁵,
M. Mylona⁶⁵, J. Nachtman³⁰⁷, T. Nakamoto⁸², M. Nardecchia⁶⁵, G. Nardini³²⁷, P. Nason¹²⁷, Z. Nergiz²³⁹,
A.V. Nesterenko¹⁴⁴, J.A. Netto³¹⁸, A. Nettsträter⁷², C. Neubüser⁶⁵, J. Neundorf⁵⁰, F. Niccoli⁶⁵, O. Nicosini^{131,270},
Y. Nie⁶⁵, U. Niedermayer²²⁹, J. Niedziela⁶⁵, A. Niemi⁶⁵, S.A. Nikitin²⁴, A. Nisati^{134,272}, J.M. No¹⁰⁶, M. Nonis⁶⁵,
Y. Nosochkov²²⁶, M. Novák¹⁷³, A. Novokhatski²²⁶, J.M. O'Callaghan²⁷⁹, C. Ochando¹⁵⁸, S. Ogur²⁰, K. Ohmi⁸²,
K. Oide⁶⁵, V.A. Okorokov¹⁸¹, Y. Okumura²³⁷, C. Oleari¹²⁷, F.I. Olness²²⁴, Y. Onel³⁰⁷, M. Ortino²³³, J. Osborne⁶⁵,
P. Osland²⁸⁹, T. Otto⁶⁵, K.Y. Oyulmaz², A. Ozansoy¹⁰, V. Özcan²⁰, K. Özdemir¹⁹⁶, C.E. Pagliarone^{53,113,115},
H.F. Pais da Silva⁶⁵, E. Palmieri¹¹⁷, L. Palumbo^{134,272}, A. Pampaloni^{125,264}, R.-Q. Pan³⁵⁰, M. Panareo^{126,266},
O. Panella^{132,271}, G. Panico²⁶³, G. Panizzo^{138,276}, A.A. Pankov⁷⁷, V. Pantsyrny¹⁷, C.G. Papadopoulos¹⁷⁷,
A. Papaefstathiou¹⁷⁶, Y. Papaphilippou⁶⁵, M.A. Parker²⁹⁹, V. Parma⁶⁵, M. Pasquali⁶⁵, S.K. Patra⁸⁸, R. Patterson⁴⁵,
H. Paukkunen³⁰⁸, F. Pauss⁶⁰, S. Peggs²¹, J.-P. Penttinen²⁰², G. Péon⁶⁵, E.E. Perepelkin¹⁴⁴, E. Perez⁶⁵, J.C. Perez⁶⁵,
G. Perez³⁴⁴, F. Pérez⁷, E. Perez Codina⁶⁵, J. Perez Morales³⁵, M. Perfilov²²², H. Pernegger⁶⁵, M. Peruzzi⁶⁵,
C. Pes⁴⁰, K. Peters⁵⁰, S. Petracca¹¹⁴, F. Petriello¹⁸⁸, L. Pezzotti^{131,270}, S. Pfeiffer²³³, F. Piccinini^{131,270}, T. Pieloni⁵⁷,
M. Pierini⁶⁵, H. Pikhartova²⁰⁵, G. Pikurs²⁰⁴, E. Pilicer²⁴⁵, P. Piminov²⁴, C. Pira¹¹⁷, R. Pittau⁴⁷, W. Placzek¹⁶⁷,
M. Plagge^{65,190}, T. Plehn²⁷⁸, M.-A. Pleier²¹, M. Ploskon¹⁶¹, M. Podeur³²⁸, H. Podlech⁹², T. Podzorny⁶⁵,
L. Poggioli³³, A. Poiron⁵⁸, G. Polesello^{131,270}, M. Poli Lener¹¹⁶, A. Polini^{119,259}, J. Polinski³⁴⁸, S.M. Polozov¹⁸¹,
L. Ponce⁶⁵, M. Pont⁷, L. Pontecorvo^{134,272}, T. Portaluri⁶⁰, K. Potamianos⁵⁰, C. Prasse⁷², M. Prausa⁸,
A. Preinerstorfer¹³, E. Premat²⁷, T. Price²⁹¹, M. Primavera¹²⁶, F. Prino^{137,275}, M. Prioli¹²⁸, J. Proudfoot¹²,
A. Provino⁴⁴, T. Pugat⁴⁰, N. Pukhaeva¹⁴⁴, S. Pulawski³²⁶, D. Pulikowski^{65,347}, G. Punzi^{133,216}, M. Putti²⁶⁴,
A. Pyarelal²⁸⁶, H. Quack²³¹, M. Quispe⁷, A. Racioppi¹⁷⁹, H. Rafique³¹³, V. Raginel⁷⁸, M. Raidal¹⁷⁹, N.S. Ramírez-Uribe¹⁰⁴,
M.J. Ramsey-Musolf³¹⁵, R. Rata⁶⁵, P. Ratoff³⁸, F. Ravotti⁶⁵, P. Rebello Teles³⁴, M. Reboud¹⁵³,
S. Redaelli⁶⁵, E. Renner²³³, A.E. Rentería-Olivo¹⁰⁵, M. Rescigno^{134,272}, J. Reuter⁵⁰, A. Ribon⁶⁵, A.M. Ricci^{125,264},
W. Riegler⁶⁵, S. Riemann⁵¹, B. Riemann²³⁰, T. Riemann³²⁶, J.M. Rifflet⁴⁰, R.A. Rimmer²³⁸, R. Rinaldesi⁶⁵,
L. Rinolfi⁶⁵, O. Rios Rubiras⁶⁵, T. Risselada⁶⁵, A. Rivetti^{137,275}, L. Rivkin¹⁹², T. Rizzo²²⁶, T. Robens²⁰⁶, F. Robert²⁷,
A.J. Robson³⁰⁵, E. Rochepault⁴⁰, C. Roda^{133,216}, G. Rodrigo¹⁰⁷, M. Rodríguez-Cahuantzi¹⁶, C. Rogan³⁰⁹, M. Roig³,
S. Rojas-Torres²⁴⁶, J. Rojo¹⁷⁶, G. Rolandi^{133,216}, P. Roloff⁶⁵, A. Romanenko⁷¹, A. Romanov⁸⁹, F. Roncarolo⁶⁵,
A. Rosado Sanchez¹⁶, G. Rosaz⁶⁵, L. Rossi^{65,267}, A. Rossi^{132,271}, R. Rossmannith^{50,147}, B. Rousset^{41,283}, C. Royon³⁰⁹,
X. Ruan³³⁰, I. Ruehl⁶⁵, V. Ruhlmann-Kleider⁴⁰, R. Ruiz⁵⁵, L. Rummyantsev^{56,223}, R. Ruprecht¹⁴⁷, A.I. Ryazanov¹⁸⁰,
A. Saba⁴⁴, R. Sadykov⁵⁶, D. Saez de Jauregui¹⁴⁷, M. Sahin³³⁹, B. Sailer²³, M. Saito²³⁷, F. Sala⁵⁰, G.P. Salam¹⁹¹,
J. Salfeld-Nebgen¹⁹⁸, C.A. Salgado¹⁰⁹, S. Salini²⁶⁷, J.M. Sallse⁵⁷, T. Salmi²⁰², A. Salzburger⁶⁵, O.A. Sampayo¹⁰⁸,
S. Sanfilippo¹⁹², J. Santiago⁴⁷, E. Santopinto¹²⁵, R. Santoro^{128,265}, A. Sanz Ull⁶¹, X. Sarasola¹⁹², I.H. Sarpün⁶,
M. Sauvain¹⁶⁰, S. Savelyeva²³¹, R. Sawada²³⁷, G.F.R. Sborlini^{46,110}, A. Schaffer³³, M. Schaubmann⁶⁵, M. Schenk⁶⁵,
C. Scheuerlein⁶⁵, I. Schienbein¹⁵⁶, K. Schlenga²³, H. Schmickler⁶⁵, R. Schmidt^{65,229}, D. Schoerling⁶⁵, A. Schoning²⁰⁷,
T. Schörner-Sadenius⁵⁰, M. Schott¹⁹⁹, D. Schulte⁶⁵, P. Schwaller¹⁴², C. Schwanenberger⁵⁰, P. Schwemling⁴⁰,
N. Schwerg⁶⁵, L. Scibile⁶⁵, A. Sciuto^{121,261}, E. Scomparin^{137,275}, C. Sebastiani^{134,272}, B. Seeber^{214,305}, M. Segreti⁴⁰,
P. Selva¹⁶², M. Selvaggi⁶⁵, C. Senatore³⁰⁵, A. Senol², L. Serin³³, M. Serluca¹⁵³, N. Serra³³⁵, A. Seryi¹⁴³,
L. Sestini^{130,268}, A. Sfyrila³⁰⁵, M. Shaposhnikov⁵⁷, E. Shaposhnikova⁶⁵, B.Y. Sharkov¹⁴⁴, D. Shatilov²⁴, J. Shelton³⁰⁶,
V. Shiltsev⁷¹, I.P. Shipsey¹⁹¹, G.D. Shirkov¹⁴⁴, A. Shivaji^{131,270}, D. Shwartz²⁴, T. Sian^{212,303,313}, S. Sidorov¹⁹²,
A. Siemko⁶⁵, L. Silvestrini^{134,272}, N. Simand²⁸, F. Simon¹⁷⁰, B.K. Singh¹⁴, A. Siódmok¹⁰⁰, Y. Sirois³³, E. Sirtori²⁹,
R. Sirvinskaite^{163,212}, B. Sitari³⁹, T. Sjöstrand³¹¹, P. Skands¹⁷², E. Skordis^{65,310}, K. Skovpen³⁴², M. Skrzypek¹⁰⁰,

E. Slade¹⁹¹, P. Slavich¹⁵⁷, R. Slovak⁶⁹, V. Smaluk²¹, V. Smirnov²²², W. Snoeys⁶⁵, L. Soffi⁴⁵, P. Sollander⁶⁵, O. Solovyanov⁹⁴, H.K. Soltveit²⁷⁸, H. Song²⁸⁶, P. Sopicki¹⁰⁰, M. Sorbi^{128,267}, L. Spallino¹¹⁶, M. Spannowsky⁵⁵, B. Spataro^{134,272}, P. Sphicas⁶⁵, H. Spiesberger¹⁹⁹, P. Spiller⁷⁸, M. Spira¹⁹², T. Srivastava⁸⁸, J. Stachel²⁷⁸, A. Stakia⁶⁵, J.L. Stanyard⁶⁵, E. Starchenko¹⁸⁰, A.Y. Starikov¹⁴⁴, A.M. Stašto²³⁶, M. Statera^{128,267}, R. Steerenberg⁶⁵, J. Steggemann⁶⁵, A. Stenvall²⁰², F. Stivanello¹¹⁷, D. Stöckinger²³¹, L.S. Stoel⁶⁵, M. Stöger-Pollach²³³, B. Strauss^{48,97}, M. Stuart⁶⁵, G. Stupakov²²⁶, S. Su²⁸⁶, A. Sublet⁶⁵, K. Sugita⁷⁸, L. Sulak¹⁹, M.K. Sullivan²²⁶, S. Sultansoy²³⁹, T. Sumida¹⁵¹, K. Suzuki⁸², G. Sylva⁴⁴, M.J. Syphers¹⁸⁷, A. Sznajder²⁵², M. Taborelli⁶⁵, N.A. Tahir⁷⁸, M. Takeuchi²³⁷, E. Tal Hod²³⁴, C. Tambasco⁵⁷, J. Tanaka²³⁷, K. Tang¹⁶⁸, I. Tapan²⁴⁵, S. Taroni³¹⁹, G.F. Tartarelli^{128,267}, G. Tassielli^{126,266}, L. Taviani⁶⁵, T.M. Taylor⁶⁵, G.N. Taylor³¹⁶, A.M. Teixeira^{31,33}, G. Tejada-Muñoz¹⁶, V.I. Telnov^{24,189}, R. Tenchini^{133,216}, H.H.J. ten Kate⁶⁵, K. Terashi²³⁷, A. Tesi^{124,263}, M. Testa¹¹⁶, C. Tetrel²⁸, D. Teytelman⁵², J. Thaler¹⁶⁸, A. Thamm⁶⁵, S. Thomas²⁰⁸, M.T. Tiirakari⁶⁵, V. Tikhomirov⁹⁶, D. Tikhonov⁸¹, H. Timko⁶⁵, V. Tisserand^{31,33}, L.M. Tkachenko¹⁴⁴, J. Tkaczuk^{41,283}, J.P. Tock⁶⁵, B. Todd⁶⁵, E. Todesco⁶⁵, R. Tomás García⁶⁵, D. Tommasini⁶⁵, G. Tonelli^{133,216}, F. Toral³⁵, T. Torims²⁰⁴, R. Torre⁶⁵, Z. Townsend⁶⁵, R. Trant⁶⁵, D. Treille⁶⁵, L. Trentadue^{127,269}, A. Tricoli²¹, A. Tricomi^{121,261}, W. Trischuk³³¹, I.S. Tropin⁷¹, B. Tuchming⁴⁰, A.A. Tudora⁶⁵, B. Turbiar¹⁰⁰, I. Turk Cakir⁷⁶, M. Turri²⁶⁷, T. Tydecks⁶⁵, J. Usovitsch²⁴¹, J. Uythoven⁶⁵, R. Vaglio⁴⁴, A. Valassi⁶⁵, F. Valchikova⁶⁵, M.A. Valdivia García²⁴⁷, P. Valente^{128,267}, R.U. Valente²⁷², A.-M. Valente-Feliciano²³⁸, G. Valentino³¹², L. Vale Silva³²⁹, J.M. Valet²⁸, R. Valizadeh²¹², J.W.F. Valle¹⁰⁷, S. Vallecorsa⁷⁵, G. Vallone¹⁶¹, M. van Leeuwen¹⁷⁶, U.H. van Rienen³²², L. van Riesen-Haupt¹⁴³, M. Varasteh⁶⁵, L. Vecchi⁵⁷, P. Vedrine⁴⁰, G. Velev⁷¹, R. Veness⁶⁵, A. Ventura^{126,257}, W. Venturini Delsolaro⁶⁵, M. Verducci^{136,274}, C.B. Verhaaren²⁹⁴, C. Vernieri⁷¹, A.P. Verweij⁶⁵, O. Verwilligen^{118,258}, O. Viazlo⁶⁵, A. Vicini^{128,267}, G. Viehhauser¹⁹¹, N. Vignaroli^{130,268}, M. Vignolo⁴⁴, A. Vitrano⁴⁰, I. Vivarelli³²⁹, S. Vlachos¹⁸³, M. Vogel²⁸⁰, D.M. Vogt³²⁸, V. Völkl⁹³, P. Volkov²²², G. Volpini^{128,267}, J. von Ahnen⁵⁰, G. Vorotnikov²²², G.G. Voutsinas⁶⁵, V. Vysotsky⁹, U. Wagner⁶⁵, R. Wallny⁶⁰, L.-T. Wang³⁰⁰, R. Wang¹², K. Wang³⁴⁹, B.F.L. Ward^{15,345}, T.P. Watson¹³⁹, N.K. Watson²⁹¹, Z. Wąs¹⁰⁰, C. Weiland¹⁹⁷, S. Weinzierl¹⁹⁹, C.P. Welsch³¹⁰, J. Wenninger⁶⁵, M. Widorski⁶⁵, U.A. Wiedemann⁶⁵, H.-U. Wienands¹², G. Wilkinson¹⁹¹, P.H. Williams²¹², A. Winter²⁹¹, A. Wohlfahrt⁷², T. Wojton¹⁰⁰, D. Wollmann⁶⁵, J. Womersley⁶⁷, D. Woog⁶⁵, X. Wu³⁰⁵, A. Wulzer^{130,268}, M.K. Yanehsari²¹⁰, G. Yang¹⁴⁹, H.J. Yang^{220,244}, W.-M. Yao¹⁶¹, E. Yazgan⁹⁸, V. Yermolchik⁹⁶, A. Yilmaz^{113,76}, H.-D. Yoo²¹⁷, S.A. Yost²³⁵, T. You²⁹⁹, C. Young²²⁶, T.-T. Yu³²⁰, F. Yu¹⁴², A. Zaborowska⁶⁵, S.G. Zadeh³²², M. Zahnd⁵⁸, M. Zanetti^{130,268}, L. Zanutto¹¹⁷, L. Zawiejski¹⁰⁰, P. Zeiler⁶⁴, M. Zerlauth⁶⁵, S.M. Zernov⁷³, G. Zevi Dell Porta²⁹⁶, Z. Zhang³³, Y. Zhang³⁴³, C. Zhang¹⁹³, H. Zhang⁹⁸, Z. Zhao³²⁴, Y.-M. Zhong¹⁹, J. Zhou^{131,270}, D. Zhou⁸², P. Zhuang²⁴³, G. Zick³, F. Zimmermann⁶⁵, J. Zinn-Justin⁴⁰, L. Zivkovic²⁸⁸, A.V. Zlobin⁷¹, M. Zbov¹¹⁶, J. Zupan³⁰¹, J. Zurita¹⁴⁷, and the FCC Collaboration³⁵².

¹ *Alikhanyan National Laboratory, Yerevan, Armenia,*

² *Bolu Abant İzzet Baysal University, Bolu, Türkiye,*

³ *Air Liquide Advanced Technologies, Sassenage, France,*

⁴ *Aix-Marseille University, Marseille, France,*

⁵ *Centre de physique théorique, Marseille, France,*

⁶ *Akdeniz University, Antalya, Türkiye,*

⁷ *ALBA Synchrotron, Cerdanyola del Vallès, Spain,*

⁸ *University of Freiburg, Freiburg im Breisgau, Germany,*

⁹ *At an institute formerly covered by a cooperation agreement with CERN,*

¹⁰ *Ankara University, Ankara, Türkiye,*

¹¹ *National High Magnetic Field Laboratory, Tallahassee, FL, United States,*

¹² *Argonne National Laboratory, Lemont, IL, United States,*

¹³ *Austrian Institute of Technology, Vienna, Austria,*

¹⁴ *Banaras Hindu University, Varanasi, India,*

¹⁵ *Baylor University, Waco, TX, United States,*

¹⁶ *Benemérita Universidad Autónoma de Puebla, Puebla City, Mexico,*

¹⁷ *At an institute formerly covered by a cooperation agreement with CERN,*

¹⁸ *Bogoliubov Laboratory of Theoretical Physics, Joint Institute for Nuclear Research, Dubna, Russia*

¹⁹ *Boston University, Boston, MA, United States,*

²⁰ *Boğaziçi University, Istanbul, Türkiye,*

²¹ *Brookhaven National Laboratory, Upton, NY, United States,*

²² *Brown University, Providence, RI, United States,*

²³ *Bruker Energy and Supercon Technologies (Bruker EST), Hanau, Germany,*

²⁴ *At an institute formerly covered by a cooperation agreement with CERN,*

²⁵ *Kyungpook National University, Center for High Energy Physics, Daegu, South Korea,*

²⁶ *Centre de physique des particules de Marseille, Marseille, France,*

- ²⁷ *Centre d'Etudes des Tunnels (CETU), Bron, France,*
- ²⁸ *Centre d'études et d'expertise sur les risques, l'environnement, la mobilité et l'aménagement, Bron, France,*
- ²⁹ *Centre for Industrial Studies (CSIL), Milan, Italy,*
- ³⁰ *Centre National de la Recherche Scientifique (CNRS), Aubière, France,*
- ³¹ *Centre National de la Recherche Scientifique (CNRS/IN2P3), Clermont-Ferrand, France,*
- ³² *Centre National de la Recherche Scientifique (CNRS), Marseille, France,*
- ³³ *Centre National de la Recherche Scientifique (CNRS), Paris, France,*
- ³⁴ *Centro Brasileiro de Pesquisas Físicas (CBPF), Rio de Janeiro, Brazil,*
- ³⁵ *Centro de Investigaciones Energéticas, Medioambientales y Tecnológicas (CIEMAT), Madrid, Spain,*
- ³⁶ *Centro de Investigación y de Estudios Avanzados (CINVESTAV), Merida, Mexico,*
- ³⁷ *Cockcroft Institute (CI Daresbury), Daresbury, United Kingdom,*
- ³⁸ *Cockcroft Institute (CI Lancaster), Lancaster, United Kingdom,*
- ³⁹ *Comenius University (CU), Bratislava, Slovakia,*
- ⁴⁰ *Commissariat à l'énergie atomique et aux énergies alternatives – Institut de Recherche sur les lois Fondamentales de l'Univers Saclay (CEA/DSM/Irfu Saclay), Gif-sur-Yvette, France,*
- ⁴¹ *Commissariat à l'énergie atomique et aux énergies alternatives – Institut Nanosciences et Cryogénie (CEA), Grenoble, France,*
- ⁴² *Consiglio Nazionale delle Ricerche (CNR), Milan, Italy,*
- ⁴³ *Consiglio Nazionale delle Ricerche – Superconducting and other Innovative materials and devices institute (CNR-SPIN), Genoa, Italy,*
- ⁴⁴ *Consiglio Nazionale delle Ricerche – Superconducting and other Innovative materials and devices institute (CNR-SPIN), Naples, Italy,*
- ⁴⁵ *Cornell University (Cornell), Ithaca, NY, United States,*
- ⁴⁶ *Departamento de Física Teórica, Universidad de València (UV), València, Spain,*
- ⁴⁷ *Departamento de Física Teórica y del Cosmos and CAFPE, Universidad de Granada (UGR), Granada, Spain,*
- ⁴⁸ *Department of Energy (DoE), Washington, DC, United States,*
- ⁴⁹ *Department of Physics, University of Tehran (UT), Tehran, Iran,*
- ⁵⁰ *Deutsches Elektronen Synchrotron (DESY), Hamburg, Germany,*
- ⁵¹ *Deutsches Elektronen Synchrotron (DESY ZEUP), Zeuthen, Germany,*
- ⁵² *Dimtel, Inc. (Dimtel), San Jose, CA, United States,*
- ⁵³ *Dipartimento di Ingegneria Civile e Meccanica, Università degli Studi di Cassino e del Lazio Meridionale (DICEM), Cassino, Italy,*
- ⁵⁴ *Duke University (DU), Durham, NC, United States,*
- ⁵⁵ *Durham University, Institute for Particle Physics Phenomenology (IPPP), Durham, United Kingdom,*
- ⁵⁶ *At an institute formerly covered by a cooperation agreement with CERN,*
- ⁵⁷ *Ecole polytechnique fédérale de Lausanne (EPFL), Lausanne, Switzerland,*
- ⁵⁸ *Ecotec Environnement SA (Ecotec), Geneva, Switzerland,*
- ⁵⁹ *Ege University (EgeU), Izmir, Türkiye,*
- ⁶⁰ *Eidgenössische Technische Hochschule Zürich (ETHZ), Zürich, Switzerland,*
- ⁶¹ *Eindhoven University of Technology (TU/e), Eindhoven, Netherlands,*
- ⁶² *Elle Marmi SARL (EM), Carrara, Italy,*
- ⁶³ *Eskişehir Technical University (ESTU), Istanbul, Türkiye,*
- ⁶⁴ *Esslingen University of Applied Sciences (HS Esslingen), Göppingen, Germany,*
- ⁶⁵ *European Organization for Nuclear Research (CERN), Geneva, Switzerland,*
- ⁶⁶ *European Scientific Institute (ESI), Archamps, France,*
- ⁶⁷ *European Spallation Source (ESS), Lund, Sweden,*
- ⁶⁸ *Fachhochschule Südwestfalen (FH-SWF), Gelsenkirchen, Germany,*
- ⁶⁹ *Faculty of Mathematics and Physics, Charles University Prague (CU), Prague, Czech Republic,*
- ⁷⁰ *Fayoum University (FU), El-Fayoum, Egypt,*
- ⁷¹ *Fermi National Accelerator Laboratory (FNAL), Batavia, IL, United States,*
- ⁷² *Fraunhofer-Institut für Materialfluss und Logistik (FIML), Dortmund, Germany,*
- ⁷³ *At an institute formerly covered by a cooperation agreement with CERN,*
- ⁷⁴ *Fujikura Ltd. (Fujikura), Sakura City, Japan,*
- ⁷⁵ *Gangneung-Wonju National University (GWNNU), Gangneung-Wonju, South Korea,*
- ⁷⁶ *Giresun University (Giresun), Giresun, Türkiye,*
- ⁷⁷ *At an institute formerly covered by a cooperation agreement with CERN,*
- ⁷⁸ *GSI Helmholtz Zentrum für Schwerionenforschung (GSI), Darmstadt, Germany,*
- ⁷⁹ *Gümüşhane University (Gumushane), Gümüşhane, Türkiye,*
- ⁸⁰ *Harvard University (Harvard), Cambridge, MA, United States,*
- ⁸¹ *Helmholtz-Zentrum Berlin (HZB), Berlin, Germany,*
- ⁸² *High Energy Accelerator Research Organization (KEK), Tsukuba, Japan,*
- ⁸³ *İşık University (Isikun), Istanbul, Türkiye,*

- ⁸⁴ *I-Cube Research (I-Cube), Toulouse, France,*
- ⁸⁵ *II. Institut für Theoretische Physik, Universität Hamburg (UNITH), Hamburg, Germany,*
- ⁸⁶ *ILF Consulting Engineers (ILF), Zürich, Switzerland,*
- ⁸⁷ *Indian Institute of Technology Guwahati (IITG), Guwahati, India,*
- ⁸⁸ *Indian Institute of Technology Kanpur (IITK), Uttar Pradesh, India,*
- ⁸⁹ *Institiut de Ciència de Materials de Barcelona (ICMAB-CSIC), Barcelona, Spain,*
- ⁹⁰ *Institiut de Physique Nucléaire d'Orsay (CNRS/IN2P3/IPNO), Orsay, France,*
- ⁹¹ *Institute for Advanced Study (IAS), Princeton, NJ, United States,*
- ⁹² *Institute for Applied Physics, Goethe University (IAP), Frankfurt, Germany,*
- ⁹³ *Institute for Astro and Particle Physics, University of Innsbruck (UIBK), Innsbruck, Austria,*
- ⁹⁴ *At an institute formerly covered by a cooperation agreement with CERN,*
- ⁹⁵ *Institute for Mathematics, Astrophysics and Particle Physics, Radboud University (IMAPP), Nijmegen, Netherlands,*
- ⁹⁶ *At an institute formerly covered by a cooperation agreement with CERN,*
- ⁹⁷ *Institute of Electrical and Electronic Engineers (IEEE), Piscataway, NJ, United States,*
- ⁹⁸ *Institute of High Energy Physics, Chinese Academy of Science, Beijing (IHEP CAS), Beijing, P.R. China,*
- ⁹⁹ *Institute of Machine Components, University of Stuttgart (IMA), Stuttgart, Germany,*
- ¹⁰⁰ *Institute of Nuclear Physics Polish Academy of Sciences (IFJ PAN), Krakow, Poland,*
- ¹⁰¹ *Institute of Physics, Academia Sinica (AS), Taipei, Taiwan,*
- ¹⁰² *Institut Jožef Stefan (IJS), Ljubljana, Slovenia,*
- ¹⁰³ *Instituto de Astrofísica de Canarias (IAC), La Laguna, Spain,*
- ¹⁰⁴ *Instituto de Física Corpuscular (CSIC-UV), Paterna, Spain,*
- ¹⁰⁵ *Instituto de Física Corpuscular (CSIC-UV), Valencia, Spain,*
- ¹⁰⁶ *Instituto de Física Teórica, Universidad Autónoma de Madrid (IFT-UAM), Madrid, Spain,*
- ¹⁰⁷ *Instituto de Física, Universitat de València (CSIC), Valencia, Spain,*
- ¹⁰⁸ *Instituto de Investigaciones Físicas de Mar del Plata (IFIMAR), Mar del Plata, Argentina,*
- ¹⁰⁹ *Instituto Galego de Física de Altas Enxerxías, Universidade de Santiago de Compostela (IGFAE), Santiago de Compostela, Spain,*
- ¹¹⁰ *International Center for Advanced Studies, Universidad Nacional de San Martín (ICAS-UNSAM), San Martín, Argentina,*
- ¹¹¹ *Iowa State University (ISU), Ames, IA, United States,*
- ¹¹² *Istanbul Aydın University (IAU), Istanbul, Türkiye,*
- ¹¹³ *Istanbul University (İÜ), Istanbul, Türkiye,*
- ¹¹⁴ *Istituto Nazionale di Fisica Nucleare, Gruppo Collegato di Salerno – Sezione di Napoli (INFN SA), Salerno, Italy,*
- ¹¹⁵ *Istituto Nazionale di Fisica Nucleare, Laboratori Nazionali del Gran Sasso (INFN LNGS), Assergi (L'Aquila), Italy,*
- ¹¹⁶ *Istituto Nazionale di Fisica Nucleare, Laboratori Nazionali di Frascati (INFN LNF), Frascati, Italy,*
- ¹¹⁷ *Istituto Nazionale di Fisica Nucleare, Laboratori Nazionali di Legnaro (INFN LNLN), Legnaro, Italy,*
- ¹¹⁸ *Istituto Nazionale di Fisica Nucleare Sezione di Bari (INFN BA), Bari, Italy,*
- ¹¹⁹ *Istituto Nazionale di Fisica Nucleare, Sezione di Bologna (INFN BO), Bologna, Italy,*
- ¹²⁰ *Istituto Nazionale di Fisica Nucleare, Sezione di Cagliari (INFN CA), Cagliari, Italy,*
- ¹²¹ *Istituto Nazionale di Fisica Nucleare, Sezione di Catania (INFN CT), Catania, Italy,*
- ¹²² *Istituto Nazionale di Fisica Nucleare, Sezione di Cosenza (INFN CS), Cosenza, Italy,*
- ¹²³ *Istituto Nazionale di Fisica Nucleare, Sezione di Ferrara (INFN FE), Ferrara, Italy,*
- ¹²⁴ *Istituto Nazionale di Fisica Nucleare, Sezione di Firenze (INFN FI), Florence, Italy,*
- ¹²⁵ *Istituto Nazionale di Fisica Nucleare, Sezione di Genova (INFN GE), Genoa, Italy,*
- ¹²⁶ *Istituto Nazionale di Fisica Nucleare, Sezione di Lecce (INFN LE), Lecce, Italy,*
- ¹²⁷ *Istituto Nazionale di Fisica Nucleare, Sezione di Milano Bicocca (INFN MIB), Milan, Italy,*
- ¹²⁸ *Istituto Nazionale di Fisica Nucleare, Sezione di Milano (INFN MI), Milan, Italy,*
- ¹²⁹ *Istituto Nazionale di Fisica Nucleare, Sezione di Napoli (INFN NA), Naples, Italy,*
- ¹³⁰ *Istituto Nazionale di Fisica Nucleare, Sezione di Padova (INFN PD), Padua, Italy,*
- ¹³¹ *Istituto Nazionale di Fisica Nucleare, Sezione di Pavia (INFN PV), Pavia, Italy,*
- ¹³² *Istituto Nazionale di Fisica Nucleare, Sezione di Perugia (INFN PG), Perugia, Italy,*
- ¹³³ *Istituto Nazionale di Fisica Nucleare, Sezione di Pisa, Università di Pisa (INFN PI), Pisa, Italy,*
- ¹³⁴ *Istituto Nazionale di Fisica Nucleare, Sezione di Roma 1 (INFN Roma 1), Rome, Italy,*
- ¹³⁵ *Istituto Nazionale di Fisica Nucleare, Sezione di Roma Tor Vergata (INFN Roma 2), Rome, Italy,*
- ¹³⁶ *Istituto Nazionale di Fisica Nucleare, Sezione di Roma Tre (INFN Roma 3), Rome, Italy,*
- ¹³⁷ *Istituto Nazionale di Fisica Nucleare, Sezione di Torino (INFN TO), Turin, Italy,*
- ¹³⁸ *Istituto Nazionale di Fisica Nucleare, Sezione di Trieste (INFN TS), Trieste, Italy,*
- ¹³⁹ *ITER (ITER), Cadarache, France,*
- ¹⁴⁰ *Ivane Javakishvili T'bilisi State University (TSU), T'bilisi, Georgia,*
- ¹⁴¹ *Izmir University of Economics (IUE), Izmir, Türkiye,*
- ¹⁴² *Johannes-Gutenberg-Universität (JGU), Mainz, Germany,*
- ¹⁴³ *John Adams Institute for Accelerator Science, Oxford, United Kingdom,*
- ¹⁴⁴ *Joint Institute for Nuclear Research, Dubna, Russia,*

145 *Julius-Maximilians-Universität Würzburg (UWUERZBURG), Würzburg, Germany,*
 146 *Kahramanmaras Sutcu Imam University (KSU), Kahramanmaras, Türkiye,*
 147 *Karlsruher Institut für Technologie (KIT), Karlsruhe, Germany,*
 148 *Katholieke Universiteit Leuven Research and Development (LRD), Louvain, Belgium,*
 149 *Key Laboratory of Theoretical Physics, Chinese Academy of Science (SKLTP ITP CAS), Beijing, P.R. China,*
 150 *King's College London (KCL), London, United Kingdom,*
 151 *Kyoto University (Kyodai), Kyoto, Japan,*
 152 *Kyungpook National University (KNU), Sankyuk-dong, South Korea,*
 153 *Laboratoire d'Annecy-Le-Vieux de Physique des Particules (CNRS/IN2P3/LAPP), Annecy, France,*
 154 *Laboratoire de l'accélérateur Linéaire, Université de Paris Sud (CNRS/IN2P3/UPSUD/ LAL), Orsay, France,*
 155 *Laboratoire de Physique Nucléaire et de Hautes Energies (LPNHE), Paris, France,*
 156 *Laboratoire de Physique Subatomique et de Cosmologie Grenoble (LPSC), Grenoble, France,*
 157 *Laboratoire de Physique Théorique et Hautes Energies (CNRS/Sorbonne/LPTHE), Paris, France,*
 158 *Laboratoire Leprince-Ringuet, Ecole Polytechnique (LLR), Palaiseau, France,*
 159 *Laboratório de Instrumentação e Física Experimental de Partículas (LIP), Lisbon, Portugal,*
 160 *Latitude Durable (LD), Geneva, Switzerland,*
 161 *Lawrence Berkeley National Laboratory (LBNL), Berkeley, CA, United States,*
 162 *Linde Kryotechnik AG (Linde), Pfungen, Switzerland,*
 163 *Loughborough University (Lboro), Loughborough, United Kingdom,*
 164 *Ludwig Maximilians University of Munich (LMU), Munich, Germany,*
 165 *Luvata Pori Oy (Luvata), Pori, Finland,*
 166 *MAN Energy Solutions Schweiz AG (MAN ES), Zürich, Switzerland,*
 167 *Marian Smoluchowski Institute of Physics, Jagiellonian University (UJ), Kraków, Poland,*
 168 *Massachusetts Institute of Technology (MIT), Cambridge, MA, United States,*
 169 *Max-Planck-Institut für Kernphysik (MPIK), Heidelberg, Germany,*
 170 *Max-Planck-Institut für Physik (MPP), Munich, Germany,*
 171 *Ministère de l'Europe et des Affaires étrangères (MEAE), Paris, France,*
 172 *Monash University (Monash), Melbourne, Australia,*
 173 *MTA Wigner Research Centre for Physics (Wigner), Budapest, Hungary,*
 174 *Mustafa Kemal Üniversitesi (MKU), Hatay, Türkiye,*
 175 *Nankai University (NKU), Tianjin, P.R. China,*
 176 *Nationaal instituut voor subatomaire fysica (NIKHEF), Amsterdam, Netherlands,*
 177 *National Centre for Scientific Research Demokritos (NCSR), Athens, Greece,*
 178 *National High Magnetic Field Laboratory, Florida State University (MagLab), Tallahassee, FL, United States,*
 179 *National Institute of Chemical Physics and Biophysics (NICPB), Tallinn, Estonia,*
 180 *At an institute formerly covered by a cooperation agreement with CERN,*
 181 *At an institute formerly covered by a cooperation agreement with CERN,*
 182 *National Science Centre Kharkov Institute of Physics and Technology (KIPT), Kharkov, Ukraine,*
 183 *National Technical University of Athens (NTUA), Athens, Greece,*
 184 *Naturhistorisches Museum Wien (NHM), Vienna, Austria,*
 185 *Niels Bohr Institute, Copenhagen University (NBI), Copenhagen, Denmark,*
 186 *Nigde Ömer Halisdemir University (OHU), Nigde, Türkiye,*
 187 *Northern Illinois University (NIU), DeKalb, IL, United States,*
 188 *Northwestern University (NU), Evanston, IL, United States,*
 189 *At an institute formerly covered by a cooperation agreement with CERN,*
 190 *Otto-von-Guericke-University at Magdeburg (OVGU), Magdeburg, Germany,*
 191 *Oxford University (UOXF), Oxford, United Kingdom,*
 192 *Paul Scherrer Institute (PSI), Villigen, Switzerland,*
 193 *Peking University (PU), Beijing, P.R. China,*
 194 *Perimeter Institute for Theoretical Physics (PI), Waterloo, Canada,*
 195 *At an institute formerly covered by a cooperation agreement with CERN,*
 196 *Piri Reis University (PRU), Istanbul, Türkiye,*
 197 *Pittsburgh Particle physics, Astrophysics and Cosmology Center and Department of Physics and Astronomy, University of Pittsburgh (PITT PACC), Pittsburgh, PA, United States,*
 198 *Princeton University (PU), Princeton, NJ, United States,*
 199 *PRISMA Cluster of Excellence, Inst. für Physik, Johannes-Gutenberg-Universität (PRISMA), Mainz, Germany,*
 200 *Pusan National University (PNU), Busan, South Korea,*
 201 *Queen's University (Queens U), Kingston, Canada,*
 202 *Tampere University (TAU), Tampere, Finland,*
 203 *Rheinisch-Westfälische Technische Hochschule Aachen (RWTH), Aachen, Germany,*
 204 *Riga Technical University (RTU), Riga, Latvia,*
 205 *Royal Holloway University (RHUL), London, United Kingdom,*

206 *Ruder Boskovic Institute (RBI), Zagreb, Croatia,*
 207 *Ruprecht Karls Universität Heidelberg (RKU), Heidelberg, Germany,*
 208 *Rutgers, The State University of New Jersey (RU), Piscataway, NJ, United States,*
 209 *Sapienza Università di Roma (UNIROMA1), Rome, Italy,*
 210 *School of Particles and Accelerators, Institute for Research in Fundamental Sciences (IPM), Tehran, Iran,*
 211 *School of Physics and Astronomy, University of Glasgow (SUPA), Glasgow, United Kingdom,*
 212 *Science and Technology Facilities Council, Daresbury Laboratory (STFC DL), Warrington, United Kingdom,*
 213 *Science and Technology Facilities Council, Rutherford Appleton Laboratory (STFC RAL), Didcot, United Kingdom,*
 214 *scMetrology SARM (scMetrology), Geneva, Switzerland,*
 215 *Scuola Int. Superiore di Studi Avanzati di Trieste (SISSA), Trieste, Italy,*
 216 *Scuola Normale Superiore (SNS), Pisa, Italy,*
 217 *Seoul National University (SNU), Seoul, South Korea,*
 218 *Sevaplan und Wurm Schweiz AG (WURM), Winterthur, Switzerland,*
 219 *Shahid Beheshti University (SBUT), Tehran, Iran,*
 220 *Shanghai Jiao Tong University (SJTU), Shanghai, P.R. China,*
 221 *Shirokuma GmbH (Shirokuma), Wetzikon, Switzerland,*
 222 *At an institute formerly covered by a cooperation agreement with CERN,*
 223 *At an institute formerly covered by a cooperation agreement with CERN,*
 224 *Southern Methodist University (SMU), Dallas, TX, United States,*
 225 *Sri Guru Tegh Bahadur Khalsa College, University of Delhi (SGTB Khalsa College), New Delhi, India,*
 226 *Stanford National Accelerator Center (SLAC), Menlo Park, CA, United States,*
 227 *Stanford University (SU), Stanford, CA, United States,*
 228 *Stony Brook University (SBU), Stony Brook, NY, United States,*
 229 *Technische Universität Darmstadt (TU Darmstadt), Darmstadt, Germany,*
 230 *Technische Universität Dortmund (TU Dortmund), Dortmund, Germany,*
 231 *Technische Universität Dresden (TU Dresden), Dresden, Germany,*
 232 *Technische Universität Graz (TU Graz), Graz, Austria,*
 233 *Technische Universität Wien (TU Wien), Vienna, Austria,*
 234 *Tel Aviv University (TAU), Tel Aviv, Israel,*
 235 *The Citadel, The Military College of South Carolina (Citadel), Charleston, SC, United States,*
 236 *The Pennsylvania State University (PSU), University Park, PA, United States,*
 237 *The University of Tokyo (Todai), Tokyo, Japan,*
 238 *Thomas Jefferson National Accelerator Facility (JLab), Newport News, VA, United States,*
 239 *TOBB University of Economics and Technology (TOBB ETU), Ankara, Türkiye,*
 240 *Tokyo Institute of Technology (Tokyo Tech), Tokyo, Japan,*
 241 *Trinity College Dublin (TCD), Dublin, Ireland,*
 242 *Tri-University Meson Facility (TRIUMF), Vancouver, Canada,*
 243 *Tsinghua University (THU), Beijing, P.R. China,*
 244 *Tsung-Dao Lee Institute (TDLI), Shanghai, P.R. China,*
 245 *Uludağ University (ULUÜ), Bursa, Türkiye,*
 246 *Universidad Autónoma de Sinaloa (UAS), Culiacán, Mexico,*
 247 *Universidad de Guanajuato (UGTO), Guanajuato, Mexico,*
 248 *Universidad de La Laguna (ULL), La Laguna, Spain,*
 249 *Universidad de la República (Udelar), Montevideo, Uruguay,*
 250 *Universidad de los Andes (Unianandes), Bogotá, Colombia,*
 251 *Universidade de São Paulo (USP), São Paulo, Brazil,*
 252 *Universidade do Estado do Rio de Janeiro (UERJ), Rio de Janeiro, Brazil,*
 253 *Universidade Federal de Pelotas (UFPel), Pelotas, Brazil,*
 254 *Universidade Federal de Rio de Janeiro (UFRJ), Rio de Janeiro, Brazil,*
 255 *Università degli Studi Roma Tre – Centro Ricerche Economiche e Sociali Manlio Rossi-Doria (EDIRC), Rome, Italy,*
 256 *Università della Calabria (UNICAL), Arcavacata, Italy,*
 257 *Università del Salento (UNISALENTO), Lecce, Italy,*
 258 *Università di Bari (UNIBA), Bari, Italy,*
 259 *Università di Bologna (UNIBO), Bologna, Italy,*
 260 *Università di Cagliari (UNICA), Cagliari, Italy,*
 261 *Università di Catania (UNICT), Catania, Italy,*
 262 *Università di Ferrara (UNIFE), Ferrara, Italy,*
 263 *Università di Firenze (UNIFI), Florence, Italy,*
 264 *Università di Genova (UNIGE), Genoa, Italy,*
 265 *Università di Insubria (UNINSUBRIA), Milan, Italy,*
 266 *Università di Lecce (UNILE), Lecce, Italy,*
 267 *Università di Milano (UNIMI), Milan, Italy,*

268 *Università di Padova (UNIPD), Padua, Italy,*
 269 *Università di Parma (UNIPR), Parma, Italy,*
 270 *Università di Pavia (UNIPV), Pavia, Italy,*
 271 *Università di Perugia (UNIPG), Perugia, Italy,*
 272 *Università di Roma Sapienza (UNIROMA1), Rome, Italy,*
 273 *Università di Roma Tor Vergata (UNIROMA2), Rome, Italy,*
 274 *Università di Roma Tre (UNIROMA3), Rome, Italy,*
 275 *Università di Torino (UNITO), Turin, Italy,*
 276 *Università di Udine (UNIUD), Udine, Italy,*
 277 *Universität Hamburg (UHH), Hamburg, Germany,*
 278 *Universität Heidelberg (HEI), Heidelberg, Germany,*
 279 *Universitat Politècnica de Catalunya (UPC), Barcelona, Spain,*
 280 *Universität Siegen (U Siegen), Siegen, Germany,*
 281 *Universität Tübingen (TU), Tübingen, Germany,*
 282 *Université Clermont Auvergne (UCA), Aubière, France,*
 283 *Université Grenoble Alpes (UGA), Grenoble, France,*
 284 *University College London (UCL), London, United Kingdom,*
 285 *University of Applied Sciences Technikum Wien (UAS TW), Vienna, Austria,*
 286 *University of Arizona (UA), Tucson, AZ, United States,*
 287 *University of Basel (UNIBAS), Basel, Switzerland,*
 288 *University of Belgrade (UB), Belgrade, Serbia,*
 289 *University of Bergen (UiB), Bergen, Norway,*
 290 *University of Bern (UNIBE), Bern, Switzerland,*
 291 *University of Birmingham (UBIRM), Birmingham, United Kingdom,*
 292 *University of Bristol (UOB), Bristol, United Kingdom,*
 293 *University of California Berkeley (UCB), Berkeley, CA, United States,*
 294 *University of California, Davis (UCD), Davis, CA, United States,*
 295 *University of California, Irvine (UCI), Irvine, CA, United States,*
 296 *University of California, San Diego (UCSD), San Diego, CA, United States,*
 297 *University of California Santa Barbara (UCSB), Santa Barbara, CA, United States,*
 298 *University of California Santa Cruz (UCSC), Santa Cruz, CA, United States,*
 299 *University of Cambridge (CAM), Cambridge, United Kingdom,*
 300 *University of Chicago (UCHI), Chicago, IL, United States,*
 301 *University of Cincinnati (UC), Cincinnati, OH, United States,*
 302 *University of Colorado Boulder (UCB), Boulder, Co, United States,*
 303 *University of Edinburgh (ED), Edinburgh, United Kingdom,*
 304 *University of Florida (UF), Gainesville, FL, United States,*
 305 *University of Geneva (UniGE), Geneva, Switzerland,*
 306 *University of Illinois at Urbana Champaign (UIUC), Urbana Champaign, IL, United States,*
 307 *University of Iowa (UIowa), Iowa City, IA, United States,*
 308 *University of Jyväskylä (JYU), Jyväskylä, Finland,*
 309 *University of Kansas (KU), Lawrence, KS, United States,*
 310 *University of Liverpool (ULIV), Liverpool, United Kingdom,*
 311 *University of Lund (ULU), Lund, Sweden,*
 312 *University of Malta (UM), Msida, Malta,*
 313 *University of Manchester (UMAN), Manchester, United Kingdom,*
 314 *University of Maryland (UMD), College Park, MD, United States,*
 315 *University of Massachusetts-Amherst (UMass), Amherst, MA, United States,*
 316 *University of Melbourne (UniMelb), Melbourne, Australia,*
 317 *University of Michigan (UMich), Ann Arbor, MI, United States,*
 318 *University of New Mexico (NMU), Albuquerque, NM, United States,*
 319 *University of Notre Dame du Lac (ND), South Bend, IA, United States,*
 320 *University of Oregon (UO), OR Eugene, United States,*
 321 *University of Rochester (Rochester), Rochester, NY, United States,*
 322 *University of Rostock (U Rostock), Rostock, Germany,*
 323 *University of Saskatchewan (USASK), Saskatoon, Canada,*
 324 *University of Science and Technology of P.R. China (USTC), Hefei, P.R. China,*
 325 *University of Science and Technology of Mazandaran (USTM), Behshahr, Iran,*
 326 *University of Silesia (USKAT), Katowice, Poland,*
 327 *University of Stavanger (UiS), Stavanger, Norway,*
 328 *University of Stuttgart (USTUTT), Stuttgart, Germany,*
 329 *University of Sussex (US), Brighton, United Kingdom,*

330 *University of the Witwatersrand (WITS), Johannesburg, South Africa,*
331 *University of Toronto (UToronto), Toronto, Canada,*
332 *University of Warsaw (UW), Warszawa, Poland,*
333 *University of Wisconsin-Madison (WISC), Madison, WI, United States,*
334 *University of Würzburg (U Würzburg), Würzburg, Germany,*
335 *University of Zürich (UZH), Zürich, Switzerland,*
336 *University Rey Juan Carlos (URJC), Madrid, Spain,*
337 *Univ. Lyon I, CNRS/IN2P3, Institut de Physique Nucléaire de Lyon (CNRS/IN2P3/IPNL), Lyon, France,*
338 *Uppsala University (UU), Uppsala, Sweden,*
339 *Usak University (Usak), Usak, Türkiye,*
340 *Vienna University of Economics and Business (WU), Vienna, Austria,*
341 *Vinca Institute of Nuclear Sciences (Vinca), Belgrade, Serbia,*
342 *Vrije Universiteit Brussel (VUB), Brussels, Belgium,*
343 *Washington University (WUSTL), St. Louis, MO, United States,*
344 *Weizmann Institute (Weizmann), Rehovot, Israel,*
345 *Werner-Heisenberg-Institut, Max-Planck-Institut für Physik (MPP), Munich, Germany,*
346 *Westfälische Wilhelms-Universität Münster (WWU), Münster, Germany,*
347 *West Pomeranian University of Technology (ZUT), Szczecin, Poland,*
348 *Wroclaw University of Science and Technology (PWR), Wroclaw, Poland,*
349 *Wuhan University of Technology (WHUT), Wuhan, P.R. China,*
350 *Zhejiang Institute of Modern Physics, Department of Physic (ZIMP), Hangzhou, P.R. China,*
351 *Zhejiang University (ZJU), Hangzhou, P.R. China,*
352 fcc.secretariat@cern.ch

Abstract

This document provides a detailed account of several studies regarding the design of the FCC-hh hadron collider that have been performed in the time period between 2019 and 2021. They extend and complement the studies reported in the conceptual design report submitted to the 2019 Update of the European Strategy for Particle Physics.

Keywords: Particle accelerators, Hadron colliders, Future Circular Collider

Foreword

The FCC-hh is the hadron collider component of the Future Circular Collider (FCC) facility proposed to be built at CERN, aimed at replacing the LHC as the worldwide flagship high-energy particle collider. A first set of comprehensive studies was performed assuming that the accelerator would provide proton-proton collisions at a centre-of-mass energy around 100 TeV and deliver a data sample corresponding to an integrated luminosity of 30 ab^{-1} . Those studies were documented in a concise conceptual design report that focused on the presentation of the potential performance and technical feasibility [1]. That early document provided the baseline inputs for the physics opportunities and performance evaluations submitted to the European Strategy for Particle Physics Update (ESPPU) of 2019 [2, 3].

The present report provides a detailed description of improved studies regarding the FCC-hh optics and key beam dynamics, at the level needed for further developments of the project, moving from conceptual discussions towards a technical design report. It includes, in particular, more extended presentations of key choices, fundamental calculations, and design optimisation, besides exposing the R&D progress achieved between 2019 and 2021. While the bulk of this volume was completed by early 2022, unfortunate events well beyond the realm of science brought its publication process to a halt. In the meantime, work continued at a steady pace. For example, the FCC-hh layout was adapted to fit together with the FCC-ee design. The most recent FCC-hh design has been described in a new document, recently submitted to the 2025 ESPPU [4]. Nevertheless, and encouraged by several stakeholders, we concluded that the publication of this report remained important, despite the significant delay, as it provides very useful information on the evolution of the project.

Daniel Schulte (Report editor), Jens Vigen (CERN SIS), Carlos Lourenço (CREB chair)
CERN, June 4, 2025

Contents

| | | |
|----------|--|-----------|
| 1 | Parameters and performance | 1 |
| 1.1 | Overview | 1 |
| 1.2 | Layout and parameters | 1 |
| 1.2.1 | Energy reach | 1 |
| 1.3 | Luminosity | 3 |
| 1.3.1 | Peak luminosity | 4 |
| 1.3.2 | Integrated luminosity | 5 |
| 1.4 | Injection considerations | 6 |
| 1.5 | Lattice design | 6 |
| 1.6 | Arc vacuum | 7 |
| 1.7 | Experimental areas | 7 |
| 1.7.1 | Main experiments | 7 |
| 1.7.2 | Additional experiments | 8 |
| 1.7.3 | RF system | 8 |
| 1.8 | Beam loss mitigation | 9 |
| 1.8.1 | Machine protection | 9 |
| 1.8.2 | Injection | 9 |
| 1.8.3 | Extraction and dump | 9 |
| 1.8.4 | Collimation | 10 |
| 1.9 | Alternatives | 10 |
| 1.9.1 | Alternative bunch spacings | 11 |
| 1.9.2 | Higher field magnets | 11 |
| 2 | Experiment insertion region concept | 13 |
| 2.1 | Overview | 13 |
| 2.2 | Machine-detector interface considerations | 15 |
| 2.3 | System layout and optics | 16 |
| 2.3.1 | Final focus triplet | 17 |
| 2.3.2 | Beam-beam effects and crossing angle | 18 |
| 2.3.3 | Dynamic aperture with triplet errors | 22 |
| 2.3.4 | Crab cavities | 24 |
| 2.4 | Energy deposition from collision debris | 25 |
| 2.5 | Photon background from synchrotron radiation | 29 |
| 2.6 | Alternative triplet and flat optics | 33 |
| 2.6.1 | Energy deposition in the alternative triplet | 35 |
| 2.7 | Low luminosity EIRs | 37 |
| 2.7.1 | Energy deposition in the low luminosity EIR | 39 |
| 2.8 | Hardware specifications | 42 |
| 3 | RF insertion | 49 |
| 3.1 | Overview | 49 |
| 3.2 | System layout and optics | 49 |
| 3.3 | Hardware specifications | 50 |
| 3.4 | Alternatives | 50 |

| | | |
|----------|--|------------|
| 4 | Injection system design for FCC-hh | 51 |
| 4.1 | Introduction | 51 |
| 4.2 | Injection system | 52 |
| 4.2.1 | Injection system layout | 52 |
| 4.2.2 | Staggered transfer | 53 |
| 4.2.3 | Synchronisation HEB-FCC | 54 |
| 4.2.4 | Injection protection design | 55 |
| 4.2.5 | Injection system for 1.3 TeV energy | 58 |
| 4.2.6 | Hardware specifications | 58 |
| 5 | Beam dump | 61 |
| 5.1 | Introduction | 61 |
| 5.2 | Extraction straight layout | 61 |
| 5.2.1 | Baseline layout using superconducting shields | 61 |
| 5.2.2 | Alternative extraction layouts | 63 |
| 5.3 | Absorber-driven system design | 64 |
| 5.3.1 | Protection absorber robustness | 64 |
| 5.3.2 | Extraction straight optics and extraction kicker parameters | 67 |
| 5.3.3 | Protection efficiency in case of asynchronous beam dumps | 68 |
| 5.4 | Dump line layout and dilution | 69 |
| 5.4.1 | Baseline dump concept and dilution requirements | 70 |
| 5.4.2 | Sensitivity of the dilution pattern to various failure cases and non-nominal operation | 70 |
| 5.4.3 | Alternative dump absorber systems | 74 |
| 5.5 | Other failures of the extraction system | 74 |
| 5.6 | Summary and outlook | 74 |
| 6 | Arc concept | 77 |
| 6.1 | Overview | 77 |
| 6.2 | System layout and optics | 77 |
| 6.3 | Key issues | 78 |
| 6.4 | Synchrotron radiation | 79 |
| 6.5 | Hardware specification | 80 |
| 6.6 | Alternatives | 81 |
| 7 | Integrated optics and single particle dynamics | 85 |
| 7.1 | Overview | 85 |
| 7.2 | Key issues | 85 |
| 7.3 | Matching | 85 |
| 7.4 | Linear corrections | 87 |
| 7.5 | Dynamic aperture | 91 |
| 7.6 | Cross talk between experiment insertion regions | 94 |
| 7.7 | Hardware specification | 98 |
| 7.8 | Alternatives and key R&D | 102 |
| 8 | Collective effects | 103 |
| 8.1 | Introduction | 103 |
| 8.2 | Electron cloud | 104 |

| | | |
|----------|--|------------|
| 8.2.1 | Multipacting thresholds | 104 |
| 8.2.2 | Stability threshold | 104 |
| 8.2.3 | Photoelectrons | 106 |
| 8.2.4 | Alternative beam options | 107 |
| 8.2.5 | Mitigation requirements and coating | 108 |
| 8.3 | Beam coupling impedances | 113 |
| 8.3.1 | Beamscreen: resistive wall, without e-cloud coating | 113 |
| 8.3.2 | Beamscreen: coating for electron cloud mitigation | 114 |
| 8.3.3 | Beamscreen: pumping holes | 114 |
| 8.3.4 | Warm beampipe: resistive wall | 114 |
| 8.3.5 | Collimators: resistive wall | 114 |
| 8.3.6 | Collimators: geometrical impedance | 114 |
| 8.3.7 | Interconnects: geometrical impedance | 115 |
| 8.3.8 | 400 MHz RF cavities | 115 |
| 8.3.9 | Crab cavities | 115 |
| 8.3.10 | Distribution of the dipolar impedance by the elements | 115 |
| 8.3.11 | Effective dipolar impedances | 115 |
| 8.4 | RF and longitudinal effects | 117 |
| 8.5 | Feedback performance | 121 |
| 8.5.1 | Emittance growth due to injection dipole errors | 122 |
| 8.5.2 | Coupled bunch instability damping | 124 |
| 8.5.3 | Operation with 5 ns or 12.5 ns bunch spacings | 126 |
| 8.5.4 | 1.3 TeV injection scheme | 126 |
| 8.6 | Beam-beam effects | 126 |
| 8.6.1 | Maximum head-on beam-beam tune shift | 126 |
| 8.6.2 | Global compensation of beam-beam long range interactions | 127 |
| 8.6.3 | Beta beating | 127 |
| 8.6.4 | Alternative schemes | 127 |
| 8.7 | Beam stability and operation strategy | 133 |
| 8.7.1 | Scaling from real LHC performance | 133 |
| 8.7.2 | Beam stability at injection | 135 |
| 8.7.3 | Beam stability at flat top | 135 |
| 8.7.4 | Beam stability during the ‘collide and squeeze’ phase | 138 |
| 8.8 | Alternatives | 143 |
| 8.8.1 | Electron lens | 143 |
| 8.8.2 | RF quadrupoles | 143 |
| 8.8.3 | HTS coating for the beamscreen | 145 |
| 8.8.4 | Beamscreen laser treatment for e-cloud mitigation | 147 |
| 8.8.5 | Intra bunch feedback | 147 |
| 8.9 | Key R&D | 148 |
| 9 | Collimation system | 151 |
| 9.1 | Introduction | 151 |
| 9.2 | Baseline collimation concept and layout | 152 |
| 9.3 | Machine aperture | 154 |
| 9.4 | Simulations of the collimation system performance | 158 |

| | | |
|-----------|--|------------|
| 9.4.1 | Simulation method | 158 |
| 9.4.2 | Betatron cleaning | 159 |
| 9.4.3 | Off momentum beam halo | 159 |
| 9.4.4 | Extraction kicker pre-fire failure | 160 |
| 9.4.5 | Influence of imperfections | 163 |
| 9.5 | Energy deposition in cold magnets | 167 |
| 9.6 | Energy deposition in the warm betatron section | 168 |
| 9.6.1 | Ozone production | 172 |
| 9.7 | Collimator robustness | 173 |
| 9.7.1 | TCS collimator | 174 |
| 9.7.2 | TCP collimator | 174 |
| 9.7.3 | Result assessment | 177 |
| 9.8 | Advanced concepts and key R&D | 177 |
| 9.9 | Conclusions | 178 |
| 9.10 | Collimators and settings | 180 |
| 10 | Operation cycle | 181 |
| 10.1 | Turn-around concept | 181 |
| 10.2 | Start-up considerations | 182 |
| 10.3 | Availability | 183 |
| 10.4 | Alternatives and key R&D | 183 |
| 11 | Machine protection concepts | 185 |
| 11.1 | Architecture and powering of magnet circuits | 185 |
| 11.2 | Magnet protection and energy extraction | 186 |
| 11.2.1 | Energy extraction system technologies | 186 |
| 11.2.2 | Quench detection technologies | 187 |
| 11.3 | Machine protection concepts | 188 |
| 11.3.1 | Damage potential and relevance of machine protection | 188 |
| 11.3.2 | Classification of FCC-hh failure modes and mitigation strategies | 189 |
| 11.3.3 | Machine-protection requirements and system layout | 191 |
| 11.3.4 | Summary | 196 |
| 12 | The FCC-hh as a nucleus-nucleus collider | 197 |
| 12.1 | Overview | 197 |
| 12.1.1 | General assumptions | 197 |
| 12.1.2 | Performance estimates | 201 |
| 12.2 | Key issues | 204 |
| 12.2.1 | Power deposition from secondary beams | 204 |
| 12.2.2 | Collimation performance | 206 |
| 12.2.3 | Ion injector chain | 209 |
| 12.3 | Additional hardware specifications | 211 |
| 12.3.1 | Dispersion suppressor collimators | 211 |
| 12.3.2 | RF system | 211 |
| 12.3.3 | Beam position monitors | 212 |
| 12.4 | Colliding other nuclei | 212 |

| | | |
|--------|----------------------------------|-----|
| 12.4.1 | Lower injection energy | 214 |
| 12.5 | Conclusion and outlook | 215 |

Parameters and performance

1.1 Overview

The FCC-hh is designed to provide proton-proton collisions with a centre-of-mass energy of 100 TeV and an integrated luminosity of $\approx 20 \text{ ab}^{-1}$ in each of the two main experiments for 25 years of operation. The combined data sets will thus significantly exceed the total of 30 ab^{-1} required by the expected physics studies. In addition, the FCC-hh offers the potential of colliding ions with protons and ions with ions. The design also allows one interaction point to be upgraded to electron-proton and electron-ion collisions. In this case, an additional recirculating, energy-recovery linac will provide the electron beam that collides with one circulating proton or ion beams. The other experiments can operate concurrently with hadron collisions.

1.2 Layout and parameters

The collider layout is shown in Fig. 1.1 and the key parameters are given in Table 1.1. The collider performance will increase from the initial to the nominal parameters.

Two high luminosity experiments are located in opposite insertions (PA and PG). This ensures the highest luminosity, reduces unwanted beam-beam effects and is independent of the beam-filling pattern. Two additional, lower luminosity experiments are located together with the injection systems in insertions PB and PL. The transverse beam cleaning is located in insertion PJ and the beam extraction in insertion PD. The longitudinal beam cleaning is placed in insertion PF and finally, the RF systems and the fast feedback are placed in insertion PH. The long arcs also contain technical points (PC, PE, PI and PK).

The collider has been placed adjacent to the CERN LHC and SPS accelerators and the two injection insertions (at PB and PL) are positioned such that one can inject beam from either the LHC or the SPS.

The circumference of the collider is 97.75 km and the insertions are 1.4 km long with the exception of the transverse collimation and beam extraction areas which are 2.8 km long. This additional length facilitates the mitigation of the challenges posed in these systems by the high stored energy.

The total length of the arcs is 83.75 km. The lattice in the arc consists of a sequence of 90° FODO cells. Each 213 m-long cell contains twelve 14 m long dipoles. The dipole filling factor is about 0.8, hence a dipole field just below 16 T is required to keep the nominal beams on the circular orbit.

1.2.1 Energy reach

Using Nb_3Sn -based conductors at a temperature of 2 K to reach this field, the dipoles are a key cost item. A focused R&D programme to increase the maximum current density in the conductors to at least 1500 A/mm^2 at 4.2 K temperature started in 2014 (currently 1200 A/mm^2 has been achieved). Based on this performance, several optimised dipole designs have been developed in the EuroCirCol H2020 EC funded project—each implementing a different design concept. This allowed the amount of conductor material to be minimised and led to the choice of the cosine-theta design as the optimum. Collaboration agreements are in place with the French CEA, the Italian INFN, the Spanish CIEMAT, the Swiss PSI and the Russian BINP organisations, to build short model magnets based on the designs. In addition, a US DOE Magnet Development Programme is working to demonstrate a 15 T

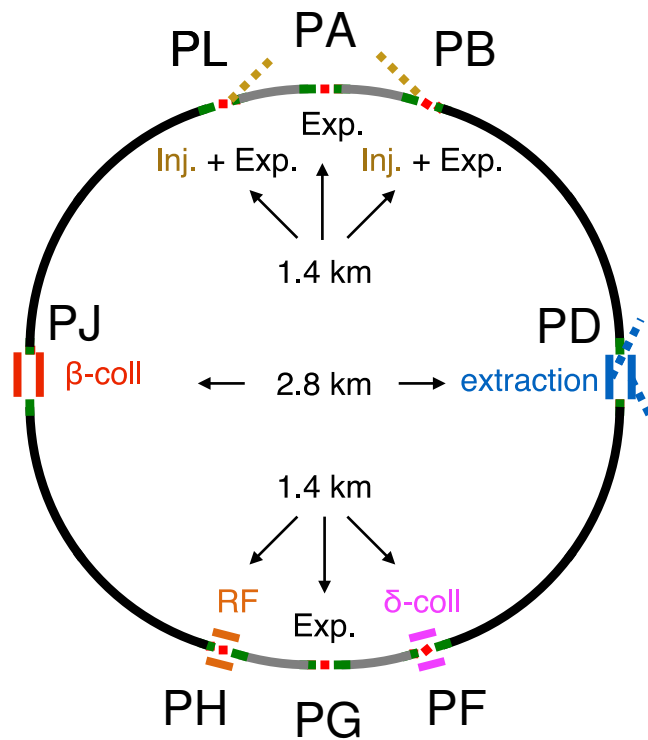


Figure 1.1: The FCC-hh layout. The two main experiments are located in PA and PG and the additional experiments in PB and PL, the latter combined with the injection. The momentum and betatron collimation systems are in insertions PF and PJ, respectively. The beam extraction is in PD and the RF and the main feedback system are integrated in PH.

superconducting accelerator magnet.

If the FCC-hh is implemented following a lepton collider (FCC-ee) in the same underground infrastructure, the time scale for design and R&D for FCC-hh is lengthened by 15 to 20 years. This additional time will be used to develop alternative technologies, e.g. magnets based on high temperature superconductors, with potentially, a significant impact on the collider parameters (e.g. increase of beam energy), relaxed infrastructure requirements (cryogenics system) and increased energy efficiency (temperature of magnets and beamscreen).

Table 1.1: FCC-hh baseline parameters compared to LHC, HE-LHC and HL-LHC parameters.

| | LHC | | HL-LHC | | FCC-hh | |
|---|-----------|------------|-------------------------|------------------|--------|--|
| | | | Initial | Nominal | | |
| Main parameters and geometrical aspects | | | | | | |
| c.m. Energy [TeV] | 14 | | 100 | | | |
| Circumference C [km] | 26.7 | | 97.75 | | | |
| Dipole field [T] | 8.33 | | < 16 | | | |
| Arc filling factor | 0.79 | | 0.8 | | | |
| Straight sections | 8 × 528 m | | 6 × 1400 m + 2 × 2800 m | | | |
| Number of IPs | 2 + 2 | | 2 + 2 | | | |
| Injection energy [TeV] | 0.45 | | 3.3 | | | |
| Physics performance and beam parameters | | | | | | |
| Peak luminosity ¹ [$10^{34} \text{ cm}^{-2} \text{ s}^{-1}$] | 1.0 | 5.0 | 5.0 | < 30.0 | | |
| Optimum average integrated lumi / day [fb^{-1}] | 0.47 | 2.8 | 2.2 | 8 | | |
| Assumed turnaround time [h] | | | 5 | 4 | | |
| Target turnaround time [h] | | | 2 | 2 | | |
| Peak no. of inelastic events / crossing | 27 | 135 (lev) | 171 | 1026 | | |
| Total / inelastic cross section σ proton [mbarn] | 111 / 85 | | 153 / 108 | | | |
| Luminous region RMS length [cm] | | | 5.7 | 5.7 | | |
| Distance IP to first quadrupole, L^* [m] | 23 | | 40 | 40 | | |
| Beam parameters | | | | | | |
| Number of bunches n | 2808 | | 10400 | | | |
| Bunch spacing [ns] | 25 | 25 | 25 | | | |
| Bunch population $N[10^{11}]$ | 1.15 | 2.2 | 1.0 | | | |
| Nominal transverse normalised emittance [μm] | 3.75 | 2.5 | 2.2 | 2.2 | | |
| Number of IPs contributing to ΔQ | 3 | 2 | 2 + 2 | 2 | | |
| Maximum total b-b tune shift ΔQ | 0.01 | 0.015 | 0.011 | 0.03 | | |
| Beam current [A] | 0.584 | 1.12 | 0.5 | | | |
| RMS bunch length ² [cm] | 7.55 | | 8 | | | |
| IP beta function [m] | 0.55 | 0.15 (min) | 1.1 | 0.3 | | |
| RMS IP spot size [μm] | 16.7 | 7.1 (min) | 6.8 | 3.5 | | |
| Full crossing angle [μrad] | 285 | 590 | 104 | 200 ³ | | |
| Other beam and machine parameters | | | | | | |
| Stored energy per beam [GJ] | 0.392 | 0.694 | 8.3 | | | |
| SR power per ring [MW] | 0.0036 | 0.0073 | 2.4 | | | |
| Arc SR heat load [W/m/aperture] | 0.17 | 0.33 | 29 | | | |
| Energy loss per turn [MeV] | 0.0067 | | 4.67 | | | |
| Critical photon energy [keV] | 0.044 | | 4.3 | | | |
| Longitudinal emittance damping time [h] | 12.9 | | 0.5 | | | |
| Transverse emittance damping time [h] | 25.8 | | 1.0 | | | |
| Dipole coil aperture [mm] | 56 | | 50 | | | |
| Minimum arc beam half aperture [mm] | ~18 | | 13 | | | |
| Installed RF voltage (400.79 MHz) [MV] | 16 | | 48 | | | |
| Harmonic number | 35640 | | 130680 | | | |

¹ For the nominal parameters, the peak luminosity is reached during the run.² The HL-LHC assumes a different longitudinal distribution; the equivalent Gaussian is 9 cm.³ The crossing angle will be compensated using the crab crossing scheme.

1.3 Luminosity

It is planned to reach the initial parameters with a maximum luminosity of $5 \times 10^{34} \text{ cm}^{-2} \text{ s}^{-1}$ in the first years. In the following years the luminosity will be increased to reach the nominal parameters with a luminosity of up to $3 \times 10^{35} \text{ cm}^{-2} \text{ s}^{-1}$. The estimated integrated luminosity is 2 fb^{-1} per day of operation for the initial and 8 fb^{-1} for the nominal parameters. A generic design for the additional experiments, which has a distance of 50 m between

the magnets of the machine, shows that a luminosity of $2 \times 10^{34} \text{ cm}^{-2} \text{ s}^{-1}$ can be reached, but further studies are required once the experiments are better defined.

1.3.1 Peak luminosity

The high luminosity is achieved with high brightness beams, a high beam current comparable to LHC parameters, and a small β^* at the collision points. The luminosity is a function of the beam current I , the beam-beam tune shift ξ , the beam gamma factor γ and the beta-functions at the collision point β^* . For a round beam it is given by:

$$\mathcal{L} = \xi \frac{I}{q} \frac{\gamma}{\beta^*} \frac{1}{r_p} F. \quad (1.1)$$

Here, r_p is the classical proton radius and q the elementary charge. The form factor F includes geometric luminosity reduction effects like the hour glass effect; it is neglected in the following discussion. Hence, to reach high luminosity, one has to use a high brightness beam (i.e. large ξ), achieve small beta functions and have a high beam current.

Larger beam-beam tuneshifts can result in more luminosity but also have undesired effects. In particular, large beam-beam tuneshifts can turn small amplitude beam-beam jitter into emittance growth which results in an increase of beam size and hence a decrease of the luminosity. They can also lead to an increase of particle losses due to non-linear effects and consequently a decrease in the beam lifetime. In FCC-hh a maximum beam-beam tuneshift of $\xi \leq 0.03$ is expected. In the initial phase each of the four experiments contributes about 0.0055 to the total remains well below the maximum. In the nominal phase each of the two main experiments reaches up to 0.013 and the tuneshift of the additional experiments has to be reduced, e.g. by separating the beams. LHC experience with the current working point confirms that this value is acceptable. The fraction of beam lost in the transverse tails remains below 10^{-3} per hour and also the emittance growth induced by beam-beam jitter remains limited. In contrast, a slightly larger tuneshift would rapidly increase the loss rate and the beam emittance would increase significantly faster for the same jitter amplitudes. Studies [5] indicate that other working points might allow even larger tuneshifts but the impact on other parts of the machine remains to be evaluated. The crossing angle of about $\theta_c \approx 200 \text{ } \mu\text{rad}$ limits the impact of parasitic beam-beam crossings and the associated luminosity reduction is mitigated by the use of crab cavities. Other means that could be added to mitigate the long-range and head-on beam-beam effects include electron lenses and current carrying wire compensators.

A small beta function, β^* , at the collision point makes the optics design for the experiment insertion demanding and requires a large aperture in the focus triplets. This poses challenges for the design of the magnet and protection systems and for the collimation which has to scrape off tails that could hit the triplets.

There are three main potential limitations for the beam current: synchrotron radiation, single beam collective effects and machine protection considerations. At the high energy of the FCC-hh, even proton beams emit significant synchrotron radiation power: together both beams emit about 5 MW. Beamscreens protect the superconducting magnets from this power, in the same way as in the LHC. The cryogenic system cools these screens to a temperature of 50 K. About 100 MW of electrical power is required to remove the synchrotron radiation power due to the Carnot inefficiency and the limited technical efficiency of the cryogenic system. A lower operating temperature would increase the power required to cool the beamscreen even further whilst a higher temperature would increase the heat transferred from the beamscreen into the magnet and hence increase the power required to cool the magnet.

The second limitation, single beam collective effects, requires advanced methods for its mitigation. These techniques include a novel beamscreen design that ensures very good vacuum. This screen also reduces the potential for single bunch instabilities by making the pumping holes invisible to the beam, a marked improvement compared to LHC [6]. A carbon layer on the surface and the specific geometry suppress the build-up of electron clouds, one of the important issues in the LHC. The same goal could be achieved by using a laser treatment to roughen the surface. Additional means to mitigate the collective effects include feedback, octupoles, and potentially RF quadrupoles and electron lenses. They are instrumental in permitting the use of a small free aperture. Combined with a compact beamscreen design a magnet aperture of only 50 mm becomes possible, which helps to limit cost.

Robust collimation and beam extraction systems protect the machine from the energy stored in the beam.

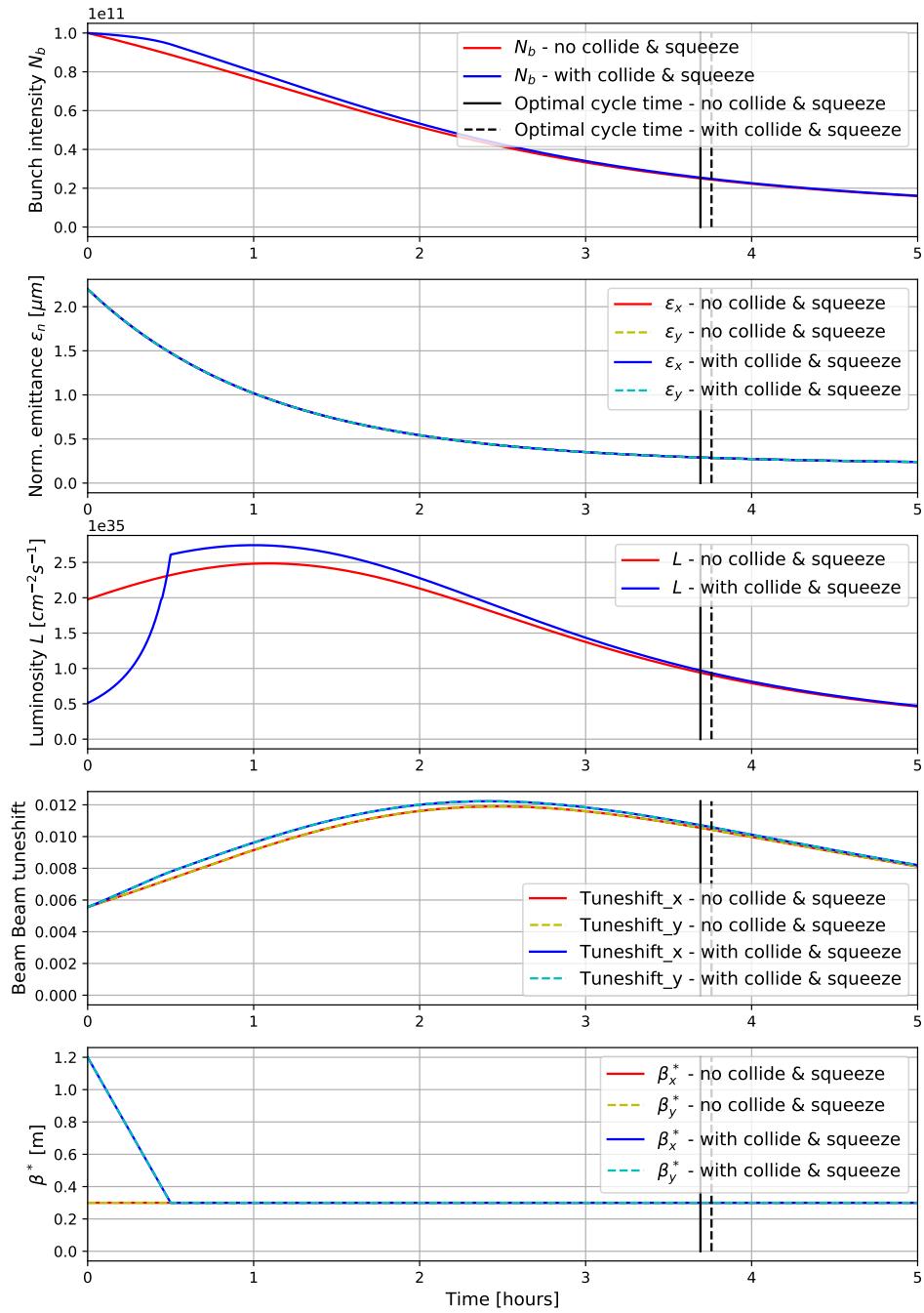


Figure 1.2: Evolution of the beam parameters and luminosity during luminosity production, for the nominal 25 ns parameter set (see Table 1.1). A vertical black line marks the optimum fill length for a turn around time of 4h. The corresponding average luminosity production rate (without down time) is 8.2 fb^{-1} per day.

1.3.2 Integrated luminosity

In the nominal phase, the beams can only be used for about 3.5 h in collision before they have to be replaced because of the fast beam burn-off. Consequently, the turn-around time from one luminosity run to the next is critical for the integrated luminosity. First detailed estimates found that theoretically a time of about 2 h can be achieved. However to include sufficient margin, turn-around times of 5 h and 4 h are assumed for initial and nominal parameters, respectively. In addition to the above, an availability of 70% is assumed for the estimate of the overall integrated luminosity.

The strong variation of the beam parameters during luminosity production have been modeled in detail [7]. Figure 1.2 illustrates the evolution of the main beam parameters taking into account the effect of intra-beam scattering, synchrotron radiation damping and quantum excitations, luminosity burn-off and an absolute emittance growth rate of 0.15 $\mu\text{m}/\text{h}$. The mathematical description of the model can be found in [8]. It is assumed that the longitudinal emittance is kept constant to maintain the size of the luminous region inside the detector. The budget for an additional source of emittance growth due to external sources of noise is conservatively based on LHC experience, where about 0.05 $\mu\text{m}/\text{h}$ is routinely observed [9]. The short period of the collide-and-squeeze scheme, which brings the beams into collision before the squeeze, is not included here as it has almost no impact on the integrated luminosity.

During the run, the emittance reduction dominates first and hence the luminosity increases up to $2.5 \times 10^{35} \text{ cm}^{-2}\text{s}^{-1}$. Then the beam burn-off starts to dominate and the luminosity decreases. A maximum beam-beam tune shift of 0.013 per IP is reached after 2 h of luminosity production. During the run the intensity decreases by a factor of 4 and the transverse emittances by a factor of 8.

Experience in LHC shows that the turnaround time from the end of luminosity production to the start of the next could be reduced to 2 h with some modifications of the injector complex [10]. The turnaround times assumed for the initial and nominal parameters are 5 h and 4 h, respectively. These times include a margin for availability limitations. An optimum average production rate of 8.2 fb^{-1} per day is obtained in these conditions – meeting the target of 8 fb^{-1} . The beams should be renewed after 3.7 h in collision.

1.4 Injection considerations

The injection energy is 3.3 TeV and beams at this energy can be provided by the LHC. The choice of this energy ensures that the beam size is small enough to provide a sufficient number of sigmas of beam stay clear for collimation and machine protection. The dynamic aperture and beam stability are also guaranteed. Some modifications of the powering scheme will allow the LHC to be ramped quickly thus providing the necessary short turnaround times. Lower injection energies have also been studied, in particular a choice of 1.3 TeV. This would allow injection from a new accelerator, either a superconducting 6 T machine in the SPS tunnel or a superferric 1.5 T one in the LHC tunnel. However, the lower energy will reduce the dynamic aperture at injection, not only due to the larger beam but also because of the increased degradation of the magnetic field quality. In addition, the collimation system and the impedance effects will become more challenging. Further design effort would therefore be required to judge whether one can adopt this injection energy.

1.5 Lattice design

The lattice design of the collider ring integrates the requirements of the different systems. It is based on the considerations below.

The lattice layout facilitates the separation of the various functions, which ensures that sensitive equipment is not affected by systems that generate significant quantities of radiation. During physics periods with stable beams in collision, the main experiments are the principle source of radiation, since most of the beam is consumed in collisions. The short arcs between the main experiment in PA and the additional experiments in PB and PL ensure that this collision debris does not cause significant background in the smaller experiments.

The collimation systems can also generate significant quantities of radiation under certain operating conditions. Therefore they are separated from all other systems. The momentum collimation system takes advantage of the dispersion from the arcs to remove energy tails. In the betatron collimation system the dispersion from the arcs is suppressed, making the removal of the transverse tails easier.

The relatively sensitive RF systems, electron lenses and the feedback systems are located in a dedicated insertion (PH) where the radiation levels are low.

Similarly, the position of the beam extraction systems in a separate insertion (PD) ensures that the extraction kicker systems are only exposed to low levels of radiation, limiting the likelihood of false kicker firing.

The injection systems are placed close to the additional experiments but the experiments will only produce significant amounts of radiation at collision energy, when injection is switched off.

With the exception of PD and PJ, the length of each insertion is 1400 m which corresponds to a scaling of the LHC insertion lengths with the square root of the beam energy. This choice allows the LHC and HL-LHC optics solutions to be implemented in the FCC-hh with the same magnet technology. Improved technologies are used to push the performance beyond that which can be achieved by scaling. In particular the final triplet magnets in

the experiment insertions use the same technology as the HL-LHC but with higher fields. This allows a relatively smaller β -function at the collision point – which naturally scales with the square root of the energy – and also increases the protection of the magnets against the higher levels of collision debris. Optics design studies have confirmed that the full 1400 m is required to achieve the performance goals.

The betatron collimation and the extraction systems are the most sensitive to beam losses under these higher performance scenarios since the increased total particle energy, the higher beam brightness and the larger number of stored protons increase the risk. Consequently, longer insertions of 2800 m have been allocated for these systems. Further studies will optimise the insertion lengths taking into account the civil engineering and implementation aspects.

1.6 Arc vacuum

The arc vacuum system defines the aperture of the magnet, which is a key cost driver and has a strong impact on the beam performance. The proposed design allows the magnet aperture to be reduced to 50 mm and still provides good conditions for the beam, i.e. good vacuum, low impedance and suppression of electron cloud effects.

The beamscreen protects the cold bore of the magnets from the 30 W/m of synchrotron radiation emitted by each beam at collision energy. The cryogenic system cools this screen to 50 K; at this temperature the heat can be removed more efficiently than with the 2 K magnet system.

A vacuum pressure of 10^{15} m^{-3} hydrogen equivalent, similar to the LHC, ensures a beam lifetime of about 100 hours, which is compatible with the integrated luminosity target. The power deposited by beam scattering on the rest gas is low enough to avoid quenches of the superconducting magnets from induced heating. However, with this lifetime up to about 40 kW (0.45 W/m) are still being deposited in the arc dipoles. To remove it requires about 30 MW of cooling power. Therefore the vacuum design aims for a significantly lower vacuum pressure of $0.2 \times 10^{15} \text{ m}^{-3}$ hydrogen, which is feasible.

The copper coating of the inner surface of the beamscreen in combination with the chosen aperture ensures that the impedance is low enough for beam stability, although a high-temperature superconductor (HTS) coating is being considered as an option to provide a higher stability margin. Pumping holes in the screen facilitate a good vacuum and in contrast to the LHC, they do not generate significant impedance because they are located in two small antechambers. The antechambers also help to reduce the amount of synchrotron radiation that is reflected back into the beam aperture. This arrangement reduces the production of seed electrons that could form an electron cloud. A thin coating of amorphous carbon on the inner part of the chamber hinders any existing electrons from producing electron showers thereby suppressing any electron cloud build-up.

1.7 Experimental areas

A detailed design of the insertion for a high luminosity experiment has been developed. The requirements for the additional experiments have not yet been established. Therefore a generic first order design of the corresponding insertion has been made to highlight the performance that can be expected.

1.7.1 Main experiments

The design of the interaction region follows the structure of the LHC interaction region: the final focus system consists of a quadrupole triplet on each side of the interaction point (IP) with a single aperture shared by the counter-rotating beams. Dipoles in the following section separate the two beams into the individual apertures used in the rest of the ring. Four quadrupoles in the straight section, the dispersion suppressor quadrupoles and trim quadrupoles in the first arc cell are used to match the optical functions between the final focus system and the regular arcs. The design of the final focus system is driven by energy deposition from collision debris from the IP. It requires a short drift space between the IP and the final focus system, as well as long, large aperture final focus quadrupoles. The opening of the detector design requires a 33 m space on either side of the IP, resulting in a total cavern length of 66 m (Fig. 1.3). The cavern is closed by a 2 m thick shielding wall followed by an absorber to protect the front of the final focus system from collision debris. This leads to a minimum drift space between the IP and the final focus system of 40 m. Systems with longer drift spaces were also considered but they featured larger chromaticity and matching of the optical functions to the arcs proved difficult within the designated insertion length. The total 107.2 m magnetic length of the triplet quadrupoles allows the use of relatively low gradient, large aperture quadrupoles. This also allows the inside of the magnets to be protected with up to 35 mm of tungsten shielding, whilst still leaving enough free aperture to accommodate a beam with a beta function at the IP of almost

$\beta^* = 0.2$ m without violating the collimation hierarchy. This beta function offers a comfortable margin to the nominal goal of $\beta^* = 0.3$ m.

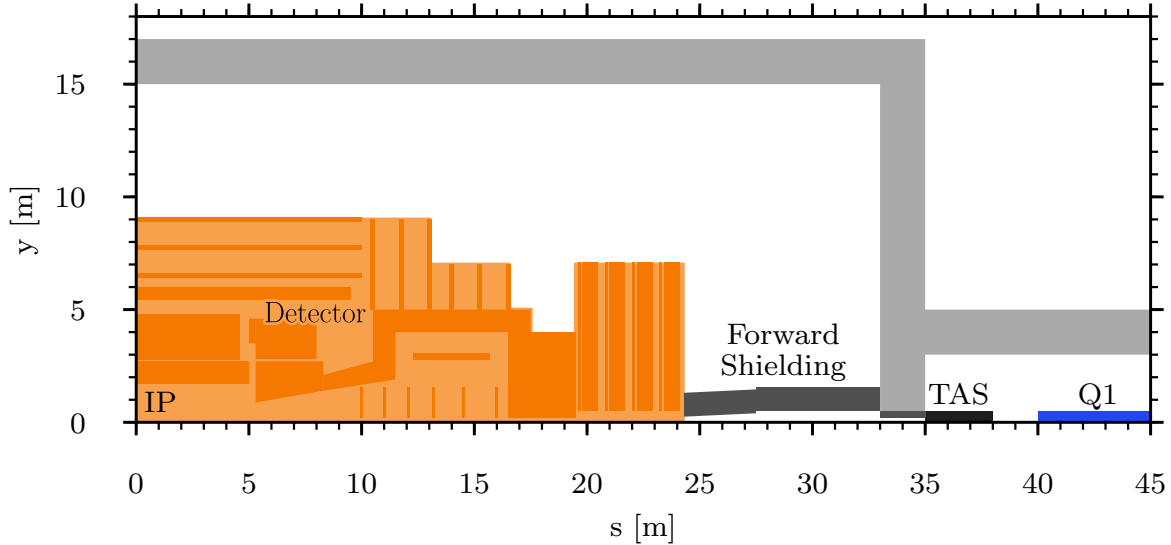


Figure 1.3: Detector region layout.

The high luminosity leads to collision debris reaching a total power of about 500 kW in each of the high luminosity detectors and a significant amount is lost in the machine section next to the detectors. A sophisticated shielding system protects the final triplet magnets from these losses. It consists of a copper shield in front of the triplet and a tungsten tube inside the magnet bore. This tube protects the magnets from charged particles (mainly pions) that enter the magnet aperture and are defocused by the field.

1.7.2 Additional experiments

The injection insertions allow the installation of two additional experiments in the collider. The first half of the insertion in the direction of the injected beam is used for injection and the detector is placed in the middle of the second half. This configuration avoids the need to bypass the detector with the transfer line and affords ample space to protect the detector from potential beam losses at injection. Currently, no specific performance requirements have been established for these experiments. A generic insertion design gives an indication of the expected performance [11]. It provides a free distance from the collision point to the focusing triplets of 25 m and can reach luminosities in the $2 \times 10^{34} \text{ cm}^{-2}\text{s}^{-1}$ range. The shielding to protect the triplet can be less massive than for the main experiments thanks to the lower luminosity.

1.7.3 RF system

The baseline RF system design is similar to that of the LHC and has a frequency of 400.8 MHz. The installed voltage will be 48 MV, three times more than in the LHC. In the longitudinal plane, an inductive longitudinal impedance budget of $\text{Im}(Z)/n = 0.2 \Omega$ is expected, similar to the one of LHC (0.1Ω). At injection, 12 MV ensures beam stability and at collision energy 42 MV is used. During ramping a maximum of 43.5 MV is used. At injection the longitudinal beam emittance is 2.3 eVs, i.e. a four-sigma bunch length of 1.42 ns and a two-sigma energy spread of $\Delta E/E = 3.25 \times 10^{-4}$ and the synchrotron tune is 2.77×10^{-3} . At collision the corresponding values are 10.2 eVs, 1.07 ns, $\Delta E/E = 1.24 \times 10^{-4}$ and 1.33×10^{-3} , respectively. Controlled longitudinal emittance blow-up (by band-limited RF phase noise) to balance synchrotron radiation damping will be required not only during the ramp but also in coast at 50 TeV.

1.8 Beam loss mitigation

After injection at 3.3 TeV, each beam has a total energy of 560 MJ. At collision energy of 50 TeV this increases to 8.3 GJ. These values exceed those of LHC by more than a factor 20. Avoiding beam loss and mitigating its consequences is thus of prime importance. This is addressed by the injection and extraction systems as well as the collimation and machine protection systems.

1.8.1 Machine protection

An adequately designed machine protection system must be conceived to mitigate the risk of beam loss. Dedicated systems will predict and detect equipment failures rapidly enough to engage protection systems that can extract the beam cleanly before it can generate harmful losses. Passive protection mitigates the impact from failure of active components, such as injection and extraction kickers. The collimation system removes the beam halo and tails and protects the machine from losses which might otherwise cause magnet quenches. The collimation system also allows continued operation of the machine with large losses in order to be able to diagnose the origin of the problem.

1.8.2 Injection

An injection system is located upstream of each of the two low-luminosity experiments within a straight section of 1.4 km. This layout allows three of the four experiments to be close to the CERN site. The injection [12, 13] utilises a fast bunch-to-bucket transfer with a normal conducting Lambertson septum to deflect the beam vertically onto the collider orbit. The horizontal angle is reduced by off-centre passage through a defocussing quadrupole and is then fully compensated by a fast kicker system. A specific injection protection system is required to protect the machine and the experiments from badly injected beams. The main constraints for the injection system at 3.3 TeV come from the total beam energy of 560 MJ of the high energy booster (HEB) to FCC transfer, coupled with the beam rigidity of 11 T km.

Investigations of LHC injection protection absorber blocks with the HL-LHC beam parameters [14] show that the threshold for absorbers to survive beam impact is around 5 MJ with the expected beam sizes. A burst-mode transfer of 130 batches, each consisting of 80 bunches, is therefore envisaged. The target filling factor of the collider is 80% (10400 bunches) and hence the gaps between batches needed for the injection kicker rise time have to be shorter than 425 ns. A fast recharging kicker system allows the full LHC beam to be transferred within several seconds and thus, the time for the injection process is negligible in comparison to the overall filling time. Many kickers will be used to achieve a fast rise time and this requires high reliability in order to achieve a low probability of any kicker misfiring. Novel solid-state kicker generator concepts are being developed to reach these short rise times. These very low failure rates will be achieved by having a very modular and easily maintainable system.

1.8.3 Extraction and dump

The dump systems [15, 16] have to abort the beam in a safe and reliable way at any energy level between injection and collision. There is one system per beam which extracts the full beam in one turn onto an external absorber block. Both active and passive beam dilution is required in the dump line to avoid damaging this block. The extraction systems for both beams are located in a dedicated 2.8 km long straight section. At collision energy, the extreme beam rigidity and stored beam energy pose serious challenges for the performance of the extraction kickers, septa and dilution kickers. In order for the dump block to survive the impact of a nominal beam dump, a dual plane dilution kicker system is required. The kicker is excited with a damped voltage pulse oscillating at 50 kHz which distributes the full beam of 10400 bunches onto a multi-branch spiral on the front face of the absorber block which is 20 m long and 55 cm in radius. Novel superconducting septa capable of deflecting these rigid beams with a reasonable power consumption are being developed.

Failures within the system which could lead to an asynchronous beam dump are of special concern due to their potential for damage and the difficulty of designing passive absorbers. These failure cases dominate the system design and dictate many of the detailed layout and parameter choices. The extraction kicker system is highly segmented. Hence, the erratic firing of a single kicker only leads to a limited level of orbit oscillation of the beam which can be accepted in the machine for a substantial fraction of a turn. This allows waiting for the next abort gap to fully extract the beam without losses. It is therefore planned to have several abort gaps in the filling pattern. This scheme prevents an asynchronous dump caused by a single kicker misfiring which could create beam

losses around the ring during the extraction. The system is designed to survive other failure modes that still might lead to a full asynchronous firing of the extraction kickers, by using passive protection elements. Since a single bunch at 50 TeV is already close to the damage limit of state-of-the-art composites, the extraction kicker rise time has to be as low as 1 μ s to avoid absorber damage caused by particles being swept across the surface during a rising kicker pulse. This constraint could be significantly relaxed if sacrificial absorbers could be used for asynchronous dump protection.

1.8.4 Collimation

As in any high-energy hadron collider, a collimation system is needed to intercept and safely dispose of unavoidable beam losses. It should clean the beam halo, to keep losses in the superconducting magnets below the quench limit and also provide passive protection during fast beam failures. The design of the collimation system also has implications for controlling the background in the experiments and/or the machine impedance. The collimation is particularly challenging due to the unprecedented stored beam energy of 8.3 GJ, which is more than a factor 20 higher than the LHC [17].

The backbone of the collimation system is housed in two dedicated insertions: PJ for betatron collimation which is 2.8 km long and PF for momentum cleaning which is 1.4 km long. The design and optics of these insertions [18, 19] are scaled-up versions of the LHC collimation system [20–23], which has been optimised and has demonstrated very good performance during operation [24, 25]. The length of the betatron system, as well as its β -functions, have been scaled up by a factor 5 from LHC to achieve collimator gaps that are similar to the LHC both in units of beam σ and in mm. This avoids excessive impedance and guarantees mechanical stability while keeping the σ -setting small enough to protect the aperture. The optics and parameters are detailed in Chapter 9.

As in the LHC, the multi-stage system consists of robust primary collimators (TCP) closest to the beam, followed by secondary collimators (TCSG), also robust, which intercept the secondary halo from the TCPs. In the LHC, the TCPs and TCSGs are made of carbon-fibre-composite (CFC), however, this would induce too high an impedance for FCC-hh. Therefore, the majority of the TCSGs are made of molybdenum-graphite instead, but with a 5 μ m molybdenum coating as in HL-LHC [26]. Active tungsten absorbers (TCLA) intercept the tertiary halo and showers from the TCSGs and are a third stage of collimation. In the same way as in the HL-LHC [27, 28], further collimators (TCLD) are introduced in the dispersion suppressor (DIS), to intercept single-diffractive protons leaking from the TCP. Furthermore, tertiary collimators (TCTs) upstream of the experiments provide local protection for the aperture bottlenecks, in particular the final focus triplets. The proposed collimation layout provides sufficient protection of the full machine at injection and also in the most demanding situation at the smallest β^* at collision.

The betatron collimation system is conservatively designed to withstand a temporary beam lifetime drop to 12 minutes over a period of 10 s, this corresponds to a beam loss power of 11.8 MW. Its performance has been successfully assessed and verified through tracking simulations [29] and energy deposition studies [30, 31].

The design of the momentum cleaning is also being studied; it mainly protects the collider from losses during the energy ramp after injection. To stay below the quench limit is less challenging at injection than with colliding beams due to the smaller beam energy. Currently, the normalised aperture is slightly smaller than in LHC due to the significantly smaller beamscreen. However, it is believed [32] that the aperture can be brought within tolerance through a careful study of error tolerances and local optics.

First studies of an asynchronous beam dump indicate that the collimation system can protect the machine and avoid any damage if a single kicker module fails. Other failure scenarios, radiation damage, shielding design and advanced collimation concepts remain to be studied.

1.9 Alternatives

Alternatives to the conceptual design can be explored. In particular the possibility has been considered of using different bunch spacings in the circulating beam with the aim of reducing the background in the detectors due to pileup. Tentative parameters characterising the performance that one might expect are given below. However detailed studies are required to establish the feasibility of these parameters. Also the use of different magnet technology to reach higher dipole fields can be considered and is discussed below.

1.9.1 Alternative bunch spacings

With the nominal parameters, a maximum of about 1000 events per bunch crossing can be reached. Novel detector design and data analysis methods need to be developed to allow the interesting physics to be extracted from this high background. Other operation modes based on reducing the bunch spacing from 25 ns to 12.5 ns or 5 ns together with proportionate changes to the charge and emittance can facilitate this task by reducing the number of events per bunch crossing. Table 1.2 shows three tentative scenarios. These options have not been considered in detail and more work is required to judge their feasibility and performance. They are more demanding for the hardware design and lead to a reduction of the integrated luminosity. The first option requires an adaptation of the injector chain to produce 12.5 ns beams. The second uses a 5 ns beam that could potentially be provided by the current injector complex, whilst the third option needs major modifications in the injector to produce the very small emittances.

If the experiments require these smaller bunch spacings an appropriate R&D programme can be launched.

Table 1.2: Key beam parameters. The initial and ultimate baseline parameters are shown together with the phase two parameters for some alternative bunch spacing scenarios.

| | Initial | Nominal | Opt 1 | Opt 2 | Opt 3 |
|--|---------|---------|-------|-------|-------|
| Bunch spacing [ns] | 25 | 25 | 12.5 | 5 | 5 |
| Protons per bunch [10^{11}] | 1 | 1 | 0.5 | 0.2 | 0.2 |
| Init. hor. transv. emittance [μm] | 2.2 | 2.2 | 1.1 | 1.1 | 0.44 |
| Init. vert. transv. emittance [μm] | 2.2 | 2.2 | 1.1 | 1.1 | 0.44 |
| Final hor. transv. emittance [μm] | 1.28 | 0.29 | 0.25 | 0.22 | 0.22 |
| Final vert. transv. emittance [μm] | 1.28 | 0.24 | 0.2 | 0.17 | 0.17 |
| Max. total beam-beam tunes | 0.01 | 0.03 | 0.03 | 0.03 | 0.03 |
| IP β -function [m] | 1.1 | 0.3 | 0.3 | 0.3 | 0.3 |
| Peak luminosity [$10^{34} \text{ cm}^{-2} \text{ s}^{-1}$] | 5.01 | 25.2 | 23.2 | 14.5 | 20.1 |
| Max. number events per crossing | 170 | 857 | 394 | 99 | 137 |
| Optimum integrated luminosity / day [fb^{-1}] | 2.27 | 8.2 | 7.5 | 5.5 | 6.2 |

The alternative bunch spacings will increase the electron cloud effect, with the 12.5 ns option being the most critical. This requires additional mitigation and improvements of the existing mitigation measures. Furthermore, the instrumentation and feedback systems must have higher bandwidth.

1.9.2 Higher field magnets

Magnets based on high-temperature superconductor (HTS) technology can potentially reach higher fields than those based on Nb_3Sn technology. This would allow the construction of an even higher energy collider in the FCC-hh tunnel. Such a scenario relies however, on the development of high-field HTS dipole and quadrupole magnets at an affordable cost, which is estimated today to take around one to two decades longer than the development of 16 T Nb_3Sn magnets. This section gives some ideas about the technical feasibility of such a higher-energy collider in the FCC tunnel, with 24 T strong magnets that would aim for a 150 TeV centre of mass energy.

At 75 TeV beam energy, the synchrotron radiation emitted by each particle increases by about a factor 5 compared to 50 TeV beam energy. To compensate this energy loss, an RF voltage of 25 MV is required, compared to 5 MV at 50 TeV beam energy. This goes together with a limited increase of the installed voltage. In the 50 TeV design the cryogenics system requires about 100 MW of power to absorb the effects of the synchrotron radiation. If the same beam current, vacuum system and magnet operating temperature were used at the higher energy, the power consumption would increase by a factor 5. The resulting impact could be mitigated by increasing the operating temperature of the magnets and the beamscreen and by limiting the beam current. An optimisation will have to be done based on a re-design of the vacuum system, a review of the magnet performance for different temperatures and on re-evaluation of the planned integrated luminosity.

The minimum affordable magnet aperture in the arcs is governed by two main factors: first, the aperture of the beamscreen has to be large enough to limit its impedance effects on the beam, to avoid instabilities. Second, sufficient space is needed between the beamscreen aperture and the magnet aperture for vacuum and cooling. A higher beam energy and in particular a lower beam current will allow the beamscreen aperture to be reduced

slightly. If the total heat load increases, more space will be needed for the cooling system. Therefore, the aperture size change is expected to remain within reasonable limits. Since the quadrupole gradient is expected to scale in proportion to the dipole field, the arc optics will not diverge significantly from the current design. With the exception of the transverse collimation and beam extraction, the lengths of the insertions should first scale with the square root of the beam energy, assuming the same aperture size.

HTS technology will also allow the quadrupole strength to be increased. Because the quadrupole gradient and the dipole strength scale together in proportion to the beam energy, the length of the final triplet could remain unchanged with the same magnet aperture and the same beta function could be achieved at the collision point. The collision debris produced in the interaction point is approximately proportional to the product of centre-of-mass energy and luminosity. Assuming the same luminosity as for 50 TeV beams, the debris would only increase by a small amount. The design of a workable experiment insertion therefore seems feasible. Studies are of course required to determine if a larger fraction of the debris deposits energy in the triplets. Since the beam needs slightly less space in the triplets, it might be possible to increase the thickness of the shielding and to close the hole in the TAS that protects the triplets from the direct losses from the collision point. Similarly, the RF insertion could maintain its optics using the stronger magnets.

The higher beam energy at the same beam current will render machine protection more critical. However, the two most challenging insertions are the transverse collimation system and the beam extraction system. These systems have the longest insertions, therefore providing some flexibility for the development of a means to address the higher risks. In particular, losses in the collimation systems can be high at certain times during machine operation. LHC experience shows that this is mostly the case for the transverse collimation system, therefore to avoid magnet quenches, normal conducting magnets are used in this insertion. However, this technology does not allow the fields to be increased. With an increase of beam energy, it could therefore be difficult to maintain the current optics design. This problem is observed in the design of the HE-LHC scenario. The beam energy doubles compared to LHC, but the length of the collimation insertion increases. For the FCC-hh baseline design this problem is avoided, because the collimation insertion is twice as long as the scaling from LHC suggests. Hence it has sufficient margin in the magnet strength to accommodate the higher beam energy. Some R&D will also have to be done on the momentum cleaning insertion to ensure that an efficient beam optics is developed.

Experiment insertion region concept

2.1 Overview

FCC-hh will provide proton-proton collisions at a centre-of-mass energy of 100 TeV, a factor 7 higher than the LHC. The goal for the integrated luminosity in each high luminosity experiment is set to 20 ab^{-1} . This ambitious goal can be reached in an operational scenario with 10 years of operation using the less ambitious parameters (baseline option) followed by 15 years of operation at the ultimate parameters. Table 2.1 shows the two parameter sets for the high luminosity IRs and compares them with the corresponding parameters of LHC and HL-LHC. The most notable difference between baseline and ultimate are the goals for the β functions at the interaction point, β^* , leading to a significant increase in instantaneous luminosity at ultimate optics. Due to the high centre-of-mass energy and the high luminosity the total power released towards each side at the IP increases from 1 kW in the LHC or 4.75 kW in HL-LHC up to 260 kW in FCC-hh with ultimate parameters. Most of this power will be absorbed in the detector but debris particles emitted at small angles will travel down the beam pipe and strike the interaction region magnets, possibly causing quenches and degrading the material. Consequently, radiation load from collision debris was identified as a key issue early in the design phase of the final focus system in the interaction regions [33]. Unifying adequate protection of the triplet magnets with high luminosity performance has been the driving factor of the interaction region layout.

In terms of the chromaticity correction, it has been estimated that the sextupoles in the arcs are able to correct around 557 units of chromaticity. The natural chromaticity for the case with $\beta^*=30 \text{ cm}$ is below this value, and therefore the chromaticity can be corrected. However this is not the case beyond the ultimate optics. While the aperture of the final focus system can accommodate a β^* of almost 20 cm for the nominal crossing angle given in Table 2.1, the strength of the sextupoles necessary to correct the chromaticity is above the maximum achievable. If operation beyond ultimate β^* is desirable, an achromatic telescopic squeezing scheme like that of the HL-LHC [34] could be used to increase the chromatic correction efficiency of the arc sextupoles.

Although the high mass of protons usually keeps the synchrotron radiation produced in hadron colliders low, the high beam energy of FCC-hh raises the concern that the photon background in the experiment regions might grow to significant levels. Hence, a closer investigation of the synchrotron radiation was necessary in order to quantify the impact, but it was concluded that the synchrotron radiation is not expected to be an issue for the experiments.

Debris from proton collisions at the interaction points may create background in the other detectors. Protons with an energy close to the nominal beam energy which travel far in the beam pipe before being intercepted, as well as muons passing through the rock between two experiments, are of particular concern. Tracking studies of the protons and an analysis of the muon range in rock were performed, concluding that the cross talk between experiments is negligible.

The high luminosity experiment interaction region (EIR) design relies on crab cavities to compensate the luminosity loss due to the crossing angle which is needed to keep long range beam-beam effects under control [35]. As this technology is currently being tested in proton accelerators for the first time it is desirable to have an alternative. Flat beam optics are a good candidate for this as the crossing angle in the less squeezed plane can be kept rather small, reducing the luminosity loss due to the geometric overlap of the colliding bunches. Corresponding optics have been developed, using an alternative triplet layout.

Table 2.1: Key parameters of FCC-hh compared to LHC and HL-LHC.

| | LHC | HL-LHC | FCC-hh | |
|---|--------|--------|---------------|------------|
| | | | Baseline | Ultimate |
| Centre-of-mass energy [TeV] | 14 | 14 | 100 | |
| Injection energy [TeV] | 0.45 | 0.45 | 3.3 | |
| Ring circumference [km] | 26.7 | 26.7 | 97.75 | |
| Arc dipole field [T] | 8.33 | 8.33 | 16 | |
| Number of IPs | 2 + 2 | 2 + 2 | 2 + 2 | |
| Number of bunches per beam n_b | 2808 | 2748 | 10600 (53000) | |
| Beam current [A] | 0.58 | 1.11 | 0.5 | |
| Peak luminosity/IP [$10^{34} \text{ cm}^{-2} \text{ s}^{-1}$] | 1 | 5 | 5 | 30 |
| Events/crossing | 27 | 135 | 170 | 1020 (204) |
| Stored beam energy [GJ] | 0.4 | 0.7 | 8.4 | |
| Synchrotron power per beam [MW] | 0.0036 | 0.0073 | 2.4 | |
| Arc synchrotron radiation [W/m/beam] | 0.18 | 0.35 | 28.4 | |
| IP beta function β^* [m] | 0.4 | 0.15 | 1.1 | 0.3 |
| Bunch spacing [ns] | 25 | 25 | 25 (5) | |
| Initial norm. rms emittance ϵ_n [μm] | 3.75 | 2.5 | 2.2 (0.45) | |
| Initial bunch population N_b [10^{11}] | 1.15 | 2.2 | 1.0 (0.2) | |
| Transv. emittance damping time [h] | 25.8 | 25.8 | 1.1 | |
| RMS bunch length [cm] | 7.55 | | 8 | |
| RMS IP beam size [μm] | 16.7 | 7.1 | 6.8 | 3.5 |
| Full crossing angle θ [μrad] | 285 | 590 | 104 | 200 |

In addition to the two high luminosity interaction regions (IRs) situated in the Points PA and PG, FCC-hh features two low luminosity interaction regions in the points PB and PL, much like the LHC. In the absence of a physics case for these two experiment regions and consequently the lack of luminosity goals or space constraints, an initial design that can reach an integrated luminosity of 500 fb^{-1} is proposed. An alternative for the low luminosity IRs is FCC-eh [1, Section 2.8], a lepton-hadron collider with an interaction region scaled up from the LHeC [36].

A filling scheme with 5 ns bunch spacing could mitigate the event pile-up in the detectors. The corresponding parameters are shown in Table 2.1 in parenthesis. This option has not been addressed in the IR design because, although it reduces aperture needs thanks to the lower emittance, it could pose operational difficulties for keeping beams in collision as the beam size reduces below $1 \mu\text{m}$ during the run due to synchrotron radiation damping.

Simulations of collective effects have led to a change of the operational mode that will now assume a collide & squeeze approach (Section 8.7.4). This is an easy way to mitigate these effects without a significant penalty in integrated luminosity. Beams will collide at a larger β^* , around 1.2 m, and the β^* squeeze will continue to the minimum beta whilst colliding. This will avoid the reduction of the stability area due to long-range beam-beam effects (see Section 8.7.4) and will provide the factor two margin in stability as was shown to be needed in LHC Run 2. Figure 2.1 shows an illustration of what an FCC-hh physics fill would look like with and without resorting to collide & squeeze.

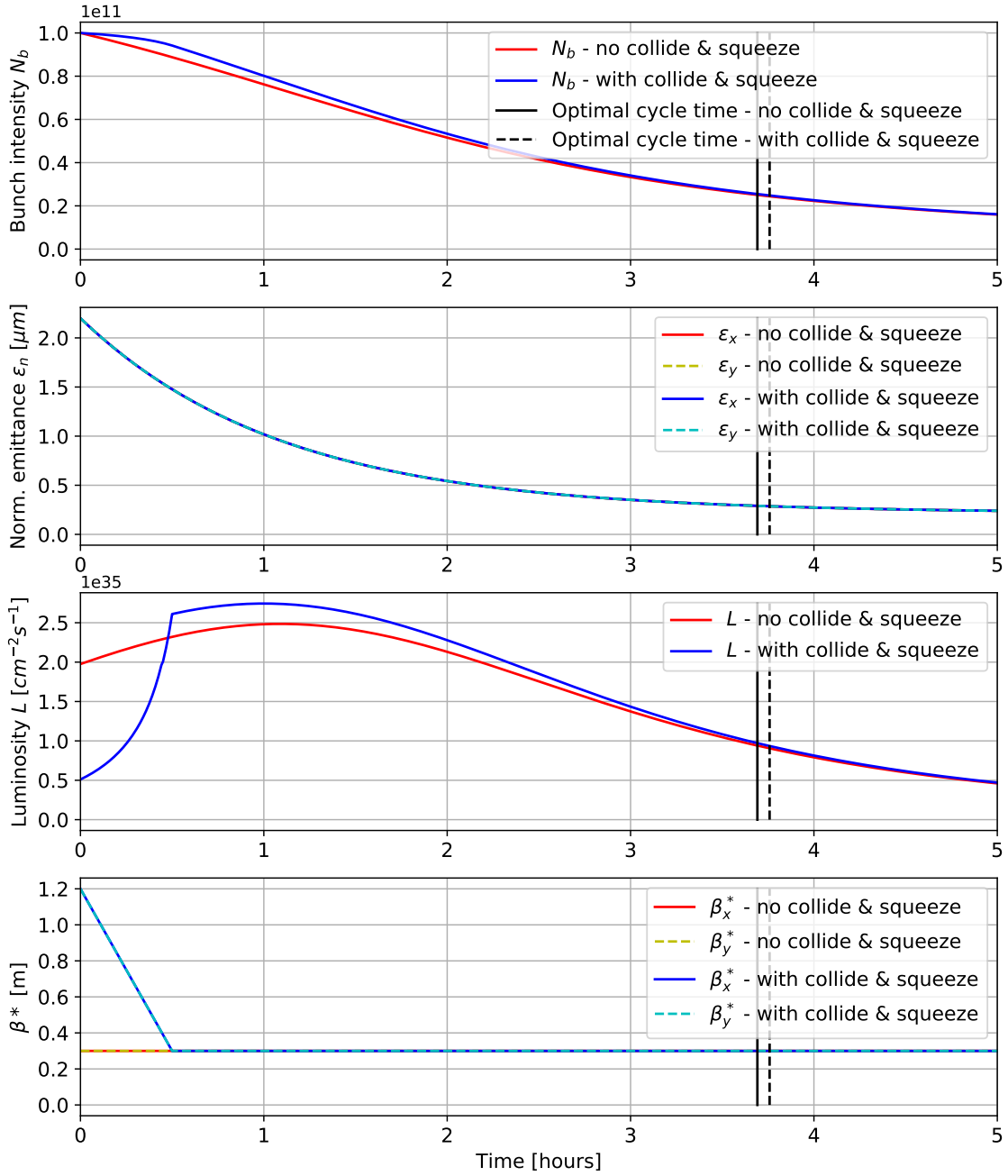


Figure 2.1: Beam parameters during FCC-hh physics fills with and without collide & squeeze.

2.2 Machine-detector interface considerations

Early studies of the final focus system layout concluded that the main contributor to the minimum β^* is the overall length of the triplet, whilst the L^* only plays a minor role [33, Sec. III D]. This led to a clear strategy to minimise β^* and having significant amounts of shielding which reduces the free aperture of the final focus magnets. The idea is to choose the smallest L^* that does not restrict the detector design and to increase triplet length until dynamic aperture or chromaticity become obstacles. In this strategy the machine-detector interface (MDI) plays a key role as it defines L^* . A sketch of the detector region layout is shown in Fig. 2.3. While the detector has a total length of about 50 m, extending to 25 m on either side of the IP, being able to open up the detector requires a total cavern length of 66 m. During operation the gap between detector and cavern wall will be occupied by the forward shielding that protects the detector from secondaries back-scattered from the TAS. The aperture in the 2 m

thick wall between cavern and tunnel is equipped with a cast iron absorber to complete the forward shielding. The TAS, a 3 m long copper absorber that protects the final focus magnets from collision debris is located 35 m from the IP. With an additional space of 2 m reserved for vacuum equipment and for the end of the magnet cryostat, first quadrupole of the final focus triplet starts at $L^* = 40$ m.

The beam pipe at the IP is made of 0.8 mm thick beryllium and has an inner radius of 20 mm. This pipe extends to 8 m at either side of the IP and is followed by a beryllium cone with an opening angle of 2.5 mrad, corresponding to $\eta = 6$. From 16 m on from the IP, the inner radius of the aluminium beam pipe is constant at 40 mm, because this is necessary for the opening of the detector.

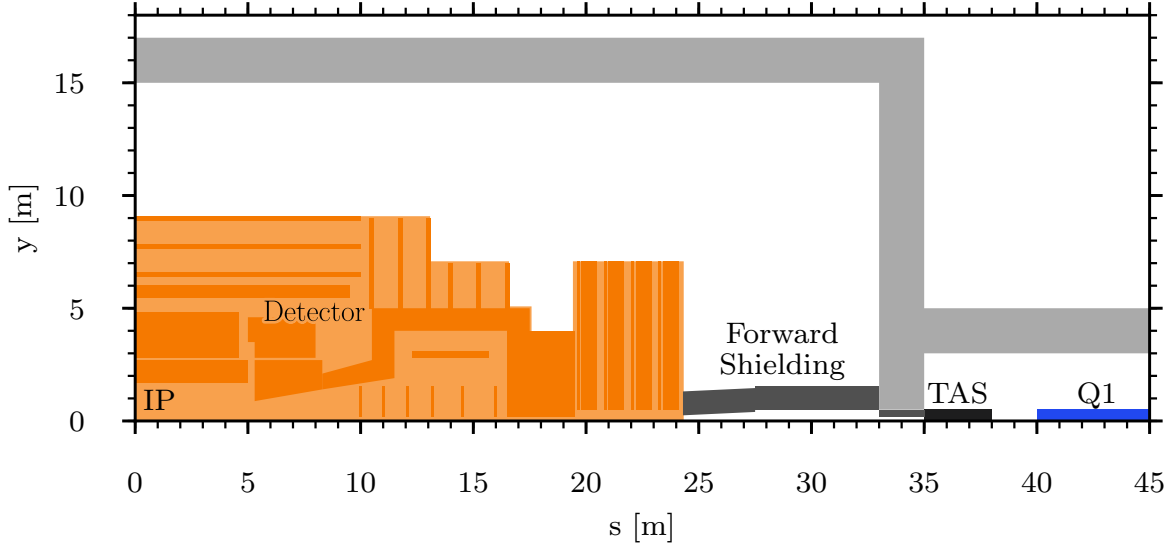


Figure 2.2: Detector and interaction region layout leading to the $L^* = 40$ m lattice. The IP is located at $(0, 0)$.

2.3 System layout and optics

The interaction region layout of FCC-hh follows the same principles as the LHC and HL-LHC interaction regions. The layout is shown in Fig. 2.3. Starting at the interaction point (IP), the strongly focused and highly divergent

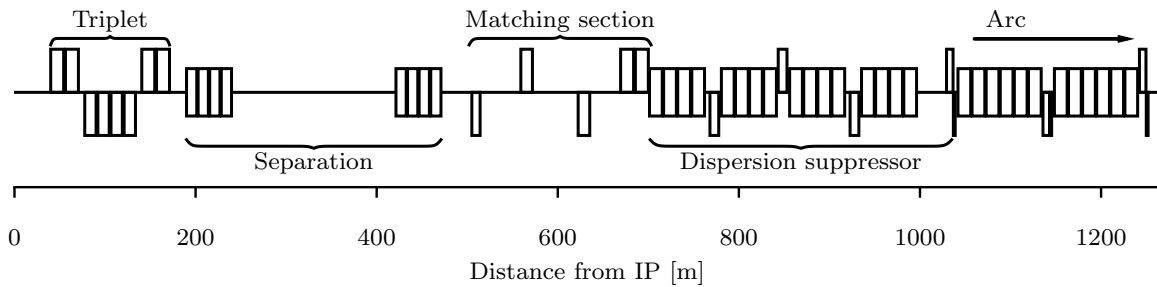


Figure 2.3: Layout of the high luminosity interaction region. The layout is antisymmetric around the IP at $(0, 0)$.

beams pass through a drift space L^* long, chosen to accommodate the detector. Following this drift space, a final focus system comprising three large aperture quadrupoles (hence called the triplet) focuses the beams in both the horizontal and vertical planes. The triplet consists of single aperture magnets that host both beams. The triplets at either side of the IP are powered antisymmetrically. This has the advantage that the triplet region is optically identical for both beams. Behind the triplet, a shared aperture dipole, D1, separates the two beams. After a drift, the double bore dipole, D2, bends the separated beams onto parallel orbits again. The resulting reference orbits are shown in Fig. 2.4. Also depicted are orbit excursions that let the two beams collide with the crossing angle which

is needed to avoid parasitic collisions outside the detector region. Four more quadrupoles, Q4-Q7, make up the following matching section that occupies the rest of the straight section. The straight section is connected to the arcs by a two cell dispersion suppressor. To provide enough degrees of freedom to match all required beam parameters from the IP to the arcs, the four matching section quadrupoles, the three individually powered quadrupoles of the dispersion suppressor, Q8-Q10, as well as three tuning quadrupoles in the first arc cell, QT11-QT13, are used for the matching procedure.

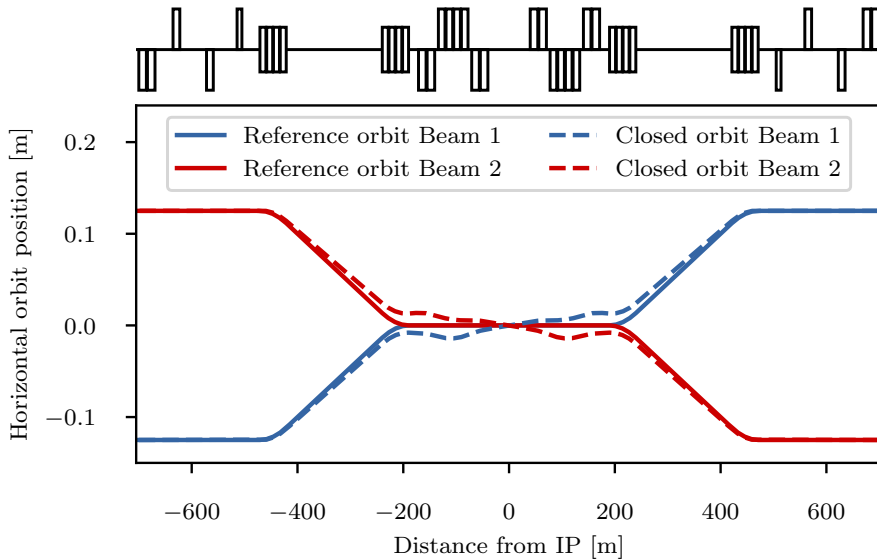


Figure 2.4: Reference orbits (solid lines) and closed orbits with crossing angles (dashed lines) in the interaction region.

2.3.1 Final focus triplet

The final focus design strategy calls for a long triplet in order to achieve small β^* values. The chromaticity and dynamic aperture were not the only limiting factors for the triplet length, but also the total length of the straight section, which determines the arc side focal length of the final focus system, as well as the strength of the Q7 quadrupole. Furthermore the lengths of individual magnets must be equal to or below 14.3 m in order to be compatible with a cryostat length of 15 m. The relative lengths of Q1, Q2 and Q3 were adopted from HL-LHC. As suggested in Ref. [37], Q1 was chosen to have a smaller aperture and higher gradient than Q2 and Q3 in order to minimise β^* . The specifications for the triplet quadrupoles are listed in Table 2.10 and the layout of the final focus triplet shown in Fig. 2.5. Q1 and Q3 are made up of two submagnets each 14.3 m long. A drift space of 2 m is reserved between the submagnets for the interconnects. The drifts between Q1–Q2 and Q2–Q3 of 7 m are longer and must house orbit correctors, BPMs and vacuum equipment. Q2 consists of four 12.5 m long submagnets. This not only allows a similar length ratio as in the HL-LHC but also placing orbit correctors in the cryostat of the outermost Q2 magnets. 18.8 m is reserved behind Q3 for higher order multipole correctors to compensate triplet field errors.

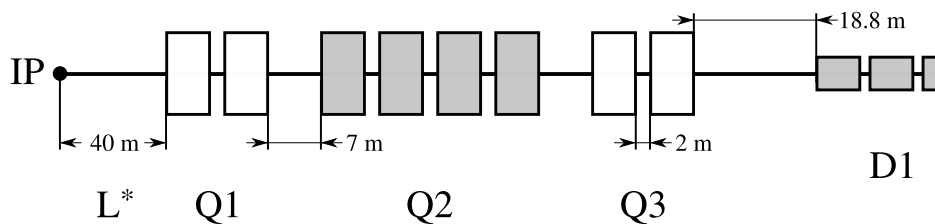


Figure 2.5: Layout of the final focus triplet.

A 35 mm thick inner shielding made from the tungsten alloy INERMET180 protects the triplet magnets from collision debris. The cold bore is scaled by 2.72 % of the coil aperture diameter. Furthermore the free aperture is reduced by a gap for the liquid helium for cooling (1.5 mm), the Kapton insulator (0.5 mm), a beamscreen (2.05 mm), a gap for the of the beamscreen insulation (2.0 mm). All of the above have been modelled as simple layers. Despite this significant reduction of the free aperture, the triplet can accommodate a beam with lower than

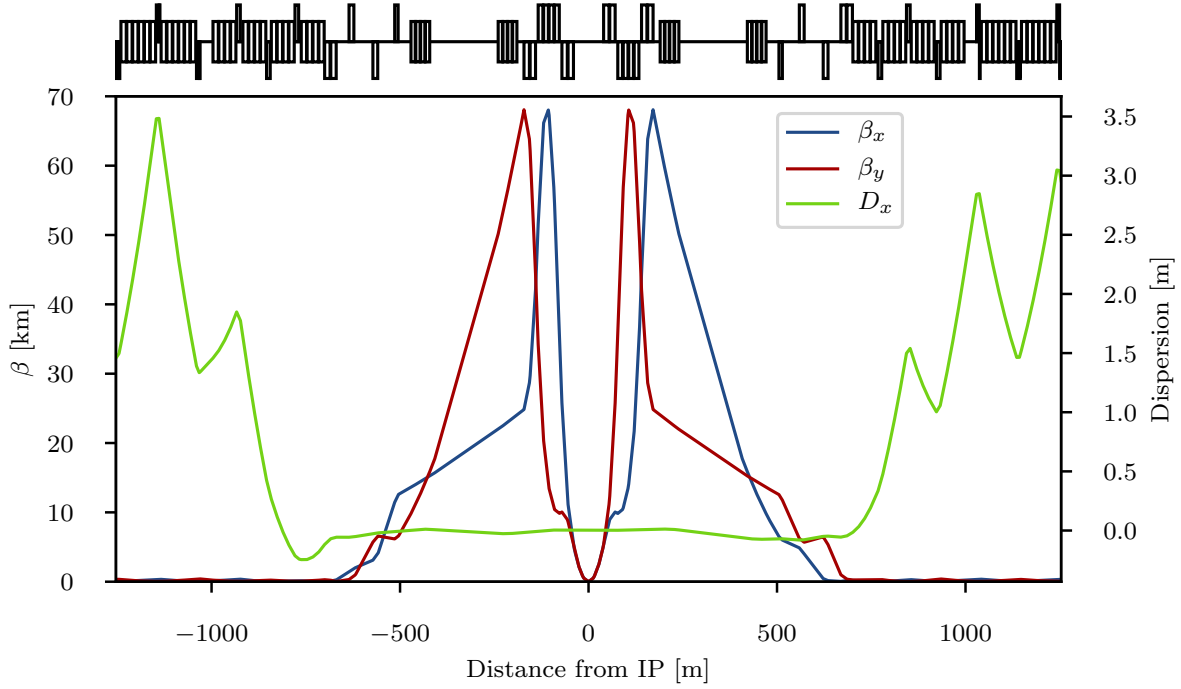


Figure 2.6: Optics of the main interaction region with $\beta^* = 0.3$ m.

ultimate β^* . Figure 2.6 shows the β functions and horizontal dispersion in the EIR and Fig. 2.7 the corresponding aperture usage. Although aperture and alignment tolerances are not included in Fig. 2.7, the beam stay clear region depicted in Fig. 2.8 clearly shows that the ultimate optics have a significant margin in terms of aperture. In fact, optics with almost $\beta^* = 0.2$ m can be achieved, although the chromaticity correction is insufficient with the current arc layout.

2.3.2 Beam-beam effects and crossing angle

The beam-beam interaction can limit the performance of a particle collider. In fact, the beam-beam interaction can induce particle losses, resulting in a reduction of the beam lifetimes and can create a high background in the experiments. In addition, the beam-beam interaction can be responsible for an elevated heat and radiation load on the collimation system, can induce emittance blow-up and can cause coherent beam instabilities with a consequent reduction of the luminosity reach. The design of FCC-hh is based on the theoretical beam-beam studies and experience in LHC [38–41]. The beams collide head-on in two high luminosity interaction points (IPA and IPG). Depending on the filling scheme used, the bunches experience different numbers of head-on and long range collisions generating two different families of bunches [42]. The so-called nominal bunches are located in the middle of a train while the PACMAN bunches are located in the head or tails of the trains. Due to empty slots at the interaction points the PACMAN bunches experience fewer long range interactions than nominal bunches, leading to different beam-beam effects. Like in the LHC and the HL-LHC, an alternating crossing scheme is chosen for the two high luminosity experiments in IPA and IPG, in order to passively compensate for tune and chromaticity shifts for PACMAN bunches [43]. In these studies it is assumed that the beam crosses with a finite horizontal angle for IPA and a vertical one in IPG as shown in Fig. 2.10. Different schemes have also been explored and they seem feasible with reduced beam-beam long-range effects [44] but will require further studies. Two additional, lower luminosity experiments are located in IPB and IPL. Assuming that the four experiments operate in proton-proton collisions with 25 ns bunch spacing, 352 long range encounters are expected compared to 120 in the LHC.

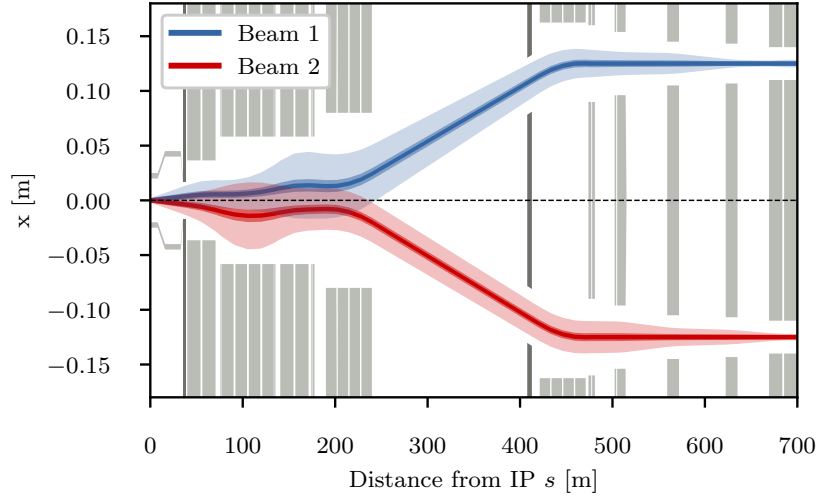


Figure 2.7: Layout of the insertion region between the IP and Q7. For each beam, the closed orbit, the 2σ envelope and the 15.5σ envelope for the ultimate β^* of 0.3 m are shown. The beam sizes include a β beating of 10% and a closed orbit uncertainty of 2 mm. Magnet apertures and the detector region beam pipe are illustrated in light grey while absorbers are shown in dark grey. The large aperture triplet magnets leave significant aperture margins.

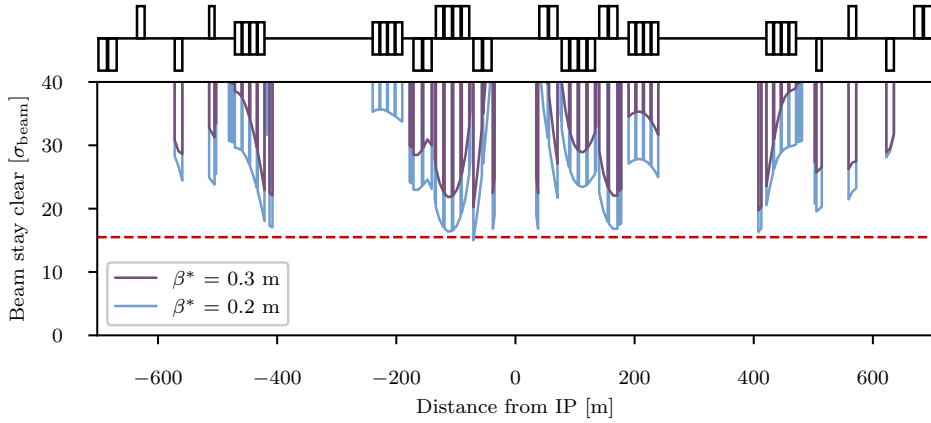


Figure 2.8: Beam stay clear values in the high luminosity EIR for horizontal crossing and ultimate as well as beyond ultimate optics. For $\beta^* = 0.2$ m the beam stay clear limit is just below the minimum of 15.5σ to the left Q1, suggesting that a slightly larger β^* can be accommodated.

Detailed beam-beam studies have been carried out based on weak-strong and strong-strong models using the SixTrack [45, 46] and COMBI [47–49] codes. The SixTrack code has been used for the computation of the area of stable motion in real space, the dynamic aperture (DA). A detailed lattice description and the LHC experiment data have been employed to benchmark the SixTrack code with and without beam-beam effects [50, 51]. The COMBI code uses a self-consistent treatment, including a simplified lattice description, and provides the evolution of macroscopic beam parameters, such as the beam intensity and the emittance together with the Landau damping of coherent beam instabilities [41, 52]. The approach used for the DA studies presented here is similar to the LHC and HL-LHC design studies [53, 54]. The LHC observations have shown that a reduction of beam lifetime starts to appear [38] below a simulated DA of 4σ . As described in Refs. [50, 55], a strong correlation exists between the beam intensity lifetime and the simulated DA for different beam configurations with and without beam-beam interactions. As shown in Fig. 2.9, a DA of 7.2σ is ensured with a crossing angle $\theta = 200 \mu\text{rad}$ in IPA and IPG for the nominal normalised emittance of $\epsilon_n = 2.2 \mu\text{m}$ and at the ultimate β^* of 0.3 m. The corresponding orbit bumps at the two interaction points are shown in Fig. 2.10 and the beam-beam long range separations in units of the transverse beam size are shown in Fig. 2.11. For the ultimate scenario with $\beta^* = 0.3$ m and the chosen crossing

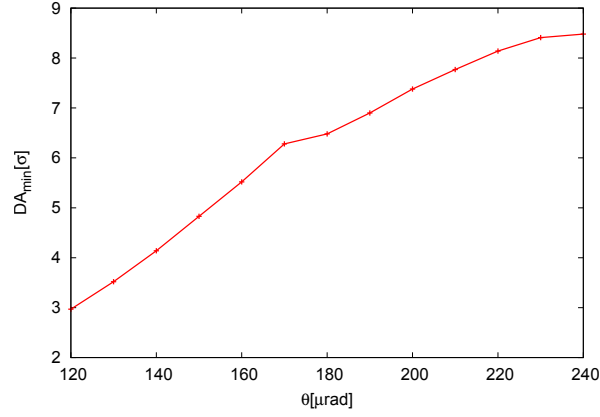


Figure 2.9: Minimum dynamic aperture in the presence of beam-beam interactions as a function of the crossing angle at the interaction points IPA and IPG for the ultimate collisions optics with $\beta^* = 0.3$ m and $L^* = 40$ m [35].

angle of $200 \mu\text{rad}$ (the blue dots), the long range separation at the first encounter is 17σ . At this separation, the value of DA (7.2σ) is well above 4σ providing sufficient margin to avoid additional particle losses on the collimation system due to beam-beam diffusive mechanisms (including a relative momentum deviation of 10^{-4}). In addition,

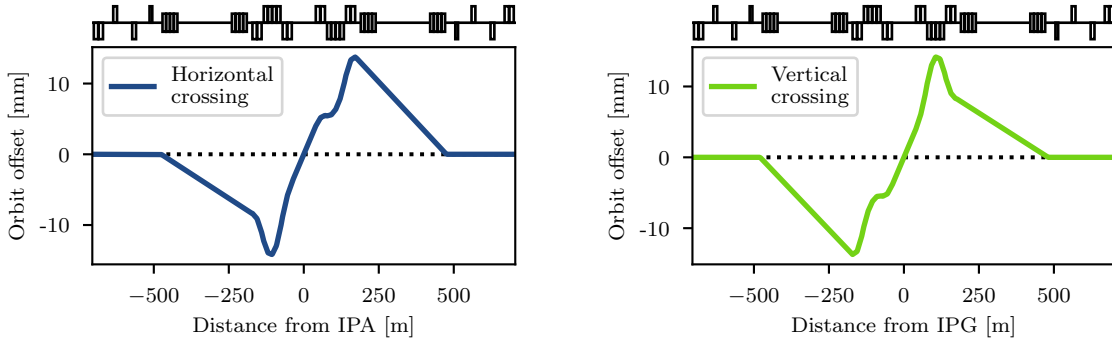


Figure 2.10: Orbit bump for a $200 \mu\text{rad}$ crossing angle required at $\beta^* = 0.3$ m in the horizontal plane for IPA and in the vertical plane for IPG.

margins are also left for high chromaticity operation (up to 20 units) if required for mitigation of coherent beam instabilities, for operating in the presence of multipolar lattice errors [56] or also for colliding in IPB and IPL. For the baseline scenario with collisions at $\beta^* = 1.1$ m, the long range beam-beam separation is well above 30σ (the red dots).

The DA as a function of the crossing angle in IPA and IPG for PACMAN bunches is shown in Fig. 2.12 (the blue and the green lines) for the H-V alternating crossing scheme. The red line corresponds to nominal bunches. As visible, the DA for PACMAN bunches is always above the DA for nominal bunches. The PACMAN effects of tune and chromaticity shifts are negligible assuming passive compensation with alternating crossing planes in IPA and IPG [44].

The expected two-dimensional tune footprints for particles up to 6σ amplitude are shown in Fig. 2.13 for the two values of β^* ($\beta^* = 1.1$ m and $\beta^* = 0.3$ m) with and without the long-range beam-beam effects. Without long-range beam-beam effects the tune spread is generated by the Landau octupoles (the blue colour) at maximum strength and powered with negative polarity as described in Ref. [57]. The tune spread is then reduced by the long-range beam-beam effects depending on the interaction strength. Fig. 2.13 shows the ultimate scenario with $\beta^* = 0.3$ m, corresponding to a minimum beam separation at the long-range encounters of 17σ (the green colour) and the the baseline scenario with $\beta^* = 1.1$ m (the red colour) at relaxed beam separations of 32σ . Despite the tune spread reduction due to the long-range beam-beam, such a configuration is preferred because it maximises the DA [58]. The strategy proposed for the FCC is to collide head-on at the two main IPs before the long-range interactions significantly reduce the tune spread provided by the Landau octupole system. Such a reduction occurs

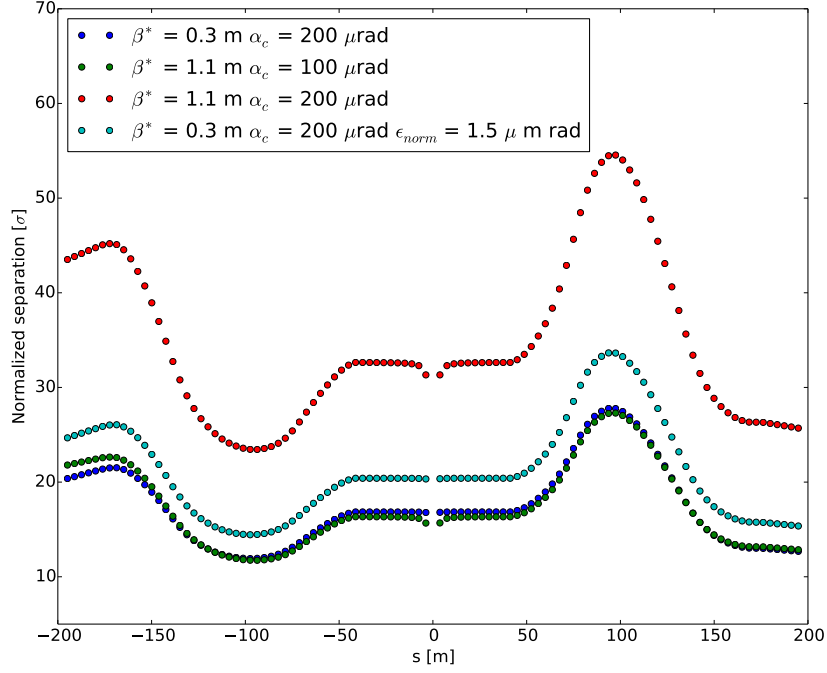


Figure 2.11: Beam-beam long range separations in units of the transverse beam size in the IR for the ultimate scenario with $\beta^* = 0.3$ m with a crossing angle $\theta = 200 \mu\text{rad}$ and the nominal normalised emittance $\epsilon_n = 2.2 \mu\text{m}$ (blue dots) and for a reduced normalised emittance of $\epsilon_n = 1.5 \mu\text{m}$ (light blue dots). The beam-beam long range for the Baseline scenario for $\beta^* = 1.1$ m are also plotted with a crossing angle $\theta = 200 \mu\text{rad}$ (red dots) and with a reduced crossing angle $\theta = 100 \mu\text{rad}$ (green dots). For this last cases the nominal normalised emittance of $\epsilon_n = 2.2 \mu\text{m}$ has been assumed.

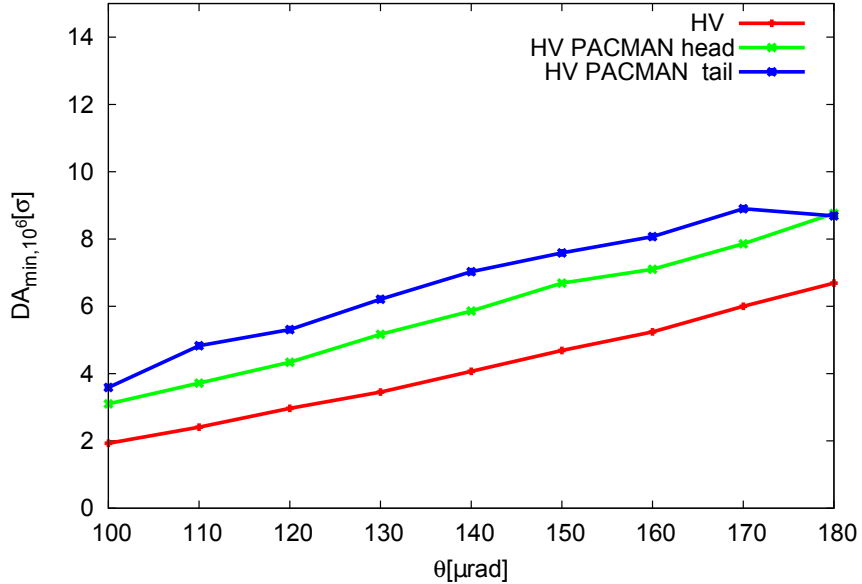


Figure 2.12: Minimum dynamic aperture, evaluated over 10^6 turns, as a function of the crossing angle in IPA and IPG for the H-V alternating crossing scheme for nominal bunches (the red line) and for PACMAN bunches in the head of a train (the green line) and in the tail of a train (the blue line) [56].

during the betatron squeeze and beams should be collided at around $1.1\text{m } \beta^*$, the value at which no reduction on

the tune footprint is visible (the red colour in Fig. 2.13) compared to the pure Landau octupoles tune spread (the blue colour in Fig. 2.13). If no coherent instabilities are observed, a reduction of the crossing angle at $\beta^* = 1.1$ m

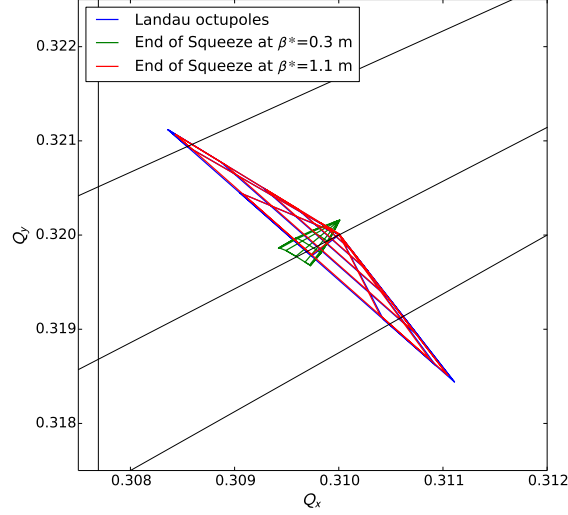


Figure 2.13: Two-dimensional tune footprints for particles up to 6σ amplitude at the end of the beta squeeze including long-range beam-beam interactions and Landau octupoles powered with negative polarity, for the ultimate scenario (the green colour) and for the baseline scenario (the red colour). For comparison the case with only Landau octupoles powered with negative polarity (maximum strength) is also shown (the blue colour).

is possible down to a minimum value of $100 \mu\text{rad}$. In fact, for this value of the crossing angle a DA of $\approx 7\sigma$ is still preserved since the long range beam-beam separations (the green dots in Fig. 2.11) are the same as the ultimate case with a crossing angle of $200 \mu\text{rad}$ (the blue dots in Fig. 2.11).

The beam parameters of the “collide & squeeze” scheme and the corresponding luminosity evolution, are shown in Fig. 2.1 as function of time. When the ultimate $\beta^* = 0.3$ m is reached the normalised emittance is reduced to $\epsilon_n = 1.5 \mu\text{m}$ due to synchrotron radiation, as shown in Fig. 2.1. The corresponding long range beam-beam separations are also shown in Fig. 2.11. As expected, the long range beam-beam separation at the first encounter is larger w.r.t. the ultimate case and it is about 20σ (the light blue dots).

In order to keep the impact of the two low luminosity experiments, IPB and IPL, in the shadow of the high luminosity ones (at IPA and IPG), a crossing angle of $180 \mu\text{rad}$ is required for the $\beta^* = 3$ m optics at these two experiments. As visible in Fig. 2.14 the DA no longer depends on the crossing angle because it is defined by the dynamics of IPA and IPG. In this configuration the long-range effects of IPB and IPL are negligible and the impact of the long-range beam-beam effects coming from these two experiments can be neglected, leaving more margin to push the performance of IPA and IPG.

The total beam-beam tune shift for two head-on collisions in IPA and IPG will be $\Delta Q_{bbho} = 0.011$. Figure 2.15 shows the two dimensional tune footprints for two head-on collisions in IPA and IPG for the baseline scenario with $\beta^* = 1.1$ m (the green colour) and for the ultimate scenario with a reduced normalised emittance $\epsilon_n = 1.5 \mu\text{m}$ (the blue colour). The latter takes into account the emittance reduction effect of the synchrotron radiation at the end of the “collide & squeeze”, as shown in Fig. 2.1. For the case with the reduced normalised emittance ($\epsilon_n = 1.5 \mu\text{m}$) the total head-on beam-beam tune shift increases up to approximately 0.016 (the blue colour in Fig. 2.15). Since the total beam-beam tune shift ΔQ_{bbho} is limited to less than 0.02 [43, 59–61] the two low luminosity experiments are required to operate with a transverse offset resulting in a maximum tune shift of $1\text{--}2 \times 10^{-3}$. However, if the total beam-beam tune shift approaches 0.03 and it can not be tolerated, it can be mitigated for example, by blowing up the transverse emittances with controlled noise.

2.3.3 Dynamic aperture with triplet errors

Dynamic aperture (DA) studies were performed to evaluate the impact of errors on the magnets and analyse possible correction schemes to achieve the minimum DA necessary to ensure the stability of the beam.

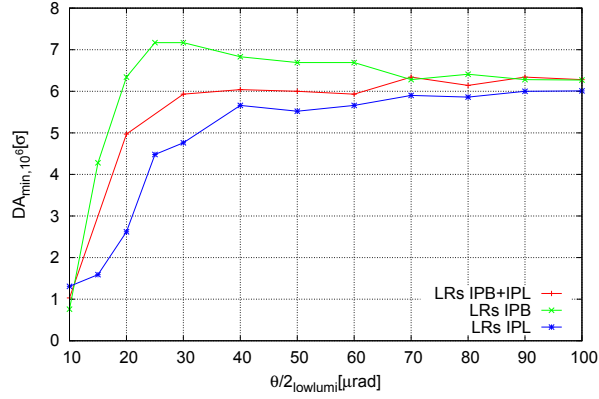


Figure 2.14: Minimum dynamic aperture, evaluated over 10^6 turns, as a function of the half crossing angle at IPB and IPL, including beam-beam long range interactions in IPB only (the green line), in IPL only (the blue line) and in both IPB and IPL (the red line) [56].

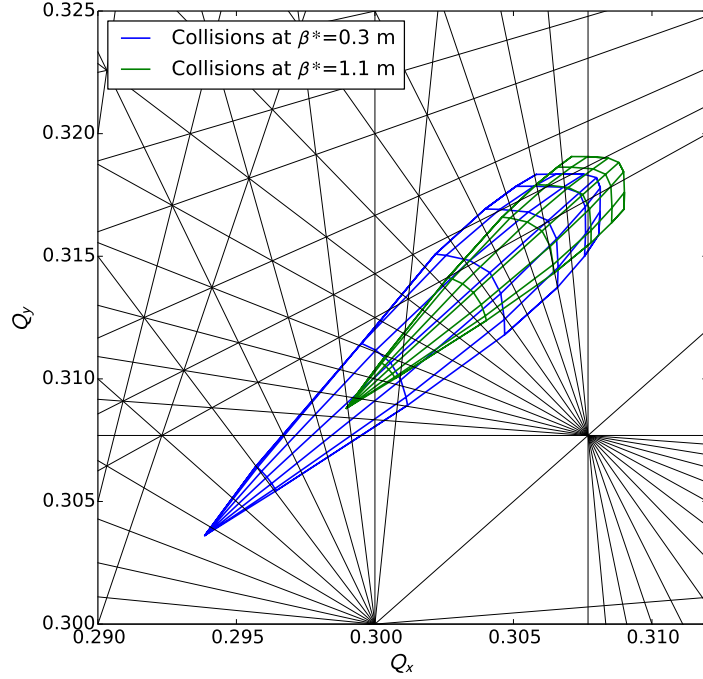


Figure 2.15: Two-dimensional tune footprints with head-on collisions in IPA and IPG for the baseline scenario with $\beta^* = 1.1$ m (green colour) and for the ultimate scenario $\beta^* = 0.3$ m with a reduced normalised emittance of $\epsilon_n = 1.5 \mu\text{m rad}$ (blue colour).

Given the large β functions and integrated length of the final focus triplet quadrupoles, the effects of systematic and random non-linear errors in the magnets had a severe impact on the stability of the beam. Therefore, DA studies at collision energy with errors on the triplet and crossing angle proved to be challenging. Several corrections were implemented to compensate for the DA reduction, but it was found that at collision energy two corrections were particularly important to achieve a DA above the target: to optimise the phase between the main IRs (IRA and IRG) and the implementation of non-linear correctors in the IR, to minimise the resonance driving terms arising from the errors in the triplet.

The minimum DA vs β^* at collision energy with errors on both the arcs and the triplets, and with and without non-linear correctors is shown on Fig. 2.16. A significant increase is observed in all cases when adding

the non-linear correctors, except for the case with $\beta^*=1.1$ m where the DA is already large without non-linear correctors. By optimising the phase advance and other corrections, the ultimate case with $\beta^*=0.3$ m shows a DA above the target of 10σ even without non-linear correctors. However, the use of non-linear correctors is still recommended in case other errors affect the DA. In the presence of beam-beam effects different optimised phases are required and detailed optimisation is necessary. The figure also shows dynamic apertures for optics with β^* below the ultimate 0.3 m. The use of non-linear correctors becomes essential for these cases. More details of the DA studies can be found in Section 7.5.

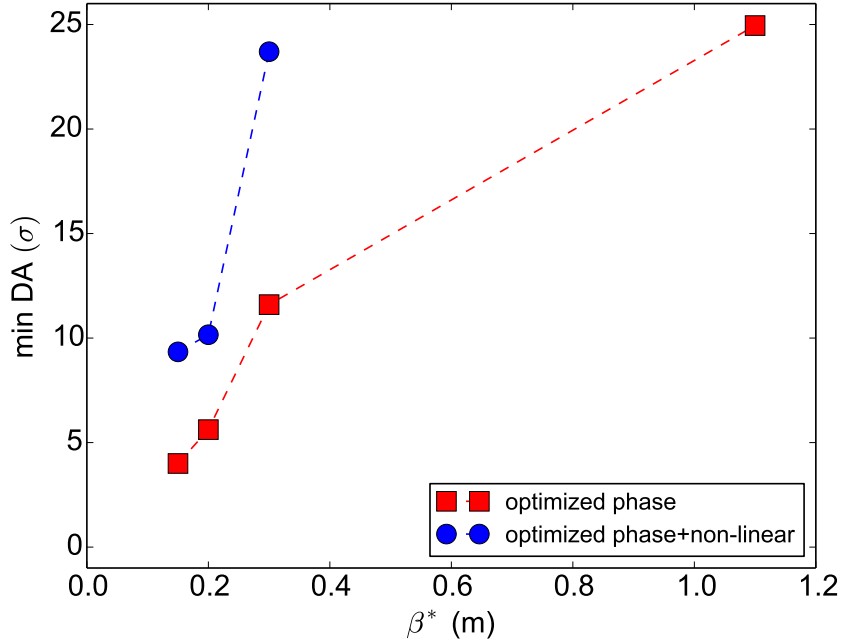


Figure 2.16: Minimum DA over 60 seeds versus β^* with and without non-linear correctors.

2.3.4 Crab cavities

In the long shared aperture section around the IP, the two counter rotating beams must be separated by an orbit bump in order to avoid the parasitic beam-beam encounters that occur every 3.75 m left and right of each IP. The two beams only cross each other at the IP with a crossing angle θ . The crossing angle determines the separation of the beam in the shared aperture and thus the long range beam-beam separations. The minimum crossing angle was determined by beam-beam studies to be $200 \mu\text{rad}$ for the ultimate β^* of 0.3 m and then scaled for other optics to provide the same normalised separation of $\approx 17\sigma$ for the maximum bunch intensity. Table 2.2 lists the crossing angle for a set of collision optics together with the luminosity reduction factor caused by the reduced geometric overlap of the bunches at the IP due to the crossing angle. For the ultimate optics and beyond, FCC-hh is not able to provide even half of the luminosity that head-on collisions would provide. It is clear that the luminosity reduction in the high luminosity EIRs must be compensated by crab cavities.

Table 2.2: Crossing angle and luminosity reduction due to crossing angle for different collision optics for an emittance of $\epsilon_n = 2.2 \mu\text{m}$.

| Optics version | β^* [m] | Full crossing angle [μrad] | Luminosity reduction factor |
|-----------------|---------------|---|-----------------------------|
| Baseline | 1.1 | 104 | 0.85 |
| Ultimate | 0.3 | 200 | 0.40 |
| Beyond ultimate | 0.2 | 245 | 0.28 |

Initial studies with crab cavities show that a crab voltage of 13.4 MV per beam on either side of each high luminosity IP is needed to provide full crabbing in the ultimate optics, corresponding to 107.2 MV in total. Half of this voltage must be horizontally deflecting in one EIR, the other half vertically deflecting in the other EIR. For

optics beyond ultimate parameters, the crab voltage increases up to 8×18.1 MV. Orbit leakage of the crab orbit into the arcs varied strongly during the evolution of the lattice. In the latest lattice version it appears to be small, causing only small orbit aberrations in the other IPs. More detailed studies should be performed to get a better control of the orbit leakage. The crab orbits and orbit leakage into the other high luminosity EIR are shown in Fig. 2.17 for ultimate optics.

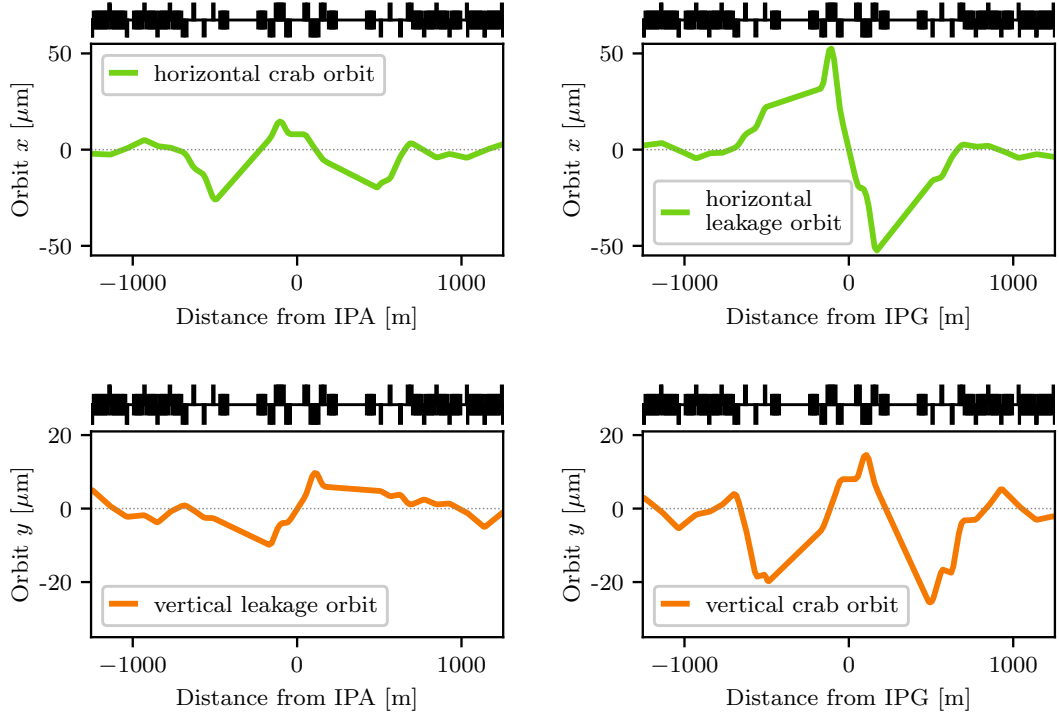


Figure 2.17: Crab orbits for $\beta^* = 0.3$ m and orbit leakage into the other high luminosity EIR.

2.4 Energy deposition from collision debris

Proton-proton inelastic collisions taking place in the FCC-hh, particularly in the two high luminosity detectors, generate a large number of secondary particles. Moving away from the interaction point (IP), this multiform population evolves even before interacting with the surrounding materials due to the decay of unstable particles such as neutral pions which decay into photon pairs. Most of these particles are intercepted by the detector and release their energy within the cavern. However, the most energetic particles, emitted at small angles with respect to the beam direction, travel farther inside the vacuum chamber and reach the accelerator elements, causing a significant impact on the magnets along the experiment insertion region (EIR), particularly in the final focusing quadrupoles and the separation dipoles. Figure 2.18 shows the particle population close to the interaction point and at the exit of the TAS: the average multiplicity of a single 100 TeV c.m. proton-proton inelastic interaction is ~ 255 . At ultimate instantaneous luminosity conditions ($30 \times 10^{34} \text{ cm}^{-2} \text{ s}^{-1}$), the 260 kW released toward each side of the IP impacts on the surrounding elements and is consequently dissipated in the machine, the nearby equipment (e.g. electronics racks) and the tunnel walls. How these particles are lost is studied in order to define the necessary protection to shield sensitive parts of the machine and in particular, the magnets.

In this context, Monte Carlo simulation of particle interaction with matter plays a crucial role and it relies on a detailed physics model and an accurate 3D description of the region of interest. The FLUKA code [62,63] has been extensively used in this conceptual design study which is based on the experience in the LHC and HL-LHC design [26] as well as the benchmarks available for these machines [64]. Figure 2.19 shows part of the FLUKA model of the EIR, for the latest layout available at the time of the simulation ($L^* = 40$ m) including 700 m of accelerator line with the inner triplet, the separation and recombination dipoles (D1 and D2), the target absorber secondaries (TAS), the target absorber neutrals (TAN) and the matching section (Q4-Q7). The following diametric

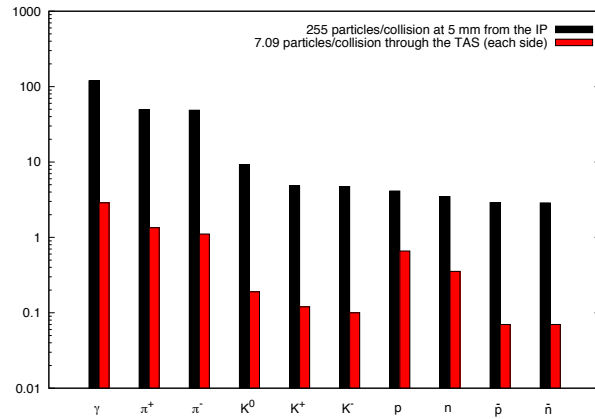


Figure 2.18: Collision debris from a single 100 TeV c.m. proton-proton inelastic reaction at 5 mm from the interaction point (black) and at the exit of the TAS (red) at 35 m from the IP.

coil apertures were used in the model: Q1 (MQXC) 164 mm, Q2 (MQXD) and Q3 (MQXE) 210 mm, orbit correctors 210 mm, Q4 (MQY) 70 mm, Q5 (MQYL) and Q6 (MQYL) 60 mm, Q7 (MQM) 50 mm. The matching section quadrupoles include a rectangle beamscreen modelled according to optics constraints. To protect the inner quadrupoles coils, a 35 mm thick tungsten shield was implemented in the mechanical design of the triplet magnets and the orbit correctors: the shielding thickness in this study is the maximum allowed in order to comply with optics requirements. The first separation dipole, D1 (MBXW), is a single aperture warm dipole, with a pole tip aperture of 170 mm. The TAN, made of a 4 m long tungsten absorber, includes twin diverging apertures of 52 mm. D2 (MBRW) is a twin aperture warm dipole: each module has been modelled with two parallel bores centred at a separation distance varying from the first to the last, in order to reach the value of 250 mm on the side away from the arc. Proton-proton collisions at 100 TeV c.m. with a vertical half crossing angle of $100 \mu\text{rad}$ have been simulated and the particle shower was tracked through all the accelerator elements [65, 66]. The study of the matching section requires an extreme computational effort to achieve a statistically meaningful outcome and therefore it is planned to be finalised at a later stage. Results for the triplet-D2 area are presented below.

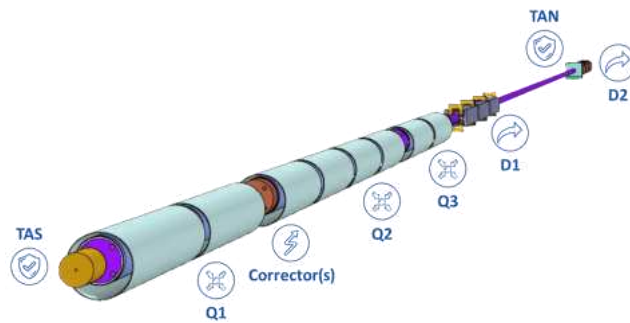


Figure 2.19: 3D rendering of the FLUKA geometry of the EIR, including ~ 700 m of beam line. The picture shows the first ~ 500 m including the TAS, the inner triplet, the TAN, the separation and recombination dipoles D1 and D2.

The total power deposited in the cold magnets (Table 2.3) is shared between the cold mass and the massive tungsten shielding, in a $\sim 15:85$ ratio. Q1B (MQXC.B1RA) turns out to be the most affected element of the triplet with a total power of about 2 kW in the cold mass and 13 kW in the shielding.

Figure 2.20 shows the absorbed power profile (in W/m) along the TAS-D2 region, where the triplet cold mass and shielding contributions are added. A linear power loss of ~ 150 W/m is reached in the Q1B cold mass. On the other hand, a preliminary evaluation based on the cooling capabilities of the beamscreen of the 16 T main

Table 2.3: Total power distribution in the EIR elements.

| Element | Total Power [kW] | | |
|--------------|------------------|-----------|-----------|
| | Cold Shielding | Cold Mass | Warm Mass |
| TAS.RA | | | 26.5 |
| MQXC.A1RA | 4.6 | 0.78 | |
| MQXC.B1RA | 13 | 1.92 | |
| MCBXDHV.A2RA | 0.06 | 0.06 | |
| MQXD.A2RA | 1.53 | 0.32 | |
| MQXD.B2RA | 0.7 | 0.09 | |
| MQXD.C2RA | 4.6 | 0.63 | |
| MQXD.D2RA | 5.93 | 0.81 | |
| MCBXDHV.B2RA | 0.51 | 0.05 | |
| MQXE.A3RA | 6.02 | 0.77 | |
| MQXE.B3RA | 7.8 | 0.95 | |
| MCBXCHV.3RA | 0.94 | 0.17 | |
| MBXW.A4RA | | | 4.99 |
| MBXW.B4RA | | | 3.57 |
| MBXW.C4RA | | | 3.57 |
| MBXW.D4RA | | | 3.96 |
| TAN.4RA | | | 107 |
| MBRW.A4RA | | | 0.07 |
| MBRW.B4RA | | | 0.01 |
| MBRW.C4RA | | | 0.003 |
| MBRW.D4RA | | | 0.002 |

dipoles, indicates that four helium tubes of 15 mm diameter, placed in a 45° pattern with respect to the mid planes, would allow the 13 kW (~ 0.8 kW/m) deposited in the Q1B shielding [66] to be dissipated. A mechanical design of shielding embedding such a cooling circuit is currently under investigation.

Figure 2.21 shows the peak power density profile in the triplet quadrupole coils, reaching a maximum of 5 mW/cm^3 at the end of the Q1B. This value matches a first conservative estimate of the quench limit with no margin. Studies to determine the latter more accurately are currently ongoing [67]. Recently, it has been shown that the 11 T Nb₃Sn HL-LHC dipoles are expected to withstand steady state loads ten times higher [68].

The absorbed dose in the magnet coils was calculated in order to estimate the integrated luminosity reach as a function of the insulator lifetime. Figure 2.22 shows the peak dose profile for the ultimate integrated luminosity goal (30 ab^{-1}). Assuming an operational limit of 30 MGy for conventional radiation resistant insulator materials, the most critical element (Q1B) exceeds this by a factor 2.5. As previously mentioned, the model already contains the maximum shielding thickness allowed by beam aperture requirements (35 mm). Nevertheless, a Q1 split featuring a larger Q1B aperture at the price of a lower gradient, to be compensated in the Q1A, would allow a corresponding increase of the shielding thickness, thereby reducing the maximum dose. Moreover, alternation of the crossing angle polarity and plane are known to significantly reduce the maximum dose, by distributing the radiation load in the coils more equally [65]. Finally, the dose limit might be increased by using insulators which are more resistant to radiation, e.g. epoxy/cyanate-ester blends [67]. Alternatively, the replacement of the inner triplet once during the FCC-hh era might be considered.

The peak dose profile in the warm dipole D1 is reported in Fig. 2.23. Both D1 and D2 have been modelled without embedding any shielding but with the return coils moved far from the beam pipe, to reduce their exposure to the collision debris. This solution provides a significant gain. However, the picture is rather similar to what was shown above for the triplet quadrupoles, with the peak dose in the first module (D1A) being three times the 30 MGy limit. In this case, a front mask as well as internal shielding can offer a substantial benefit. With regard to D2, the highest value expected at the D2A IP end is below 10 MGy, while peak doses ten times lower have been found in the D2C and D2D. As a result of the protection provided by the TAN, the D2 presents no major concerns

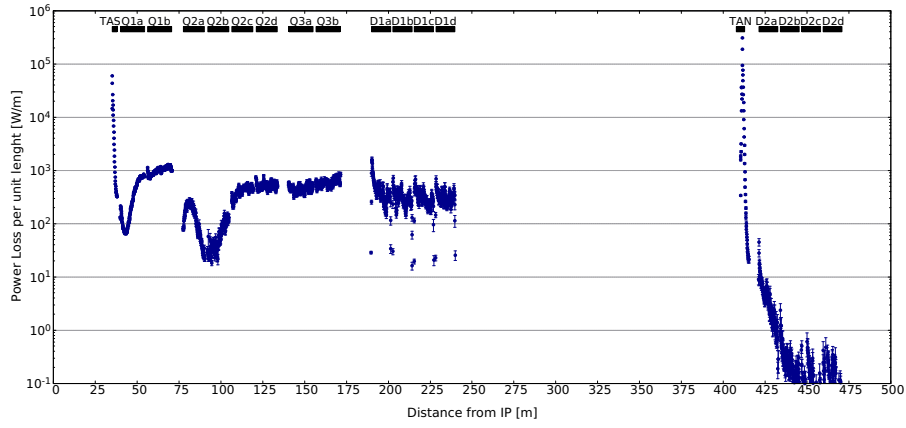


Figure 2.20: Absorbed power profile in the elements of the TAS-D2 region at the ultimate instantaneous luminosity of $30 \times 10^{34} \text{ cm}^{-2} \text{ s}^{-1}$.

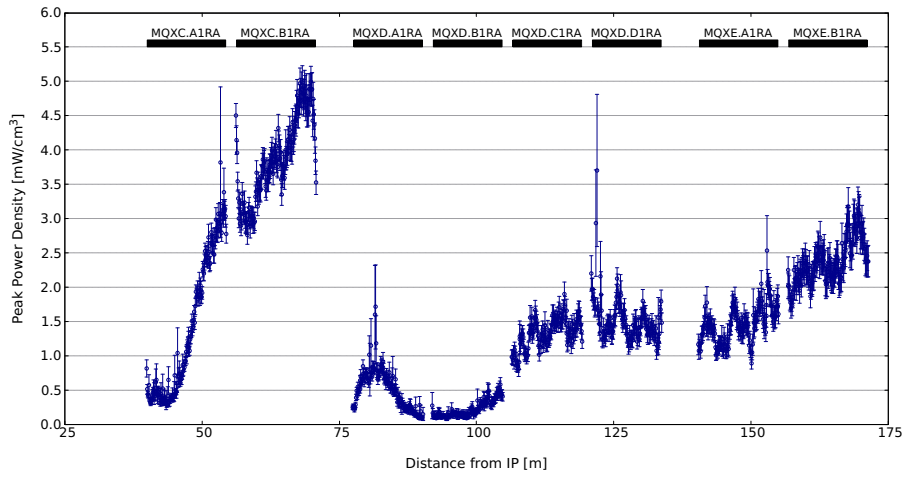


Figure 2.21: Peak power density profile in the triplet quadrupole coils at the ultimate instantaneous luminosity of $30 \times 10^{34} \text{ cm}^{-2} \text{ s}^{-1}$. Values are averaged over the radial cable thickness, with an azimuthal resolution of 2° . Vertical bars indicate the statistical error.

for the coil insulator lifetime, even for the ultimate integrated luminosity target.

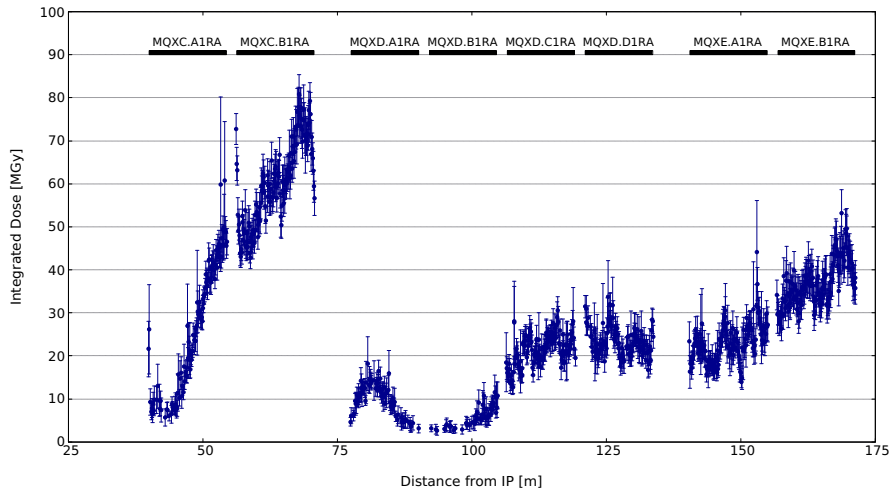


Figure 2.22: Peak dose profile in the triplet quadrupole coils for the ultimate integrated luminosity target (30 ab^{-1}). Values refer to a radial and azimuthal resolution of 3 mm and 2° , respectively. Vertical bars indicate the statistical error.

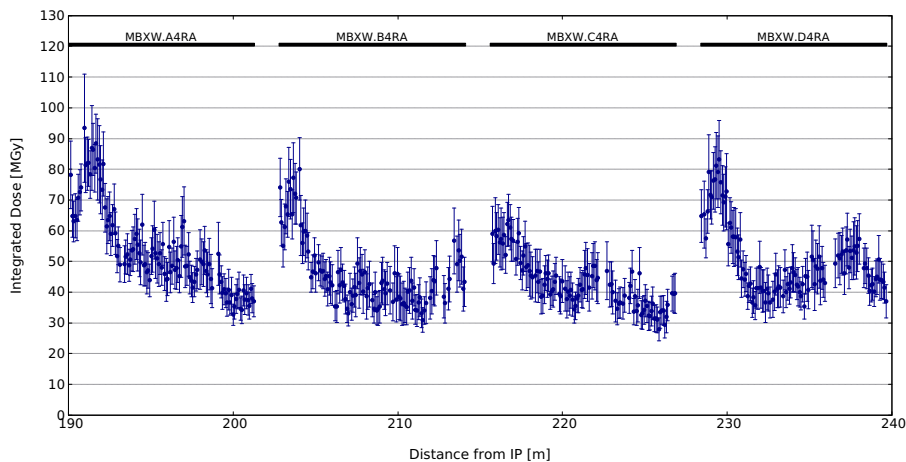


Figure 2.23: Peak dose profile in the D1 warm separation dipole coils for the ultimate integrated luminosity target (30 ab^{-1}). Values are averaged over a $3 \text{ mm} \times 3 \text{ mm}$ transverse area. Vertical bars indicate the statistical error.

2.5 Photon background from synchrotron radiation

The amount of power radiated by synchrotron radiation (SR) strongly depends on the relativistic Lorentz factor, γ , of the moving particle and thus on its energy to mass ratio: $P \propto \gamma^4 \rightarrow P \propto (E/m)^4$ [69].

SR emitted by protons is usually a very small source of backgrounds in the experiments due to their mass, even in very high energy proton beams such as LHC. However, in the FCC case, this possible source of background should be carefully evaluated.

The critical energy of the SR emitted scales with the Lorentz factor γ and bending radius ρ according to γ^3/ρ . While the increase of FCC-hh centre-of-mass energy with respect to the LHC is about a factor 7, the critical energy of emitted photons increases by a factor 100, shifting the energy spectrum from hard ultraviolet for LHC (which is easily absorbed) into soft X-rays of several keV for FCC. Since the beryllium of the inner beam pipe starts to become transparent at these energies, some of these photons could traverse the beam pipe and potentially generate background in the detectors.

A specific software tool has been developed, validated and used for this study. MDISim [70] is a toolkit that combines existing standard tools MAD-X [71], ROOT [72] and GEANT4 [73]. It reads the MAD-X optics files,

and it uses its Twiss (and optionally Survey) output file to export the geometry and the magnetic field information in a format which can be directly imported in GEANT4 to perform particle tracking, including the generation of secondaries and detailed modelling of the relevant absorption processes.

Based on the baseline and ultimate optics where β^* is 1.1 m and 0.3 m respectively, lattice version LATTICE_V9 has been used for this study. The free length between the IP and the first quadrupole L^* is 40 m. MDISim has been used to reconstruct the region from -700 m to 700 m around the interaction point A (IPA), see Fig. 2.24 for a top view. The study also applies to the second interaction point, IPG, that has the same design and is located approximately 50 km away from IPA.

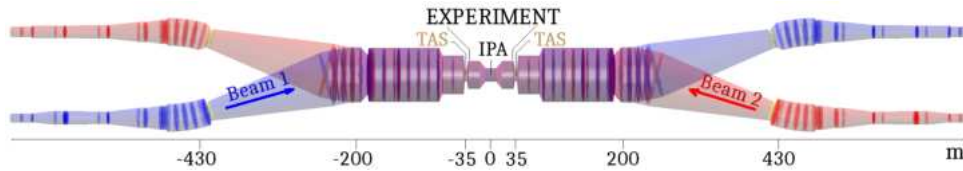


Figure 2.24: FCC-hh interaction region top view from MDISim, from -700 m to 700 m. The beam pipe is in blue for beam 1 and in red for beam 2. The transverse dimensions have been scaled up 500 times for visualisation.

The beam pipe apertures upstream and downstream of IPA are symmetrical. From IPA to ± 8 m, the beam pipe is made of 0.8 mm thick beryllium with an inner radius of 20 mm, making it a critical region due to its proximity to the vertex detector. The following 8 m are covered by a beryllium cone with an opening angle of 2.5 mrad. From ± 16 m to ± 35 m, the material is aluminium and the beam pipe radius is 40 mm. The entire detector layout occupies the region between ± 25 m, followed by a forward shielding section from ± 25 m to ± 35 m. At ± 35 m from IPA, outside the detector and shield area, the target absorber secondaries (TAS), with 20 mm radius apertures, protect the insertion quadrupoles from collision debris. The radii of the aperture outside the region between the two TAS are larger than 56 mm, up to the TAN collimator at ± 412 m where it is reduced to 29 mm.

The dipoles in the experiment region shown in Fig. 2.24 are 2 T magnets 11.3 m long, unlike the nominal arc dipoles which have a field of 16 T. These low field dipoles are located at about 200 m and 430 m, upstream and downstream of IPA, providing a bending angle of 135 μ rad each. The aim of the study was to evaluate the SR which comes from these dipoles and enters the TAS, or crosses the beryllium beam pipe from -8 m to 8 m around IPA and which might strike the detector. Figure 2.25 shows a zoom of this region.

The TAS was chosen as the reference position. The power of the photons passing through the TAS is input data and where these photons were generated is determined in detail, the energy spectra and hit positions downstream are calculated and the fraction of photons hitting the inner beryllium pipe is determined.

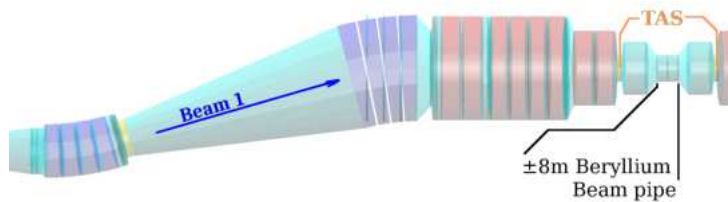


Figure 2.25: Top view of the beam pipe 3D-model obtained with MDISim. Dipoles are in violet, drifts in light blue, quadrupoles in orange, collimators in yellow.

Table 2.4 gives the exact longitudinal position of the last eight dipoles 470 m upstream of the IPA. The critical energy in the dipoles is 0.536 keV, the mean energy 0.165 keV and the power emitted by each dipole is 6.4 W. In total, their emitted power is about 50 W. However, only a fraction of these photons will reach the experiment area, due the geometry and to the presence of the TAS, and even fewer of them will hit the ± 8 m beryllium beam pipe.

As described above MDISim was used to produce the description of the geometry and the magnetic field. GEANT4 has been used to perform the detailed simulation, starting at approximately -700 m from IPA with a Gaussian beam with the expected size and emittance. These protons were tracked with the Monte Carlo algorithm,

Table 2.4: Longitudinal position of the last eight dipoles 470 m upstream the IPA. They all have a field of 2 T and are 11.3 m long, their critical energy is 0.536 keV, the mean energy is 0.165 keV and each emits a power of 6.4 W. In total, the emitted power is about 50 W.

| Dipole name | Distance from IPA [m] |
|--------------|-----------------------|
| MBXW.A4LA.H | 190.0 |
| MBXW.B4LA.H | 202.8 |
| MBXW.C4LA.H | 215.6 |
| MBXW.D4LA.H | 228.4 |
| MBRW.A4LA.H1 | 421.3 |
| MBRW.B4LA.H1 | 434.1 |
| MBRW.C4LA.H1 | 446.9 |
| MBRW.D4LA.H1 | 459.7 |

taking into account the production of SR photons and their subsequent propagation. The baseline and ultimate optics were used with and without the horizontal crossing angle for this study. The results of this simulation, summarised in Table 2.5, suggest that about 10 W are expected to enter the experiment area with no crossing angle. The power of the photon flux at the inner beryllium pipe located from -8 m to 8 m around IPA remains below 1 W. A possible 10 Tm spectrometer placed around the detector would increase this value by one Watt. Even if the power deposited on the beryllium pipe remains small, the simulations show that the number of photons is significant and merits closer investigation. To evaluate the quantity of particles that can pass through the beryllium, a more localised GEANT4 simulation was used. The photon energy spectra obtained from the beams was used for photons striking the 0.8 mm beryllium pipe at a grazing angle of $200 \mu\text{rad}$, to compute an upper limit for the ultimate crossing angle.

Table 2.5: Summary of the SR power emitted per beam in the last 700 m upstream of IPA that reaches the experiment area P_{TAS} , and the fraction that impacts the inner Be beam pipe P_{Be} , for the baseline and ultimate configurations with and without crossing angle. The number of photons hitting the Be, $N_{\gamma Be}$ and their mean energy E_{mBe} are also shown.

| Lattice | Version | Half Crossing Angle μrad | P_{TAS} [W] | P_{Be} [W] | $N_{\gamma Be}$ [10^9] | E_{mBe} [keV] |
|----------|------------|-------------------------------------|---------------|--------------|----------------------------|-----------------|
| Baseline | LATTICE_V9 | 0 | 8.5 | 0.74 | 1.1 | 0.166 |
| Ultimate | LATTICE_V9 | 0 | 8.7 | 0.73 | 1.1 | 0.163 |
| Baseline | LATTICE_V9 | 52 | 26.5 | 1.17 | 1.8 | 0.163 |
| Ultimate | LATTICE_V9 | 100 | 46.4 | 12.86 | 16.0 | 0.198 |

Table 2.5 summarises the study of the SR impacting equipment in the experiment area. Without crossing angle, the SR emitted in the last magnetic elements upstream of IPA by protons in the beam, is small and is only a minor source of background for the experiments. With crossing angle, there is a small increase in power and a more significant increase in the number of photons reaching the experiment area. A small part of the increase is due to the extra SR generated by the field of the corrector magnets that generate the crossing angle (shown in Table 2.6). The

Table 2.6: Correctors upstream of IPA used in the optics lattices with crossing angle.

| Corrector name | Distance to IPA [m] | Length [m] | B field [T] | |
|----------------|---------------------|------------|-------------|----------|
| | | | Baseline | Ultimate |
| MCBXDHV.A2LA.H | 75.8 | 1.3 | -0.168 | -0.562 |
| MCBXCHV.3LA.H | 174.2 | 1.3 | 1.226 | 1.957 |
| MCBRDH.4LA.H1 | 474.0 | 3.0 | -0.821 | -1.536 |

power from the SR of the corrector magnets is 0.6 W for the baseline and 1.8 W for the ultimate lattices, or a rather small increase compared to the power produced by the 11.3 m long 2 T dipoles. Figure 2.26 shows the z-position

at the origin of the photons reaching the TAS. It can be seen that without crossing angle (left plot of Fig. 2.26), almost all photons entering the experiment originate in the 2 T dipoles located -450 and -200 m upstream of IPA, and that only few of these hit the beryllium beam pipe. The simulation includes the SR from quadrupoles which significantly increases with crossing angle over the last 100 m as can be seen in Fig. 2.26. With crossing angles many of these photons and in particular those generated by the quadrupole magnets MQXD.A2LA.H at -77.6 m and MQXC.B1LA.H at -56.3 m will hit the beryllium pipe. The magnetic field gradient of the quadrupoles in

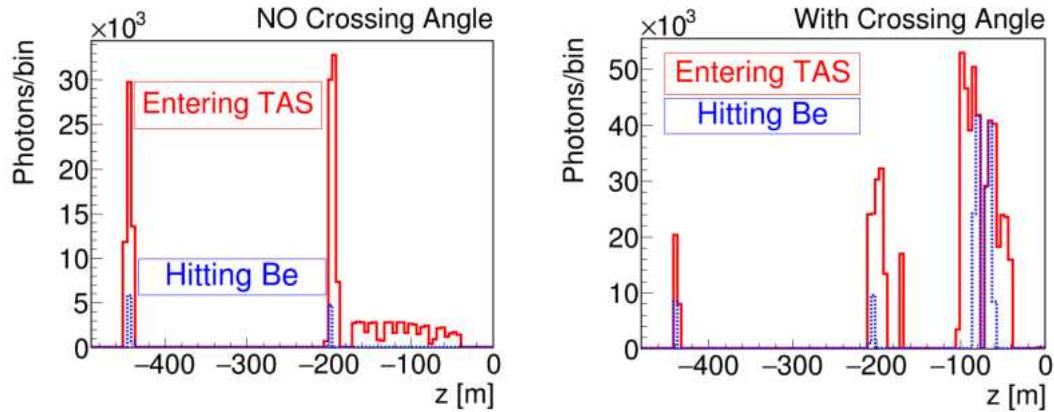


Figure 2.26: Histogram of SR photon generation upstream of IPA for the ultimate optics, where IPA is at $z = 0$. **Left:** The two peaks at -450 and -200 m are photons produced by 2 T dipoles that reach the two TAS regions (in red), but few of them hit the Be pipe (in blue). In addition, few photons are generated by quadrupole magnets downstream -200 m, and none of them hit the Be beam pipe. **Right:** With crossing angle, additional radiation comes from quadrupole magnets in the last 100 m. Radiation coming from MQXD.A2LA.H at -77.6 m and MQXC.B1LA.H at -56.3 m hits the Be pipe.

the last 100 m does not vary much amongst the various optics configurations. Much of the increase with crossing angle is from the last quadrupoles.

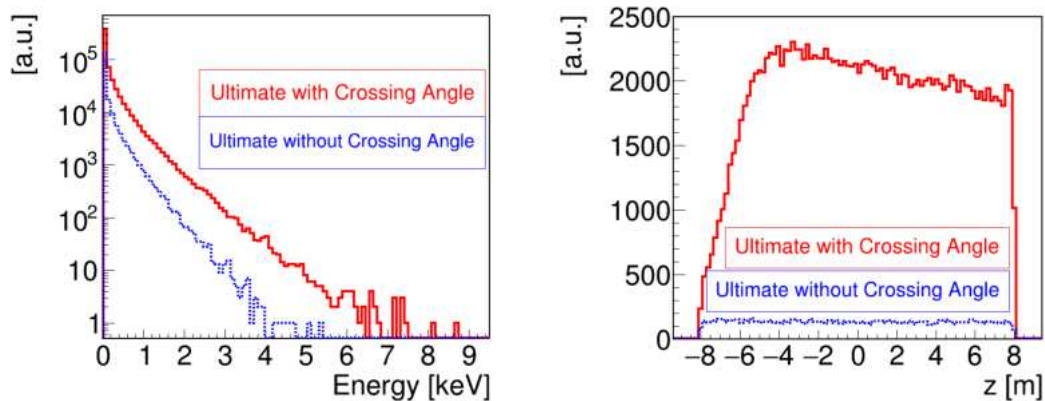


Figure 2.27: Left: Photon energy distribution entering the TAS with crossing angle (in red), and without crossing angle (in blue) for the ultimate optics. **Right:** Photons hitting in the last -8 m to 8 m Be beam pipe around IPA which is located at $z = 0$. Without crossing angle (in blue) the photons are uniformly distributed, while with crossing angle (in red) they accumulate towards the centre.

The contribution of SR photons in the experiment area has been addressed using GEANT4 and MDISim and similar studies were also carried out for other lattice versions [74] and the results have been benchmarked with SYNRAD [75], and very good agreement was found. The results of this work show that the synchrotron radiation backgrounds are not expected to be an issue in the experiment areas.

2.6 Alternative triplet and flat optics

In parallel with the design of the final focus triplet described in Section 2.3.1, an alternative triplet has been designed [76]. This alternative was produced using an algorithm that systematically scans the parameter space to find the shortest possible triplet that has a sufficient beam stay clear region and shielding [77]. In a first approximation, the code scans through the entire parameter space using the thin lens approximation to estimate the beam stay clear region. It then does a more precise scan using the MAD-X aperture module in a smaller area identified by the approximation.

The design was worked on iteratively with energy deposition studies to determine the right amount of shielding required to protect the triplet from the collision debris. In a first iteration, the optimisation code was used to find the shortest triplet with 1.5 cm of tungsten shielding. This triplet was integrated into the baseline EIR and energy deposition studies were performed to estimate the amount of shielding needed. Next, the triplet was optimised again with the new shielding estimate and again integrated and tested. This process was repeated several times until a triplet was found that is as short as possible whilst still having sufficient beam stay clear region and shielding.

In the course of this optimisation it was found that peaks in energy deposition could be minimised if all triplet quadrupoles had similar coil radii [78, 79]. Therefore, the optimisation code was modified to find triplets made of quadrupoles of equal radii. In order to fulfil the technical requirements, the quadrupoles of the ideal solution had to be split into sub-magnets that were no longer than 15 m. The resulting triplet consisted of seven 15 m sub-magnets with equal radii and similar gradients. The details of the magnets in this triplet are shown in Table 2.7. Like the baseline triplet, the main quadrupoles in the alternative triplet are separated by 7 m drifts to leave space for correctors and instrumentation, whilst the sub-magnets only need a 2 m separation for connectors.

Table 2.7: Properties of quadrupole groups in the alternative triplet.

| Parameter | Quadrupole | | |
|-----------------------|------------|------|------|
| | Q1 | Q2 | Q3 |
| Sub-Magnets | 2 | 3 | 2 |
| Sub-Magnet Length [m] | 15 | 15 | 15 |
| Coil Radius [mm] | 96.5 | 96.5 | 96.5 |
| Gradient [T/m] | 106 | 112 | 99 |
| Shielding [mm] | 44.2 | 33.2 | 24.2 |

The triplet was integrated in the same EIR as in Section 2.3.1, leaving the same 18.8 m drift between Q3 and the first separation dipole for the correction package. The matching quadrupoles in the EIR were used to match the Twiss functions to the arc. The resulting optics in the triplet are shown in Fig. 2.28, which also shows the beam orbit for a 200 μ rad crossing angle in the horizontal plane.

Once the triplet was integrated, the beam stay clear region in the individual quadrupoles was reassessed and the shielding was increased wherever possible. This led to an increase in shielding in Q2 and Q1 by 9 mm and 20 mm respectively. These increases are possible because the β functions and orbit are smaller near the front of the triplet, leaving more space for potential shielding. This distribution in shielding is advantageous since most of the collision debris will hit the magnets closer to the IP. The exact amounts of shielding are also shown in Table 2.7.

Whilst the ultimate collision optics aims for a $\beta_{x,y}^*$ of 0.3 m, the shielding was designed to leave 15.5σ for an optics with a $\beta_{x,y}^*$ of 0.2 m to provide a luminosity handle. The aperture studies were performed using the same technical specifications for the cooling, cold bore and beamscreen as outlined in Section 2.3.1 and the results are shown in Fig. 2.29. As one can see from Fig. 2.29, the alternative triplet can comfortably reach a β^* of 0.3 m and even 0.2 m. Figure 2.29 also shows the beam stay clear region for a case with $\beta^* = 0.15$ m, whilst this is lower than required it may still be a viable option should the beam current be low enough to adjust the collimator settings accordingly. A low beam current may be one of the reasons why the β^* would need to be decreased to compensate for the consequent loss in luminosity.

The alternative triplet can also be used for a flat optics, which can be exploited to compensate for the luminosity loss in case of any problem with the crab cavities [78, 80]. This can be achieved without changing the gradients in the triplet but re-matching the β functions using the matching section quadrupoles. In this initial study a 1.2 m \times 0.15 m flat optics was assumed but further detailed studies should be conducted. Table 2.8 shows a comparison between the main parameters of the round and flat optics.

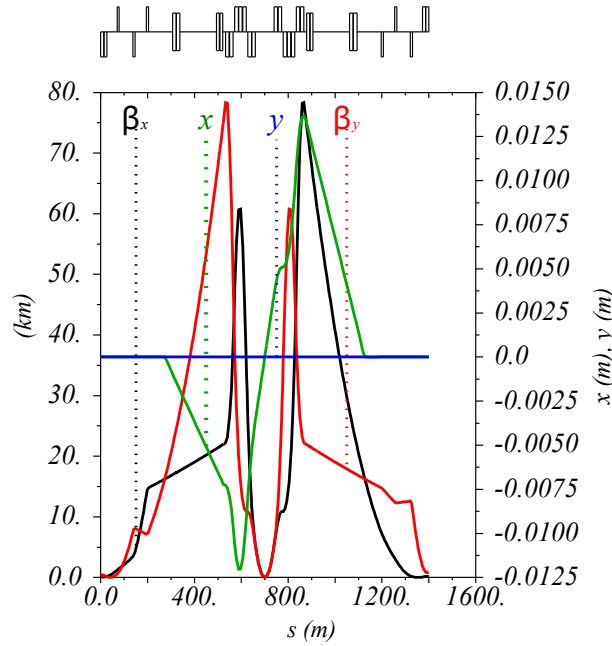


Figure 2.28: β functions and orbit for EIR optics with alternative triplet and $\beta_{x,y}^* = 0.3$ m.

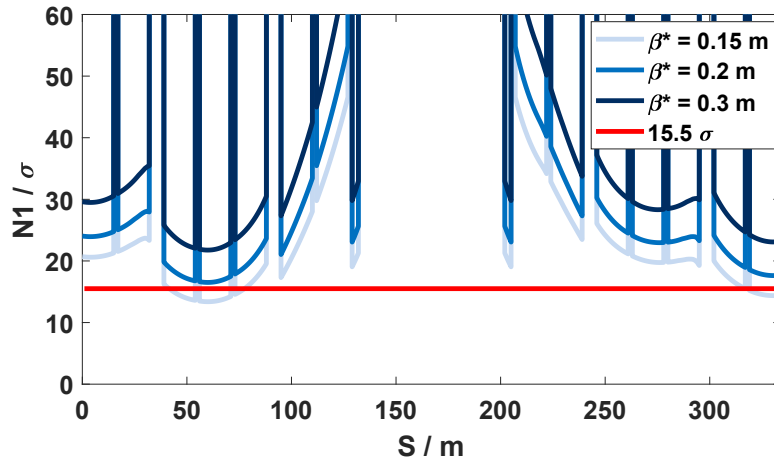


Figure 2.29: Plot showing BSC region for $\beta^* = 0.15$ m, 0.2 m and 0.3 m for the alternative triplet.

Beam-beam studies have shown that with the flat optics an increase in beam to beam separations is required at the long-range encounters in order to keep the dynamic aperture similar to the equivalent round optics case. This is because the tune of the particles differ from the round case. Therefore the normalised separation for the flat optics is set at a value 30% higher than for round optics by increasing the crossing angle. The average tune shift can be corrected. However, the variation of the tune with particle amplitude also differs from the round case leading to the beam occupying a different tune space compared to the round case. Preliminary results can be found in Ref. [81]. For a final beta ratio of 8, an 80% larger normalised beam separation is needed. However thanks to

Table 2.8: Parameters of the various optics for the alternative triplet.

| Parameter | Round | Flat |
|-----------------------------------|-------|------|
| β_x^* [m] | 0.3 | 1.2 |
| β_y^* [m] | 0.3 | 0.15 |
| Full crossing angle [μ rad] | 200 | 130 |
| Beam-beam separation [σ] | 17 | 22 |

the collide and squeeze scheme this is only required when the beam emittances have shrunk significantly and the beam intensities have reduced by 10%. It is therefore assumed that only a 30% larger normalised separation is required for this study.

Figure 2.30 shows the EIR optics for the flat option. The corresponding BSC regions are shown in Fig. 2.31. The flat optics still provides sufficient BSC.

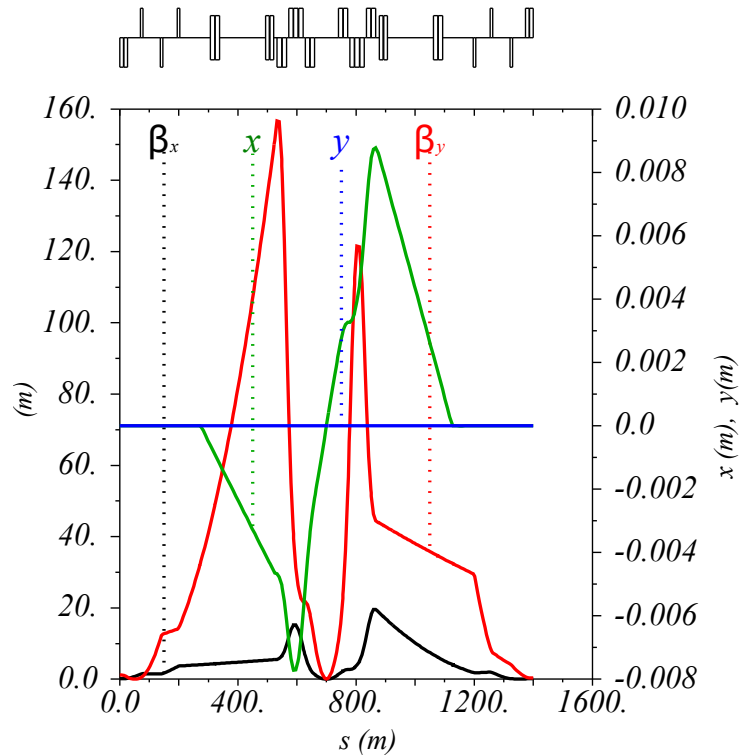


Figure 2.30: β Functions and orbit for 1.2×0.15 m flat EIR collision optics with alternative triplet and $\beta_x^* = 1.2$ m, $\beta_y^* = 0.15$ m.

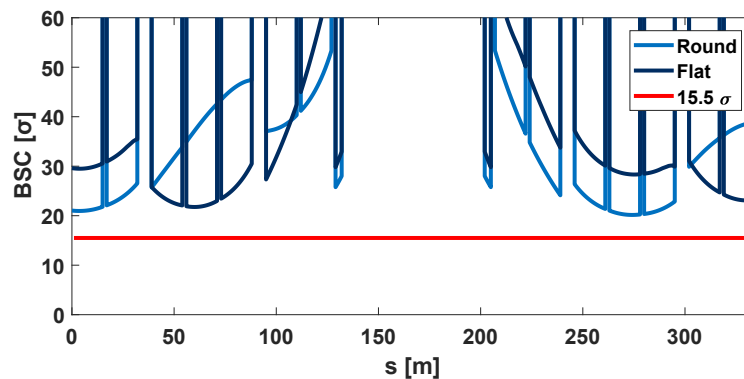


Figure 2.31: Plot showing BSC in triplet for flat and round optics.

2.6.1 Energy deposition in the alternative triplet

Figure 2.32 shows the peak dose in the triplet magnets along the longitudinal axis. The maximum dose is found at Q3, with a maximum of $30 \text{ MGy}/10 \text{ ab}^{-1}$ (excluding the peak at the beginning, that can be reduced by reducing the missing gap for the interconnects). Which means that if the magnet can withstand 65 MGy in its entire life, an integrated luminosity of 18.5 ab^{-1} can be achieved. The dose can also be reduced when using the alternate crossing scheme, in a similar way as for the baseline triplet [33, 65]. The peak dose profile for the alternative flat

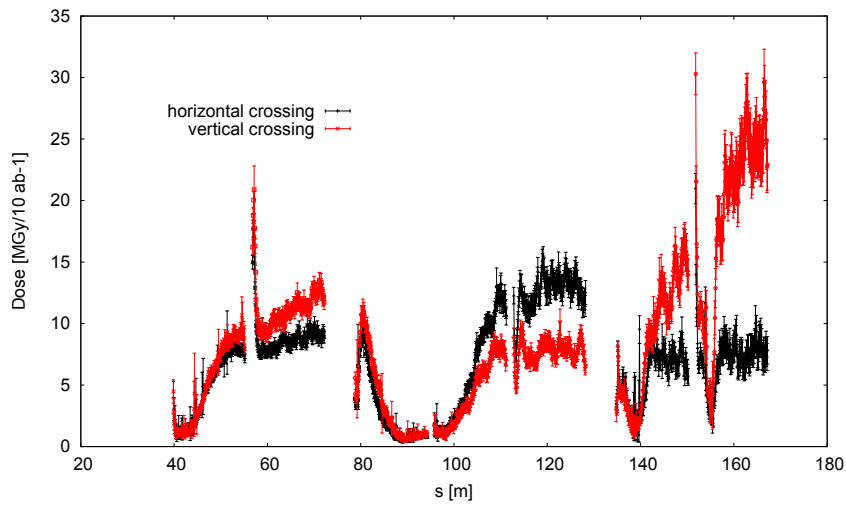


Figure 2.32: Peak dose profile for alternative triplet (round optics).

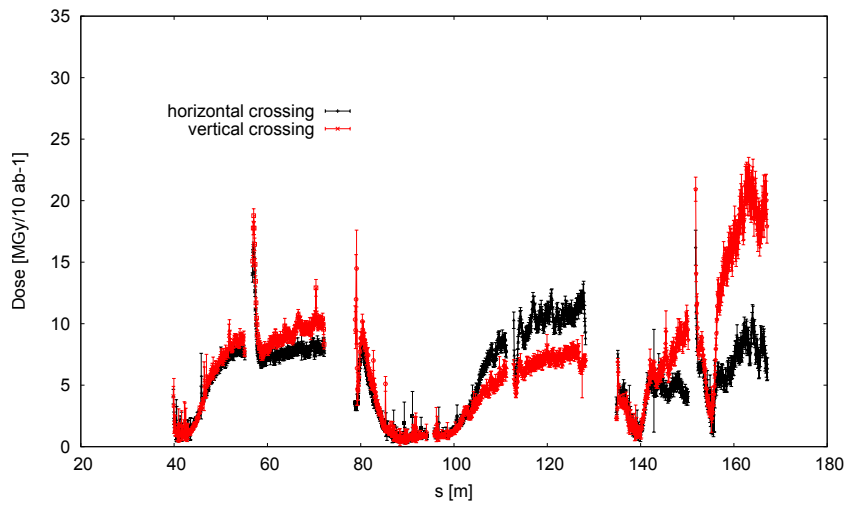


Figure 2.33: Peak dose profile for the alternative triplet (flat optics).

beam option is shown in Fig. 2.33. The peak dose is reduced to from 55 to 42 MGy for 18.5 ab^{-1} , due to the lower crossing angle allowed by the flat beam optics.

2.7 Low luminosity EIRs

In addition to the high luminosity IRs located in Points PA and PG, the FCC-hh will also host two low luminosity experiment insertions in Points PB and PL. Like the LHC, beams will be injected upstream of the experiments in these insertions. Following initial injection hardware considerations, the length of half cells containing injection equipment has been set to 150 m. Unlike the LHC injection/experiment insertions, two additional half cells were added after the injection cells. These give the possibility of adding more elements to protect both the superconducting magnets and experiment from mis-injected beam. As a result of this, the interaction point is not located in the centre of the straight section but rather 250 m further downstream. Unlike the high luminosity experiment insertions, currently no performance requirements have been specified for these low luminosity experiments and consequently no target β^* can be specified. Similarly, due to the lack of a detector design and required cavern length, the L^* has been tentatively set to 25 m. The layout of this combined injection/experiment insertion for Point PB based on these considerations is presented in Fig. 2.34.

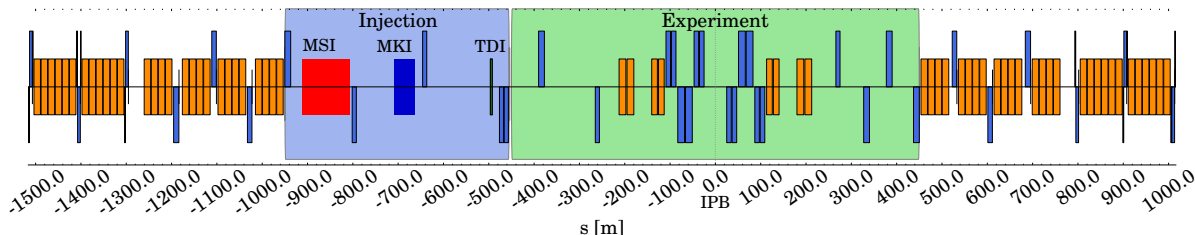


Figure 2.34: Layout of the low luminosity insertion in Point B.

The final focus triplet left and right of the interaction point consists of three quadrupoles. Each of these quadrupoles is split into two submagnets to keep the magnet length below 15 m. Each of the Q1 and Q3 submagnets has a length of 10 m whereas each Q2 submagnet is 15 m long. A 2 m long drift space has been reserved for the interconnects between each submagnet. All triplet quadrupoles have the same coil aperture of 64 mm. The specifications of the triplet quadrupoles can be found in Table 2.16. This aperture is further reduced, by the presence inside the coil of a liquid helium layer, a kapton insulator layer and the stainless steel cold bore, as described in Section 2.3.1. Finally a 10 mm thick tungsten (INERMET180) shield is put inside the cold bore to protect the superconducting coils. The radial aperture available for the beam is therefore reduced to 18.25 mm.

In order to keep the separation section after the triplet as short as possible, a superconducting solution was chosen. Using two 12.5 m long shared aperture separation dipoles, D1, with a field strength of 12 T and two 15 m long double aperture recombination dipoles, D2, with a field strength of 10 T, the length of this section can be kept under 100 m. Due to the aforementioned injection hardware constraints and the additional cells, the matching sections in these insertions feature a different length and layout.

On the non-injection side of the insertion, four matching quadrupoles make up the matching section which is 235 m long. The 735 m long matching section on the injection side of the insertion comprises six matching quadrupoles. The injection septum (MSI) which deflects the injected beam in the vertical plane is located between Q8 and Q9. The injection kicker system (MKI) which provides a horizontal kick to put the injected beam on the closed orbit is installed in the following half cell between Q7 and Q8. The quadrupole, Q8, between the MSI and the MKI was chosen to be horizontally defocussing to provide an additional horizontal kick which helps to reduce the kick strength of the injection kickers. A 4 m long absorber (TDI) is installed in the cell between Q6 and Q7 to protect superconducting magnets further downstream from mis-injected beam. Each of these half cells is 150 m long.

Both the optics for collision energy and injection energy are presented in Fig. 2.35. At collision energy a minimum β^* of 3 m has been matched. The crossing angle for these insertions has been obtained by scaling the normalised separation of the high luminosity insertion [82] by the reduced number of long range encounters. This leads to a normalised separation of 5.25σ , corresponding to a half crossing angle of $19.5 \mu\text{rad}$. With this crossing angle, the beam stay clear region in the triplet is well above the minimum allowed value of 15.5σ and could be further increased, as illustrated in Fig. 2.36. However, a crossing angle of $180 \mu\text{rad}$ at full intensity as detailed in Section 2.3.2 would lead to a beam stay clear value below the limit of 15.5σ . To comply with both constraints, the β^* at the beginning of collisions has to be set to 19 m. The minimum β^* of 3 m could then be reached after 1.5 hours, assuming a reduction of the separation to 20σ at this time. During collision, the beams always collide with a transverse offset to keep the head-on beam-beam tune shift from these two experiments below $1-2 \times 10^{-3}$.

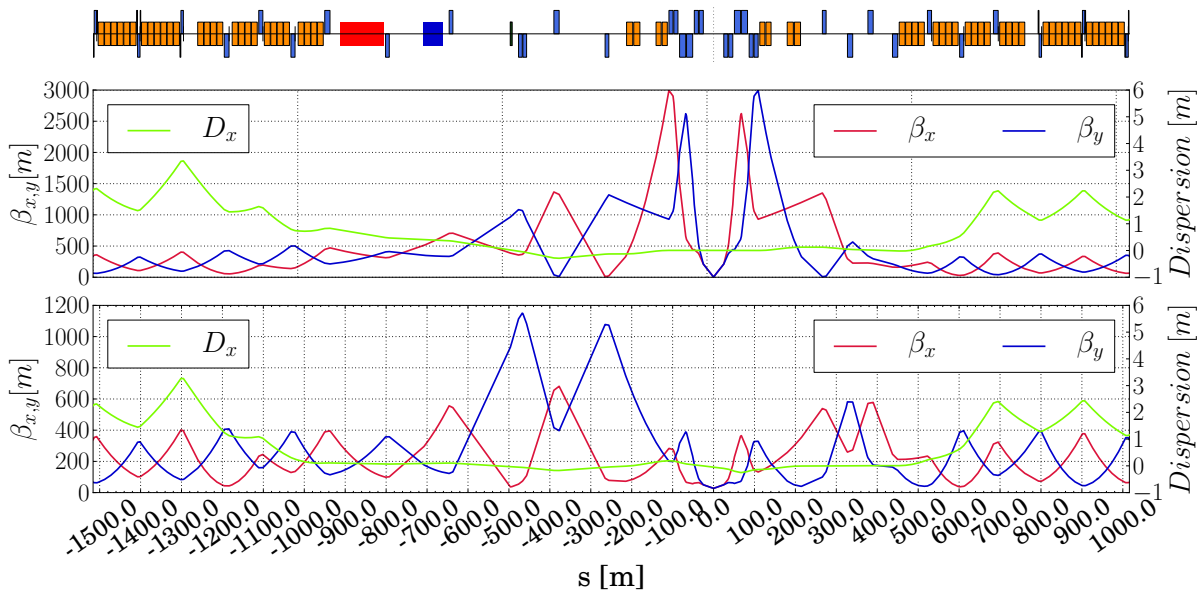


Figure 2.35: Collision optics (top) and injection optics (bottom) for the low luminosity insertion in Point B.

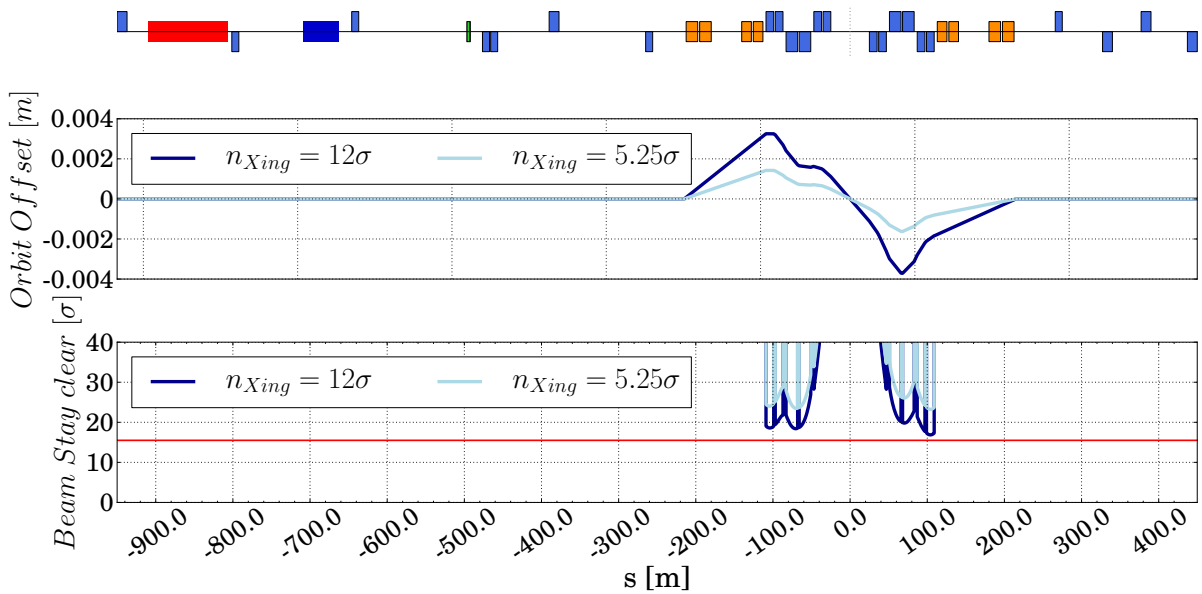


Figure 2.36: Crossing angle and corresponding aperture in the low luminosity insertion in Point B. The minimum allowed beam stay clear of 15.5σ is indicated in red.

At injection energy, the crossing angle is limited by the triplet aperture to a beam separation of 7σ . Further studies are required to assess the viability of this separation. If the separation proves to be insufficient, the shielding in the triplet could be reduced, in turn potentially also decreasing the achievable integrated luminosity.

For the injection optics various constraints had to be taken into account to provide optimum injection protection efficiency. The horizontal phase advance between the MKI and the TDI should be 90° to ensure that any kicker failure translates into an orbit offset at the TDI. The beta functions at the TDI were matched to the largest possible values to increase the beam size which in turn reduces the peak energy density in case of an injection kicker malfunction. Furthermore, the dispersion function in the straight section is kept below 30 cm.

As the injection of beam 2 will take place in Point PL the low luminosity insertion for this straight section is mirrored with respect to s . Here the interaction point is located 250 m upstream of the middle of the straight section for beam 1. Both the collision optics with a β^* of 3 m and injection optics with a β^* of 27 m are illustrated

in Fig. 2.37.

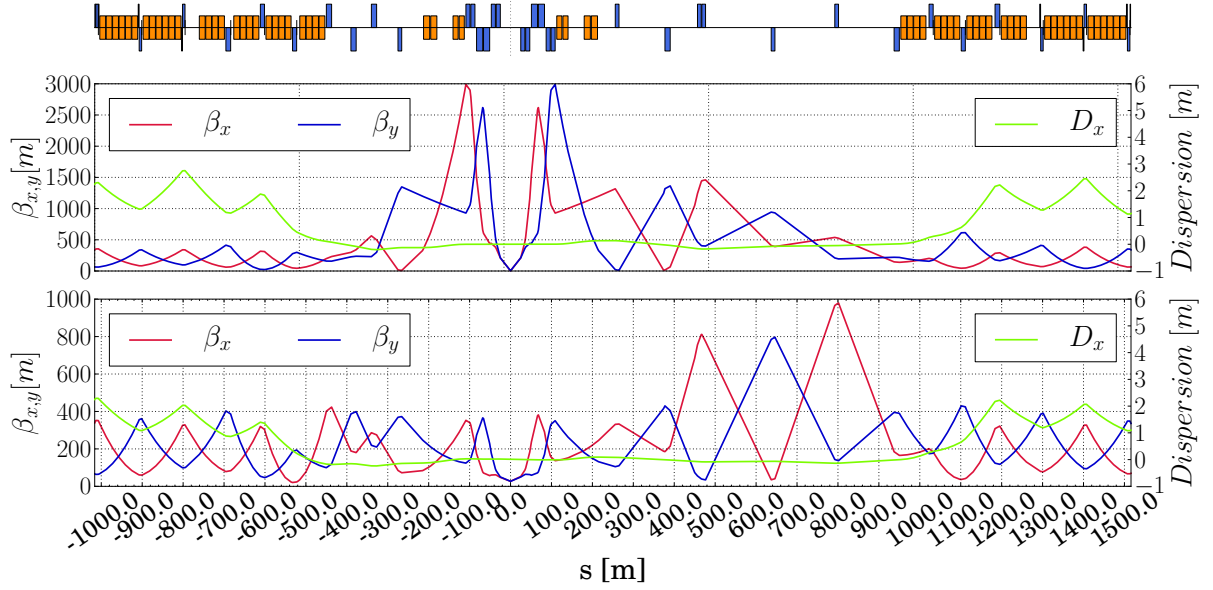


Figure 2.37: Collision optics (top) and injection optics (bottom) for the low luminosity insertion in Point L.

2.7.1 Energy deposition in the low luminosity EIR

The energy deposition in the low luminosity EIR has been assessed using FLUKA simulations, for both vertical and horizontal crossings. The insertion region has been modelled as shown in Fig. 2.38 for this purpose. The quadrupole design is very similar to the one for the main EIR described in Section 2.3.1, but the model has been scaled down to cope with the smaller coil radius of 32 mm. In order to better protect the superconducting magnets, the 10 mm thick tungsten shielding is prolonged in the interconnect cold bore, with tentative gaps of 700 mm. In addition to this, a mask has been put in front of Q1A, to shield its entrance. The mask is clearly visible in Fig. 2.38 and it is modelled as a 760 mm long tungsten (INERMET180) cylinder with an external radius of 81 mm and a free radial aperture of 13.26 mm.

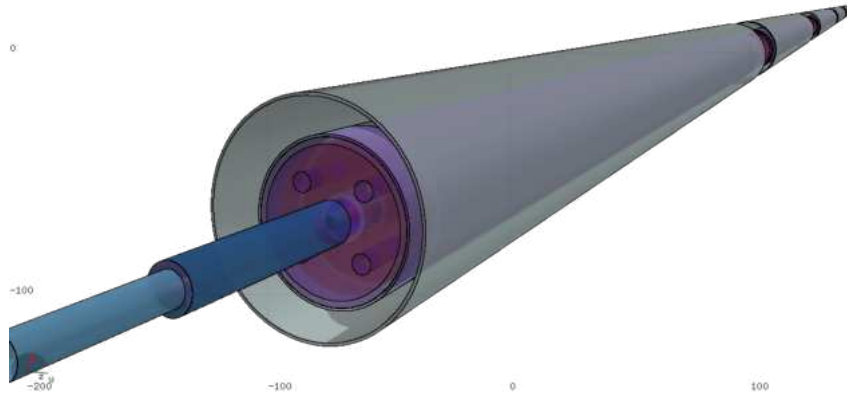


Figure 2.38: Low luminosity triplet geometry as modelled in FLUKA.

The power impacting on each magnet is listed separately in Table 2.9 for the shielding and the cold mass, assuming an instantaneous luminosity of $5 \times 10^{33} \text{ cm}^{-2} \text{ s}^{-1}$. Even if the mask in front of Q1A intercepts about 280 W, this magnet remains the most exposed and the total power on the cold mass is about 150 W for both crossing schemes.

Less than 40% of the total power generated in the collision is deposited in the inner triplet. The remaining 63%, which corresponds to about 2.7 kW for an instantaneous luminosity of $5 \times 10^{33} \text{ cm}^{-2} \text{ s}^{-1}$, escapes downstream on both sides of the IP and it will be deposited elsewhere in the accelerator.

Table 2.9: Total power in the magnets of the inner triplet for vertical and horizontal crossing, assuming an instantaneous luminosity of $5 \times 10^{33} \text{ cm}^{-2} \text{ s}^{-1}$. The contribution to the shielding and the cold mass are quoted separately.

| Magnet | Vertical Crossing [W] | | | Horizontal Crossing [W] | | |
|--------------|-----------------------|------------|------------|-------------------------|------------|------------|
| | Total | Shielding | Cold Mass | Total | Shielding | Cold Mass |
| Q1A | 249 | 101 | 147.9 | 251 | 102 | 149 |
| Q1B | 268 | 183 | 85 | 269 | 184 | 85 |
| C1 | 27 | 19 | 8 | 28 | 19 | 8 |
| Q2A | 118 | 82 | 36 | 119 | 83 | 36 |
| Q2B | 204 | 147 | 57 | 191 | 137 | 54 |
| Q3A | 111 | 77 | 34 | 113 | 80 | 33 |
| Q3B | 113 | 81 | 31 | 132 | 95 | 37 |
| C2 | 15 | 11 | 4 | 18 | 13 | 5 |
| Total | 1105 | 701 | 404 | 1121 | 714 | 407 |

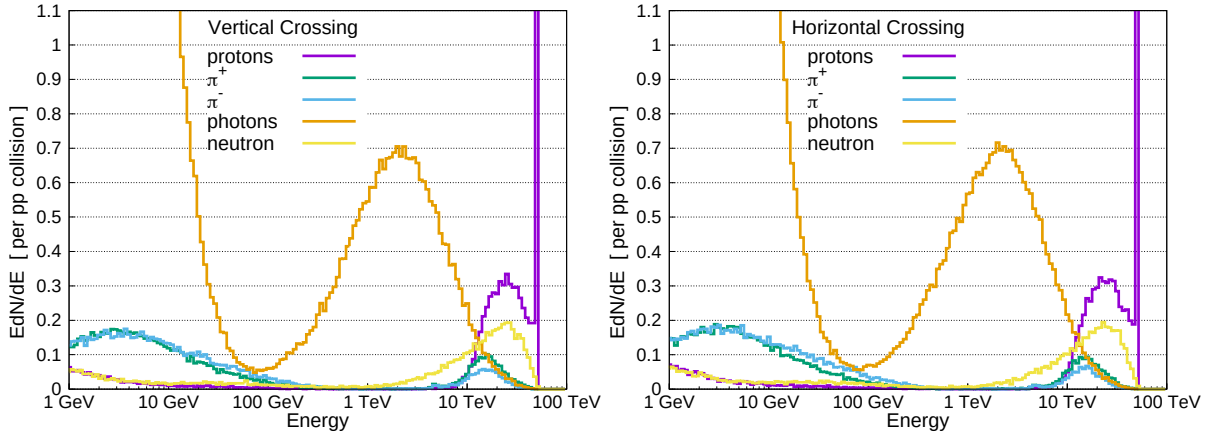


Figure 2.39: Spectra of collision debris particles in the vacuum chamber at the exit of Q3B for vertical crossing (left) and horizontal crossing (right) schemes. The distributions are normalised to one proton-proton collision.

Figure 2.39 shows the spectra of particles at the exit of Q3B for vertical crossing on the left and horizontal crossing on the right. The peak at 50 TeV is due to protons produced in single diffractive events. These protons travel much further in the accelerator and are expected to impact in the dispersion suppressor region. The charged pions and the protons of a few tens of TeV will be lost on D1, on the TAN or in the matching section instead. Many high energy photons and neutrons escape downstream of Q3 as well and they will be captured by the TAN or even at longer distances from the IP, depending on their angle. In order to assess the impact of these particles in the accelerator components precisely, new calculations which will extend the simulation to the matching section are planned, as has been done for the main interaction region.

The peak power density in the inner cable of the magnet is presented in Fig. 2.40 as a function of the distance from the interaction point for vertical and horizontal crossings. For both cases, the values are safely below the quench limit for the superconducting coils. The maximum is 1 mWcm^{-3} and it is reached at the entrance of Q1A. Without the presence of the mask, this value would be more than 30 times higher and would significantly exceed quench limits. The presence of a peak at the entrance of each magnet is due to the shielding gaps in the interconnects.

The maximum dose is also reached at the entrance of Q1A for both schemes and, for an integrated luminosity of 500 fb^{-1} , it remains below 30 MGy, which is the limit currently assumed for the damage of insulators and organic materials.

The cause of the shape difference between the red and the blue curves in Fig. 2.40 is the different collision crossing schemes. The crossing choice also influences the azimuthal position of the peaks. This can be seen from

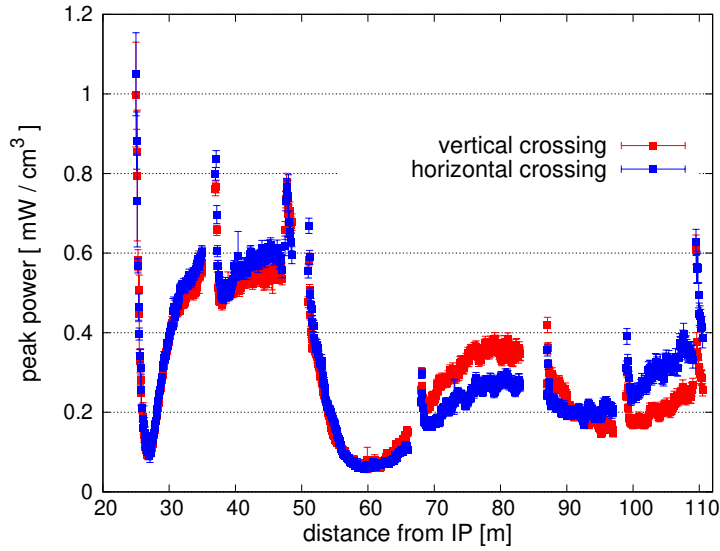


Figure 2.40: Peak power density in the innermost cable of the inner triplet magnets as a function of the distance from the IP, for an instantaneous luminosity of $5 \times 10^{33} \text{ cm}^{-2} \text{ s}^{-1}$. The resolution along the z-axis is 10 cm and the resolution on the azimuthal direction is 2 deg. A radial average is considered along the cable thickness (18.6 mm for quadrupoles and 5 mm for correctors) and the maximum over the azimuthal direction is considered.

Fig. 2.41, which shows the dose distribution in the innermost strands of the magnet coils as a function of the distance from the IP and of the azimuthal angle Φ , for vertical crossing on the top and horizontal crossing on the bottom. The asymmetric pattern observed is due to the combined effects of the crossing angle and plane and of the focusing/defocusing action of the quadrupoles, which sweep low energy secondary particles into the magnets preferentially along the vertical and horizontal planes.

The triplet polarity is DFD in the horizontal plane for positive particles, which are more abundant in p-p collisions. In Q1 positive particles are therefore deflected in the horizontal plane and, in the case of vertical crossing, hit the coil symmetrically at 0 and π . In the vertical plane, negative particles impact at $-\frac{\pi}{2}$ ¹, because of the crossing angle offset. In the horizontal crossing case, positive particles impact mainly at π , because of the initial crossing angle. For this reason both peak power density and peak dose values in Q1A and Q1B are higher for this case. The lower peaks at $\pm\frac{\pi}{2}$ are due to negative particles deflected symmetrically in the vertical plane. Due to the polarity change in Q2, positive particles are deflected in the vertical plane and impact at $\frac{\pi}{2}$ for the vertical case, because of the initial crossing angle. In the case of h-crossing two symmetric and lower peaks are present at $\pm\frac{\pi}{2}$. Finally in Q3, where the polarity is inverted again, positive particles are deflected in the horizontal plane and are collected at 0 for h-crossing, while for v-crossing they hit symmetrically at 0 and at π . Higher power density and dose values are therefore observed in Q3B for the horizontal crossing.

¹The position of the peak is $-\frac{\pi}{2}$, because the crossing angle is negative. In the case of positive crossing, the peak would have been at $\frac{\pi}{2}$.

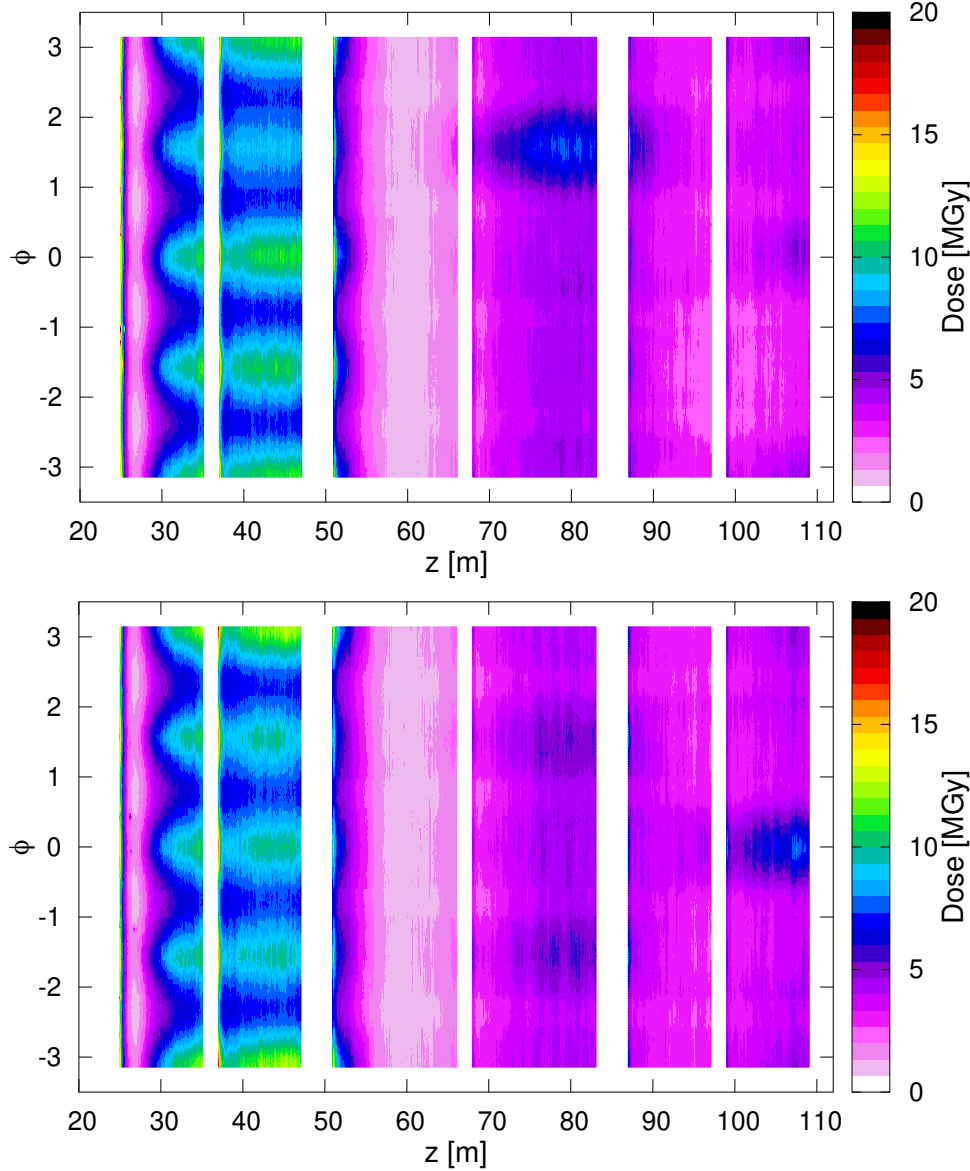


Figure 2.41: Dose distribution averaged over the innermost 3 mm of the magnet coils, as a function of z and of the azimuthal angle for vertical (top) and horizontal (bottom) crossing, normalised to an integrated luminosity of 500 fb^{-1} .

2.8 Hardware specifications

Table 2.10 lists the specifications for the magnets of the high luminosity EIRs. The cryostats of the triplet quadrupoles will have to be designed so they can support thick and consequently heavy shielding inside the coil apertures. The field quality specifications of the triplet magnets used in dynamic aperture studies are shown in Tables 2.11 and 2.12.

For the separation and recombination dipoles, D1 and D2, in the high luminosity EIRs, normal conducting dipoles similar to the MBXW and MBW designs of the LHC, were chosen because of the radiation environment and because they can provide better field quality. The field qualities assumed are listed in Tables 2.13 and 2.14.

The strengths required for the non-linear corrector package behind the triplet were obtained from the dynamic aperture studies. The coil apertures are the same as in the triplet quadrupoles Q2 and Q3 in order to avoid exposure to collision debris. With this, the possible field strengths could be determined and the length requirements calculated. The sextupole and octupole correctors only require lengths of a few centimetres. Thus it is possible to further increase the coil apertures of the sextupole and octupole correctors in order to reduce energy deposition, if necessary.

Table 2.10: Magnet parameters of the high luminosity EIRs.

| Magnet | Length [m] | Field strength | Coil aperture diameter [mm] | Number per IP |
|---|------------|-----------------------|-----------------------------|---------------|
| Triplet quadrupoles | | | | |
| Q1 | 14.3 | 130 T/ m | 164 | 4 |
| Q2 | 12.5 | 105 T/ m | 210 | 8 |
| Q3 | 12.5 | 105 T/ m | 210 | 4 |
| Separation and recombination dipoles | | | | |
| D1 | 11.3 | 2 T | 170 | 8 |
| D2 | 11.3 | 2 T | 91 | 8 |
| Matching quadrupoles | | | | |
| Q4 | 9.1 | 200 T/ m | 70 | 2 |
| Q5/6 | 12.8 | 260 T/ m | 60 | 4 |
| Q7 | 14.3 | 400 T/ m | 50 | 4 |
| Non-linear correctors | | | | |
| Sextupole (normal/skew) | 0.07 | 460 T/m ² | 210 | 2/2 |
| Octupole (normal/skew) | 0.21 | 4000 T/m ³ | 210 | 2/2 |
| Orbit correctors | | | | |
| MCBX | 1.3 | 3 T | 210 | 6 |
| MCBRD | 3.0 | 4 T | 70 | 4 |
| MCBYM | 1.5 | 4 T | 60 | 4 |
| MCB | 1.2 | 4 T | 50 | 4 |

Table 2.10 also lists the hardware specifications of the high luminosity IR orbit correctors. The single aperture MCBX magnets have nested coils, allowing them to deflect the beam in both planes. Each matching section quadrupole is equipped with one orbit corrector of the same aperture, hence the need for three classes. The MCB class is identical to the arc orbit correctors and two units are placed next to Q7 in order to provide enough strength. No strength requirements for the low luminosity EIR orbit correctors have been established so far, but it is expected that four single aperture correctors per IP will be required in the triplet region, as well as five double aperture correctors with 70 mm coil aperture per IP and 5 double aperture correctors with 50 mm coil aperture per IP.

Orbit correction studies have shown that the alignment tolerances for the high luminosity EIR elements listed in Table 2.15 result in a residual orbit below 1 mm (90th percentile). It should be noted that the residual orbit is very sensitive to misalignments of the strong Q7 quadrupoles. Thus those elements need to be aligned more precisely than the other matching quadrupoles, possibly requiring a remote alignment system as proposed for the HL-LHC [83].

For collision optics beyond ultimate parameters (with β^* down to 0.2 m) a crab voltage of 18.1 MV per beam on either side of each high luminosity IP was sufficient to provide full crabbing. This corresponds to 145 MV in total. Following direct scaling from the HL-LHC lattice, 20 m of space were allocated for the crab cavities on each side of the two main IPs. No detailed studies of the number of cavities or cryostat design have been done yet. It should be noted that a radiation mitigation strategy to protect the triplet is to change the crossing plane on the two main IPs at least once during the lifetime of the machine. This will also require an exchange of the crab cavities (horizontally/vertically deflecting). Since IPA and IPG will always run with different crossing planes, it should be possible to simply exchange the hardware between the two main IPs during a shutdown. This should be taken into account when designing the cryostats and RF connections.

The specifications for the triplet quadrupoles in the low luminosity experiment insertions are listed in Table 2.16. Unlike the high luminosity EIRs, the separation and recombination dipoles in the low luminosity EIRs are chosen to be superconducting. This allows a significantly shorter separation, providing more space for both experiment and injection hardware.

Table 2.11: Field error components of Q1 and Q3 with $R_{\text{ref}} = 55$ mm for Q1 and $R_{\text{ref}} = 70$ mm for Q3.

| Normal | Systematic | | Uncertainty | | Random | |
|-------------|------------|------------|-------------|------------|-----------|------------|
| | Injection | High Field | Injection | High Field | Injection | High Field |
| b_1 | 0.000 | 0.000 | 0.000 | 0.000 | 0.000 | 0.000 |
| b_2 | 0.000 | 0.000 | 0.000 | 0.000 | (10) | (10) |
| b_3 | 0.000 | 0.000 | 0.82 | 0.82 | 0.82 | 0.82 |
| b_4 | 0.000 | 0.000 | 0.57 | 0.57 | 0.57 | 0.57 |
| b_5 | 0.000 | 0.000 | 0.42 | 0.42 | 0.42 | 0.42 |
| b_6 | -19.947 | -0.357 | 1.1 | 1.1 | 1.1 | 1.1 |
| b_7 | 0.000 | 0.000 | 0.19 | 0.19 | 0.19 | 0.19 |
| b_8 | 0.000 | 0.000 | 0.13 | 0.13 | 0.13 | 0.13 |
| b_9 | 0.000 | 0.000 | 0.07 | 0.07 | 0.07 | 0.07 |
| b_{10} | 3.664 | -0.129 | 0.2 | 0.2 | 0.2 | 0.2 |
| b_{11} | 0.000 | 0.000 | 0.26 | 0.26 | 0.26 | 0.26 |
| b_{12} | 0.000 | 0.000 | 0.18 | 0.18 | 0.18 | 0.18 |
| b_{13} | 0.000 | 0.000 | 0.009 | 0.009 | 0.009 | 0.009 |
| b_{14} | 0.158 | -0.866 | 0.023 | 0.023 | 0.023 | 0.023 |
| b_{15} | 0.000 | 0.000 | 0.000 | 0.000 | 0.000 | 0.000 |
| Skew | | | | | | |
| a_1 | 0.000 | 0.000 | 0.000 | 0.000 | 0.000 | 0.000 |
| a_2 | -0.877 | -0.877 | 0.000 | 0.000 | (10) | (10) |
| a_3 | 0.000 | 0.000 | 0.65 | 0.65 | 0.65 | 0.65 |
| a_4 | 0.000 | 0.000 | 0.65 | 0.65 | 0.65 | 0.65 |
| a_5 | 0.000 | 0.000 | 0.43 | 0.43 | 0.43 | 0.43 |
| a_6 | 0.062 | 0.062 | 0.31 | 0.31 | 0.31 | 0.31 |
| a_7 | 0.000 | 0.000 | 0.19 | 0.19 | 0.19 | 0.19 |
| a_8 | 0.000 | 0.000 | 0.11 | 0.11 | 0.11 | 0.11 |
| a_9 | 0.000 | 0.000 | 0.08 | 0.08 | 0.08 | 0.08 |
| a_{10} | 0.002 | 0.002 | 0.04 | 0.04 | 0.04 | 0.04 |
| a_{11} | 0.000 | 0.000 | 0.026 | 0.026 | 0.026 | 0.026 |
| a_{12} | 0.000 | 0.000 | 0.014 | 0.014 | 0.014 | 0.014 |
| a_{13} | 0.000 | 0.000 | 0.01 | 0.01 | 0.01 | 0.01 |
| a_{14} | -0.004 | -0.004 | 0.005 | 0.005 | 0.005 | 0.005 |
| a_{15} | 0.000 | 0.000 | 0.000 | 0.000 | 0.000 | 0.000 |

Table 2.12: Field error components of Q2 with $R_{\text{ref}} = 70$ mm.

| Normal | Systematic | | Uncertainty | | Random | |
|-------------|------------|------------|-------------|------------|-----------|------------|
| | Injection | High Field | Injection | High Field | Injection | High Field |
| b_1 | 0.000 | 0.000 | 0.000 | 0.000 | 0.000 | 0.000 |
| b_2 | 0.000 | 0.000 | 0.000 | 0.000 | (10) | (10) |
| b_3 | 0.000 | 0.000 | 0.82 | 0.82 | 0.82 | 0.82 |
| b_4 | 0.000 | 0.000 | 0.57 | 0.57 | 0.57 | 0.57 |
| b_5 | 0.000 | 0.000 | 0.42 | 0.42 | 0.42 | 0.42 |
| b_6 | -19.752 | -0.317 | 1.1 | 1.1 | 1.1 | 1.1 |
| b_7 | 0.000 | 0.000 | 0.19 | 0.19 | 0.19 | 0.19 |
| b_8 | 0.000 | 0.000 | 0.13 | 0.13 | 0.13 | 0.13 |
| b_9 | 0.000 | 0.000 | 0.07 | 0.07 | 0.07 | 0.07 |
| b_{10} | 3.631 | -0.132 | 0.2 | 0.2 | 0.2 | 0.2 |
| b_{11} | 0.000 | 0.000 | 0.26 | 0.26 | 0.26 | 0.26 |
| b_{12} | 0.000 | 0.000 | 0.18 | 0.18 | 0.18 | 0.18 |
| b_{13} | 0.000 | 0.000 | 0.009 | 0.009 | 0.009 | 0.009 |
| b_{14} | 0.151 | -0.865 | 0.023 | 0.023 | 0.023 | 0.023 |
| b_{15} | 0.000 | 0.000 | 0.000 | 0.000 | 0.000 | 0.000 |
| Skew | | | | | | |
| a_1 | 0.000 | 0.000 | 0.000 | 0.000 | 0.000 | 0.000 |
| a_2 | -1.003 | -1.003 | 0.000 | 0.000 | (10) | (10) |
| a_3 | 0.000 | 0.000 | 0.65 | 0.65 | 0.65 | 0.65 |
| a_4 | 0.000 | 0.000 | 0.65 | 0.65 | 0.65 | 0.65 |
| a_5 | 0.000 | 0.000 | 0.43 | 0.43 | 0.43 | 0.43 |
| a_6 | 0.071 | 0.071 | 0.31 | 0.31 | 0.31 | 0.31 |
| a_7 | 0.000 | 0.000 | 0.19 | 0.19 | 0.19 | 0.19 |
| a_8 | 0.000 | 0.000 | 0.11 | 0.11 | 0.11 | 0.11 |
| a_9 | 0.000 | 0.000 | 0.08 | 0.08 | 0.08 | 0.08 |
| a_{10} | 0.002 | 0.002 | 0.04 | 0.04 | 0.04 | 0.04 |
| a_{11} | 0.000 | 0.000 | 0.026 | 0.026 | 0.026 | 0.026 |
| a_{12} | 0.000 | 0.000 | 0.014 | 0.014 | 0.014 | 0.014 |
| a_{13} | 0.000 | 0.000 | 0.01 | 0.01 | 0.01 | 0.01 |
| a_{14} | -0.007 | -0.007 | 0.005 | 0.005 | 0.005 | 0.005 |
| a_{15} | 0.000 | 0.000 | 0.000 | 0.000 | 0.000 | 0.000 |

Table 2.13: Field error components of D1 with $R_{\text{ref}} = 46$ mm. The values are based on the MBXW magnet design for LHC.

| Normal | Systematic | | Uncertainty | | Random | |
|-------------|------------|------------|-------------|------------|-----------|------------|
| | Injection | High Field | Injection | High Field | Injection | High Field |
| b_1 | 0.000 | 0.000 | 0.000 | 0.000 | 0.000 | 0.000 |
| b_2 | -0.200 | -0.300 | 0.000 | 0.000 | 0.100 | 0.200 |
| b_3 | 0.100 | -0.900 | 0.000 | 0.000 | 0.300 | 0.000 |
| b_4 | 0.000 | 0.000 | 0.000 | 0.000 | 0.000 | 0.000 |
| b_5 | -0.100 | -0.100 | 0.000 | 0.000 | 0.200 | 0.000 |
| Skew | | | | | | |
| a_1 | 0.000 | 0.000 | 0.000 | 0.000 | 0.000 | 0.000 |
| a_2 | -0.200 | -0.100 | 0.000 | 0.000 | 0.200 | 0.100 |
| a_3 | 0.000 | 0.000 | 0.000 | 0.000 | 0.000 | 0.100 |
| a_4 | 0.000 | 0.000 | 0.000 | 0.000 | 0.000 | 0.000 |
| a_5 | 0.000 | 0.000 | 0.000 | 0.000 | 0.000 | 0.100 |

Table 2.14: Field error components of D2 with $R_{\text{ref}} = 28$ mm. The values are based on the MBW magnet design for LHC.

| Normal | Systematic | | Uncertainty | | Random | |
|-------------|------------|------------|-------------|------------|-----------|------------|
| | Injection | High Field | Injection | High Field | Injection | High Field |
| b_1 | 0.000 | 0.000 | 0.000 | 0.000 | 0.000 | 0.000 |
| b_2 | 0.300 | -1.400 | 0.000 | 0.000 | 1.800 | 1.100 |
| b_3 | 1.500 | -0.400 | 0.000 | 0.000 | 0.400 | 0.800 |
| b_4 | 0.000 | 0.300 | 0.000 | 0.000 | 0.400 | 0.800 |
| b_5 | -0.400 | -0.500 | 0.000 | 0.000 | 0.300 | 0.200 |
| b_6 | 0.000 | 0.000 | 0.000 | 0.000 | 0.400 | 0.300 |
| b_7 | -0.300 | -0.200 | 0.000 | 0.000 | 0.200 | 0.200 |
| b_8 | 0.000 | 0.100 | 0.000 | 0.000 | 0.200 | 0.200 |
| b_9 | -0.100 | 0.000 | 0.000 | 0.000 | 0.000 | 0.200 |
| b_{10} | 0.000 | 0.100 | 0.000 | 0.000 | 0.000 | 0.200 |
| b_{11} | 0.000 | 0.100 | 0.000 | 0.000 | 0.000 | 0.100 |
| Skew | | | | | | |
| a_1 | 0.000 | 0.000 | 0.000 | 0.000 | 0.000 | 0.000 |
| a_2 | 0.100 | 0.200 | 0.000 | 0.000 | 0.100 | 0.200 |
| a_3 | 0.000 | -0.100 | 0.000 | 0.000 | 0.100 | 0.300 |
| a_4 | 0.000 | 0.100 | 0.000 | 0.000 | 0.000 | 0.200 |
| a_5 | 0.000 | -0.100 | 0.000 | 0.000 | 0.000 | 0.100 |
| a_6 | 0.000 | 0.000 | 0.000 | 0.000 | 0.100 | 0.200 |
| a_7 | 0.000 | -0.100 | 0.000 | 0.000 | 0.000 | 0.100 |
| a_8 | 0.000 | 0.000 | 0.000 | 0.000 | 0.000 | 0.100 |

Table 2.15: Alignment specifications for the high luminosity EIR elements.

| Element | Error | Units | Value | Comments |
|----------------------------|---------------------------|-------|-------|------------------|
| Separation dipole D1 | roll angle $\sigma(\phi)$ | mrad | 1.0 | |
| Recombination dipole D2 | roll angle $\sigma(\phi)$ | mrad | 1.0 | |
| Triplet quadrupoles Q1-Q3 | $\sigma(x), \sigma(y)$ | mm | 0.2 | remote alignment |
| Matching quadrupoles Q4-Q6 | $\sigma(x), \sigma(y)$ | mm | 0.5 | |
| Matching quadrupole Q7 | $\sigma(x), \sigma(y)$ | mm | 0.2 | |
| BPM | $\sigma(x), \sigma(y)$ | mm | 0.3 | accuracy |
| | $\sigma(\text{read})$ | mm | 0.05 | |

Table 2.16: Magnet parameters of the low luminosity EIRs.

| Magnet | Length [m] | Field strength | Coil aperture diameter [mm] | Number per IP |
|---|------------|----------------|-----------------------------|---------------|
| Triplet quadrupoles | | | | |
| Q1 | 10 | 270 T/ m | 64 | 4 |
| Q2 | 15 | 270 T/ m | 64 | 4 |
| Q3 | 10 | 270 T/ m | 64 | 4 |
| Separation and recombination dipoles | | | | |
| D1 | 12.5 | 12 T | 100 | 4 |
| D2 | 15 | 10 T | 60 | 4 |
| Matching quadrupoles | | | | |
| Short type | 9.1 | 200 T/ m | 70 | 6 |
| Long type | 12.8 | 300 T/ m | 50 | 5 |

RF insertion

3.1 Overview

The RF insertion will house RF cavities for ramping and beam stability. The total cavity voltage required is 48 MV at the frequency of 400.8 MHz (see Table 1.1 in Chapter 1). The total length of the RF insertion is 1400 m, which is sufficient to accommodate all of the cavities. Additional dipoles are added at the entrance and the exit of the RF insertion to enhance the beam separation from 250 mm to 420 mm, as is done in LHC.

3.2 System layout and optics

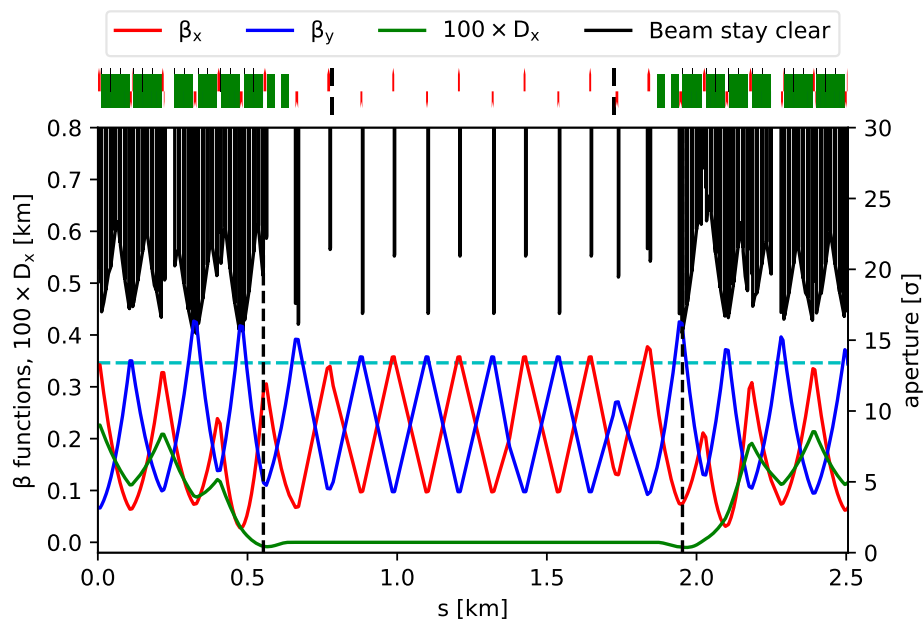


Figure 3.1: Optical functions in the RF insertion (β_x in blue, β_y in red, and $100 \times D_x$ in green). The beam stay clear region is shown in black at injection energy (3.3 TeV). The cyan horizontal line shows the specified target of 13.4σ .

The RF insertion is composed of 219.292 m long FODO cells. The phase advance per FODO cell is 72° in both planes. This phase advance is chosen as a compromise to keep a global tune Q_x/Q_y near the target values of 109.31/107.32 in collision and to keep the beam stay clear region and maximum quadrupole gradients within the specifications. Nevertheless, there is still room for optimisation of the phase advances in the RF insertion. The entrance and exit of the RF insertion host two separation dipoles and two recombination dipoles to enhance the beam separation from 250 mm to 420 mm. The distance between separation and recombination dipoles is adjusted

to keep the same distance between matching quadrupoles. The optical functions, the dispersion function, and the beam stay clear limit are shown in Fig. 3.1. The minimum beam stay clear limit at injection is 15.5σ , well above the specified target of 13.4σ .

3.3 Hardware specifications

The FODO cells have quadrupoles similar to those of the arcs with same length and aperture. The only difference is the beam separation which is 420 mm compared to 250 mm in the arcs. Each quadrupole is surrounded by a dipole corrector and a BPM, similar to the arcs. The RF insertion houses RF cavities operating at the frequency of 400.8 MHz with a total voltage of 48 MV. If the same technology as in LHC is used, a gain of 2 MV per cavity can be expected and thus a total of 24 cavities per beam is required [84–86]. The hardware specifications are summarised in Table 3.1.

Table 3.1: Magnet parameters of the RF insertion.

| Magnet | Length [m] | Field strength | Beam separation [mm] | Number |
|---|------------|----------------|----------------------|--------|
| Quadrupoles | | | | |
| MQR | 6.4 | 290 T/m | 420 | 8 |
| Q5/6 | 9.1 | 230 T/m | 420 | 4 |
| Q7 | 9.1 | 360 T/m | 250 | 2 |
| Separation and recombination dipoles | | | | |
| D1 | 12.5 | 12 T | 250 | 4 |
| D2 | 12.5 | 12 T | 420 | 4 |
| Orbit correctors | | | | |
| MCBR | 1.2 | 4 T | 420 | 12 |
| MCB | 1.2 | 4 T | 250 | 2 |

3.4 Alternatives

The space required for cavities (a few tens of metres) will be small compared to the total available in the RF insertion. Therefore, there is still room to insert diagnostics or correction schemes, like trim quadrupoles to correct the global tune. The RF section can also house other devices like electron lenses or RF quadrupoles to mitigate collective effects as explained in Section 8.8. An optics scaled from the RF insertion of LHC can be an alternative lattice.

Injection system design for FCC-hh

4.1 Introduction

The relevant parameters for the beam transfer systems are summarised in Table 4.1.

Table 4.1: Beam parameters at FCC injection and extraction.

| Beam parameters | Unit | Injection | Extraction |
|-----------------------|---------------|-------------|-------------|
| Kinetic energy | TeV | 3.3 | 50 |
| β_{rel} | | ≈ 1 | ≈ 1 |
| γ_{rel} | | 3518 | 53290 |
| Revolution period | μs | 333 | 333 |
| Magnetic rigidity | T.m | 11011 | 166785 |
| # bunches | | 10400 | 10400 |
| Transverse emittances | μm | 2.2 | 2.2 |
| Total beam energy | GJ | 0.56 | 8.5 |

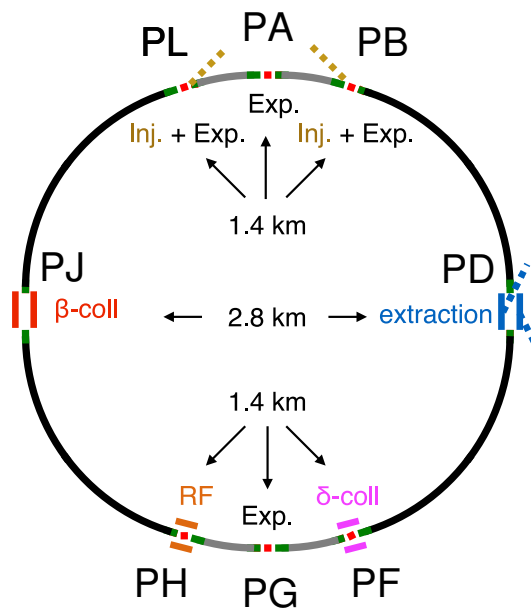


Figure 4.1: Layout of the FCC collider.

4.2 Injection system

4.2.1 Injection system layout

An overall ring layout optimisation resulted in straight sections LSS-B and LSS-L housing injection and a side experiment (see Fig. 4.1). Even though unfavourable from the machine protection and availability point of view, the present straight section and experiment cavern dimensions only allow placing the injection system upstream of the experiment. The injection system requires three half-cells or about 450 m for its equipment. Additional half cells upstream and downstream of the low beta insertion are required to install auxiliary protection elements (see Section 4.2.4) and to provide the matching between dispersion suppressors, injection and low beta optics (see Fig. 4.2).

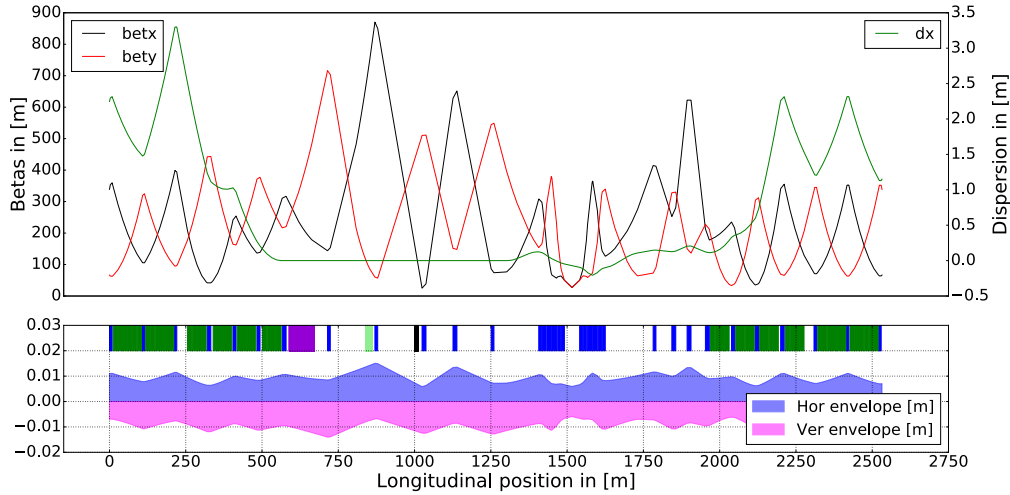


Figure 4.2: Optics and beam envelopes for the injection straight (LSS-B) with an increased cell length of 145 m. In violet the septum, in light green the kickers and in black the injection dump. The low beta insertion for the side experiment is placed at around 1550 m.

The FCC injection is a fast bunch-to-bucket transfer. The injected beam enters the septum with an offset in angle and position in both planes with respect to the ring orbit (Fig. 4.3). The injection system uses a Lambertson septum to deflect the beam vertically onto the FCC orbit. The horizontal angle is reduced by off-centre passage through a quadrupole and finally compensated by a fast kicker system. In order to estimate the required kick angles the following assumptions have been taken:

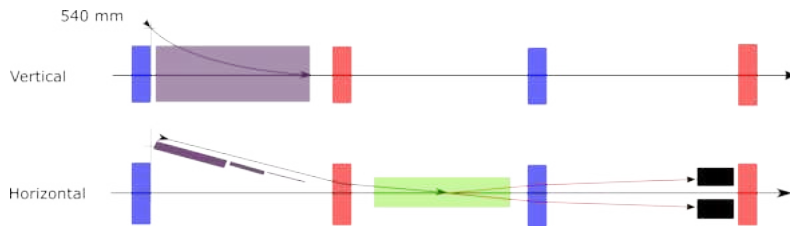


Figure 4.3: Layout of the injection system. Focussing (blue) and defocussing (red) quadrupoles build a FODO lattice. The Lambertson septum (violet) which is horizontally aligned with the incoming trajectory angle deflects the beam vertically onto the orbit, and the kicker (green) compensates for the remaining angle in the horizontal plane. The injection dump (black) intercepts miskicked beam.

- The half width of the cryostat for FCC quadrupoles is 500 mm which leads to a required clearance of 540 mm.
- The rms betatron beam size in FCC at the exit location of the injection septum amounts to 0.34 mm. Assuming $\pm 15.5\sigma$ for the beam and ± 4 mm for orbit and alignment tolerances, the minimum required beam stay clear diameter is 19 mm.

- The septum blade closest to the kicker is assumed to have an apparent thickness of 8 mm, which leads to a minimum beam opening of 27 mm at the end of the septum closest to the kicker.
- The quadrupole gradient between septum and kicker amounts to 97 T/m.

Figure 4.4 shows the septum field required as a function of the half cell length. For mechanical feasibility, a septum filling factor of 95% is assumed. The available length and position are defined by the beam separation allowing for the 6 mm thick blade. Considering these assumptions, the required field for the standard arc half cell length of 100 m is 3.5 T. Since injection is an inherently high beam loss process, superconducting septa will not be used. For a half cell length of more than 125 m, normal conducting Lambertson septa can be envisaged. To account for additional instrumentation, vacuum equipment and steering elements, the half cell length in the injection area was fixed at 145 m. This corresponds to a septum field well below 1 T.

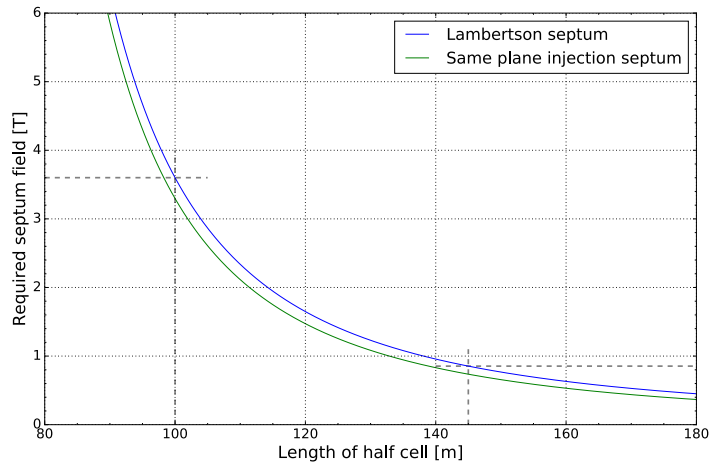


Figure 4.4: Required field of the injection septum as a function of the half cell length. Dashed lines denote the required field of 3.5 T for a standard arc half cell length of 100 m and 0.7 T for the increased half cell length in the injection area of 145 m.

The kicker deflection is defined by the quadrupole strength between septum and kicker and the septum thickness. The kicker magnet system is kept as short as possible for beam impedance reasons and, if centrally placed, requires about half the available drift to avoid exceeding the maximum possible current of the pulse generator. By moving the system as far downstream as possible in the available drift, the deflection required from the kicker system and therefore also its length can be reduced further. The final kick angle for a 40 m long magnet system is to 0.18 mrad. The resulting beam offset in the quadrupole is 20 mm which leads to a total horizontal diameter required inside the vacuum chamber of 58 mm. Figure 4.2 shows the optics for the injection straight (LSS-B) with an increased cell length of 145 m. The gradient of the quadrupole between septum and kicker is fixed at 97 T/m and the horizontal phase advance between kicker and injection dump at 90° . These constraints must be fixed whenever the kicker generators are charged to provide protection of downstream elements in case of spontaneous kicker firing.

4.2.2 Staggered transfer

A main limitation for the injection system comes from the total beam energy of 560 MJ during High Energy Booster (HEB) to FCC transfer. Present investigations of the feasibility of absorber blocks for HL-LHC injection protection show that HL-LHC and even LHC standard beam parameters with small emittances are at the limit for both mechanical stresses and attenuation of primary particles to provide protection of downstream elements. The beam energy of the HEB to FCC transfer is about a factor 120 higher than for the SPS to HL-LHC transfer. Thus, a staggered transfer of batches with a reduced number of bunches is envisaged. Figure 4.5 shows the achievable bunch filling factor as a function of the injection kicker rise time for different beam transfer energies. Energy deposition studies for the injection dump result in a maximum allowed number of 80 bunches per transfer [87, 88]. The maximum number of bunches in FCC is determined by the acceptable synchrotron radiation heat load and amounts to 10400 bunches or 78% fill factor.

In order to reach this fill factor with 80 bunches per transfer and assuming 10 μ s for distributed abort

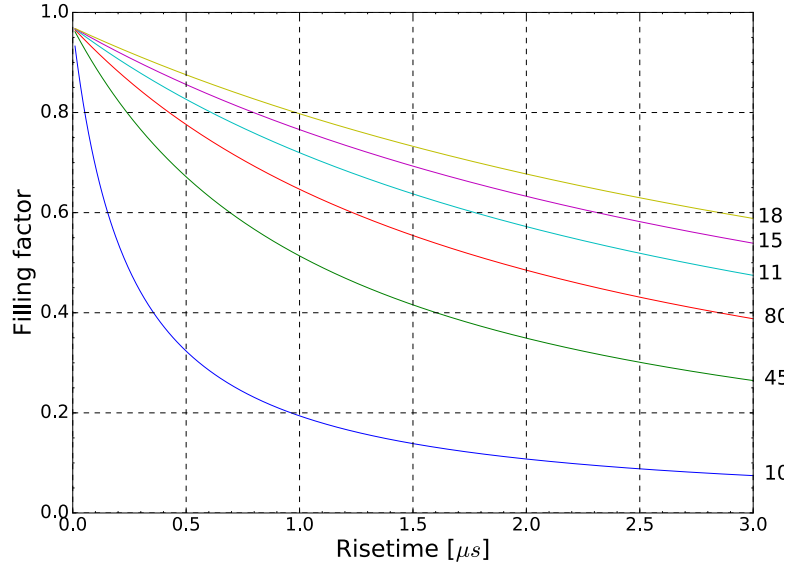


Figure 4.5: FCC bunch fill factor as a function of the injection kicker rise time for different beam transfer energies. The planned filling factor of 78% is reached for HL-LHC energies (about 4.8 MJ) for a rise time of 0.490 μs . The filling factor never reaches 100% because 10 μs are allowed for distributed abort gaps.

gaps, the kicker rise time has to be less than 0.490 μs . A total of 130 batches with 80 bunches each need to be transferred. Some margin on the rise time needs to be taken into account to allow for low and intermediate intensity beam injections to probe the machine and steer the transfer line trajectories. This leads to a rise time specification for the injection kicker hardware of 0.43 μs .

4.2.3 Synchronisation HEB-FCC

The time between batch transfers is dominated by the synchronisation between the HEB and FCC and beam quality checks. Between each transferred batch both machines have to be synchronised on the common frequency:

$$f_c = \frac{f_{rev,HEB}}{N_{FCC}} = \frac{f_{rev,FCC}}{N_{HEB}} \quad (4.1)$$

where N_{FCC}/N_{HEB} is a simple fraction such that $N_{FCC}/N_{HEB} = C_{FCC}/C_{HEB}$.

This common frequency corresponds¹ to the desired recharge rate for the HEB extraction and FCC injection kickers. Table 4.2 lists common frequencies for a few interesting FCC examples for the case of LHC or SPS as HEB.

Table 4.2: Common frequencies of FCC and SPS or LHC for a few interesting circumferences.

| C_{FCC}/C_{LHC} | C_{FCC}/C_{SPS} | C_{FCC} (km) | $f_{c,LHC}$ (Hz) | $f_{c,SPS}$ (Hz) |
|-------------------|-------------------|----------------|------------------|------------------|
| 98/27 | 98/7=14/1 | 96.8 | 115 | 3098 |
| 99/27=11/3 | 99/7 | 97.7 | 1022 | 438 |
| 100/27 | 100/7 | 98.7 | 112 | 434 |
| 102/27=34/9 | 102/7 | 100.7 | 331 | 430 |
| 105/27=35/9 | 105/7=15/1 | 103.7 | 104 | 2892 |
| 108/27=4/1 | 108/7 | 106.7 | 2811 | 402 |

The common frequency defines the maximum frequency that the beam can be transferred in a synchronised way between two rings, thus, defining the upper value for the kicker recharge frequency. Assuming a kicker recharge frequency of 100 Hz, transferring the full LHC beam to FCC takes about one second.

¹On the condition that the batch spacing in the FCC and the HEB is the same.

Synchronisation of the two rings and recharging the kicker system do not significantly contribute to the time required for the overall beam transfer. More time could be needed to validate the injection quality after each transfer: currently this takes several seconds for the LHC. For a staggered transfer, the injection quality check has to rely on observables which can be monitored and interlocked directly in the hardware in the timeframe of tens of ms. These observables would include power supply voltages, magnet currents, and the collimator positions of the extraction, transfer line and injection equipment. Beam parameters such as intensity, emittance and satellite bunch population need to be validated before extraction. Any beam quality deterioration during the transfer process which is not related to magnet currents can only be detected via beam loss monitors which should stop further injections. Very fast, order of ns, beam loss monitors based on diamond detectors could be placed at sensitive locations like collimators. While the kicker recharging frequency is not significant for the overall filling time, it is important for ensuring a safe and reliable injection process. As a reasonable balance, a recharging frequency of 10 Hz is planned.

4.2.4 Injection protection design

The injection protection design is described in detail in Ref. [89]. Its main results concerning the injection system design and impact on other FCC-hh systems are presented in the following paragraphs.

4.2.4.1 Failure scenarios

The main sources for fast injection failures requiring passive protection are the injection kicker (MKI) and its trigger system. Failure scenarios for the inductive adder (IA) as a potential kicker generator are shown in Table 4.3. Most faults can have an impact on either the circulating or injected beam, in the form of positive and negative miskicks. The amplitudes $|a|$ of the main potential miskicks measured in beam size σ_x are:

- $|a| < 0.36 \sigma_x$ due to erratic or missing branches or layers.
- $|a| \approx 0 - 8.7 \sigma_x$ due to e.g. vacuum flash-overs, single erratics or missing IAs.
- $|a| \approx 130 - 148 \sigma_x$ due to e.g. synchronisation errors or missing triggers of the entire system.

A miskick of $|a| = 6.5 - 10.5 \sigma_x$ results in grazing or quasi-grazing impact at the TDI. Although the probability of deflections other than those above is assessed to be low, it cannot be excluded as the failure might occur during the generator discharge at the end of the fill. Therefore, irrespective of any failure probabilities, the worst case failure scenario for the current design of the injection protection system is: grazing impact of a miskicked circulating beam with an extended MKI flat-top length of 3 μs and a resulting deflection of 100 bunches.

4.2.4.2 Injection protection layout

A layout for the system to intercept a beam miskicked by the MKI system has been proposed analogous to the LHC and HL-LHC injection protection system. It is composed of the injection dump (TDI) and two auxiliary absorbers, the TCLIA and TCLIB. The TDI is installed with a horizontal phase advance of $\Delta\mu_x = 90^\circ$ downstream of the MKI system, 20 m upstream of Q6, and it absorbs the miskicked beam in case of MKI failures. A 6 m graphite absorber is planned as TDI. It consists of a 2.5 m segment with a density 1.4 g/cm^3 and a 3.5 m long segment of 1.8 g/cm^3 . Additionally, 1 m stainless steel masks are planned to protect the downstream quadrupoles from hadronic showers.

The auxiliary absorbers, TCLIA and TCLIB, are to be installed with $\Delta\mu_x = 180 - 20^\circ$ and $\Delta\mu_x = 360 + 20^\circ$ from the TDI to compensate for any potential phase errors between MKI and TDI. Currently there have been no further design studies for TCLIA and TCLIB. As a preliminary dummy design for the current simulations, 2 m absorbers made of low density graphite ($\rho = 1.4 \text{ g/cm}^3$) are inserted into the lattice for TCLIA and TCLIB. However, it has to be noted that no material studies have been conducted and these parameters are expected to change, depending on the necessity of survival of direct impact of the full injection batch in case of phase errors.

First studies result in a TDI aperture setting of 8.5σ , based on collimation settings scaled from HL-LHC (secondary collimator at 8.4σ) [19, 29].

FLUKA [62, 63] simulations have been conducted to validate the energy deposition in the absorber itself as well as the protection efficiency. The impact of 80 bunches with an impact parameter of 1σ (quasi-grazing impact) at 3.3 TeV was simulated as a worst case impact for TDI robustness and shower production.

The simulations are based on the latest optics version, which features $\beta_x = 37 \text{ m}$ and $\beta_y = 932 \text{ m}$ at the entrance of the absorber. A maximum temperature of 1200°C is obtained in the TDI. Referring to latest HiRadMat results [90], there should be a margin of at least a few tens of percent for the acceptable number of impacting

Table 4.3: Failure scenarios of the MKI system, based on the IA as pulse generator

| | Erratic (Missing) Layer/Branch | Erratic (Missing) System |
|---|---|---|
| Cause | Spurious (missing) trigger, short (open) switch, single event burnout (SEB),... | Spurious (missing) trigger |
| Probability | medium - high | low-medium |
| Kick | $< 0.26 \%$ / 0.36σ | 100 % / 139σ |
| Impact | negligible, no losses | full impact at TDI, quench of downstream MQ in IPB |
| Reaction | continue operation, with spare layers if necessary | beam abort, downtime |
| Limitation $< 3 \mu\text{s}$ | not necessary | obligatory |
| Severity | very low | medium |
| | Erratic /Missing IA | Magnet Short Circuit |
| Cause | spur./miss. trigger | vacuum flash-over |
| Probability | very low | circ: very low; inj: medium |
| Kick | $5 - 6.2 \%$ / $6.8 - 8.7 \sigma$ | circ: $94 - 106 \%$ / $130 - 148 \sigma$, inj: -6.2 to $+6.2 \%$ / -8.7 to 8.7σ |
| Impact | grazing impact at TDI, losses in IPB / IPJ (quench) | circ: full impact at TDI, inj: graz. impact (high losses in IPB / IPJ; quench) |
| Reaction | beam abort / downtime | beam abort / downtime |
| Limitation $< 3 \mu\text{s}$ | obligatory | obligatory |
| Severity | high | very low - high |

bunches. The energy deposited by hadronic showers in the Nb₃Sn cables of the downstream quadrupoles is in the order of a few 10 J/cm³. This is at least one order of magnitude below the first estimate of the damage limit determined by material tests in the HiRadMat facility, reported in Ref. [91].

It can be stated that the survival of the TDI and the downstream quadrupoles is guaranteed for a worst case beam impact. The remaining margin of a few 10s of bunches needs to be maintained due to the potential extended pulse lengths from selected MKI failures. A maximum of 100 impacting bunches will therefore be used for all further simulations.

4.2.4.3 Tracking studies for assessing the minimum protected aperture with grazing impact

First assessments of the downstream losses in case of a grazing TDI impact due to an MKI failure are based on tracking studies using MAD-X [71] and the scattering routine pycollimate [92]. This results in a first estimate for the TDI aperture settings and the downstream minimum protected aperture, depending on the maximum TDI and TCLI set-up errors assumed. An range of expected set-up errors is summarised in Table 4.4 and explained in Ref. [89].

The survival function $S(a)$ estimates the number of protons escaping with a phase space amplitude $r > a$ and is defined as

$$S(a) = \frac{1}{N_0} \int_a^\infty f(r) dr \quad (4.2)$$

with $N_0 = 10^{13}$ p+, i.e. 100 bunches. In analogy to studies for HL-LHC [93] the maximum $r = \max(X, Y)$ is applied to define the amplitude in the transverse plane. The studies are based on a preliminary estimate for the damage limit at 3.3 TeV of 10^{10} p+ corresponding to a survival function of $S = 10^{-3}$, based on [94].

Table 4.4: Maximum assumed errors at the TDI and TCLIs in order to evaluate the downstream protected aperture in case of kicker failure. The value listed in brackets is considered as the expected error for a scenario, which is studied in more detail in Ref. [89]

| | HL-LHC [92] | FCC-hh |
|-----------------------|----------------------------------|--|
| Mechanical tolerances | $\pm 0.2\text{mm} / 0.35 \sigma$ | $\pm 0.3 \text{ mm} / 1.7\text{-}2 (1.7) \sigma$ |
| Injection precision | 0.35σ | $\sim 0.3\text{-}1 (0.5) \sigma$ |
| Setting up optics | 0.71σ | $\sim 0.5 (0.5) \sigma$ |
| Local orbit | 1.1σ | $\sim 1\text{-}3 (1.8) \sigma$ |
| Total | 2.5σ | $3.5\text{-}6.5 (4.5) \sigma$ |

The estimated survival functions $S(a)$ downstream the TDI and at the downstream end of the insertion are illustrated in Fig. 4.6, for a nominal TDI setting of 8.5σ and different set-up errors. The results show that a part of the protons are scattered at the TDI with large scattering angles independently of the TDI errors, and hence the effective aperture. These large scattering angles translate to phase space amplitudes $a > 15.5\sigma$. Downstream of the TDI, this fraction amounts to approximately 0.9% of the impacting beam, corresponding to $9 \cdot 10^{10}$ p+ and is explained by the small horizontal beam size at the TDI, i.e. $\sigma_x = 0.15$ mm. Doubling the beam size would already decrease $S(a = 15.5 \sigma)$ from 0.9% to approximately 0.5%.

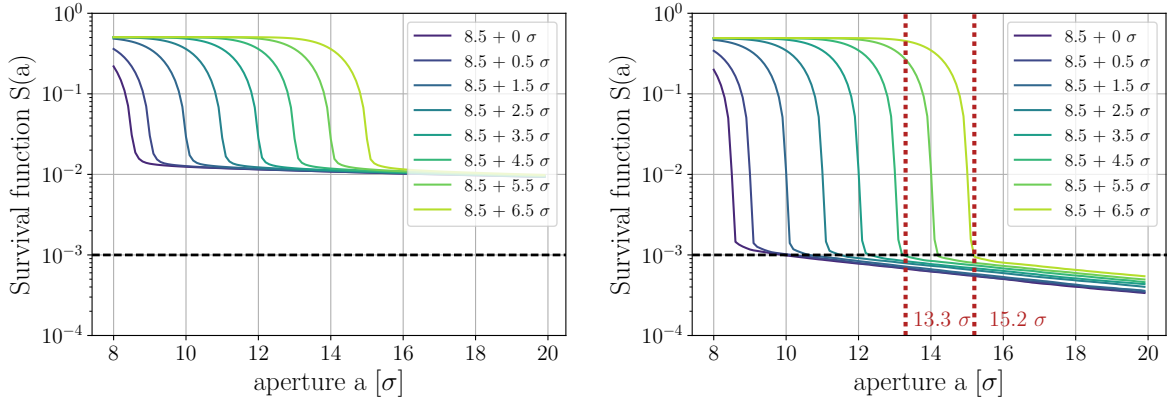


Figure 4.6: $S(a)$ for different TDI errors, observed at the downstream end of the TDI (left) and the insertion (right)

Most of the scattered protons are subsequently lost in the injection insertion. A loss map of the injection insertion is shown in Fig. 4.7. The local losses exceed the previously defined damage limit of 10^{10} p+ at neighbouring quadrupoles. However, these losses are scattered transversely resulting in a maximum density of $5 \cdot 10^8$ p+/mm². Further, FLUKA studies considering both hadronic showers and scattered protons [88] show an acceptable energy deposition in neighbouring quadrupoles in case of grazing impact. Repeating the FLUKA simulations with suppressed hadronic showers and a comparison of the energy deposition may lead to an increase of the damage limit for further studies. As the safe beam flag is mainly defined for localised losses it is therefore not directly translatable to the scattered losses in case of injection failures.

Nevertheless, respecting this first pessimistic damage limit as a threshold, the results obtained for the downstream end of the insertion show that for a total TDI error of 4.5σ a protected arc aperture of 13.3σ can be guaranteed. The worst case TDI errors of 6.5σ result in a protected aperture of 15.2σ . Evidently, the prediction of the protected arc aperture strongly depends on the estimation of the TDI set-up errors summarised in Table 4.4. An estimate of a total error of 4.5σ seems feasible, if the errors defined are taken as design specifications for further developments. However, detailed studies should be conducted, especially regarding estimation of the local orbit offset, as this value has a large impact on the predicted set-up error. The large error contributions of mechanical

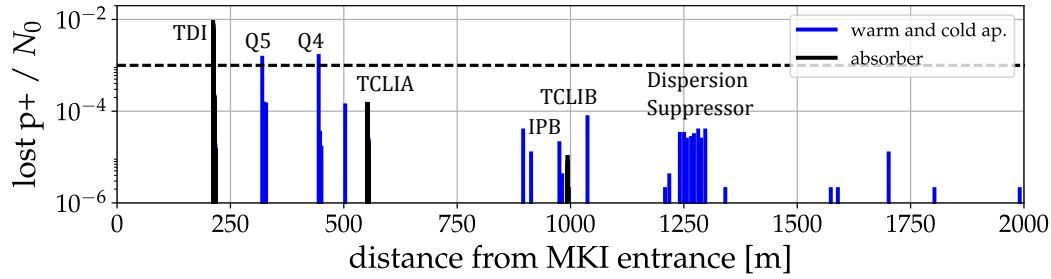


Figure 4.7: Losses in the injection insertion in case of grazing impact for TDI settings of 8.5 sigma, including accumulated alignment and orbit errors of 6.5 σ (bin width: 1 cm).

tolerances and the local orbit errors are due to the small horizontal beam size at the TDI. Hence, an alternative optics layout featuring an increased beam size would improve the protection efficiency and the protected aperture by both reducing the TDI set-up errors and by reducing the number of protons scattered with large angles.

The losses in the remainder of the collider, mainly in the collimation insertion, strongly depend on the phase between MKI and TCP. The beam may either impact directly on the TCP or not be intercepted by the TCP but directly impact on a secondary collimator. This results in losses affecting different magnets. For both cases the losses exceed the safe beam flag of 10^{10} p+ at certain locations, but are still considered as acceptable based on reasoning similar to that used for the injection insertion.

4.2.5 Injection system for 1.3 TeV energy

The injection system described in the previous paragraphs is conceived for a transfer energy of 3.3 TeV. For the option to inject a 1.3 TeV beam from a superconducting machine in the SPS tunnel, certain technology choices might change.

A lower injection energy will allow the integrated magnetic field required to be reduced but will require the magnet openings to increase. Whilst these changes might not affect the septa design strongly, it could have an impact on the field rise time and beam impedance of the kickers [95].

With reduced beam energy, the number of bunches per transfer can be increased from 80 to around 160 depending on the optics parameters at the injection dump [88]. With longer trains, the kicker pulse length required increases whereas the batch spacing required can be relaxed. For these specifications, the present choice for the kicker generator (Inductive Adder [96–98]) would have to be revised.

4.2.6 Hardware specifications

The required kicker and septum parameters are summarised in Table 4.5. The parameters for the individual septa families are summarised in Table 4.6.

Table 4.5: Parameters of kicker and Lambertson septum at FCC injection.

| Hardware parameters | Unit | Kicker | Septum |
|---|-------------|-----------------------|-------------------|
| Deflection | mrad | 0.18 | 9.8 |
| Integrated field | T.m | 2.0 | 92 |
| System length | m | 40 | 104 |
| Effective length | m | 31.8 | 84 |
| Rise time | μ s | 0.43 | - |
| Recharge frequency | Hz | ≈ 10 | - |
| Flattop length | μ s | 2.0 | ≥ 2.0 |
| Flattop stability ² | | $\pm 5 \cdot 10^{-3}$ | $\pm 10^{-5}$ |
| GFR inj. beam h/v (radius) | mm | - | 9/- |
| Beam stay clear circ. beam h/v (radius) | mm | 16/16 | 9/14 (first unit) |
| Septum width (first unit) | mm | - | 8 |

Table 4.6: Parameters of the Lambertson injection septa.

| Hardware parameters | Unit | Family A | Family B | Family C |
|------------------------------------|-------------|-----------------|-----------------|-----------------|
| Apparent blade thickness | mm | 8 | 12 | 18 |
| System length | m | 10 | 30 | 64 |
| Number of modules | m | 2 | 6 | 13 |
| Effective module length | m | 4 | 4 | 4 |
| Flux Field | T | 0.7 | 1 | 1.2 |
| BdL | Tm | 5.6 | 24 | 62.4 |
| Circ. beam stay clear h/v (radius) | mm | 9/14 | 9/14 | 11/13 |
| Inj. beam stay clear h/v (radius) | mm | 9/14 | 9/14 | 11/13 |

Beam dump

5.1 Introduction

The FCC-hh dump systems have to abort the beam in a safe and reliable way at any energy level between injection and collision. The stored beam energy and high beam rigidity at collision energy, see Table 5.1, pose a serious challenge for the extraction and dilution systems. Failure cases within the system which could lead to an asynchronous beam dump are of special concern and dominate the system design.

Table 5.1: Beam parameters for FCC injection and extraction.

| Beam parameters | Unit | Injection | Extraction |
|-----------------------|---------------|-------------|---------------|
| Kinetic energy | TeV | 3.3 | 50 |
| β_{rel} | | ≈ 1 | ≈ 1 |
| γ_{rel} | | 3518 | 53290 |
| Revolution period | μs | 326 | 326 |
| Magnetic rigidity | T.m | 11011 | 166785 |
| Bunch spacing | ns | | 25 (5) |
| # bunches | | | 10400 (52000) |
| Bunch intensity | 10^{11} | | 1 (0.2) |
| Transverse emittances | μm | | 2.2 (0.44) |
| Total beam energy | GJ | 0.55 | 8.3 |

The dump system is triggered by an external signal from an interlock system. There is one dump system per beam which extracts the full beam in one turn onto an external dump block. In order to avoid an uncontrolled sweep of particles during the field rise of the extraction kicker, there are one or several abort gaps in the filling pattern. Active and passive beam dilution are applied according to the damage limits of the dump block.

5.2 Extraction straight layout

The ring layout has two extended straight sections, each of 2.8 km length, to house the extraction and betatron collimation systems, as shown in Fig. 5.1.

5.2.1 Baseline layout using superconducting shields

The proposed dump system is based on a single plane extraction. The extraction kickers deflect the beam in the vertical plane, helped by off-centre passage through a focusing quadrupole, to clear the width of a thin superconducting shield (SuShi) which screens an external magnetic field of about 2-3 T [99]. Around 20 m of SuShi are required to clear a septum blade of a 4 T truncated cosine-theta magnet which is several tens of mms thick. Around 50 m of this septum type will deflect the 50 TeV beam outside the cryostat of the downstream lattice quadrupole, see Fig. 5.2. A detailed description of the extraction septa can be found in Ref. [100].

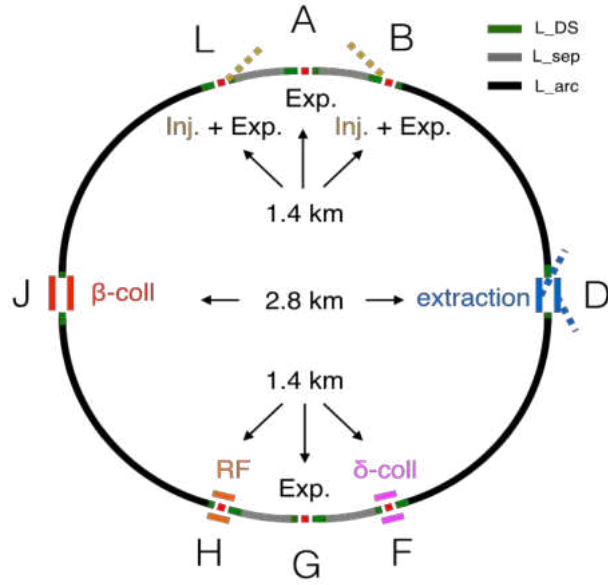


Figure 5.1: Layout of the FCC collider.

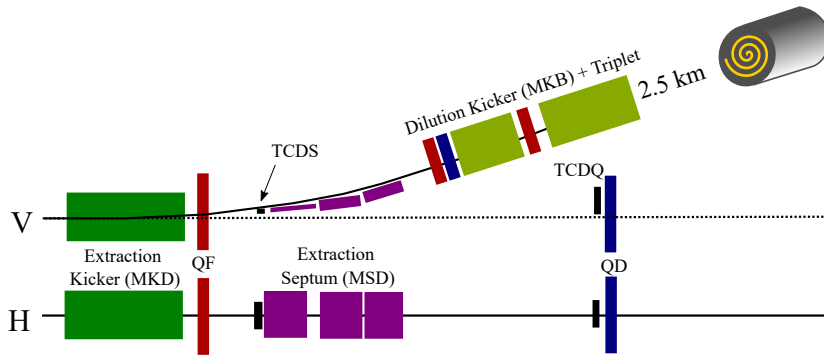


Figure 5.2: Schematic layout of the extraction system, illustrating both planes (not to scale). The septum and quadrupole protection absorbers are labelled TCDS and TCDQ, respectively.

Specific protection absorbers are needed to shield magnets, septa and other equipment in case of kicker malfunctions or timing errors during extraction. The damage limit of the absorbers and therefore the particle distribution in the dump, drive the layout of the extraction insertion and are discussed in more detail below. Energy deposition calculations presented here show that sufficient attenuation to avoid damaging the superconducting coils of the downstream quadrupoles can be provided with a single stage absorber system combined with fixed aperture masks. Therefore, additional cells for extra collimation stages between the two extraction systems are not needed and the two extraction systems can be overlaid as much as possible. The symmetry point of the dump systems is given by the septum protection absorbers which are placed at equal longitudinal location for both systems. The septa are separated longitudinally allowing for superconducting septum technology which probably requires larger transverse dimensions.

The most critical failure case is a beam abort which is not synchronised with the abort gap. In such a case some bunches will be swept over the aperture due to the rise time/shape of the kicker pulse. To protect the superconducting quadrupole and machine elements further downstream, one absorber is placed upstream of the first superconducting quadrupole (see Fig. 5.7). The absorber needs to be ~ 10 m long and a few cm wide to attenuate the longitudinal and radial shower components sufficiently. The longitudinal distance between kicker system and absorber is chosen so that the energy deposition from the secondary particle shower from a beam impact is below the damage limit of the quadrupole coils. For the LHC, the damage limit of NbTi coils from fast beam losses is assumed to be several 100 J/cm^3 [101, 102]. As a first estimate, it can be assumed that the limit is of the same order of magnitude for FCC magnet coils. To mitigate damage to the absorber, it is placed as far downstream from the

kicker magnets as possible in order to increase the bunch separation during the sweep. Losing the full beam on the same spot on the protection absorber is unacceptable because it would lead to hydrodynamic tunneling [103].

The transverse distance between the quadrupole protection and the beam is defined by the hierarchy of the collimation system. Assuming a three stage cleaning system [17], the extraction protection absorber must be placed in the transverse shadow of the secondary collimators in order to avoid deteriorating the cleaning efficiency and to minimise activation of the downstream area in standard operational conditions. On the other hand, this protection element has to shadow tertiary absorbers, which are made of high atomic number materials and therefore have lower damage thresholds for primary particle impact [104]. Depending on the collimation system design and the energy, this position might be around 8 to 12 betatron σ from the beam (current settings for the quadrupole protection: 10.7σ with the secondary collimator at 9.7σ).

The septum protection is designed to protect a septum with a maximum length of 200 m in case of an asynchronous beam abort. A transverse extension between 21.5 and 49.5 mm with respect to the centre of the beam pipe is required to avoid a core bunch impacting on either the beam screen or the extraction channel vacuum pipe. For a reduced system length, the transverse extension of the upper edge of the septum protection absorber can be reduced by up to 0.5 mm. For a nominal beam abort, a beam stay clear distance to the septum protection of $5.1\sigma + 4$ mm tolerance and $>6.2\sigma + 4$ mm to the septum vacuum pipe is guaranteed. In case a larger beam stay clear value is required, the strength of the extraction kickers can be increased.

The β^* reach and consequently the luminosity, are limited by having to respect the above-mentioned protection element hierarchy and taking into account tolerances for optics, orbit, setup errors and mechanical alignment. Any non-zero dispersion in the extraction region has to be taken into account and this will further limit luminosity performance. Aiming at a dispersion contribution of less than half a σ limits the maximum dispersion to about 40 cm in the extraction region. Since the extraction deflection is in the vertical plane, this should be a minor constraint.

The common aperture strategy for the FCC is for all hardware elements to be designed for $\pm 15\sigma \pm 4$ mm beam-stay-clear area. The 4 mm portion accounts for orbit offsets, alignment tolerances and optics uncertainties. The required kicker and septum parameters are summarised in Table 5.2.

Table 5.2: Kicker and septum parameters at FCC extraction.

| Hardware parameters | Unit | Kicker | Septum |
|--|---------|------------|------------|
| Deflection | mrad | 0.045 | 1.15 |
| Integrated field | T.m | 7.5 | 190 |
| System length | m | 120 | 70-90 |
| Effective length | m | 90 | 50-70 |
| Effective septum thickness (first unit) 90 | mm | - | 25 |
| Maximum leak field | T.m | - | < 0.6 |
| Rise time | μ s | 1 | - |
| Flattop length | μ s | ≥ 326 | ≥ 326 |
| Flattop stability | % | ± 5 | ± 1 |
| GFR h/v (radius) | mm | 22.5/16.5 | 26/26 |

5.2.2 Alternative extraction layouts

The extraction layout described above is based on novel septa designs to minimise the space required and power the consumption. These designs have to be carefully evaluated in operating and failure scenarios with respect to their quench and damage limits. If these novel techniques do not meet the required levels of availability and reliability, a fall back solution using superferric Lambertson septa was devised. The septa parameters for the two solutions are compared in Table 5.3. The layouts for the baseline and the alternative option are shown in Fig. 5.3.

There are several additional options which are independent of the single or double plane extraction that ease the requirements for the extraction elements. Adding a bump which moves the beam close the septum blade can be used to reduce the kicker deflection. This bump would need to be off at injection energy where the beam size is largest and ramped up to its maximum at collision energy, thereby reducing the kick strength when the beam is most rigid but also smallest in size.

Table 5.3: Comparison of novel septa (SuShi and truncated cos-Theta) and superferric Lambertson septa at FCC extraction.

| Hardware parameters | Unit | Novel septa | SC Lambertson |
|--|------|-------------|---------------|
| Deflection | mrad | 1.15 | 1.15 |
| Integrated field | T.m | 190 | 204 |
| System length | m | 70-90 | 190 |
| Effective length | m | 50-70 | 150 |
| Effective septum thickness (first unit) 90 | mm | 25 | 25 |
| Maximum leak field | T.m | < 0.6 | < 0.6 |
| Flattop stability | % | ± 1 | ± 1 |
| Beam stay clear h/v (radius) | mm | 26/26 | 23/19 |

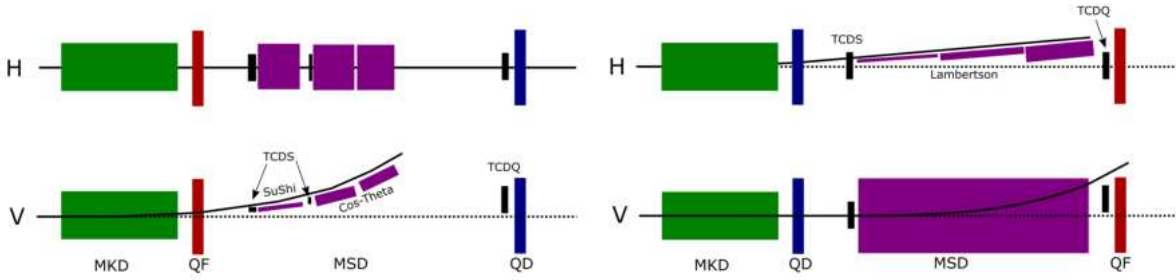


Figure 5.3: Schematic illustration of single (left) and double plane (right) extraction. The single plane deploys novel septa technologies and is considered the baseline. MKD: Extraction kicker; MSD: Extraction Septa; TCDS: Septum protection; TCDQ: Quadrupole protection.

The septum strength can be significantly reduced if the beam does not need to pass outside the downstream quadrupole but can pass through an opening in the cryostat. The downstream drift can be used to place further dipole magnets to direct the extracted beam into the dump channel.

Both options require additional hardware, either for the bumper system and its powering, or a new hardware design of presently planned elements like the quadrupole with an extra opening in the cryostat for the passage of the beam.

5.3 Absorber-driven system design

The FCC dump system and in particular the extraction and the dilution kickers (described below) are designed to respect machine protection requirements. This was studied and documented in detail in [89]. The main focus lies on surviving an asynchronous beam abort and hence preparing an appropriate protection absorber design. Secondly, the probability of such an event has to be reduced. Both aspects are summarised in the following sections.

5.3.1 Protection absorber robustness

The energy deposited by 50 TeV proton bunches in absorber materials poses a severe challenge for the robustness of protection devices. The maximum energy deposition density and temperature inside an absorber are governed by the electromagnetic showers which are concentrated along the shower core. Electromagnetic showers are mainly induced by the decay products (γ -pairs) of π^0 -mesons produced in hadronic cascades. On average, the π^0 s carry about one third of the energy released in hadron-nucleus collisions. The energy deposition density in absorber materials increases compared to the LHC due to the higher proton energy and the smaller angular opening of showers.

Depending on the transverse bunch size ($\sigma_x \times \sigma_y$), and hence the β_x - and β_y -functions at the absorber location, a single 50 TeV FCC bunch can damage some of the most robust absorber materials like graphite or carbon-fibre reinforced carbon (CfC) currently used for intercepting high-energy particle beams. The stresses generated by the thermal shock can compromise the integrity of such materials well below their maximum service temperature, which is typically around 3000°C for graphite or CfC in vacuum. In order to safely absorb FCC

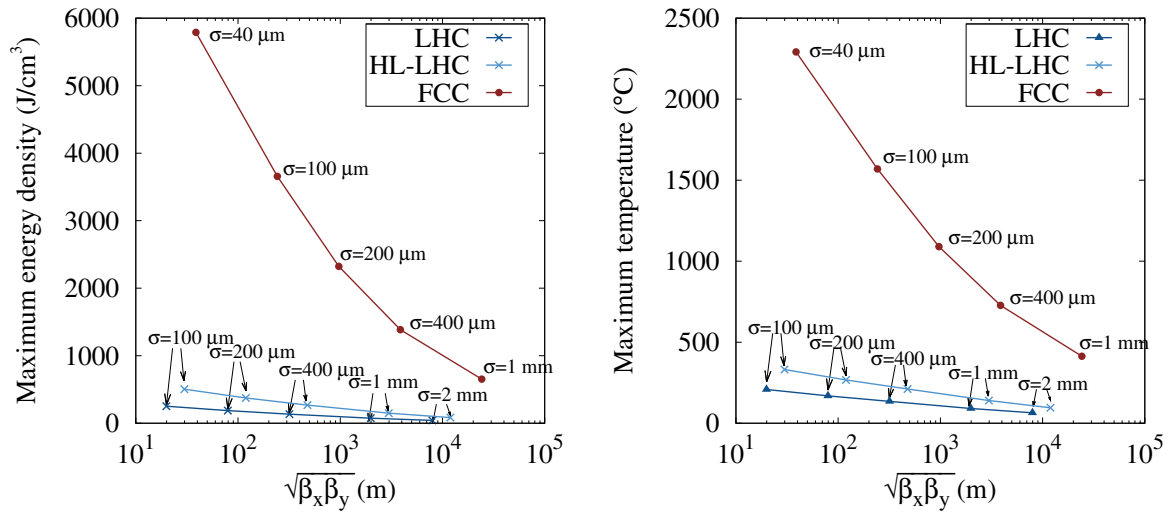


Figure 5.4: Maximum energy deposition density (left) and temperature (right) versus $\sqrt{\beta_x \beta_y}$, induced by a single LHC, HL-LHC and FCC proton bunch in a CfC absorber with a density of 1.4 g/cm^3 . The energy densities were obtained with FLUKA simulations, assuming that beams are round ($\beta_x = \beta_y$). The physical beam size ($\sigma = \sigma_{x,y}$) is displayed next to the data points. The FCC bunch parameters are specified in Table 5.1. The LHC and HL-LHC beam parameters are detailed in the text.

bunches swept across the aperture in an extraction accident, the bunch size needs to be sufficiently large and bunches need to be sufficiently diluted across the absorber front face. In the following, some constraints for the extraction region optics are derived assuming that the robustness of materials is similar to those used for LHC absorbers.

Figure 5.4 shows the maximum energy deposition density and temperature induced by a single FCC bunch in a CfC composite with a density of 1.4 g/cm^3 , as a function of $\sqrt{\beta_x \beta_y}$. The contribution of the dispersive component to the beam size is neglected, i.e. $\sigma_{x,y} = \sqrt{\varepsilon \beta_{x,y} / \beta \gamma}$, where ε is the transverse normalised emittance and $\beta \gamma$ is the product of the relativistic factors. The emittance and bunch intensity were taken from Table 5.1. The results were derived with particle shower simulations using the FLUKA Monte Carlo code [62, 105]. For comparison, the figure also shows the peak energy deposition density and temperature induced by a nominal 7 TeV LHC (HL-LHC) bunch, with a normalised transverse emittance of 3.5 (2.1) $\mu\text{m}\cdot\text{rad}$ and a bunch intensity of 1.15 (2.2) $\times 10^{11}$ protons. For the same β -functions, an FCC bunch gives rise to ~ 25 - 27 times higher peak energy densities than an LHC bunch, and ~ 10 - 12 times higher energy densities than an HL-LHC bunch. Depending on the bunch size and beam energy, the maximum energy deposition and hence the hottest spot occurs at depths between 1.5 and 3 m inside the absorber. To illustrate the effect of the beam energy, Fig. 5.5 compares two-dimensional energy deposition density maps for a 7 TeV and a 50 TeV bunch, assuming that the physical beam size (σ) is the same. The depth of the maximum energy deposition density differs by less than 1 m between the two beam energies.

Composites such as the one in Fig. 5.4 are the material for the core of several protection devices in the LHC extraction region [106]. They combine good mechanical strength with a low density, which reduces the shower-induced peak load. As demonstrated in Fig. 5.4, the peak temperature induced by a FCC bunch exceeds 1000°C if $\sqrt{\beta_x \beta_y}$ is less than $\sim 1 \text{ km}$, and reaches 1500°C if $\sqrt{\beta_x \beta_y}$ is less than $\sim 300 \text{ m}$. Thermo-structural studies carried out for the LHC (see e.g. Ref. [107]) showed that tensile stresses typically exceed the tensile strength of the CfC composites used in LHC absorbers if beam-induced peak temperatures are as high as 1500°C . These results indicate that β -functions at absorber locations need to be larger than several hundred metres in order to safely absorb a single FCC bunch in an LHC-like absorber.

If multiple bunches are swept across an absorber by an asynchronous beam dump, the energy deposition density and temperature induced are driven by the overlap of transverse shower profiles of individual bunches. In addition to the β -functions, the peak energy deposition density therefore depends on the number of bunches intercepted by the absorber and on their transverse separation during impact. For the layouts and system parameters presented here, the maximum number of bunches intercepted by protection absorbers in the extraction region is

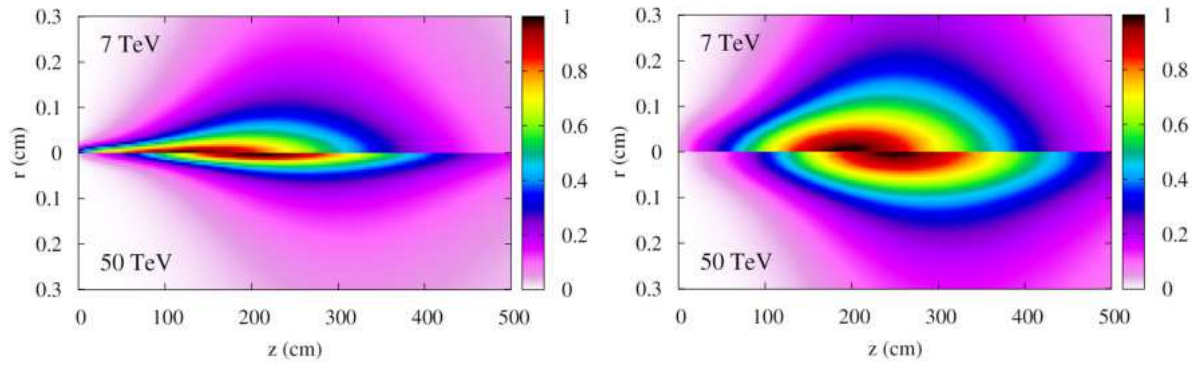


Figure 5.5: Energy deposition density maps, calculated with FLUKA, for a 7 TeV bunch (top half) and a 50 TeV bunch (bottom half) in a CfC absorber with a density of 1.4 g/cm^3 . The beam size (σ) is assumed to be $100 \mu\text{m}$ in the left figure, and $400 \mu\text{m}$ in the right figure. The beam direction is from the left to the right. The z -variable indicates the absorber depth and the r -variable the radial distance from the beam axis. All maps are expressed as a fraction of the maximum energy deposition density.

less than 20. Figure 5.6 shows the peak temperature generated by multiple bunches impacting on a CfC absorber, assuming that $\sqrt{\beta_x\beta_y}$ is $\sim 1 \text{ km}$, which is the minimum $\sqrt{\beta_x\beta_y}$ at absorbers in the extraction optics presented in the next section. The curves in the figure show the effect of different transverse bunch separations. In order to absorb 20 bunches and keep the maximum temperature around 1500°C , neighbouring bunches need to be separated by about 2 mm . The separation can be somewhat smaller if fewer bunches impact on the absorber or if $\sqrt{\beta_x\beta_y}$ is higher than the 1 km assumed.

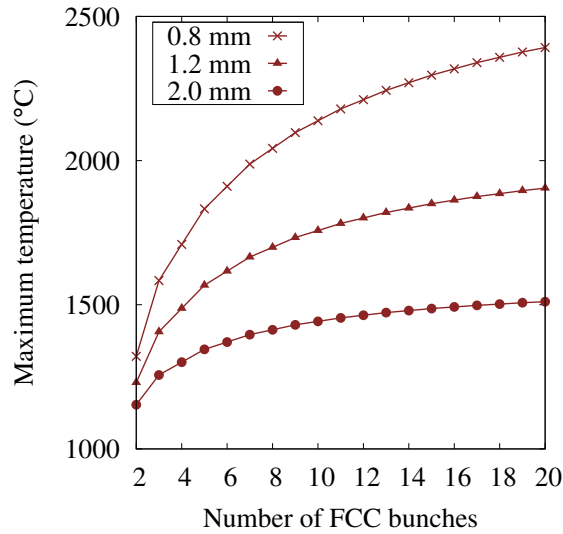


Figure 5.6: Maximum temperature in a CfC absorber (1.4 g/cm^3) as a function of the number of FCC bunches swept across the absorber front face. The temperatures were calculated in adiabatic limit, using FLUKA energy deposition results. The transverse bunch size (σ) was assumed to be $200 \mu\text{m}$, which corresponds to $\sqrt{\beta_x\beta_y} \approx 1 \text{ km}$. The different curves assume a different transverse bunch separation in the sweep direction.

The temperature limit adopted only allows a first approximate assessment of constraints arising from limited absorber robustness. Thermo-structural studies are necessary to refine these constraints based on the stresses generated by the beam-induced temperature gradients inside the absorbers. In addition, the limits derived are based upon the assumption that carbon composites similar to those of the LHC are used. The qualification of new or improved materials with a better resistance to high-energy particle beams will, to some extent, relax these requirements. Beam impact tests such as in the CERN HiRadMat [108] facility are essential for probing material limits and for quantifying the dynamic response to extreme thermal shocks. Examples of promising candidate materials for future absorbers are 3D carbon composites or carbon foams. Some of these materials are already

being tested in the framework of the LIU and HL-LHC projects [109, 110]. An alternative approach to cope with the extreme energy deposition in the FCC could be the use of sacrificial absorbers which are replaced after accidental beam loss damage. Robustness to beam impact is however, not the only criterium for selecting absorber materials. They must also exhibit a low outgassing rate to meet vacuum specifications, and they should have a good electrical conductivity to minimise the resistive wall heating.

5.3.2 Extraction straight optics and extraction kicker parameters

There are two main reasons for adapting the optics: beam dilution on the absorbers and minimum oscillation from a single kicker pre-fire, Fig. 5.7.

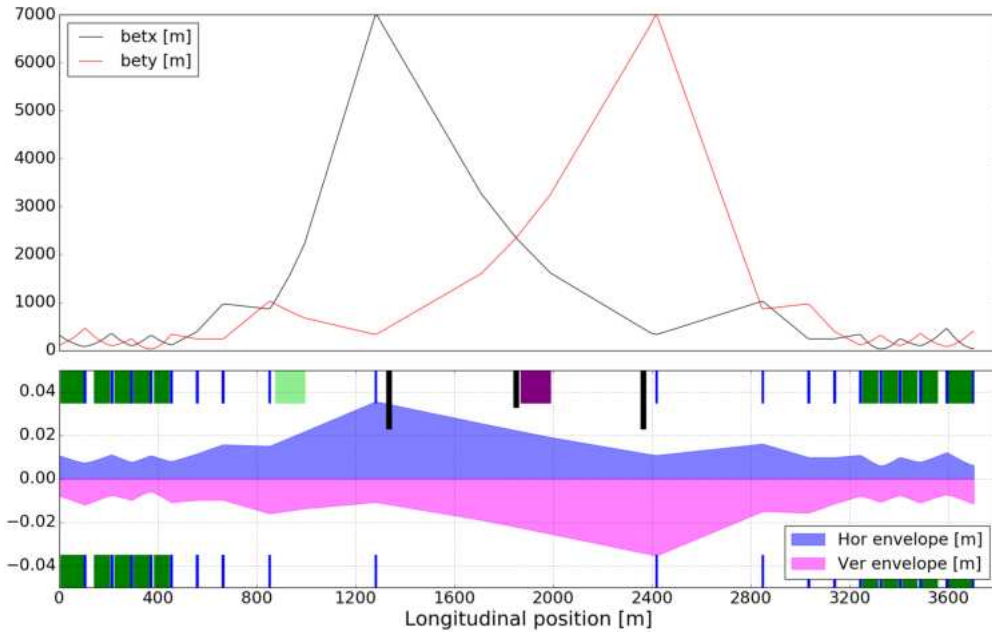


Figure 5.7: Optics and beam envelopes of the extraction straight section.

High betatron functions in both planes ($\sqrt{\beta_x \beta_y} > 1$ km) at the protection absorbers are designed to reach the required dilution for single bunch impact. In addition, a fast rise time of the kickers ($1 \mu\text{s}$) is needed to limit the number of bunches striking the protection absorbers and to increase the transverse bunch separation in the sweep direction. Figure 5.8 shows the resulting beam deflection and particle distribution on absorbers for an asynchronous beam dump. About seven bunches, separated by 4-5 mm, impact on the quadrupole protection absorber (TCDQ), and about 12 bunches, separated by about 2 mm, impact on the septum protection absorber (TCDS). In both cases, the shower-induced temperatures in the absorber are acceptable ($<1500^\circ\text{C}$) according to the constraints presented in the previous section.

The failure scenario considered above assumes that all kickers fire simultaneously, but asynchronously with the abort gap. This could happen in case of a timing error, for example. Another failure scenario is the erratic pre-fire of one or more kickers. In the case that only a single kicker pre-fires, it is proposed to accept an oscillation of about 1.5σ for up to one turn followed by a dump synchronised to the next abort gap. In order to keep the beam displacement from a single kicker unit as small as possible, the kicker system is being designed with a high segmentation of about 150 units and the betatron function in the bending plane is minimised. For the dump system in the LHC, a kicker pre-fire is detected internally and all the remaining kickers are re-triggered within 800 ns. To reduce the time between a pre-fire and synchronisation with the abort gap, it is beneficial to have several abort gaps in the machine. Another driver of the high segmentation of the kicker system is the possibility to have ‘hot’ spares installed. If a small number of modules fails, a clean extraction can still be guaranteed and therefore the repair can be scheduled in a technical stop.

The feasibility of this concept with respect to the load on the collimation system and beam-beam effects is discussed in Ref. [89] and Chapter 9. This scenario should be compared to other failure scenarios leading to a

sudden beam orbit excursion in order to define the maximum acceptable oscillation amplitude.

The overall extraction parameters were chosen so that for 150 modules a single kicker switch has to hold off a moderate voltage of around 5 kV, and switch 4 kA/ μ s. To reach the challenging rise time of 1 μ s, the length of one module is 0.6 m. The betatron function in the non-bending plane is minimised to lower the aperture in the corresponding plane and hence the system inductance. Balancing the electrical parameters against the number of modules is illustrated in Fig. 5.9. The complete preliminary parameter list of the extraction kickers is shown in Table 5.5.

Alternative switch topologies like crow-bars and series switches lead to different failure probabilities and would change the optimum number of modules. A detailed hardware study including prototyping is required before choosing the switch design.

5.3.3 Protection efficiency in case of asynchronous beam dumps

Apart from being robust enough, a protection device needs to sufficiently shield downstream equipment from the showers generated by the 50 TeV protons. For a CfC absorber, like the one considered above, the shower maximum occurs at a depth of roughly 3 m. To optimise the absorption of secondary showers, other materials, like higher-density graphite, can be used further downstream where the shower-induced energy deposition density is lower. Similar sandwich solutions have been adopted for the LHC [106]. For the FCC, a total absorber length of the order of 10 m is sufficient to protect equipment components which are in its geometrical shadow. FLUKA shower simulations indicate that for the worst case where 12 bunches are swept across the septum protection absorber, the temperature increase in the steel septum blade is a few 10 K if a 10 m long LHC-like absorber sandwich of low- and high-density CfC is used.

If mis-steered FCC bunches impact close to the absorber edge or if they graze the absorber, the energy deposition in downstream equipment is dominated by secondary particles leaking through the absorber gap. For such accident scenarios, one can only achieve a limited gain by increasing the absorber length and in addition one needs mask-like shower absorbers just upstream of the magnet or septum to protect components which are not shaded by the primary absorber.

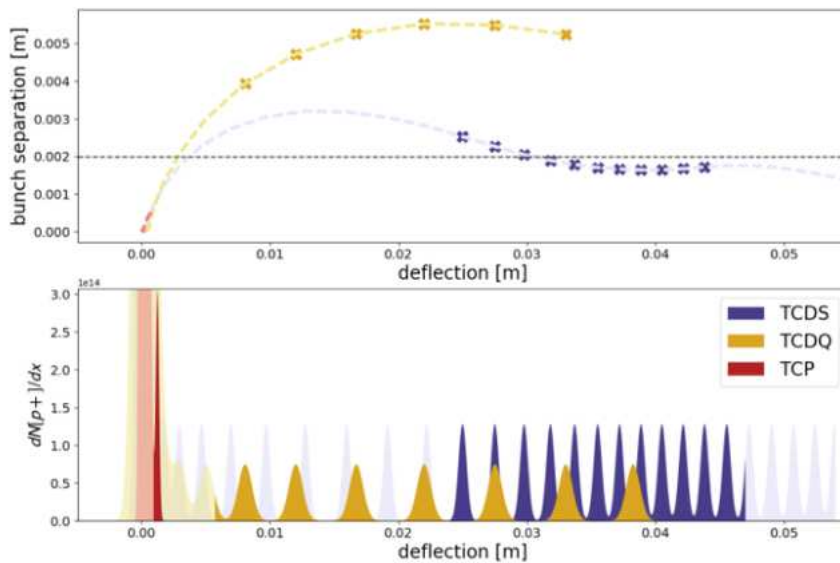


Figure 5.8: Particle distribution and bunch separation for bunches impacting the primary collimators (TCP), quadrupole (TCDQ) and septum protection (TCDS) in an asynchronous dump with an MKD rise time of 1 μ s.

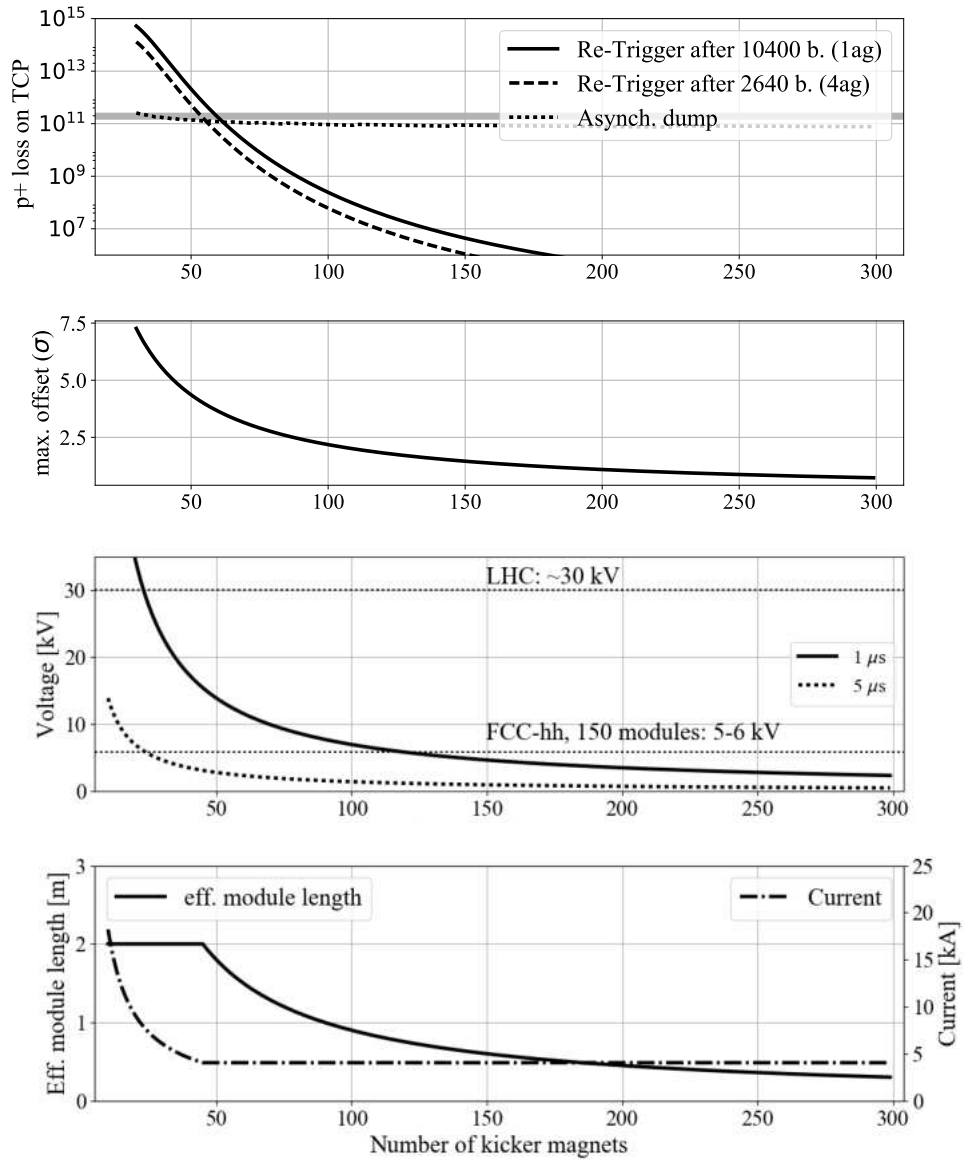


Figure 5.9: Impact of segmentation choice on hardware parameters and losses in the case of pre-firing MKDs. From top to bottom: Approximate losses at TCP for different abort strategies for a single erratic MKD; maximum mis-kick in case of single failing MKD; capacitor voltages required for an MKD rise time of $1 \mu\text{s}$ and $5 \mu\text{s}$; module length and current required.

5.4 Dump line layout and dilution

The extracted proton beams must be disposed of on a beam dump which absorbs a large fraction of the energy carried by the beam particles. The dump needs to be surrounded by heavy shielding to reduce the activation of the surrounding environment. As indicated in the previous sections, the FCC proton beams are highly destructive for any solid material and must be swept transversely across the front face of the dump by dilution kickers to avoid excessive temperatures and stresses in the dump core. Graphite has been the preferred material choice for most high-energy hadron dumps at CERN [111, 112] and other facilities (see e.g. [113–115]) because of its low atomic number, its high thermal shock resistance and its high melting point. Low-density variants like graphite foams ($<0.5 \text{ g/cm}^3$) or innovative solutions like carbon powder-based dumps are promising directions of study for the FCC, but a first estimate of the dilution requirements and the minimum dump dimensions can be derived by assuming a conventional LHC-like graphite core. These aspects, including the kicker parameters and the sensitivity to dilution failures and abnormal operating conditions, are presented below. Some considerations of alternative dump concepts are briefly outlined at the end of the section. These include dilution-free dumping systems based

on water or gas dumps. Such concepts have been studied within the FCC project and in previous high-energy collider studies, but these systems imply other challenges such as dump vessels which are hundreds of metres long.

5.4.1 Baseline dump concept and dilution requirements

The baseline option is to extract the beam onto a LHC-like dump made of low-density graphite sheets or blocks ($\sim 1 \text{ g/cm}^3$). In order not to exceed temperatures of about 1500°C in the dump core, the bunch train needs to be diluted. Assuming a spiral shaped bunch pattern on the dump, consecutive bunches have to be separated by about 2 mm and branches of the spiral need to be separated by about 20 mm. This means that the sweep path length must be at least 22 times longer than for the LHC (1.2 m). It is planned to provide this pattern with a combination of horizontal and vertical kickers, which are powered with a damped sinusoidal pulse, i.e. the spiral radius is maximum at the beginning of the sweep and decreases continuously throughout the sweep.

The footprint of the spiral pattern on the dump depends on the dilution kicker frequency and would be smallest if the frequency is modulated along the sweep path. This would, however, increase the complexity of the system and would enhance the sensitivity to dilution failures and non-ideal operating conditions like small frequency offsets between individual kicker modules. It is therefore envisaged to maintain a constant kicker frequency of 50 kHz. Such a frequency is needed to keep the temperature below 1500°C when dumping a full 25 ns FCC-hh beam with 10400 bunches and 10^{11} protons per bunch. The initial spiral radius is assumed to be 550 mm, which, for a 2.5 km long dump line, requires a pulse strength of 30 T.m. These parameters are presently considered very challenging, but in reach given that the time scale of the project allows for sufficient research and development.

Like in the LHC dump, the low-density graphite segment only needs to extend a few metres around the shower maximum, i.e. in the region where the shower-induced energy densities and temperatures are the highest. In order to make the dump more compact, the low-density part can be combined with higher-density graphite blocks at the up- and downstream ends. These blocks enhance the initial shower build-up and increase the attenuation of particles beyond the shower maximum, therefore reducing the total core length. Since the shower length only scales logarithmically with beam energy, the core length only increases moderately compared to the LHC, i.e. the length of a LHC-like FCC-hh dump would be of the order of 10-20 m (compared to about 8 m in case of the LHC). The radius of the dump needs to be at least 70-80 cm to have sufficient distance to the housing of the core.

One way to reduce the requirements for this safety critical system is to introduce a focusing structure in the dump line. This allows the optics functions at the dump to be controlled independently of the collider optics. Diluting the beam by increasing the spot size on the dump does not significantly decrease the peak energy deposition due to the overlap of the transverse shower of consecutive bunches. However, by over-focusing the deflected beam trajectory after the first dilution kickers, not only can the deflection strength of these kickers be reduced, but also the non-bending plane aperture of the downstream kicker system. Figure 5.10 shows the beam envelope range along the dump line. While in the very beginning of the line the effective beam envelope is given by the beam size, after the first dilution kickers, the effective area covered by beam is given by the beam size around the deflected trajectories. The maximum deflection is shown in Fig. 5.10. The top part of Fig. 5.11 shows the effect of reducing the horizontal kick strength and the bottom part shows the reduction in required vertical kicker aperture when comparing a dump line with and without focusing structure.

5.4.2 Sensitivity of the dilution pattern to various failure cases and non-nominal operation

The sensitivity of the sweep pattern to different operational scenarios and failure cases has been studied. Here, a sweep pattern with a branch separation of 20 mm and a minimum bunch separation of 1.8 mm is assumed, resulting in a maximum radius of 55 cm.

Asynchronous beam dump

The MKB rise time is $5 \mu\text{s}$, whereas the MKD rise time is $1 \mu\text{s}$. During a nominal dump, the MKD are triggered $4 \mu\text{s}$ after the MKB generators to provide the preparation time required for the MKB system. In case of an asynchronous beam dump however, the MKB generators are only re-triggered once the MKD field rises and hence bunches pass through the MKB system during the rising edge of the field. This results in an increased energy deposition at the beginning of the the dilution pattern, as illustrated in Fig. 5.12. The sweep pattern based on a modulated frequency does not provide margin for this increased energy deposition and survival of the dump would not be guaranteed (peak dose of $>8 \text{ kJ/g}$). The updated sweep pattern based on the constant frequency results in

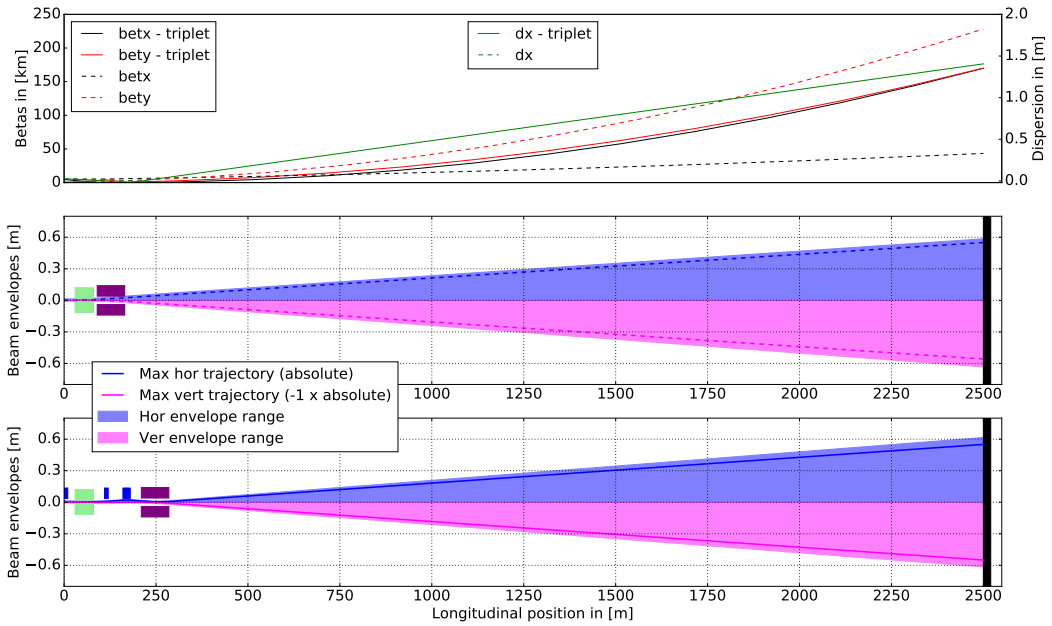


Figure 5.10: Optics and beam envelopes of the dump lines. Horizontal dilution kickers in green, vertical ones in purple. The beam envelopes in blue show the absolute value of the horizontal beam stay clear area. The envelopes in magenta show the vertical absolute beam stay clear area multiplied by -1. The solid and dashed lines compare the maximum deflection trajectories in both planes for a dump line with and without focusing structure.

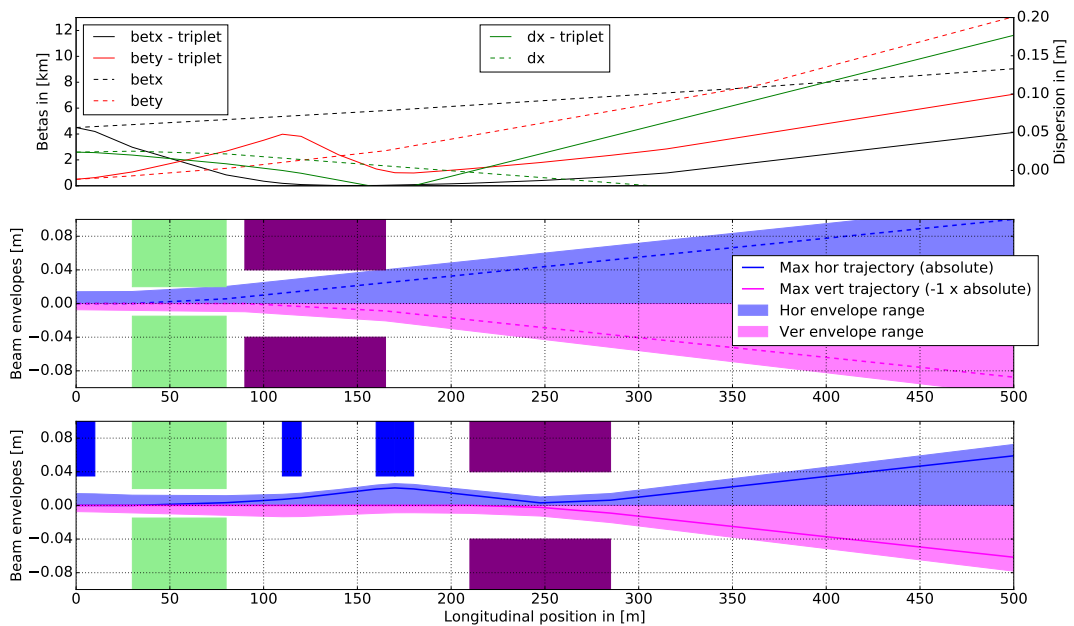


Figure 5.11: Zoom into the dump line area around the dilution kickers. The reduction for the horizontal beam stay clear area in the vertical dilution kickers for the dump line with focusing structure is shown.

lower energy deposition values for an asynchronous dump, i.e. a peak dose of ~ 4 kJ/g and a maximum temperature of 2150°C . Further material tests are needed to judge if such a shock heating leads to local damage inside the

graphite core but it is nevertheless expected that the dump remains functional in such an event. The impact on other equipment, such as the vacuum windows upstream and downstream the TDE, has to be evaluated in further studies.

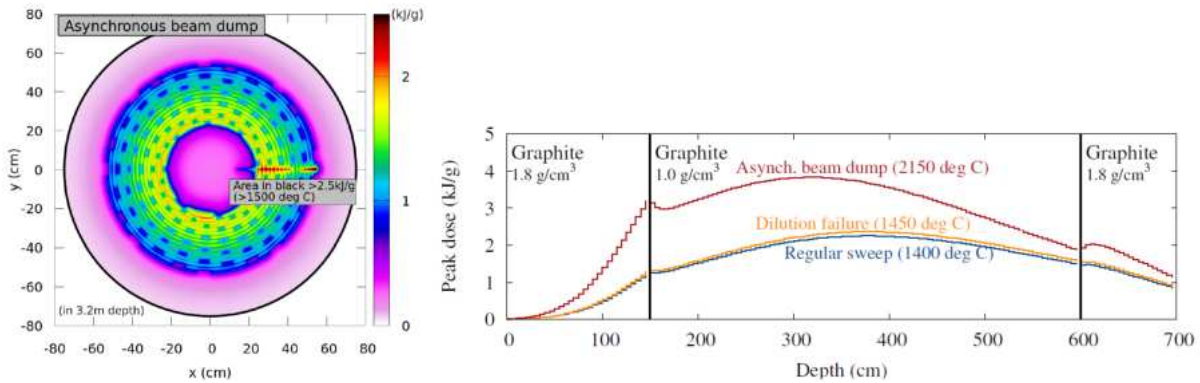


Figure 5.12: Left: Sweep pattern and peak dose for an asynchronous dump. Right: Peak dose in the TDE for a regular sweep (blue), an asynchronous dump (red) and 90% horizontal dilution (yellow).

Missing extraction and dilution kicker

The system is designed to run with a reduced number (i.e. 90%) of MKB and MKD to increase the availability. The resulting peak dose for operation with 10% missing horizontal and vertical MKB corresponds to a maximum temperature of 1450°C, which is comparable to the maximum temperature of the regular sweep (1400°C), as illustrated in Fig. 5.12. A reduced MKD kick strength does not result in any distortion of the sweep pattern but it shifts the entire pattern by ~4 cm.

Dilution kicker frequency mismatch

Due to the long sweep path, the high frequency oscillation is sensitive to frequency mismatches. The following scenarios have been studied:

- A systematic frequency mismatch $\Delta\nu$ of the horizontal and vertical system,
- Random errors of all generators with an RMS error of $\Delta\nu$.

The results of the FLUKA simulations are illustrated in Figs. 5.13-5.15. It can be preliminarily concluded, that for a frequency mismatch between MKBV and MKBH a maximum error of $\Delta\nu/\nu = 0.2\%$ is tolerated. This results in a temperature increase of ~100°C compared to the nominal sweep pattern. The impact of randomly distributed frequency errors of all generators is less critical and errors larger than $\Delta\nu/\nu = 0.2\%$ might be acceptable. A threshold for these random errors is to be evaluated in further studies to complement the MKB generator specifications.

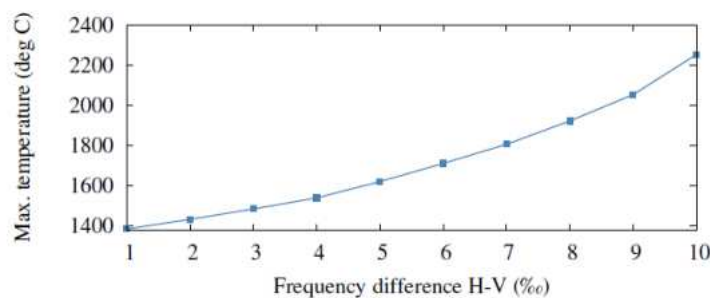


Figure 5.13: Maximum temperature increase for dilution patterns with a systematic frequency mismatch between horizontal and vertical MKB system .

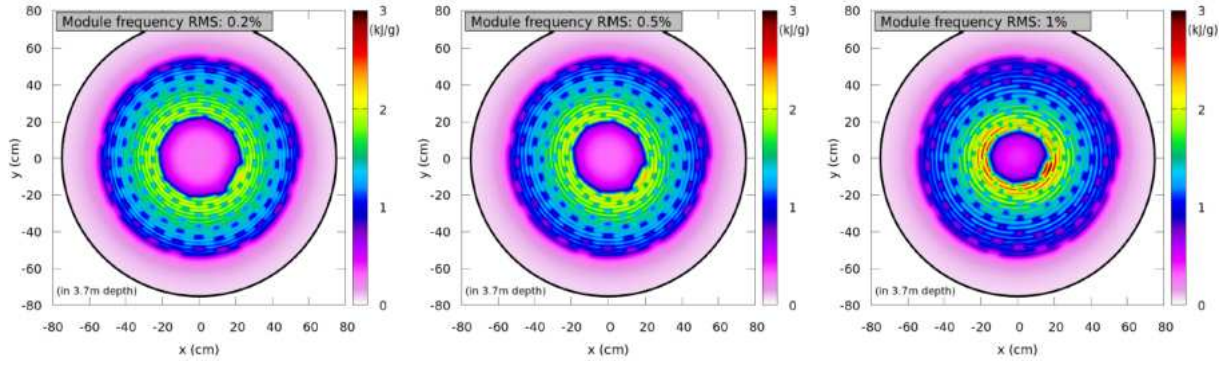


Figure 5.14: Dilution pattern with random frequency errors of all generators with a RMS error of $\Delta\nu/\nu$.

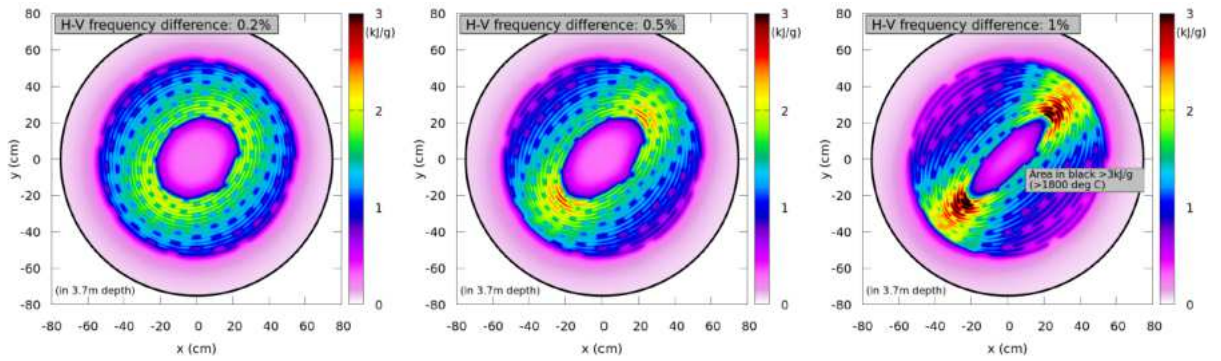


Figure 5.15: Dilution pattern for a systematic frequency mismatch $\Delta\nu/\nu$ of the horizontal and vertical system.

Combination of non-nominal operation of multiple systems

A combination of the above mentioned cases has been evaluated to complete the studies of the sensitivity of the dilution pattern to non-operational scenarios. In addition, the impact of the MKD flat top variation has been investigated by scaling the LHC waveform to FCC timescales. The resulting maximum temperatures are listed in Table 5.4. It can be seen that the intrinsic dilution due to the MKD flat-top ripple results in a marginally reduced maximum temperature (1360°C compared to 1400°C). A loss of 10% dilution in both planes leads to a temperature increase of 200°C. Random frequency deviations do not increase the temperature significantly. However, simulations using different seeds may need to be conducted to evaluate the impact of such random errors in more depth. A frequency mismatch of 0.2% between MKBV and MKBH results in a temperature increase of another 100°C. To conclude, a non-nominal operational scenario with 90% dilution in both planes, 90% MKD kick strength and a frequency mismatch, results in a maximum temperature of 1630°C which is acceptable from the current point of view. The impact of an asynchronous dump for such a case will be evaluated in further studies. It has to be noted, that the maximum temperature depends on the value assumed for the heat capacity of the dump core material and is therefore subject to changes. However, the relative difference between the various operational scenarios is apparent as all cases are computed with the same heat capacity.

Table 5.4: Peak temperature for different operational scenarios.

| Case | 0 | 1 | 2 | 3 | 4 | 5 | 6 | 7 | 8 | 9 | 10 | 11 | 12 |
|--|-----|------|------|------|------|------|------|------|------|------|------|------|------|
| MKD flattop var. | n | y | y | y | y | y | y | y | y | y | y | y | y |
| Rel. MKD kick | 1 | 1 | 0.9 | 1 | 0.9 | 1 | 0.9 | 1 | 0.9 | 1 | 0.9 | 1 | 0.9 |
| Rel. MKBH kick | 1 | 1 | 1 | 0.9 | 0.9 | 1 | 1 | 0.9 | 0.9 | 1 | 1 | 0.9 | 0.9 |
| Rel. MKBV kick | 1 | 1 | 1 | 0.9 | 0.9 | 1 | 1 | 0.9 | 0.9 | 1 | 1 | 0.9 | 0.9 |
| $\Delta\nu/\nu$ random [%] | 0 | 0 | 0 | 0 | 0 | 0.2 | 0.2 | 0.2 | 0.2 | 0 | 0 | 0 | 0 |
| $\Delta\nu/\nu$ h-v [%] | 0 | 0 | 0 | 0 | 0 | 0 | 0 | 0 | 0 | 0.2 | 0.2 | 0.2 | 0.2 |
| Max. T [10^3°C] | 1.4 | 1.36 | 1.36 | 1.56 | 1.55 | 1.37 | 1.36 | 1.57 | 1.56 | 1.44 | 1.44 | 1.64 | 1.63 |

5.4.3 Alternative dump absorber systems

The dilution system described above is complex and failure scenarios need to be carefully evaluated. Compared to the graphite and carbon reinforced carbon composites used in the LHC, some benefits in terms of beam dilution can be expected from carbon foam- or powder-based dumps, but the dilution requirements will be substantial in this case. Alternatively, one could envisage dump concepts where no beam dilution is required. Depending on the material and the transverse bunch size, even a few or a few tens of FCC proton bunches would provoke a phase transition in a solid or liquid absorber if the beam is not diluted. The resulting shock waves lead to a reduction of material density along the beam path and, as a consequence, the following bunches can penetrate deeper inside the target. This effect is called hydrodynamic tunnelling. As proposed in Ref. [116], a dilution system can be avoided if the beam is dumped on a water absorber which is sufficiently long to contain the tunnelled FCC beam. The dimension of the water container required is estimated to be a few hundreds of metres [116]. The feasibility of this dump concept still has to be studied, in particular the vacuum system, the beam windows, the container confinement and radiation protection aspects.

5.5 Other failures of the extraction system

Further failure scenarios have only been briefly analysed at this stage due to their lower impact or probability. MSD powering failures are not expected to be critical due to the large time constant of the current decay for superconducting magnets. The field decay of the SuShi and truncated cosine theta septa following a quench should be studied further. An internal surveillance system directly linked to the TSU and independent of the BIS might be necessary to guarantee a fast synchronous beam abort in case of septa failures.

A further failure, which is worth mentioning, is the so-called ‘dead lock situation’: if the MKD are triggered asynchronously during the injection process the injection process must be stopped as described in [89].

Table 5.5: Approximate MKD and MKB parameters for the lumped inductance magnets and generators studied.

| Parameters | Unit | MKD | MKBH | MKBV |
|---|---------|------------|-------------|-------------|
| Deflection | mrad | 0.045 | 0.13 | 0.25 |
| Integrated Field | Tm | 7.5 | 22 | 42 |
| System length | m | 120 | 57 | 110 |
| Magnetic length | m | 90 | 43.5 | 83.5 |
| Modules | # | 150 | 29 | 56 |
| Module length | m | 0.6 | 1.5 | 1.5 |
| Rise time | μ s | 1 | 5 | 5 |
| Capacitor voltage | kV | 5 | 12 | 19 |
| Peak current | kA | 4 | 12 | 16 |
| Flattop length | μ s | ≥ 326 | - | - |
| Flattop stability | % | ± 5 | ± 5 | ± 5 |
| Good Field Region (GFR) h/v (\emptyset) | mm | 45/33 | 24/24 | 34/40 |
| Aper. h/v (\emptyset) | mm | 61/49 | 30/30 | 40/46 |
| Inductance | μ H | 0.75 | 2.3 | 2.6 |
| Frequency | kHz | - | 50 | 50 |
| $\frac{\Delta\nu}{\nu}$ mismatch | - | - | $\pm 0.2\%$ | $\pm 0.2\%$ |

5.6 Summary and outlook

The dump system design described above is a consistent and self-contained concept covering kicker, septa, absorber and optics design.

Several alternatives have been envisaged for each subsystem like the kickers (segmentation, switch topology, frequency beating), for septa hardware (superconducting shield, cos-theta magnets, mass-less septa, super-ferric and normal conducting Lambertson, respectively), the absorber material for the dump (water, gas, foam, powder), and conceptual aspects (asynchronous beam dump in case of erratic, sacrificial absorber design, beam passage through magnet cryostat, several beam dump systems). Most of these alternatives are described in more detail in references [89, 100, 117].

Prototyping of kicker switch topologies will be necessary to define the optimum choice with respect to machine protection and availability. The novel superconducting shield septum concept promises to have very performance; it requires further studies to ensure its feasibility regarding material properties, damage limits and quench characteristics. The choice of Lambertson septa remains a back-up solution.

Certain absorber alternatives like the water dump are not chosen as baseline since their feasibility cannot be judged without making a detailed engineering design where most of the challenges are expected.

With the present knowledge of limits in hardware elements, the dump system described above is optimum in performance and feasibility. There are currently two main challenges which need further action. First is a need for a careful validation against all known failure scenarios for the dilution system and dump absorber together with a feasibility study of the dilution kicker hardware. The second main challenge is the triggering system which has to be different from the LHC architecture to reach demanding short system re-trigger delays, for example.

Arc concept

6.1 Overview

Like LHC, the arcs are made of FODO lattices with a phase advance of about 90° in both planes. A phase advance of 90° has several advantages: the ratio between maximum betatron function and cell length is near the minimum, the dispersion function is quite small and it facilitates more efficient correction schemes. The length of the arc cells is optimised as a trade-off between the filling ratio, the normalised aperture available, the achievable gradients and civil engineering constraints [118, 119]. Civil engineering studies have shown that short arc regions (SAR) should be 3.4 km long. Since the length of the SAR is an integer multiple of the arc cell length, the possible space is thus strongly constrained. The FODO cell length is fixed at 213.04 metres [120] and as a result the long arc regions (LAR) contain 78 FODO cells and the SARs contain 20 FODO cells.

The global tune and the phase advances between interaction points are set by adjusting the phase advance of the FODO cells in each long arc. In other terms, the phase advance within each of the 4 LAR is 90° plus ϵ , the value of ϵ being calculated to get the desired tune values. The phase advance in the FODO cells of the SAR is still 90° . The cross-talk through the yoke between the two dipole chambers gives a systematic b_2 component of 6 units in the dipoles for a beam separation of 250 mm at injection. At collision energy, the value of b_2 is near 0. The sign of b_2 is negative/positive in the inner/outer aperture for $\cos\theta$ or block configurations. This b_2 component is corrected by the main arc quadrupoles to maintain the phase advances in the FODO cells and the impact on the optical functions stays small (a few percent).

6.2 System layout and optics

The arc cells are made of 12 dipoles and 2 short straight sections (SSS). The distance between two dipoles of 1.5 m is to allow for the interconnections, the distance between the dipoles and the SSS is 1.3 m not including BPMs. Each SSS contains one BPM, one sextupole to correct the chromaticity, one main quadrupole, one multipole (trim/skew quadrupole or octupole), and one dipole corrector. The distance between two magnets inside the SSS is 0.35 m. The total length of the SSS is 11.3 m. Dipoles and main quadrupoles will use Nb_3Sn technology whereas other multipoles will use NbTi. The maximum dipole field is 15.81 T. The layouts of the arc half-cell, of the cryo-dipole and of the short straight section are shown in Figs. 6.1, 6.2 and 6.3, respectively.

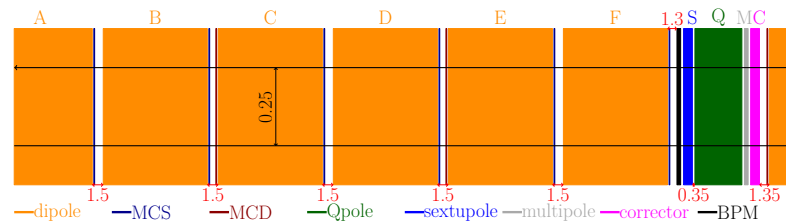


Figure 6.1: Layout of the half-cell in the arcs.

The global chromaticity is corrected by arc sextupoles. Octupoles are integrated in the arcs for Landau damping or compensation of beam-beam effects. Feedback systems are used for the fundamental mode of collec-

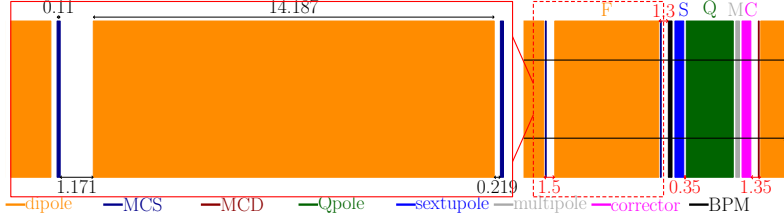


Figure 6.2: Layout of the dipole in the arcs.

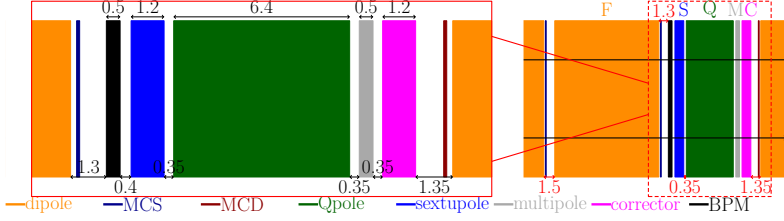


Figure 6.3: Layout of the short straight section in the arcs.

tive oscillations. The strength and the number of the octupoles are chosen to maintain the beam in the stability region from injection to collision [121] (see Section 8.7.1).

The optical functions and normalised aperture in the arc cell are shown in Fig. 6.4 at the injection energy where b_2 is positive in the dipoles. The small difference between the maximum value of β_x and β_y comes from the systematic value of b_2 in the dipoles. The beam stay clear limit is 16.9σ , well above the specifications of 13.4σ .

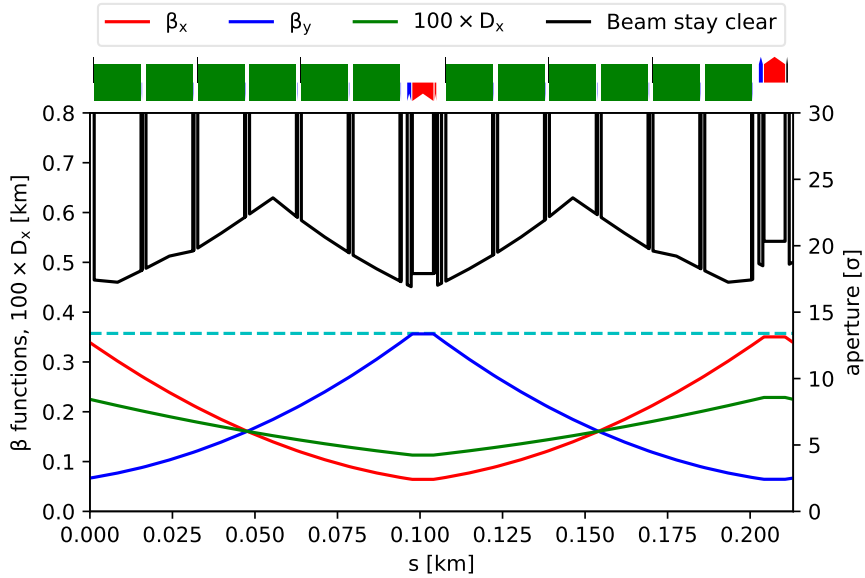


Figure 6.4: Optical functions in the arc cells (β_x in blue, β_y in red, and $100 \times D_x$ in green). The beam stay clear region at injection energy (3.3 TeV) is shown in black. The cyan horizontal line shows the target value of 13.4σ .

6.3 Key issues

One of the main cost driving items of the FCC-hh ring is the dipole and more particularly the maximum dipole field. Early in the design phase, arcs cells were optimised to maximise the filling ratio and thus to minimise the dipole field needed [119]. Therefore anything which contributes to the reduction of the filling ratio, like interconnection distances or the SSS components lengths, requires careful study.

6.4 Synchrotron radiation

At 50 TeV, the proton beam will radiate significant quantities of photons in the arc dipoles. The synchrotron radiation (SR) fluxes expected in FCC-hh are shown and compared to LHC and FCC-ee in Fig. 6.5. This flux results in a heat deposition of the order of 30 W/m on the beamscreen. In order to evacuate this power a new design of the beamscreen in the main arc dipoles has been proposed, prototyped and tested in a light source [122]. The beamscreen design has longitudinal slots in the plane where the SR photon fan is directed, as shown in Fig. 6.6.

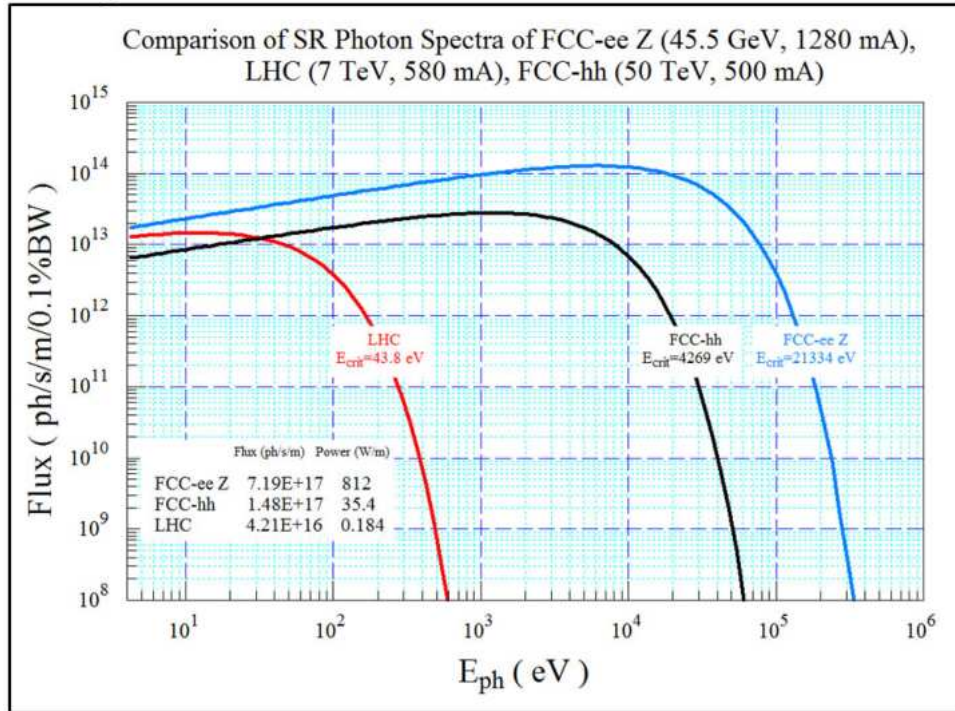


Figure 6.5: Synchrotron radiation photon flux spectra for LHC, FCC-ee (Z-pole) and FCC-hh beams.

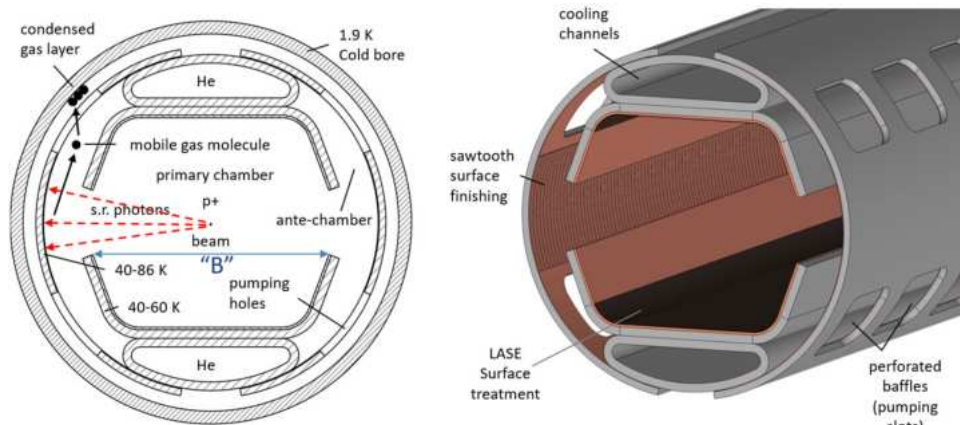


Figure 6.6: Latest beamscreen design. The internal part has a height of 26.9 mm and a width "B" of 27.55 mm.

The height of these longitudinal slots has been optimised to limit their effects on the impedance budget. At the same time they preserve the vacuum quality, capturing a large fraction of primary SR photon fan during the acceleration phase [1, Section 3.3.2]. Calculations have also shown that they reduce electron cloud build up (see Chapter 8).

The SR mitigation has an impact on the beam stay clear region in the arcs. For this reason the present beamscreen design is used in the calculation of the available machine aperture, as explained in Section 9.3. The calculation also takes into account SR absorbers placed about 0.6 m downstream of every arc dipole to protect

the connection to the next magnet. This reduces the horizontal aperture by 1.630 mm at these absorbers (see Section 9.3). Nevertheless, the beam stay clear limit is above the target value in the arcs at both collision and injection energies, as shown in Fig. 6.4.

The use of longitudinal slots in the beam screen to evacuate the SR photon energy affects the linear correction schemes, adding tolerances on the residual orbit and beam angle (see Section 7.4). This also limits the use of orbit bump techniques in the arcs to correct or to measure optical quantities.

Finally, SR damps the emittance of proton beams at 50 TeV. Considering the classical radiation and quantum excitation given by SR, the equilibrium emittance for the present lattice is :

$$\epsilon_{x0} = C_q \gamma^2 \frac{I_5}{j_x I_2} \approx 1 \times 10^{-12} [\text{m}] \quad (6.1)$$

where $C_q = \frac{55\hbar}{32\sqrt{3}m_p c} = 2.08692 \times 10^{-16}$ is a constant, γ is the relativistic gamma, I_5, I_2 are the synchrotron radiation integrals (which are affected by the lattice design) and j_x is the horizontal damping partition number. The estimated SR damping time is of the order of hours which is enough to give luminosity enhancement in the ~ 4 h collision phase (see Section 1.3.2), but it is not enough to damp instabilities, for which feedback systems and Landau damping octupoles are still required (see Chapter 8).

6.5 Hardware specification

The maximum gradients in the Nb₃Sn quadrupoles and in the trim/skew NbTi quadrupoles are 360 T/m and 220 T/m respectively [123, 124]. The maximum gradient for the NbTi sextupoles is 7000 T/m². At collision and at $\beta^* = 0.3$ m, the integrated sextupole field is 8370 T/m. The sextupole length was fixed at 1.2 m to keep the maximum gradient in the sextupoles below the recommended value of 7000 T/m².

Dynamic aperture studies have shown that sextupole correctors, MCS, and decapole correctors, MCD, are mandatory near each dipole (see Section 7.5) to correct the b_3 and b_5 components defined in [125–127] as:

$$b_3 = \frac{1}{2} \frac{R_{\text{ref}}^2}{B_0} \frac{\partial^2 B_y}{\partial x^2} \quad (6.2)$$

$$b_5 = \frac{1}{24} \frac{R_{\text{ref}}^4}{B_0} \frac{\partial^4 B_y}{\partial x^4} \quad (6.3)$$

where $R_{\text{ref}} = 17$ mm is the reference radius and B_0 is the dipole field. It must be taken into account that the sextupole gradient S is defined by $S = \frac{1}{2} \frac{\partial^2 B_y}{\partial x^2}$ and $|B|(r) = S r^2$. The MCS/MCD correct the b_3/b_5 dipole components respectively if their integrated gradient is equal to that of the sextupole/decapole component in the dipoles. In this case:

$$S_{\text{MCS}} = \frac{L_{\text{dipole}}}{L_{\text{MCS}}} \frac{B_0}{R_{\text{ref}}^2} b_3 \quad (6.4)$$

$$S_{\text{MCD}} = \frac{L_{\text{dipole}}}{L_{\text{MCD}}} \frac{B_0}{R_{\text{ref}}^4} b_5 \quad (6.5)$$

The NbTi technology allows a gradient in an MCS of 2800 T/m² with an aperture of 50 mm. For comparison, the spool pieces currently used in LHC have a maximum gradient of 1630 T/m² and an aperture of 58 mm. Up to $b_3 = 4/60$ units (1 unit is 1/10,000 parts of the main field) can thus be corrected at collision/injection energy (50 TeV/3.3 TeV), if the MCS is 0.11 m long. The last dipole field quality requires a correction of 25 units at injection, which leaves margin for the b_3 correction.

The NbTi technology allows a gradient in a simple MCD of 4.3×10^6 T/m⁴ with an aperture of 58 mm and in a nested MCDO (decapole and octupole correctors) 2.8×10^6 T/m⁴ with an aperture of 63 mm. The magnetic length of an MCD is 0.066 m although its physical length is still 0.11 m because the coiling of the head requires more space. If the LHC scheme is used with one MCD every other dipole, the gradients required are 2.775×10^6 T/m⁴/1.385 $\times 10^6$ T/m⁴ with the half-pinning/pinning error table at injection respectively. At collision energy, the systematic value of b_5 in the dipoles is negligible and is not an issue. The gradient required for the MCD is thus within the limits of NbTi technology.

The arc elements for one arc cell are listed in Table 6.1. The main dipoles and the MCS can be powered in series in each arc (and for each beam). The main quadrupoles and sextupoles need at least two powering systems

each (focusing and defocusing quadrupoles). Main octupoles should be powered with two powering systems, however, the baseline uses the same current in all octupoles (see Section 8.7.4). A single powering system may be acceptable even if there is a loss of flexibility for the correction system. It is worth noting that octupoles are not present in all arc cells. Where necessary, they are replaced by trim or skew quadrupoles for correction purposes. MCB correctors will need at least 4 powering systems (2 for each plane). MQT and MQS correctors will need specific powering systems (at least 2 powering systems to correct the spurious dispersion and 2 powering systems to correct the tune).

Table 6.1: Parameters of main elements in the arcs. Trim quadrupoles, skew quadrupoles or octupoles are not present in all FODO cells. Nevertheless, there are always two multipoles per cell.

| Magnet | Coil aperture diameter [mm] | Max. field | Length [m] | Number per cell |
|---------------------------|-----------------------------|--|------------|-----------------|
| Main Dipole (MB) | 50 | 16 T | 14.187 | 12 |
| Dipole Corrector (MCB) | 50 | 4 T | 1.2 | 2 |
| Main Quadrupole (MQ) | 50 | 360 T/m | 6.4 | 2 |
| Trim Quadrupole (MQT) | 50 | 220 T/m | 0.5 | max. 2 |
| Skew Quadrupole (MQS) | 50 | 220 T/m | 0.5 | max. 2 |
| Main Sextupole (MS) | 50 | 7,000 T/m ² | 1.2 | 2 |
| Sextupole Corrector (MCS) | 50 (single) | 3,000 T/m ² | 0.11 | 12 |
| Decapole Corrector (MCD) | 58 (single) | 4,300 × 10 ³ T/m ⁴ | 0.066 | 6 |
| Main Octupole (MO) | 50 | 200,000 T/m ³ | 0.5 | max. 2 |
| BPM | 50 (single) | - | 0.5 | 2 |

6.6 Alternatives

Two alternatives were investigated:

- Phase advances of 60° instead of 90° in the arc cells.
- Longer arc cells.

Phase advances of 60° in the arc cells (as against 90° in the baseline) have several advantages. First of all, for a FODO cell of length L_c and phase advance μ with the thin lens approximation, the integrated strength in the quadrupoles KL_q is given by [128, 76–77]:

$$KL_q = \pm \frac{4 \sin \frac{\mu}{2}}{L_c} \quad (6.6)$$

Therefore, the ratio between the integrated strength for a phase advance of 60° against 90° is $\frac{\sin \frac{\pi}{6}}{\sin \frac{\pi}{4}} = \frac{\sqrt{2}}{2}$. In the FCC-hh case, the quadrupoles can be much shorter (4.5 m vs. 6.4 m) and thus the dipoles can be longer and weaker. The SSS has been shortened from 11.3 m to 9.3 m. The dipole field required is then 15.44 T (as against 15.81 T) for a length of 14.52 m (vs. 14.19 m). The arc cell is a bit longer (because the dispersion suppressors are a bit shorter too): 213.09 m compared to 213.04 m. Another advantage of using phase advances of 60° is that weaker sextupoles are required to correct the global chromaticity. Indeed, sextupoles are more efficient thanks to larger dispersion functions in the arcs and a larger minimum betatron function. For instance, the maximum sextupole gradient to correct the chromaticity (for the collision optics with $\beta^* = 0.3$ m) is 3215 T/m² compared to 6974 T/m². The strength of the octupoles is relaxed thanks to a larger average betatron function: the maximum betatron function is similar to the 90° case, whereas the minimum betatron function is larger with 60°. The impact on the dynamic aperture needs to be evaluated because the magnitudes of the driving terms are modified (for instance, the resonance $3Q_x - \nu$).

Phase advances of 60° have, however, several drawbacks. The corrections schemes need to be modified and the residual orbit after correction needs to be evaluated to check the impact of this alternative. Phase advances of 90° between correctors and BPMs are more efficient. Correction schemes for the tune or the beta-beating have to be modified. With phase advances of 90°, a set of 4 trim quadrupoles located near main focusing quadrupoles

(defocusing quadrupoles for the vertical plane) enables independent correction of the tune (if same polarity), the dispersion (if opposite polarity between first and third quadrupoles, or second and fourth quadrupole) or the betatron function (by alternating polarities). With a phase advance of 60° per cell, a suggestion is to use a set of 4 trim quadrupoles by alternating locations between focusing and defocusing quadrupoles. In this way, phase advances of 90° between trim quadrupoles can be obtained. Nevertheless, since the betatron functions are not the same in all trim quadrupoles, the magnitude of the field in the trim quadrupoles (at focusing or defocusing positions) will be different. Finally, the main drawback of using 60° instead of 90° is a reduction of the beam stay clear region resulting from larger dispersion functions, as shown in Fig. 6.7. The beam stay clear value is 12.29σ , below the target of 13.4σ . Nevertheless, the beam stay clear limit is calculated assuming that the dipoles are straight. The sagitta of 1.26 mm in the dipoles is the source of a decrease of the beam stay clear value by about 2σ . In the case of sector dipoles, the beam stay clear value for this alternative becomes 15σ – above the requirements of 13.4σ .

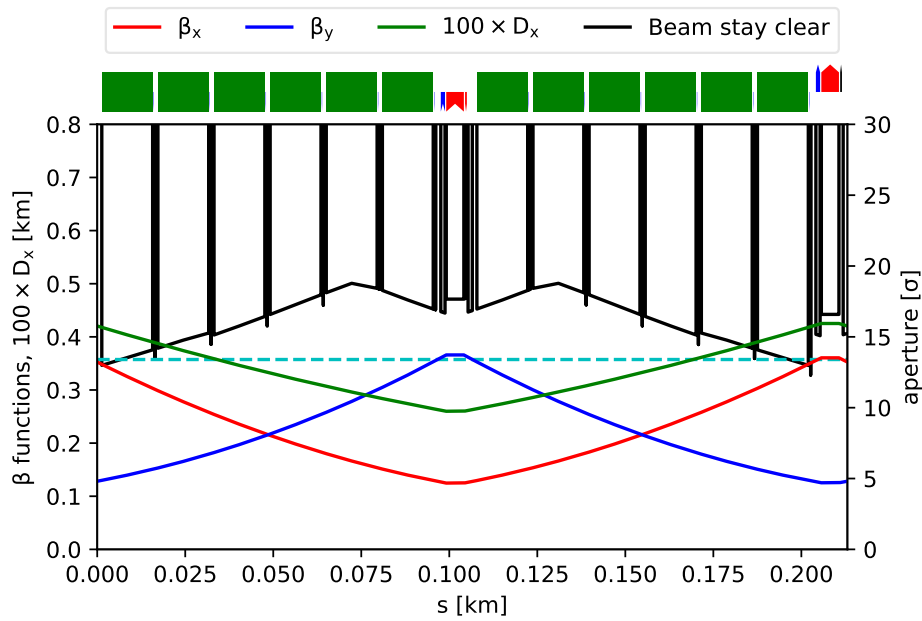


Figure 6.7: Optical functions in the arc cells for the alternative with a phase advance of 60° (β_x in red, β_y in blue, and $100 \times D_x$ in green). The beam stay clear limit is shown in black at injection energy (3.3 TeV). The cyan horizontal line shows the specified target of 13.4σ .

Another proposed method to increase the filling factor in the arcs is to use longer cells. Indeed, longer cells require fewer, weaker, and shorter quadrupoles, which enables the filling factor to be increased. However, optical functions are proportional to the cell length. The advantage is making sextupoles and octupoles more efficient with longer cells but a direct consequence is to decrease the beam stay clear region. Another drawback is having less place for correctors. The alternative considered is an arc cell of 307.09 m as against 213.04 m and with 18 dipoles per cell (vs. 12 dipoles in the baseline). The length of the main quadrupoles is 4.5 m. The SSS has been shortened from 11.7 m to 9.3 m. The dipole field required is then 15.01 T (vs. 15.81 T) for a length of 14.41 m (vs. 14.19 m). The maximum sextupole gradient to correct the chromaticity (for the collision optics with $\beta^* = 0.3$ m) is 3244 T/m^2 as against 6974 T/m^2 . The main drawback of using longer arc cells is a reduction of the beam stay clear size because of larger betatron and dispersion functions as shown in Fig. 6.8. The beam stay clear value is 11.44σ : below the target of 13.4σ .

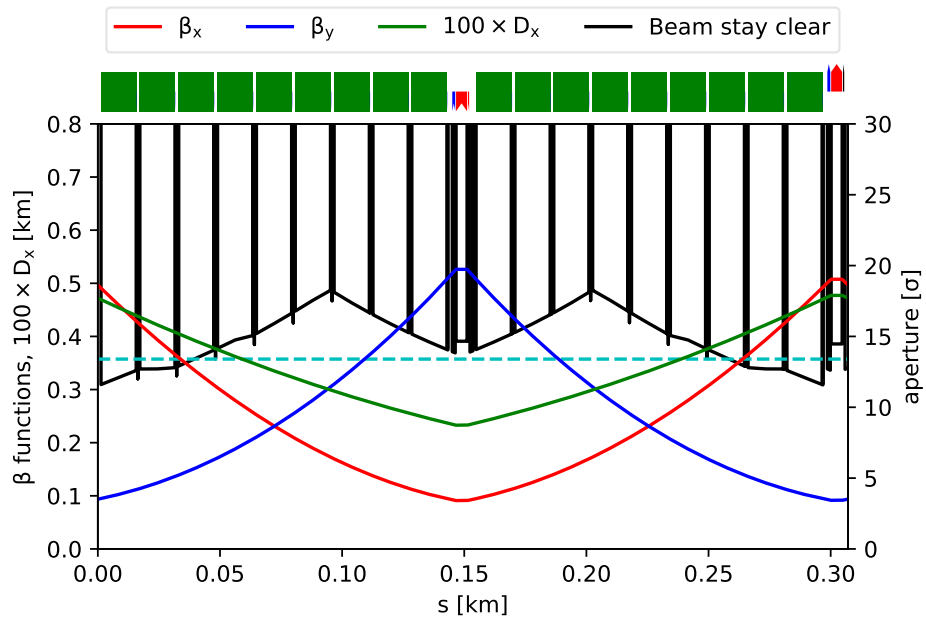


Figure 6.8: Optical functions in the arc cells for the alternative with a longer arc cell of 307.09 m (β_x in red, β_y in blue, and $100 \times D_x$ in green). The beam stay clear limit is shown in black at injection energy (3.3 TeV). The cyan horizontal line shows the specified target of 13.4σ .

Integrated optics and single particle dynamics

7.1 Overview

The different insertions in the FCC-hh ring are presented in Chapters 2, 3, 4, and 9 and the arcs in Chapter 6. The whole optics was integrated by using dispersion suppressors to match the arcs with the insertions. The phase advance in the long arcs is calculated to get the global horizontal/vertical tune Q_x/Q_y of 109.31/107.32 at collision and 109.28/107.31 at injection. The fractional part of the tune is identical to that of HL-LHC. The integer part of the tune was chosen to minimise the difference between the phase advance in LAR cells and 90° at collision energy. The main sextupoles are adjusted to get a global chromaticity Q'_x/Q'_y of 2.

7.2 Key issues

The matching between the arcs and insertions faces various issues. The first one is a lack of flexibility of the matching sections. Different constraints need to be fulfilled, such as betatron and dispersion functions at the arc entrances and sometimes phase advance between the arc entrance and the insertions. Another issue is the reduction of the beam stay clear region because of larger betatron and dispersion functions in these sections than in the arcs. Some space has to be allocated for collimators to protect the arc entrances from the debris coming from the insertions. This topic is developed specifically in Chapter 9. The dynamic aperture can be dramatically reduced when non linear errors in the triplet (mainly at collision energy) or in the main dipoles (mainly at injection energy) are applied. Correction with non linear correctors is essential to keep the dynamic aperture above target values.

7.3 Matching

Each arc start and end has an adjacent dispersion suppressor (DIS). The DIS is LHC-like with the 3 first half-cells with a length equal to two thirds of the arc cell (with 8 instead of 12 dipoles). The following half-cell contains 4 dipoles but has the same length as the arc cell. The matching between the insertions and the arcs is done with the quadrupoles MQDA 8, 9, and 10 and the long trim quadrupoles MQTL near the main quadrupoles 11, 12, and 13. In some insertions like the experiment insertion regions (EIR), additional matching quadrupoles were added. In the experiment insertions, quadrupole 7 is the bottleneck for matching and it was necessary to double it. The layout of the DIS is shown in Fig. 7.1. The quadrupoles MQDA 8, 9, and 10 are similar to the main quadrupoles, MQs, but are longer to increase the integrated gradient available for matching: they are 9.1 m long. One-metre-long collimators have been inserted to protect the arc entrances from the debris coming from the insertions (mainly cleaning and EIR).

Another constraint is to keep the beam stay clear values above the targets of 13.4σ at injection and 15.5σ at collision. These values are defined to maintain some margin in the collimation hierarchy. Special care was taken in the design to avoid betatron and dispersion peaks. The optical functions and the beam stay clear region at injection energy in the whole ring is shown in Fig. 7.2. The aperture is within the specifications in the DIS. At collision

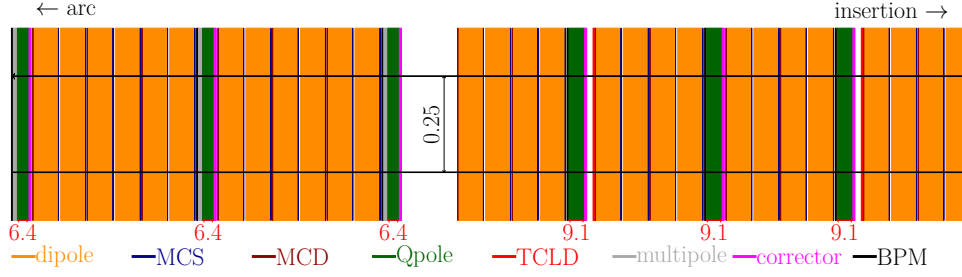


Figure 7.1: Layout of the dispersion suppressor (DIS).

energy, thanks to a smaller momentum spread and RMS emittance, the beam stay clear value is well above the specifications in the DIS.

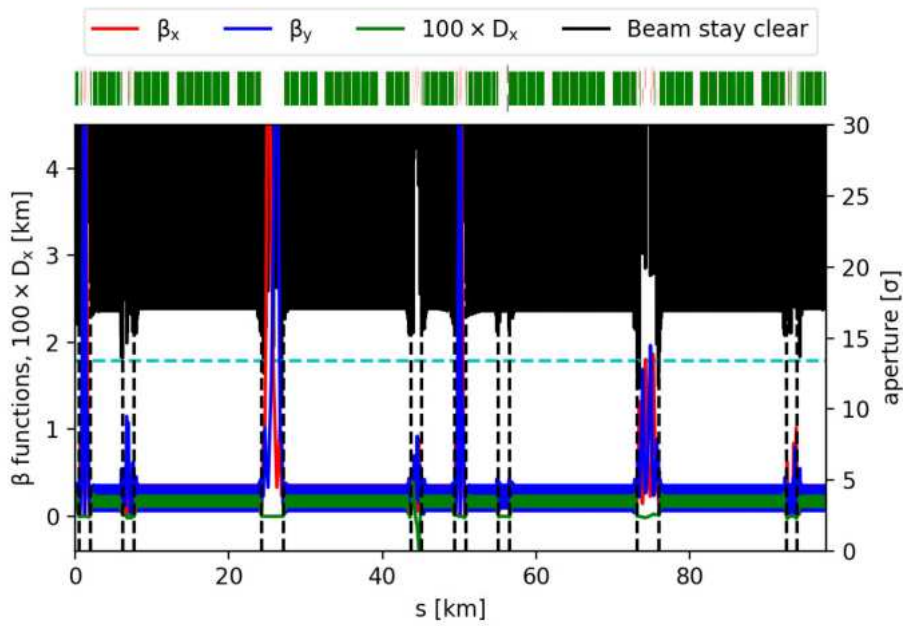


Figure 7.2: Optical functions in the FCC-hh ring at injection (β_x in blue, β_y in red, and $100 \times D_x$ in green). The beam stay clear limit is shown in black (3.3 TeV). The cyan line shows the target of 13.4σ . The vertical dashed line shows the boundaries of the insertions.

The matching section also has to correct the spurious dispersion generated by the crossing scheme at the IP. Two approaches were investigated: the HL-LHC scheme [34] using an orbit distortion in the arc quadrupoles or the SSC scheme [129] using trim or skew quadrupoles. With HL-LHC scheme, the bump needed goes up to 9 mm [118] in the arcs, which cannot be accepted. Nevertheless, the SSC scheme is less efficient for correction of the vertical spurious dispersion because of the reduced dispersion function at the defocusing quadrupole. The baseline uses a set of 4 trim/6 skew quadrupoles to correct the horizontal/vertical spurious dispersion respectively. The optical functions in the EIR with the crossing scheme off and on are shown in Fig. 7.3. The crossing angle is $100 \mu\text{rad}$ in the horizontal plane at IPA and in the vertical plane at IPG. The spurious dispersion is well corrected after a few arc cells.

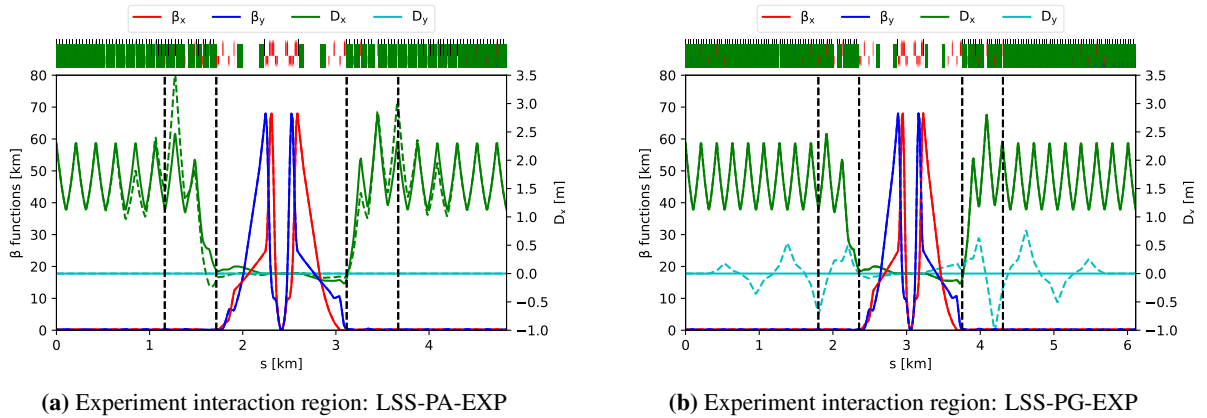


Figure 7.3: Optical functions in the LSS-PA-EXP and LSS-PG-EXP insertions when the crossing scheme is off (solid line) and on (dashed line, crossing angle of $100 \mu\text{rad}$ in the horizontal/vertical plane at IPA/IPG) (β_x in blue, β_y in red, and D_x in green). The DIS is delimited by vertical black lines.

7.4 Linear corrections

Alignment errors of the magnets used for the optics and field errors of the main components (dipole, quadrupole and their skew equivalents) can lead to errors in beam transport e.g. perturbations in the position, size or dispersive effects, as well as global parameters like the beam tunes. The main contributors to the beam orbit error are the quadrupole position error in the transverse planes, x and y , and the b_1 dipole component error. The main contributions to the beam size error or *beta-beating* are the a_2 skew quadrupole component error, the quadrupole rotation error around the longitudinal axis or *roll angle* and the b_2 quadrupole component error. The main contributions to the dispersion error or *dispersion beating* are the a_2 skew quadrupole component error, the quadrupole rotation error around the longitudinal axis or *roll angle* for the vertical dispersion and the b_2 quadrupole component error for the horizontal dispersion.

It is very important to be able to correct all these contributions by adding correction elements in the lattice. For this purpose, three different types of correctors have been inserted, together with BPM (Beam Position Monitor) diagnostic elements:

- Dipole correctors to cancel the beam position around the optical axis
- Skew quadrupole correctors to cancel the coupling contributions
- Normal quadrupole correctors to restore the beam tunes to their nominal values

Correction elements are inserted inside the short Straight Section (SSS) units or their equivalent in the insertions. A schematic layout of an arc SSS unit, with a quadrupole and its neighbouring correctors, is shown in Fig. 6.3.

Dipole correctors are inserted in all sections of the collider, whether it is the arc, dispersion suppressors (DIS) or insertions sections. In the arc and DIS sections the correctors act on the plane corresponding to the focusing plane of the neighbouring quadrupole, they are separated by a phase advance of 90° (or distant by two SSS units). There is a single dipole corrector in each SSS unit. The same occurs in the matching sections of the insertion sections. In the inner parts of the insertion sections (including focusing triplets) there are two correctors, one for each plane, next to the quadrupole. The list of correctors and their main characteristics are displayed in Table 7.7. The main constraint for the correctors in the arc sections is a maximum field of 4 T with NbTi technology, allowing an integrated field of 4.8 Tm with 1.2 m correctors. At this stage, all correctors are independent, meaning that in the arc sections there are currently 348 correctors with independent strengths acting on each plane.

Skew quadrupoles are inserted around the centre of long arc sections, as 2 families of 8 correctors separated by a phase advance of 90° , making a total of 8 families. Such a scheme cannot be inserted in short arc sections, because the space is already allocated for the spurious dispersion correction (see Section 7.3). The driving term due to the a_2 field component error has been calculated, as it is the main contribution to coupling, and the necessary corrector strengths applied according to the calculation shown in Equation 7.1:

$$\Delta c_- = \int_L ds \sqrt{\beta_x \beta_y} k_s e^{i(\mu_x - \mu_y)} \quad (7.1)$$

Trim quadrupoles are inserted near the entrance and exit of each long arc. Skew quadrupoles are not inserted in the short arc sections: they are arranged in two families of 8 quadrupoles per arc, making a total of 8 families. Each family is shifted from the other by a 45° phase advance, so two quadrupoles of the same family are separated by 90°. They correct the global horizontal and vertical tunes.

The main characteristics of skew quadrupoles (MQS) and trim quadrupoles (MQT) are displayed in Table 7.5. Using NbTi technology, the maximum gradient allowed for both skew and trim quadrupoles is 220 T/m.

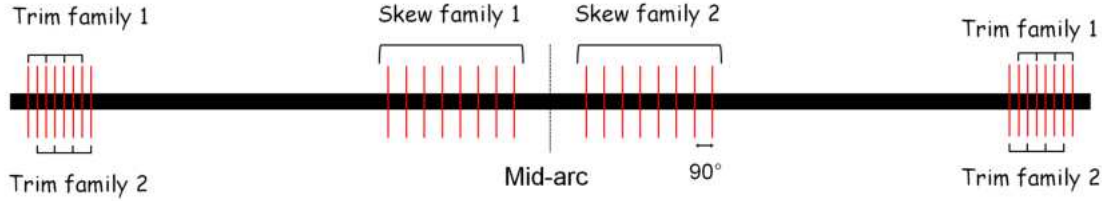


Figure 7.4: Overview of the skew and trim quadrupole correction schemes for a long arc section of FCC-hh.

The errors are generated using the RMS tolerance values defined for the arc and DIS elements according to Table 7.1 and for the insertion elements according to Table 7.2. Currently the tolerances have been estimated for the IR sections and they are considered to be identical in all other insertions.

Table 7.1: RMS tolerance values for the elements in the arcs and DIS. LHC design values taken from [127] are shown for comparison.

| Element type | Error type | Description | Units | FCC | LHC | Comments |
|--------------|------------------------|---------------|-----------------|------|------|-----------------------------------|
| Dipole | $\sigma(\psi)$ | roll angle | mrad | 0.50 | n/a | LHC value includes $\sigma(\psi)$ |
| | $\sigma(\Delta B/B)$ | random b_1 | % | 0.10 | 0.08 | |
| | $\sigma(\Delta B/B)$ | random b_2 | 10^{-4} units | 0.92 | 0.80 | |
| | $\sigma(\Delta B/B)$ | random a_2 | 10^{-4} units | 1.1 | 1.6 | |
| | $\sigma(\Delta B/B)$ | uncert. a_2 | 10^{-4} units | 1.1 | 0.50 | |
| Quadrupole | $\sigma(x), \sigma(y)$ | | mm | 0.50 | 0.36 | |
| | $\sigma(\psi)$ | roll angle | mrad | 1.0 | 0.50 | |
| | $\sigma(\Delta B/B)$ | random b_2 | % | 0.10 | 0.10 | |
| BPM | $\sigma(x), \sigma(y)$ | | mm | 0.30 | 0.24 | relative to quad. accuracy |
| | $\sigma(read)$ | | mm | 0.20 | 0.50 | |

The error correction is applied in a 3-step procedure:

1. Analytical correction of the a_2 contribution to the coupling with skew quadrupoles
2. Horizontal and vertical orbit correction with dipole correctors
3. Tunes correction with trim quadrupoles

A statistical study was performed by generating errors for 200 separate machines, with a different seed for each machine. Each machine is corrected with the aforementioned procedure. The following observables are studied at each element position and for each corrected machine:

- Horizontal and vertical residual orbit
- Horizontal and vertical residual angle
- Horizontal and vertical beta-beating $\Delta\beta = (\beta - \beta_{ref})/\beta_{ref}$
- Horizontal and vertical dispersion beating $\Delta D = (D - D_{ref})/\sqrt{\beta_{ref}}$
- Dipole and quadrupole corrector strengths

Table 7.2: RMS tolerance values for the elements in the interaction regions. Values are for injection energy, and they also apply at collision energy unless specified. The values are used for all elements of the other insertion regions (if applicable).

| El. type | Error type | Description | Units | Triplet | Other | Comments |
|------------|------------------------|--------------|--------------|---------|-----------|---------------------------|
| Dipole | $\sigma(\psi)$ | roll angle | mrad | | 1.0 | |
| | $\sigma(\Delta B/B)$ | random b_1 | % | | 0.05 | |
| | $\sigma(\Delta B/B)$ | random b_2 | 10^{-4} u. | | 0.10/1.8 | IR only (coll. 0.10/1.1) |
| | $\sigma(\Delta B/B)$ | random a_2 | 10^{-4} u. | | 0.20/0.10 | IR only (coll. 0.10/0.20) |
| Quadrupole | $\sigma(x), \sigma(y)$ | | mm | 0.20 | 0.50 | Q7 in IR has 0.20 |
| | $\sigma(\psi)$ | roll angle | mrad | 0.20 | 0.50 | TBD for IR |
| | $\sigma(\Delta B/B)$ | random b_2 | % | TBD | 0.05 | |
| BPM | $\sigma(x), \sigma(y)$ | | mm | 0.30 | 0.30 | relative to quad. |
| | $\sigma(read)$ | | mm | 0.05 | 0.05 | accuracy |

The study was performed for two settings of the collider, at 3.3 TeV injection energy with a β^* of 4.6 m ('baseline injection'), and at 50 TeV collision energy with a β^* of 0.3 m ('nominal') and crossing scheme. For each observable the mean value, standard deviation and maximum value were computed over the 200 machines. The maximum value distribution was used to obtain the 90-percentile value, the value for which 90% of the data points of a given distribution are included. In other words, the 90-percentile value gives a number for which 90% of the machines do not have an element of the beam line for which this number is exceeded.

The beam observable results obtained for the injection settings are shown in Figures 7.5 and 7.7. The results obtained for the collision settings are shown in Figures 7.6 and 7.8. The corrector strengths for the collision setting are displayed in Figure 7.9. The 90-percentile values obtained are summarised in Table 7.3.

Table 7.3: 90-percentile results obtained for the injection and collision cases.

| Observable | Injection | Collision |
|---------------------------------|---|---|
| Horizontal orbit | 0.80 mm | 0.79 mm |
| Vertical orbit | 0.73 mm | 0.73 mm |
| Horizontal angle | 26 μ rad | 26 μ rad |
| Vertical angle | 25 μ rad | 27 μ rad |
| Horizontal beta-beating | 22 % | 34 % |
| Vertical beta-beating | 24 % | 42 % |
| Horizontal dispersion beating | $2.3 \times 10^{-2} \frac{1}{\sqrt{m}}$ | $3.6 \times 10^{-2} \frac{1}{\sqrt{m}}$ |
| Vertical dispersion beating | $2.8 \times 10^{-2} \frac{1}{\sqrt{m}}$ | $2.7 \times 10^{-2} \frac{1}{\sqrt{m}}$ |
| Hori. orbit correctors strength | | 4.7 Tm |
| Vert. orbit correctors strength | | 4.2 Tm |
| Skew quadrupoles strength | | 148 T/m |
| Trim quadrupoles strength | | 140 T/m |

The results indicate that the residual orbit stays below 1 mm in both planes and for almost all machines. The residual angle does not exceed 35 μ rad at injection. At collision the residual angles are very similar. Assuming a drift of 11 m for synchrotron radiation before it hits the chamber walls and an ejection cone of 19 μ rad, a total vertical shift of 1.2 mm can be expected, far from the 7.5 mm half-aperture of the beamscreen.

The beta-beating is relatively high at injection, with a 90-percentile value close to 25% in both planes, and well above the target of 10% assumed for beam stay clear calculations (see Section 2.3.1). For collision settings it becomes significantly higher, up to 34% in horizontal plane and 42% in vertical plane. Currently there is no dedicated correction of the beta-beating, and the coupling and tune corrections do not cancel it very efficiently. The results for dispersion beating seem satisfactory at injection, with 90-percentile values below the LHC design values. The horizontal dispersion beating for the collision settings is slightly higher than the LHC design constraints. A

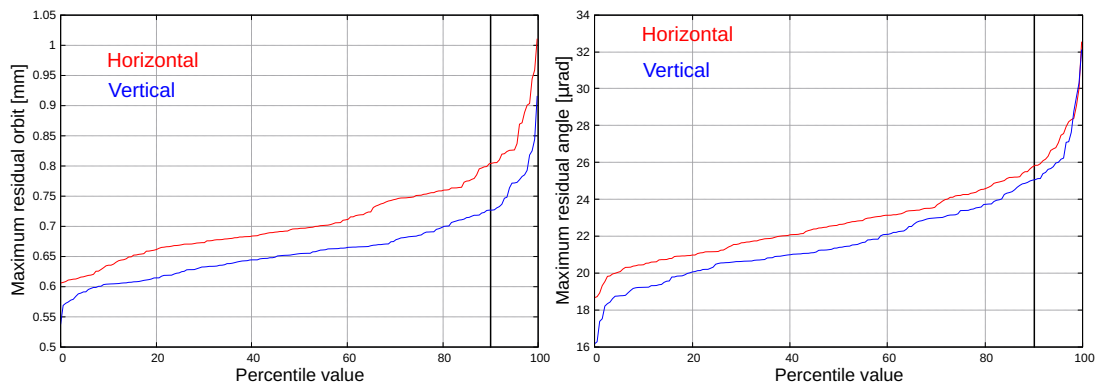


Figure 7.5: Evolution of the residual orbit and residual angle with percentile value for the injection case. The 90% value is indicated with a vertical solid line.

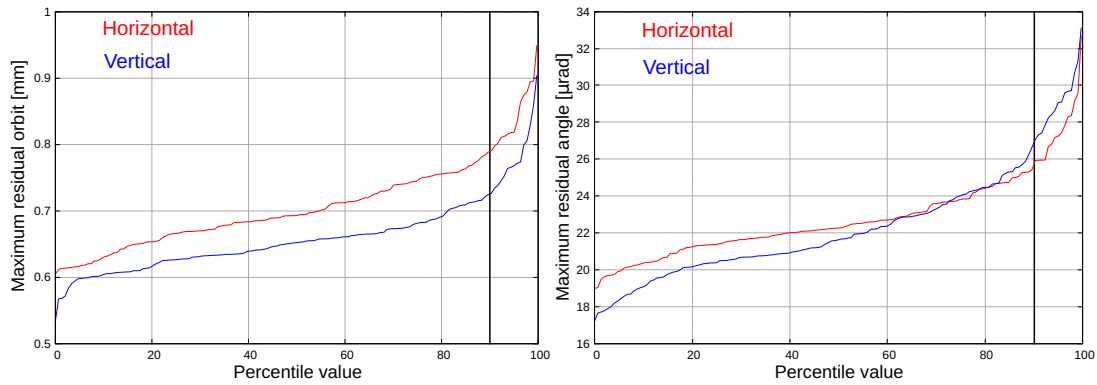


Figure 7.6: Evolution of the residual orbit and residual angle with percentile value for the collision case. The 90% value is indicated with a vertical solid line.

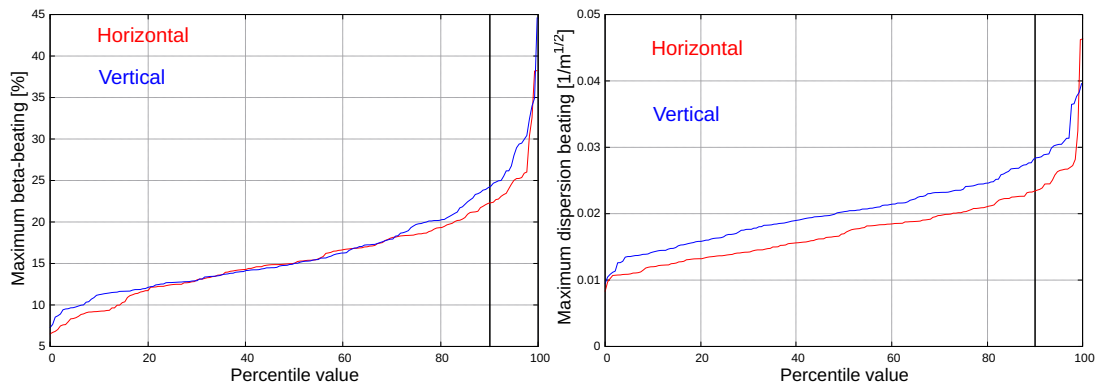


Figure 7.7: Evolution of the beta-beating and dispersion beating with percentile value for the injection case. The 90% value is indicated with a vertical solid line.

specific correction is envisaged to improve the results for the beta-beating.

The orbit corrector strengths are below the NbTi limit at a 90% level, and vertical correctors only exceed the limit for a few machines. Skew quadrupoles values are all below 200 T/m. Trim quadrupoles are also within the NbTi limit at the 90% level and it appears that with 220 T/m quadrupoles one can correct up to 0.03 tune fractions.

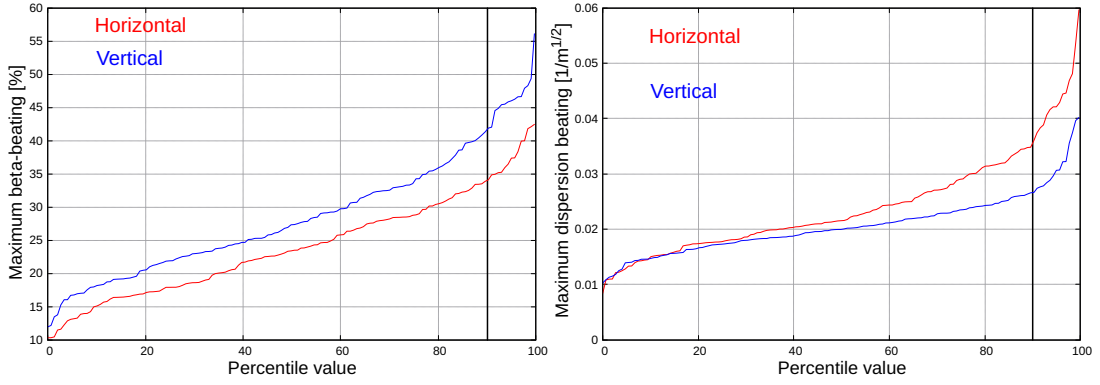


Figure 7.8: Evolution of the beta-beating and dispersion beating with percentile value for the collision case. The 90% value is indicated with a vertical solid line.

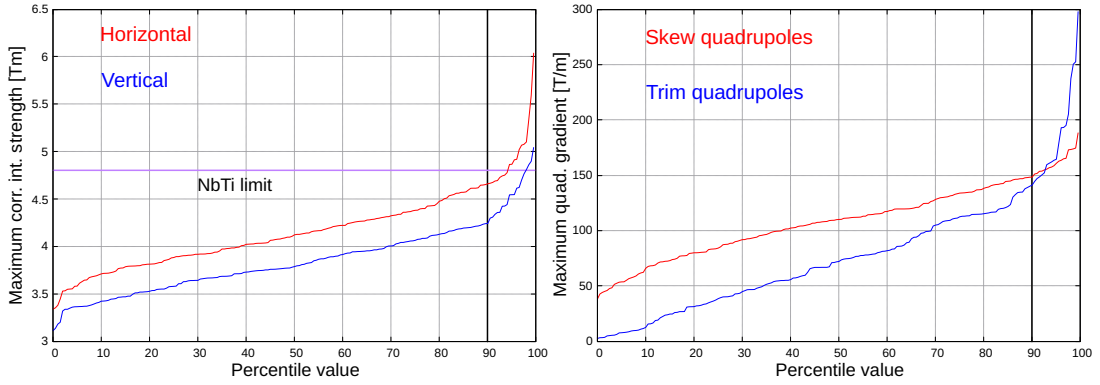


Figure 7.9: Evolution of the corrector strengths with percentile value for the collision case. The 90% value is indicated with a vertical solid line.

7.5 Dynamic aperture

The dynamic aperture (DA) is the region in transverse phase space where the particle motion is stable. Resonances, excited by the multipole errors of the magnets, limit the maximum amplitude particles can reach, without being lost. The behaviour of the particles in presence of these magnet imperfections cannot be corrected by specific feedback. Therefore, it is important to know the multipole errors in advance and to be able to correct for them if they reduce the DA below the safety limit. The DA is computed by tracking simulations, using the SixTrack code [45]. The particle motion is simulated over 10^5 turns, using a set of initial conditions distributed on a polar grid, in such a way that there are 30 particle pairs for each interval of 2σ . Five different angles of the ϵ_x , ϵ_y phase space have been used. The normalised rms beam emittance is $\epsilon_n = 2.2 \mu\text{m}$ for both injection and collision energies (3.3 and 50 TeV, respectively). The initial momentum offset is set to 2.8×10^{-4} at injection and 1.3×10^{-4} at collision (corresponding to 2/3 of the RF acceptance, for a maximum voltage of 12 MV and 42 MV at injection and collision respectively). The DA value is defined as the maximum amplitude of particles not lost in 10^5 turns. As far as the field imperfections are concerned, sixty different machines (also called seeds) have been generated. Each multipole harmonic entering in the magnet field expansion is modelled as the sum of three contributions [127]:

$$b_n = b_{n_S} + \frac{\xi_U}{1.5} b_{n_U} + \xi_R b_{n_R} \quad (7.2)$$

where ξ_U and ξ_R denote the random numbers with Gaussian distribution truncated at 1.5 and 3σ , respectively. In particular, the ξ_U is kept constant for all dipoles of the same arc and for the interaction region (IR) magnets of the same type, while ξ_R changes for each magnet. The separation dipoles field errors are based on the magnetic model of the normal-conducting magnets MBXW of the LHC [130], while the inner triplet errors are based on the HL-LHC magnets [131] scaled to fit the FCC quadrupole apertures. The main dipole field quality tables used for the DA studies are described in Section 7.7. After the field errors are added to the lattice, several corrections are

performed. Using the main quadrupoles of the arc, the tunes are corrected to have the same working point for each of the 60 machines (namely, .28, .31 at injection and .31, .32 in collision). Early DA studies have shown the need for local compensation of the sextupole (b_{3_s}) component of main dipoles [132]. This is corrected with sextupole correctors at each dipole of the arcs; their length is 0.11 m (as in the LHC) and their strength is of 3000 T/m^2 , which is achievable with Nb-Ti technology. Linear chromaticity is then matched to 2, using the main sextupoles of the arcs. When inner triplet and separation dipole errors are included, the residual dispersion generated by the crossing angle and coupling in the main IRs are also corrected, using normal and skew correctors in the IR and the adjacent arcs.

At the nominal injection energy of 3.3 TeV, the minimum DA (over the sixty seeds) is below 12σ due to the main dipole field errors only, and using a gradient of 1205 T m^{-2} for the sextupole correctors of the systematic and uncertainty b_3 component over the arcs. If local correction of the b_{5_s} of main dipoles is added, the minimum DA stays above the 12σ target. Therefore, local correction of the b_{5_s} component of main dipoles or its strong reduction is required. In particular, assuming that the same scheme as LHC (one decapole corrector every other dipole) is adopted, a maximum gradient of 2.950 T m^{-4} was found over the 60 different seeds simulated. This is still compatible with NbTi technology as discussed above in Chapter 6. The local correction of the b_4 component is, however, not required since the tune shift with momentum stays below 0.01 and the minimum DA doesn't improve significantly when the b_{4_s} component is set to zero. The high luminosity IRs triplet and separation dipole errors do not reduce DA at injection even when taking the crossing scheme into account. If octupoles for Landau damping are powered to 15/720 A, which is required for stability, the minimum DA shrinks to 9.5σ . The value is still acceptable as it is above the primary collimators settings but it leaves no margin for additional sources of DA reduction. It is worth noting that the minimum DA value for the on-momentum particles is close to the 12σ target even with the Landau damping octupoles.

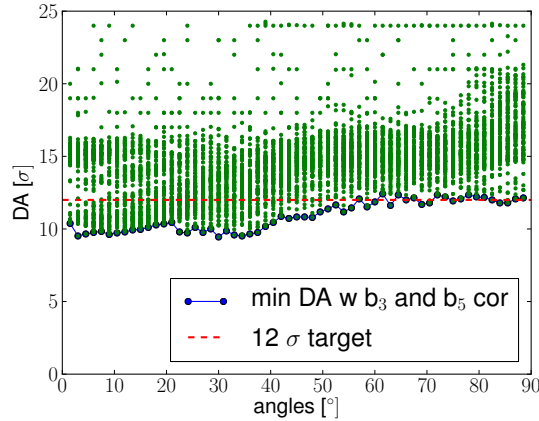


Figure 7.10: DA values at injection computed for 100 seeds and 59 angles. It includes main dipoles, triplet and separation dipole field errors and the octupole for Landau Damping powered to 15/720 A. The systematic b_3 and b_5 components of the main dipole are corrected as explained in Chapter 6. Green dots are DA values for each seed and angle. Blue dots represent the minimum DA values for each angle. We greatly acknowledge all BOINC volunteers who supported LHC@Home project, giving their CPU time for free and allowing these results to be produced

Curved (LHC type) dipoles are assumed in all the studies. For straight dipoles (the current choice for Nb_3Sn material) the effect of the sagitta on the multipole errors has been calculated using the feed-down formula [125]. In particular, the additional b_{3_R} is smaller than the original random component of the present field quality table. The feed-down of b_{5_s} to b_{4_s} is of the same order as the present b_{4_s} error, giving an extra argument for a local correction of the b_{5_s} error. The impact on DA of the residual arc linear imperfections (mainly orbit, β -beating and coupling) and of the main quadrupole field quality remains to be checked.

As mentioned before, several corrections were implemented to compensate for the reduction of DA from errors in the magnets. For collision energy it is found that both optimising the phase between the main IRs and the implementation of non-linear correctors significantly increase the DA. The change of phase advance between main IPs has a big effect on the resulting DA, particularly in the vertical plane where a small change in phase ($\Delta = \pm 0.1$) results in a significant increase/decrease in DA. A scan has therefore been performed to find the optimum changing

the phase between the main IRs using the trim quadrupoles in the long arcs between IRA and IRG, whilst using the trim quadrupoles from IRG to IRA to adjust the total tune. Figure 7.11 presents the impact of phase on the DA for a previous version of the lattice. Two zones can be identified as optimal and one of them (bottom left) has been used for subsequent versions of the lattice.

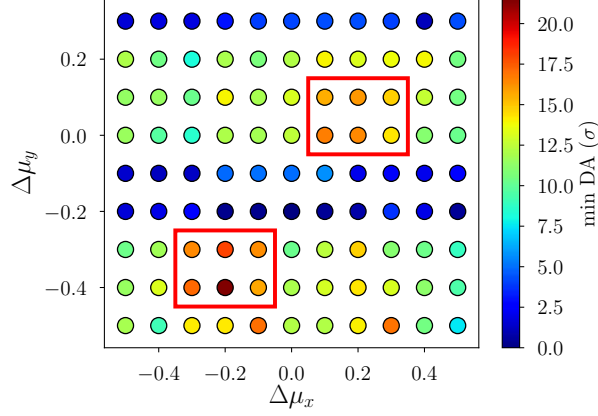


Figure 7.11: Minimum DA for 10 seeds vs a change in horizontal and vertical phase between n IRs. Two zones with higher DA have been identified and marked with red boxes.

Non-linear correctors are implemented next to the triplet, left and right of both main IRs (IRA and IRG). With one corrector located at each side of the two low β interaction points, each pair of correctors has the possibility of correcting the resonance driving terms (RDTs) arising from two different resonance lines. The RDTs to be corrected have been chosen for the proximity of their associate resonance lines to the working point and are: $c(b_3;1,2)$, $c(b_3;3,0)$, $c(a_3;0,3)$ and $c(a_3;2,1)$ for the normal and skew sextupolar correctors; b_3 and a_3 , $c(b_4;0,4)$, $c(b_4;4,0)$, $c(a_4;3,1)$ and $c(a_4;1,3)$ for the octupolar correctors; b_4 and a_4 and finally $c(b_6;0,6)$ and $c(b_6;6,0)$ for the dodecapolar correctors. It is found that the DA increases proportionally with the number of correctors, as shown in Fig. 7.12. This was done for a previous version of the lattice without phase optimisation and therefore a very low DA when no non-linear correctors were applied ($\approx 2\sigma$) which helps to illustrate the increase of DA for each corrector. This study also included the correctors a_5 , b_5 and a_6 , but it was found that correcting only the RDTs above is enough for the purpose of these studies.

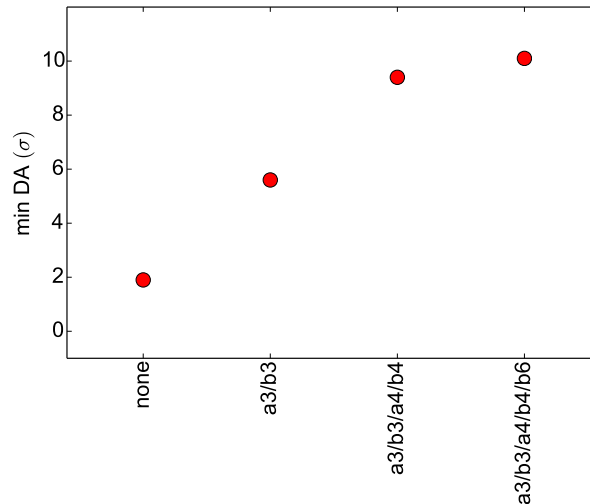


Figure 7.12: Minimum DA at collision energy with respect to the non-linear correctors used in the lattice for 60 different seeds for the errors in the triplet.

For the ultimate case with $\beta^* = 0.3$ m and errors in the arcs and the triplets, a DA of 11.6σ is obtained by implementing all corrections including optimisation of the phase advance but without the non-linear correctors. When the sextupolar and octupolar non-linear correctors (a_3 , b_3 , a_4 and b_4) are included the DA increases to 23.7σ .

For this case the dodecapolar corrector b_6 was not included because the strength required was too large and only resulted in a 1σ increase in DA.

Given that the non-linear corrections relied on the assumed magnet errors, which normally differ from those found in reality, the strengths of the non-linear correctors were calculated in the same way, but modifying the non-linear contributions by a certain percentage (up to 50% off). It was found that even with this strength difference on the correctors no significant reduction of the DA was observed.

As shown in Fig. 2.16 the case with $\beta^*=1.1$ m has a large DA (over 20σ) even without non-linear correctors. The most challenging cases are the optics with $\beta^*=0.15$ and 0.2 m, where a DA above 10σ can only be achieved with non-linear correctors. For the latter cases, the strength limits of the arc sextupoles have been ignored in order to allow full chromaticity correction. The alternative design for round ($\beta^*=0.3$ cm) and flat beams ($\beta^*=0.15$ m and 1.2 m) presents similar results to the baseline with a DA of 16.4σ for round beams and 12.2σ for flat beams; when non-linear correctors are included, the DA increases to 25.4σ and 20.4σ for round beams and flat beams, respectively.

In conclusion most of the designs have a DA above the 10σ target at collision energy, even without the use of non-linear correctors; however, the use of non-linear correctors is still recommended in case other errors affect the DA, offering a reliable increase even when the correction is not 100% accurate; furthermore, the use of non-linear correctors is essential to achieve an acceptable DA for the cases with lower β^* .

7.6 Cross talk between experiment insertion regions

Proton collisions at the interaction points of the FCC-hh may contribute losses around the ring between the detectors and to background in the subsequent detector. As the proton luminosity is high, this may be of concern.

The debris from the 50 TeV proton-proton collisions with vertical crossing is generated using the upgraded version of the DPMJET-III event generator [133] inside FLUKA [62]. Due to the rigidity of the charged particles, only protons are transported by the accelerator. Muons are the only other major concern, and are treated separately. The energy distribution of protons is large, this is shown in Fig. 7.13.

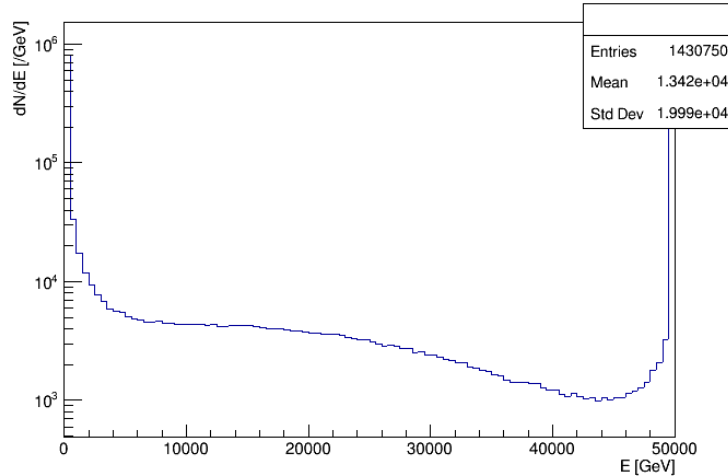


Figure 7.13: Proton energy distribution 3 m downstream of IPA for 10^6 pp collisions.

For proton cross-talk, the energy of 49.95 TeV is used as a threshold. Protons from the collision with an energy greater than this are defined as ‘elastic’, and those with energy below this are defined as ‘inelastic’ protons. PTC [134] and MERLIN [135] are used to perform tracking of both elastic and inelastic protons to determine the cross-talk. That is, the number of collision debris protons that will reach the next detector. The debris is generated at IPA and tracked to IPB.

For elastic protons, nearly all reach IPB with a spot size similar to that of the beam. This is likely to lead to an emittance growth, but should pose no major concern. Around 2 inelastic protons per bunch crossing will arrive at IPB under nominal settings, rising to ≈ 9 under ultimate settings. The mean energy of these few protons is 49.89 TeV, and they are unlikely to be of concern in terms of cross-talk.

What is of greater concern is the loss of inelastic protons between the two IPs. Most are lost in the short straight section and dispersion suppressor (DS) regions around IPA. A detailed study of losses in the detector, inner

triplet, and separation and recombination dipoles has been conducted with FLUKA. This is reported in Section 2.4. Therefore the focus here is on losses after these elements: of greatest concern are the DS losses as it is a bottleneck for off-momentum particles and the proton energy is high.

It was decided to mitigate these losses using HL-LHC style ‘TCLD’ collimators in the DS. Two 1 m long TCLD collimators were placed before the first quadrupole in cells 8 and 10, at the points where the dispersion rises rapidly. With these collimators in place, the DS losses are minimised, as all particles are intercepted by the TCLDs. In these simulations all apertures are treated as black absorbers. The collimators are placed in regions of relatively low β function, thus allowing larger jaw gaps so as not to violate the collimation hierarchy. A jaw half-gap of 35σ was found to be sufficient. Using MERLIN, the power and energy of particles lost in the short straight section with the two TCLD collimators, were computed and are shown in Fig. 7.14. It should be noted that all losses are shown per element, therefore the largest peak in the power plot corresponds to the loss over the full length of a ≈ 200 m long drift.

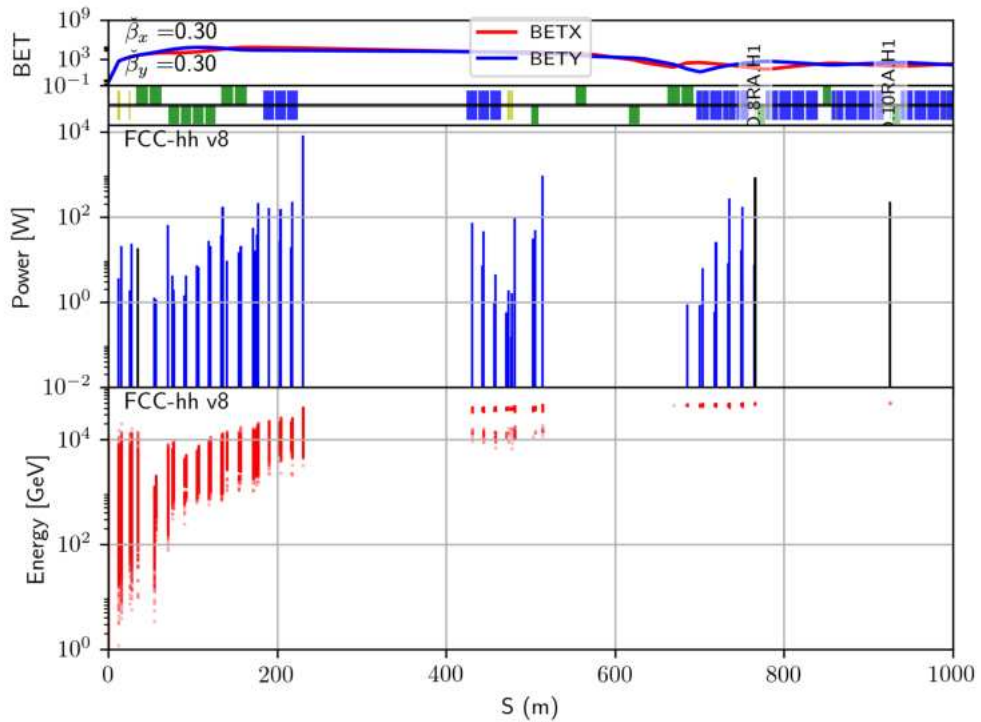


Figure 7.14: Proton losses between IPA and IPB. The top plot shows power deposition per element when including the TCLD collimators, the bottom plot shows the energy distribution of the losses.

Collimators clean the ‘primary’ halo but, in turn, produce a ‘secondary’ halo. In order to verify that this secondary shower would not exceed the maximum energy deposition allowed on the subsequent superconducting quadrupole, a two step simulation was used. Firstly using MERLIN, the inelastic protons were transported from IPA to the TCLDs to generate hits on the collimator jaws. These hits were fed into a FLUKA model, shown in Fig. 7.15, which consists of the first TCLD collimator, a drift space, followed by a 50 cm long mask prior to the superconducting quadrupole. The quadrupole coils are simulated as a mixture of 50% Nb_3Sn and 50% copper. INERMET180 has been chosen as the material for the TCLD jaw and quadrupole mask, as in the current LHC absorbers. The distance between the collimator and the mask and quadrupole gives space for the shower to spread, thus minimising the load on the quadrupole coils.

As the first collimator (in cell 8) has the higher load, it was used for shower simulations. A jaw half-gap of 35σ was shown to intercept all inelastic protons whilst not violating the betatron collimation hierarchy. There is the possibility that this could still interfere with the momentum cleaning hierarchy as the momentum cleaning was not defined at the time of this investigation.

It is evident from Fig. 7.16, which shows the maximum energy deposition in the first quadrupole post-

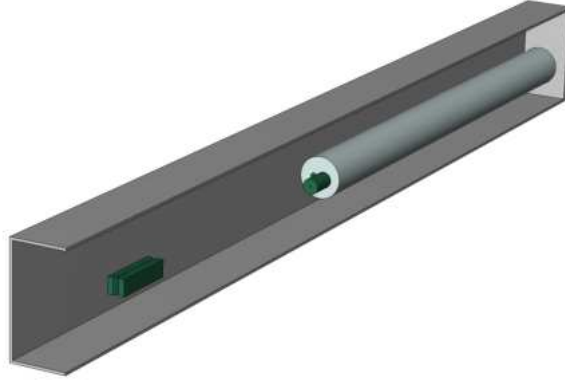


Figure 7.15: FLUKA model used for shower simulations in the dispersion suppressor. The green objects are first the TCLD collimator, followed by a 50 cm long mask, both made of INERMET180. Following this is the first quadrupole in the DS. The particles are loaded 63 cm before the collimator.

TCLD, that the 50 cm mask is required in order to stay below the limit of $\approx 5 - 10 \text{ mW cm}^3$ [136] at ultimate parameters. For baseline parameters the mask is not required. Thus the DS losses due to inelastic protons from collision debris can be mitigated using the two 1 m long INERMET180 TCLDs, placed in cells 8 and 10, before the first quadrupole in the cell.

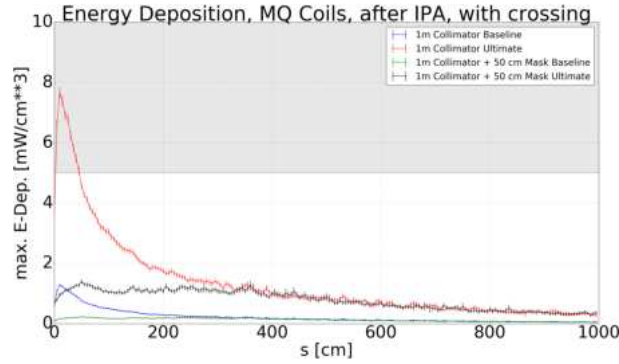


Figure 7.16: Maximum energy deposition per cm^3 in 5 cm bins along the first quadrupole in cell 8 after IPA for baseline and ultimate configurations.

As muons have a large mean free path, they can travel kilometres in dense materials, therefore muon cross-talk may be a concern. The muon energy distribution generated from 10^6 50 TeV pp collisions using DPMJET-III inside FLUKA is shown in Fig. 7.17. The highest energy muon produced is around 20 TeV.

Muon energy loss can be separated into; ionisation, bremsstrahlung, production of electron-positron pairs, and through photo-nuclear and photo-nucleon interactions. This approach is summarised in equation 7.3 [137]:

$$\left\langle \frac{-dE}{dx} \right\rangle = a(E) + b(E)E, \quad (7.3)$$

where $a(E)$ is the ionisation contribution, and $b(E) = b_b(E) + b_p(E) + b_n(E)$ is the sum of the contributions of bremsstrahlung, pair production, and photo-nuclear/nucleon interactions [138]. In the continuous slowing down approximation the range is given by

$$R(E) = \int_{E_0}^E (a(E') + b(E')E')^{-1} dE'. \quad (7.4)$$

At high energy a and b are constant, and this becomes

$$R(E) \approx \frac{1}{b} \ln \left(1 + \frac{E}{E_c} \right), \quad (7.5)$$

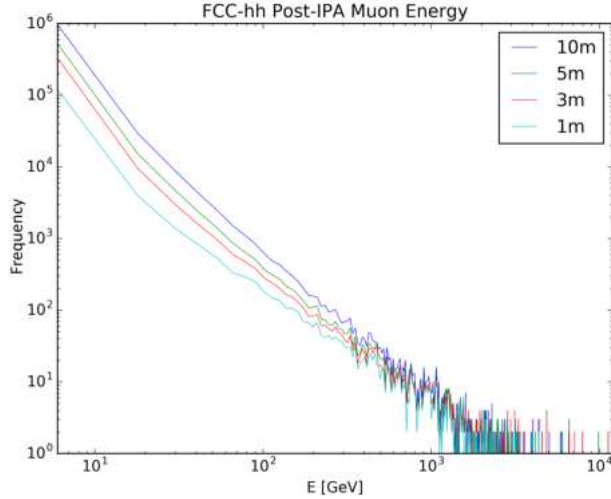


Figure 7.17: Muon energy distribution at intervals downstream of IPA, generated using DPMJET-III in FLUKA, with no detector or accelerator model.

where the electronic and radiative losses are equal at the critical energy E_c . This approach is used to calculate the theoretical range of muons in standard rock, which has a specific gravity of 2.65 g cm^{-3} and $\langle \frac{Z}{A} \rangle = 0.5$, and in which the muon critical energy is 693 GeV. The result of this calculation, shown in Fig. 7.18, gives a maximum range of 3.3 km for FCC-hh collision debris muons through standard rock. This analytical calculation does not include the interaction of collision debris with the detector.

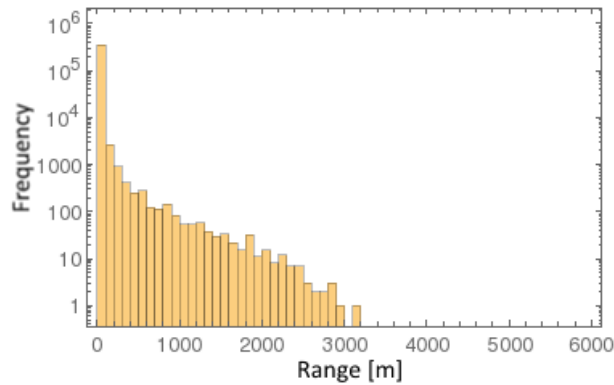


Figure 7.18: Theoretical range of collision debris muons in rock.

In order to verify the analytical expectation, 5×10^4 pp collisions were generated using DPMJET-III inside FLUKA with a complete model of the detector [139] in order to generate the initial muon distribution. These muons were then tracked in FLUKA using a total of 10^9 histories through the tunnel model shown in Fig. 7.19.

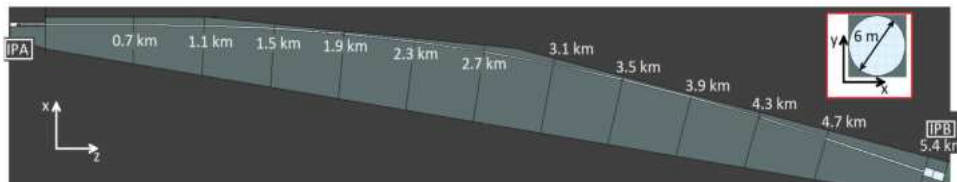


Figure 7.19: Cross section of the FLUKA FCC-hh tunnel model. The distance from IPA to each point along the tunnel central line is indicated. IPB is located 5.4 km away from IPA. The lighter grey area is modelled as standard rock. Note that this model was based on an older version of the FCC-hh lattice.

The muon energy distributions along the tunnel model are shown in Fig. 7.20. From this it is clear that no muons travel beyond 2.7 km, thus it can be concluded that muon cross-talk should not be an issue at the FCC-hh.

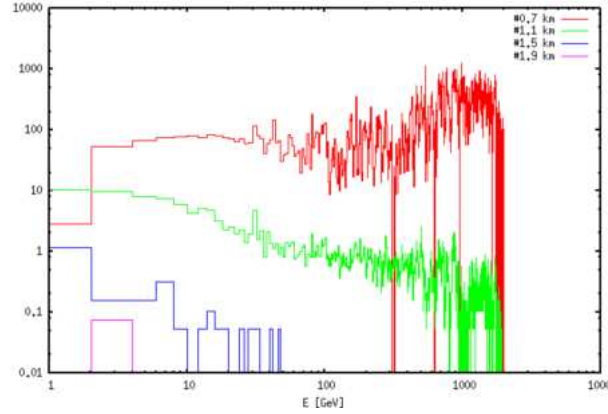


Figure 7.20: Muon distribution at different positions along the tunnel.

In summary, elastic protons with an energy greater than 49.95 TeV from collisions at IPA nearly all reach IPB with a spot size similar to the beam. This should result in an emittance growth of the beam. Inelastic protons, with an energy less than 49.95 TeV pose a greater threat. Only 2 - 9 inelastic protons per bunch crossing are expected to reach IPB: this is deemed negligible. The losses from inelastic protons in the short straight section and dispersion suppressor regions post IPA are of concern. By using two 1 m long TCLD collimators with INERMET180 jaws, the losses in the DS region after IPA were mitigated. Shower simulations of the inelastic proton impacts on the first TCLD in cell 8 were performed in order to gauge secondary shower damage on the next superconducting element, the first quadrupole in the cell. Results show that for baseline parameters the energy deposition is below the suggested limit, and for the ultimate parameters the addition of a 50 cm long INERMET180 mask would be required to protect the quadrupole coils [140].

Despite high energy muons of up to 20 TeV being created in the pp collisions, it has been shown with analytical and Monte Carlo methods that muons should not travel far enough through rock or the accelerator tunnel to reach the subsequent detector [141].

Photons and other charged hadrons in the collision debris are ignored as their rigidity means that they will not be accepted in the accelerator, and thus cannot be transported to IPB.

7.7 Hardware specification

The hardware specifications for the various insertions are explained in Chapters 2, 3, 4, and 9 and for the arcs in the Chapter 6. The hardware specification for the whole ring is summarised for the dipoles in Table 7.4, for the quadrupoles in Table 7.5, for the other multipoles in Table 7.6 and for the dipole correctors in Table 7.7. The total number of BPMs in the integrated optics is 906 per beam.

Table 7.4: Parameters of dipoles in the whole FCC-hh ring.

| Type | Number | Coil aperture diameter [mm] | Max. field [T] | Length [m] | Material | Type |
|------|--------|-----------------------------|----------------|------------|--------------------|---------------|
| MB | 4672 | 50 | 16 | 14.187 | Nb ₃ Sn | straight |
| MBA | 8 | 50 | 13 | 12.5 | Nb ₃ Sn | separation |
| MBB | 8 | 50 | 13 | 12.5 | Nb ₃ Sn | recombination |
| MBWM | 12 | 50 | 1 | 7.764 | NC | straight |
| MBRE | 8 | 60 | 10 | 15 | NbTi | recombination |
| MBRW | 16 | 91 | 2 | 11.3 | NC | recombination |
| MBW | 8 | 50 | 2 | 17 | NC | separation |
| MBXB | 8 | 100 | 12 | 12.5 | NbTi | separation |
| MBXW | 16 | 170 | 2 | 11.3 | NC | separation |

The main dipole field quality used for dynamic aperture calculations is given in Table 7.8.

The dipole and quadrupole errors of the main dipole used for the linear correction studies are given in

Table 7.5: Parameters of quadrupoles in the whole FCC-hh ring.

| Type | Number | Coil aperture diameter [mm] | Max. gradient [T/m] | Length [m] | Material |
|-------|--------|-----------------------------|---------------------|------------|--------------------|
| MCQS | 4 | 50 | 220 | 1.6 | NbTi |
| MCQSX | 4 | 50 | 220 | 1.6 | NbTi |
| MQ | 744 | 50 | 360 | 6.4 | Nb ₃ Sn |
| MQDA | 48 | 50 | 360 | 9.1 | Nb ₃ Sn |
| MQE | 2 | 50 | 220 | 6.8 | NbTi |
| MQI | 2 | 50 | 220 | 6.8 | NbTi |
| MQM | 8 | 50 | 360 | 14.3 | Nb ₃ Sn |
| MQML | 10 | 50 | 360 | 12.8 | Nb ₃ Sn |
| MQMO | 18 | 50 | 360 | 9.1 | Nb ₃ Sn |
| MQR | 8 | 50 | 360 | 6.4 | Nb ₃ Sn |
| MQS | 96 | 50 | 220 | 0.5 | NbTi |
| MQT | 88 | 50 | 220 | 0.5 | NbTi |
| MQTL | 48 | 50 | 220 | 2.2 | NbTi |
| MQTLH | 12 | 50 | 220 | 6.5 | NbTi |
| MQTLM | 12 | 50 | 220 | 2.969 | NbTi |
| MQWA | 20 | 50 | 50 | 15.54 | NC |
| MQWB | 4 | 50 | 50 | 15.54 | NC |
| MQWC | 20 | 50 | 50 | 7.097 | NC |
| MQWD | 4 | 50 | 50 | 7.097 | NC |
| MQXA | 16 | 64 | 270 | 10.0 | Nb ₃ Sn |
| MQXB | 8 | 64 | 270 | 15.0 | Nb ₃ Sn |
| MQXC | 8 | 164 | 130 | 14.3 | Nb ₃ Sn |
| MQXD | 16 | 210 | 105 | 12.5 | Nb ₃ Sn |
| MQXE | 8 | 210 | 105 | 14.3 | Nb ₃ Sn |
| MQY | 18 | 70 | 200 | 9.1 | Nb ₃ Sn |
| MQYL | 8 | 50 | 360 | 12.8 | Nb ₃ Sn |

Table 7.6: Parameters of multipoles in the whole FCC-hh ring. The number of elements is given per beam. In case of single aperture, the number is doubled for the whole machine.

| Type | Number | Coil aperture diameter [mm] | Max. gradient | Length [m] | Material | aperture |
|------|--------|-----------------------------|------------------------------------|------------|----------|----------|
| MS | 696 | 50 | 7000 T/m ² | 1.2 | NbTi | double |
| MCS | 4672 | 50 | 3000 T/m ² | 0.11 | NbTi | single |
| MO | 480 | 50 | 2.0×10^5 T/m ³ | 0.5 | NbTi | double |
| MCD | 2336 | 58 | 4.3×10^6 T/m ⁴ | 0.066 | NbTi | single |

Section 7.4. The interaction region magnet field quality is discussed in Chapter 2. The correction of the systematic b_3 at injection and at collision, using spool piece correctors (MCS) at each dipole, is discussed in Section 7.5. In the presence of MCS misalignment, the resulting rms beta-beating due to feed-down of the systematic b_3 to a random b_2 can be a concern. In order to keep this rms beta-beating of the order of 5% (same order due to the original random b_2 reported in Table 7.8), a relation for the relative alignment of the MCS with respect to the dipole as a function of the systematic b_3 value [126] has been derived. The results are shown in Fig. 7.21.

For a systematic b_3 component of about 25 units, as reported in Table 7.8, a relative MCS alignment of about 300 μm is required in order to limit the beta-beating due to feed-down to 5%.

Table 7.7: Parameters of dipole correctors in the whole FCC-hh ring.

| Type | Number | Coil aperture diameter [mm] | Max. field [T] | Length [m] | Material |
|---------|--------|-----------------------------|----------------|------------|----------|
| MCBCH | 1 | 50 | 4 | 2.055 | NbTi |
| MCBEXPH | 4 | 50 | 4 | 3.4 | NbTi |
| MCBH | 426 | 50 | 4 | 1.2 | NbTi |
| MCBRDH | 8 | 50 | 4 | 3.0 | NbTi |
| MCBWH | 2 | 50 | NC | NC | NC |
| MCBXCH | 4 | 50 | 4 | 1.0 | NbTi |
| MCBXDH | 4 | 50 | 4 | 1.0 | NbTi |
| MCBXH | 4 | 50 | 4 | 2.25 | NbTi |
| MCBCV | 1 | 50 | 4 | 2.064 | NbTi |
| MCBRDV | 8 | 50 | 4 | 3.0 | NbTi |
| MCBV | 422 | 50 | 4 | 1.2 | NbTi |
| MCBWV | 2 | 50 | NC | NC | NC |
| MCBXCV | 4 | 50 | 4 | 1.0 | NbTi |
| MCBXDV | 4 | 50 | 4 | 1.0 | NbTi |
| MCBXCHV | 4 | 50 | 4 | 1.3 | NbTi |
| MCBXDHV | 8 | 50 | 4 | 1.3 | NbTi |

Table 7.8: Main dipole Field Quality: the values are in units of 10^{-4} at $R_{ref} = 17$ mm.

| Normal | systematic inj b_{n_S} | systematic col b_{n_S} | uncertainty b_{n_U} | random b_{n_R} |
|--------|--------------------------|--------------------------|-----------------------|------------------|
| 3 | -25.121 | 0.1060 | 0.6680 | 0.6680 |
| 4 | 0.795 | 0.3130 | 0.4670 | 0.4670 |
| 5 | 5.1700 | 0.1820 | 0.2830 | 0.2830 |
| 6 | 0.6730 | 0.3470 | 0.1870 | 0.1870 |
| 7 | -1.3300 | 0.1840 | 0.1090 | 0.1090 |
| 8 | 0.4630 | 0.3750 | 0.0720 | 0.0720 |
| 9 | 2.0550 | 0.5680 | 0.0470 | 0.0470 |
| 10 | 0.2210 | 0.1300 | 0.0280 | 0.0280 |
| 11 | 1.0480 | 1.0500 | 0.0150 | 0.0150 |
| 12 | 0.0810 | 0.0880 | 0.0100 | 0.0100 |
| 13 | -0.2270 | -0.2450 | 0.0050 | 0.0050 |
| 14 | 0.0260 | 0.0280 | 0.0030 | 0.0030 |
| 15 | -0.0200 | -0.0220 | 0.0020 | 0.0020 |
| Skew | a_{n_S} | a_{n_S} | a_{n_U} | a_{n_R} |
| 3 | 0.0000 | 0.0000 | 0.7540 | 0.7540 |
| 4 | 0.0000 | 0.0000 | 0.4730 | 0.4730 |
| 5 | 0.0000 | 0.0000 | 0.3290 | 0.3290 |
| 6 | 0.0000 | 0.0000 | 0.0205 | 0.0205 |
| 7 | 0.0000 | 0.0000 | 0.0114 | 0.0114 |
| 8 | 0.0000 | 0.0000 | 0.0690 | 0.0690 |
| 9 | 0.0000 | 0.0000 | 0.0380 | 0.0380 |
| 10 | 0.0000 | 0.0000 | 0.0230 | 0.0230 |
| 11 | 0.0000 | 0.0000 | 0.0150 | 0.0150 |
| 12 | 0.0000 | 0.0000 | 0.0080 | 0.0080 |
| 13 | 0.0000 | 0.0000 | 0.0050 | 0.0050 |
| 14 | 0.0000 | 0.0000 | 0.0030 | 0.0030 |
| 15 | 0.0000 | 0.0000 | 0.0020 | 0.0020 |

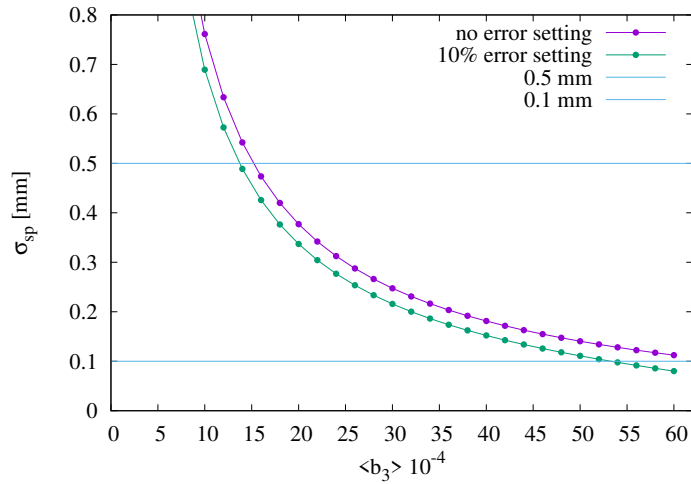


Figure 7.21: MCS relative alignment as function of the systematic b_3 value at injection, in order to have 5% residual beta-beating due to feed-down.

7.8 Alternatives and key R&D

The alternatives are the integrated optics with the alternative triplet in the EIR as described in Chapter 2, or with a different arc cell (phase advance of 60° instead of 90° or longer cells) as described in Chapter 6.

If the alternative of phase advance of 60° in the arc cells is maintained, a specific correction scheme for optics with 60° FODO cells should be developed. Studies have shown that the misalignment of Q7 in the EIR is critical for the beam orbit. Developing a system to improve the alignment of Q7 will relax the constraints on dipole correctors and matching section to the EIR.

Collective effects

8.1 Introduction

Taking into account the experience gained at the LHC, the studies for the FCC-hh focus on collective effects induced by the beam pipe and other low and high frequency contributions to the impedance spectrum. Electron cloud buildup and collective effects induced by the cloud have been studied for the detailed pipe design. The impedance of the beam pipe has been considered in more detail, taking into account the design geometry and possible coatings for electron cloud mitigation. The contribution to the broadband impedance spectrum from pumping holes, interconnects and other possible sources have been estimated. Instability growth rates and stability thresholds have been computed from analytical models and simulation codes (mode coupling and particle tracking with collective effects) using the impedance database. The simulations include models for the transverse feedback system as well as Landau damping octupoles. In addition, growth rates and stability thresholds have been estimated with scaling laws using the LHC as a baseline (Subsection 8.7.1).

The simulations have been applied to various operational scenarios, for example bunch spacing and injection energies, with and without beam-beam interaction. Transverse feedback, for injection transients and rigid ($k=0$) bunch modes together with Landau octupoles for higher-order ($k>0$) modes should stabilise transverse single and coupled bunch modes sufficiently. In addition Landau damping by electron lenses and RFQs has been studied in analytical models and in simulations. Both mechanisms promise stronger Landau damping (also stabilising the $k=0$ coupled bunch modes), with fewer implications for the dynamic aperture than the baseline octupoles. However, future simulation and experimental studies will focus on a more detailed comparison of these mechanisms and the resulting stability boundaries. Compared to electron lenses and RFQs, octupoles still have the advantage that they will always stabilise the beam, but at the cost of an enlarged transverse emittance.

Simulations of electron cloud buildup have been performed using two simulation tools (PyELOUD and openELOUD). The contribution of residual photoelectrons has been carefully considered in the electron buildup simulations, which confirm that the beamscreen design will be able to sufficiently suppress photoelectrons entering the inner part of the pipe and interacting (via space charge forces) with the circulating bunches. Unlike the pipe impedance, the electron cloud density only depends weakly on the detailed geometry of the pipe. The simulations indicate, that the amorphous carbon (a-C) coating of the upper/lower parts of the screen will reduce the SEY sufficiently to lower the electron densities below the instability thresholds. Laser surface treatment for SEY reduction as well as HTS coating for impedance reductions have been studied, but neither is part of the baseline scenario. Both of these coatings have the disadvantage of causing increased impedance at high frequencies, with corresponding TMCI thresholds approaching the design bunch intensities. Intrabeam scattering, relevant on longer time scales, will be too weak to affect coherent instability thresholds. Transverse space charge effects have also been ignored, as their effect on the threshold can be neglected for the FCC-hh parameters.

Longitudinal beam stability is ensured by having the RF voltage sufficiently high to prevent the loss of Landau damping, and by controlled emittance blow-up during the ramp (Section 8.4). The baseline strategy to ensure transverse beam stability evolves throughout the operational cycle as described below. At injection, a factor of 3 safety margin in stability is achieved by using both the transverse feedback system and the Landau octupoles (Section 8.7.2). During the ramp, the impedance increases due to the tighter collimator gaps, nevertheless the instability growth rates decrease due to the higher beam rigidity. This leads to the lower damping rate required

from the feedback, however, the octupole current must increase as their stabilising effect falls rapidly with the energy. As a result, the same factor of 3 in the safety margin is maintained at the top energy before the squeeze (Section 8.7.3). The negative octupole polarity is chosen as the preferred option for single beam stability and for the dynamic aperture in the presence of long-range beam-beam effects. However, at this polarity, the long-range beam-beam effects act against the stabilising effect of the octupoles. To prevent the reduction of beam stability, the beams are brought into collision early during the squeeze phase at $\beta^* = 1.1$ m (Section 8.7.4). The safety margin of stability falls below 3 over a short period of time while bringing the beams into collision, but does not pose a problem as the instability rise time is much longer than this period. Once in collisions, the beams are stabilised by the head-on beam-beam tune spread. Similar to the LHC, the transverse feedback is kept on during collisions.

8.2 Electron cloud

Electron cloud mitigation in the FCC-hh relies on suppressing electron cloud build-up by reducing the emission of both primary and secondary electrons in the regions around the beam. Primary electrons due to photoemission are reduced by the beamscreen design, which directs the bulk of the synchrotron radiation into a secondary chamber. Secondary electron numbers are reduced by having surfaces with low secondary electron emission where necessary. In this section, simulation studies of electron cloud build-up and beam stability in the presence of electron clouds are presented and the requirements for surface treatments and photoelectron suppression are identified. Except where otherwise mentioned, the studies have been performed with the PyECLOUD code [142, 143], using a secondary emission model [144–146] parameterising measurements of LHC Cu co-laminated beamscreen samples [147–149].

8.2.1 Multipacting thresholds

The secondary electron emission yield (SEY) of a surface is defined as the ratio between the impinging and the emitted electron current, and is a function of the energy and angle of incidence of the impinging electrons. For a given surface, the maximum value of the secondary emission yield curve (SEY_{max}) can be used to parameterise the secondary electron yield of the surface.

The maximum secondary electron yield values above which electron cloud build-up occurs, i.e. the multipacting thresholds, have been estimated in arc dipoles, quadrupoles and drifts for both injection and collision energies. Figure 8.1 shows the estimated heat load per beam for the baseline beam option with 25 ns bunch spacing at injection and collision energy. In accordance with the constraints from injection considerations (Chapter 4), the filling pattern consists of trains of 80 bunches, separated by 17 empty 25 ns bunch slots. The curves in the figure have been scaled with the fraction of length occupied by each type of element in the arcs, such that the sum of the curves gives the weighted average heat load in the arcs. The multipacting thresholds are clearly visible in the figure, and are summarised in Table 8.1. The maximum secondary emission yield is required to be 1.1 in the arc quadrupoles, 1.5 in the dipoles and 2.0 in the field free regions. Furthermore, even above the multipacting threshold, i.e. when electron cloud build-up occurs, the heat loads are low compared to the expected heat load from the synchrotron radiation, see Table 2.1.

8.2.2 Stability threshold

An estimate of the threshold electron density, above which the electron cloud drives single-bunch head-tail instabilities, can be derived by approximating the force that the electron cloud exerts on the beam as a wakefield [150, 151]. The density can be written as [152, 153]

$$\rho_{e,th} = \frac{2\gamma Q_s}{\sqrt{3}Qr_p\beta_{x,y}L}, \quad (8.1)$$

where r_p is the classical proton radius, L is the length over which the electron cloud extends and Q is the quality factor of the wakefield, which is taken to be $Q = \min(\omega_e\sigma_z/c, 7)$. Here ω_e is the electron oscillation frequency near the beam centre, which depends on the line density of the bunch $\lambda_z = N_b/4\sigma_z$ (assuming a uniform longitudinal distribution) and the transverse beam size as follows

$$\omega_e = \sqrt{\frac{2\lambda_z r_e c^2}{\sigma_{x,y}(\sigma_x + \sigma_y)}}, \quad (8.2)$$

where r_e is the classical electron radius. Assuming electron cloud along the arcs of the machine, the estimated density thresholds are 1×10^{11} e/m³ at injection energy and 5×10^{11} e/m³ at collision energy. These estimates

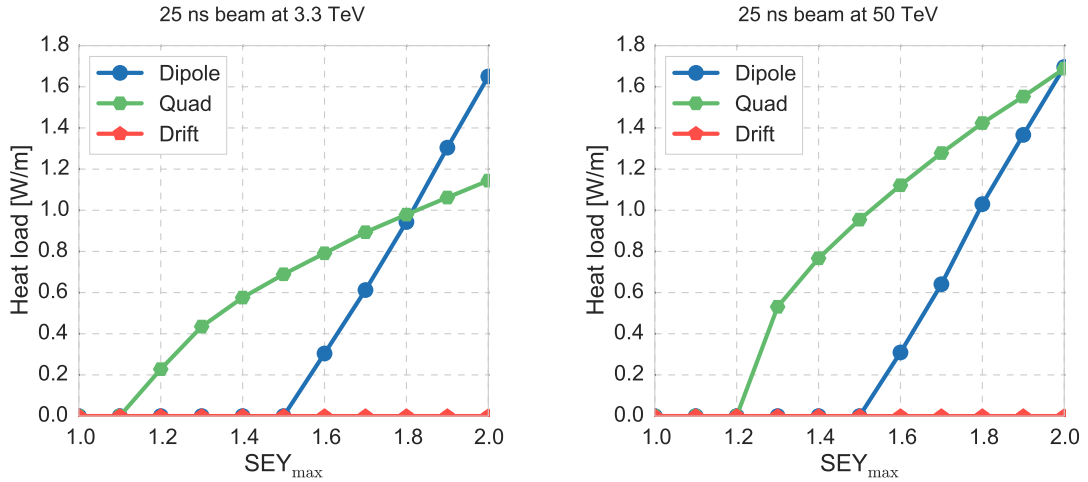


Figure 8.1: Heat load per beam as a function of SEY_{max} in the main arc elements at injection and collision energy.

are independent of the bunch spacing, as long as the beam brightness remains fixed.

The single-bunch stability in the presence of electron clouds has also been studied with macro-particle simulations, using the PyECLOUD-PyHEADTAIL simulation suite [143]. The stability has been evaluated in the arc dipoles at injection and collision energies for the baseline beam option with 25 ns bunch spacing, as well as for an alternative beam option with 5 ns bunch spacing (option 3 in Table 1.2). At collision energy the RF voltage is set to 32 MV, which gives a somewhat conservative estimate with respect to the baseline RF parameters given in Section 8.4. The threshold electron densities predicted by the simulations are similar to or slightly higher than the analytical estimate, around 10^{11} e/m^3 at injection and 10^{12} e/m^3 at collision energy. To avoid electron cloud-induced instabilities, the average electron density in the arcs should stay well below these threshold values.

The simulated electron density in the centre of the beam chamber as a function of the maximum secondary electron yield in the main arc elements is shown in Fig. 8.2, for the baseline beam at injection and collision energies. As was done for the heat loads above, the curves have been scaled with the fraction of length occupied by each

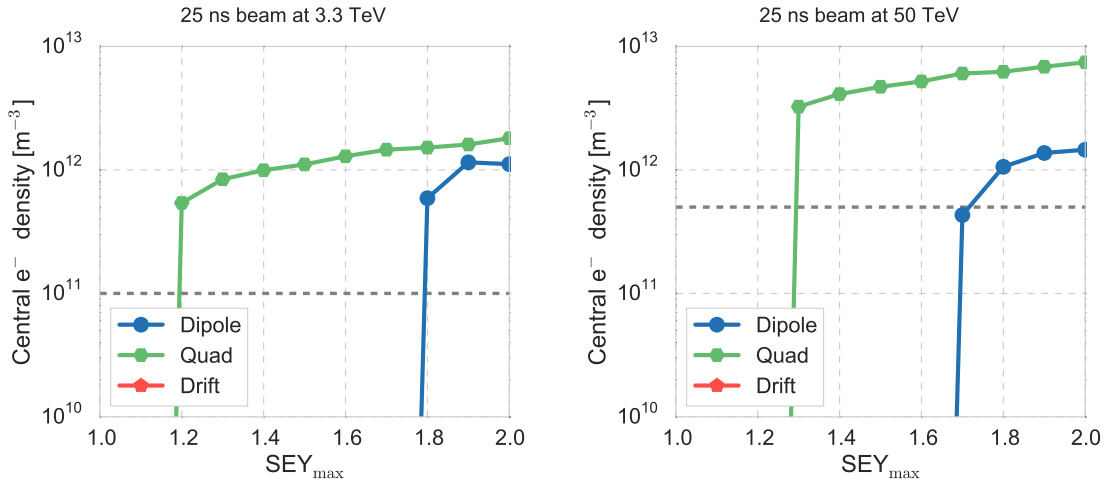


Figure 8.2: Central electron density as a function of SEY_{max} in the main arc elements at injection and collision energy.

type of element in the arcs, such that the sum of the curves gives the weighted average central electron density in the arcs. In the quadrupoles, the electron density exceeds the stability threshold whenever the SEY is above the multipacting threshold. Also in the dipoles the density exceeds the stability threshold when the SEY is large, whereas below the multipacting threshold the density is well within the tolerance. This shows that, in the absence of strong primary electron seeding, electron-cloud-induced beam instabilities can be avoided by ensuring that the SEY_{max} of the surface is no larger than the multipacting threshold.

8.2.3 Photoelectrons

In addition to the secondary emission yield, the impact of primary electron emission in the form of synchrotron radiation-induced photoelectrons has been evaluated. A study of their effect was done with preliminary simulations using a chamber geometry based on an early design of the beamscreen, where photoelectrons were emitted from the chamber walls at a rate depending on the angle from the synchrotron radiation impact point. These studies show

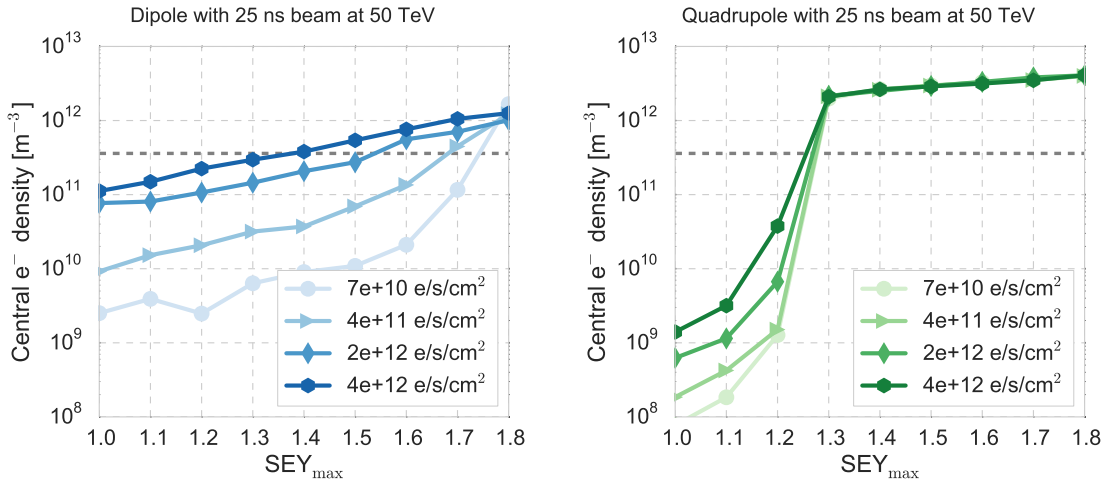


Figure 8.3: Central electron density as a function of SEY_{max} for varying photoelectron flux in dipoles (left) and quadrupoles (right) at collision energy. An early version of the beamscreen design from 2015 was used.

that if a significant flux of photoelectrons is induced by the synchrotron radiation, the central electron density can exceed the instability threshold even in the absence of electron cloud build-up through multipacting. In Fig. 8.3, the simulated central electron densities at collision energy are shown for different photoelectron fluxes (no significant photoelectron emission is expected at injection energy). The effect of the photoelectrons can be seen mainly below the multipacting threshold, where the central electron density increases with increasing photoelectron flux. Based on these studies, constraints on the photoelectron flux to ensure beam stability were determined and conveyed to the beamscreen design team. The constraints have been successfully taken into account in the current design where the photon reflector initially planned at the radiation impact point has been replaced by a saw-tooth surface that directs the photons into the secondary chamber [154].

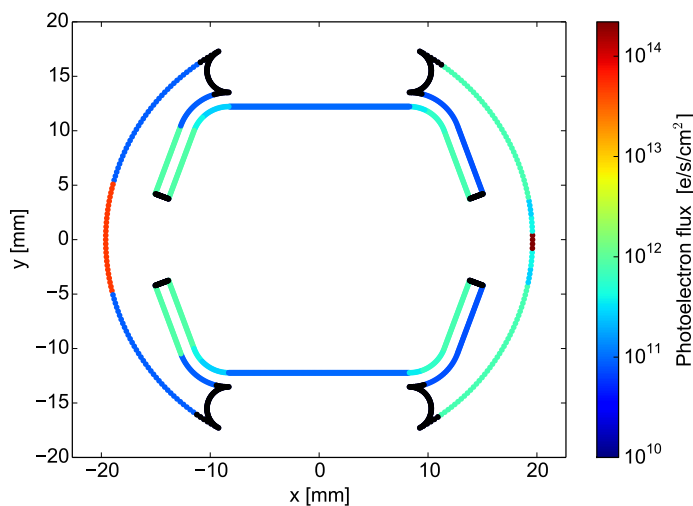


Figure 8.4: Transverse cross-section of the beamscreen showing the local photoelectron flux applied to the chamber in simulations. The fluxes in this example are determined by synchrotron radiation tracking simulations and photoemission measurements of a Cu co-laminated beamscreen sample [122, 155, 156].

To verify the validity of the updated beamscreen design, simulations with a more accurate photoelectron

emission model have been implemented. In this model, a local photoelectron flux can be applied to different parts of the chamber surface with arbitrary spatial resolution. In this way, photoelectron flux distributions based on synchrotron radiation ray-tracing simulations and photoemission measurements could be used in the build-up simulations [154]. In simulations of the dipoles and quadrupoles two different photoelectron distributions which were based on photoelectron yield measurements on co-laminated Cu surfaces and LASE treated surfaces (see Section 8.8.4) [156] were considered. In the first case, shown in Fig. 8.4, Cu photoemission is assumed on all the inner surfaces of the beam chamber, while in the other case LASE photoemission is assumed on the areas most exposed to electron cloud build-up, i.e. on the top, bottom and corners of the inner chamber. Simulated central electron densities with the two photoemission distributions are shown in Fig. 8.5. The electron density stays well below the instability threshold in the absence of electron multipacting for both models, confirming that the beamscreen design efficiently suppresses photoelectron production.

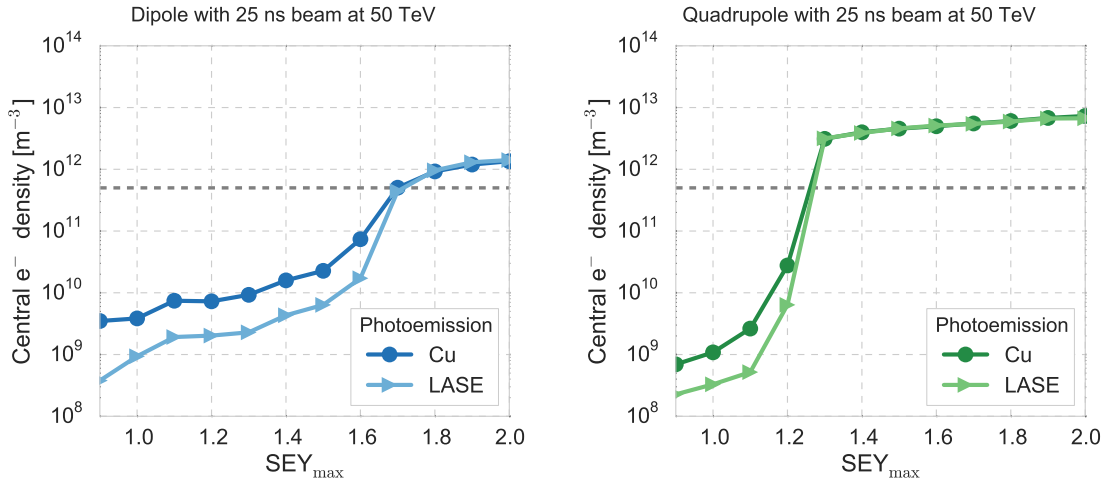


Figure 8.5: Central electron density as a function of SEY_{max} at collision energy using segment-wise photoelectron emission with Cu and LASE photoelectron yield models.

The effect of photoelectrons has been considered at two different locations in the interconnection regions. The highest photoelectron flux is expected in the region of the absorber for the synchrotron radiation from the neighbouring magnets. At this location, the absorber itself is assumed to be LASE treated, whereas Cu photoemission is assumed for the chamber surfaces. In addition, a location further from the magnets has been studied, where some of the reflected synchrotron radiation hits the chamber wall, assuming Cu photoemission from the chamber surface. The simulated central electron densities in the two locations are shown in Fig. 8.6. The electron density only depends weakly on the SEY, since no multipacting occurs in the interconnection regions for the SEY_{max} values considered. At low SEY_{max} , the densities are significantly higher than the corresponding densities estimated in the arc magnets, although they remain below the estimated instability threshold in both locations.

In addition to the central electron density, electron impingement rates and the average energy of impinging electrons have been determined based on the segment-wise photoelectron simulations used for estimating the electron stimulated desorption rates for vacuum stability [154, 155].

8.2.4 Alternative beam options

As discussed in Section 1.9, alternative operation modes with the bunch spacing reduced from the nominal 25 ns to 12.5 ns or 5 ns together with proportionate changes to the bunch charge and emittance have been considered, in order to reduce the number of collision events per bunch crossing. Since electron cloud build-up depends strongly on the bunch spacing and, in addition, the bunch intensity significantly impacts the distribution of the electron cloud, the studies with the nominal beam cannot be assumed to be representative of the alternative cases. To evaluate their feasibility, electron cloud effects have also been studied for the alternative beam configurations, in particular options 1 and 3 in Table 1.2.

Figure 8.7 shows the estimated heat load per beam with the alternative bunch spacings at injection and collision energy. The bunch trains are assumed to have the same length and total charge as the nominal case, and thus consist of 400 bunches with 5 ns spacing and 160 bunches with 12.5 ns spacing, respectively. Compared to the corresponding results for the nominal beam, Fig. 8.1, the multipacting thresholds for the alternative beam options

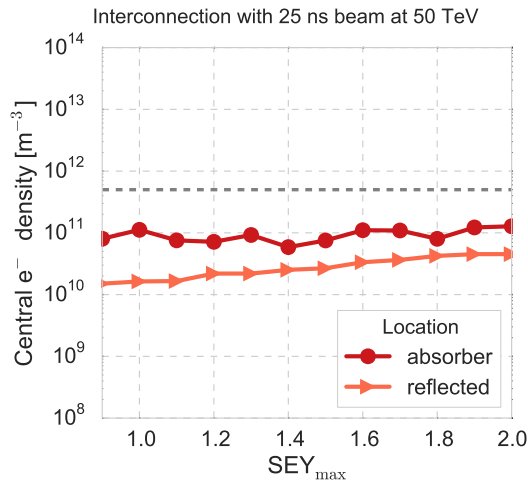


Figure 8.6: Central electron density as a function of SEY_{max} at collision energy with segment-wise photoelectron emission in two different locations of the interconnection regions.

are considerably lower. For both alternatives significant electron cloud build-up occurs in the quadrupoles for $SEY_{max} = 1.1$. The 12.5 ns beam option is the most challenging case, with relatively low multipacting thresholds also in the dipoles and field-free regions. For both options, the heat loads above the multipacting threshold are considerably higher than with a 25 ns bunch spacing, although still significantly lower than the expected heat load from the synchrotron radiation.

The estimated electron density in the centre of the beam chamber with the alternative bunch spacings at injection and collision energy are shown in Fig. 8.8. In most cases, the central electron density exceeds the instability threshold whenever SEY_{max} is above the the multipacting threshold. In these cases SEY_{max} must not be larger than the multipacting threshold to ensure beam stability. The central electron density above the multipacting threshold is particularly high with the 5 ns bunch spacing.

The effect of photoelectron emission on the electron cloud build-up has also been studied for the alternative beam options. As with the 25 ns bunch spacing, two different photoelectron distributions based on photoelectron yield measurements on co-laminated Cu surfaces and LASE treated surfaces were studied for the dipoles and quadrupoles. The simulated central electron densities with the two photoemission distributions are shown in Fig. 8.9. Slightly lower central densities are estimated with the LASE photoemission model, however neither model's photoemission has a significant impact on the conclusions drawn above.

In the interconnection regions the effects of photoelectrons have been considered in the same two locations as the 25 ns bunch spacing: the absorber region and a region with reflected synchrotron radiation. The simulated central electron densities in the two locations are shown in Fig. 8.10. For the 5 ns beam, it is estimated that the stability threshold is reached in the absorber region even with low SEY due to the photoemission. With 12.5 ns bunch spacing the central density remains below the estimated instability threshold in both locations.

8.2.5 Mitigation requirements and coating

The surface requirements in terms of maximum secondary electron yield to ensure electron cloud suppression in the main arc components are summarised in Table 8.1 for all beam options studied. For comparison, an unconditioned LHC beamscreen surface has an SEY_{max} of around 2.0. Under electron irradiation, the surfaces condition to a lower SEY. In laboratory measurements, the surfaces can be conditioned down to an SEY_{max} of around 1.15 [157, 158].

Since electron bombardment occurs naturally in the presence of electron clouds, the beamscreen surfaces should gradually condition to lower SEY values during machine operation. Such a reduction of the SEY has been indirectly observed in the LHC through a decrease of the measured heat load on the beamscreen [159]. However, some heat loads currently measured in the LHC are only compatible with an SEY much higher than expected from laboratory measurements [160]. This implies that some of the beamscreen surfaces in the LHC cannot be conditioned to the expected levels, even after several years of operation with significant electron clouds. As long as this phenomenon is not fully understood, it remains unclear to what extent scrubbing can be relied on for electron

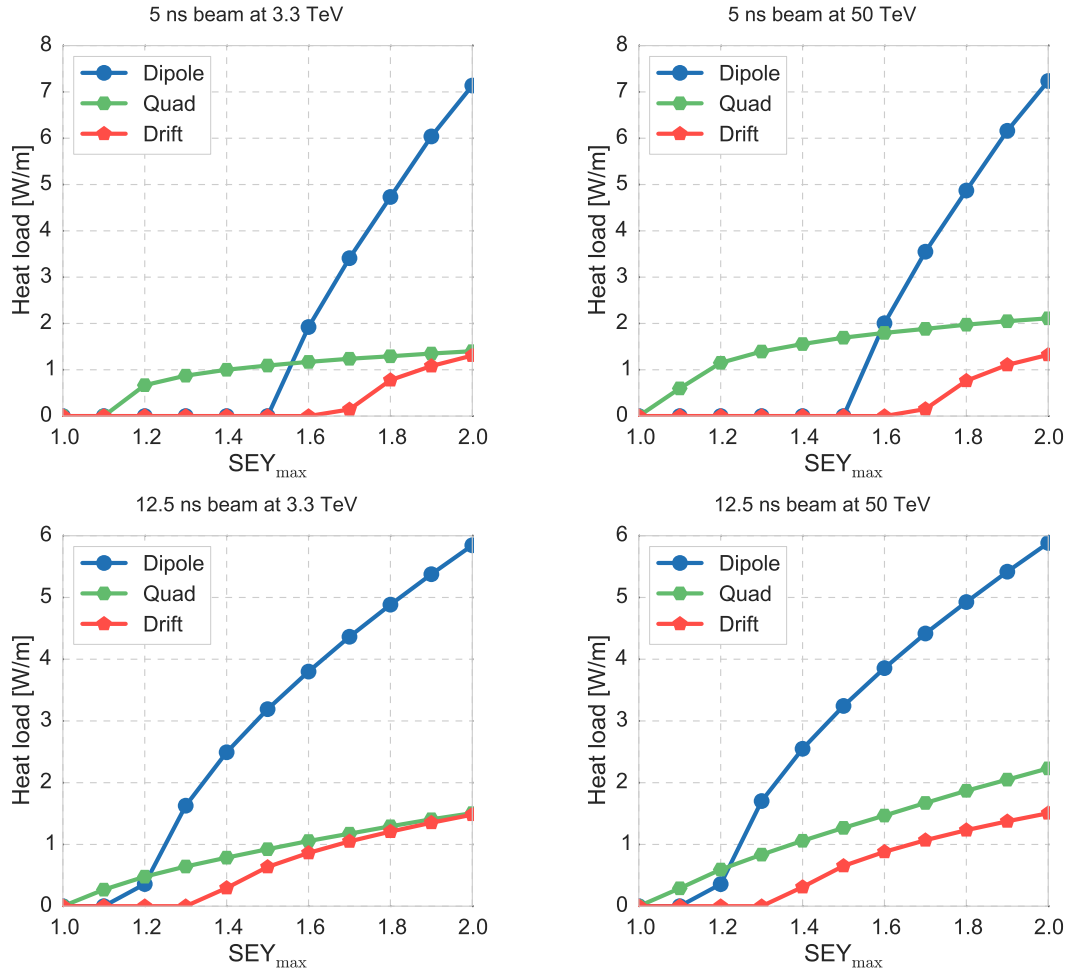


Figure 8.7: Heat load per beam as a function of SEY_{max} in the main arc elements with 5 ns bunch spacing (top) and 12.5 ns bunch spacing (bottom) at injection (left) and collision (right) energy.

cloud mitigation. Therefore, coating is the preferred strategy for lowering the SEY of the FCC-hh beamscreens.

For the baseline beam option, the maximum secondary emission yields required for electron cloud suppression are moderate and can be achieved with low-SEY surface treatments. An amorphous carbon (a-C) coating [161], which lowers the SEY to around 0.95-1.05, or LASE surfaces [162, 163], which typically have lower SEY, would both be sufficient. Due to the lesser impact on the machine impedance (see Section 8.3) a-C is the baseline coating option. Based on the transverse distribution of the electron cloud in different magnetic fields, illustrated in Fig. 8.11, the coating should be applied over the top and bottom surface of the beamscreen in dipoles, whilst in quadrupoles the coating is required on the sides, at 45° to the horizontal plane. In the field-free regions the SEY required is sufficiently high that no dedicated coating is necessary. For the alternative beam options, the multipacting thresholds are considerably lower. In particular, in the quadrupoles, SEY_{max} may need to be kept no larger than 1 for these beam options. This could be achieved by high performance a-C coatings, or LASE surfaces. In addition in the field free regions, a surface coating or other mitigation measures, e.g. solenoid fields or electron-clearing electrodes, should be considered.

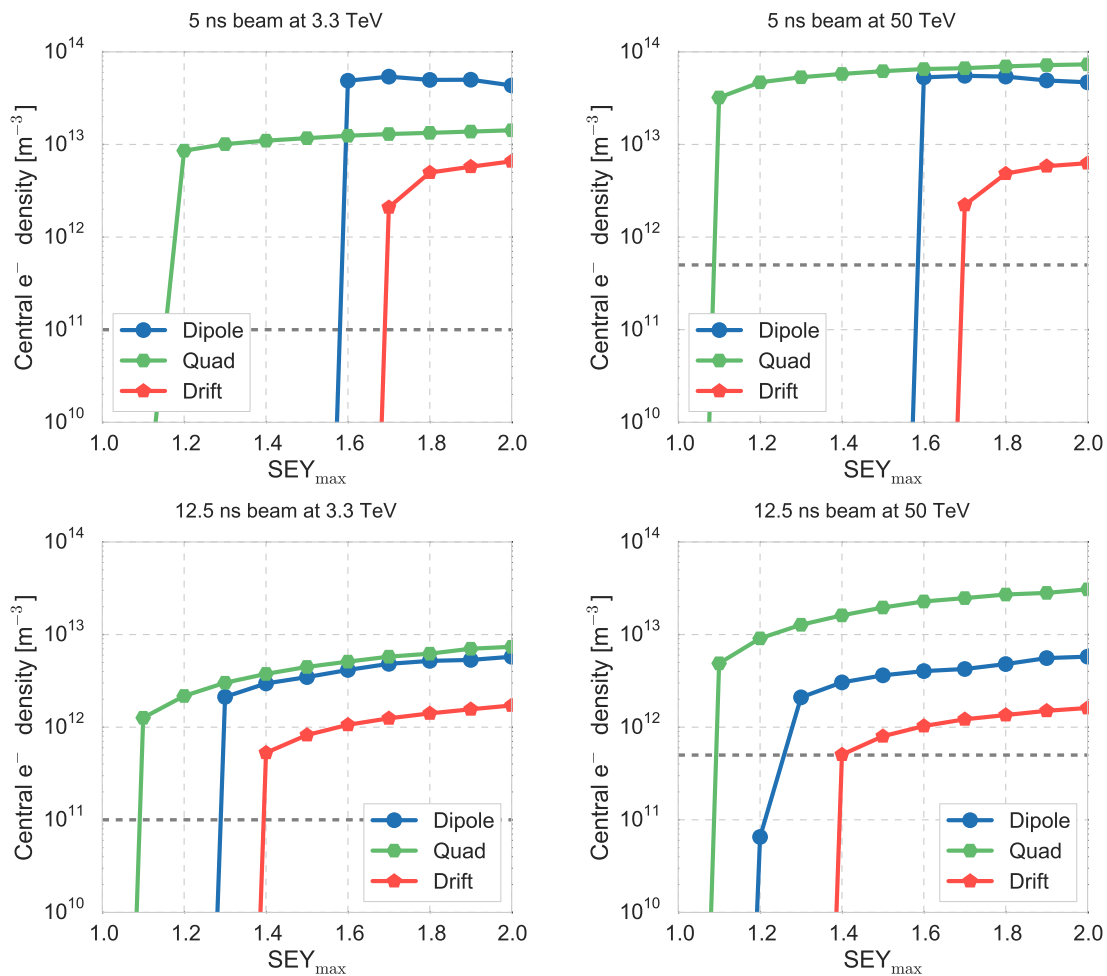


Figure 8.8: Central electron density as a function of SEY_{max} in the main arc elements with 5 ns bunch spacing (top) and 12.5 ns bunch spacing (bottom) at injection (left) and collision (right) energy.

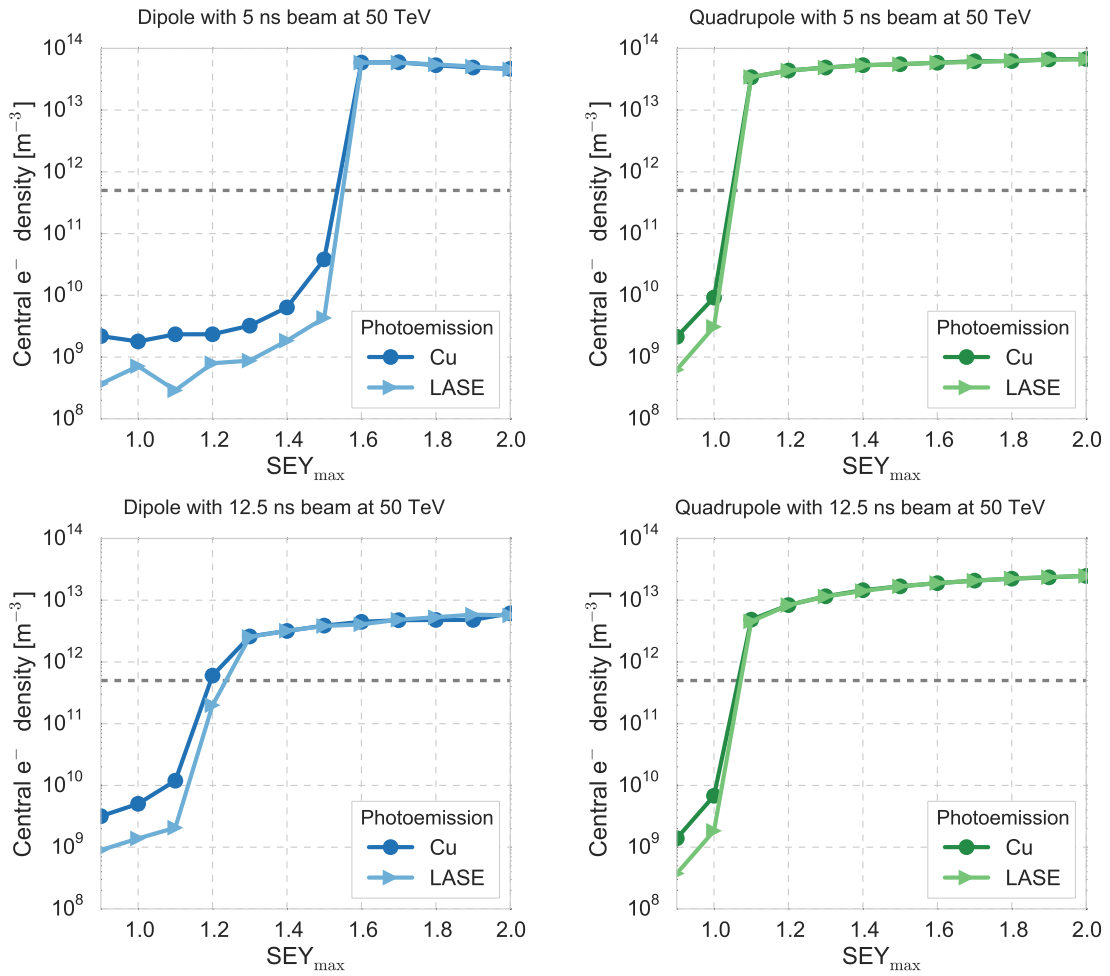


Figure 8.9: Central electron density as a function of SEY_{max} at collision energy with segment-wise photoelectron emission with Cu and LASE photoelectron yield models with 5 ns bunch spacing (top) and 12.5 ns bunch spacing (bottom) in dipoles (left) and quadrupoles (right).

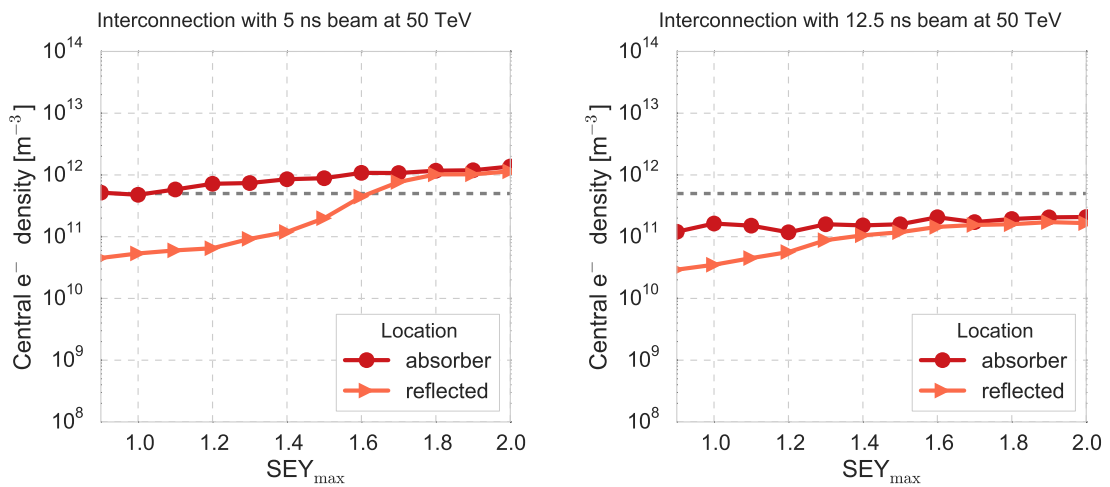


Figure 8.10: Central electron density with segment-wise photoelectron emission in two different locations of the interconnection regions with 5 ns bunch spacing (left) and 12.5 ns bunch spacing (right).

Table 8.1: Multipacting thresholds for electron cloud build-up in the arc elements at injection and collision energy.

| Arc element | 25 ns injection / top energy | 12.5 ns injection / top energy | 5 ns injection / top energy |
|-------------|---------------------------------|-----------------------------------|--------------------------------|
| Dipole | 1.5 / 1.5 | 1.1 / 1.1 | 1.5 / 1.5 |
| Quadrupole | 1.1 / 1.2 | 1.0 / 1.0 | 1.1 / 1.0 |
| Drift | 2.0 / 2.0 | 1.3 / 1.3 | 1.6 / 1.6 |

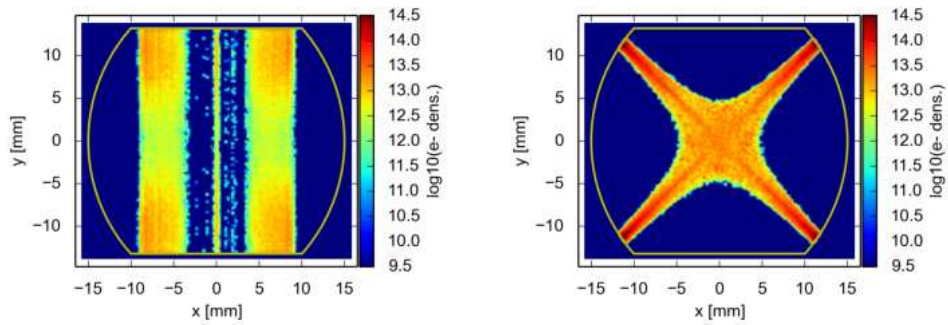


Figure 8.11: Electron cloud distribution with the nominal beam in a dipole (left) and quadrupole (right) for an early version of the beamscreen design.

8.3 Beam coupling impedances

The FCC-hh impedance model includes the monopole longitudinal impedance $Z_z(f)$ and the dipolar transverse impedances in the horizontal and the vertical planes $Z_x(f)$, $Z_y(f)$. The total impedances Z_z and Z_y (the most critical transverse plane) are shown in Fig. 8.12 at the injection energy (3.3 TeV) and the collision energy (50 TeV). For the dipolar impedances, contributions of different elements are weighted by their ratio of their local β -functions to the smooth approximation β : $\beta_{x,y}^{\text{ref}} = C/(2\pi Q_{x0,y0})$, where C is the circumference and $Q_{x0,y0}$ are the unperturbed horizontal and vertical betatron tunes.

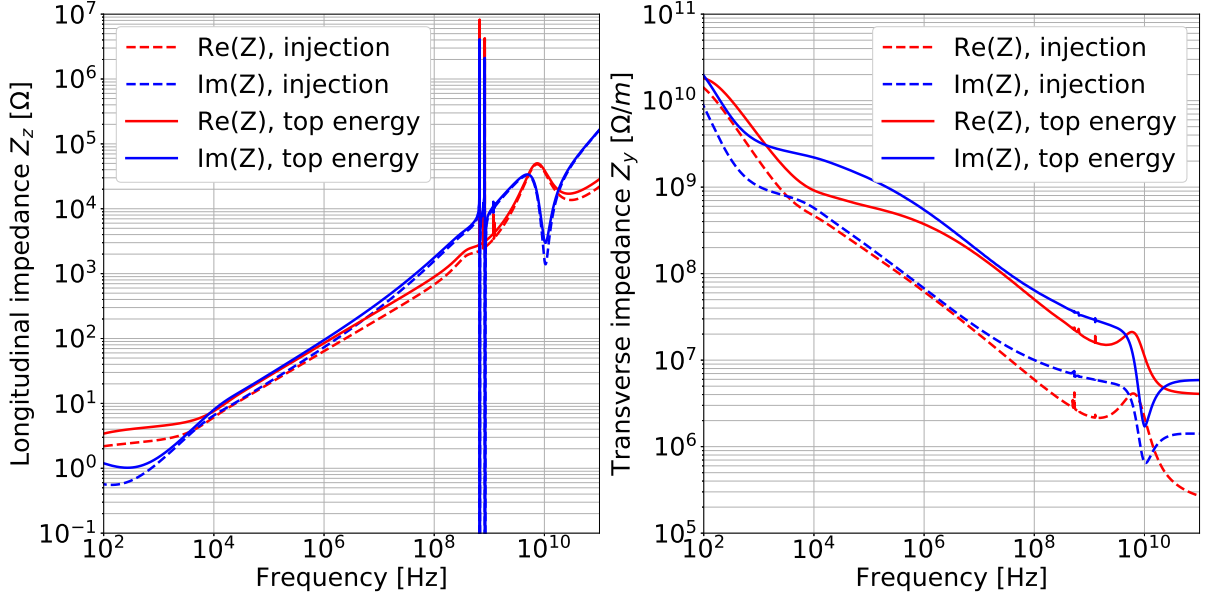


Figure 8.12: Total FCC-hh impedances as functions of frequency.

8.3.1 Beamscreen: resistive wall, without e-cloud coating

The beamscreen which occupies 86% of the collider circumference, separates the particle beam from the magnet cold bore in the long and the short arc sections. Its walls are made of stainless steel (grade P506, resistivity $6 \times 10^{-7} \Omega\text{m}$), with the sides facing the beam co-laminated with a 300 μm thick layer of copper. The copper layer is assumed to have an RRR of 70, similar to the LHC beamscreen (see Ref. [164], p.185). Note that it would be possible to have purer copper with an RRR of 100. The temperature of the beamscreen walls is set to 50 K, resulting in a resistivity of $7.5 \times 10^{-10} \Omega\text{m}$ for the copper in the absence of an external magnetic field. The resistivity increases with the dipole magnetic field according to Kohler's rule [165], becoming $7.9 \times 10^{-10} \Omega\text{m}$ at injection and $1.4 \times 10^{-9} \Omega\text{m}$ at the top energy. The impedance of the two-layer walls is calculated with the ImpedanceWake2D [166] code for a circular pipe with a radius of 12.22 mm - the vertical aperture of the beamscreen. Then, form factors are applied to account for the non-circular cross-section: $F_x = 0.45$, $F_y = 0.83$, $F_z = 0.82$, as estimated with the CST wakefield solver [167]. Finally, the dipolar impedances are weighted with the average β -functions in the arc FODO cell. However, the transverse impedance for the complex beamscreen geometry can be calculated using a frequency domain solver BeamImpedance2D [168].

In the current design the copper coating is absent on some walls which do not face the beam but nevertheless affect the impedance due to the non-zero surface electromagnetic fields. In particular, at the edges of the slit, a small area of uncoated stainless steel is exposed, which affects the dipolar impedance in the horizontal plane. Several solutions to this issue exist, including re-shaping the edge or applying a thin copper coating. The latter option is possible using cold or plasma spraying. However, the copper applied by this method is likely to have different properties to the co-laminated one, leading to increased impedance, which in turn, affects the collective effects. The current impedance estimate does not include the potential increase due to the exposed stainless steel region.

8.3.2 Beamscreen: coating for electron cloud mitigation

A coating is applied to the inner surface of the beamscreen in order to prevent an electron cloud build-up by reducing the secondary emission yield (SEY) of the surface. In the current impedance model, an amorphous carbon coating is assumed. This material has a low secondary emission yield δ_{max} and a relatively weak effect on the machine impedance [169]. The thickness of the a-C coating required to decrease the SEY below 1 is approximately 30 nm, corresponding to 100-150 carbon monolayers [170]. The thickness and the resistivity of the coating are assumed to be 200 nm, and 10^{-4} Ωm , respectively. Such a thickness is sufficient to avoid the electron clouds in the beam pipe and will not have a large impact on the TMCI threshold, and at the same time it avoids roughness of the material. The method above is used to find the resistive wall impedance of the beamscreen, after the extra layer of coating has been added. Subtracting the impedance of the uncoated beamscreen gives the impedance contribution of the coating. In the frequency range of interest, the coating impedance is purely imaginary and is independent of the exact value of the resistivity. In case of applying a titanium-nitride layer of the same thickness the impedance will be the same. The longitudinal impedance is proportional to the frequency, and the transverse impedance is constant with frequency.

Alternatively, a laser treatment of the beamscreen surface can be used if the impedance increase is found acceptable. This option is discussed further in Section 8.8.4.

8.3.3 Beamscreen: pumping holes

Pumping holes connect the space inside the beamscreen to the outer region from where the air is pumped out. The novel design of the beamscreen significantly reduces the impedance of the pumping holes by shielding them from the beam. The complexity of the beamscreen geometry prevents the use of analytical methods to estimate the impedance of the holes. In order to estimate the broadband dipolar impedance of the holes, numerical simulations were carried out accounting for travelling waves synchronous with the beam [6]. If the slit width is artificially increased, the impedance becomes high enough to be simulated with the time-domain wakefield solver of CST. Both the travelling wave result and the extrapolation to the actual slit width of the time-domain results show that the integrated effect of all the holes amount to less than 0.1 M Ω /m of broadband dipolar impedance in the horizontal plane. The real part of the longitudinal impedance can potentially lead to an excessive heat loss in the cold bore, but is expected to also decrease rapidly with the slit width.

8.3.4 Warm beampipe: resistive wall

The warm beampipe is the vacuum chamber of varying cross-section that surrounds the particle beam in the straight sections (outside of the arcs). The resistive impedance is calculated by using the thick-wall formula that applies in a sufficiently wide frequency range, and weighting the impedance of each section with the local β -function [171]. At injection, the most critical contributions come from the extraction insertion, PD, and the collimation insertion, PJ. At the top energy, the main experiment insertions PA and PG, dominate due to the high β -functions.

8.3.5 Collimators: resistive wall

Jaws of collimators and protection devices have a significant impact on the overall impedance model due their proximity to the beam (half-gap on the order of 1 mm for the ‘squeezed’ settings). The jaws of all primary collimators and the first secondary collimator in the betatron-cleaning section are made of CFC to sustain the high heat load. Jaws of all other secondary collimators are made of molybdenum-graphite with a 5 μm thick pure molybdenum coating in order to reduce their impedance. The resistive impedance is calculated with the code ImpedanceWake2D. For each collimator, the dipolar impedances are rotated by the angle of the collimator position in the $x - y$ plane and weighted with the local β -functions.

8.3.6 Collimators: geometrical impedance

The geometrical impedance of the collimators is associated with the taper transitions from the beam pipe to the jaws (two tapers per collimator). To find the low-frequency broadband impedances, approximate analytical formulas for rectangular tapers [172] are used. Similar to the LHC collimators, the tapers are assumed to be 97 mm long, 70 mm wide, and to have a 17.6 mm step in the plane of collimation. The broadband resonator model (see Ref. [164], p.71) is used to extrapolate the low-frequency impedances to the full frequency range. The resonance is assumed to have a very low quality factor ($Q = 1$) and is placed at the beampipe cut-off frequency. For each collimator, the

dipolar impedances are rotated by the angle of the collimator position in the $x - y$ plane and weighted with the local β -functions.

8.3.7 Interconnects: geometrical impedance

The arc FODO cell consists of 12 cryodipoles and 2 short straight sections containing quadrupoles and other magnets. Thus, each FODO cell contains 14 interconnects between the cryo-modules, with a total number of 5516 interconnects in the ring. Each interconnect has tapers that transform the complex beamscreen shape to a circle on both sides such that the two sides can be connected with RF fingers. Unlike in the LHC, such a transformation involves an abrupt change in the cross section, although only behind the shielding. Additionally, the upstream taper is made of the taper-down and the taper-up parts to form a barrier that prevents the intense synchrotron radiation from hitting the RF fingers. The low-frequency broadband impedances of the tapers are simulated with the CST Wakefield Solver [167]. The low-frequency impedances are extrapolated to the entire frequency range using the broadband resonator model, similar to the impedance of the collimator tapers (see above). The dipolar impedances are weighted with the average β -functions at the location of the interconnects, which are approximately equal to the average β -function in the arcs.

8.3.8 400 MHz RF cavities

The frequencies, shunt impedances, and damped Q-factors are assumed to be that of the LHC cavities. The shunt impedances for one 4-cell module [173] were multiplied by 6, assuming that 24 cells are needed to provide 48 MV of RF voltage. The fundamental mode at 400.79 MHz is not considered in the impedance model, except for its contribution to the broadband longitudinal impedance (broadband resonator model with $Q = 1$ is used). The dipolar impedances are weighted with the average β -functions for the two groups of cavities.

8.3.9 Crab cavities

Eigenmode data for the WOW crab cavities is used, containing 6 modes: two monopole modes at 667 MHz and 827.2 MHz, three dipole modes in the deflecting plane at 400.0 MHz, 638.3 MHz and 1276 MHz, and one dipole mode in the non-deflecting plane at 643.8 MHz. The fundamental ‘crabbing’ mode 400.0 MHz is only included in the model with its broadband contribution (broadband resonator model with $Q = 1$ is used). The number of cavities is assumed to be 24, with half of the cavities crabbing in the horizontal plane, half in the vertical plane. The dipolar impedances were weighted with the average β -functions at the location of the cavities. Unlike for the 400 MHz RF cavities, the β -functions at the locations of the crab cavities vary strongly between the injection settings and the collision settings, making the impedance of the crab cavities energy-dependent.

8.3.10 Distribution of the dipolar impedance by the elements

Distribution of the weighted dipolar impedance over the different elements is shown in Fig. 8.13. Two frequency ranges are distinguished: the kHz range driving the coupled bunch instabilities (the left side of the graphs), and the GHz range driving the single bunch instabilities (the right side of the graphs). The growth rate of the coupled bunch instability is dominated by the resistive wall impedance of the beamscreen both at injection and at the top energy. As far as the single bunch instabilities are concerned, the situation varies according to the energy. Namely, at injection, the growth rate and the real tunes shift of the head-tail modes are dominated by several elements, among which the beamscreen coating is an important contributor. At the top energy, the collimator impedance dominates (consisting of both the resistive and the geometrical parts) due to the squeezed collimator settings.

8.3.11 Effective dipolar impedances

Effective impedances are defined for the head-tail mode with the azimuthal and the radial indexes $k = 0$, $q = 0$ at zero chromaticity, similar to what was done for the LHC ([17] pp 98 - 101). The effective impedances facilitate a comparison of contributions of the different elements, and provide rough estimates of the stability margins (actual stability simulations will follow in Section 8.7). For each machine element placed at a location with betatron functions $\beta_{x,y}$, and characterised by the dipolar coupling impedances $Z_{x,y}$, the effective coupled bunch impedance is defined as

$$\operatorname{Re} (Z_{x,y})_{\text{eff}}^{\text{CB}} = \frac{\beta_{x,y}}{\beta_{x,y}^{\text{ref}}} \sum_{k=-\infty}^{k=\infty} \operatorname{Re} (Z_{x,y}(\omega_k)) h_{0,0}(\omega_k), \quad (8.3)$$

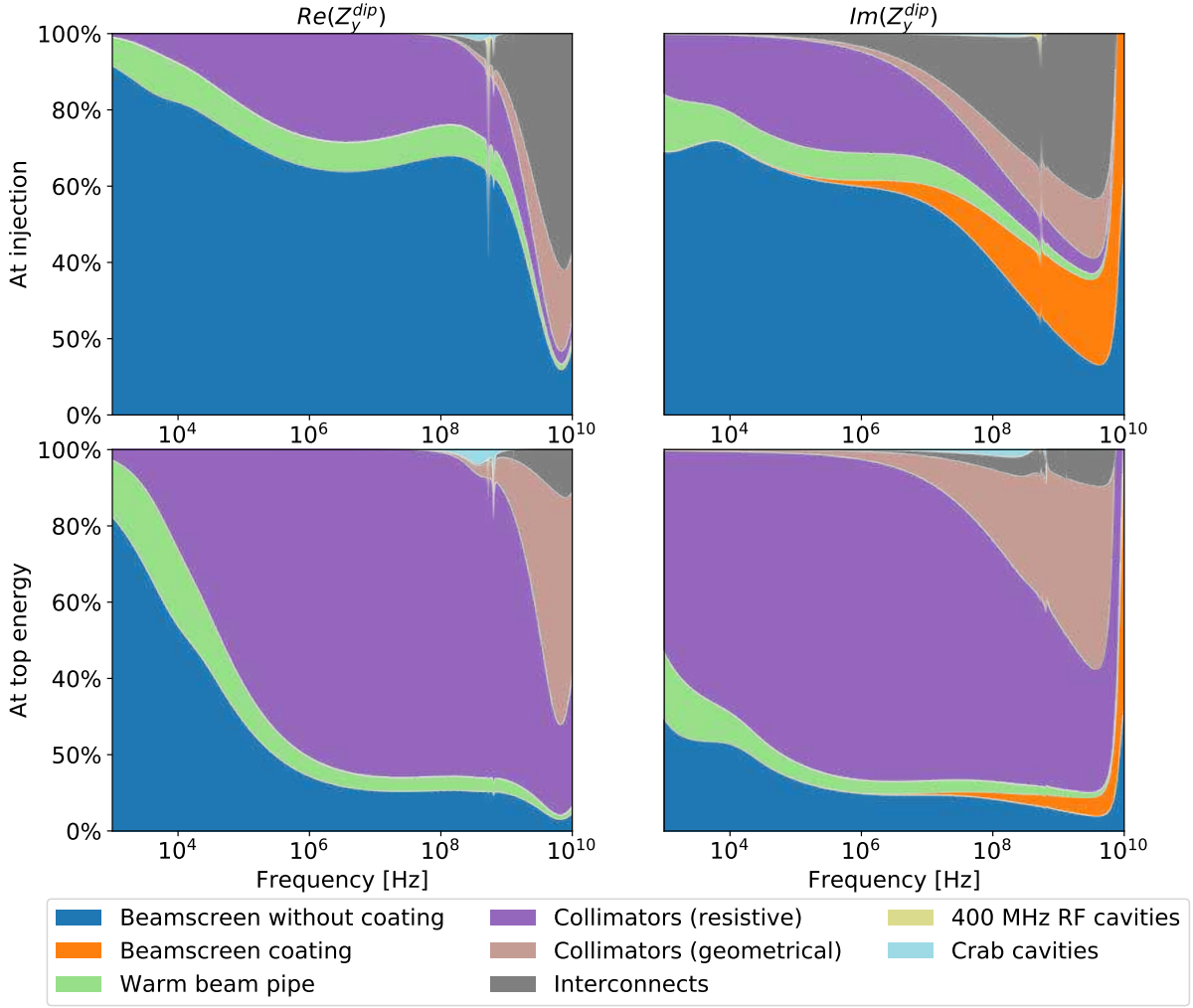


Figure 8.13: Dipolar impedance distribution by element (y -plane).

where the sum is done over the frequency lines $\omega_k = (\text{frac}[Q_{x0,y0}] - 1 + kM)\Omega_0$ for the most unstable coupled bunch mode number $n_{cb} = -(\text{int}[Q_{x0,y0}] + 1)$. Here $h_{0,0}(\omega) = e^{-(\omega\tau_b/4)^2}$ is the head-tail mode power spectrum for the Gaussian bunch shape, M is the total number of bunches in the ring, $\Omega_0 = 2\pi f_{rev}$ is the angular revolution frequency, τ_b is the 4σ bunch length in seconds.

Similar to the coupled bunch case, for an element with $\beta_{x,y}$ and $Z_{x,y}$ the single bunch effective impedance is defined as

$$\text{Im}(Z_{x,y})_{\text{eff}}^{\text{SB}} = \frac{\beta_{x,y}}{\beta_{x,y}^{\text{ref}}} \frac{\sum_{k=-\infty}^{k=\infty} \text{Im}(Z_{x,y}(\omega_k)) h_{0,0}(\omega_k)}{\sum_{k=-\infty}^{k=\infty} h_{0,0}(\omega_k)}, \quad (8.4)$$

where in this case the summation is done over the frequency lines $\omega_k = (k + Q_{x0,y0})\Omega_0$. Both the coupled-bunch and the single bunch effective impedances are shown in Table 8.2. For comparison approximate instability thresholds are also listed, also estimated at zero chromaticity (some numbers differ slightly from those listed in Refs. [174] and [1] due to the adjusted damper strength). For the coupled bunch threshold, the strongest possible feedback damping rate of 20 turns (injection) and 150 turns (top energy) are assumed. For the single bunch threshold, an RF voltage of 12 MV (injection) and 32 MV (top energy) are assumed.

Table 8.2: Effective transverse coupled bunch (CB) and single bunch (SB) impedances for the rigid mode ($k = 0$) at zero chromaticity. Impedances in the most critical (vertical) plane are shown.

| Source of impedance | Re $(Z_y)_{\text{eff}}^{\text{CB}}$ [M Ω /m] injection / top energy | Im $(Z_y)_{\text{eff}}^{\text{SB}}$ [M Ω /m] injection / top energy |
|--|---|---|
| Resistive impedance of beamscreen (no coating) | -940 / -1610 | 3.4 / 4.5 |
| Beamscreen coating | Negligible | 1.1 |
| Pumping holes | Negligible | ≤ 0.1 |
| Resistive impedance of warm beam pipe | -100 / -400 | 0.4 / 1.5 |
| Resistive impedance of collimators | -30 / -150 | 1.0 / 34.5 |
| Geometrical impedance of collimators | Negligible | 0.9 / 11.9 |
| Interconnects | Negligible | 2.4 |
| RF cavities | Negligible | Negligible |
| Crab cavities | Negligible | Negligible / 0.5 |
| Total | -1070 / -2160 | 9.2 / 56.5 |
| Instability threshold | -4070 / -8230 | 35 / 220 |

8.4 RF and longitudinal effects

The beam and machine parameters that are directly relevant to the design of the RF system are given in Table 8.3. The minimum bunch spacing of 5 ns defines the maximum bucket length and gives the lower limit of the RF

Table 8.3: Main ring and beam parameters.

| Parameter | Unit | Value |
|---|------|----------------------|
| Circumference | km | 97.75 |
| Energy (injection/collision) | TeV | 3.3/50 |
| Transition gamma | | 99.33 |
| Energy loss per turn at 50 TeV | MeV | 4.67 |
| Longitudinal emittance damping time at 50 TeV | h | 0.54 |
| Bunch spacing | ns | 25 (5) |
| 4σ bunch length at 50 TeV | ns | 1.07 |
| Bunch intensity | ppb | 1.0×10^{11} |

frequency of 200 MHz. The bunch length during physics of 1.07 ns limits the maximum RF frequency to 400 MHz, which corresponds to a 2.5 ns bucket length. Landau damping provides single bunch stability if the following criterion is satisfied [175, 176]

$$\text{Im}Z/n < (\text{Im}Z/n)_{\text{th}} = \frac{F|\eta|E}{e^2 N_b \beta^2} \left(\frac{\Delta E}{E} \right)^2 \frac{\Delta f_s}{f_s} \tau_b, \quad (8.5)$$

where $\text{Im}Z/n$ and $(\text{Im}Z/n)_{\text{th}}$ are the inductive longitudinal impedance and its threshold value, respectively. F is the form factor defined by the particle distribution in the bunch (in the LHC, the experimentally determined value is $F = 0.43$ [177]), $\eta = 1/\gamma_t^2 - 1/\gamma^2$ is the slip factor, γ_t is the transition gamma, ΔE is the half bunch energy spread (approximately twice RMS energy spread), E is the energy of a synchronous particle, and Δf_s is the full synchrotron frequency spread. For constant bunch length the threshold longitudinal impedance scales approximately as [178]

$$(\text{Im}Z/n)_{\text{th}} \propto V f_{\text{rf}}^3 \tau_b^5. \quad (8.6)$$

where f_{rf} is the RF frequency. It shows that, for stability of a bunch with the same length, about 8 times more RF voltage is required in a 200 MHz RF system than in a 400 MHz RF system. Thus the RF frequency of 400 MHz was chosen. The synchronisation with injectors sets the harmonic number $h = 130680$ [85].

The minimum RF voltage and the longitudinal emittance ϵ_z at 50 TeV are defined by single bunch stability. In Fig. 8.14 the threshold values of inductive impedance at flat top are shown as a function of bunch length for

different RF voltages together with $\text{Im}Z/n = 0.2 \Omega$ assumed as impedance budget of FCC-hh (in the LHC, the calculated and measured $\text{Im}Z/n = 0.09 \Omega$ [177]). The RF voltage of 42 MV provides the stability of bunches with the expected $\pm 5\%$ bunch length spread as the threshold curve crosses the impedance budget value at 95% of the design bunch length. In the previous calculations [86] the form factor $F = 1$ was used and 32 MV RF voltage was sufficient to prevent the transverse mode coupling instability (TMCI) which is shown in Fig. 8.15. In the present situation with higher RF voltage the transverse stability is further improved. The threshold impedance,

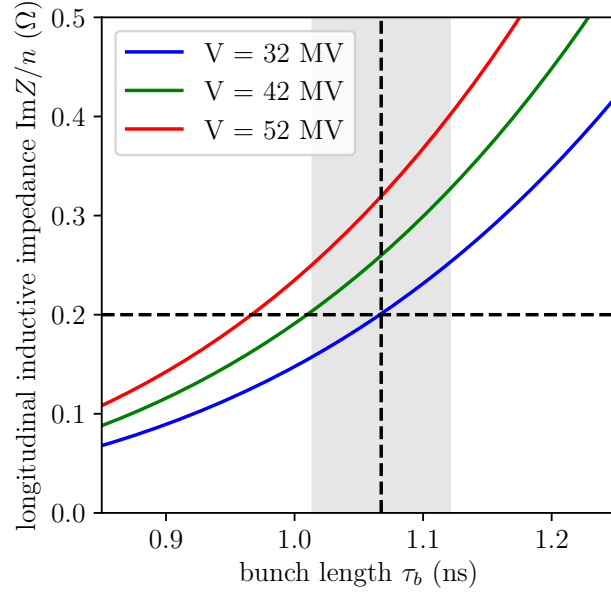


Figure 8.14: Threshold for the loss of Landau damping as a function of bunch length for $N_b = 1.0 \times 10^{11}$, $F = 0.43$, and different RF voltages. The horizontal dashed line is the impedance budget of 0.2Ω . The vertical dashed line is the design bunch length at 50 TeV. The grey region is $\pm 5\%$ bunch length spread.

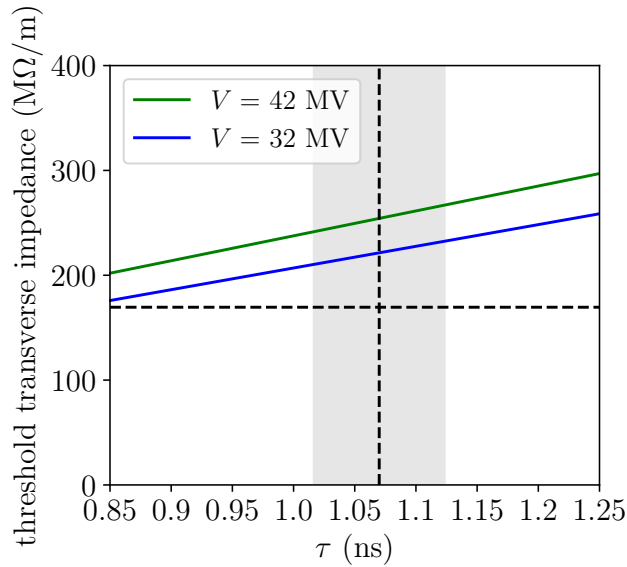


Figure 8.15: Threshold for the transverse mode coupling instability as a function of bunch length for $N_b = 1.0 \times 10^{11}$ and different RF voltages. The horizontal dashed line is the 3 times effective impedance at 50 TeV (see Table 8.2). The vertical dashed line is the design bunch length. The grey region is $\pm 5\%$ bunch length spread.

$(\text{Im}Z/n)_{\text{th}}$, which corresponds to loss of Landau damping, strongly depends on the longitudinal bunch emittance (to the power 2.5). During physics, emittance would be quickly reduced by synchrotron radiation damping with a characteristic time of half an hour. For the given parameters this means that controlled emittance blow-up is needed to maintain longitudinal beam stability and an additional 800 MHz RF system might be beneficial for this purpose [179].

The choice of RF and beam parameters at the FCC injection energy of 3.3 TeV is more flexible but there are the following constraints which should be taken into account:

- The present LHC RF system can provide up to 16 MV RF voltage.
- The length of bunches injected in the FCC-hh should be below 1.6 ns to avoid capture losses due to injection errors (similar to the LHC and HL-LHC).
- The longitudinal beam stability should be maintained for $\text{Im}Z/n = 0.2$ with margins for $\pm 5\%$ bunch length spread.

Having the same bucket area at the LHC extraction and the FCC injection will minimise the mismatch of injected bunches (but leaves no space for energy errors). The half bucket height is [180]

$$\Delta E_B = \sqrt{\frac{2\beta^2 E e V}{\pi h |\eta|} \left| \cos \phi_s - \frac{\pi - 2\phi_s}{2} \sin \phi_s \right|}, \quad (8.7)$$

where ϕ_s is the synchronous phase. Thus the ratio $V/(h|\eta|)$ should be the same for both machines as synchrotron radiation is negligible at 3.3 TeV and $\phi_s = \pi$. For the maximum RF voltage in the LHC (16 MV) with $\gamma_t = 53.65$ and $h = 35640$ the corresponding matched voltage in the FCC is 17 MV. For this voltage, beam stability at injection requires the 1.3 ns long bunches (taking into account $\pm 5\%$ bunch length spread (see Fig. 8.16)). Similar calculations show that for the maxim bunch length (1.6 ns) at injection, the required matched RF voltage is 7 MV. For the moment 12 MV RF voltage is chosen, but further optimisation can be done if required.

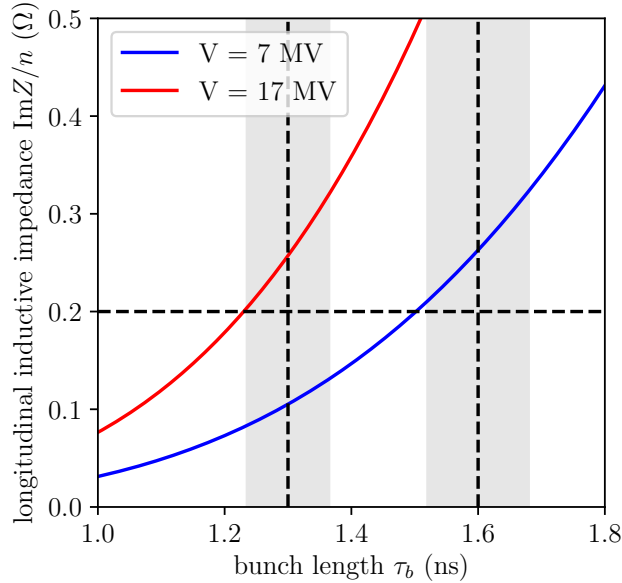


Figure 8.16: Threshold for the loss of Landau damping as a function of bunch length for $N_b = 1.0 \times 10^{11}$, $F = 0.43$, and different RF voltages at 3.3 TeV. The horizontal dashed line is the impedance budget of 0.2 Ω . The vertical dashed lines at 1.3 ns and 1.6 ns are the bunch lengths required for beam stability for 17 MV and 7 MV, respectively. The grey regions are $\pm 5\%$ bunch length spreads.

The proposed 20 minute momentum ramp from 3.3 TeV injection energy to 50 TeV consists of parabolic, linear, and again parabolic parts with 10%, 80%, and 10% of the total energy increase, respectively (see the left-hand plot in Fig. 8.17). The controlled emittance blow-up with longitudinal emittance $\epsilon_z \propto \sqrt{E}$ is required for longitudinal beam stability during the cycle [178]. The maximum voltage during the ramp will depend on the

filling factor in energy $q = \Delta E/\Delta E_B$, the ratio of the half bunch energy spread to the half bucket height. Based on LHC experience, $q < 0.9$ is required to avoid particle losses from the bucket. The maximum RF voltage is about 48 MV for maximum $q = 0.85$ (the right-hand plot in Fig. 8.17) and the longitudinal beam stability is maintained as the calculated threshold impedance is higher than the assumed impedance budget of 0.2Ω (see Fig. 8.18). To provide this RF voltage an installation of at least 24 single-cell cavities that operate with minimum voltage of 2 MV/cavity is required.

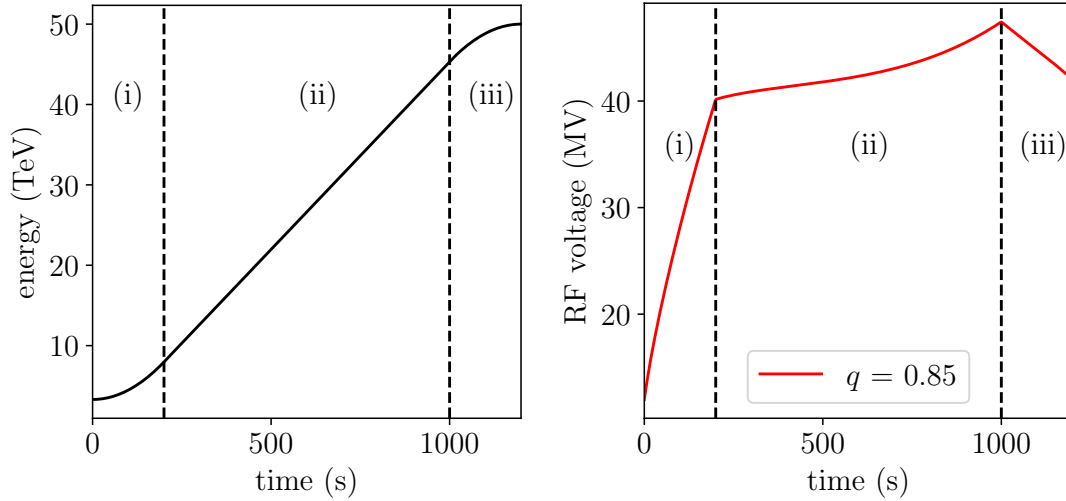


Figure 8.17: Left: energy evolution during the acceleration in the FCC-hh. Right: corresponding voltage programme. The dashed lines separate different parts of the momentum ramp: (i) the parabolic, (ii) linear, and (iii) parabolic parts.

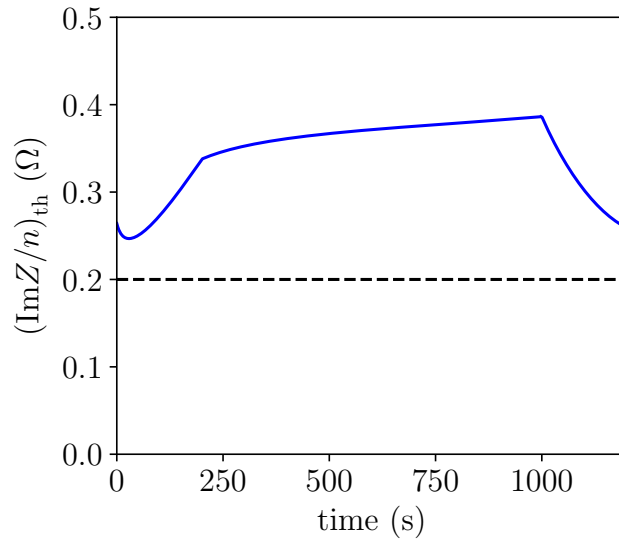


Figure 8.18: Threshold for the loss of Landau damping during acceleration for $N_b = 1.0 \times 10^{11}$, $F = 0.43$, and $q = 0.85$. The horizontal dashed line is the impedance budget of 0.2Ω .

The maximum generator power calculated for the case of half-detuning beam loading compensation scheme [181] and $q = 0.85$ is about 500 kW/cavity (see Fig. 8.19). This scheme was used in the LHC until 2014 and then a power saving algorithm (the LHC full detuning) was implemented [182]. The FCC-hh ramp requires larger energy gain per turn compared to the LHC ramp which results in significant deviation of the synchronous phase from π . Optimisation of the power consumption in the FCC-hh is ongoing [183].

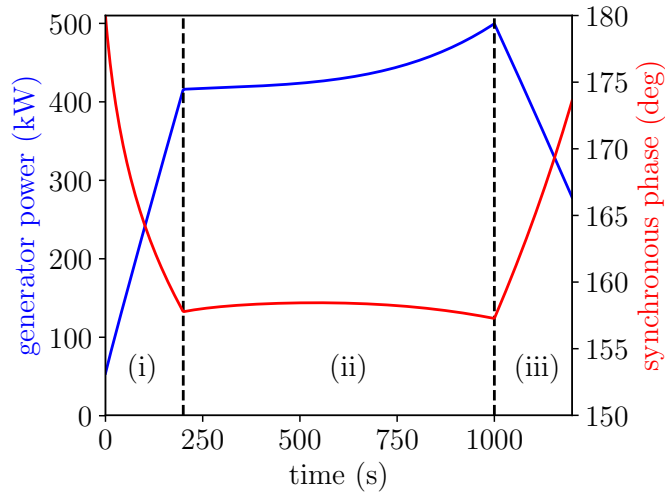


Figure 8.19: Evolution of the generator power and synchronous phase for the half-detuning beam loading compensation scheme during the momentum ramp shown in Figure 8.17 for $q = 0.85$.

Finally, relevant parameters at flat bottom and flat top are summarised in Table 8.4.

Table 8.4: RF and longitudinal beam parameters.

| Parameter | Unit | Flat bottom energy | Flat top energy |
|------------------------------------|------|---------------------------|---------------------------|
| Emittance | eVs | 2.3 | 10.2 |
| RF voltage | MV | 12 | 42 |
| 4σ bunch length | ns | 1.42 | 1.07 |
| Relative energy spread (twice RMS) | | $\pm 3.25 \times 10^{-4}$ | $\pm 1.24 \times 10^{-4}$ |
| Synchrotron tune | | 2.77×10^{-3} | 1.33×10^{-3} |
| Bucket filling factor in energy | | 0.78 | 0.68 |

8.5 Feedback performance

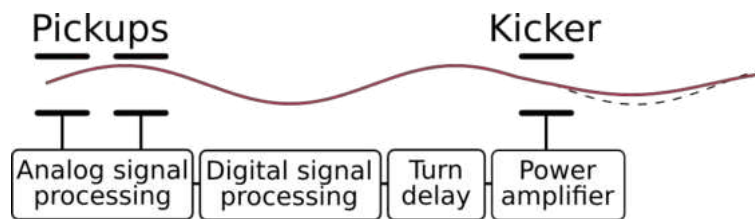


Figure 8.20: Schematic picture of the main components of a transverse feedback system.

Transverse feedback systems are used in the FCC-hh for injection oscillation damping and stabilisation of transverse coherent beam instabilities. A schematic picture of a transverse feedback system is presented in Fig. 8.20. Beam oscillations are measured with pickups. As in similar large accelerators, correction kicks are applied one turn after the pickup readings due to the finite signal processing time. The correction for the betatron motion during signal processing, as well as power amplifier and kicker phase errors are compensated through digital signal processing. Finally, the correction signal is fed to the kickers through the power amplifiers.

The history of transverse feedback systems at CERN goes back to the late 1960s [184, 185] and they are currently in operational use in all of the synchrotrons of the CERN accelerator complex [186]. Most of these

systems were originally designed for injection oscillation damping, but recently they have also been used for coupled bunch instability damping during all the beam cycle phases including collisions in the LHC.

The FCC-hh sets new challenges both in terms of injection oscillation damping and instability mitigation. Due to the higher injection energy, the kick strength required for injection oscillation damping is higher than in any existing system. On the other hand, after the injection error damping, the kick strength required for instability mitigation is orders of magnitude lower, but challenges arise from beam dynamics. The coupled bunch instability (CBI) growth rate in the FCC-hh is significantly higher than in the LHC and its mitigation relies on the transverse feedback system in all operation phases from injection to collision.

Because of the different requirements for the injection oscillation damping and instability mitigation, feedback performance for these scenarios are studied separately in Sections 8.5.1 and 8.5.2. Studies for the different operational schemes and possible future investigations are discussed in Sections 8.5.3, 8.5.4 and 8.8.5.

All the results presented in this section are based on multibunch macroparticle simulations with the PyHEADTAIL simulation code [187], which was optimised for multibunch simulations [188]. Transverse feedback system models were implemented with a new PyHEADTAIL module originally developed for these studies [189].

The accelerator parameters used in the simulations are described in Section 1.1. In order to take into account uncertainties and safety margins, a beam intensity 3×10^{11} protons per bunch is used instead of the design value 1×10^{11} . The September 2019 version of the impedance model (see Section 8.3) and the 3.3 TeV filling scheme (see Section 4.2) were included in the simulations.

The transverse feedback system models applied are based on the LHC transverse feedback system (ADT) including signal processing steps described in Refs. [190, 191]. The FCC-hh baseline system is the LHC ADT system scaled to 2.35 MHz cut-off frequency because of the shorter injection gaps (425 ns vs. 975 ns). The scaling of the simulation model included the phase linearisation FIR filter and the final analogue lowpass filter representing bandwidth limitations of the power amplifiers and the kicker structures.

In addition to the 2.35 MHz baseline model, the direct LHC ADT transverse feedback model ($f_c = 1$ MHz) was used in the coupled bunch instability simulations. The damping of the coupled bunch instabilities is sensitive to the exact frequency response above the cut-off frequency which depends on the final technical design. The direct LHC ADT model gives flexibility for the final technical design providing sufficient damping for the FCC-hh but also allowing improvements.

8.5.1 Emittance growth due to injection dipole errors

Due to the imperfections in the beam transfer and injection to the FCC-hh, the beam is injected with an offset. Without active damping this offset, together with non-linearities, would cause beam emittance growth. The most significant non-linearities are from chromaticity and octupoles in the transverse plane and from the RF-system in the longitudinal plane. Although these may not cause transverse emittance growth alone, when they interplay they can contribute to growth.

The FCC-hh specified limit for injection emittance growth is below 5% growth of the $2.2 \mu\text{m}$ normalised bunch emittance when the beam is injected with less than 0.5 mm ripple amplitude together with less than 0.5 mm DC offset at $\beta_{inj}=700$ m. Emittance growth of the specified oscillation limits are studied as a worst case scenario together with options of the 20 turn and 40 turn active damping time.

The baseline transverse feedback system for the FCC-hh is a scaled version of the LHC ADT. The bandwidth requirements for the injection oscillation damping come from the batch spacing between the injections and the main frequency component of the MKI kicker ripple. The injection batch spacing on the FCC-hh is 425 ns which scales the LHC feedback system (0.975 μs batch spacing) from 1 MHz to 2.35 MHz.

Typical bunch-by-bunch emittance growths for the injected batch are presented in Fig 8.21 for 12 MV RF voltage and $Q'=14$. In the worst case scenario of a 1 mm flat injection error, the emittance growth is virtually constant in the middle of the batch and only larger for the few bunches on the edges of the injected batch. The MKI magnet ripple model for the injection error (0.5 mm ripple amplitude and 0.5 mm DC offset) gives significantly lower average emittance growth than the flat offset. This is because the MKI kicker ripple decays in approximately 400 ns therefore only affecting the first 16 bunches and the DC component of the offset is only 0.5 mm. However, in reality, the MKI power supply imperfection might also have a contribution which is not included into the simulations. Therefore, the flat 1 mm injection error is used in the more detailed studies for the operational margins for the chromaticity and octupoles. More information about the MKI kicker system of the FCC-hh can be found in Chapter 4.

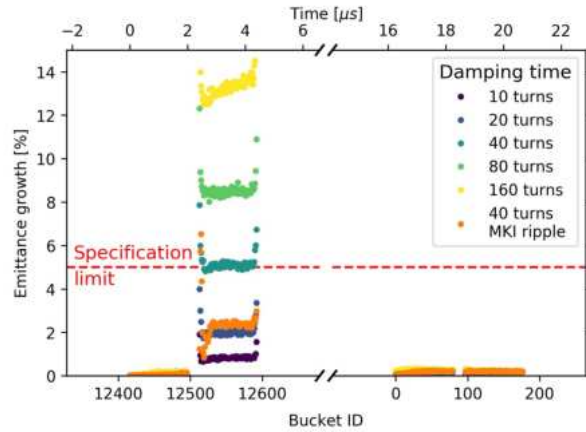


Figure 8.21: Bunch by bunch emittance growth from the injection for the injected and adjacent batches. A constant 1 mm injection error together with the 2.35 MHz scaled LHC damper model is used for damping times from 10 turns to 160 turns. A total 1 mm oscillation amplitude (DC + ripple) is used for the simulation with the MKI ripple.

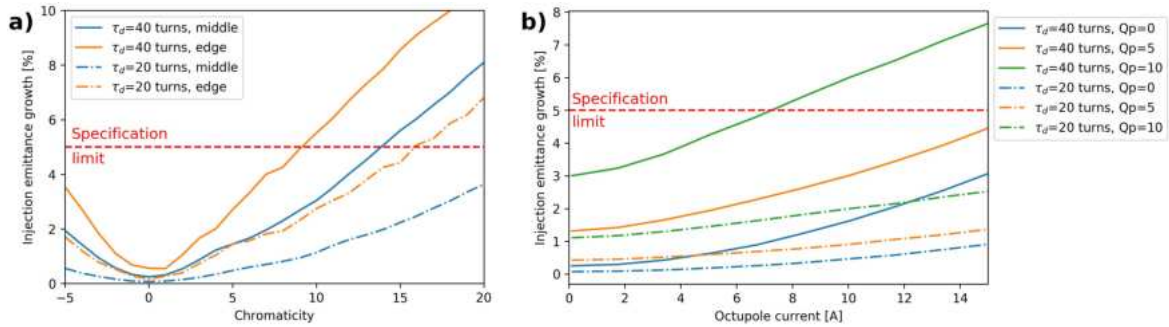


Figure 8.22: a) Injection emittance growths on the edge and the middle of the injected batch as a function of chromaticity without octupoles. b) Injection emittance growths on the middle of the injected batch as a function of octupole current for different chromaticities. A 1 mm flat injection error was used in all simulations.

In practice, the FCC-hh will be operated with chromaticity and octupoles during injection. The operational ranges allowed for these imperfections have been scanned in Fig 8.22 by assuming the flat 1 mm injection offset. Chromaticity up to 14 units is acceptable if the accelerator is operated without octupoles and a larger emittance is allowed for the edge bunches. Operating with both chromaticity and octupoles, octupole currents from 7 A ($Q' = 10$) to >20 A ($Q' = 0$) can be applied while keeping the emittance growth within specifications. These values are the worst case scenario for the option of the 40 turn damping time with the 1 mm flat offset. The majority of the bunches have only 0.5 mm offset, if the specified 0.5 mm injection ripple affects only a few first bunches as with the MKI kicker ripple in Fig 8.22. The operational margins with 0.5 mm flat offset for most of the bunches are at least two times larger, if over 5% emittance growth is allowed for a few bunches. Furthermore, the operational margins can be increased more by decreasing damping time with a stronger kicker system or active gain control on the damping.

In some alternative FCC-hh schemes for the baseline (e.g. with the lower injection energy) the coupled bunch instability growth times are shorter than the baseline damping time for the injection oscillations. In these cases simulations imply that faster damping time is only required for coupled bunch instability stabilisation below a certain small oscillation amplitude. This kind of faster damping for small amplitude oscillations can be implemented without stronger (larger) kicker structures by simply using dedicated digital signal processing or a separate weak feedback system for coupled bunch instabilities.

All these studies suggest that the LHC ADT damper system scaled to 2.35 MHz is sufficient as a baseline for the FCC-hh. However, it is worth noting that separate feedback systems for injection oscillation damping and

coupled bunch instability mitigation could allow further optimisation of the system size and performance. For example, separate systems would allow feed-forward damping of injection oscillations with possibly more flexible solutions and replacement of the baseline tetrode amplifier technology.

Feed-forward signal processing is possible because once a beam has been injected into a synchrotron and injection oscillations have been measured from the first turn, digital signal processing allows relatively high accuracy predictions for the transverse momentum corrections in the following turns. This means that the correction waveforms can be optimised for every injection in order to minimise the emittance growth for each bunch. Therefore, the overall performance can be achieved with a variety of technologies, for example, by combining non-linear or saturated amplifiers or power sources generating discrete kicks (e.g. capacitor banks) as a part of the system.

8.5.2 Coupled bunch instability damping

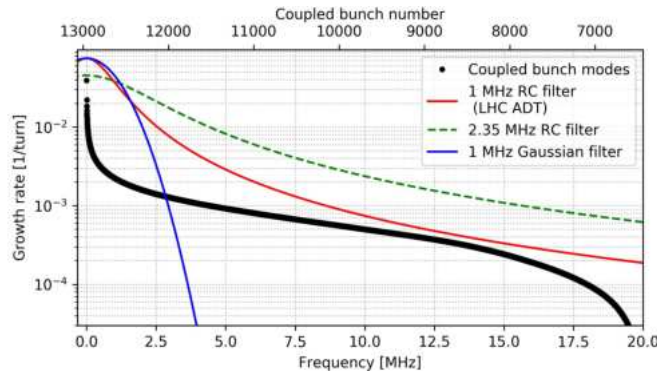


Figure 8.23: Theoretical growth rates for the coupled bunch instability modes in the FCC-hh with every bucket filled (13068 bunches). The modes where growth rates are lower than the damping rates of the plotted transverse feedback models are stable.

The baseline mitigation for the fastest growing (lowest frequency) coupled bunch instability modes relies entirely on the transverse feedback system. The higher order modes are mitigated by the combination of the transverse feedback system and Landau damping (octupoles, electron lenses and/or RF quadrupoles).

In theory, stabilisation of the coupled bunch instabilities with a transverse feedback system can be studied analytically by assuming that every beam bucket is filled. This is presented in Fig. 8.23, where theoretical growth rates for the coupled bunch instability modes are plotted together with the frequency responses of the transverse feedback models. The fastest growing instability modes can be damped with very low damper bandwidth, while the damping of the high frequency modes is very sensitive to the exact frequency response of the feedback system above the cutoff frequency.

Without a feedback system, the PyHEADTAIL simulations give 24.6 and 184 turns coupled bunch instability growth times at injection and top energies respectively. For an ideal bunch-by-bunch feedback system, the feedback damping time required would correspond to the growth time of the fastest coupled bunch instability mode. In practice, the finite bandwidth signal processing chain of the feedback system together with the filling pattern cause deviations from these theoretical values. Therefore, passband damping times which correspond to the damping time of a smooth sinusoidal signal at the passband frequency range of the feedback system are used in this section. In other words, a passband damping time corresponds to an operational set value of feedback gain, which together with a maximum oscillation amplitude sets technological requirements for the kicker system and the damper loop stability.

The simulations for the transverse feedback system performance included realistic models for the accelerator, the filling pattern and the feedback system. The performance criterion for the feedback system is set to stabilise the entire frequency range of the coupled bunch instabilities. In order to keep a connection to the working systems, the direct model of the the LHC transverse feedback system (ADT) ($f_c = 1$ MHz, total bandwidth 20 MHz) is used in the simulations¹. This choice gives realistic frequency response above the cut off frequency and also ensures that the experience from the LHC/HL-LHC operations is straightforwardly applicable to the FCC-hh. However, it

¹The current LHC ADT system and the FCC-hh baseline system use established tetrode amplifier technology, the future

is worth noting that a system with a higher cut-off frequency and at least similar response above the cut-off is also sufficient, e.g. the 2.35 MHz FCC-hh baseline transverse feedback system.

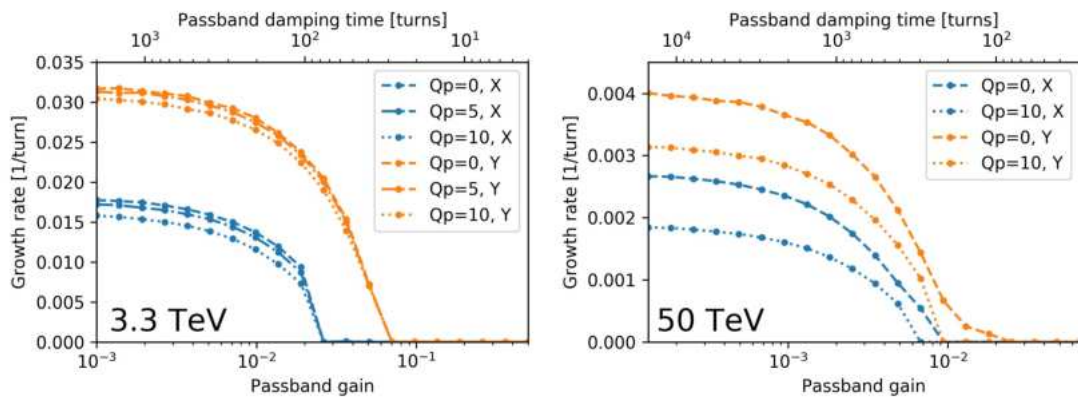


Figure 8.24: Coupled bunch instability growth rate as a function of feedback set gain for different chromaticities at 3.3 TeV and 50 TeV beam energies. Results for the horizontal plane are plotted in blue and for the vertical plane in orange.

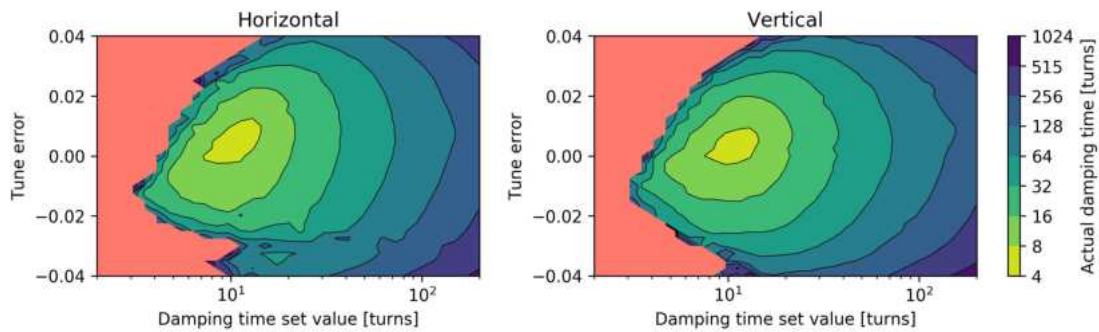


Figure 8.25: Single bunch damping times as a function of the damper gain set value and tune deviation. The red area is unstable.

The feedback performance for coupled bunch instability damping is evaluated by simulating CBI growth rate as a function of passband feedback gain and chromaticity. The results for the direct LHC ADT damper model are presented in Fig. 8.24 for the 3.3 TeV injection and 50 TeV collision energies. The transverse feedback system similar to the LHC ADT system is able to stabilise coupled bunch instabilities when the passband damping time is below 30 turns at the injection energy and below 100 turns at the collision energy. Chromaticity and the damper cutoff frequency (1 MHz vs 2.35 MHz) do not have significant effects on the required damping times when the frequency response above the cutoff frequency follows the characteristics of the LHC ADT system.

The operational margins for gain variations and tune acceptance have been studied by simulating single bunch injection damping times and full beam CBI growth rates as a function of damper gain and tune error. Simulations imply that the CBI stability approximately follows the contours of the single bunch injection damping times presented in Fig. 8.25. If 30 turn passband damping time is required, the LHC ADT signal processing allows ± 0.02 tune variation and set gain variation between 5–30 turn damping time. It is worth noting that the operational margins can be significantly affected and improved with digital filters.

availability of which is uncertain. Replacement technology with solid state amplifiers might lead to different characteristics above the cutoff frequency. The detailed characteristics of the system depend on the final amplifier and kicker design.

All the simulations imply that a feedback system similar to the LHC ADT system is able to stabilise coupled bunch instabilities both during injection and at top energy in the FCC-hh.

8.5.3 Operation with 5 ns or 12.5 ns bunch spacings

The nominal bunch spacing in the FCC-hh is 25 ns. Alternative options are 5 ns or 12.5 ns, which would, for example, relax the single bunch instability thresholds and reduce pile-up density in the experiments.

The requirements for injection oscillation damping are predominantly determined by the gaps between the injections and the injection offset, which do not depend on the bunch spacing. However, the smaller transverse emittance would increase the injection oscillation amplitude in the units of bunch transverse sigmas. It requires shorter damping times and subsequently a stronger kicker system, if the specification limits for the injection emittance growth and operational margins for non-linearities (chromaticity and octupoles) stay constant.

Nevertheless, the bunch spacing sets the upper bandwidth requirement for the coupled bunch instability damping. The maximum CBI oscillation frequency is 20 MHz for the 25 ns bunch spacing. The 5 ns bunch spacing would shift it to 100 MHz, but simulations show that only a minor extension is required to the baseline system. A very weak additional transverse feedback system is able to damp the extended frequency range of the coupled bunch instabilities.

8.5.4 1.3 TeV injection scheme

The 3.3 TeV injection energy from the LHC as an injector is the baseline concept for the FCC-hh. One of the alternative concepts relies on the scSPS with 1.3 TeV injection energy to the FCC-hh. With this injection concept, one injection consists of four 80-bunch batches and there is a 1 μ s gap between the injections in the filling pattern.

The 1.3 TeV injection scheme relaxes the requirements for the injection oscillation damping, because the lower injection energy requires less kick strength and the longer injection gap allows a lower feedback system bandwidth such as in the 1 MHz LHC ADT system. From the injection emittance growth point of view, the lower injection energy would also allow longer damping time for the injection oscillations because the beam oscillation amplitude in sigmas is smaller if the normalised emittance is fixed.

The challenges for the lower injection energy arise from coupled bunch instability mitigation. Without a reduced beam impedance budget, the CBI growth rates are approximately three times higher than with the 3.3 TeV injection energy. Taking into account the factor of three safety margin in the beam intensity, the specification point is in a highly non-linear regime of the coupled bunch instabilities. The beam dynamics of this regime is not well studied and, therefore, reliable estimates for the technological challenges and risks for the transverse feedback system operated in this regime would need further studies. However, in principle, it is technologically feasible to build a distributed transverse feedback system which is capable of damping continuous unstable sinusoidal waves with growth times below ten turns.

8.6 Beam-beam effects

The optimal beam-beam configuration for the FCC-hh has been discussed in detail in Section 2.3.2. It includes a full crossing angle $\alpha_c = 200 \mu\text{rad}$ in IPA and IPG that guarantees a dynamic aperture above 7.2σ . The two low luminosity experiments in IPB and IPL will collide with a crossing angle of $180 \mu\text{rad}$ in order to keep the DA above 6σ when the beams collide in the four IPs.

8.6.1 Maximum head-on beam-beam tune shift

In the FCC-hh baseline scenario, the total head-on beam-beam tune shift will reach a maximum of $\Delta Q_{\text{Tot}} = 0.011$. Due to evolution of the beam parameters, it will reach a maximum of 0.03 in the ultimate scenario, see Fig. 1.2. Whether this is acceptable with regard to the long-term degradation of the beams is discussed here. The situation was examined using a simplified model in CABIN, including two IPs with head-on interactions only, phase advances between the IPs, and chromaticity [61]. The simplified model allows accurate calculations of loss rates and emittance growth rates in long-term simulations, by reducing the numerical complexity. CABIN has shown agreement with experimental tests in the LHC with strong beam-beam interactions [56]. The head-on interaction is assumed to be the dominant non-linear effect in FCC-hh. The absence of long range interactions in this model is justified by the FCC-hh design, as discussed in Section 8.6.

If the crossing angle can be cancelled with crab cavities and one can make the phase advance between the IPs symmetrical, the head-on interactions pose no limit in the relevant range at the LHC working point, as can be seen in Fig. 8.26a. The symmetric phase advance effectively cancels even beam-beam resonances. For $\Delta Q_{\text{Tot}} = 0.03$, the required precision in phase is about $0.01 \times 2\pi$ [61]. The cancellation does not work for odd resonances, which can be excited by a crossing angle, an offset of the head-on interaction, or by long range interactions. Without the cancellation due to a symmetric phase advance, the head-on interaction limits the beam quality at the LHC working point, as shown in Fig. 8.26b. A working point optimisation has been performed, finding two alternative working points (0.315, 0.325) and (0.475, 0.485), which both allow for the ultimate head-on tune shift. Note that this is without odd resonances. The working point close to the half-integer resonances could be limited by lattice non-linearities that are not modelled in CABIN, and would have to be investigated further.

In the scenario where crab-cavities cannot cancel the crossing angle, the head-on interactions will excite odd resonances. With $\phi_{\text{PIW}} = 1$, as presented in Fig. 8.26c, the head-on beam-beam interaction becomes limiting on the loss rate close to the baseline tune shift, at both the LHC working point and (0.315, 0.325). As the footprint is shifted further away from odd resonance lines close to the alternative working point (0.315, 0.325), the degradation of the beam does not worsen further until a tune shift of 0.02. The increased degradation due to a small nonzero crossing angle is minimal for $\phi_{\text{PIW}} = 0.1$ [61]. The impact of odd resonances excited by other mechanisms needs further investigation.

8.6.2 Global compensation of beam-beam long range interactions

Figure 8.27 shows the minimum dynamic aperture as a function of the horizontal and vertical phase advances between the two high luminosity interaction points (IPA and IPG) including head-on and long range beam-beam collisions in IPA and IPG (centre plot) and also including the Landau octupoles powered with negative (left plot) and with positive polarity (right plot) for the fully squeezed optics with the ultimate $\beta^* = 0.3$. The negative octupole polarity is preferred. It not only provides larger beam stability with single beam at flat top energy (as discussed in Section 8.7.3) but it also provides more margin in terms of dynamic aperture in the presence of beam-beam interactions thanks to a global compensation of the long range beam-beam effects [58] when in collisions. Additional studies of the optics parameter optimisation show that an increase of up to 7.5σ for negative octupole polarity (Fig. 8.27) is possible.

8.6.3 Beta beating

The beam-beam interaction causes non-linear amplitude detuning. However for small amplitude particles ($< 1\sigma$) the kick is linear and causes a linear change of the β -function. The increase of the beating is proportional to the beam-beam parameter ξ_{bb} . The studies have been carried out for $L^* = 40$ cm optics and the ultimate $\beta^* = 30$ cm with full crab-crossing (H-V crossing scheme). Figure 8.28 shows the β -beating including head-on collisions in IPA and IPG. The red line is the case for a total beam-beam parameter $\xi_{bb} = 0.03$ for which the β -beating reaches a value of 22% while the green line is the case with a total beam-beam parameter $\xi_{bb} = 0.011$ for which the β -beating reaches a value of 8%. This optics distortion becomes another parameter for optimisation and needs to be kept below a value of 10%, as in the LHC, in order to limit the effects on the collimation system.

8.6.4 Alternative schemes

Alternative crossing schemes have been explored and show larger flexibility in terms of dynamic aperture with optimised tunes. Figure 8.29 shows the minimum dynamic aperture for nominal bunches as a function of the crossing angle in IPA and IPG with collisions in the two high-luminosity experiments. The H-V crossing scheme (the red line) is compared to the H-H crossing scheme (the blue line) and to the V-V crossing scheme (the green line). As can be seen, the H-H crossing is equivalent to the H-V crossing. The V-V crossing scheme is not acceptable at the (0.31, 0.32) working point due to the strong impact of the 3rd order resonance. However this could be improved by making use of mirrored tunes.

As can be seen in Fig. 8.30 in both cases for H-H crossing and in Fig. 8.31 for V-V crossing, the PACMAN bunches (bunches that are at the head or in the tail of a train missing long range collisions) always show a better dynamic aperture w.r.t the nominal bunches which experience all of the long range interactions. As a result of this study it is possible to conclude that there is room for flexibility in configuration if energy deposition studies show this to be necessary.

The flat optics is the natural back-up solution in case the crab-cavities do not perform as expected. In this

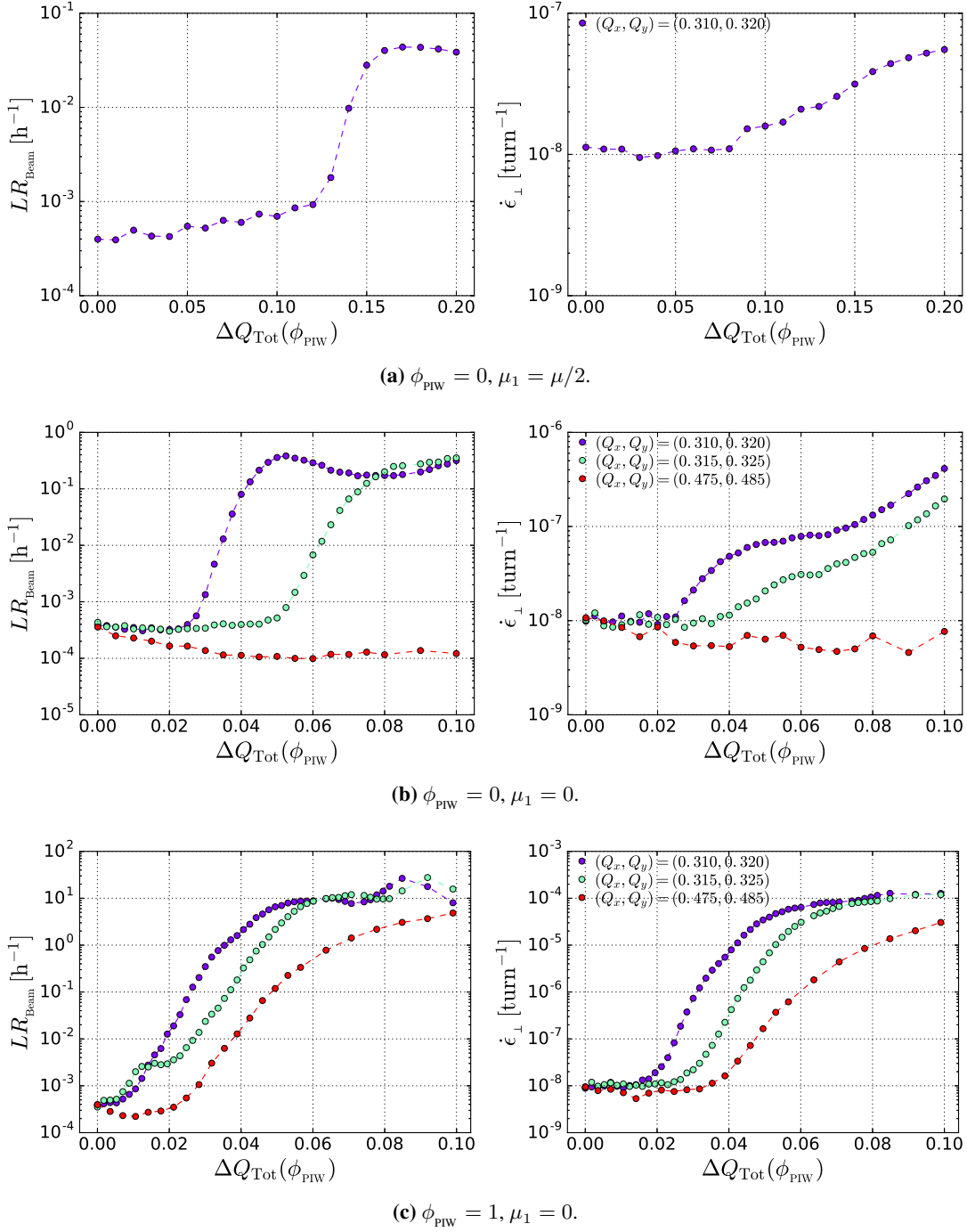


Figure 8.26: Beam quality reduction for increasing beam-beam parameter, ξ_{Tot} , until a threshold is found. Simulations were run for a large chromaticity, $Q' = 15$, $\sigma_{\Delta p/p} = 10^{-4}$, and a significant hourglass effect, $\beta^* = 30$ cm. The crossing angle, intermediate phase advance and working point have been varied. The loss rate (LR) and average transverse emittance growth rate ($\dot{\epsilon}_{\perp}$) are presented as functions of ΔQ_{Tot} , taking into account the reduction due to the crossing angle. Courtesy of [61].

case, due to the trains and the broken passive compensation, the long range interactions cause tune shifts and the head-on collisions create a larger tune spread, with a direct impact on the dynamic aperture. The dynamic aperture as a function of the long range beam-beam separation for collisions in IPA and IPG, with H-V crossing and a β -ratio= 4 is shown in Fig. 8.32. The red line is the case for round optics, the green line is the case of flat optics and the blue line is the case with flat optics and re-matched tunes. The corresponding tune footprints are shown in Fig. 8.33. The flat optics needs $\approx 40\%$ more long range separation w.r.t. the round optics. Correcting for tune

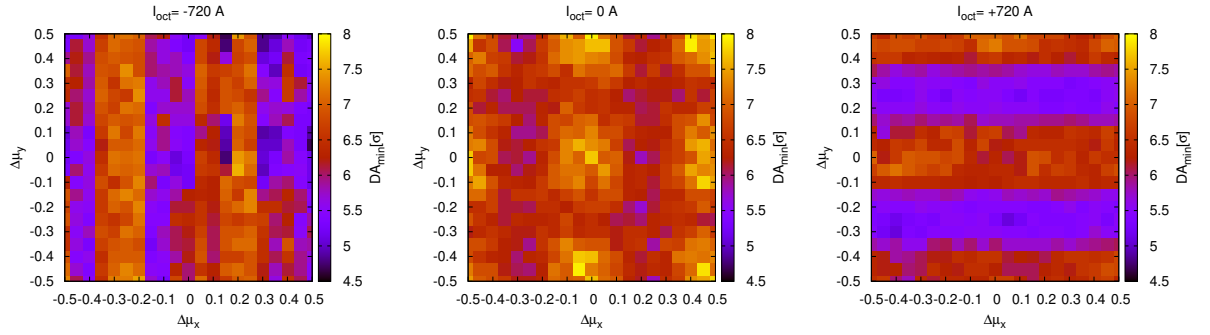


Figure 8.27: Minimum dynamic aperture, evaluated over 10^6 turns, as a function of the phase advance between the high luminosity interaction points (IPA and IPG) in the presence of head-on and long range beam-beam interactions (centre plot) and also including the Landau octupoles powered with negative (left plot) and positive (right plot) polarity. Simulations have been carried out using the fully squeezed optics with the ultimate $\beta^* = 0.3$.

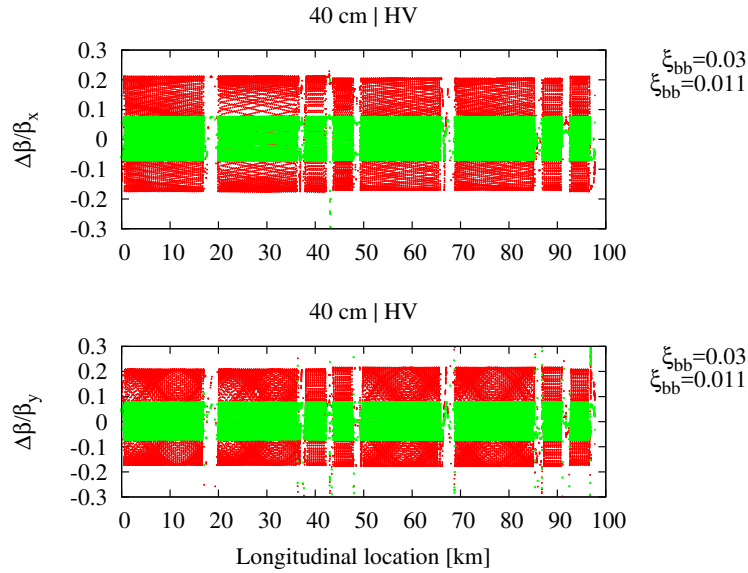


Figure 8.28: Evaluated β -beating with two head-on collisions in IPA and IPG for the ultimate case with $\beta = 0.3$ m and full crab-crossing. The red line shows to the case with a total beam-beam parameter $\xi_{bb} = 0.03$ and the green line corresponds to the case with a total beam-beam parameter $\xi_{bb} = 0.011$.

shifts (the blue line) improves the dynamic aperture, although a larger separation of $\approx 26\%$ is still needed. Further studies are needed in order to fully compensate for the unwanted effects introduced by the flat optics.

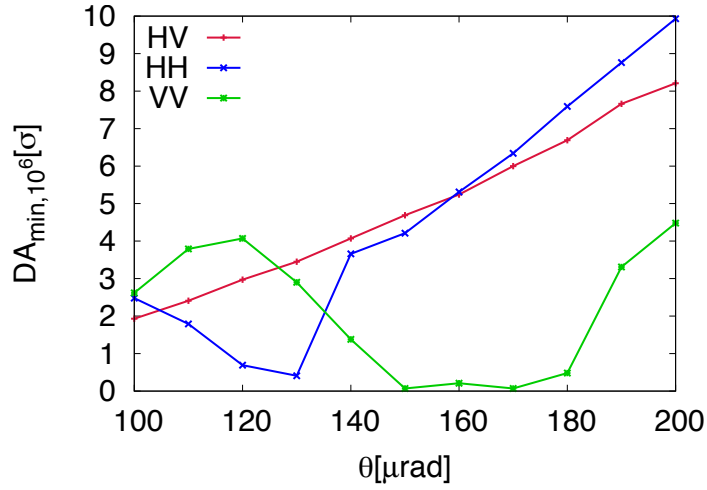


Figure 8.29: Minimum dynamic aperture for nominal bunches, evaluated over 10^6 turns, as a function of the crossing angle in IPA and IPG with H-H (blue line), H-V (red line) and V-V (green line) crossing schemes [56].

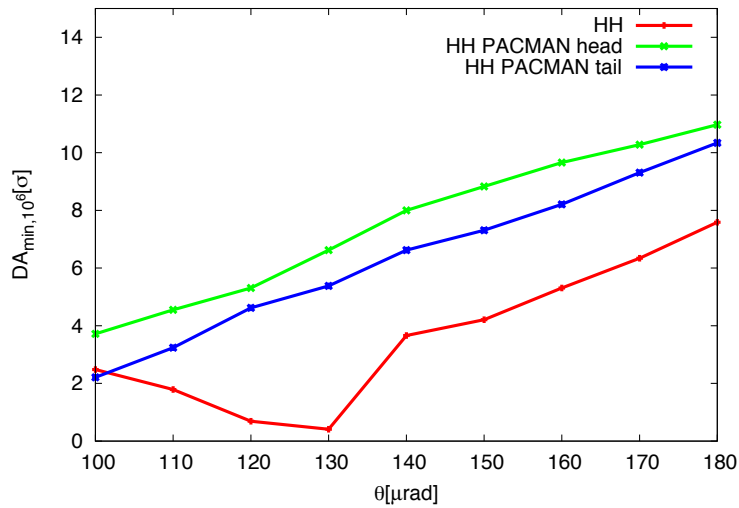


Figure 8.30: Minimum dynamic aperture, evaluated over 10^6 turns, as a function of the crossing angle in IPA and IPG with H-H crossing scheme for nominal bunches (the red line) and for PACMAN bunches at the head (green line) and in the tail (blue line) of a train [56].

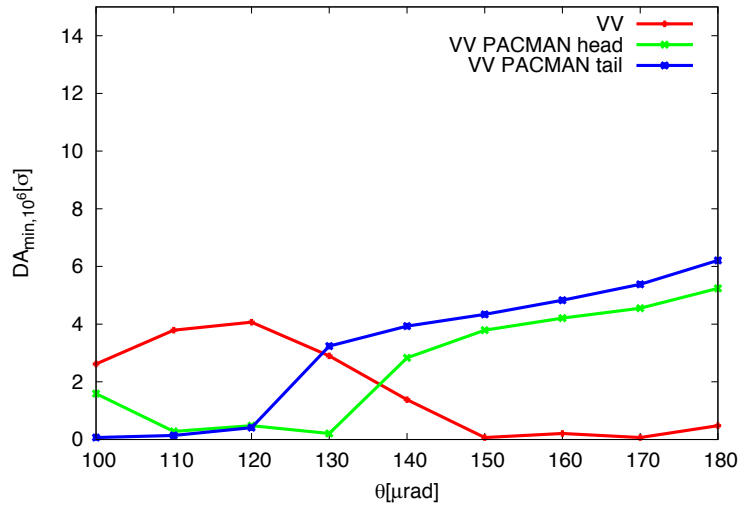


Figure 8.31: Dynamic aperture, evaluated over 10^6 turns, as a function of the crossing angle in IPA and IPG for V-V crossing scheme for nominal bunches (red line) and for PACMAN bunches at the head (green line) and in the tail (blue line) of a train [56].

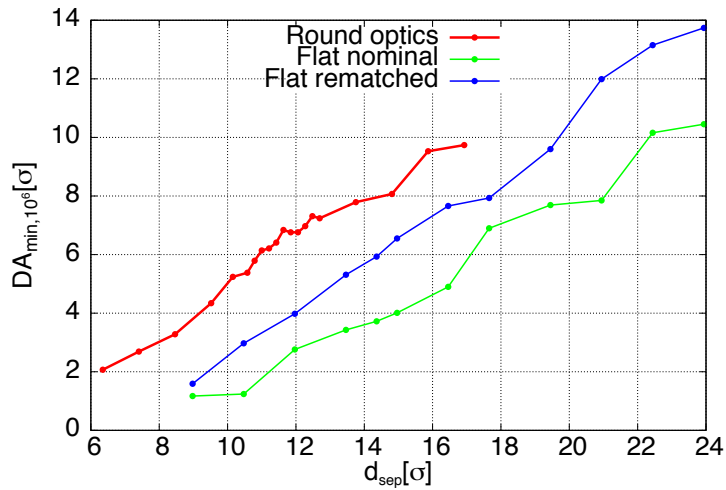


Figure 8.32: Minimum dynamic aperture evaluated over 10^6 turns for the ultimate $\beta^* = 30$ cm, including beam-beam interactions (head-on and long range) for round optics (red line) and flat optics (green line) with the H-V crossing scheme. The re-matched case for flat optics with $Q_x = 0.31$ and $Q_y = 0.32$ is also shown (blue line).

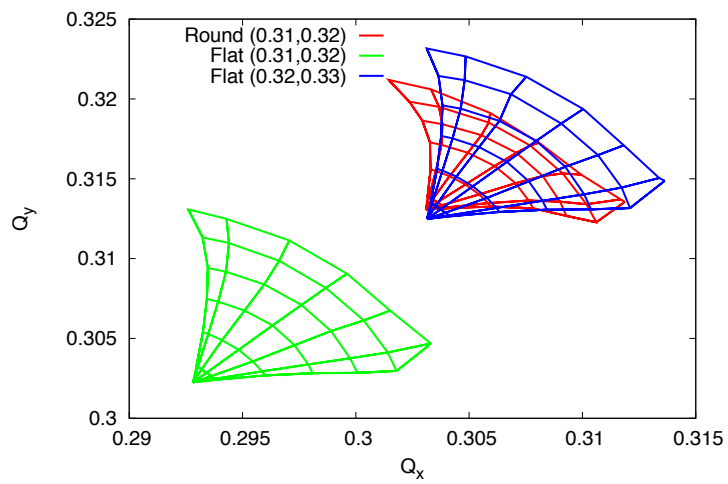


Figure 8.33: Two-dimensional tune diagram for particles up to 6σ amplitude (ultimate $\beta^* = 30$ cm) for the round optics (red), for the flat optics (green) and the rematched case for flat optics with $Q_x = 0.31$ and $Q_y = 0.31$ (blue).

8.7 Beam stability and operation strategy

8.7.1 Scaling from real LHC performance

Given the FCC-hh impedances from Section 8.3, instabilities can be compared to the LHC using simple scaling laws. Detailed computational studies will follow in Section 8.7.2 and 8.7.3. The LHC parameters used below are those from the 2017 run, rather than the design values (see Table 8.5). The main difference between the 2017 run and the LHC design is that the collimator gaps are set tighter in order to increase the luminosity. The tighter gaps result in significantly higher broadband impedance. Nevertheless, even with this impedance the machine was running without requiring the maximum allowed octupole current. Using the 2017 settings therefore provides scaling from the realistic LHC performance, retaining the safety margins of normal operation. Some of the FCC-hh parameters listed in Table 8.5 were updated (see Section 8.4). In particular, the bunch length at injection and the synchrotron tune at the top energy were increased, with both changes favourable for stability.

Table 8.5: Parameters of the LHC (2017 run) and the FCC-hh used for the scalings.

| | LHC 2017 injection / flat top | FCC-hh injection / flat top |
|--|---|---|
| Energy E | 0.45 / 6.5 TeV | 3.3 / 50 TeV |
| Bunch intensity N_b | 1.2×10^{11} | 10^{11} |
| Avg. β -function (smooth approximation) | 72 m | 141 m |
| Bunch spacing | 25 ns | 25 ns |
| Coupled-bunch frequency f_{CB} | 7.8 kHz | 2.1 kHz |
| Full (4σ) bunch length τ_b | 1.5 / 1.08 ns | 1.07 / 1.07 ns |
| Single-bunch frequency f_{SB} | 0.66 / 0.93 GHz | 0.93 / 0.93 GHz |
| Impedance $\text{Re}(Z_{\perp})$ at the frequency f_{CB} | $6.1 \times 10^7 / 1.6 \times 10^8 \Omega/\text{m}$ | $1.1 \times 10^9 / 2.1 \times 10^9 \Omega/\text{m}$ |
| Impedance $\text{Re}(Z_{\perp})$ at the frequency f_{SB} | $4.7 \times 10^5 / 1.2 \times 10^7 \Omega/\text{m}$ | $2.3 \times 10^6 / 1.8 \times 10^7 \Omega/\text{m}$ |
| Impedance $\text{Im}(Z_{\perp})$ at the frequency f_{SB} | $3.5 \times 10^6 / 2.1 \times 10^7 \Omega/\text{m}$ | $6.2 \times 10^6 / 3.3 \times 10^7 \Omega/\text{m}$ |
| β -function at the octupoles | 176 m | 352 m |
| Normalised emittance ϵ_n (flat top) | 2.5 μm | 2.2 μm |
| Octupolar strength O_3 (flat top) | $6.31 \times 10^4 \text{ T/m}^3$ | $2 \times 10^5 \text{ T/m}^3$ |
| Octupolar length L_{oct} | 32 cm | 50 cm |
| Number of octupoles N_{oct} | 168 | 480 |
| Synchrotron tune Q_s | $5.1 \times 10^{-3} / 2.2 \times 10^{-3}$ | $2.8 \times 10^{-3} / 1.2 \times 10^{-3}$ |

8.7.1.1 Transverse coupled bunch instability

When comparing different proton rings, the growth rate (in turns⁻¹) induced by the head-tail instability can be estimated to scale as

$$n_{turns}^{-1} \propto \frac{N_b \beta_{avg}}{\gamma \Delta s} \text{Re}(Z_{\perp}(f_{CB})), \quad (8.8)$$

where N_b is the bunch intensity, $\beta_{avg} = C/(2\pi Q_{\beta})$ is the smooth approximation average betatron function, C is the circumference, Q_{β} is the betatron tune, γ is the relativistic gamma, Δs is the bunch spacing, $Z_{\perp}(f_{CB})$ is the weighted transverse dipolar impedance taken at the characteristic frequency of the coupled bunch instability $f_{CB} = f_0(1 - \text{frac}(Q_{\beta}))$, and f_0 is the revolution frequency. Using the parameters from Table 8.5, gives:

$$\frac{(n_{turns}^{-1})_{FCC}}{(n_{turns}^{-1})_{LHC}} \approx \begin{cases} 4.0 & \text{at injection,} \\ 2.9 & \text{at flat top.} \end{cases} \quad (8.9)$$

Therefore, the coupled bunch instability in the FCC-hh is expected to be 3 – 4 times faster (in turns⁻¹) or roughly equally fast in the absolute units of time. The gain of the proposed FCC-hh transverse feedback is sufficiently high to counteract this instability.

8.7.1.2 Transverse head-tail instability and Landau octupoles

Provided that the transverse feedback is sufficiently strong and high-frequency trapped modes are sufficiently damped, the growth rate of the multi-bunch system is reduced to the level of single bunch head-tail instability. A simple scaling law allows a comparison of the head-tail instability growth rate for the transverse feedback turned off. When comparing different proton rings, the growth rate (in turns⁻¹) induced by the head-tail instability scales as:

$$n_{turns}^{-1} \propto \frac{N_b \beta_{avg}}{\gamma \tau_b} \text{Re}(Z_{\perp}(f_{SB})), \quad (8.10)$$

where τ_b is the full (4σ) bunch length in seconds, and $Z_{\perp}(f_{SB})$ is the weighted transverse dipolar impedance taken at the characteristic frequency of single bunch instabilities $f_{SB} = 1/\tau_b$. Using the parameters from Table 8.5, gives:

$$\frac{(n_{turns}^{-1})_{FCC}}{(n_{turns}^{-1})_{LHC}} \approx \begin{cases} 1.5 & \text{at injection,} \\ 0.3 & \text{at flat top.} \end{cases} \quad (8.11)$$

Therefore, the growth rate (in turns⁻¹) of the head-tail instability is expected to be somewhat higher (at injection) or a few times lower (at flat top) than in the LHC.

Similar to the LHC, this instability cannot be completely mitigated by the means of the transverse feedback alone, and Landau damping by octupole magnets is required. The maximum growth rate that can be mitigated by the octupoles scales as

$$\max(n_{turns}^{-1}) \propto \frac{\beta_{oct}^2 \epsilon_n}{\gamma^2} O_3 L_{oct} N_{oct}, \quad (8.12)$$

where β_{oct} is the betatron function at the location of the octupoles, ϵ_n is the normalised emittance, O_3 is the octupolar strength, L_{oct} is the length of one octupole, and N_{oct} is the total number of octupoles. Due to the factor $1/\gamma^2$ the limiting case happens at flat top, assuming that the necessary octupole current at injection is allowed by the dynamic aperture considerations. Using the parameters from Table 8.5, gives:

$$\frac{\max(n_{turns}^{-1})_{FCC}}{\max(n_{turns}^{-1})_{LHC}} \approx 0.8 \text{ at flat top.} \quad (8.13)$$

This ratio, together with the ratio of the impedance-induced growth rate, suggests that the FCC-hh should have even higher safety margins in terms of the available octupole strength, than the LHC.

There may be an operational scenario in which the beams are taken out of collisions after the normalised emittance has shrunk due to the synchrotron radiation. In that case, the octupoles would have to be used again to stabilise the head-tail modes, although their efficiency would be lower. However, at the same time, the instability growth rates would also be lower due to the reduced bunch charge. Due to the beam-beam tunes shift requirement, the ratio of N_b/ϵ_n is set to go up by not more than a factor of 3 during the collision cycle. Therefore, at any point during collisions, the ratio of $\max(n_{turns}^{-1})$ provided by the octupoles to n_{turns}^{-1} induced by the instability is expected not to be worse than in the LHC at flat top.

8.7.1.3 Transverse mode coupling instability

When comparing different proton rings, the ratio of the bunch intensity to the mode coupling threshold, N_b^{th} , scales as

$$N_b/N_b^{th} \propto \frac{N_b \beta_{avg}}{\gamma \tau_b Q_s} \text{Im}(Z_{\perp}(f_{SB})), \quad (8.14)$$

where Q_s is the synchrotron tune. Using the parameters from Table 8.5, gives:

$$\frac{(N_b/N_b^{th})_{FCC}}{(N_b/N_b^{th})_{LHC}} \approx \begin{cases} 1.0 & \text{at injection,} \\ 0.6 & \text{at flat top.} \end{cases} \quad (8.15)$$

This means that in the FCC-hh the TMCI threshold is roughly as distant from the nominal bunch intensity, as in the LHC.

8.7.2 Beam stability at injection

The transverse coupled bunch instability is primarily driven by the high resistive wall impedance of the beamscreen. The growth rate of the rigid ($k = 0$) coupled bunch mode is several times higher than in the LHC, while the octupole stability region is comparable to the LHC (Section 8.7.1). More than that, the growth rate that can be stabilised by the octupoles drops for head-tail modes that have a high real tune shift $|\text{Re}(\Delta Q)|$ (see Fig. 8.34b). The undamped $k = 0$ mode has the highest $|\text{Re}(\Delta Q)|$ of all head-tail modes, making its stabilisation by octupoles inefficient. For these reasons damping of the rigid coupled bunch mode is achieved by active stabilisation, i.e. the transverse feedback system. The feedback is required to damp the rigid mode completely without relying on Landau octupoles. In the worst case of zero chromaticity, full suppression of the mode is achieved by a feedback operating at the damping rate of 65 turns. A safety factor of 3 is placed on the maximum damping rate that can be achieved by the feedback, resulting in the specification of 20 turns. These values were obtained consistently by two Vlasov solvers DELPHI and Nested Head-Tail [192], assuming the fully filled ring. They are in good agreement with the 24.6 turns growth rate obtained from the tracking simulations reported in Section 8.5.2, especially when accounting for the 20% overestimation due to using the fully filled ring rather than the actual filling scheme.

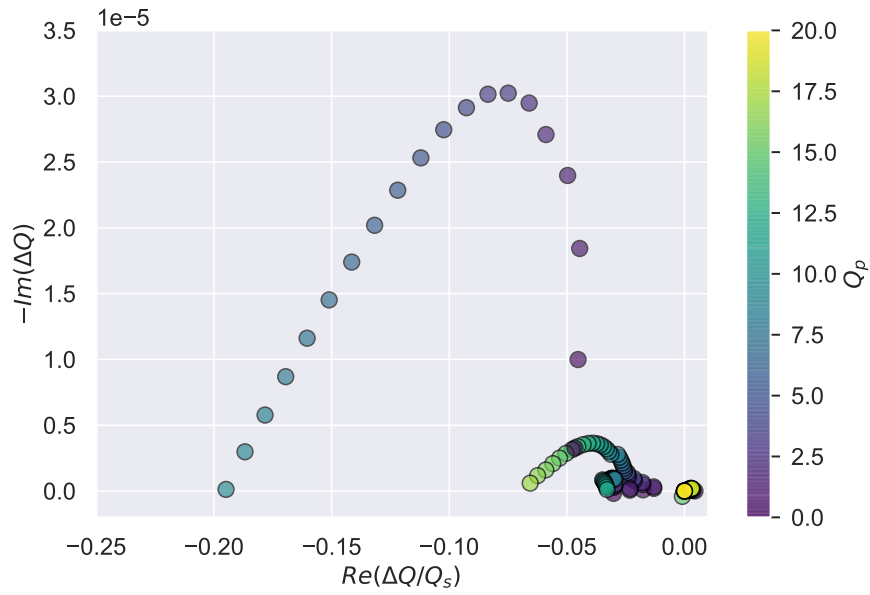
The head-tail instability is also primarily driven by the resistive wall impedance of the beamscreen. This impedance induces positive growth rates to higher order head-tail modes ($|k| \geq 1$) at $Q' > 0$, as can be seen in Fig. 8.34a. The LHC experience shows that the possibility of operating in a wide range of chromaticities is needed. Stabilisation of the $|k| \geq 1$ modes in the range $0 < Q' < 20$ is achieved by the octupole magnets with the current set to 15 A (of the maximum 720 A). The transverse feedback also provides partial suppression of the higher order head-tail modes thanks to their non-zero coherent oscillation amplitudes at $Q' > 0$. As a result, even for the weakest feedback capable of fully suppressing the rigid bunch mode (65 turns), all $|k| \geq 1$ modes lie well within the octupole stability region (Fig. 8.34b). In terms of the required octupolar strength, a safety factor of 4.0 is achieved, assuming the negative octupole polarity. The safety factor is even higher if the proposed 20 turns feedback is used.

The transverse mode coupling instability (TMCI) at injection is driven by the impedance of several different elements, among which the beamscreen, the collimators, and the interconnects are the most prominent. This instability is analysed in Fig. 8.35 at zero chromaticity as the worst case. As expected in the short-bunch regime, the mode coupling happens between the azimuthal modes $k = 0$ and $k = -1$. The single bunch mode coupling in the absence of the transverse feedback occurs at the bunch intensity of 4.5×10^{11} – well above the nominal bunch intensity (Fig. 8.35a, left). If necessary, the TMCI threshold can be pushed even further by using the feedback system in the reactive mode [193]. On the other hand, the proposed 20 turns resistive feedback does not move the threshold, and even gives a small positive growth rate at intensities below the threshold (Fig. 8.35a, right) – this effect is described in Ref. [194]. However, this potential destabilisation does not pose any problem in FCC-hh as the modes are still within the octupole stability region (Fig. 8.34b).

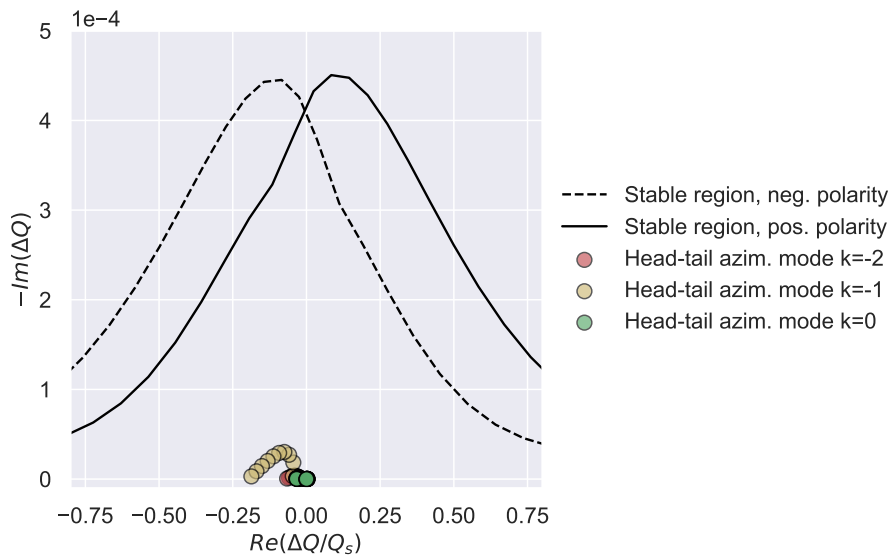
In the multi-bunch case, the ‘mode crossing’ happens at the much lower intensity of 1.2×10^{11} , shortly after the nominal bunch intensity (Fig. 8.35b, top). Such a difference between the mode crossing in the single bunch case and the multi-bunch case is much more prominent in the FCC-hh than in the LHC due to the strong low-frequency impedance peak from the beamscreen. Although mode coupling instability is traditionally considered to be a purely single-bunch phenomenon, this effect was described in Ref. [195] as the ‘multi-bunch mode coupling’. In the absence of the feedback, the growth rate remains as a linear function of the bunch intensity despite the mode crossing (Fig. 8.35b, bottom left). With the feedback on, a small growth on the order of $\text{Im}(\Delta Q) \sim 10^{-5}$ is retained at $0 < N_b < 3 \times 10^{11}$ (Fig. 8.35b, bottom right). The plots in Fig. 8.35b are cut at 3×10^{11} in order to see this small $\text{Im}(\Delta Q)$ which would otherwise be invisible in comparison to the rigid coupled bunch instability. Such a slow instability should be damped by the octupoles (see the stability diagram in Fig. 8.34b). Nevertheless, this subject deserves deeper investigation, as the stability diagram formalism is not strictly applicable due to the mode coupling. In any case, going to non-zero chromaticities greatly reduces the effect, because the mode crossing is pushed to a higher intensity, and because the $|k| \geq 1$ will be damped by the feedback.

8.7.3 Beam stability at flat top

It is assumed that stability at the flat top is not affected by the beam-beam effects since the normalised beam separation stays high until the squeeze phase (described in Subsection 8.7.4). At the flat top, instability mechanisms and stabilisation schemes are the same as at injection. Therefore, the discussion is not mentioned here, instead only the differences from the injection phase are cited. On one hand, growth rates of instabilities are increased by higher impedances of the beamscreen (due to the magneto-resistance) and the collimators (due to the squeezed gaps). On the other hand, the growth rates are reduced by a factor of 15 due to the relativistic γ , which more than compensates



(a) Real and imaginary tune shifts of head tail modes as functions of chromaticity



(b) Same data as above, plotted together with the octupole stability region

Figure 8.34: Tune shifts of head-tail modes on a stability diagram (injection energy, y-plane). Real and imaginary tune shifts caused by the impedance are shown in round dots, as calculated with DELPHI (13068 bunches). Each dot corresponding to a value of chromaticity in the range $0 < Q' < 20$. The transverse feedback is operating at a damping rate of 65 turns in the ‘resistive’ phase. The black lines represent the stability region provided by the 480 Landau octupoles operating at a fraction 15 A / 720 A of the maximum current. The FCC-hh parameters for simulations were taken from Table 8.5.

the increased impedance.

Similar to the injection phase, the transverse coupled bunch instability is primarily driven by the resistive wall impedance of the beamscreen. Full suppression of the mode is achieved by a feedback operating at a much lower damping rate of 460 turns, and the proposed feedback specification is 150 turns. Again, this damping rate is in a good agreement with the 184 turns growth rate obtained from the tracking simulations described in Subsection 8.5.2, especially if the 20% overestimation due to using the fully filled ring rather than the actual filling scheme is taken into account.

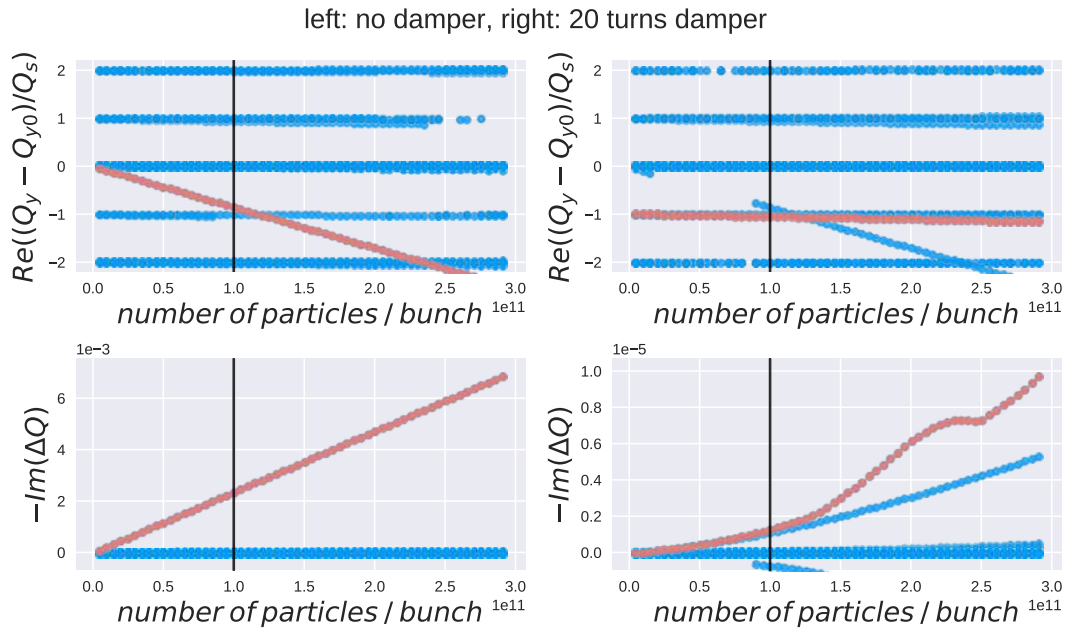
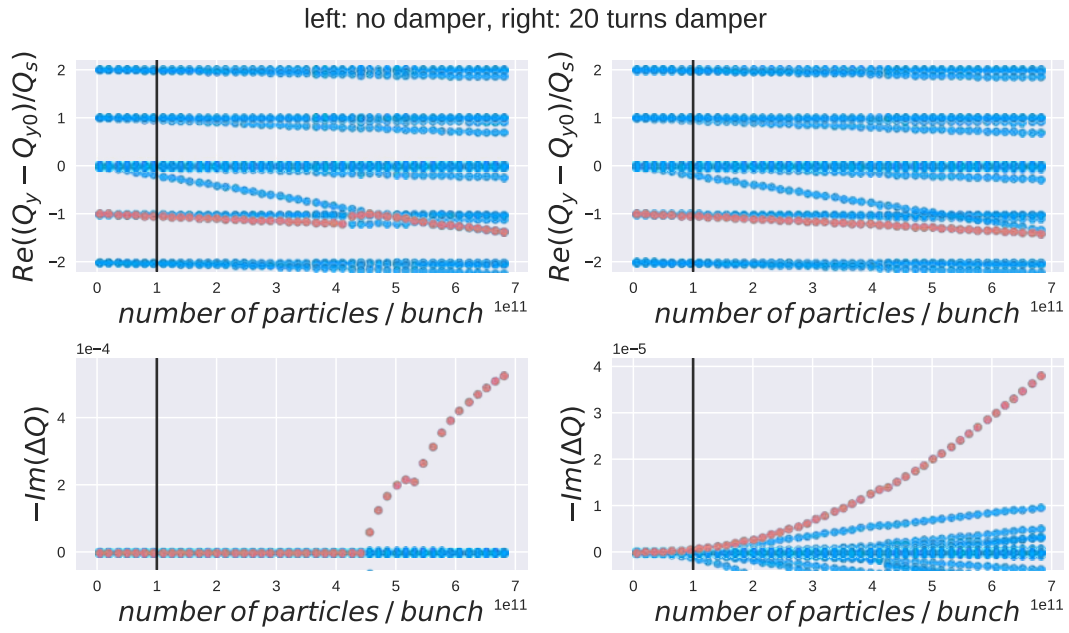


Figure 8.35: Real and imaginary tune shifts as functions of the bunch intensity (injection energy, y-plane, $Q' = 0$). The blue dots represent all azimuthal and radial head-tail modes, and the red dots represent the most unstable mode. Only the most unstable coupled bunch mode is shown. The transverse feedback operates in the ‘resistive’ phase. The black line represents the nominal bunch intensity. The FCC-hh parameters for simulations were taken from Table 8.5.

Unlike at injection, the head-tail instability at the flat top is primarily driven by the impedance of the collimators. The stability diagram for the weakest feedback capable of fully suppressing the rigid bunch mode (460 turns), is shown in Fig. 8.36. The safety factor in the octupolar strength is 4.0, similar to that at injection. If necessary, a stronger feedback damping rate can bring the growth rates even lower, increasing the safety margin, however, care should be taken to make sure that feedback-amplified noise does not cause excessive emittance

growth.

The transverse mode coupling instability is also primarily driven by the impedance of the collimators. The corresponding bunch intensity scans are shown in Fig. 8.37 for zero chromaticity. Similar to the injection phase, the single bunch mode coupling in the absence of the transverse feedback occurs at the bunch intensity of 4.3×10^{11} (Fig. 8.37a, left). The multi-bunch “mode crossing” happens at the intensity $N_b = 2.0 \times 10^{11}$ (Fig. 8.37b, top). Again, in the absence of the damper, this multi-bunch mode crossing produces no noticeable perturbation to the already existing growth rate of the coupled-bunch instability (Fig. 8.37b, bottom left). With the 150 turns damper on, only a small growth rate at the level of $\text{Im}(\Delta Q) \sim 10^{-5}$ is left at $0 < N_b < 3 \times 10^{11}$ (Fig. 8.37b, bottom right), and should be damped by the octupoles.

8.7.4 Beam stability during the ‘collide and squeeze’ phase

During the operational cycle the Landau octupole strength required to provide sufficient transverse beam stability in relation to the relativistic γ and the growth rates of instabilities (as described in Subsection 8.7.1.2). However, in the presence of the beam-beam interactions, the transverse beam stability provided by the Landau octupoles is modified [196]. In fact, the detuning with amplitude (tune spread) driven by the Landau octupole magnets changes during the operational phases in which the beam-beam interactions are not negligible i.e. at the end of the betatron squeeze, during the collapse of the separation bumps and in head-on collisions [196]. When the beams collide head-on, the transverse beam stability is maximised due to the large tune spread provided by the head-on beam-beam interaction [197]. However, at the end of the betatron squeeze and during the collapse of the separation bumps, the tune spread, and therefore the beam stability, might be strongly affected by the beam-beam interactions. For this reason, a detailed analysis of the transverse beam stability during these operational phases is required in order to maximise the beam stability and define the optimal strategy for operations.

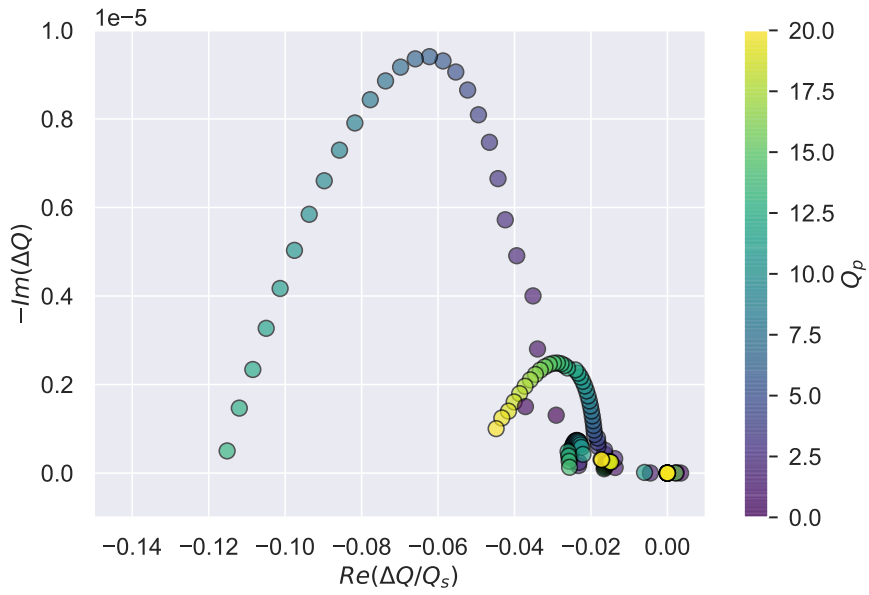
The transverse stability of the beams has been evaluated by solving the dispersion integral in the presence of both Landau octupoles and beam-beam interactions for the machine configurations corresponding to the various operational phases. The computation of the stability diagram was performed using the PySSD code [52]. The detuning with amplitude for the different collision configurations is evaluated by using the MAD-X tracking module [198, 199]. Table 8.5 shows the main features of the FCC octupole magnet system that has been included in the optics model. The analysis has been carried out for both positive (LOF>0) and negative (LOF<0) polarity of the Landau octupoles.

Figure 8.38 shows the detuning with amplitude in the two-dimensional tune diagram (Q_x, Q_y) for particles up to 6σ amplitude at flat top energy with the Landau octupoles powered at their maximum strength. The purple and the green colours represent the tune diagram at the end of the betatron squeeze, for positive and negative octupole polarity respectively, with the ultimate $\beta^* = 30$ cm. At this β^* value with the nominal normalised emittance of $2.2 \mu\text{m}$ rad, the normalised long range beam-beam separation is $\approx 17\sigma$ (Subsection 2.3.2). In the same figure, the two-dimensional tune diagrams at flat top energy with single beam for both positive (the light blue colour) and negative (the orange colour) octupole polarity are also shown for comparison. As visible at the end of the betatron squeeze, with the ultimate $\beta^* = 30$ cm, the tune spread in the beams increases for positive octupole polarity while it reduces for negative octupole polarity. Although the positive octupole polarity provides a larger tune spread, a better dynamic aperture is expected in the presence of negative octupole polarity thanks to the global compensation of the long range beam-beam effects [58, 200], as discussed in Section 8.6.

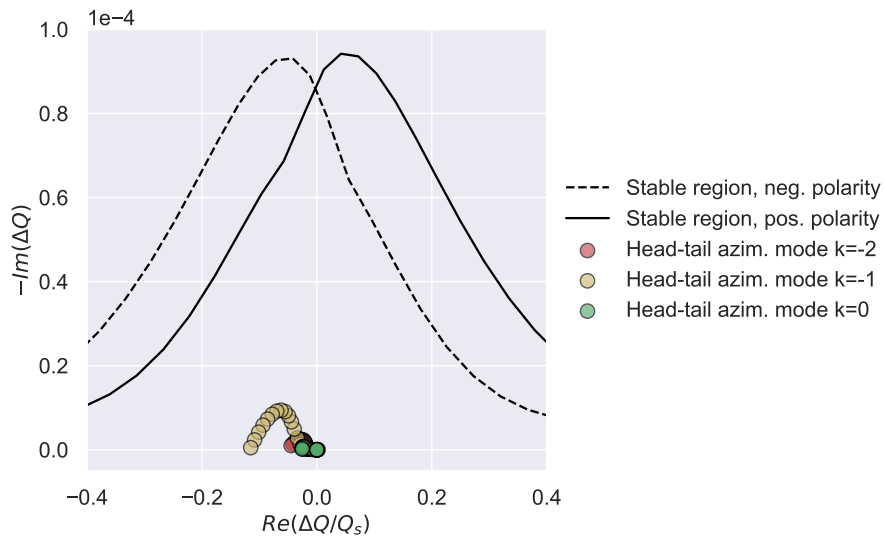
The stability diagram at the end of the betatron squeeze with $\beta^* = 30$ cm in the presence of negative octupole polarity is shown in Fig. 8.39 (the green line) where the head-tail coupled bunch modes are also shown for an ADT gain of 460 turns (Section 8.7.3) and as a function of the chromaticity (the vertical colour bar). For comparison, the stability diagrams at flat top energy with single beam for negative (the orange colour) and positive (the light blue colour) octupole polarity are shown in the same figure.

Although the coherent modes lie within the stability diagram at the end of the betatron squeeze ($\beta^* = 30$ cm) with negative octupole polarity, additional margins are required. In the LHC in order to stabilise the beams, a factor 2 more octupole strength w.r.t. the stability predictions is required [201]. Recent experimental studies in the LHC have shown that the transverse stability of the beams is reduced in the presence of noise [196, 202] or a small external excitation [203]. Therefore, in order to maximise the beam stability, collisions at larger β^* are planned. Similar to the HL-LHC’s operational scenario [26, 204], the ‘Collide and Squeeze’ will be applied in the FCC-hh.

Figure 8.40 shows the reduction of the stability diagram as a function of the β^* at IPA and IPG (dotted blue line). For each β^* value, the reduction is evaluated as the relative difference of the negative real part at the



(a) Real and imaginary tune shifts of head tail modes as functions of chromaticity

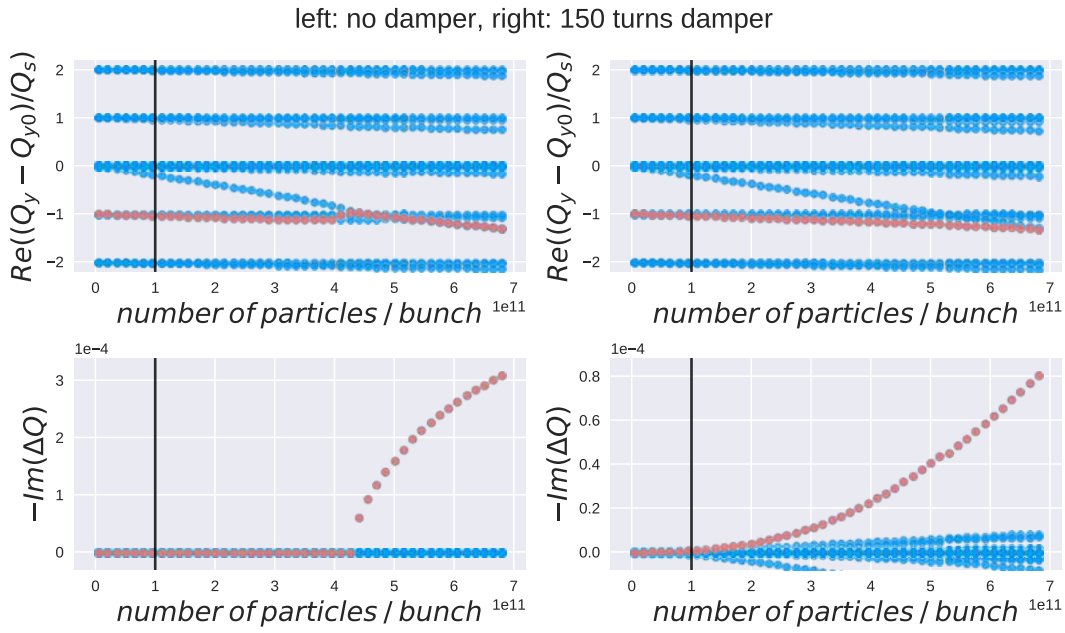


(b) Same data as above, plotted together with the octupole stability region

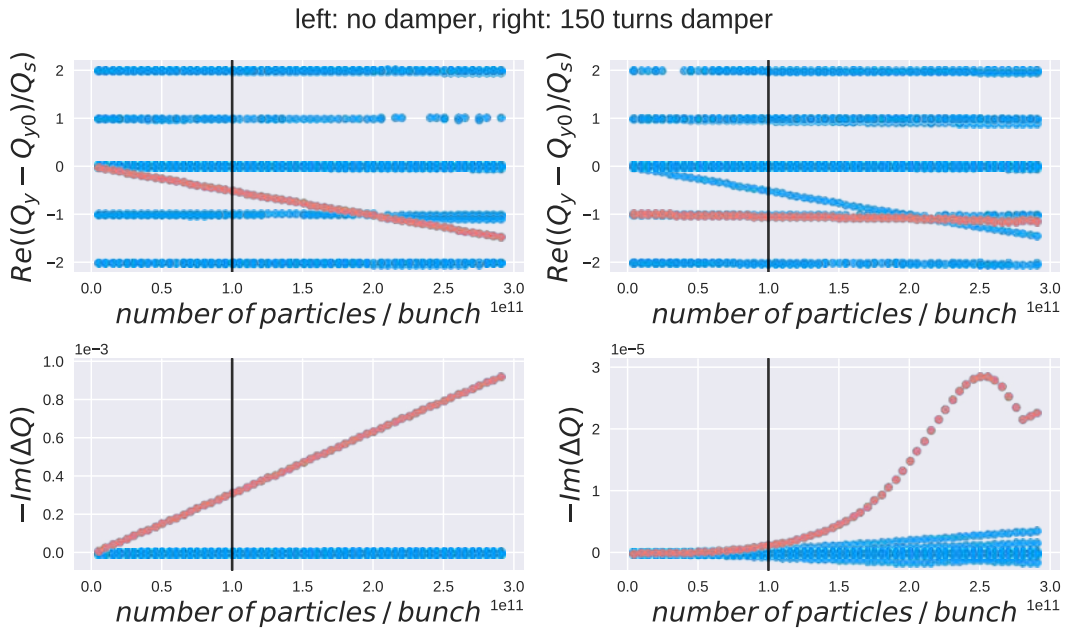
Figure 8.36: Tune shifts of head-tail modes on a stability diagram (flat top, y-plane). Real and imaginary tune shifts caused by the impedance are shown as round dots, calculated with DELPHI (13068 bunches). Each dot corresponds to a value of chromaticity in the range $0 < Q' < 20$. The transverse feedback is operating at a damping rate of 460 turns in the 'resistive' phase. The black lines represent the stability region provided by the 480 Landau octupoles operating at the maximum current. The FCC-hh parameters for simulations were taken from Table 8.5.

half-height between the stability diagram in the presence of negative octupole polarity and beam-beam long range interactions and the stability diagram at flat top energy (single beam) with negative octupole polarity. The dashed black line corresponds to the relative difference between the stability diagram with positive octupole polarity and the stability diagram with negative octupole polarity at flat top energy for the single beam case. For $\beta^* \approx 1.1$ m the reduction is negligible ($\approx 5\%$). As a result of these studies, the collisions are planned to have an initial $\beta^* = 1.1$ m.

The evolution of the stability diagram during the collapse of the separation bumps at the $\beta^*=1.1$ m is shown



(a) Single bunch regime



(b) Multi-bunch regime

Figure 8.37: Real and imaginary tune shifts as functions of the bunch intensity (top energy, y-plane, $Q' = 0$). The blue dots represent all azimuthal and radial head-tail modes, and the red dots represent the most unstable mode. Only the most unstable coupled bunch mode is shown. The transverse feedback operates in the ‘resistive’ phase. The black line represents the nominal bunch intensity. The FCC-hh parameters for simulations were taken from Table 8.5.

in Fig. 8.41a. The stability diagrams have been evaluated as a function of the transverse beam offset at IPA and IPG. During this process two minima have been identified: one at 5σ separation (solid red line in Fig. 8.41b) and a second one at 1.75σ (dashed red line in Fig. 8.41b). The first one is ≈ 2 times larger than the stability diagram at the end of the betatron squeeze at $\beta^* = 30$ cm with negative octupole polarity (the green line in Fig. 8.41b). The second one is slightly above the end of the betatron squeeze case with $\beta^* = 30$ cm. For comparison, the stability

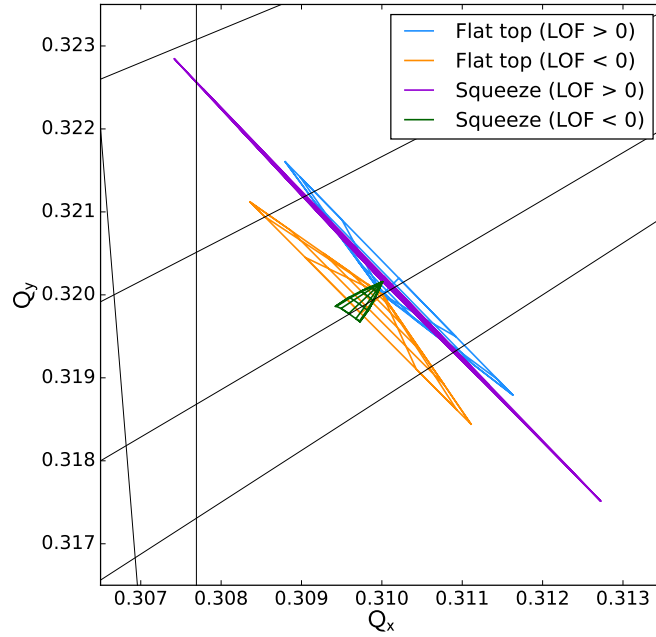


Figure 8.38: Two-dimensional tune diagram for particles up to 6σ amplitude at flat top energy evaluated for both positive (the light blue colour) and negative (the orange colour) octupole polarity without long range beam-beam interactions. The purple and the green colours represent the tune diagram at the end of the betatron squeeze (with the ultimate $\beta^* = 0.3$ m) including the long range beam-beam interactions for positive and negative octupole polarity respectively.

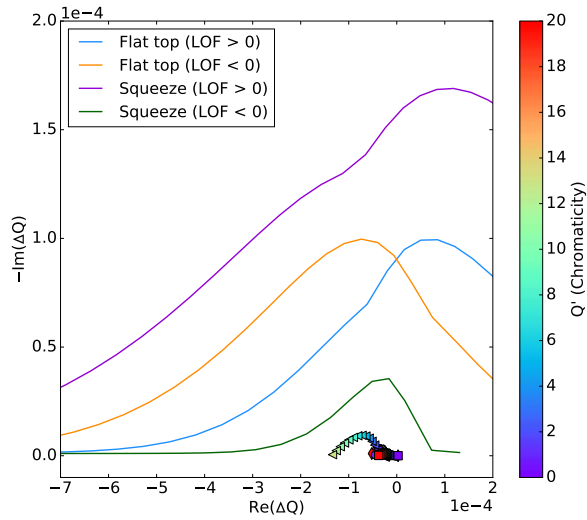


Figure 8.39: Stability Diagrams at the end of the betatron squeeze ($\beta^* = 30$ cm) in the presence of long range beam-beam interactions for negative (green line) and positive octupole polarity (purple line). For comparison, the stability diagrams at flat top energy (single beam) are also plotted for both negative (orange colour) and positive (light blue colour) octupole polarity. The head-tail coupled-bunch modes ($k=-1$) for a transverse feedback gain of 460 turns (Subsection 8.7.3) are also included as a function of the chromaticity values (vertical colour bar).

diagram at flat top (single beam) with negative octupole polarity (the orange line) is also shown in the same figure, where the black line represents the stability diagram at the start of the collision process at $\beta^*=1.1$ m. These two reductions of stability cannot be avoided, therefore, in order to prevent coherent beam instabilities during the collapse of the separation bump process, it is recommended that the beams pass through these minima faster than

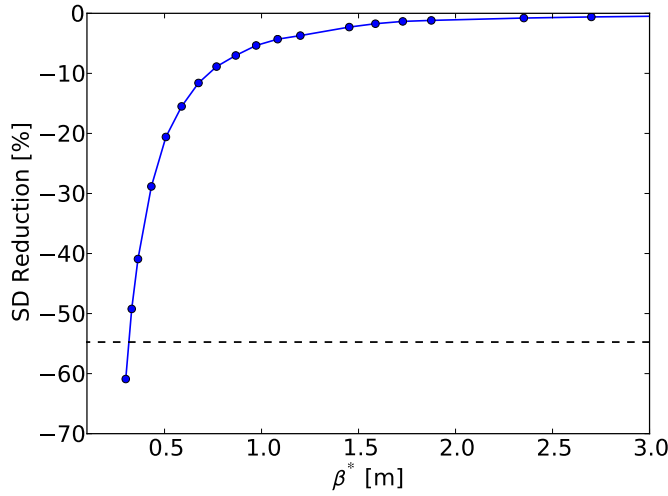


Figure 8.40: Stability diagram reduction in the presence of long range beam-beam interactions w.r.t the stability diagram evaluated at flat top energy with negative octupole polarity (single beam) as a function of the β^* at the high luminosity Interaction Points (IPA and IPG). The dashed black line corresponds to the relative difference between negative real part at half height of the stability diagram with positive octupole polarity and the stability diagram with negative octupole polarity at flat top energy (single beam).

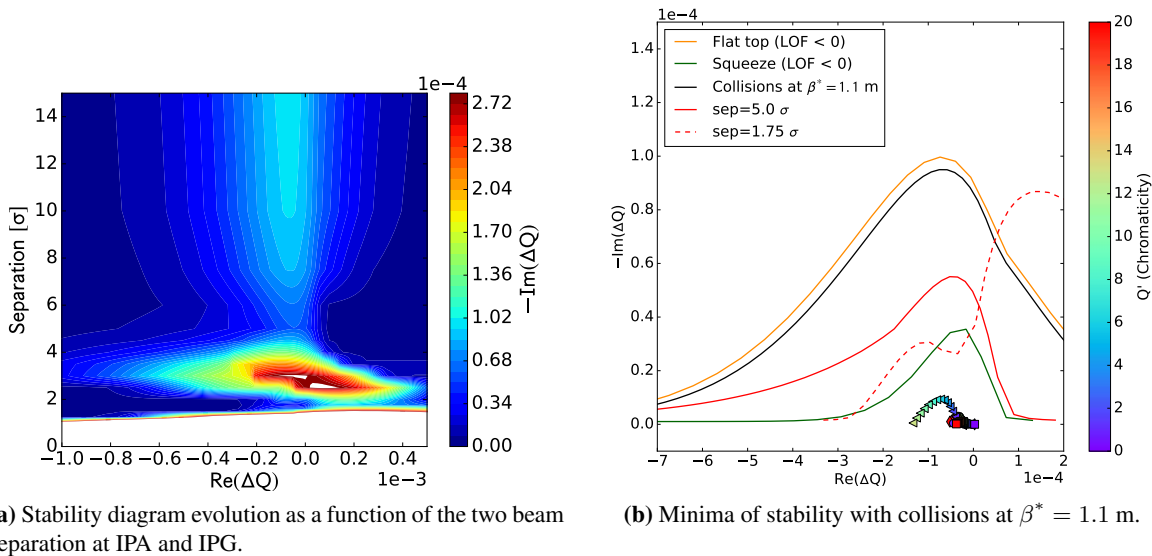


Figure 8.41: Stability diagram evolution during the collapse of the separation bumps for collisions at $\beta^* = 1.1$ m (left). The minima of stability diagram during this process are shown on the right plot (dashed and solid red lines) compared to the stability diagram at flat top with negative octupole polarity (the orange line) and to the end of the betatron squeeze (ultimate $\beta^* = 0.3$ m.) with negative octupole polarity (the green line). The black line represents the stability diagram at the start of the collision process. The head-tail coupled-bunch modes are also plotted as a function of the chromaticity (vertical colour bar) for $k = -1$ and a transverse feedback gain of 460 turns.

the instability growth rate. As presented in Subsection 8.7.3 the faster instability rise time is about 5 s for $k = -1$ for a chromaticity range of $\approx 8 - 6$ units with a transverse feedback gain of 460 turns.

8.8 Alternatives

8.8.1 Electron lens

The alternative of using an electron lens (e-lens) in the FCC-hh for Landau damping [205] has been explored. Like the head-on beam-beam interaction, the electromagnetic interaction of the proton beam with the electron beam of the e-lens acts mostly on small amplitude particles thus providing an effective Landau damping of coherent instabilities. Figure 8.42 shows the comparison between the stability diagram for Landau octupoles at flat top energy (light blue line for the positive octupole polarity and orange line for the negative octupole polarity) and the stability diagram for a two metre long electron lens [205]. The detuning with amplitude provided by the electron lens is computed using the COMBI code [49]. An electron lens powered with 140 mA [121] provides Landau damping of the most unstable coupled-bunch mode ($k = -1$) with sufficient margins with a transverse feedback of 460 turns, up to a chromaticity value $Q' = 15$ units. Further studies have to be carried out covering the collapse of the separation bumps in particular, since the tune spread provided by the electron lens might modify the tune spread, and therefore the transverse stability provided by the head-on collisions [206] during this process.

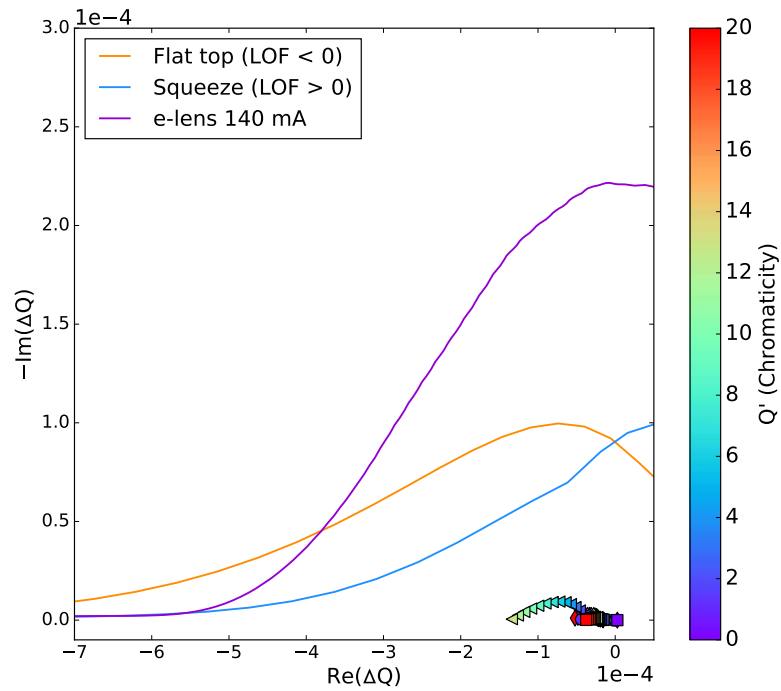


Figure 8.42: Stability diagram evaluated from the tune spread provided by an electron lens at flat top energy (purple line) compared to the stability diagram provided by the FCC octupole system (light blue line for positive octupole polarity and orange line for negative octupole polarity). The most unstable coupled-bunch mode ($k = -1$) is plotted as a function of the chromaticity Q' (vertical colour bar) with a transverse feedback gain of 460 turns.

8.8.2 RF quadrupoles

The use of RF quadrupole cavities to suppress coupled-bunch modes was first discussed in Refs. [207, 208], and later to raise the intensity threshold of the transverse mode-coupling instability in Refs. [209, 210]. For FCC-hh, RF quadrupoles operate in yet another regime. The objective is to use them as an alternative to Landau octupoles to mitigate weak single-bunch head-tail modes through Landau damping [211–213]. Whilst the Landau octupoles described above produce an incoherent betatron tune spread $\Delta Q_{x,y}$ which depends on the transverse actions (J_x, J_y) of the beam particles, the RF quadrupole generates betatron tune spread as a function of the longitudinal action $\Delta Q_{x,y}(J_z)$ [214, 215]. The latter approach is more efficient, particularly for the high-energy, small transverse emittance beams of FCC-hh². Numerical and analytical studies have been carried out in Refs. [215] and [216] respectively, explaining and demonstrating the working principle of the device. A first experimental

²At 50 TeV, the longitudinal action spread ΔJ_z is up to six orders of magnitude larger than in transverse planes $\Delta J_{x,y}$.

proof-of-principle on single-bunch beams employing the second-order chromaticity, which introduces a stabilising mechanism similar to that of the RF quadrupole, was also carried out [217].

Cavity designs, performance optimisation, and potential limitations

Two designs for a superconducting RF quadrupole cavity have been proposed and optimised, primarily for integrated quadrupolar gradient, but also for transverse and longitudinal beam coupling impedance, and peak electric, E_{pk} , and magnetic, B_{pk} , surface fields. The first cavity type uses an elliptical geometry and operates in a transverse magnetic quadrupolar mode. The second one is a four-vane cavity operating in a transverse electric quadrupolar mode. The geometry and field distributions of the latter design are shown in Fig. 8.43. The main advantages of the four-vane cavity compared to the elliptical one are: (i) the quadrupolar field strength is two to five times larger than that of the elliptical design, given that the aperture has a radius < 50 mm, and (ii) the four-vane cavity is more compact and hence requires smaller cryomodules and less cooling power. As a result, such a system provides the same amount of Landau damping, but with fewer cavities and at reduced impedance and cost. Both cavity types have been designed to operate at a frequency of 800 MHz to match the bunch length of the beams. The cavity design studies are discussed extensively in Ref. [218].

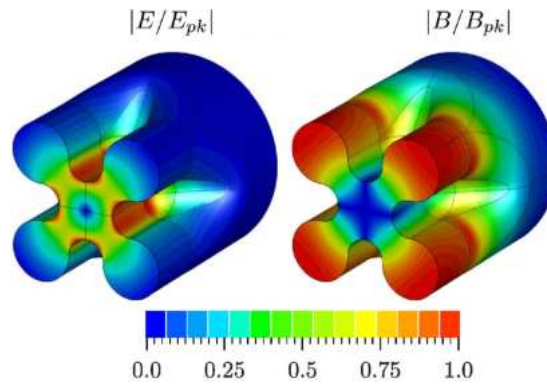


Figure 8.43: Normalised electric (left) and magnetic (right) fields of the four-vane RF quadrupole cavity [218].

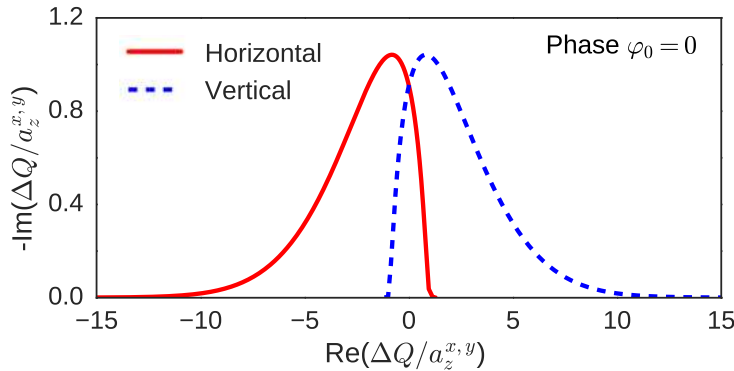


Figure 8.44: Horizontal and vertical stability diagrams in the complex tune space normalised to the RF quadrupole detuning coefficient $a_z^{x,y}$ for a single family operating at a phase $\varphi_0 = 0$ (see Ref. [215] for definitions of φ_0 and $a_z^{x,y}$).

A single RF quadrupole produces incoherent tune spreads with opposite signs in the transverse planes. This is a consequence of the quadrupolar nature of the device. Theory predicts that the stability diagrams also follow this asymmetry meaning that the stabilising efficiency in the transverse planes can be different for a given head-tail mode [215]. This is illustrated in Fig. 8.44 where the stability diagrams are shown for a single RF quadrupole. This impracticality can be overcome by installing two independent RF quadrupole families that operate with a phase difference at two different locations in the machine lattice: one of them at high β_x , low β_y to improve beam stability mainly in the horizontal plane, and the other one at low β_x and high β_y for stability mainly in the vertical plane. The aim is to keep the difference between the local beta functions as large as possible to avoid significant compensation of the detuning effect from the other family. The advantages of this scheme were demonstrated using macroparticle tracking simulations and the outcome is presented in Ref. [215]. It was shown that the asymmetry in

the quadrupolar field strengths required to stabilise the two transverse planes can be removed and lowered overall. Using this scheme for the FCC-hh is therefore highly recommended.

In the studies conducted so far, the RF quadrupole system shows a great potential in terms of the stabilisation of collective instabilities. They also shed light on potential limitations of the device and open questions, however. First, apart from introducing Landau damping described by the dispersion relation and the corresponding stability diagrams [216,219], the RF quadrupole directly modifies the interaction between the beam and the impedance with the result that the effective impedance and the complex coherent tune shifts of the head-tail modes change [212,216,217]. This makes it more difficult to make general statements about the stabilisation of head-tail modes through stability diagram theory. Particle tracking simulations are therefore required to address the requirements of an RF quadrupole system for beam stability as discussed in the following. Second, incoherent effects that may be introduced by the RF quadrupole need to be investigated (resonances, dynamic aperture, beam lifetime). Third, the experimental verification of the stabilising mechanisms from an RF quadrupole needs to be addressed by means of a proof-of-principle experiment. This also includes the construction and test of a prototype cavity. Finally, tolerance studies will be carried out to understand the effect of the device on, for example, bunches entering the cavity off-axis (RF dipole feed-down, closed orbit distortions).

RF quadrupole requirements for FCC-hh

6D macroparticle tracking simulations with PyHEADTAIL [220] were performed to study the transverse single-bunch instabilities expected at injection (3.3 TeV) and collision (50 TeV) energies. The transverse dipolar wakefield model of the machine (November 2017) was used. It was *multiplied by a factor three* to account for uncertainties as well as additional contributions from structures that may be included in the future. The RF quadrupole effect is applied as a thin-lens kick, according to the model described and benchmarked in Ref. [215]. The simulations were carried out with first-order chromaticity $Q'_{x,y}$ set to 0, 5, and 10, and with an idealised transverse bunch-by-bunch feedback system with a damping time of $\tau_{fb} = 60$ turns at injection energy, and 300 turns or 600 turns at collision energy respectively. For each of these settings, a scan in integrated RF quadrupolar field gradient b_2 was performed to determine the number of cavities required for beam stabilisation for each operational scenario. The simulation setup uses FCC machine and beam design parameters. The bunch is modelled as a collection of 4×10^5 macroparticles tracked over 6×10^5 turns. Two RF quadrupole families operating with a phase difference of $\Delta\varphi_0 = \pi$ are installed at locations with $\beta_x = 80 \text{ m} / \beta_y = 360 \text{ m}$ and $\beta_x = 360 \text{ m} / \beta_y = 80 \text{ m}$ respectively. The values for the beta functions originate from a MAD-X lattice calculation and refer to locations $s_1 = 54,000 \text{ m}$ and $s_2 = 54,820 \text{ m}$ respectively, in the main RF straight section. The results of the simulation campaign are summarised in Table 8.6. At injection energy, the number of cavities required is relatively low. This is mainly thanks to the low beam rigidity and thus the stronger effect of the quadrupole kicks. At collision energy, the strength required is up to a factor 20 larger. This is roughly in agreement with the ratio (≈ 15) of the Lorentz factors γ between collision and injection energies and illustrates that the efficiency of the RF quadrupole scales with $1/\gamma$ with increasing beam rigidity. The studies indicate that beam stability for all the operational scenarios could be provided by 25 RF cavities per family. Furthermore, thanks to the two-family scheme, the stabilising quadrupole strengths are approximately the same in both planes.

A further reduction of the number of cavities could be achieved by optimising the beta functions at the locations of the RF quadrupole system. With fewer cavities, the (more critical) longitudinal impedance of the RF quadrupole system can also be reduced linearly [218]. The same applies to the number of cryomodules and this would greatly reduce the cost. Overall, the transverse impedance of the system will remain roughly the same. In addition, by further optimising the ratio of β_x and β_y at the locations of the two RF quadrupole families, the mutual partial compensation of the horizontal or the vertical tune spreads can be minimised.

8.8.3 HTS coating for the beamscreen

Beam stability margins from beam coupling impedance may be improved by coating the interior of the beamscreen with a high temperature superconductor (HTS). Estimates of the surface resistance have been carried out for the two most promising material candidates, namely REBCO and Tl-1223, selected for their known HTS parameters and the baseline operating conditions of the beamscreen. The results reported in Fig. 8.45 show that a large gain over copper at 50 K and 16 T can be expected over a large frequency range both for REBCO [221] and Tl-1223 [222], and an even higher gain can be expected at injection field. First estimates of beam coupling impedance also confirm these results [223].

Experimental studies have thus been initiated in collaboration between CERN and several European institutes in order to investigate the feasibility of applying HTS to the beamscreen. One possible option is to use

Table 8.6: Summary of RF quadrupole strengths required for stable single-bunch operation for various FCC-hh scenarios. The number of cavities is based on the four-vane design with an aperture radius of 30 mm and lowest taper angle (per cavity strength of $b_2^{\text{cavity}} = 0.35$ Tm/m with an active length of about 0.3 m, see Ref. [218]).

| | Scenario | | Head-tail mode | b_2^{stable} (Tm/m) | | # cavities (per family) |
|------------------|------------|----------------------------|----------------|------------------------------|-----------------|-------------------------|
| | $Q'_{x,y}$ | τ_{fb} (turns) | | Horizontal | Vertical | |
| Injection | 0 | 60 | -1 | 0.45 ± 0.05 | 0.45 ± 0.05 | 2 |
| | 5 | 60 | 1 | 0.15 ± 0.03 | 0.20 ± 0.03 | 1 |
| | 10 | 60 | 0 | 0.1 ± 0.1 | 0.4 ± 0.1 | 2 |
| Collision | 0 | 300 | -1 | 8.6 ± 0.4 | 6.8 ± 0.4 | 25 |
| | 5 | 300 | -1 | 8.6 ± 0.4 | 6.4 ± 0.4 | 25 |
| | 10 | 300 | 2 | 1.9 ± 0.1 | 1.9 ± 0.1 | 6 |
| | 0 | 600 | 0 | 7.1 ± 0.4 | 5.6 ± 0.4 | 21 |
| | 5 | 600 | -1 | 7.9 ± 0.4 | 6.4 ± 0.4 | 23 |
| | 10 | 600 | -1 | 6.4 ± 0.4 | 7.1 ± 0.4 | 23 |

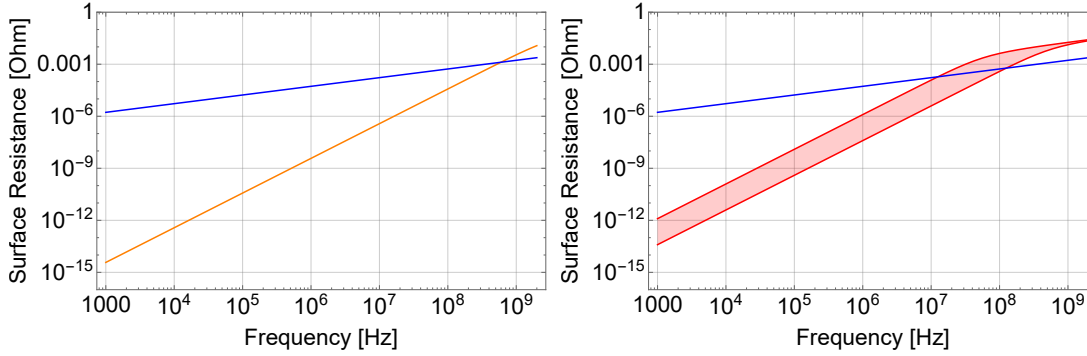


Figure 8.45: Expected surface resistance of REBCO based HTS (left) and TI-1223 HTS (right) based on standard material parameters from the literature, compared to copper (blue lines) at 50 K and 16 T.

existing commercial REBCO coated conductors (CC), typically 12 mm wide tapes available in lengths of several hundred metres, by soldering them on the inner parts of the beamscreen during the manufacturing process. An extensive programme is currently ongoing to validate the mechanical, superconducting DC and RF properties of several commercial CC samples, in parallel to the soldering process development. As an alternative, the coating of TI-1223 by electroplating is being developed at the sample scale. The programme starts with a solution of the individual constituents and is coupled to extensive structural and transport analyses. A relatively straightforward scalability of electroplating to larger sizes is expected. The higher critical temperature of TI-1223 might open up the possibility of operating the beamscreen at ≈ 100 K.

Several RF experimental results on selected REBCO conductors and the first measurement of a non-optimised TI-1223 sample are presented in Fig. 8.46. These have been measured with a dielectric loaded resonator, operating at 8.05 GHz and at variable temperature and magnetic field, up to 9 T. The results go beyond expectations, in particular for REBCO tapes with artificial pinning centres that might be even further customised. The behaviour with magnetic field follows \sqrt{B} as predicted [221]. Scaling to lower frequencies ($\propto \nu^2$ for HTS compared to $\propto \nu^{1/2}$ for copper) and to 16 T shows that a gain of at least one order of magnitude compared to copper could be attainable for frequencies of 1 GHz and below. First measurements of TI-1223 samples at zero field also show the potential for improvements compared to copper, and further improvement is expected for textured TI-1223.

In parallel, studies are being carried out on e-cloud mitigation by amorphous carbon coatings, resistance to synchrotron radiation and nuclear irradiation, activation and lifecycle issues and on the effect on the dipole magnetic field accuracy and possible mitigation strategies [224]. No showstoppers have been identified.

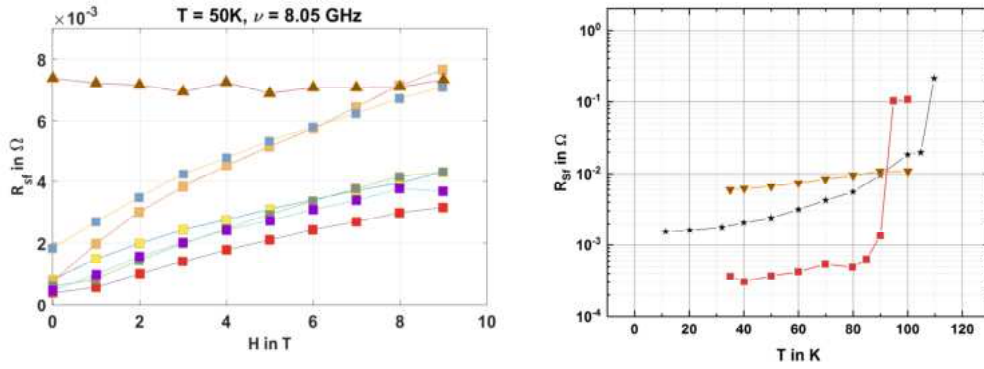


Figure 8.46: (left) Measured surface resistance of REBCO coated conductors (squares) compared to copper (triangles) as a function of applied magnetic field. The lower four curves correspond to materials which have artificial pinning centres. (right) Measured surface resistance for copper (triangles), the best CC (squares) and Tl-1223 HTS (stars) at zero field as a function of temperature, showing a T_c of ≈ 110 K for the latter compared to ≈ 90 K for REBCO.

8.8.4 Beamscreen laser treatment for e-cloud mitigation

Laser ablation surface engineering (LASE), or laser-engineered surface structures (LESS) can be applied to the beam-facing surfaces of the beamscreen in order to mitigate the electron cloud build-up. Indeed, there is evidence that the rough surface possesses a lower secondary electron yield (SEY) [162, 163]. The treated surface exhibits two types of roughness: large parallel grooves that trace the laser trajectory, and micron-level balls chaotically placed on top of the grooves. The micron-level roughness is a result of condensation of the evaporated material and is a necessary tool for reducing the SEY.

However, the surface roughness inevitably leads to the increase of the beam coupling impedance. In particular, the increased imaginary part of the transverse dipolar impedance can cause the transverse mode coupling instability (TMCI). Studies are on-going [225] to estimate the impact of the laser-treated surface on the impedance over a wide frequency range and in realistic conditions (cryogenic temperatures and a high external magnetic field). Some preliminary measurements show that the increase of the real part of the impedance is tens of percent when the grooves are made parallel to the direction of the beam, or several-fold if they are made perpendicular. Based on these measurements, the imaginary part of the impedance can be estimated to be similarly increased [226]. If these conclusions are confirmed by measurements, only the parallel grooves would be acceptable from the beam stability point of view.

8.8.5 Intra bunch feedback

Active feedback systems for the intra-bunch instabilities have been under development during recent years (see e.g. ref. [227, 228] and refs. therein). These kinds of system have been proposed to be used against intra-bunch oscillations, e.g. from TMCI, electron cloud and slow head-tail instabilities. Recently, it was also demonstrated experimentally in the SPS that the accelerator can be operated above the TMCI threshold with the wideband feedback system [229].

In the FCC-hh, a wideband feedback system could be used to mitigate intra bunch instabilities, whereas in the baseline configuration its suppression relies on Landau damping. Some of the most challenging damping requirements in the FCC-hh are the intensity threshold at injection energy and the slow head-tail instabilities during the squeeze. The bandwidth³ and gain requirements for these cases have been studied with single bunch PyHEADTAIL simulations. The wideband feedback systems is assumed to be an additional feedback system working in parallel with the baseline bunch-by-bunch system.

Single bunch intensity thresholds for the different feedback options are presented in Fig. 8.47. Without a transverse feedback system, the TMCI threshold can be observed at an intensity of 4.5×10^{11} protons per bunch. An ideal bunch-by-bunch feedback system generates slow intra-bunch instabilities even below the TMCI threshold.

³In these studies the bandwidth of the intra-bunch feedback system is determined as a cutoff frequency of a Gaussian lowpass filter. Note that the bandwidth requirement is sensitive to the exact frequency response above the cutoff frequency, which depends on the final design of the amplifiers and the kickers.

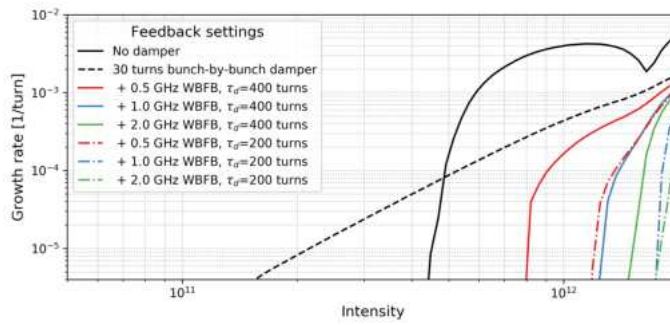


Figure 8.47: Effects of a bunch-by-bunch and wideband feedback systems on the TMCI threshold at injection energy. Simulations are based on the 01/2018 impedance model.

An additional 1 GHz transverse feedback system can both stabilise the instability caused by the bunch-by-bunch feedback and push the (TMCI) intensity threshold to above 1×10^{12} protons per bunch.

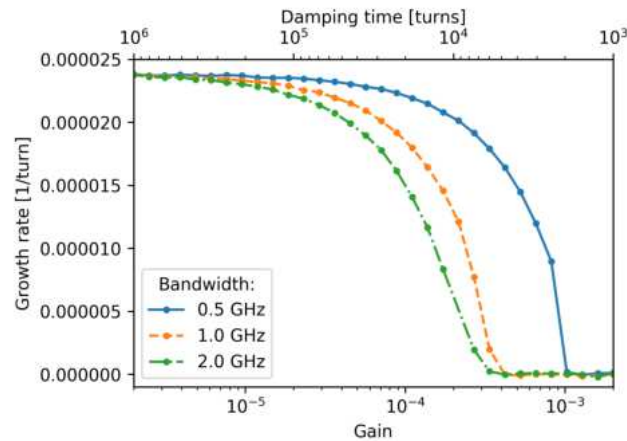


Figure 8.48: Slow head-tail instability growth rate as a function of wideband feedback system gain at collision energy when $Q'=11$ and the damping time of the bunch-by-bunch damper system is 20 turns. Simulations are based on the 01/2018 impedance model.

The bandwidth and gain requirements for the wideband feedback system were also studied at top energy. In these simulations the wideband feedback system works together with the 20 turns bunch-by-bunch damper in the worst case scenario for slow head tail instability when $Q'=11$ without Landau octupoles. The simulations presented in Fig 8.48 show that the 1 GHz bandwidth together with 5000 turns damping time is sufficient to stabilise the beam without Landau octupoles.

From the technological point of view, the 1 GHz bandwidth required for the intra-bunch feedback system is feasible and already demonstrated with the existing wideband feedback system in the SPS. Also its capability against the intra-bunch TMCI instabilities has been demonstrated experimentally. However, it is essential to get more experimental data from beam dynamics studies in order to identify the key technological challenges for the FCC-hh. In particular, the effects of WFBF noise on the FCC-hh beams and the requirements for the possible electron cloud instability mitigation need more studies.

8.9 Key R&D

Several of the most important R&D topics are described above in Section 8.8 and in addition the following theoretical, computational, and experimental work would be helpful:

- Theoretical understanding of the stability diagram in high-tuneshift regime when interaction between different azimuthal modes cannot be neglected
- Calculation of the impedances of the few remaining complex components, e.g. the injection kicker magnet with shielding
- Demonstration of the transverse mode-coupling instability (TMCI) in the LHC in both the single bunch and the multi-bunch regimes
- Effect of the crab cavities on beam stability (will be thoroughly studied in the HL-LHC)

Collimation system

9.1 Introduction

In order to achieve a high luminosity at 50 TeV, a high beam current is required in the FCC-hh. Combined with the 50 TeV particle energy, this results in a stored beam energy of about 8.3 GJ, assuming the baseline parameters of 10400 bunches of 10^{11} protons per bunch. This is about a factor 24 higher than the nominal LHC and a factor 12 higher than the HL-LHC. Therefore, the FCC-hh beams are highly destructive and open up a new regime in terms of beam halo cleaning and machine protection considerations. Absorbing the energy of even very small beam losses becomes challenging.

To achieve the high energy per particle, strong magnetic fields are needed, which demands the use of superconducting magnets operating at cryogenic temperatures. A loss of a small fraction of the beam can deposit enough energy to quench a magnet. To avoid this, a collimation system must be installed to protect the magnets from beam losses and this is the main topic of this chapter. The development of the design of the various aspects of FCC-hh collimation has been documented in previous publications [18, 19, 29, 30].

In addition to the routine cleaning losses, the collimation system must also protect machine elements from damage from irregular and accidental beam losses that could occur, e.g. injection and extraction kicker misfires, or failures of other elements. If needed, the collimators can be sacrificed in order to prevent beam losses in more critical locations, such as the experiment detectors. Furthermore, the collimation system should also localise the losses and hence concentrate the radiation dose in controlled areas, and if needed, help in reducing machine-induced experiment backgrounds. At the same time the machine impedance must be kept within acceptable limits. This latter point is discussed in Subsections 8.3.5 and 8.3.6.

Beam loss rates in the FCC-hh are very hard to predict and depend on a number of unknowns, but regular operation and tuning of the machine requires that a reasonable range of beam lifetimes (BLT) can be handled without a beam dump, quench or collimator damage. For the design and specification of the collimation system, the target is that the FCC-hh should be able to sustain betatron losses due to a BLT drop down to 12 minutes over a period of 10 s, and a BLT of 1 h in steady state. The former scenario corresponds to an extreme instantaneous beam loss power of 11.6 MW. These design scenarios have been adopted from the LHC design [230]. Although LHC operation in Run 2 very rarely resulted in such pessimistic losses, these criteria are conservatively used for the FCC-hh design.

For off-momentum losses, the most critical scenario is taken to be the losses at the start of the energy ramp, where any off-energy tail outside of the RF buckets is rapidly lost as the acceleration starts [231]. Based on LHC experience, the design criterion for the collimation system is that the machine should be able to routinely handle losses of 1% of the total beam intensity over 10 s [232]. This assumes that the rate of change of the energy at the start of the ramp is similar to that of the LHC.

The baseline FCC-hh collimation system is based on the design and operation of the LHC system [20–25, 233], as well as the planned upgrades for HL-LHC [26–28, 234, 235].

9.2 Baseline collimation concept and layout

Two main collimation insertions are used; a betatron system in IRJ for removing particles that have a large amplitude in transverse phase space, and a momentum collimation system in IRF, for removing particles with a large rigidity offset. In addition to these two insertions, there are collimators around each experiment insertion, for both the incoming and outgoing beams. Finally collimators are placed around the injection and extraction regions to protect against regular injection and extraction losses, and also against failure modes.

In IRJ and IRF, a scaled-up version of the LHC multi-stage cleaning system is used. It has primary collimators (TCP) closest to the beam, followed by secondary collimators (TCS), and absorbers (TCLA). As in the LHC, the main bottleneck in terms of cleaning losses is expected to be in the dispersion suppressor (DS) downstream of the betatron collimation insertion, where the dispersion generated due to the superconducting dipoles increases rapidly. Protons that have lost energy in single diffractive scattering event in the TCP and which have a small enough angular deviation to bypass the TCSs risk being lost in this area [24]. In order to alleviate these losses, it is planned to install DS collimators (TCLD) in the cold region, similar to the upgrades planned for HL-LHC [26]. It is planned to install TCLDs in IRF as well, and also downstream of the experiments in order to catch off-energy collision debris that would otherwise risk putting too high a load on the DS. The optics and collimator positions in IRJ and IRF are shown in Figs. 9.1a–9.2b, and the full list of collimators with their names, positions, materials, settings through the cycle, and orientations are shown in Table 9.1. In addition to the above mentioned collimators, TCL physics debris absorbers will be added to the lattice for the outgoing beams around each experiment IP. The exact placements are still under study. It is expected that each IP will have 3 TCLs per beam, making a total of 12 additional collimators.

The baseline betatron collimation insertion is a scaled version of the current LHC system, with the constraint that there is a minimum mechanically feasible jaw gap size. In order to keep similar settings to the LHC in units of beam σ , the smaller geometric emittance of the 50 TeV beam is compensated by a larger β -function.

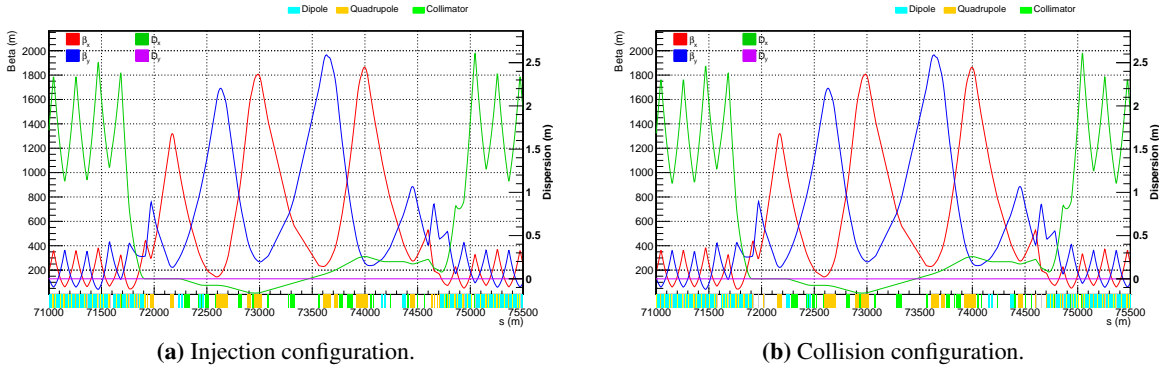


Figure 9.1: The optics in the betatron collimation insertion (IRJ).

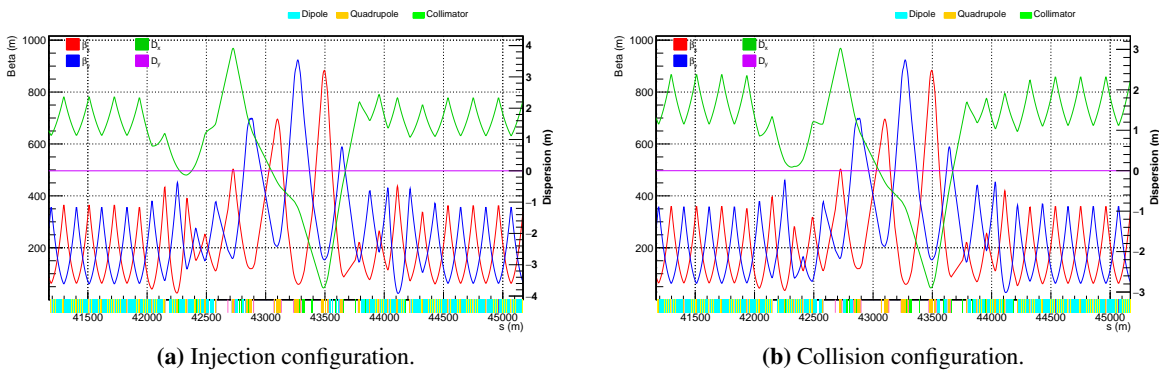


Figure 9.2: The optics in the energy collimation insertion (IRF) at collision configuration.

Therefore, all β -functions have been scaled by $\sqrt{\frac{E_{FCC}}{E_{LHC}}} = \sqrt{\frac{50}{7}} \approx 2.67$. To achieve this, all magnet lengths

and separations have been increased by 2.67, and the total length of the insertion is 2.7 km. This ensures that the magnetic fields in the warm magnets are of the same magnitude and therefore can be constructed. The increase in focusing required by the energy increase w.r.t. LHC comes from the increase in magnetic length.

For the momentum cleaning insertion, the baseline is also a layout similar to that of the LHC but scaled up by the same factor as the betatron system. This is the lattice used for the studies presented later in this report. However, work on alternative designs is underway, and a first version of a new optics for the off-momentum cleaning insertion has been created. This is based on an optimisation of the normalised dispersion at the off-momentum TCP, whilst keeping favourable phase advances to secondary and tertiary collimators. This alternative design has shown some promising results in terms of geometric acceptance and protection of the downstream arc, however, more work is needed on the optimisation of potential aperture bottlenecks at injection, as well as tracking studies to optimise the collimator placement.

The collimators for the present studies are assumed to be of a design similar to those used in the LHC, i.e. pairs of movable collimator jaws constructed of sections of amorphous materials, with a single tank per beam for each collimator - a design that is well established and optimised for high losses. The infrastructure requirements are also similar: cooling water is required, and the controls infrastructure needs to be implemented so that no sensitive electronic components are placed in areas where they risk radiation damage. A previous design of the FCC-hh lattice, with the extraction kickers placed close to the collimators, was abandoned due to the high radiation load on the kickers. Since the collimation insertion will be a high-radiation area, remote inspection and handling capabilities are necessary in order to reduce the dose to personnel. The TCPs and TCSs need to be very robust. It is planned to use carbon-fibre composite (CFC) for the TCPs and the first TCS, which are the most critical devices in terms of robustness. Molybdenum-graphite (MoGr) with a 5 μm coating of Mo is used for the downstream TCSs, which are less loaded. This, together with an optics design providing for larger jaw gap sizes, allows the machine impedance to be reduced to acceptable levels. This material, which will be used in the HL-LHC [26], has a significantly lower impedance than CFC. In this document it is assumed that such collimators can be reliably produced within specifications. Using coated graphite has been considered as a backup solution. Iterations on the mechanical design, with improvements on the LHC solution, could be made in the future to ensure optimum response to the expected loads from the whole collimator structure.

Other collimators, such as the TCLAs and the tertiary collimators (TCTs) in the experiment insertions, are further away from the beam centre and have lower robustness requirements but higher requirements for absorption. As in the LHC, these collimators are made of a heavy tungsten alloy (Inermet 180).

Table 9.1: The FCC-hh collimator materials, numbers (per beam), and settings throughout the cycle. The settings are given for the normalised emittance reference value of 2.2 μm .

| Collimator | Material | Number | Injection ($n\sigma$) | Collision ($n\sigma$) |
|-----------------|----------|--------|-------------------------|-------------------------|
| β TCP | CFC | 2 | 7.6 | 7.6 |
| β TCSG | CFC/MoGr | 11 | 8.8 | 8.8 |
| β TCLA | W | 5 | 12.6 | 12.6 |
| β TCLD | W | 3 | 21.0 | 35.1 |
| δ TCP | CFC | 1 | 10.8 | 18.7 |
| δ TCSG | MoGr | 4 | 13.0 | 21.7 |
| δ TCLA | W | 5 | 14.4 | 24.1 |
| δ TCLD | W | 4 | 21.0 | 35.1 |
| TCT | W | 12 | 14.0 | 10.5 |
| Experiment TCLD | W | 8 | 21.0 | 35.1 |
| TCDQ | CFC | 1 | 9.8 | 9.8 |
| Extraction TCLA | W | 2 | 11.8 | 11.8 |
| Extraction TCLD | W | 1 | 21.0 | 35.1 |

After initial simulation results, the design diverged from the LHC system, which has three betatron TCPs (in the horizontal, vertical and skew planes). Initial energy deposition simulations showed that the power load from secondary particles on the skew TCP was too high. The collimator would have been unlikely to survive. To achieve acceptable power loads, some changes have been made to the collimator materials and design. The length of the primary betatron collimators has been reduced from 60 cm to 30 cm and their thickness has been

increased from 2.5 cm to 3.5 cm. This reduces the power load inside the collimator jaws and metallic support structure. Removal of the skew TCP allows the secondary particle showers to expand and reduce their energy density. The subsequent collimator that these secondary particles will hit is the first secondary collimator. The initial energy deposition simulations found that the secondary particles would not directly hit the collimator jaw, but the mounting mechanism behind it. Because of this, the thickness of the jaws of the first secondary collimator has been increased from 2.5 cm to 4.5 cm.

Particles interacting with the collimation system can lose energy, but survive and exit the collimation region. Following the collimation insertions, the dispersion is matched to that of the arc region in the DS. Inside the DS, the dispersion rapidly rises. Any sufficiently off-momentum particles will strike the beam pipe aperture due to the dispersion. This will quench magnets if specific protection is not installed. Because of this, DS collimators, known as TCLDs are installed in this region to catch these off-momentum particles, as planned for HL-LHC [26]. Each experiment IR has 2 sets of TCLDs installed, and due to the higher particle load in the collimation regions these have additional TCLDs. In the betatron insertion, 3 TCLDs are used, and in the energy collimation, 4 are used. In addition, due to optical changes between injection and collision, the peak dispersion position changes between the injection and collision optics. The additional TCLD (w.r.t. the HL-LHC number) is also required to cover both the injection and collision cases.

In the experiment straight sections, it was found that one set of TCT collimators (horizontal and vertical) was insufficient. Beam losses were found both inside the matching section and also between D1 and D2. An extra pair of TCT collimators was installed in the matching part of the straight section, in order to catch these losses. This strategy, which has been adopted for the IR upgrade in the HL-LHC, should also reduce experiment backgrounds.

For the extraction insertion, debris from the extraction protection (TCDQ) was found to strike the beam pipe at the end of the straight section. The level of losses in this region was found to be excessive for a 12 min BLT. To protect the machine, an extra pair of TCLA type collimators was added in the straight section after the TCDQ; one in the horizontal and one in the vertical plane. In addition, a TCLD type collimator was added at the start of the arc, which provides additional protection in case of a failure of the dump system.

9.3 Machine aperture

For the collimation system to work properly, the beam-stay-clear region around the FCC-hh ring must be sufficient. This is usually most critical at injection energy in the arcs, where the geometric emittance is larger. Aperture bottlenecks usually also arise in the inner triplet at top energy, when the β -functions are squeezed at the collision points.

To study the available aperture, the same approach as for the LHC and HL-LHC is used [93, 236, 237]. The aperture module of MAD-X [71] is used to quantify the smallest distance, in units of beam σ , between the beam centre and the mechanical aperture anywhere on the 2D cross section of the beamscreen. The calculations are performed at several longitudinal locations in each element in order to obtain the minimum beam-stay-clear value as a function of s . Various imperfections are included: a radial closed orbit offset x_{co} , a fractional change k_β in beam size from β -beating, a momentum offset δ_p , and a relative parasitic dispersion f_{arc} coming from the arc.

The values assumed for these tolerances are shown in Table 9.2. Since it is very hard to accurately estimate these for FCC-hh, they have been derived from the HL-LHC assumptions [93, 236, 237], which in turn have been shown to be pessimistic compared to the aperture measurements performed in the LHC [238–247]. Similarly, the alignment and manufacturing tolerances of each magnet have been adopted from similar magnets of the HL-LHC. It should be noted that the values of the momentum offsets are pessimistic compared to the calculated RF bucket height in Chapter 7. This gives a small additional safety margin, however, it should be noted that these values may change. The last line of Table 9.2 shows the protected aperture, i.e. the smallest calculated aperture that is allowed in any machine element. As a working assumption, this value has been scaled from HL-LHC by the ratio of the square-root of the emittances. This assumption is, however, not trivial and needs to be studied in greater detail. The value of the protected aperture depends on the distribution and intensity of the halo that escapes the collimation system, as well as the halo that escapes the protection devices during failures, which have to be combined with detailed knowledge of the quench limit and damage limits of the machine elements [237]. Such studies have not yet been performed in detail for the FCC and, pending them, the HL-LHC parameters are assumed.

In the calculations, the design of the arc beamscreen as of July 2018 has been adopted, as shown in Fig. 9.3. It should be noted that all arc dipoles are straight, which gives rise to a reduction in aperture due to the sagitta. This aperture reduction has been pessimistically modelled as a constant decrease of mechanical aperture of half of the

Table 9.2: The parameters used in the MAD-X model for FCC-hh aperture studies at top energy and injection.

| Parameter set | FCC-hh injection (3.3 TeV) | FCC-hh top energy (50 TeV) |
|--|----------------------------|----------------------------|
| Primary halo extension | 6σ | 6σ |
| Secondary halo, hor./ver. | 6σ | 6σ |
| Secondary halo, radial | 6σ | 6σ |
| Normalised emittance ϵ_n | $2.2 \mu\text{m}$ | $2.2 \mu\text{m}$ |
| Radial closed orbit excursion x_{co} | 2 mm | 2 mm |
| Momentum offset δ_p | 6×10^{-4} | 2×10^{-4} |
| β -beating fractional beam size change k_β | 1.05 | 1.1 |
| Relative parasitic dispersion f_{arc} | 0.14 | 0.1 |
| Protected aperture (σ) | 13.4 | 15.5 |

sagitta on each side of the beamscreen along the full length of the magnets. A sagitta of 2.524 mm was used for the aperture calculations. A synchrotron radiation absorber protects the interconnection to the next magnet at about 0.6 m downstream of every arc dipole (see Ref. [1, Section 3.3.2]). Whilst the dimensions of the inner chamber of this absorber are the same as for the beamscreen, the slits are not as deep and the sagitta is larger due to the longer distance from the dipole centre, resulting in a horizontal aperture reduction of 1.630 mm at the absorbers.

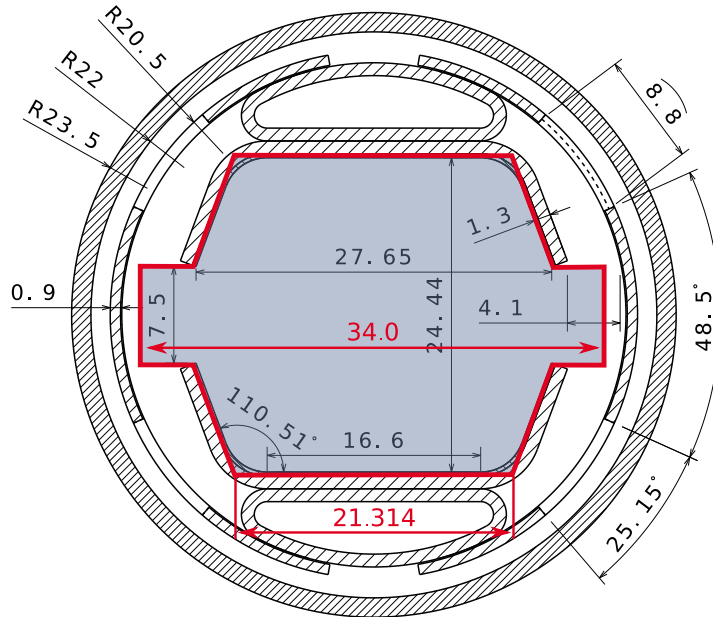


Figure 9.3: The transverse cross section of the arc beamscreen, the MAD-X model for the aperture calculations is outlined in red.

Several assumptions had to be made about the mechanical aperture, in particular that similar tolerances to those of the LHC [248] for manufacturing and alignment apply. The FCC-hh arc beamscreen in Fig. 9.3 features antechambers to channel synchrotron radiation. This was considered unnecessary for the straight section magnets, thus a scaled LHC-like beamscreen design with a larger free aperture was assumed. Some detailed studies are required to determine whether this is justified for straight section magnets close to the arcs that might still receive some synchrotron radiation. The aperture tolerances were adopted from LHC elements. The vacuum chamber apertures in the warm sections for collimation and extraction should also be reviewed.

Using the parameters in Table 9.2, the aperture around the FCC-hh was evaluated at injection and top energy using the optics version 10. The results show that the apertures of the full ring, including the triplets in front of

the high-luminosity experiments, are above the protected aperture. The top-energy triplet aperture at the high-luminosity experiments in IRA and IRG is shown in Fig. 9.4 for the ultimate optics with $\beta^* = 30$ cm, and it can be seen that there is still some margin left. This margin could potentially be used to squeeze the optics further down to around $\beta^* \approx 21$ cm. This includes an increased crossing angle to keep the normalised separation constant.

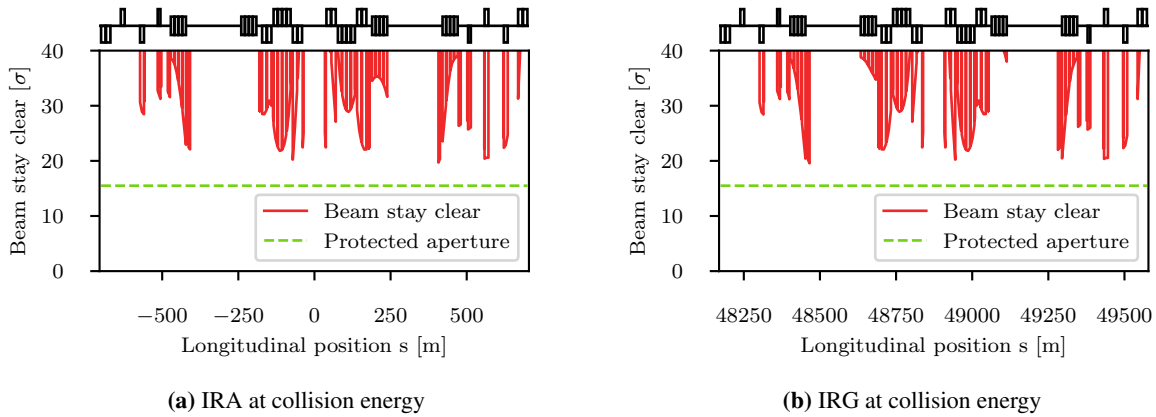


Figure 9.4: The calculated aperture at top energy, using the ultimate optics with $\beta^* = 30$ cm, as a function of distance s in the high-luminosity experiments in IRA and IRG, shown together with the criterion for the minimum aperture.

At injection, most elements around the ring are found to be within specification, in particular in the arcs, in spite of the pessimistic modelling of the beamscreen. An example is shown in Fig. 9.5. A few elements do not meet the criterion and have too small a beam-stay-clear region. These are listed in Table 9.3. As can be seen, there are only three types of magnets affected: orbit correctors in the extraction and betatron collimation section (elements starting with MCB) as well as matching quadrupoles (MQMO) and tuning quadrupoles (MQTLH) of the betatron collimation section. Figure 9.6 shows the aperture bottlenecks in IRJ. The aperture issues of the MCB and MQMO magnets can be solved simply by replacing them with larger aperture magnets of the MCBY and MQY classes respectively. These magnet classes are already used in various locations around the ring and provide sufficient strengths. The MQTLH magnet issues also have to be solved for the final design but are not believed to be show-stoppers.

Previous lattice versions showed aperture limitations in the DS where the optics required a certain degree of freedom in terms of beam size but the aperture is given by the arc dipole design. Several mitigation measures have been proposed if these issues re-emerge as the lattice evolves. One such measure involves pursuing the studies to refine the aperture criterion and the parameters in Table 9.2 and to investigate whether any of them can be improved. The mechanical tolerances on the manufacturing and alignment could possibly also be improved. In particular, in the few locations concerned, magnets could be installed that are better than the specification, either by sorting the magnets and simply taking the best ones from the full production, or by designing a special beamscreen for these magnets only.

In conclusion, using the preliminary aperture parameters that are taken over, or scaled from the HL-LHC, it has been demonstrated that the aperture of FCC-hh is adequate for the presently considered optics scenarios, with the vast majority of the elements around the FCC-hh ring meeting the specification. While there are a few outliers, most of them can be cured by a simple switch of magnet type. For the remaining ones in magnets of the MQTLH type, some further design studies are needed, however, it is not believed to be a showstopper. The calculations should be repeated in the future using updated parameters specifically tailored to the FCC-hh.

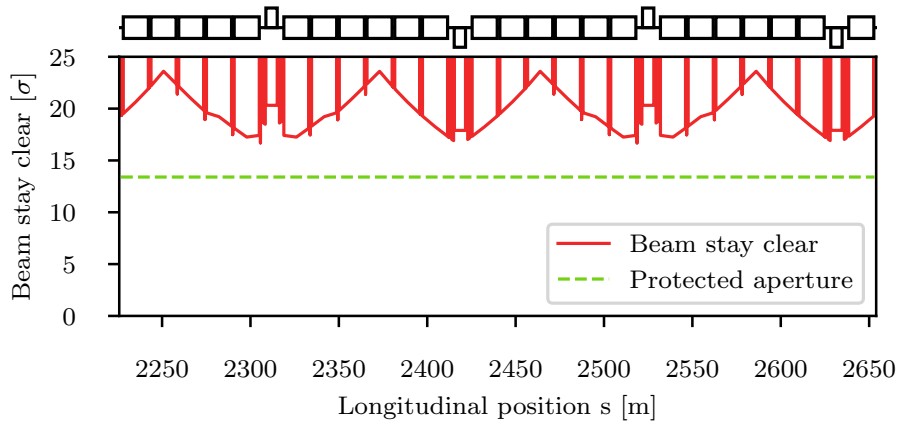


Figure 9.5: The calculated aperture at injection energy, as a function of distance s over two arc cells, shown together with the criterion for the minimum aperture.

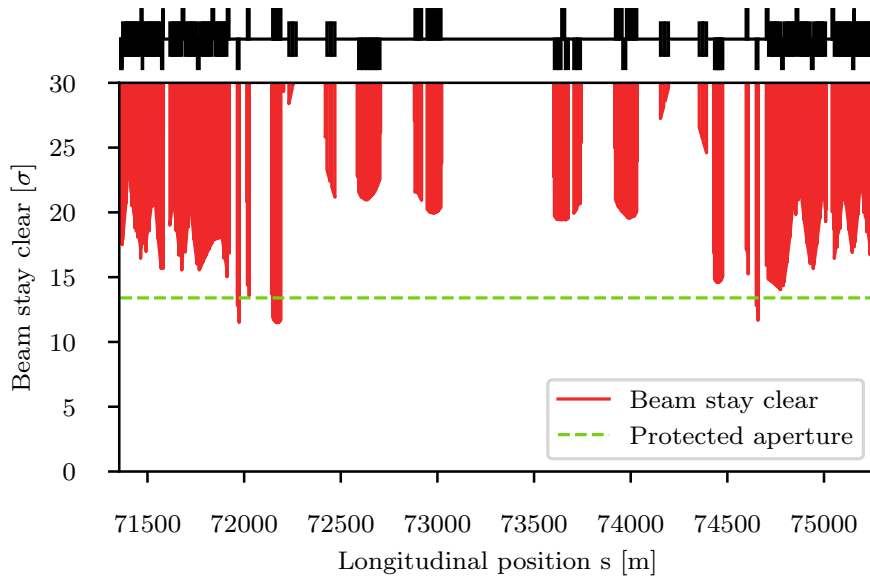


Figure 9.6: The calculated aperture at injection, using the standard injection optics with $\beta^* = 4.6$ m, as a function of distance s in IRJ (betatron collimation). It can be seen that a few elements in the DS fall below the criterion for the minimum aperture.

Table 9.3: Elements found below the minimum aperture at injection energy.

| Element name | s -location (m) | Calculated aperture |
|-------------------|-------------------|---------------------|
| MCBV.6RD.H1 | 25629 | 10.2σ |
| MQTLH.[A-F]6LJ.H1 | 72169 | 11.5σ |
| MCBH.6LJ.H1 | 71974 | 11.5σ |
| MCBV.6RJ.H1 | 74659 | 11.7σ |
| MCBH.6LD.H1 | 23254 | 12.5σ |
| MQMO.6LJ.H1 | 71974 | 12.6σ |
| MQMO.6RJ.H1 | 74658 | 12.8σ |

9.4 Simulations of the collimation system performance

Tracking simulations of the loss pattern around the ring to evaluate the cleaning performance of the system are reported in this section. Various loss mechanisms are considered, and the output is used for further studies of energy deposition (in Sections 9.5–9.6) and the thermomechanical response (in Section 9.7).

During collisions, the beam is squeezed to a small size at the interaction point, and in doing so, it is blown up in the inner triplet magnets. These become the aperture restriction of the machine. At the same time, the crossing angle is enabled to prevent parasitic head on collisions and long range beam beam effects. This reduces the available aperture. For the studies at top energy, this worst case for the aperture is the configuration that is simulated. Studies were also done at injection with un-squeezed optics, where the aperture restriction is in other regions of the machine, such as the arcs and DS. The optics parameters used in the simulations are summarised in Table 9.4, and the collimator settings in Table 9.6.

Table 9.4: A table showing the FCC-hh optics configuration used in this work.

| Parameter | Unit | Value |
|------------------------------------|-----------------|-------|
| Optics version | | 9 |
| Injection energy | TeV | 3.3 |
| Collision energy | TeV | 50.0 |
| Injection β^* (IPA,IPG) | m | 4.6 |
| Injection β^* (IPB,IPL) | m | 27.0 |
| Collision β^* (IPA,IPG) | m | 0.3 |
| Collision β^* (IPB,IPL) | m | 3.0 |
| Injection crossing angle (all) | μrad | 0 |
| Collision crossing angle (IPA,IPG) | μrad | 100 |
| Collision crossing angle (IPB,IPL) | μrad | 26 |

Additionally an asynchronous dump is simulated at collision energy. This is an accidental loss scenario, where the extraction kicker magnets do not fire at the correct time, or do not fire with sufficient strength to extract the circulating beam at its first passage, resulting in the beam not being fully extracted correctly from the storage ring.

9.4.1 Simulation method

At both injection and collision, 3 possible beam loss scenarios are simulated. These are beam losses in the horizontal plane, vertical plane, and both planes simultaneously (referred to as skew). Simulations were carried out using the coupling [249–251] between SixTrack [24, 45, 46, 252] and FLUKA [62, 253], where the first code tracks the particles through the whole ring and the second describes their interactions in the collimator material, until they are lost in the latter by a nuclear inelastic reaction or they reach the machine aperture boundary elsewhere. This framework has been benchmarked against measurements with LHC beam losses, and the simulations agree well with the measurements [254].

The input beam distribution corresponds to a given loss scenario (e.g. losses in the horizontal or vertical plane), while the output gives two components. The first is the energy deposited by particles in each collimator after each pass of the simulated bunch. In addition, the full phase space and location of each particle is dumped if it touches the beam pipe aperture. These particles are considered to be lost. The combination of the collimator and aperture losses give a description of the energy flow around the machine. These losses are then histogrammed to produce what is called a loss map, which shows the loss locations around the ring. A longitudinal binning size of 10 cm was used for this work.

In the FLUKA coupling framework, only positively charged stable baryons are tracked around the ring - i.e. protons and heavy ions. All other particles are killed and are not tracked - their energy is considered to be lost in the collimator or shortly after. An energy cut of 30% was used in FLUKA for this work, meaning that particles below 70% of the initial energy are killed.

In analogy to Ref. [21], the local cleaning inefficiency is defined as

$$\eta_c(s) = \frac{E(s)}{E_{\text{tot}}\Delta s}, \quad (9.1)$$

where η_c is the cleaning inefficiency, Δs is the longitudinal binning size (10 cm in this work), E is the energy that impacts the physical aperture in a given bin, and E_{tot} is the total energy deposited in the full simulation (including inside collimator jaws). The required value of η_c that keeps all magnets below quench level depends on the loss scenario and beam energy

9.4.2 Betatron cleaning

To study the betatron cleaning performance, where the halo is assumed to impact on the primary betatron collimators, a ring of particles is generated in the phase space of the collimation plane (e.g. x, x', y, y') with sufficient amplitude to just touch the primary collimator jaw, usually with a flat distribution between 7.57 and 7.570001σ for a primary cut at 7.57σ . There is no amplitude in the vertical or longitudinal plane; particles are injected on the reference orbit.

The halo, usually containing 100 million particles and generated at IPA, is then tracked for 400 turns, which is sufficient for most particles to interact with a primary collimator and be lost on a collimator in an inelastic interaction, or on the physical beam pipe aperture.

To calculate the required cleaning performance, a quench limit of 10 mW/cm^3 , radially averaged over the superconducting cable, is conservatively assumed for a continuous power load into the magnet coils at 50 TeV. This is slightly higher than the design assumption for the LHC magnets at 7 TeV [255]. It should be noted that recent studies of the 11 T dipole magnet for the LHC, which is made from a similar Nb_3Sn technology, have shown significantly higher quench limits [256], and extrapolations of those studies indicate that the real quench limit of the FCC magnets might be above 70 mW/cm^3 at the peak (see Section 3.2 of the short CDR [1] for further details on the magnet design assumptions).

However, the collimation design studies in this section were performed before this update and are based on 10 mW/cm^3 . The more relaxed, updated number introduces a good safety factor.

The losses at quench can then be calculated as $2.2 \times 10^5 \text{ p/m/s}$ by scaling the LHC design loss rate at quench ($7.8 \times 10^6 \text{ p/m/s}$ [23]) by a factor 35, which is the estimated increase in energy deposition per proton at 50 TeV compared to 7 TeV [257]. Then, assuming an instantaneous loss rate corresponding to a 12 minute BLT and full intensity, a maximum allowed cleaning inefficiency of $\eta_{c,\text{max}} = 3 \times 10^{-7}/\text{m}$ is found. Similarly, for a 12 minute BLT at injection energy, the quench limit is estimated as $\eta_{c,\text{max}} = 3 \times 10^{-5}/\text{m}$.

The simulated betatron cleaning at injection is shown in Figs. 9.7–9.8b. The highest cold losses around the ring stay well below $\eta_c = 10^{-5}/\text{m}$ and are thus considered safe.

The estimated losses at collision energy are shown in Figs. 9.9–9.10b. This is considered to be the most critical scenario. It can be seen that also in this case, the cleaning inefficiency around the ring is below the estimated quench limit of $\eta_{c,\text{max}} = 3 \times 10^{-7}/\text{m}$, which means that for a perfect case, the collimation system should be able to protect the cold aperture even in the rather demanding scenario for a 12 minute BLT. The results shown are for a horizontal beam halo but they are not substantially different for vertical losses.

With the removal of the skew TCP from the layout, the skew beam halo at collision provides an interesting test of the performance of the system with this updated layout. Figure 9.12a shows losses in the betatron collimation insertion with the skew primary removed, for a halo with equal horizontal and vertical amplitudes. Instead of striking a TCP, the beam first hits the less robust TCSs. From a cleaning perspective, the performance is maintained; the losses into the cold regions of the machine are not excessive thanks to the TCLDs, although significant losses appear downstream of IPA. The robustness of the most exposed skew secondary collimators is a potential concern for these losses. From LHC operational experience, skew losses are very rare. The solution is to place a stricter limit on the BLT due to losses in the skew plane, consistent with the damage limit of the TCSs and the LHC operational experience.

9.4.3 Off momentum beam halo

For off-momentum losses, the cleaning efficiency at the start of the ramp was studied first. The losses from uncaptured beam at the start of acceleration were simulated by injecting a pencil beam of off-momentum particles

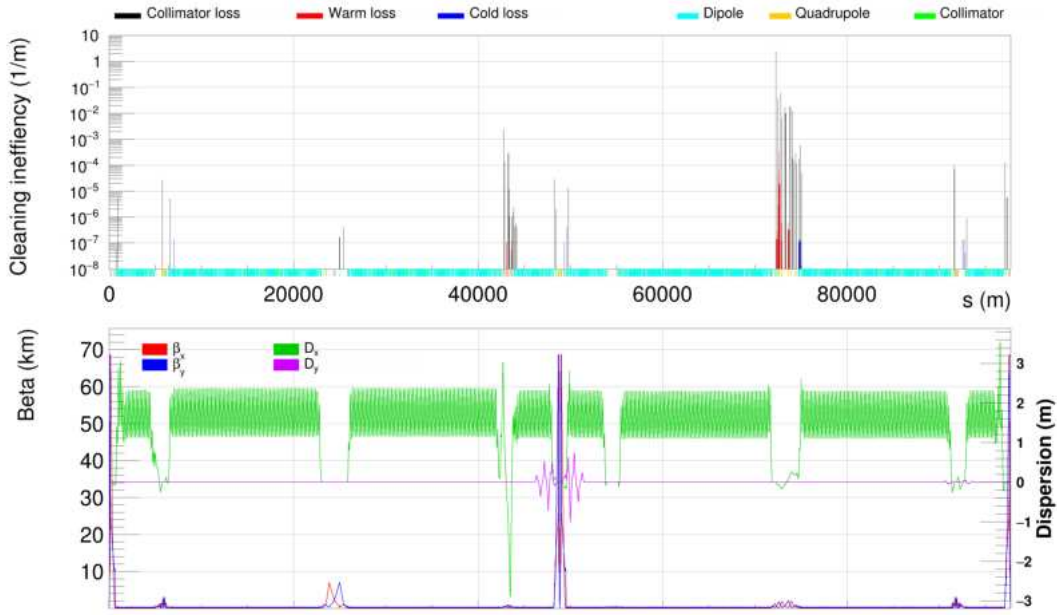


Figure 9.7: Image showing the full ring loss map at injection for a horizontal beam halo.

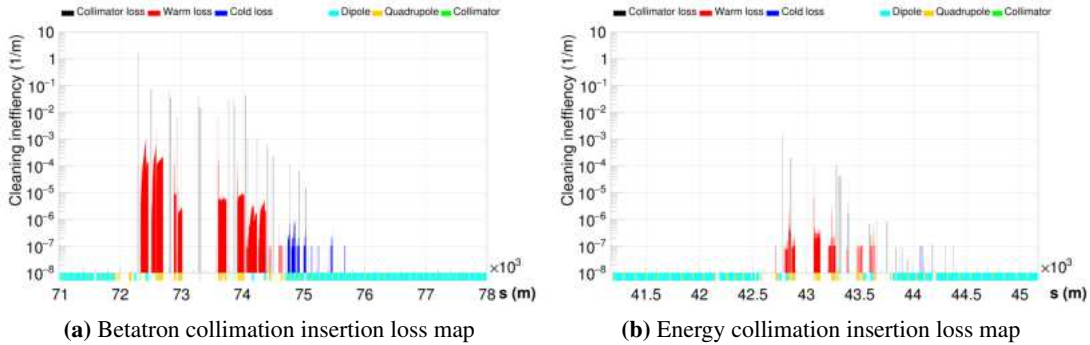


Figure 9.8: Loss maps at injection for a horizontal beam halo.

without betatron amplitude but with a δ_p/p such that they just impacted on the primary momentum collimator jaw (an energy of 3294.8025 GeV was used instead of the reference 3300.0 GeV, which gives a $\delta_p/p = -0.001575$).

The resulting losses are shown in Fig. 9.13. Assuming a 1% beam loss over 10 s, the instantaneous lifetime is about 17 minutes, which requires the inefficiency to stay below $\eta_{c,max} = 4 \times 10^{-5}/m$. As can be seen, all losses fulfil the criterion with some margin.

In collision, off-momentum losses can also be caused by uncaptured beam, but these losses are expected to occur at a slow steady rate, and not as a brief pulse. Therefore the cleaning criterion is not as strict as for the betatron case, where faster losses are more likely. Irregular losses could be faster, e.g. during a fault of the RF system, however, such events are expected to be very rare. Simulations are needed to quantify a limit on the loss rate allowed from the off-momentum halo at collision energy.

9.4.4 Extraction kicker pre-fire failure

The collimation system must also withstand losses resulting from fast failures, in particular single-turn failures where there is no time to dump the beam before losses occur. One such failure scenario, which is one of the most critical failures for the LHC, is a kicker pre-fire in the beam extraction system (see Chapter 4). In this case, one or more extraction kickers could pre-fire asynchronously with the abort gap and hence cause an erroneous deflection of the circulating beam. In the LHC, such a failure would almost immediately re-trigger the remaining extraction kickers, causing an asynchronous beam dump with the risk that mis-kicked beam directly impacts the collimators

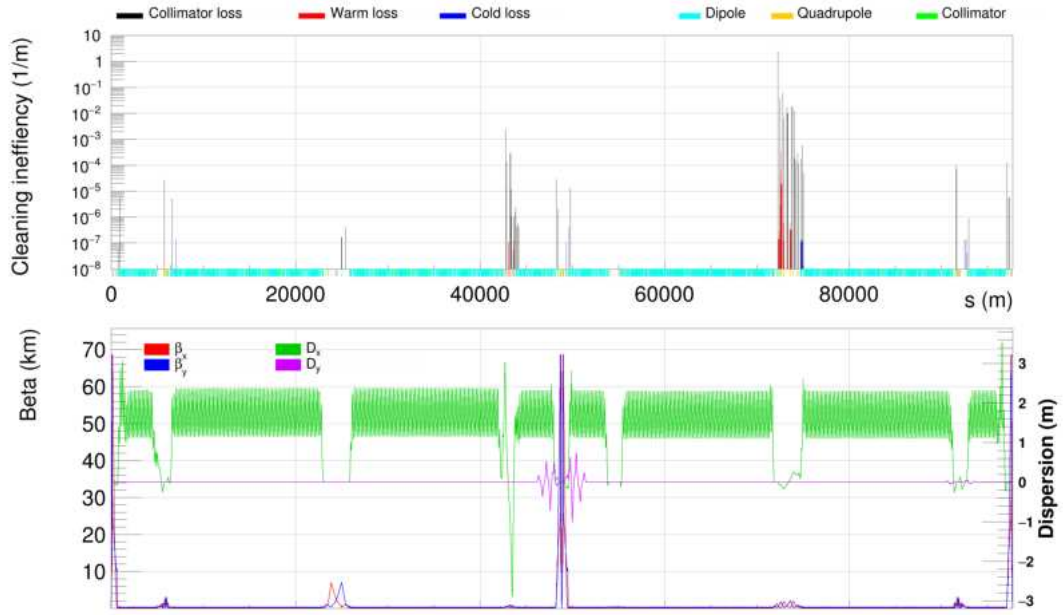


Figure 9.9: Image showing the full ring loss map at collision for a horizontal beam halo.

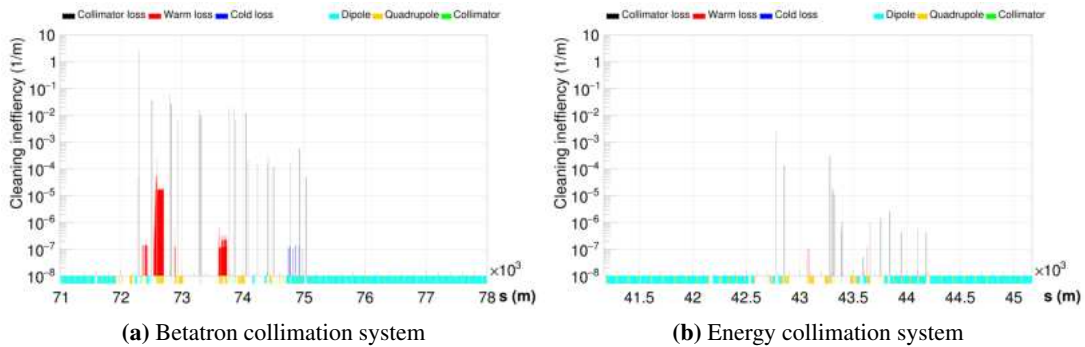


Figure 9.10: Image showing collimation systems at collision for a horizontal beam halo.

and machine aperture.

For the FCC-hh, the proposed alternative abort strategy uses a delayed synchronous beam dump, resulting in mis-kicked beam oscillating for up to one additional turn, as presented in detail in Chapter 4 and in Ref. [89]. This is made possible by distributing the kick, necessary to extract the beam, over 150 extraction kickers instead of the 15 kickers used in the LHC, so that the oscillation amplitude induced by a single failing kicker is much smaller. In the version of the FCC used (V10), the extraction takes place in the vertical plane, and the amplitude of the betatron oscillation induced by a single failing kicker at maximum field is about 1.4σ . For a single kicker pre-fire, there is therefore no risk of the beam core striking the machine aperture.

Specific collimators (TCDQ), as well as septum protection devices (TCDS), are in place to protect against mis-kicked beam. However, beam could leak out of the TCDQ or pass it if there was an error in the TCDQ position, or potentially sensitive collimators or aperture bottlenecks could arise due to errors at apertures effectively smaller than the TCDQ. The collimation system should be able to survive such an accident.

The goal of this study was to obtain the maximum number of kicker magnets that could fire at the same time before damage occurs at a collimator. In the simulation, the beam was tracked for 1 turn, n extraction kickers were enabled on turn 2, the beam was then tracked for one further turn and extracted. The initial conditions are for a full beam, including the core. The distribution corresponds to the sum of two gaussians: the core consists of 95% of particles, with a 1σ standard deviation, while the halo makes up the remaining 5%, with a 1.8σ standard deviation. This distribution is based on experimental results from the LHC, extracted from the Van der Meer scans

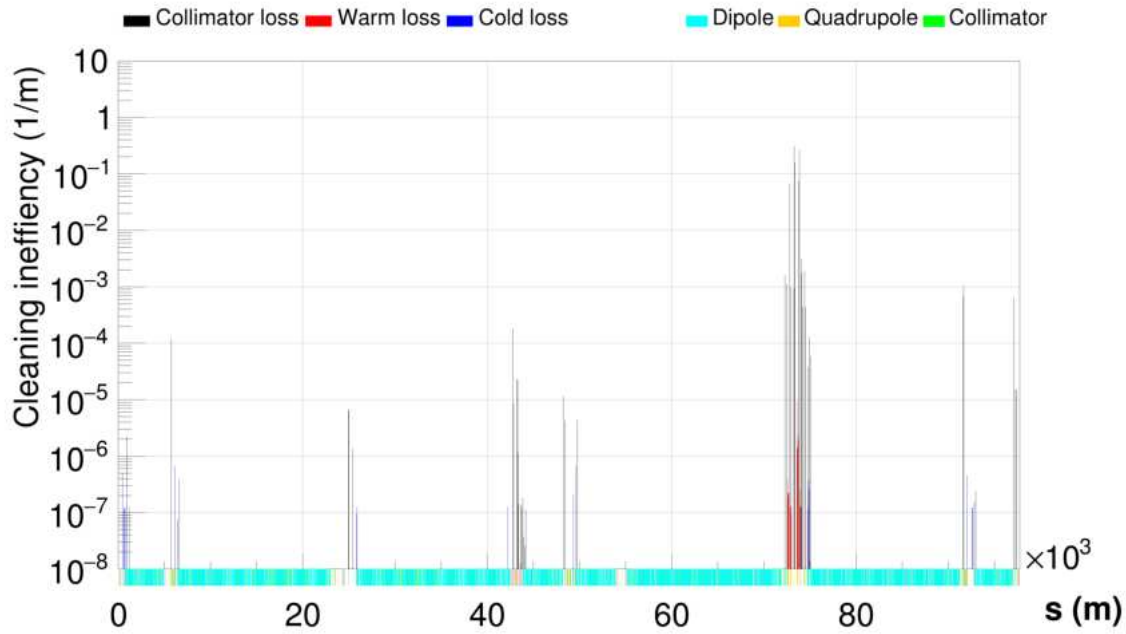


Figure 9.11: Image showing the full ring loss map at collision for a skew beam halo.

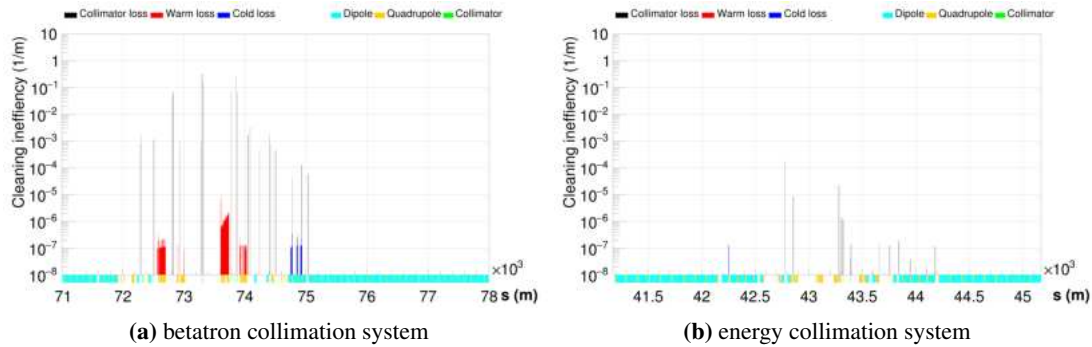


Figure 9.12: Image showing collimation systems at collision for a skew beam halo.

in Ref. [258]. Particles are generated up to the TCP cut, in this case 7.57σ .

The resulting losses, for different numbers of kickers firing and normalised to the absolute number of impacting protons, are shown in Fig. 9.15a–9.15d. As can be seen, almost all miss-kicked protons are lost on the collimation system, and the most exposed cold magnets see losses of up to a few 10^7 protons. The results in Fig. 9.15a–9.15d can be compared to an estimated collimator damage limit of 1×10^{11} protons. From the plots, it can be seen that up to 4 kickers can fire safely but for more than 4 it is potentially not safe. These simulations were performed on a perfect lattice, i.e. one with no magnetic field or alignment errors of either magnets, apertures or collimators. Further studies have been performed on the system sensitivity to collimator alignment errors. With 4 kickers firing and the secondary collimator (TCSG.D2LJ.H1) where the peak loss occurs closed by 0.5σ , the peak loss reaches about 1.5×10^{11} , above the safe single bunch threshold. Closing the TCP or TCDQ collimators by 0.5σ does not change any of the conclusions above. The reason the TCSG intercepts the beam, and not the TCP, is that in this case the phase advance between the dump kickers and the TCP is such that the beam passes through the TCP gap without being collimated, but does impact the TCSG. If this phase advance changes in future lattice iterations, then the conclusions of this study will also change. One can conclude that although for a perfect machine 4 kickers could safely pre-fire, for a machine with errors this is not the case, and the kicker pre-fire limit should be dropped to 3. If the phase advance between the extraction kickers and TCP changes, then this limit could drop even further. Future studies should be performed on a machine with a full set of errors and imperfections.

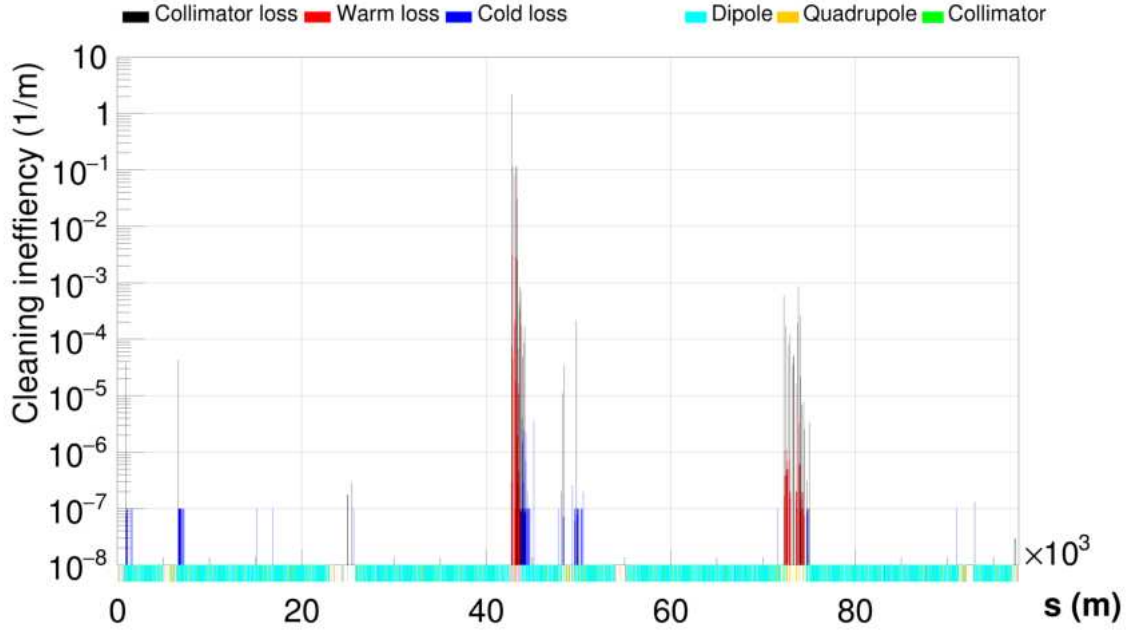


Figure 9.13: Image showing the full ring loss map at injection for an off momentum beam halo.

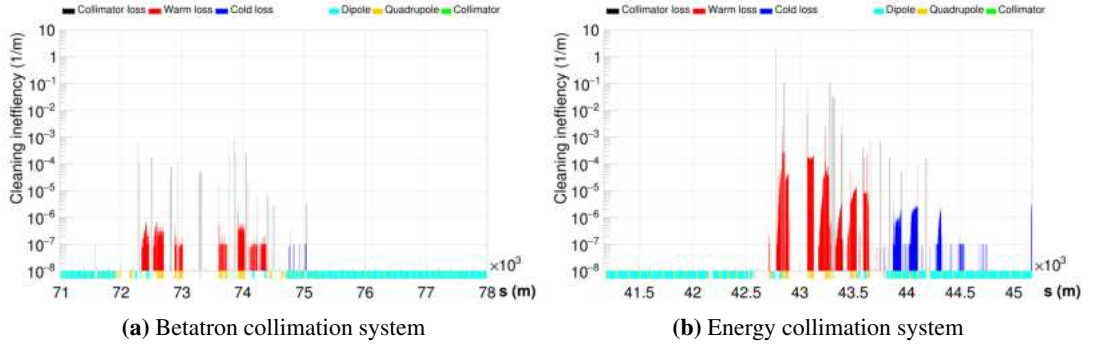


Figure 9.14: Image showing the collimation systems at injection for an off momentum beam halo.

9.4.5 Influence of imperfections

The results in the previous sections refer to an ideal machine but in reality, unavoidable imperfections of the collimators and the rest of the machine affect the cleaning performance of the collimation system. In order to evaluate their influence, several cases with combined imperfections have been simulated. The error model was introduced in SixTrack following the procedure and experimental data used for the LHC as follows [23, 24]:

1. Imperfections of the jaw flatness can reduce the length of material seen by the impacting protons. The jaw flatness error is modelled by a second order polynomial applied over a number of slices:

$$\pm 4 \cdot 10^{-4} \left(\frac{s^2}{l} - s \right) [m] \quad (9.2)$$

where s is the longitudinal position along the jaw and l is the jaw length in m. In this study four slices are used with the deformation bent outwards the beam as shown in Fig. 9.16.

2. The beam orbit and centre of the collimator gap are not always perfectly aligned. These were modelled by random offsets of the centres of collimators with a standard deviation of 100 μm (see Fig. 9.17).
3. Angular misalignments of the collimator jaws with respect to the beam axis were added with an rms tilt angle of 200 μrad (see Fig. 9.17).

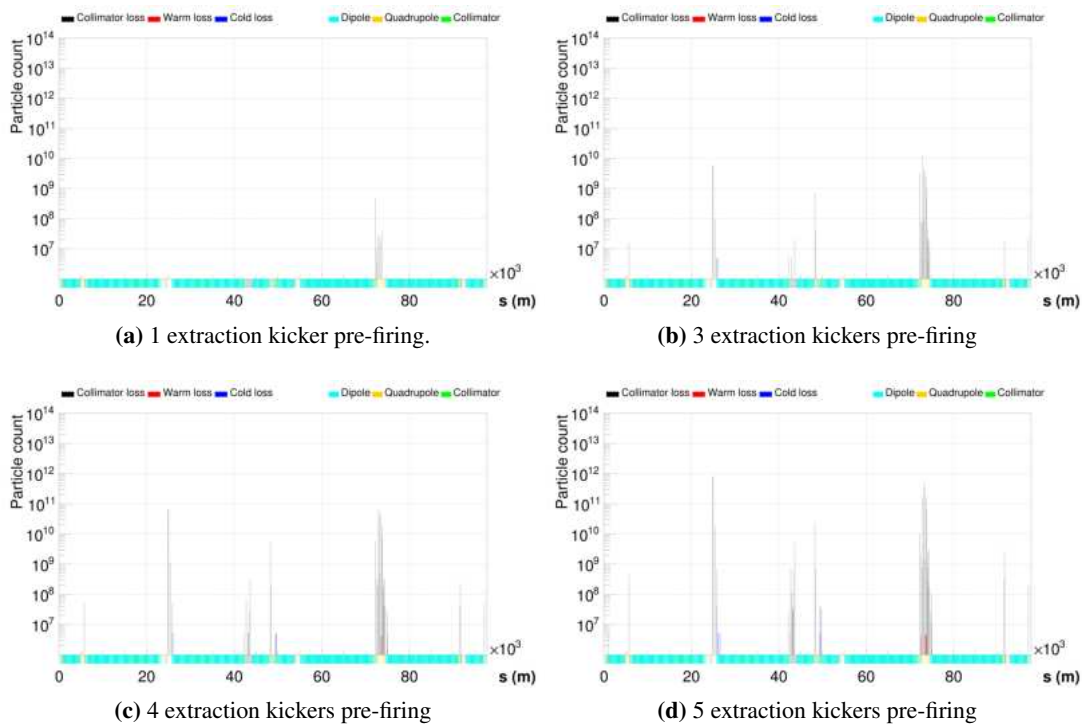


Figure 9.15: Loss distribution for pre-firing kickers.

4. Random errors were applied with a standard deviation of 0.17σ to collimator gaps, corresponding to an rms β -beating of 4% as assumed for FCC-hh [259].
5. Tolerances of aperture misalignments for the different types of magnets are used to introduce imperfections in the alignment of the accelerator elements.

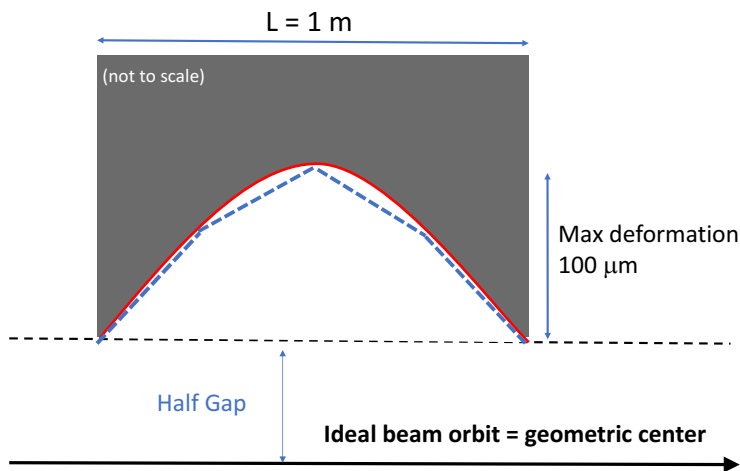


Figure 9.16: Jaw deformation for 1 m long collimator modelled by a 2nd degree polynomial in red and the 4 slices approximation used in SixTrack in dashed blue.

A full study of optics imperfections, adding magnetic and alignment errors in the lattice through MAD-X and partially correcting them to get a realistic β -beating and orbit, has not been performed but is planned. Phase advance and dispersion beating can only be introduced with this second method. Apart from the jaw flatness error,

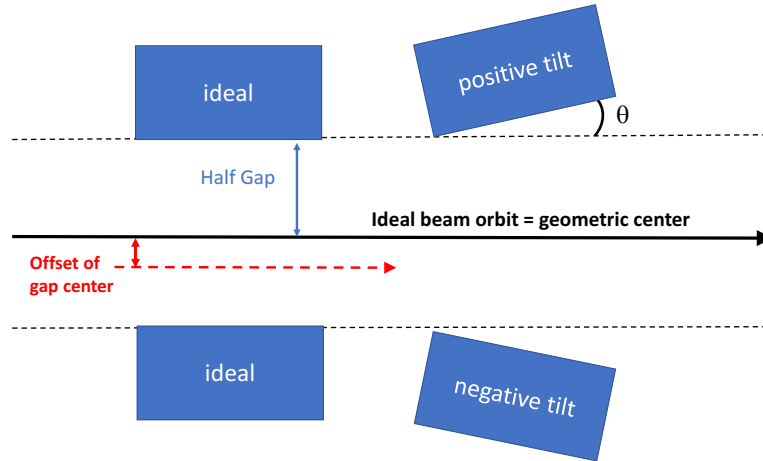


Figure 9.17: Illustration of the various errors applied to collimator in simulation.

all the imperfections follow a Gaussian distribution cut at 3σ and are controlled by a seed. Twenty seeds are used for each scenario with combined imperfections. The number of seeds is limited by computational time, which represents several decades of computer CPU time for this study.

The FCC-hh lattice used in this study for the beyond ultimate case with $\beta^* = 15$ cm at collision was V9 to investigate the most challenging scenario. The horizontal betatron loss maps have been simulated for multiple imperfection scenarios. The SixTrack version used for this study relied on the internal scattering module [252] and the cleaning inefficiency in the following plots represents the fraction of protons lost in a longitudinal bin normalised by the bin length ($\eta = N_{lost}^{\Delta s} / [N_{lost} \Delta s]$). The collimation system was the one of Table 9.6, however, in an earlier version with the skew TCP in IRJ still in and all the TCSs made of CFC. The length of the TCPs is 60 cm and the TCDQ is 10 m whereas other collimators are 1 m. The simulation setup is identical to the one in Section 9.4, but with an impact parameter of 0.0015σ .

In Figs. 9.18–9.19 the loss maps for the ideal case and an example with all imperfections are presented. As expected, most protons are lost in the collimation regions IRF and IRJ. These results allow the prediction of where possible quenching events may occur, and give an indication about how to modify the collimator settings along the accelerator in order to improve the system performance. The loss map for the ideal machine in Fig. 9.18 shows very few cold losses compared with several blue spikes present in the loss map with imperfections. Most of the cold losses appear between the detector IRA and IRB, around the dump insertion region, IRD, and downstream of the RF insertion IRH. The majority of loss maps for all imperfections activated show similar behaviour.

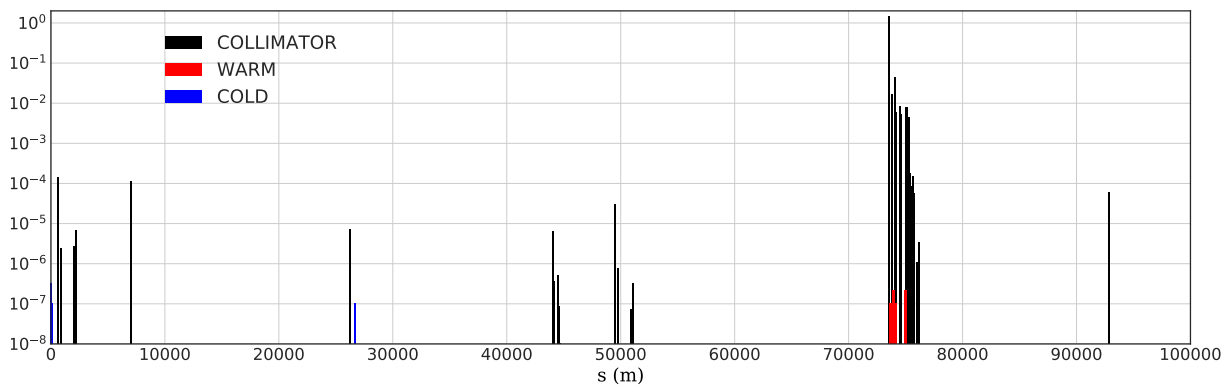


Figure 9.18: Horizontal loss map for the ideal case without imperfections.

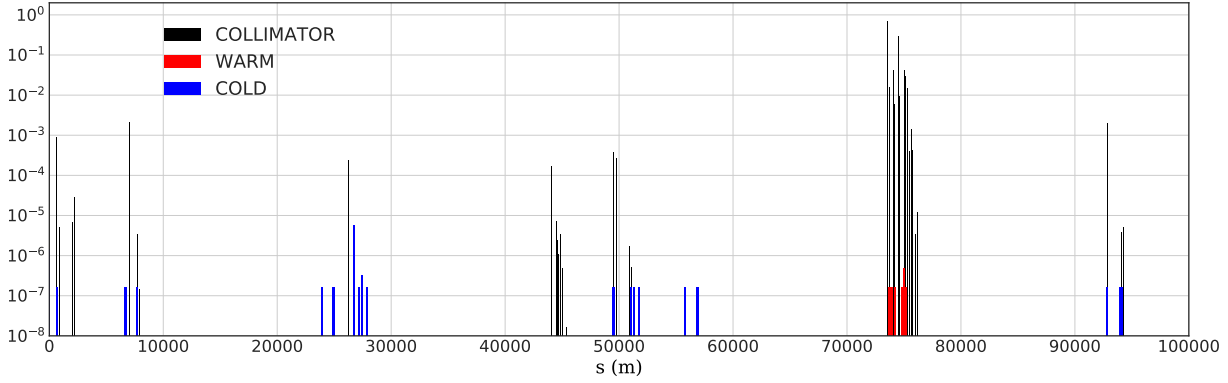
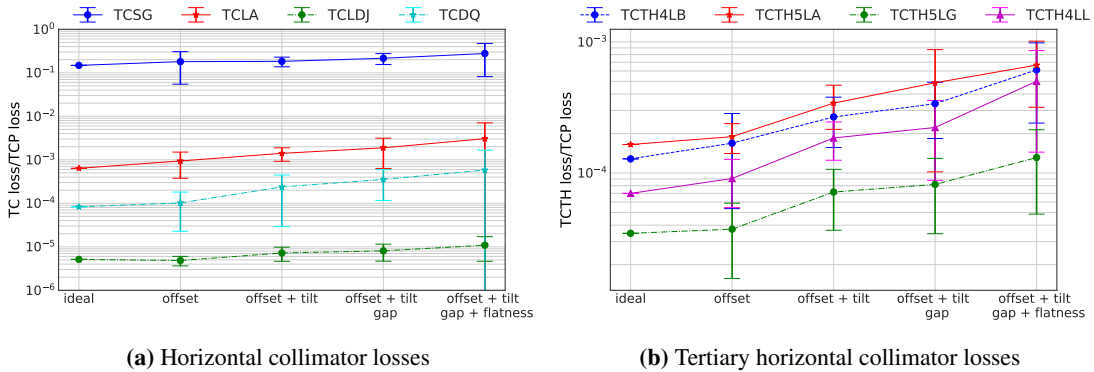


Figure 9.19: Example of horizontal loss map with all imperfections.

The influence of various imperfection types on the collimator losses is summarised in Fig. 9.20a where the ratio of losses on different collimator families to the losses on the TCP is presented. The horizontal axis presents increasing complexity of imperfections. Each point represents an average over the 20 seeds and the error bar indicates their standard deviation. The ratio including the error bars of below one for all cases indicates that no breaking of the hierarchy was observed in the simulations. A slight increase can be observed with wider error bars for TCLAs, TCDQ and TCLDs. The ratio between the TCT losses and the TCP losses is presented in Fig. 9.20b. In this case, the TCT losses increase as more imperfections are included. It can be seen that with all imperfections, losses in tertiaryaries are about 4 times higher with respect to the ideal case, which could have a potential impact on the machine-induced background.



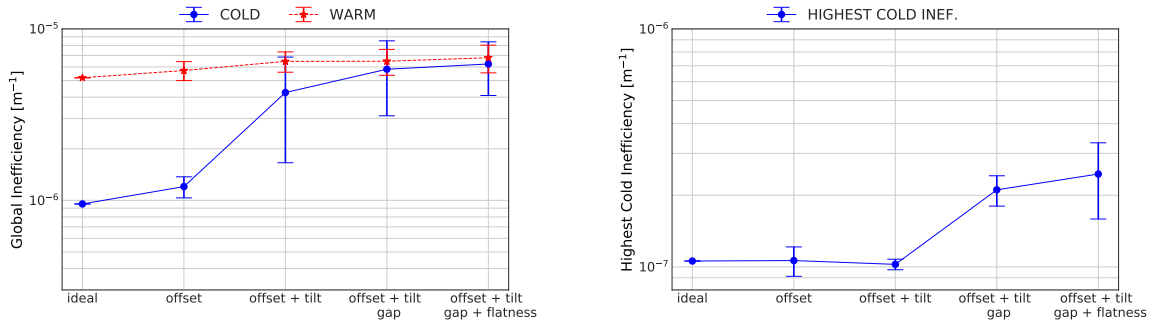
(a) Horizontal collimator losses

(b) Tertiary horizontal collimator losses

Figure 9.20: Influence of imperfections on collimator losses as simulated by SixTrack.

The warm and cold global inefficiencies, defined as the sum of all inefficiencies in warm and cold apertures of the machine, are shown in Fig. 9.21a. The changes to the global inefficiency for warm elements is within the error bars. For cold elements an increase by a factor 2 with respect the ideal case is observed after introducing offset errors for the collimator gaps. Including tilt errors, the global inefficiency is about a factor 5 higher than in the ideal case, while adding gap and flatness errors gives a final increase by a factor of about 6.

The highest cold losses in a single 10 cm bin are presented in Fig. 9.21b. Most of the simulations with imperfections show an almost complete loss of all protons (more than 95%). For the ideal case the number of protons simulated was increased to 140M to have a similar quantity of total losses and a comparable η_c for a loss of a single particle in the simulation. Fig. 9.21b indicates that on average only one proton is lost in a single longitudinal bin for the ideal case and for the offset-tilt cases. When adding gap errors and flatness imperfections the inefficiency in a single location increases by up to 3 times the single event inefficiency, however, most seeds stay within the estimated requirement of $\eta_{c,max} = 3 \times 10^{-7}/m$, which gives confidence in the system performance. For the ultimate optics case of this study, the highest cold peak increases on average by a factor 2 and the global cold inefficiency by a factor of 4.



(a) Global cold inefficiency calculated as sum of all collimator imperfections for all combined scenarios.

(b) Highest cold inefficiency in a single longitudinal bin of 10 cm for different combined scenarios.

Figure 9.21: Cold inefficiencies for different combined scenarios.

9.5 Energy deposition in cold magnets

The tracking simulations described in the previous sections give the distribution of protons lost on the apertures around the ring. Based on this, an approximate estimate was made of whether the protection of the cold aperture is adequate. For a detailed assessment of particularly critical locations, it is necessary to perform local energy deposition studies. In particular, the protons impacting on the collimators cause secondary particle showers that are not evaluated in the tracking simulations and which can extend into neighbouring magnets. The expected energy deposition in the DS of IRJ, which is the most critical cold part of the machine, and in particular, in the cold magnets installed downstream of the TCLDs is examined in this section.

The Monte Carlo program FLUKA [62, 253] was used to evaluate the energy deposition in the cold region around a TCLD, downstream of the betatron cleaning insertion straight section [31]. The distribution of protons leaking out of the upstream betatron collimators at the start of cell 8 was used as starting conditions. They were extracted from tracking simulations carried out at 50 TeV using the MERLIN code [260, 261], and the FCC-hh lattice of 2017 [118]. Only cell 8, including the TCLD, was simulated, on the assumption that the situation around the other TCLD in cell 10 would be similar or better. An identical result and mitigation strategy can thus be assumed for cell 10.

A 3D geometry of the region was implemented as shown in Fig. 9.22, including the TCLD and two downstream magnets (a quadrupole and a dipole). Since at the time of the study a detailed geometry of the dipole was not available, simplified models based on the current LHC magnets with the addition of the FCC coil design and beamscreen were used [262]. Magnetic fields were included in both magnets, modelled as perfect quadrupolar or dipolar fields, extending over the vacuum chamber, beamscreen and cold bore. The collimators were modelled as two parallel blocks of the tungsten alloy Inermet 180, including a tapering part. The masks were modelled as cylinders of the same material. Full details can be found in Ref. [31].

In the FLUKA simulations, typically 4×10^6 protons were simulated, and the energy deposition was scored in the coils of the dipole and quadrupole. To normalise the simulated energy deposition per lost proton, a 12 minute BLT was assumed for the nominal FCC-hh beam parameters at 50 TeV, with all losses on the primary collimator, in order to obtain the power load in the superconducting coils.

For the studies, several layouts of TCLDs and masks were tested and iteratively adjusted until a satisfactory solution was found. The final layout proposed includes a main 1.0 m long TCLD, followed by a second 1.5 m TCLD, and a 0.5 m mask in front of the quadrupole. An additional 1.5 m TCLD and a 0.15 m mask were placed in front of the dipole. For this layout, labelled “Updated design”, the resulting energy deposition along the length of the coils of the quadrupole and dipole is shown in Fig. 9.23. For each longitudinal position, the figure shows the transverse maximum over all bins.

In the figure, the simulated power load has been scaled up by a safety margin of a factor 8. This factor includes both the effect of imperfections, not included in the tracking simulations used here, and the underestimation of the measured energy deposition found in previous studies of the LHC [24], even after imperfections were included.

It can be seen in Fig. 9.23 that for a previous layout iteration consisting of only two 1 m TCLDs and a single mask, the power load exceeds the estimated quench limit of 10 mW/cm^3 , whilst for the final layout with 3 TCLDs

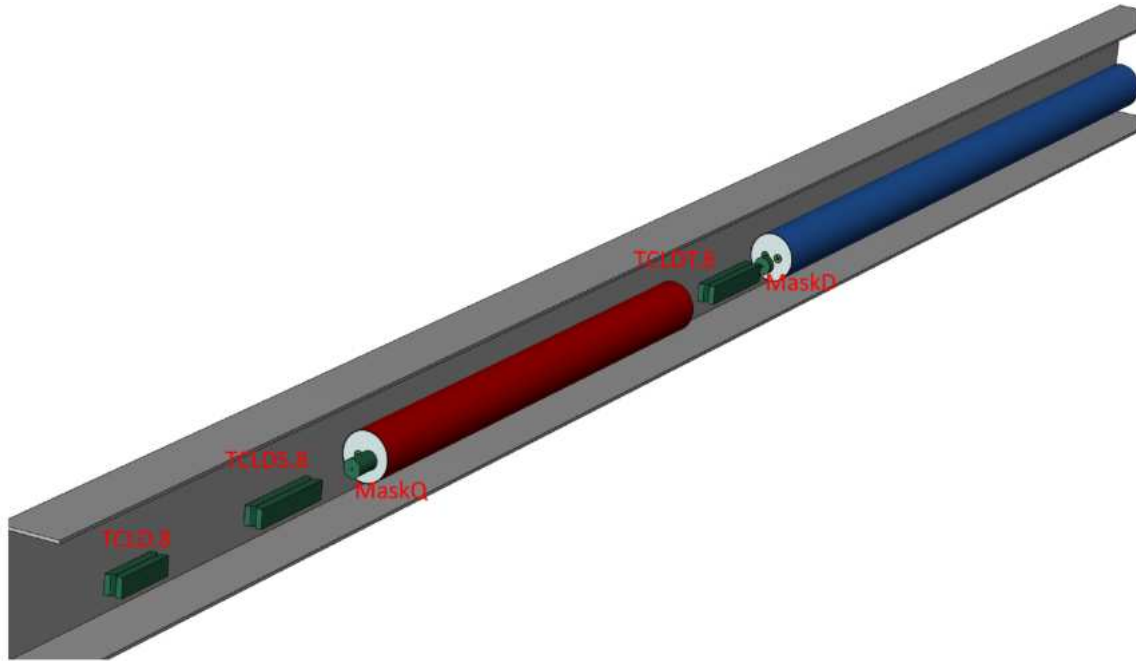


Figure 9.22: FLUKA geometry as implemented in cell 8 in the dispersion suppressor of IRJ, including three TCLDs and two fixed masks [31]. The collimators and masks are shown in green, the quadrupole in red, and the dipole in blue.

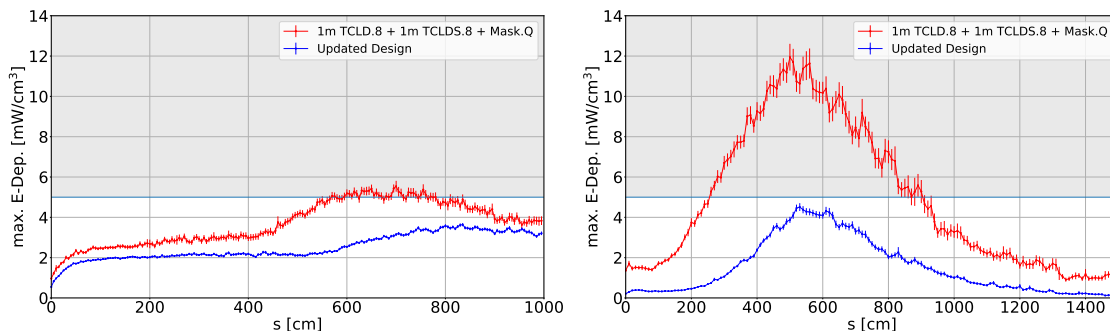


Figure 9.23: Peak power density along the quadrupole (left) and dipole (right) in cell 8 for the final protection design and the previous solution with the a factor 8 safety margin included [31].

and two masks, it is well below. As noted before, this limit is likely to be pessimistic in view of the recent estimates of a 100-200 mW/cm^3 quench limit of the 11 T magnet [256] developed for HL-LHC and also based on Nb_3Sn technology. This gives a significant safety margin in the final design which, based on these simulation results, should be able to protect the cold aperture of the ring against quenches from a 12 minute BLT. Although these studies should be redone for the latest version of the FCC-hh lattice, which might cause minor layout changes, it is unlikely that the qualitative conclusions will change.

9.6 Energy deposition in the warm betatron section

The power deposition is of high importance not only for the superconducting magnets, but also for the collimators themselves and other elements in the warm section. The extreme load during a 12 minute BLT drop corresponds to a beam loss power of 11.6 MW, which is 24 times higher than for the nominal LHC and it should be sustained for up to 10 s. This represents a severe challenge for the robustness of the collimators and other exposed elements. This section presents FLUKA energy deposition studies of all elements in the warm section.

A cut of the initial part of the FLUKA model of the whole 2.7 km insertion is shown in Figure 9.24. An earlier version of the collimator configuration was used, which is identical to the one in Table 9.6 except that all

TCSs are made of CFC. As in the LHC, three passive absorbers (TCAP), made of tungsten and copper, with lengths of 1.5 m, 0.4 m and 1 m, respectively, are placed in front of the most exposed magnets. Figure 9.25 shows the components of the collimator jaws as modelled and a 3D view of a part of the tunnel is given in Fig. 9.26.

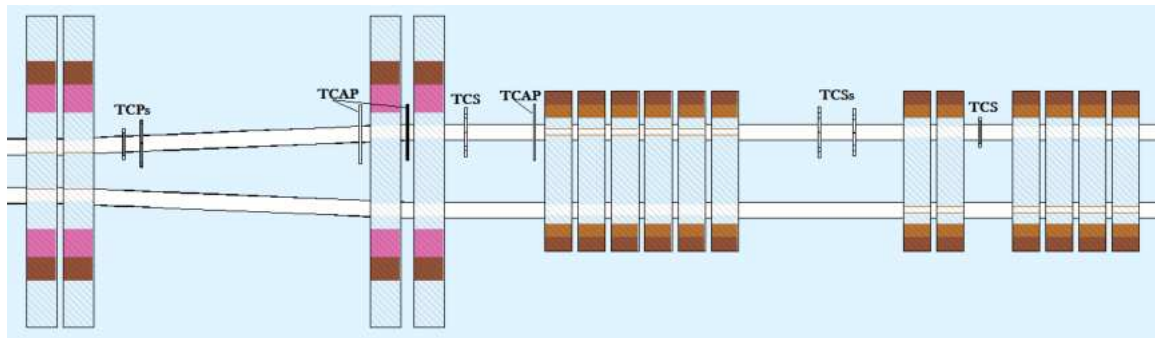


Figure 9.24: FLUKA model of the first 800 metres of the betatron collimation insertion.

In order to perform particle shower simulations and calculate energy deposition in the various beam line elements, maps of beam halo protons touching the collimator jaws are fed into FLUKA. These are produced by the above-mentioned online coupling between SixTrack and FLUKA. The relevant phase space details of each collimator hit is dumped as input for the second step of the simulation, performed by the FLUKA geometry model (partially shown in Figure 9.24). Before being removed from the halo by either hitting the aperture or inelastic interactions inside a collimator, a halo proton touches the collimators on average more than once. Its hits are only kept in the maps if they occur in distinct turns, since possible multiple hits in the same turn are replicated as part of the shower propagation.

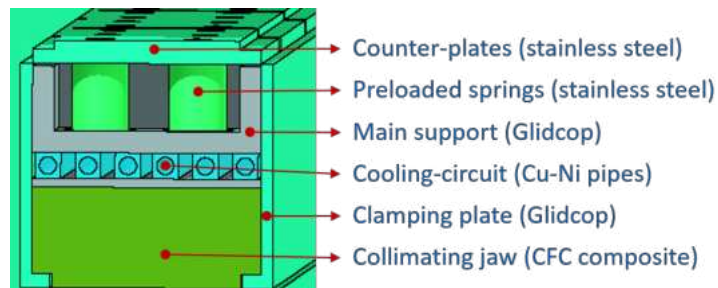


Figure 9.25: FLUKA model of a collimator jaw.

The vertical halo scenario, where hits are concentrated in the first TCP, was investigated through successive iterations as a representative case. This case is more critical than horizontal losses, since the vertical TCP is the furthest upstream and there is therefore more distance over which the shower can develop. In order to limit the power deposition on the jaws, three design measures were implemented. First, the TCP active length was halved (from 60 cm to 30 cm) with respect to that of the LHC TCP, reducing the shower development inside the absorbing material. Then the jaw thickness was increased (from 2.5 cm to 3.5 cm and 4.5 cm, for TCPs and TCSGs, respectively), since the metallic parts of the jaw cooling circuit turned out to be subject to the highest power density, because they were too close to the core of the secondary particle shower. Finally, the skew primary collimator was removed, because it was still collecting a total power which significantly exceeded 100 kW for the design BLT of 12 minutes, because it was downstream of the horizontal and vertical primaries.

The power deposition on the beam line elements and the infrastructure for the resulting configuration is given in Fig. 9.27. Almost half of the power is taken by the tunnel walls and a significant fraction is absorbed along the 2.7 km by the beam pipes.

Table 9.5 gives the loads on the collimation system elements. Among those in CFC, the first secondary collimator represents the most critical case. However, despite an integral load 14 times lower, the primary collimator which is directly impacted by the beam halo (TCP.D) is exposed to the highest power density, due to the multi-turn ionisation by primary protons at extremely small impact parameters.

Figures 9.28a and 9.28b show the power density distribution in the vertical TCP. For the design BLT of 12 minutes, the maximum value is 50 kW/cm^3 on the jaw surface layer, but $100 \mu\text{m}$ inside it is already an order of

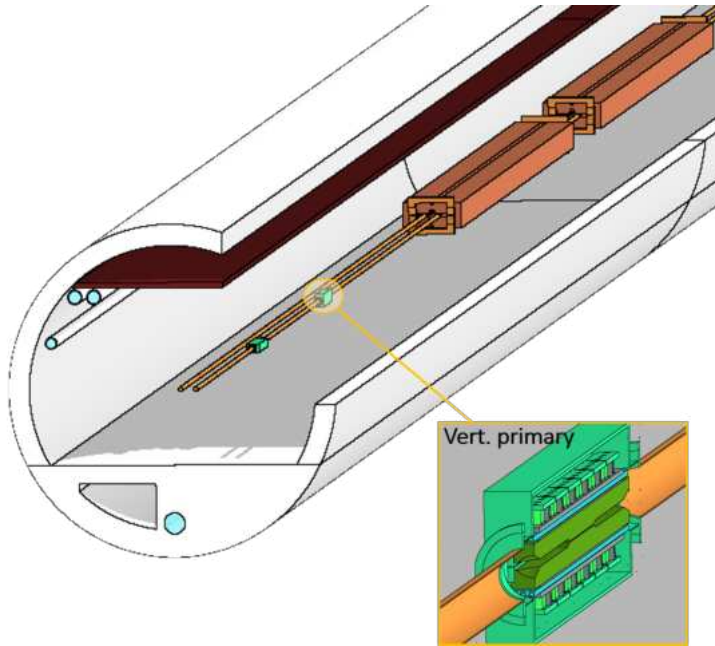


Figure 9.26: 3D view of the FLUKA model of the betatron cleaning insertion dogleg, hosting the primary collimators.

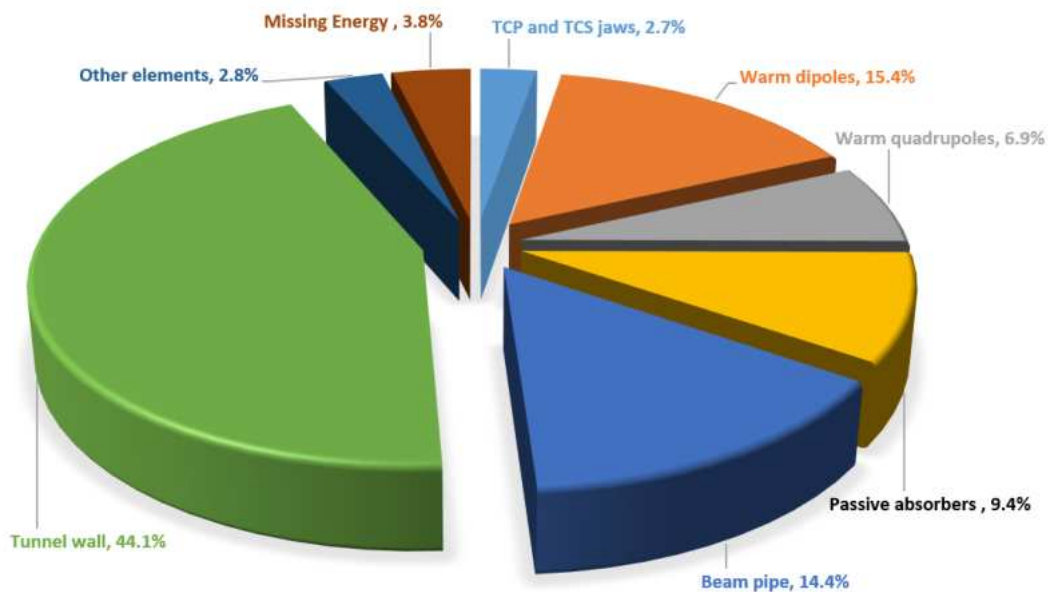


Figure 9.27: Power sharing in the betatron collimation insertion. The missing energy fraction refers to the energy spent in endothermic nuclear reactions as well as that carried away by the neutrinos generated.

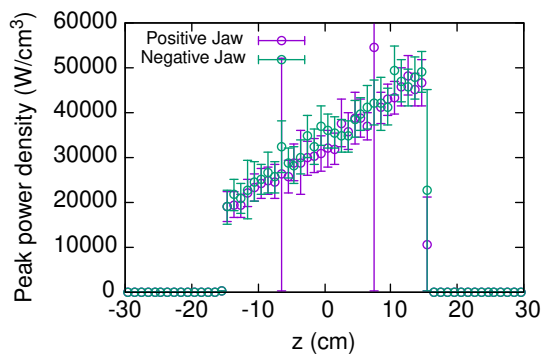
magnitude lower.

The horizontal TCP, which is rather exposed to the particle shower from the upstream collimator in the scenario studied, takes a total power 12 times higher than the latter, but its peak power densities are dramatically lower, up to 55 W/cm^3 , albeit extended to a much larger volume.

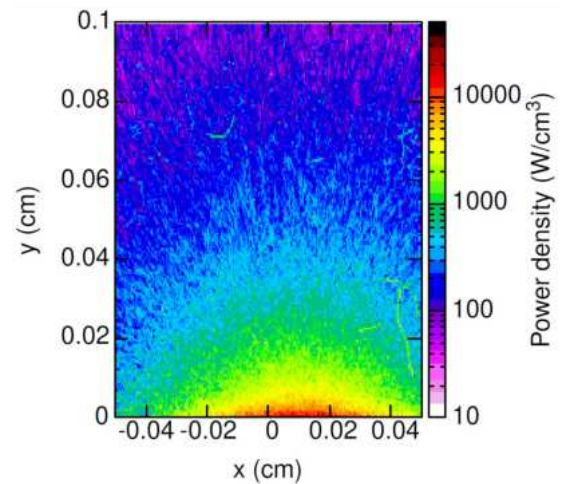
As pointed out above, the first TCS is affected by more severe conditions (in terms of total load). Figure 9.29 illustrates the 3D distribution of the nearly 100 kW, also showing the picture obtained with the standard LHC jaw thickness of 2.5 cm that induces power density values up to 800 W/cm^3 in the cooling pipes and an integrated load almost 2.5 times higher. With the proposed thickness increase to 4.5 cm, a maximum of 115 W/cm^3 is found in the absorbing material instead. For the following collimators, this is less critical. Further studies of the

Table 9.5: Total power on collimators and absorbers for 12 min BLT

| Primaries | Power (kW) |
|--------------------------|-------------------|
| TCP.D6L | 6.5 |
| TCP.C6L | 80 |
| Secondaries | Power (kW) |
| TCSG.A6L | 92 |
| TCSG.B5L | 9.8 |
| TCSG.A5L | 41 |
| TCSG.D4L | 33 |
| TCSG.B4L | 6.4 |
| TCSG.A4L | 12 |
| TCSG.A4R | 14 |
| TCSG.B5R | 3.3 |
| TCSG.D5R | 7.2 |
| TCSG.E5R | 12.5 |
| TCSG.6R | 2.3 |
| Active absorbers | Power (kW) |
| TCLA.A6R | 36.5 |
| TCLA.B6R | 2.0 |
| TCLA.C6R | 2.2 |
| TCLA.D6R | 1.6 |
| Passive absorbers | Power (kW) |
| TCAPA.6L | 545 |
| TCAPB.6L | 78 |
| TCAPC.6L | 484 |



(a) Peak power density profile along the length of the two jaws of the vertical TCP.



(b) Transverse power density distribution in the most impacted area (1 mm x 1 mm) of the vertical TCP. The jaw surface is at y=0. Values are given for 12 min BLT, with a transverse (x/y) resolution of 5 μ m and a longitudinal (z) resolution of 1 cm.

Figure 9.28: Power density distributions

thermo-mechanical response of the most critical collimators are shown in Section 9.7.

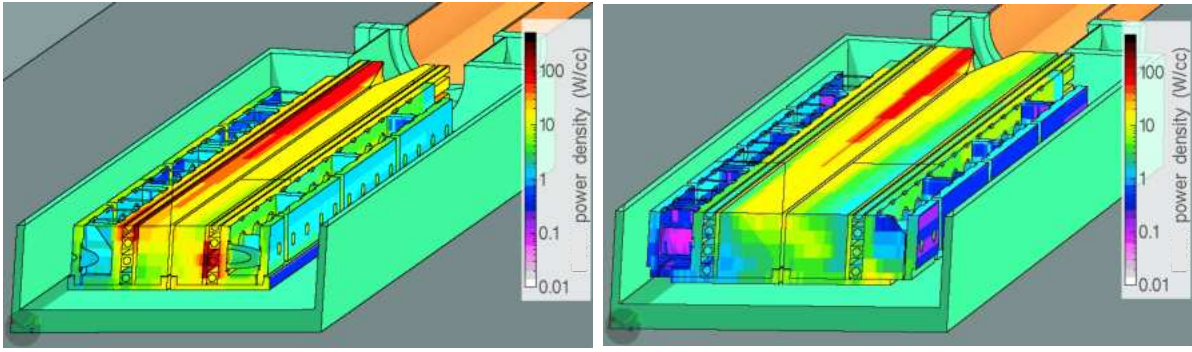


Figure 9.29: Power density distribution in the first secondary collimator for 12 min BLT. Left: LHC jaw thickness of 2.5 cm. Right: proposed jaw with thickness of 4.5 cm.

The two 17 m long warm dipoles that close the dogleg are particularly impacted, since they are exposed to the particle showers from the primary collimators. In the presence of the shortest passive absorber in front of it, the second module collects more than 1 MW for a 12 min BLT. For reference, the LHC module, which is 5 times shorter, would receive 22 kW assuming the same BLT with nominal beam parameters. As shown in Fig. 9.30, the MBW.A6 non-IP face reaches 270 kW/m, whereas over most of its length the absorbed power is at about 60 kW/m, which translates into a linear load between 10 kW/m and 100 W/m for more regular BLTs of 1 to 100 hours, respectively. This calls for a suitable cooling system and further optimisation of the front face protection, given that the first metre of the magnet absorbs more than 10% of the total power.

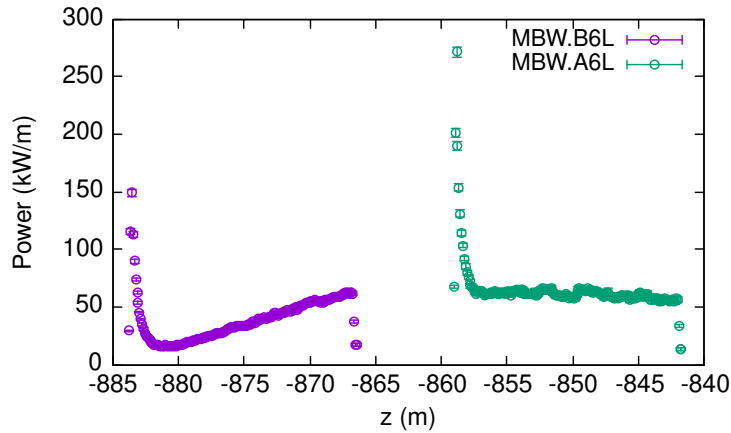


Figure 9.30: Integral power profile on the two warm dipoles after the primary collimators, for a 12 min BLT.

Looking at the dose accumulated in the coils, it is clear from Fig. 9.31 that the mechanical design provides a critical gain, by keeping the return coils as far as possible from the beam pipe. If the LHC design with return coils closer to the beam had been used, one order of magnitude higher localised peak dose would be expected.

9.6.1 Ozone production

From the calculation of energy deposition in air, one can estimate the resulting concentration of ozone with the formula:

$$N_{O_s} (ppm) = 9.28 \times 10^{-15} \times G(eV^{-1}) \frac{P_{eV} \left(\frac{eV}{s}\right) \tau(s)}{V(cc)} [1 - e^{-\frac{t}{\tau}}] \quad (9.3)$$

where the numerical constant is the ratio between the O_2 concentration and the number of air molecules per cm^3 , G is the number of O_3 molecules produced by the absorption of 1 eV (typically 0.06 to $0.074 eV^{-1}$) and

$$\tau(s) = \frac{1}{\left(\alpha + \frac{1}{\tau_{vent}} + \frac{kP_{eV}}{V}\right)} \quad (9.4)$$

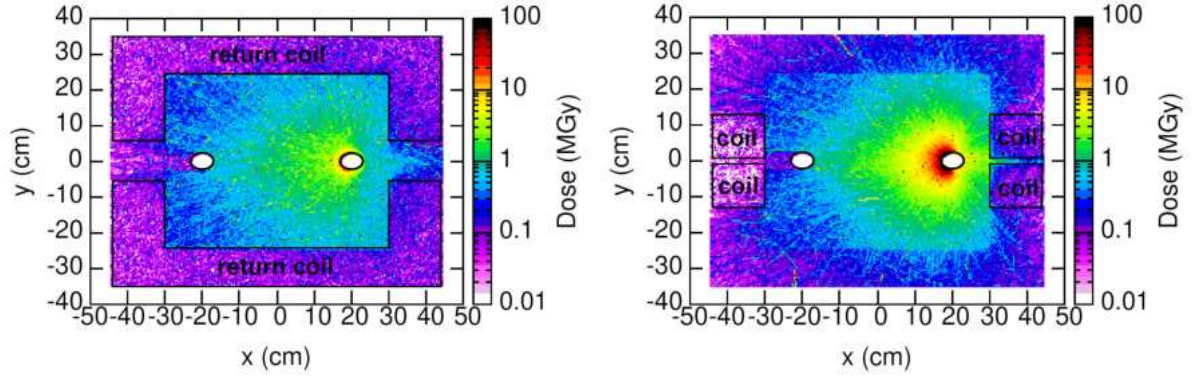


Figure 9.31: Transverse dose distribution at the MBW.B6 non-IP end, for a cumulative loss on the collimation system of 10^{16} top energy protons. Left: Return coil layer. Right: First internal layer. The coil position is indicated. Values are averaged over the respective layer length of 8 cm.

and

$$\alpha\left(\frac{1}{s}\right) = 2.3e - 4 \quad \& \quad k(\text{eV}^{-1}\text{cm}^3) = 1.4 \times 10^{-16} \quad (9.5)$$

being the ozone dissociation and decomposition constants, respectively. The second addend of the sum in equation 9.4 is the air renewal rate, i.e. the inverse of the ventilation time τ_{vent} needed to fully renew the volume of air, V , concerned.

In this model, the assumption of an average loss rate corresponding to 10^{16} protons per beam lost in the collimation system over an annual operation time of 5000 beam-hours yields a power deposition of 100 W in an air volume of 58000 m^3 . Since $\frac{1}{\alpha} = 1.2 \text{ h}$, a ventilation time larger than several hours would give an ozone concentration of 0.03 ppm for this power density in air. Ideally, to achieve a factor 10 reduction, a ventilation time of 8 minutes would be required.

9.7 Collimator robustness

Preliminary finite element analyses have been conducted on the most loaded TCS and TCP jaws. Simulations were carried out using the Ansys v18.2 finite element software. To begin with, a thermal analysis was performed, using the beam-induced energy deposition from FLUKA as input (see in Section 9.6). A static structural analysis was then coupled to the thermal study to obtain the mechanical response of the system. A detailed explanation of the method and of the relevant assumptions can be found in Ref. [263].

Starting with LHC specifications, the most loaded collimators are built from CFC. Losses during both 1 h and 12 minute BLT are studied for the secondary collimator, whereas only the 12 minute scenario is used for the TCP. This choice is driven by the fact that the 1h BLT scenario for the TCP involves a smaller amount of power than the 1 h BLT case for the TCS (which features the same overall geometry as the TCP). This means that the assessment of the TCP's global response (i.e. in terms of thermally-induced deflections of the jaws) results a less severe case. Therefore, since the goal is to analyse the robustness of the TCP components, which is mainly affected by peak energy deposition density, only the more severe case of a 12 minute BLT is considered.

In the 1 h BLT scenario, the beam-induced power deposition is applied in steady state. For the 12 minute BLT scenario, starting from this steady condition, the associated losses are ramped up during 10 ms and then kept for 10 s, to be subsequently ramped down again in 10 ms to the previous 1 h BLT load (see Fig. 9.32).

All analyses were carried out for heat loads for a scenario with the skew TCP removed, the TCPs shortened to 30 cm and the thickness of TCPs and TCSs increased to 3.5 cm and to 4.5 cm respectively. Moreover, given the preliminary nature of the study, some simplifying assumptions were made: a perfect bonding between the CFC absorbers and the Glidcop housing was assumed, as well as a linear constitutive law (i.e. the material response, in terms of strain produced under a given stress (and vice-versa) is linear, and the proportionality constant is the young's modulus, therefore the model cannot predict any plastic, pseudo-plastic, or viscous deformation) for the absorbers and a constant temperature profile for the water flowing inside the cooling circuit. The following sections discuss the results.

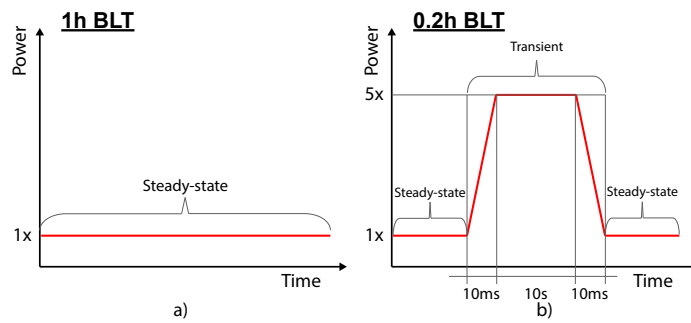


Figure 9.32: Load profiles considered in the thermo-structural analyses for a) the 1h BLT and b) the 0.2h BLT load case.

9.7.1 TCS collimator

The design of LHC TCSP collimators is considered as the base for the analysis of the most loaded TCS, namely the TCSG.A6L. The only difference between the two designs is that the former has Glidcop tapers to host the beam position monitors (BPMs), while the latter features CFC tapers (and no BPMs), and that the CFC thickness is increased by 2 cm.

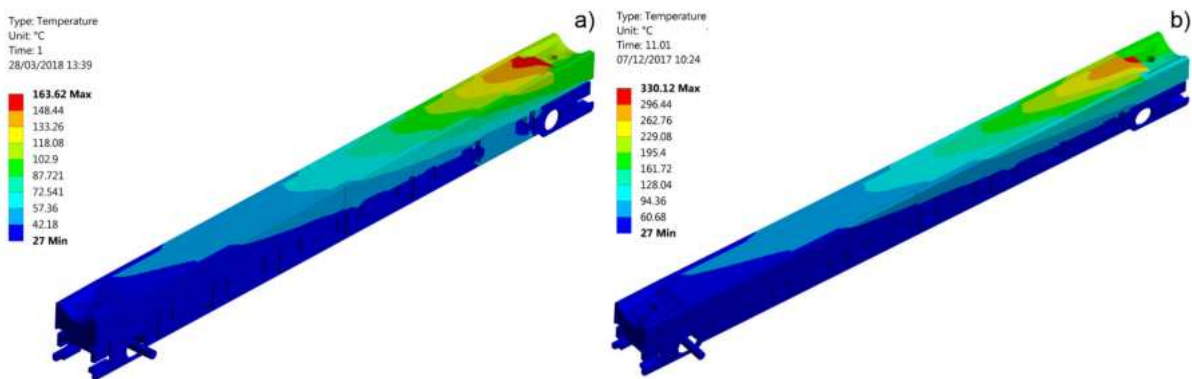


Figure 9.33: Beam-induced temperature fields on the first TCS for 1 h BLT (left) and 12 minute BLT (right).

The peak temperatures found on the jaw for the 1 h and 12 minute BLT cases are about 164°C and 330°C, respectively, as shown in Fig. 9.33. This induces thermal deformations, strains and stresses on the various components, due to the temperature gradient and the thermal-expansion coefficient mismatch among the different materials constituting the jaw. Temporary beam-induced deflections of up to 185 μm and 246 μm are obtained for the 1 h and 0.2 h BLT cases, respectively (see Fig. 9.34). Non-negligible strains are present in the contact region between the CFC absorbers and the housing: these values are mostly due to the bonded contact introduced in the model (perfect bonding) and to the linear character of the constitutive law adopted in the analyses of the absorbers, which both lead to an overestimation of the rigidity of the structure.

Finally, the cooling pipes were found to experience plasticity (see Fig. 9.35). The elastic limit of the CuNi 90-10, from which they are made, is about 100 MPa and it is largely exceeded both in the 1 h and in the 12 minute BLT case. This issue is not a showstopper, as it can be mitigated by adopting a higher yield-strength material for the cooling circuit.

9.7.2 TCP collimator

As done for the TCS collimators, with which TCPs share the same geometry apart from the absorber thickness, the design of LHC TCSP collimators is taken as the base design for the analyses of the vertical TCP, which is exposed to the highest peak power deposition density. In this case, however, only a 30 cm long region of the 3.5 cm thick absorbers has been subject to power deposition. The maximum temperature found on the CFC is about 660°C, as shown in Fig. 9.36. As a result, a maximum stress of 45 MPa is induced in the absorber-housing contact region along the direction normal to the planes of the CFC absorber, with an associated strain estimated to be about 8000

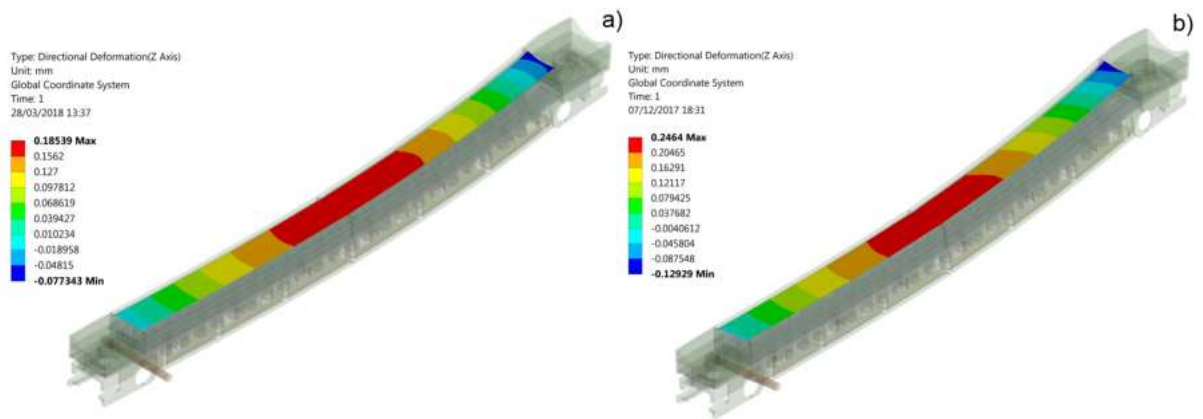


Figure 9.34: Normal deflections of the TCS jaw for 1 h BLT (left) and 12 minute BLT (right).

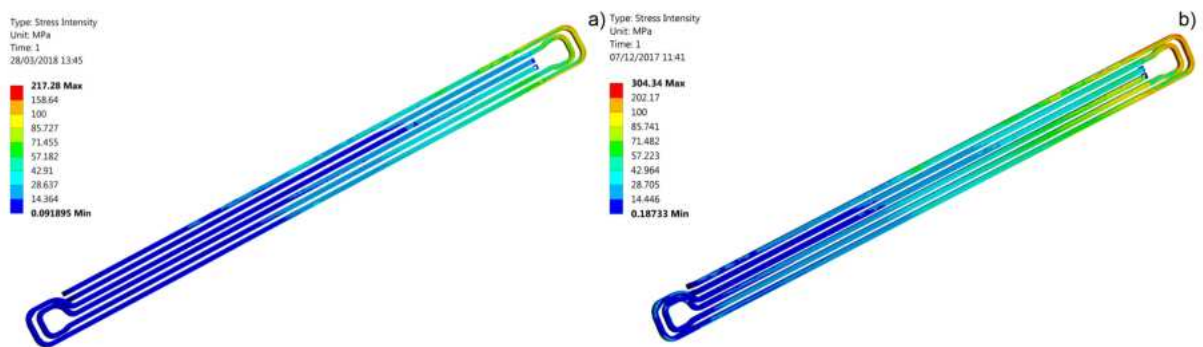


Figure 9.35: Stress intensity for the first TCS in the CuNi 90/10 cooling pipes for 1 h BLT (left) and 12 minute BLT (right).

$\mu\text{m/m}$. Theoretically this would lead to failure (see Fig. 9.37).

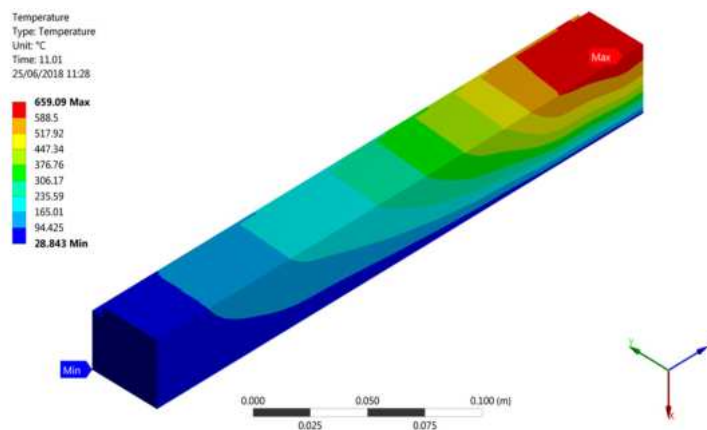


Figure 9.36: Beam-induced temperature fields on the vertical TCP for the 12 minute BLT case.

However, similar temperatures have already been achieved repeatedly on CFC absorbers during past experimental campaigns, without any sign of failure [264, 265]. In the HRMT-23 experiment [264], CFC absorbers reached a peak temperature of 685°C when impacted by 288-bunches with a total intensity of 3.79×10^{13} protons with $\sigma=0.35\text{mm}$. Furthermore, in the HRMT-36 experiment [265], CFC samples experienced a grazing pulse of 288 bunches, with a total intensity of 3.72×10^{13} protons and $\sigma=0.25\text{mm}$. No failure was found in either case, despite thermal gradients which largely exceed those of the present study shown in Fig. 9.38.

The high values of stress and strain obtained are therefore thought to be largely due to the simplified nature of the absorber-housing contact adopted in the analysis, as well as the hypothesis of linear elasticity for CFC. Both

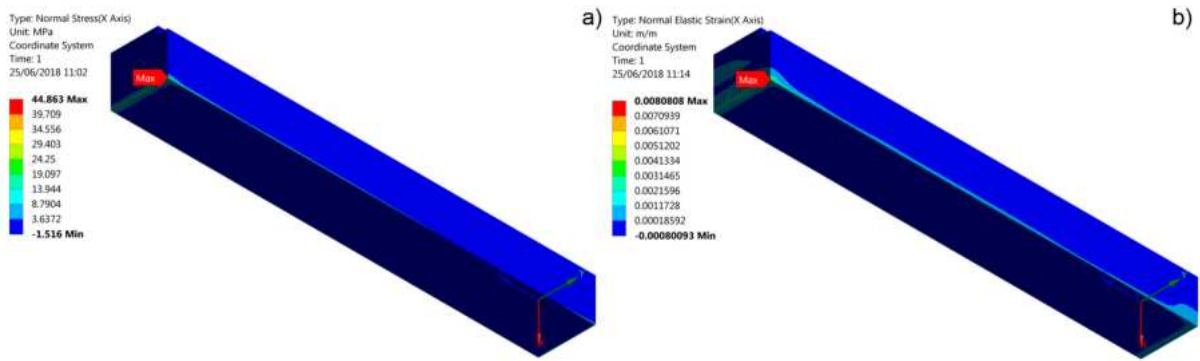


Figure 9.37: The estimated stress (left) and strain field (right) on the CFC absorber of the vertical TCP for the 12 minute BLT case.

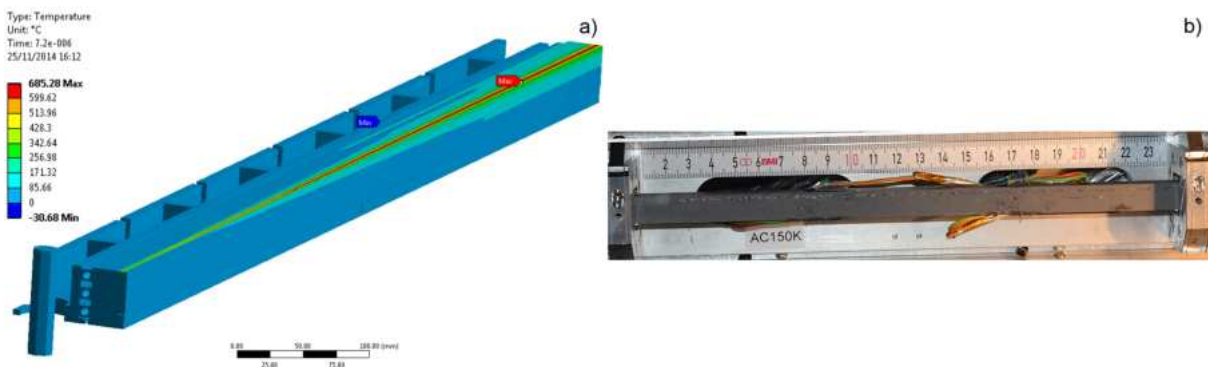


Figure 9.38: The temperature field over the CFC absorbers in HRTM-23 [264] (left) and the Mo-coated CFC sample impacted by a grazing shot which melted the coating and left the CFC substrate unbroken [265] (right).

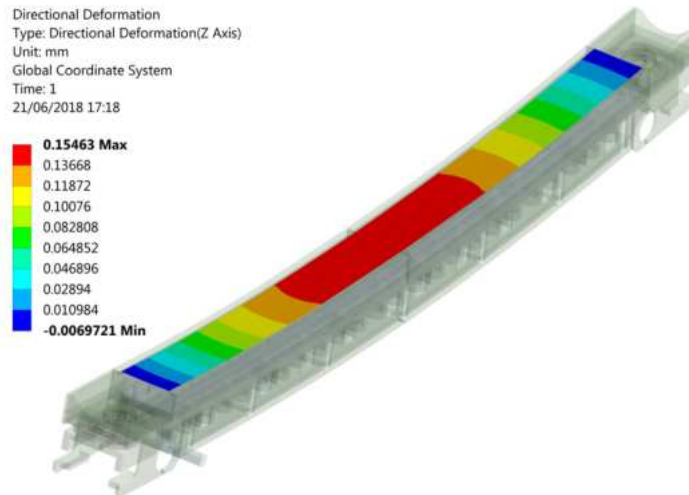


Figure 9.39: Beam-induced normal deflection on the vertical TCP for the 12 minute BLT case.

these assumptions create a much stiffer structure than is the real case. For the same reason, the beam-induced bending deflection of 155 μm shown in Fig. 9.39 is believed to underestimate the real deformation of the jaw. A maximum stress of 26 MPa was found for the cooling circuit, much below the elastic limit for CuNi 90-10. No plasticity was observed in the housing either, where a stress peak of 106 MPa is estimated compared to a yield stress for Glidcop of 294 MPa (see Fig. 9.40).

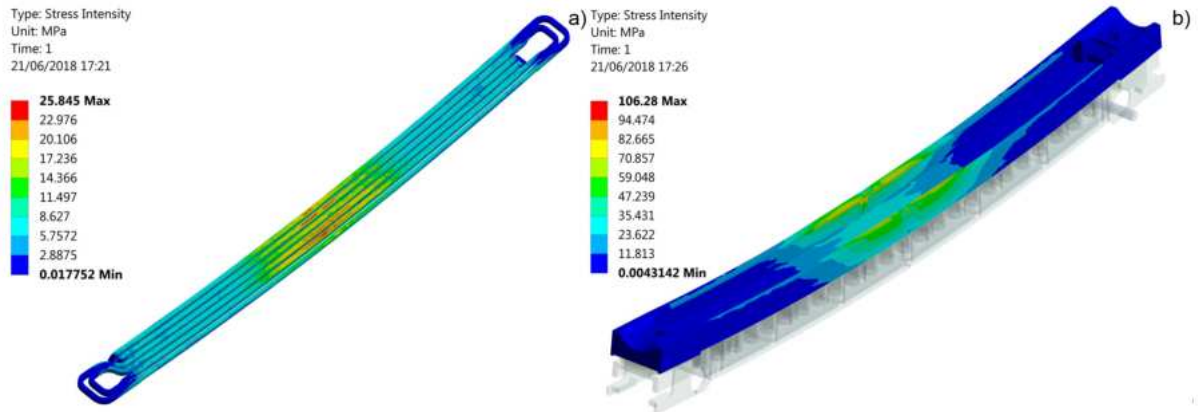


Figure 9.40: Stress intensity in the CuNi 90/10 cooling pipes (left) and the Glicop housing (right) of the vertical TCP during 12 minute BLT losses.

9.7.3 Result assessment

Thermo-mechanical analyses conducted on the most loaded TCS and TCP collimators highlighted some critical points which, without representing any clear showstopper at this stage, will need to be addressed in future design developments. The only case where permanent deformations occur is in the cooling pipes of the TCS, however, it is believed that this can be mitigated in a straight-forward way by a different material choice for the pipes.

Temperature peaks up to 660°C are observed in the CFC absorber of the vertical TCP, theoretically leading to failure. However, past tests have shown that no failure occurred in CFC absorbers at these temperatures [264, 265]; the numerical overestimation of stresses and strains is thought to be largely ascribable to the simplifying hypotheses introduced in the numerical models, leading to a stiffer structure. For the same reason an underestimation of the beam-induced bending deflections must be considered for both the case of TCS and TCP, where temporary deformations stay above 100 µm for all the load cases analysed. In the future it should be assessed if this has an impact on the cleaning inefficiency. Another potential concern is that the outgassing from graphitic materials such as CFC risks being very high at the simulated temperatures. The resulting beam vacuum and the possible need for additional pumping should also be evaluated in future studies.

Different avenues for improvement could be considered to address the points raised above – proposals include:

- lighter absorbers, to minimise the energy density on the jaw, e.g. carbon foams [266];
- more rigid housing and stiffener;
- higher water flow in the cooling pipes;
- monitoring, and possibly deformation-correcting, systems. A project in this sense has been launched by CERN and the University of Huddersfield under the framework of HL-LHC [267].

9.8 Advanced concepts and key R&D

The studies presented above are based on a collimation system that is scaled up from the LHC but using similar physical hardware. The simulations show that special measures such as the removal of the skew TCP, have to be taken to ensure safe operation with acceptable collimator loads during BLT drops. One important path for general improvements of the collimation system is to study novel materials with improved robustness and acceptable impedance. A better optimised and robust system design could be obtained with such materials if the skew TCP could be kept. A novel mechanical collimator design could also be investigated as an option to improve the robustness. Furthermore, the cleaning performance might be improved through iterations on the optics design, the layout of the two collimation insertions and the potential addition of more fixed masks.

An alternative collimation technique, such as crystal collimation [268], is a potential path for future study. With this technique, bent crystals are used to channel impacting halo particles, giving them an angular kick that is large enough to make them impact deeply at a downstream absorber. Experiments using an LHC test installation [269] have shown a significant improvement of the cleaning efficiency with Pb, Xe, and proton beams [270]. However, since the power deposition of the lost particles will be concentrated on the absorber, its design is very

challenging.

Another area for future studies is the control of the beam halo. It has been estimated that for the HL-LHC, the amount of energy present above 3.5σ in betatron amplitude is 35 MJ [271]. With a factor 12 higher total stored beam energy in the FCC-hh, the total energy in the halo alone risks to be of the order of 400 MJ, which is more than the total 362 MJ stored energy of the LHC beam. Any movement or jitter in the orbit risks causing large losses and beam dumps, that reduce the machine availability. One solution could be to use a hollow electron lens, as studied for HL-LHC [26]. By controlling the diffusion speed of halo particles, one can act on the time profile of the losses, for example by introducing a steady and controlled halo depletion, so that static halo population is significantly reduced. This would reduce the amount of beam scraped during any orbit movement. The parameters and feasibility of a hollow electron lens for FCC-hh remain to be studied.

9.9 Conclusions

A detailed design of the FCC-hh collimation system, including the collimators and the beam optics has been presented in this document. The hardware design of the collimators is based on concepts from the LHC and HL-LHC but with some further development to cope with the very high power loads expected from the FCC-hh beam loss scenarios. Like the LHC, infrastructure requirements include cooling water circuits, controls, and remote inspection and handling in high-radiation areas.

The performance of the FCC-hh collimation system has been studied in detail through particle tracking, energy deposition, and thermo-mechanical simulations. In spite of a stored beam energy of 8.3 GJ, it has been shown that the cleaning performance largely meets the requirements and that the machine can be protected from quenches during lifetime drops down to 12 minutes, which is pessimistically taken as a specification for the betatron cleaning. This has been achieved through the use of a system based on the LHC design but with the addition of extra dispersion suppressor collimators as well as local protection to alleviate losses at some critical locations. The cleaning of off-momentum losses at the most critical scenario, where the unbunched beam is lost rapidly at the start of the ramp, has also been found to be within the estimated limits.

The collimators themselves will be subject to very high loads during sharp BLT drops and this is a major challenge for the system design. Energy deposition studies and thermo-mechanical simulations have been used to study and optimise the loads, and through changes in the collimator design the peak power load can be brought down to manageable levels. Some issues still remain to be solved but they are not believed to be showstoppers. Other elements in the warm collimation section, such as the passive absorbers and the warm dipoles, receive very high instantaneous power loads, and the design and cooling of these elements need further study and optimisation.

Table 9.6: The full list of FCC-hh movable collimators, including their materials, angles, active jaw lengths, and settings throughout the cycle. The settings are given for the reference value of the normalised emittance of 2.2 μm .

| Collimator | Material | Angle (rad) | Length (m) | Injection ($n\sigma$) | Collision ($n\sigma$) |
|--------------|----------|-------------|------------|-------------------------|-------------------------|
| TCP.D4LJ.H1 | C | 1.57 | 0.3 | 7.6 | 7.6 |
| TCP.C4LJ.H1 | C | 0 | 0.3 | 7.6 | 7.6 |
| TCSG.A4LJ.H1 | C | 2.46 | 1 | 8.8 | 8.8 |
| TCSG.B3LJ.H1 | MoGR | 2.5 | 1 | 8.8 | 8.8 |
| TCSG.A3LJ.H1 | MoGR | 0.71 | 1 | 8.8 | 8.8 |
| TCSG.D2LJ.H1 | MoGR | 1.57 | 1 | 8.8 | 8.8 |
| TCSG.B2LJ.H1 | MoGR | 0 | 1 | 8.8 | 8.8 |
| TCSG.A2LJ.H1 | MoGR | 2.35 | 1 | 8.8 | 8.8 |
| TCSG.A2RJ.H1 | MoGR | 0.808 | 1 | 8.8 | 8.8 |
| TCSG.B3RJ.H1 | MoGR | 2.47 | 1 | 8.8 | 8.8 |
| TCSG.D3RJ.H1 | MoGR | 0.897 | 1 | 8.8 | 8.8 |
| TCSG.E3RJ.H1 | MoGR | 2.28 | 1 | 8.8 | 8.8 |
| TCSG.4RJ.H1 | MoGR | 0.00873 | 1 | 8.8 | 8.8 |
| TCLA.A4RJ.H1 | Iner | 1.57 | 1 | 12.6 | 12.6 |
| TCLA.B4RJ.H1 | Iner | 0 | 1 | 12.6 | 12.6 |
| TCLA.C4RJ.H1 | Iner | 1.57 | 1 | 12.6 | 12.6 |
| TCLA.D4RJ.H1 | Iner | 0 | 1 | 12.6 | 12.6 |
| TCLA.A5RJ.H1 | Iner | 0 | 1 | 12.6 | 12.6 |
| TCLD.8RJ.H1 | Iner | 0 | 1 | 21.0 | 35.1 |
| TCLD.10RJ.H1 | Iner | 0 | 1 | 21.0 | 35.1 |
| TCLD.11RJ.H1 | Iner | 0 | 1 | 21.0 | 35.1 |
| TCP.5LF.H1 | C | 0 | 0.3 | 10.8 | 18.1 |
| TCSG.4LF.H1 | MoGR | 0 | 1 | 13.0 | 21.7 |
| TCSG.3RF.H1 | MoGR | 0 | 1 | 13.0 | 21.7 |
| TCSG.A4RF.H1 | MoGR | 2.98 | 1 | 13.0 | 21.7 |
| TCSG.B4RF.H1 | MoGR | 0.189 | 1 | 13.0 | 21.7 |
| TCLA.A4RF.H1 | Iner | 1.57 | 1 | 14.4 | 24.1 |
| TCLA.B4RF.H1 | Iner | 0 | 1 | 14.4 | 24.1 |
| TCLA.5RF.H1 | Iner | 0 | 1 | 14.4 | 24.1 |
| TCLA.6RF.H1 | Iner | 0 | 1 | 14.4 | 24.1 |
| TCLD.8RF.H1 | Iner | 0 | 1 | 21.0 | 35.1 |
| TCLD.10RF.H1 | Iner | 0 | 1 | 21.0 | 35.1 |

9.10 Collimators and settings

| Collimator | Material | Angle (rad) | Length (m) | Injection ($n\sigma$) | Collision ($n\sigma$) |
|---------------|----------|-------------|------------|-------------------------|-------------------------|
| TCLD.8RA.H1 | Iner | 0 | 1 | 21.0 | 35.1 |
| TCLD.10RA.H1 | Iner | 0 | 1 | 21.0 | 35.1 |
| TCLD.8RG.H1 | Iner | 0 | 1 | 21.0 | 35.1 |
| TCLD.10RG.H1 | Iner | 0 | 1 | 21.0 | 35.1 |
| TCLD.8RB.H1 | Iner | 0 | 1 | 21.0 | 35.1 |
| TCLD.10RB.H1 | Iner | 0 | 1 | 21.0 | 35.1 |
| TCLD.8RL.H1 | Iner | 0 | 1 | 21.0 | 35.1 |
| TCLD.10RL.H1 | Iner | 0 | 1 | 21.0 | 35.1 |
| TCLD.7RF.H1 | Iner | 0 | 1 | 21.0 | 35.1 |
| TCLD.11RF.H1 | Iner | 0 | 1 | 21.0 | 35.1 |
| TCLAV.6RF.H1 | Iner | 1.57 | 1 | 14.4 | 24.1 |
| TCLD.8RD.H1 | Iner | 0 | 1 | 21.0 | 35.1 |
| TCLA.3RD.H1 | Iner | 1.57 | 1 | 11.8 | 11.8 |
| TCLA.4RD.H1 | Iner | 0 | 1 | 11.8 | 11.8 |
| TCTH.5LA.H1 | Iner | 0 | 1 | 14.0 | 10.5 |
| TCTVA.5LA.H1 | Iner | 1.57 | 1 | 14.0 | 10.5 |
| TCTH.5LG.H1 | Iner | 0 | 1 | 14.0 | 10.5 |
| TCTVA.5LG.H1 | Iner | 1.57 | 1 | 14.0 | 10.5 |
| TCTH.4LB.H1 | Iner | 0 | 1 | 14.0 | 10.5 |
| TCTV.4LB.H1 | Iner | 1.57 | 1 | 14.0 | 10.5 |
| TCTH.4LL.H1 | Iner | 0 | 1 | 14.0 | 10.5 |
| TCTV.4LL.H1 | Iner | 1.57 | 1 | 14.0 | 10.5 |
| TCTH.4LA.H1 | Iner | 0 | 1 | 14.0 | 10.5 |
| TCTVA.4LA.H1 | Iner | 1.57 | 1 | 14.0 | 10.5 |
| TCTH.4LG.H1 | Iner | 0 | 1 | 14.0 | 10.5 |
| TCTVA.4LG.H1 | Iner | 1.57 | 1 | 14.0 | 10.5 |
| TCDQA.A3RD.H1 | C | 1.57 | 10 | 9.8 | 9.8 |

Operation cycle

10.1 Turn-around concept

Operational cycles consist of a collision phase (or ‘physics production phase’), and a turn-around phase that prepares the machine for collisions. The optimum collision phase time for FCC with the nominal parameters [272] is 3.7 hours. This time is short when it is compared to LHC’s 10-20 hours long collision phases. As a result, the FCC’s production efficiency will be highly dependent on the average turnaround time.

Table 10.1 shows the breakdown of the FCC turn-around cycle phases and compares them to the LHC experience. The FCC values are goals for technical performance and not the values that the machine reaches during operation. To take into account the operational inefficiencies the luminosity production estimates use 4 hours (nominal) and 5 hours (initial) turnaround times [272]. These times also take into account the fact that due to failures some fills do not reach the collision phase. In these cases, the turn-around cycle needs to be restarted after the machine has recovered from the failure. However, the actual downtime is not included in these values.

Table 10.1: Technical performance targets for FCC-hh turnaround cycle [10], and observed minimum and mean turnaround times in 2017 [273].

| Phase | FCC target [min] | LHC min 2017 [min] | LHC mean 2017 [min] |
|-----------------------|------------------|--------------------|---------------------|
| Setup | 10 | - | - |
| Injection | 40 | 28.0 | 77.1 |
| Prepare ramp | 5 | 2.3 | 5.0 |
| Ramp-Squeeze-Flat top | 20+5+3 | 20.2+13.4+2.8 | 20.5+18.1+4.5 |
| Adjust | 5 | 3.3 | 7.9 |
| Ramp down | 20 | 36 | 153.2 ^a |
| Total | 108 (1.8 h) | 106.0 (1.8 h) | 286.3 (4.8 h) |

^aThe ramp down phase includes the recovery time from failures.

Reference [10] describes the FCC cycle phases in more detail, but a summary is also given here. During a setup phase, the magnet fields are set to the injection level and systems are prepared for beam injection. The injection phase starts with the injection of low energy probe beams that are used for measurements and correction of machine settings. This procedure reduces the risk of single-turn failures leading to severe fast beam losses, as the energy stored in a probe beam is non-damaging. After the measurements, the nominal beams are injected. The baseline scenario assumes that the LHC is the final injector for the FCC. In this case, filling of the FCC requires four LHC cycles that each last 10-12 minutes. Once the machine is filled, the systems are prepared for the ramp.

The ramp time depends on the performance of the power converters that provide current for the magnets. So-called beta-squeeze is also performed during the ramp. This procedure has been demonstrated in the LHC and is successfully used in other colliders [274]. After the ramp, beams are brought into collision with each other, and will also be required for this and additional preparations at the flat top energy. Ramp down is performed after the beam is dumped. FCC will have four quadrant power converters which will decrease the ramp down time

compared to the LHC.

When the FCC target times are compared to the LHC performance, two values stand out: the injection time and the ramp down time. Based on LHC experience, the current injection process could be improved by (i) adding beam diagnostics in the injectors to help identify beam quality issues as close as possible to the source, (ii) having fast diagnostics to understanding the cause of rejected injections, and (iii) improved synchronisation and coordination with the injectors [275]. The recorded LHC ramp-down time is misleadingly long. The time is dominated by failure recovery times, which are mostly cleared during this phase.

10.2 Start-up considerations

Hardware commissioning (HWC) prepares the machine for safe beam operations. In the LHC, main HWC steps are: 1) warm electrical quality assurance tests, 2) cool-down, 3) cold electrical quality assurance tests, 4) powering tests, 5) magnet training. The initial LHC commissioning, in 2008, would have taken more than 164 days [276]. Unlike the LHC, FCC magnets will be able to be powered up to the nominal field without experiencing training quenches which will avoid taking the long time required to train them in the machine.

A new collider will not immediately reach the nominal performance. In the LHC, the objective for the first operational years was to establish safe operations that created a basis from which to improve the performance. The LHC surpassed its nominal instantaneous luminosity performance in the fourth operational year. Figure 10.1 shows the evolution of the LHC's instantaneous luminosity. Similar performance evolution has also been witnessed in other colliders [277]. In the LHC, this evolution was the result of increasing the beam intensity and decreasing the β^* , crossing angle, and emittance [278]. As for the LHC, a start with relaxed machine and beam parameters gives a margin on the aperture that can be decreased as the knowledge of the machine accumulates.

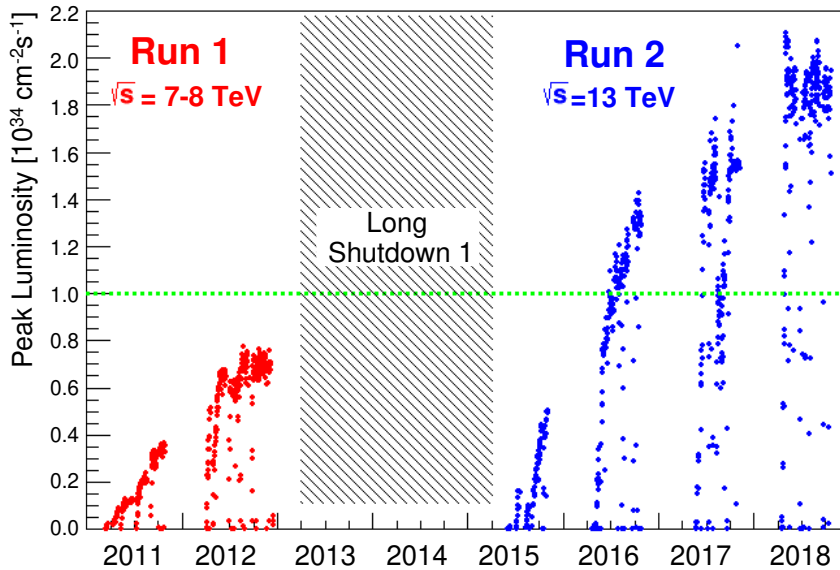


Figure 10.1: Peak luminosity evolution in the LHC [278]

Although the LHC has reached the design luminosity performance, it has not reached the design energy of 7 TeV. From 2010 - 2012, the energy in the LHC was limited to 3.5 TeV due to issues with superconducting splices [279]. Also, during the period 2015 - 2018 the energy was limited to 6.5 TeV. This limitation was mainly due to the time it takes to train magnets to the new higher energy level [280].

For the intensity, it can be assumed that the LHC experience can be repeated and that the FCC will reach the nominal performance in 4 ± 1 years. The intensity ramp could be faster, but this would limit the amount of early physics production with a limited intensity which, for a new machine, is still valuable for the experiments. Reaching the energy performance should be easier in the FCC, thanks to the expected improvements in magnet training performance.

10.3 Availability

Reaching the physics goals set for FCC-hh requires about 70% machine availability [272]. This is defined as the ability for the machine to perform operational cycles (collision and turnaround phases), i.e. the probability of not being in a fault state. Comparable availability figures have been reached with the LHC in the 2016-2017 runs [281, 282]. However, considering the increased machine complexity and the introduction of an additional injector in the chain, achieving the target availability poses major challenges for system design.

The key contributors for the LHC unavailability have been: the injector complex, cryogenics system power converters, quench protection system, beam dumping system, cooling & ventilation, radio frequency, electrical network, and beam loss monitors [281, 282]. Almost all of these systems will scale in complexity from the LHC to the FCC. Special attention needs to be given to the injector chain which will be increasingly important due to the short physics production time. The cryogenics system is itself relatively reliable, but it requires a long recovery time if the system heats up. Many of the failures observed are associated with electronics and therefore the effect of radiation on electronics needs to be taken into account during the design.

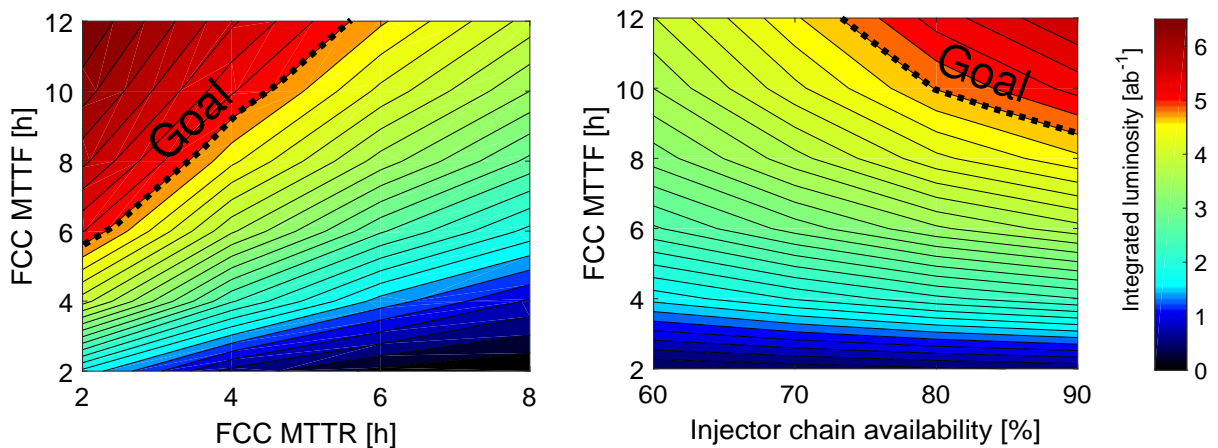


Figure 10.2: Effect of reliability, recoverability and injector availability on integrated luminosity with ultimate parameters [283].

Figure 10.2 (left) shows the evolution of the integrated luminosity as a function of the global machine mean-time-to-failure (MTTF) and mean-time-to-repair (MTTR) [283]. This figure is used to identify an acceptable parameter space for FCC systems availability to be identified. Figure 10.2 (right) shows the sensitivity of the integrated luminosity to the availability of the injector chain, setting an overall goal of 80-90%, depending on the MTTF. This figure is derived from a simulation [283, 284] that takes into account the operation cycle phases, luminosity production, and the system failures. This calculation uses parameters for nominal operation scenario as input and assumes 900 days for proton physics during a nominal operations period. LHC's availability is today 80%. As an injector for the FCC, the LHC energy and beam intensity will be lower and this will help the availability goals to be reached.

10.4 Alternatives and key R&D

A simple scaling from LHC, accounting for the increased system complexity indicates that it is necessary to develop innovative designs for new systems. General guidelines should be established for designing intrinsically reliable systems with built-in redundancy, remote diagnostic capabilities and limited exposure to the radiation. This will reduce the number of spurious beam aborts. Investing in advanced fault diagnostic and remote and autonomous maintenance can reduce the time for interventions and logistics. Further study of this topic giving high priority to critical systems (e.g. cryogenic system, beam dump, etc.) is needed for the definition of a strategy for spare part management.

The combination of FCC's increased dependence on the injector performance and the age of the CERN's injector complex in the FCC era make the consideration of alternative injectors options interesting. Further studies will identify the best injector option taking into account: availability, beam quality, available magnet technologies, capital investment to build a new superconducting machine or for consolidation of the existing CERN complex and operational expenditures. The injector option can also affect the injection time.

Along with availability studies, the short optimum luminosity production time and increased complexity show the need for studies to improve the operational efficiency. The main element which prolongs the LHC operation cycle is the time it takes to fill the machine. Discovering ways to reduce this time could benefit the FCC. Another aspect that has a direct impact on the cycle time is related to the power converters. Increasing the ramp and ramp down times may decrease the requirements for the converter design but this will have an adverse effect on luminosity production.

The LHC was able to surpass its design performance thanks to improvements in the beam and machine parameters. The performance is mostly a result of improved emittance preservation in the injectors and reduced β^* and crossing angle in the LHC. The operation procedures and principles for HL-LHC are currently being tested in the LHC and similar activities could be planned for the FCC procedures.

The impact of design changes that would have an effect on operation and production can be evaluated with accelerator availability modelling based on Monte Carlo simulations. These analyses allow the integrated luminosity to be predicted for different operating scenarios. Such models should be maintained and updated as the machine design evolves. The ongoing availability studies have determined the modelling concept [284]. The aim of studies is the global optimisation of the machine design for sustainable operation including: system availability budget, capital and operational expenditures, and energy efficiency. A modelling approach has been established for these analyses [285, 286].

Machine protection concepts

11.1 Architecture and powering of magnet circuits

For the FCC, the stored energy in the $\cos\theta$ dipole magnets (37 MJ) is 5 times higher than in the LHC and the arc between two access points is almost 3 times longer (8 km) than that of the LHC. In order to avoid excessive voltages to ground during fast power aborts in the FCC, there must be multiple circuits per arc and/or energy extractors distributed along the tunnel. The circuit layout adopted has multiple circuits per arc, each equipped with a power converter (PC) and a single energy extraction system (EE) located close to the access points. This solution optimises space in the tunnel and makes maintenance of PCs and EEs easier. Moreover, the availability of a superconducting link in the tunnel, already under study for the HL-LHC project [26], would greatly simplify the powering of multiple circuits.

An FCC powering sector (PS) is defined as half of the 8 km arc as shown in Fig. 11.1. The number of PS for the entire accelerator, (N_{PS}), including the 3.2 km long mini arcs, is 20. Figure 11.2 shows how each PS is subdivided into 5 independent circuits so that the total number of dipole circuits, N_{cir} , is 100. Since one PC and one EE are present for each circuit, N_{cir} is also the total number of these devices. The main parameters of the proposed dipole circuit layout are given in Table 11.1.

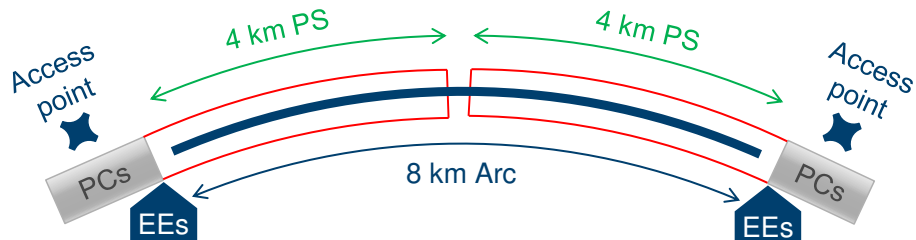


Figure 11.1: Layout of an FCC Powering Sector (PS). The location of power converters (PCs) and energy extractors (EEs) is also shown.

As shown in Table 11.2, the ramp-up time proposed for the FCC is the same as for the LHC in order to limit the turnaround time of the machine. Another relevant circuit parameter is the maximum voltage to ground which is the sum of half of the EE voltage (provided that the EE is grounded at the mid point) and the internal voltage developed during a magnet quench. Table 11.3 shows that, with half of the EE voltage (see details in EuroCirCol specification in Ref. [287]) being 1.3 kV, the time constant for the fast power abort is 110 s, slightly higher than that of the LHC. A fast discharge limits the number of neighbouring magnets which quench and thereby reduces the recovery time of the cryogenics. The higher time constant for the FCC is compensated by the lower nominal current so that the same integral of I^2 during discharge (MIITs) and cross-section of the copper busbar are obtained.

The main drawback of the proposed circuit layout is the relatively high number of powering devices which could lead to a reduction of the overall availability of the circuit. This aspect has been studied and the results are presented in Section 10.3.

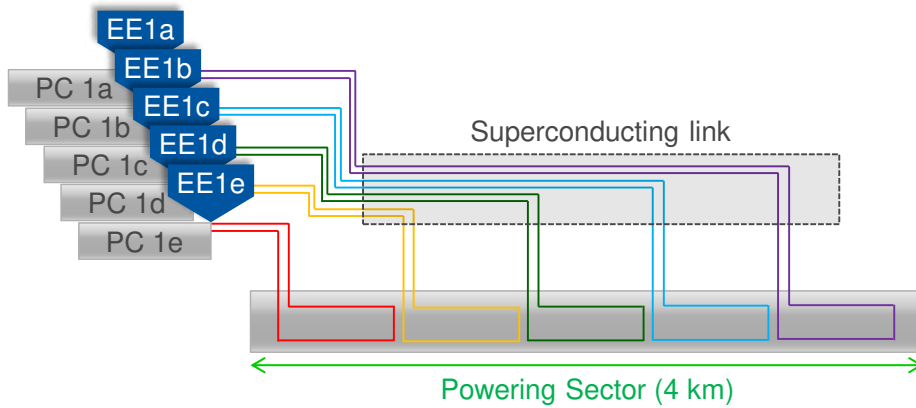


Figure 11.2: Schematic diagram of the dipole circuit architecture.

Table 11.1: FCC and LHC dipole circuit parameters.

| | Number of circuits N_{cir} | Nominal current | Magnets in series | Energy | Apparent inductance |
|-----|------------------------------|-----------------|-------------------|--------|---------------------|
| FCC | 100 | 11.2 kA | 44 | 1.6 GJ | 26 H |
| LHC | 8 | 11.9 kA | 154 | 1.1 GJ | 15 H |

Table 11.2: FCC and LHC dipole circuit parameters.

| | Ramp-up time | Max PC voltage | Max PC net power |
|-----|--------------|----------------|------------------|
| FCC | 20 min | 240 V | 2.7 MW |
| LHC | 20 min | 150 V | 1.8 MW |

Table 11.3: Fast power abort of FCC dipole circuit compared with LHC.

| | Half of EE voltage | Discharge time constant | MIITs | Busbar copper cross-section |
|-----|--------------------|-------------------------|-------------------------------------|-----------------------------|
| FCC | 1.3 kV | 110 s | $7 \cdot 10^3 \text{ MA}^2\text{s}$ | 270 mm^2 |
| LHC | 0.45 kV | 100 s | $7 \cdot 10^3 \text{ MA}^2\text{s}$ | 270 mm^2 |

The circuit architecture presented above is based on the parameters of the baseline magnet design, i.e. the $\cos-\theta$ option. When alternative magnet designs are considered, two groups can be identified: $\cos-\theta$ and block-coil designs have similar nominal currents and energies and, therefore, they lead to the same circuit layout. Common coil and canted $\cos-\theta$ options have higher stored energies, which is a clear disadvantage for circuit protection. At the same time however, they have lower inductances, which is an advantage. Applying the same circuit layout to these magnets would lead to larger MIITs (almost twice) and a faster discharge (about 20% lower time constant).

The powering of quadrupole magnets and correctors is considered less critical and will follow the same strategy as the dipole circuits.

11.2 Magnet protection and energy extraction

11.2.1 Energy extraction system technologies

Two distinct methods are proposed for the extraction of energy from the main dipole circuits. Discharging the energy into passive resistors as is currently done for the LHC magnet chains, and active energy extraction and recuperation. In the first option, a circuit breaker (a classical electro-mechanical switch or a switch based on a quenching superconductor) will be connected in series with the magnet chain, allowing for the dissipation of the stored energy in a dump resistor. Alternatively, an active energy extraction system with energy recovery capability, comprising a converter module is proposed. This module will maintain a constant voltage across the magnet chain during the extraction process and transfer the energy to a temporary storage unit, where it can be re-used

for example in the following energy ramp. The challenges encountered for the first option are the considerable duration of energy extraction, which is determined by the maximum allowed extraction voltage as well as the financial and environmental impact of releasing the energy stored in the magnets in the form of heat.

The second option offers a twofold solution to the aforementioned challenges. By performing the extraction at constant maximum voltage, the extraction time can be considerably reduced compared with a resistor-based system and also the energy recovery reduces operational losses and therefore has a smaller environmental impact. Although the powering architecture mentioned earlier will not be altered, the reduced extraction time could allow fewer independent circuits: their number can be reduced by 33% whilst keeping the same circuit MIITs. In turn, the solution will require an additional power converter as well as an intermediate energy storage unit, coupled with the proposed DC-grid powering and be capable of handling the high amounts of energy. The system reliability must remain high to ensure safe extraction of energy at all times in spite of the added complexity.

11.2.2 Quench detection technologies

The core strategy for an evolution of the quench detection system (QDS) for the FCC-hh is based on the concept of centralised data processing and quench detection as presented in Fig. 11.3. It enables the instrumentation units located in the tunnel (QS) to be considerably simplified, thus reducing their susceptibility to the expected levels of ionising radiation. A development challenge is to evolve them into a set of versatile distributed intelligent sensors capable of providing the reconfigurable, high bandwidth and high resolution instrumentation required by all FCC superconducting circuits. A high level of standardisation of the equipment located in the tunnel will facilitate maintenance, which likely will evolve towards fully autonomous maintenance provided by robotic means. However, this requires careful mechanical integration developed closely in conjunction with the electronic and electrical design processes. The central data processing units (QPU) will be located outside the FCC tunnel and interconnected with high speed and highly deterministic data links to the intelligent instrumentation sensors. The centralisation enables data acquisition from multiple sources, which allows novel quench instrumentation technologies to be employed. These will improve noise suppression and accuracy by performing correlation across multiple channels of the superconducting circuits. A considerable challenge for the development of the global protection scheme is designing a digital system based on a fast and reliable software-defined quench detection system which is also capable of dealing with very large data volumes.

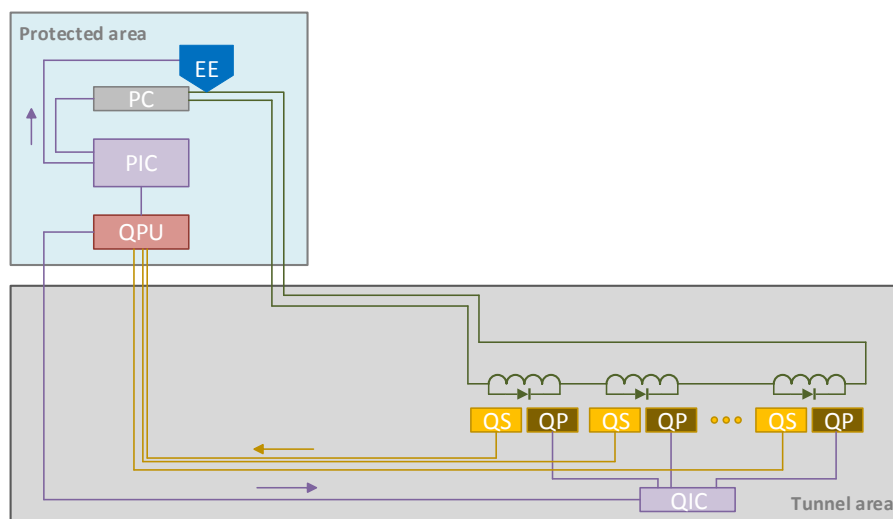


Figure 11.3: Overview of proposed QDS architecture for one of the 8 dipole circuits in an FCC arc.

Deep learning neural networks could complement the centralised quench detection scheme, in order to provide an accurate assessment of the operational state of the system. Given the vast amount of data, neural networks could also provide additional input to the quench detectors to improve their resolution and accuracy. However, in order to distribute interlock signals among protection devices located in the FCC tunnel (QP), significant changes are required in local interconnections (QIC) by the developing high speed, low latency and high reliability optical data links. A packet based solution has been proposed to provide the required timing accuracy and precise addressing of single or groups of protection units. Furthermore, enhanced embedded error detection and correction

mechanisms will allow constant assessment of the state of the data link by monitoring the bit error rates. The proposed evolution of the quench detection system will significantly ease the fully autonomous analysis of events and faults in the FCC machine.

11.3 Machine protection concepts

11.3.1 Damage potential and relevance of machine protection

In the LHC, the energy stored in one of the two counter-rotating proton beams reaches 360 MJ, for the nominal beam parameters, of 2808 bunches at 7 TeV with a bunch intensity of 1.15×10^{11} protons [17]. This energy is sufficient to melt 500 kg of copper when heated from room temperature. The energy stored in the beams will be doubled in the HL-LHC [26] compared to LHC. In FCC the nominal number of bunches per beam will be 10 400 and the bunch intensity will be 1.0×10^{11} , leading to an energy of 8.3 GJ stored in each beam, which is 20 times higher than in the LHC. As the proton energy increases, the quench limit of the superconducting dipole magnets in terms of protons lost per metre per second drops to 5×10^5 p⁺/m/s at 50 TeV, 15 times lower than that of the LHC at 7 TeV [288, 289]. For many failure cases, the beam energy would be concentrated on a spot size smaller than 1 mm², making it even more destructive if a beam accident occurs. In the case of the 50 TeV FCC beam and a normalised emittance of $\epsilon_{n,rms} = 2.2 \mu\text{m}$, the beam size will be 0.09 mm for a typical betatron function of 200 m. Thus, the beam energy density will be of the order of 200 GJ mm⁻², about a factor of 150 higher than at LHC (assuming a typical β function of 100 m and a beam σ of 0.22 mm for the LHC).

To provide a quick assessment of beam impact on FCC-hh components and its injector chain, the energy deposition of protons in copper and in graphite has been simulated using the Monte-Carlo code FLUKA [62, 63]. The proton energy range from 50 MeV to 50 TeV, and three representative beam sizes for each energy sample [290] were selected for the simulation. Results for an RMS beam size of 0.2 mm are shown in Fig. 11.4. For this beam size, one nominal bunch with 1.0×10^{11} protons at injection energy of 3.3 TeV can melt the copper around the energy deposition peak. At the top proton energy of 50 TeV, one bunch is sufficient to evaporate copper.

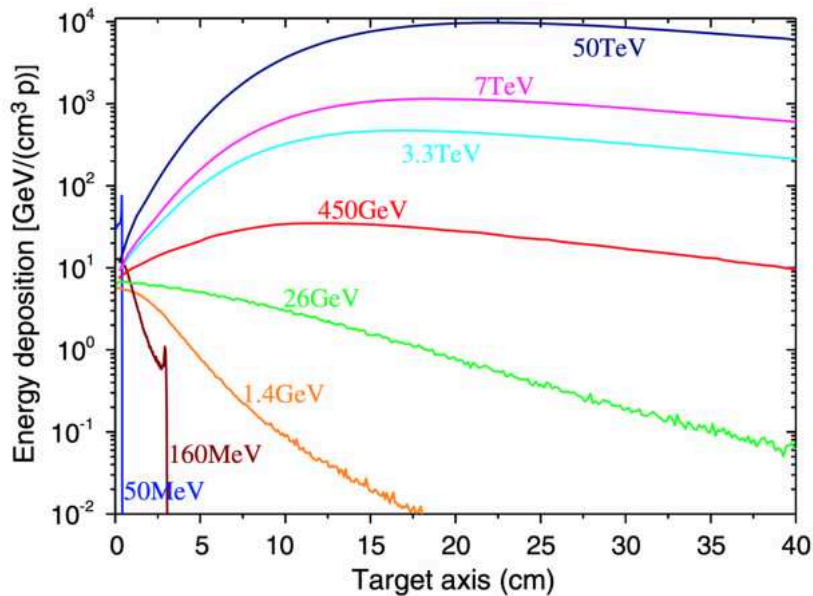


Figure 11.4: Simulated energy deposition along the axis per impacting proton as a function of depth in a cylindrical copper target. For the simulations, the RMS beam size was kept at 0.2 mm, while the beam energy was changed between 50 MeV and 50 TeV.

The number of protons needed to melt copper at the maximum energy-deposition point for different energies and beam sizes is given in Table 11.4. Based on these simulations, a beam intensity to maintain a reasonable safety margin with respect to the estimated damage limit has been defined as 5.0×10^8 protons. This is a vital concept for the initial commissioning and setup of the machine at 50 TeV. This number is also important for the definition of the dynamic range required for beam instrumentation devices which will interact with the Machine Protection System (MPS).

Table 11.4: Number of protons needed to melt copper at the maximum energy-deposition point for different energies and beam sizes [290]. The safe beam intensity at 50 TeV has been defined as 5.0×10^8 protons.

| Energy [TeV] | RMS beam size [mm] | N_p |
|--------------|--------------------|----------------------|
| 0.45 | 0.1 | 6.4×10^{11} |
| | 0.2 | 1.1×10^{12} |
| | 0.8 | 3.1×10^{12} |
| 3.3 | 0.1 | 4.6×10^{10} |
| | 0.2 | 8.0×10^{10} |
| | 0.4 | 1.5×10^{11} |
| 7.0 | 0.1 | 1.8×10^{10} |
| | 0.2 | 3.3×10^{10} |
| | 0.4 | 6.2×10^{10} |
| 50 | 0.1 | 1.9×10^9 |
| | 0.2 | 3.9×10^9 |
| | 0.4 | 7.5×10^9 |

In a worst-case failure scenario, a large number of bunches can be lost at the same place. This could occur e.g. during beam injection or extraction due to an erroneous deflecting angle. If this happens, an effect known as hydrodynamic tunnelling [291–293] will become significant. In this process following bunches will penetrate deeper into the target because the material density around the beam has been substantially reduced by the strong radial shock wave generated by the preceding bunches. To simulate this phenomenon it is therefore necessary to run an energy deposition code and a hydrodynamic code iteratively. Simulations in which the FLUKA and BIG2 codes were coupled showed that the penetration depth of a nominal LHC beam with an RMS beam size of $\sigma_{x,y} = 0.2$ mm was about 35 m in copper [293]. In graphite, the penetration depth reached 25 m with $\sigma_{x,y} = 0.5$ mm [294]. Recent simulations illustrated that the full 50 TeV FCC beam would penetrate 350 m in copper with $\sigma_{x,y} = 0.2$ mm [103].

11.3.2 Classification of FCC-hh failure modes and mitigation strategies

The significance of beam-related failures depends on the amount of beam energy lost and on the time scale of the losses. Table 11.5 shows typical beam lifetimes for different operational and failure scenarios comparing FCC-hh and LHC.

Based on the speed of the failure onset and the subsequent increase of induced beam losses, one can distinguish three main failure categories:

- *Slow failures* (see Table 11.6): This includes power converter failures, magnet quenches or RF failures that lead to a beam lifetime of the order of one second. If the failure is detected properly, there is enough time to dump the beam. However, recurring faults might lead to increased induced radioactivity.
- *Fast failures* (see Table 11.7): This includes unidentified falling objects (UFOs) [295, Chapter 5], fast equipment failures like power supply failures of magnets installed at positions with high β -function or with short time constant field decays, resulting in a beam lifetime of the order of a few ms (tens of turns). The majority of such failures lead to fast movements of the orbit or fast emittance growth. Protection from such events relies on monitoring of the hardware systems and fast detection of the failure onset directly at the source. An example is the monitoring of magnet currents using a fast magnet current change monitor (FMCM) [296]. Monitoring of the hardware systems must be complemented by fast beam loss and beam position monitoring. For all fast failures it is important that the beams are dumped as soon as possible. Fast magnet failures are very likely to occur during the operation of the FCC-hh, since more than 5000 main dipole and quadrupole magnets will be installed, together with a large number of normal conducting magnets, orbit correctors, etc. Experience from other accelerators indicates that thunderstorms frequently lead to trips of power converters, as well as a large number of utilities/services, leading to correlated failures. Collimator jaw positions, expressed in the transverse beam size σ , are typically placed at a position between 5σ and 9σ for efficient beam cleaning. A beam displacement of up to 1.5σ during 2 ms is just acceptable, assuming that 1 ms is needed to dump the beam. If the beam displacement happens faster, the damage

Table 11.5: Beam Losses and Protection Strategies for Various Operation and Failure Scenarios

| Beam lifetime | Beam Power Lost | | Scenario | Strategy and Remarks |
|--------------------------|------------------|--------------|---|---|
| | LHC | FCC-hh | | |
| 100 h | 1 kW | 23 kW | <i>Optimum operating conditions.</i> | (Possible) upgrade of the collimation system after some years of operating experience. |
| 10 h | 10 kW | 230 kW | <i>Steady beam loss</i> , acceptable operating conditions (expected during early operation). | Operation acceptable; collimators must absorb large fraction of beam energy. |
| 12 min | 500 kW | 12 MW | <i>Abnormal operating conditions</i> (during change of optics, tuning, collimation aperture setting, etc). | Operation only possible for a short time (≈ 10 s); requires efficient collimator system and active cooling of the jaws. |
| 1 s | 362 MW | 8.3 GW | <i>Slow failures</i> (powering failures, magnet quenches, RF failures, ...). | Detection of failure; beam must be dumped rapidly. |
| A few ms (tens of turns) | ≈ 100 GW | \approx TW | <i>Fast failures</i> (UFOs, fast equipment failures, e.g. magnet failures at high beta function or with short time constant). | Fast detection of hardware failures or beam losses; beam dump as fast as possible. |
| 1 turn to a few turns | < 4 TW | < 26 TW | <i>Ultrafast failures</i> (Single-passage beam losses during injection and extraction; ultrafast equipment failures, e.g. phase jump of crab cavities). | Passive protection with collimators and absorbers (made of novel or sacrificial materials) is required; as a last resort, an asynchronous dump might be needed. |

limit of the collimators might be exceeded before the beam is dumped completely. This limit defines the minimum time constant of the field decay for a dipole kick. For quadrupoles, the limit is estimated by allowing a tune change of 0.01 or a β beating of 20% within 2 ms. [297]

Various magnet failures have been analysed using the existing beam optics design of the FCC-hh. The most critical magnet failures are listed in Table 11.7. The study showed that critical failures are quenches of superconducting magnets at positions with very high β -functions (low-beta triplets) and powering failures of normal conducting magnets with fast field decay (separation dipoles). The consequences of combined magnet failures, e.g. separation dipoles in interaction regions IRA and IRG failing simultaneously, could be much more severe depending on the phase advance between the elements. However, such combined failure modes have a low probability of occurrence, so the risk is low. For normal conducting magnets installed in areas with high β -functions, the powering circuits have to be designed with a large enough time constant for the field decay. Alternatively, the magnet could be connected in series with a superconducting solenoid to increase the time constant for the field decay, thereby relaxing the parameters for the protection system.

- *Ultrafast failures* (see Table 11.8): This includes single-passage beam losses during injection and extraction [298, 299], ultrafast equipment failures like phase jumps of crab cavities leading to intense beam losses within a few turns [300, 301], missing beam-beam deflection during beam extraction [302] and quench heater firings [303]. Since the failure occurs on a timescale that is smaller than the minimum time required to detect and extract the beam, protection from such specific failure cases relies entirely on passive protection devices, i.e. beam absorbers and collimators that need to be positioned close to the beam to capture the particles that are accidentally deflected.

All typical failure modes are summarised in Tables 11.6, 11.7, and 11.8, together with the failure scenarios, potential consequences, and mitigation strategies.

Table 11.6: Slow failures and possible mitigation strategies for FCC-hh

| Failure mode | Consequences | Mitigation strategies |
|---|---|---|
| Powering failure of normal conducting magnets with moderate β function. | Distortion of the closed orbit, or tune change. | – After detection of failure or abnormal beam parameters, dump the beam rapidly if necessary. |
| Quench of one main dipole or quadrupole. | Change of the closed orbit or optics. | – After detection of failure or abnormal beam parameters, dump the beam rapidly if necessary. |
| RF accelerating cavity failures. | More particles in the tail due to dephasing, more particles in the beam-free abort gap. | – After detection of failure or abnormal beam parameters, dump the beam rapidly if necessary. – Improved abort-gap cleaning. |

11.3.3 Machine-protection requirements and system layout

For the operation of accelerators with high-power beams or for sub-systems with large stored energy, machine protection involves methods and technologies to identify, mitigate, monitor and assess the technical risks from failure modes which might substantially damage accelerator systems or cause a significant interruption to operation [307]. It includes an ensemble of hardware and software systems, commissioning and operational procedures. There are several general requirements for the protection systems. The first is to protect the accelerator equipment from damage and the superconducting magnets from quenches. The second is to protect the beam, i.e. the protection systems should only dump the beam when necessary. Unnecessary (‘false’) beam dumps should be avoided in order to preserve machine availability. The third is to collect relevant data: in case of failure, complete and coherent diagnostics data should be provided to understand what caused the failure and if the protection systems worked correctly.

Table 11.7: Fast failures and possible mitigation strategies for FCC-hh

| Failure mode | Consequences | Mitigation strategies |
|---|--|--|
| Powering failure of normal conducting separation dipole ‘D1’ in insertions IRA/IRG. | The beam can be displaced quickly from nominal orbit, leading to fast beam losses. | <ul style="list-style-type: none"> – Time constant of the field decay must be >15 s (optics dependent). – Connect a superconducting solenoid in series to increase the time constant, if the powering circuit cannot fulfil the requirement for the time constant. – Detect failure at hardware level (e.g. FMCM). – Detect initial impact of the failure on the beam (fast BPM, BLM, etc). – Dump beam as fast as possible. |
| Quench of one magnet in the low- β triplets. | <p>Tune change and β-beating, leading to resonances and beam instabilities.</p> <p>In addition, a fast dipole kick (250 μm in 20 ms) due to current redistribution in a triplet quench was observed at the LHC [304].</p> | <ul style="list-style-type: none"> – Fast detection of the quench. – Time constant of the field decay must be >140 ms (optics dependent). – Dump beam as fast as possible. |
| UFOs, type 1 and type 2. | Beam instabilities and fast beam losses. Significant beam losses on a millisecond time scale at the LHC, e.g. 16L2 events [305]. | <ul style="list-style-type: none"> – Fast detection of initial effects on the beam and trigger dump. – Make use of the conditioning effect during machine operation. |
| Beam transverse damper excites beam resonantly. | Fast beam deflections. | <ul style="list-style-type: none"> – Avoid coherent excitation of transverse dampers/correctors. |
| Vacuum valve or beamscreen in the beam pipe. | Aperture reduction and fast beam losses. | <ul style="list-style-type: none"> – Accurate control and position interlocking of movable devices. – Dump beam if a device approaches the beam. |
| Vacuum leak or wire scanner in the beam. | Beam scattering and fast beam losses. | <ul style="list-style-type: none"> – Hardware interlock for wire scanner. – Fast detection of initial beam losses and trigger dump. |
| Beam instability due to too high a beam current/e-clouds. | Fast beam losses. | <ul style="list-style-type: none"> – Fast detection of beam losses and/or beam position. – Dump beam as fast as possible. |

Table 11.8: Ultrafast failures and possible mitigation strategies for FCC-hh

| Failure mode | Consequences | Mitigation strategies |
|--|--|---|
| Wrong deflecting angle of injected beam (injection kicker failure or wrong angle from transfer line). | Large number of bunches lost at the same location in the accelerator. | <ul style="list-style-type: none"> – Transfer line collimators. – Injection absorber. – More detailed studies in Ref. [15]. |
| Wrong deflecting angle of extracted beam (energy tracking, kicker or septa failure during extraction). | Large number of bunches lost at the same location in the accelerator or dump line. | <ul style="list-style-type: none"> – Two-sided protection absorbers for septum and other magnets. – More detailed studies in Ref. [15]. |
| Dilution kicker failure. | Higher energy density deposited in the dump block due to reduced dilution. | <ul style="list-style-type: none"> – Dump block designed to survive when 90% dilution capability is kept. – Possibly, a liquid dump material which would not need dilution kickers. Assuming a water target, the beam would penetrate about 1.3 km into the target for a beam size of $\sigma_{x,y} = 0.4$ mm [306]. Hence, the beam size would have to be increased to centimetres to reduce the tank length and allow the use of a beam window separating the beam transfer line and the water. [116] |
| For crab cavities (CCs), voltage/phase changes exponentially with a time constant of $\tau = 2Q_{ext}/\omega$ due to equipment failure, or faster due to quenches or multipacting [301]. In the worst case, phase could jump 90° in one turn. | Beam centre could be deflected of the order of one σ in one turn, leading to significant beam losses in 3 turns 90° [301]. | <ul style="list-style-type: none"> – Increase Q_{ext} and the number of CCs per beam per IP side. – Avoid simultaneous failures of multi-cavities and multi-cavity feedback for field-error compensation. – Hollow e-lens to deplete halos. – Make phase advance between CCs and certain collimators close to 90°. – For the fastest CCs failure, there might be no time to extract the beam in a controlled way, thus, passive protection and/or an asynchronous dump trigger might be needed. |
| Absence of beam-beam deflection due to the non-simultaneous extraction of the two beams. | Fast deflection of the remaining circulating beam, high losses on collimators if the beam halo is populated. [302] | <ul style="list-style-type: none"> – Deplete and control the beam halo population using e-lens. – Monitor the halo population. If the halo becomes too large, dump the beams. |
| Quench heater or CLIQ magnet protection firing on the circulating beam. | Current discharge produces a magnetic field deflecting the beam. [302] | <ul style="list-style-type: none"> – Ensure beam is dumped before triggering quench heaters or CLIQ. – Reduce probability of spurious firing and reduce effect on beam by optimised connection scheme. |

The machine protection strategy for FCC-hh [297, 298, 308] will be based on the remarkably successful layout of the LHC Machine Protection System [307, 309, 310], which has allowed safe and reliable operation without beam accidents and with high availability for almost 10 years. In the LHC, momentum and betatron collimators are installed to clean the beam halos. Collimators define the aperture during operation, so that beam-induced quenches of the superconducting magnets can be avoided as much as possible. Dedicated beam diluters provide passive protection against ultrafast beam losses e.g. during injection or extraction failures. Fast and reliable instrumentation and beam monitoring systems actively detect element failures and abnormal beam parameters (for example, beam loss rates). These are able to trigger a beam dump request before damage thresholds are reached. A beam interlock system (BIS) provides highly reliable transmission of the dump request from the monitoring system to the beam dumping system. In case of a failure, the beam is extracted from the ring as fast as possible and guided into a beam stopper. The extraction kicker magnets of the beam dumping system are triggered during a particle-free abort gap (synchronous beam dump), to prevent particle losses during the kicker rise time. The beam is then extracted in a single turn. Other kickers installed in the extraction line dilute the energy density, and the beam is dumped on a block designed to withstand the impact of the diluted full beam.

The machine protection systems have to work correctly during the entire operation cycle. The various challenges throughout the cycle are illustrated in Fig. 11.5.

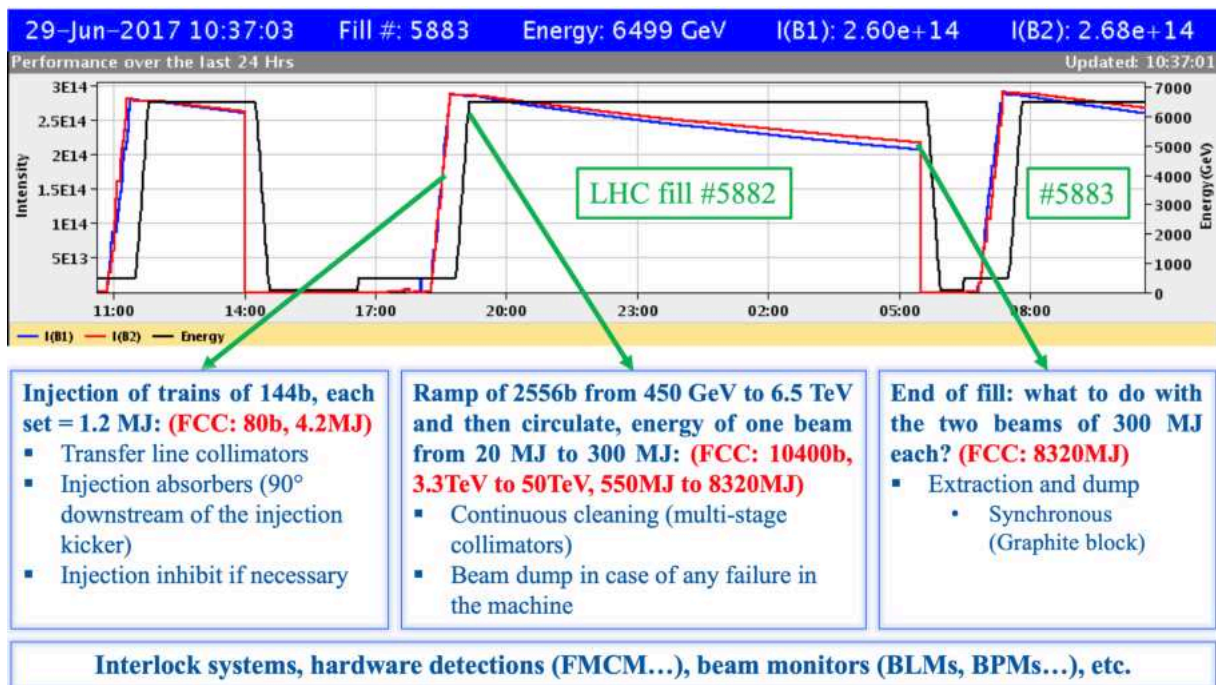


Figure 11.5: Machine-protection challenges throughout an FCC-hh cycle and a typical LHC cycle (using the example of LHC fill #5883). The FCC-hh parameters are highlighted in red.

During the whole cycle, beam permit loops are active to transmit beam dump requests from a large variety of critical equipment to the beam dumping system. The number of elements capable of triggering a beam dump for FCC-hh will exceed 100 000 [297, 308]. A schematic drawing of the BIS and its main client systems is shown in Fig. 11.6.

Three important system requirements of the beam interlock system for FCC-hh are high reliability, high availability and short system reaction time. The reliability requirement is driven by the large stored beam energy as described above. The likelihood of a missed dump should not exceed one occurrence in 1000 years. This can only be achieved with redundancy in the system design, covering the user system requesting the beam dump up to the beam dumping system itself. Frequent testing of the system, guaranteeing the full redundancy of channels, is a prerequisite for such a highly reliable system. The consequences for the machine in case of a beam dump not working on request could be reduced by driving a sacrificial dump block into the beam or by using massive absorbers around the beam (outside the standard collimator hierarchy) that protect the accelerator but not the collimators. Both of these strategies are, however, very challenging for such destructive beams. Therefore, the main strategy is to reduce the likelihood of such an event happening. If the beam dumping system became unavailable during

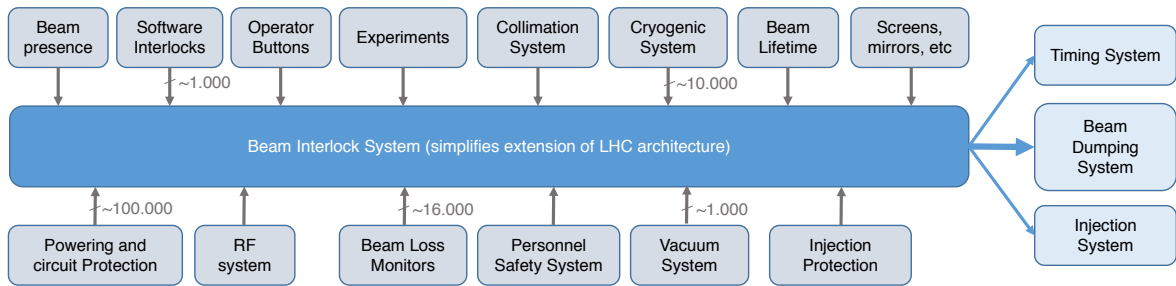


Figure 11.6: Architecture and client systems of the beam interlock system (BIS).

stable beam operation, the beam could be depleted in another safe way, e.g. by slow scraping using collimators, as proposed for the LHC [311].

The availability requirement will be very challenging for the FCC due to the extent of the system and the many users connected. A balance between availability and reliability can be achieved by introducing a voting logic across redundant interlock channels. Such a voting logic – of at least three redundant connections – will also facilitate the continuous testing of the beam interlock system. [312]

The third requirement concerns the reaction time, i.e. the delay between the event requiring a beam dump and the time that the beam is completely extracted from the accelerator. Here, the acceptable delay between the beam dump request and the extraction of the last particles is determined by the beam density distribution and by the speed with which the fault moves the beam transversely, creating losses at the collimators or at the aperture. LHC experience shows that the tails in the transverse beam halo population are more intense than expected in a Gaussian distribution. It was observed that around 5% of the beam population is stored in the tails above 3.5 beam σ (compared to 0.22% for a Gaussian distribution) [313]. The use of a hollow electron lens [313, 314] could deplete the proton population in the beam halo, and thus increase the acceptable delay between the occurrence of the failure and the beam dump. On the other hand, the presence of a beam halo allows an early and very valuable detection of beam movements or instabilities by the beam loss monitors at the collimators. However, this could still be provided by a few witness bunches, with a larger halo population than the cleaned bunches. In addition, the beam halo population could be monitored directly, e.g. with an adapted synchrotron light monitor, triggering a beam dump if the intensity in the halo increases above a pre-defined threshold.

As illustrated in Fig. 11.7, the reaction time from a fault occurrence to the full beam being dumped comprises four main contributions: 1) Failure detection, 2) Communication between BIS and beam dumping system, 3) Synchronisation with the particle-free abort gap, and 4) Beam extraction. For LHC, the longest delay time to

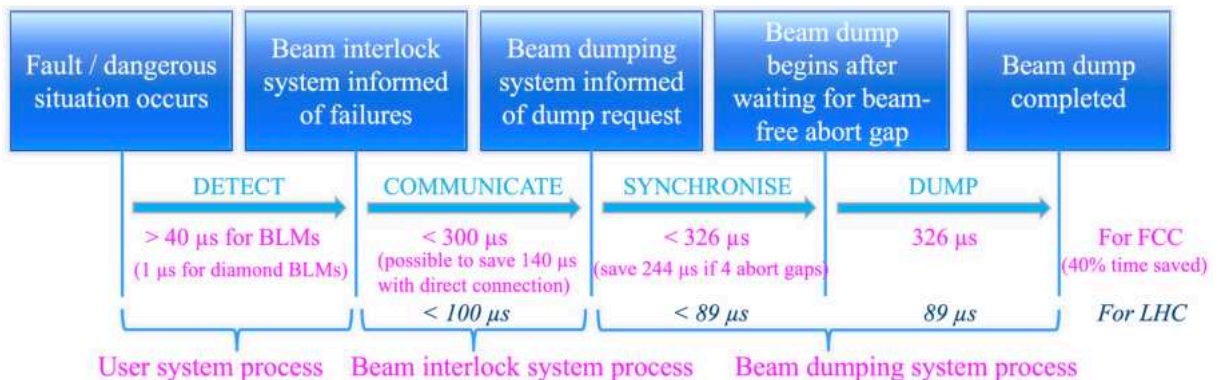


Figure 11.7: Reaction time of the machine protection system from fault detection to beam dump.

extract the beam completely after the initial detection of a failure (Steps 2 to 4), is close to three beam revolutions. This corresponds to a delay of almost 300 μs . With the larger ring of FCC-hh, this delay would increase to approximately 1 ms, which might be critical for some of the fast failures described in Table 11.7. However, the reaction time can be reduced by implementing the measures listed below.

- Reduce *failure detection time*
 - The detection time strongly depends on the failure type. For LHC, the beam loss monitors are among the most important and fastest dump triggers for which the minimum time delay, including the electronics delays, is around $80\ \mu\text{s}$. For FCC, this delay could be shortened significantly to around $1\ \mu\text{s}$ by using faster detectors at aperture limitations, e.g. diamond detectors [315], silicon detectors [316], or Čerenkov fibres [317] equipped with faster read-out electronics.
 - The detection time could be further improved by monitoring bunch-by-bunch beam losses [315, 316] at aperture limitations and sensitive areas, e.g. in the triplet and collimation regions, and connecting these signals directly to the interlock system.
 - Interlock the derivative of the beam losses measured by a distributed beam loss system or put an interlock on the derivative of the total beam current. This would allow faster detection, especially for large losses distributed all around the machine.
 - UFO induced quenches in the FCC could be avoided more effectively if the beam losses were detected between the beam and the superconducting coils directly, in contrast to today’s LHC beam loss monitors which are located outside the cryostat. Possible options are fast diamond detectors distributed over the superconducting magnets behind the beamscreens, a continuous optical fibre close to the beam aperture or, as a third option, a superconducting cable with a very low quench threshold close to the beam aperture in the cryostat. In the last case, the beam could be dumped when this superconducting wire quenches and therefore before the quench threshold of the magnets was reached.
- Reduce communication time
 - The communication time is the time that the dump-request signal needs to travel along the beam interlock loop to the beam dumping system. For FCC, the delay is estimated to be $300\ \mu\text{s}$. Here, time can be gained by making one or several ‘direct’ connections across the ring or by maintaining a short distance between the beam dumping system and the collimation system, where losses will most frequently be seen first. Using a direct signal path from the betatron collimation insertion ‘J’ to the extraction insertion ‘D’ instead of using signal transmission cables through the arc, could reduce the communication time required by about $145\ \mu\text{s}$.
 - For certain failure cases, the use of additional beam loss monitors with a direct link to the beam dumping system, without passing through the BIS, can reduce the communication time required [318]. Furthermore, this approach increases the overall reliability because the trigger signal will be propagated to the beam dumping system even in case of a BIS failure.
- Reduce synchronisation time between the extraction kickers and the particle free abort gap
 - For FCC, this delay would amount to $330\ \mu\text{s}$ when using one beam-free abort gap, as is presently done in the LHC. The time can be shortened by introducing multiple abort gaps. With four abort gaps, the time until the beam is fully extracted from the FCC could be reduced by up to $3/4$ of a turn, i.e. by $244\ \mu\text{s}$.
 - As a last resort, the direct trigger of an asynchronous beam dump could be considered for particularly critical ultrafast failure cases.
- Reduce beam extraction time
 - The extraction time equals the time that the whole beam needs to travel around the FCC circumference to the extraction point, i.e. approximately $330\ \mu\text{s}$. The only way to reduce this time would be to have multiple extraction points and, hence, to install multiple beam dumping systems. However, this would be very expensive and unless, for example, limitations in the material robustness require multiple dump systems this will not be part of the baseline.

11.3.4 Summary

The FCC-hh Machine Protection System will be based on the successful strategy adopted for LHC. The main requirements are the reliability, availability and fast reaction time of the system. However, improvements in several key areas are needed. This includes the reduction of the overall MPS reaction time, faster monitoring of beam losses based on detectors with nanosecond resolution, improved control of the decay time constant of magnet power converters to avoid beam losses building up too fast in case of failures, and, last but not least, the efficient control and monitoring of the transverse beam profile, e.g. by using a hollow electron lens or equivalent devices.

The FCC-hh as a nucleus-nucleus collider

12.1 Overview

In the scope of a second major physics programme on QCD matter at high density and temperature, otherwise known as ‘heavy-ion physics’, the FCC-hh could operate as a nucleus-nucleus or proton-nucleus collider, similar to the LHC. Because of the success of the LHC heavy-ion programme, these collisions were considered from an early stage in the FCC-hh conceptual design [319, 320]. In the meantime, the expected performance has evolved considerably in line with what has been achieved at the LHC [3, 321–323].

While the major hardware systems of the FCC-hh ring are compatible with heavy-ion operation, the beam dynamics and performance limits with nuclear beams are quite different to those of protons in a number of respects. In order to keep cost and effort reasonable, the ion programme is designed to rely on the baseline assumptions made for proton-proton operation, in particular, the equivalent beam energy and same optics.

This chapter assumes fully stripped lead ($^{208}\text{Pb}^{82+}$) ions as the primary species, producing Pb–Pb or p–Pb collisions. Nevertheless, because of the potential physics interest and the design challenges imposed by the secondary beams from ultra-peripheral interactions, the performance of a set of lighter species is briefly discussed. These secondary beams already imposed luminosity limits in the LHC where, at peak luminosities a few times above the design value, the power deposited is able to quench the superconducting magnet which they strike. Because the awareness of this effect only emerged in the late design stage of the LHC, hardware changes to mitigate it could only be made several years after first operation. The FCC-hh enters new territory where heavy-ion operation is impossible without implementing countermeasures in the initial collider design.

At the time of writing, the physics community has not decided if there will be a dedicated heavy-ion experiment¹ in one of the secondary interaction points (IP), or if one or two of the multi-purpose detectors in the main IPs will study heavy-ion collisions. Since the latter seems more likely at present, all estimates made here are based on beams colliding in either one or two main IPs.

Beam and luminosity evolution, as well as estimates for the integrated luminosity are given. The performance projections presented assume the LHC to be the final injector in the chain. The beam parameters are defined by the present and expected performance (for HL-LHC) of the current pre-injector chain.

12.1.1 General assumptions

Beam parameters

In order to provide a broad overview of the potential of the FCC as an ion collider, several operational scenarios are compared throughout the chapter:

- Two cases for beam parameters (see Table 12.1) : *baseline* and *ultimate*, which differ in the β -function at the interaction point and the bunch spacing, defining the maximum number of circulating bunches.

¹like ALICE in the LHC

Table 12.1: Beam and machine parameters.

| | Unit | Baseline | | Ultimate | |
|---|--|------------------|-------------------|------------------|-------------------|
| | | Pb-Pb | p-Pb ^a | Pb-Pb | p-Pb ^a |
| Operation mode | - | Pb-Pb | p-Pb ^a | Pb-Pb | p-Pb ^a |
| General beam parameters | | | | | |
| Beam energy (injection) | [TeV] | 270.6 | 3.3 | 270.6 | 3.3 |
| Beam energy (collision) | [TeV] | 4100 | 50 | 4100 | 50 |
| Energy per nucleon (collision) | [TeV] | 19.7 | 50 | 19.7 | 50 |
| Relativistic γ -factor | - | 21168 | 53289 | 21168 | 53289 |
| Centre-of-mass energy per nucleon | [TeV] | 39.4 | 62.8 | 39.4 | 62.8 |
| No. of bunches | - | 2760 | | 5400 | |
| Bunch spacing | [ns] | 100 | | 50 | |
| No. of particles per bunch | [10 ⁸] | 2 | 164 | 2 | 164 |
| Transverse normalised emittance | [$\mu\text{m}\cdot\text{rad}$] | 1.5 ^b | 3.75 ^b | 1.5 ^b | 3.75 ^b |
| RMS bunch length | [m] | 0.08 | | 0.08 | |
| RMS energy spread | [10 ⁻⁴] | 0.6 | | 0.6 | |
| Total RF voltage | [MV] | 32 | | 32 | |
| Stored energy per beam | [MJ] | 362 | | 709 | |
| Stored energy per beam at injection | [MJ] | 24 | | 47 | |
| Intrabeam scattering (IBS) & synchrotron radiation | | | | | |
| Initial longitudinal IBS emittance growth time | [h] | 19.6 | 3069 | 19.6 | 3069 |
| Initial horizontal IBS emittance growth time | [h] | 20.8 | 3233 | 20.8 | 3233 |
| Longitudinal emittance radiation damping time | [h] | 0.24 | 0.48 | 0.24 | 0.48 |
| Horizontal emittance radiation damping time | [h] | 0.48 | 0.97 | 0.48 | 0.97 |
| Luminosity | | | | | |
| β -function at the IP | [m] | 1.1 | | 0.3 | |
| Initial rms beam size at IP | [μm] | 8.8 ^b | | 4.6 ^b | |
| Number of IPs in collision | - | 1 or 2 | | 1 or 2 | |
| Initial luminosity | [10 ²⁷ cm ⁻² s ⁻¹] | 34 | 2800 | 248 | 20400 |
| Peak luminosity ^c | [10 ²⁷ cm ⁻² s ⁻¹] | 77 | 13300 | 310 | 55500 |
| LHC turn around time | [min] | 25.4 | | 25.4 | |
| Integrated luminosity ^d (1 experiment) | [nb ⁻¹ /run] | 35 | 8000 | 105 | 29000 |
| Integrated luminosity ^d (2 experiments) | [nb ⁻¹ /run] | 23 | 6000 | 62 | 18000 |
| Total cross-section | [b] | 636 | 2 | 636 | 2 |
| Peak BFPP beam power | [kW] | 18 | 0 | 70 | 0 |

^a p-Pb operation uses the same Pb beam as in Pb-Pb operation. The parameters listed in this column correspond to the proton beam.

^b Pb emittances are based on LHC experience. Proton emittances are chosen to give the same geometric beam size, which is larger than in p-p operation, where $\epsilon_n = 2.2 \mu\text{m}$.

^c One experiment in collisions.

^d Per experiment. Including an performance efficiency factor of 50% to take account of down time due to failures. Assuming a LHC turn-around time of 28 minutes.

- Collisions at either one or two experiments, which share the total available luminosity.

Table 12.1 summarises the assumed beam and machine parameters. In the case of the *baseline* scenario the parameters of the injected beam in an LHC cycle are based on those obtained in the 2016 p–Pb run of the LHC [324]. This could be comfortably achieved by simply maintaining the present LHC source and injector chain at the performance levels of LHC Run-2. In addition to this, the *ultimate* scenario assumes a shorter bunch spacing of 50 ns, the principal improvement of the LHC injector chain planned for high-luminosity (HL-LHC) operation in LHC Run-3². Note that, in 2018, the LHC already approached the *ultimate* scenario as it ran with injected bunch intensities beyond those of the baseline scenario and a 75 ns basic bunch spacing. The choices of β^* (β -function at the IP) follow the p–p proposal (see Chapter 1)

Filling pattern

The exact filling pattern in the FCC depends mainly on what is possible in the injectors but it may also be adjusted to meet the experiments’ detector requirements. At the time of writing, studies of a new, potentially improved, heavy-ion injector chain for FCC-hh have not been performed. The estimates given here assume that the existing pre-injector chain can be re-used for FCC, providing the beam quality planned for LHC during the HL-LHC era. Additionally, the upgrades considered for the LHC as the last injector in the chain before the FCC-hh (faster ramp rate, injection and extraction kicker rise time and flat top length) are adopted from the proton programme, see also Chapters 4 and 10. The ion beam production in the injectors is therefore very similar to what is currently done for the LHC.

Starting from the source and Linac 3, the Low Energy Ion Ring (LEIR) produces a batch of two bunches. In the Proton Synchrotron (PS) those are then split into four and, with the aid of RF batch compression, the bunch spacing of the inner batch is adjusted to 100 ns. This batch of four bunches is transferred into the SPS, where a number of PS fillings are accumulated. The total number of PS transfers defines the length of the SPS train that is injected into the LHC.

For protons, the FCC injection energy determines the damage limit for the injection protection devices. This imposes a limitation on the total intensity and thus maximum train length that can safely be transferred from the LHC into the FCC. This limit is of the order of a few tens of proton bunches per transfer (see Chapter 4). A fast extraction kicker with a short flat top length is required to only extract a few of the bunches circulating in the LHC. In heavy-ion operation the bunch intensities are about one order of magnitude below those of the high-intensity proton bunches. From the injection protection point of view it would therefore be permissible to transfer longer trains³. Nevertheless the specifications of the extraction kicker for proton operation are more demanding, imposing the same kicker flat top length limit for ion bunch trains. For that reason a maximum of 20 bunches (5 times 4 bunches) are allowed per train in the LHC. It is convenient to already adjust the train length in the SPS to meet the subsequent extraction requirements. In this way the gaps imposed by the injection kicker can have the same length as required for the extraction. Limiting the SPS train length to 5 PS injections has the advantage that the dwell time on the SPS injection plateau is rather short.⁴ This limits the degradation of the bunch quality due to beam dynamic effects in the SPS [325].

An example of an FCC filling pattern for the baseline scenario is shown in Fig. 12.1. The first row illustrates the first LHC beam to be injected in the FCC ring. It includes a pilot bunch⁵, and 36 trains of 20 bunches. Each of the 37 injections arriving from the SPS must also be individually transferred to the FCC once accelerated to 3.3 TeV. This filling includes an abort gap of 3 μ s for the LHC beam dump kickers. The second to fourth LHC fillings (middle row) assume no pilot bunches and consist of 34 nominal trains only. They are shorter in order to optimise the space in the FCC. In total, four LHC fillings are required to fill the full circumference of the FCC with 138 trains, containing 2760 bunches. The counter-rotating rings of the LHC can produce the beams for the two FCC rings in parallel.

²Assuming that the HL-LHC era for heavy-ion operation starts in 2021.

³The trains still have a smaller number of bunches compared to proton operation, because of the larger bunch spacing.

⁴For LHC ion operation 12 PS injections were regularly taken to construct a train.

⁵Required for setting up (test of all systems with low intensity beam; tune, chromaticity and orbit corrections) the LHC and FCC for injection of trains

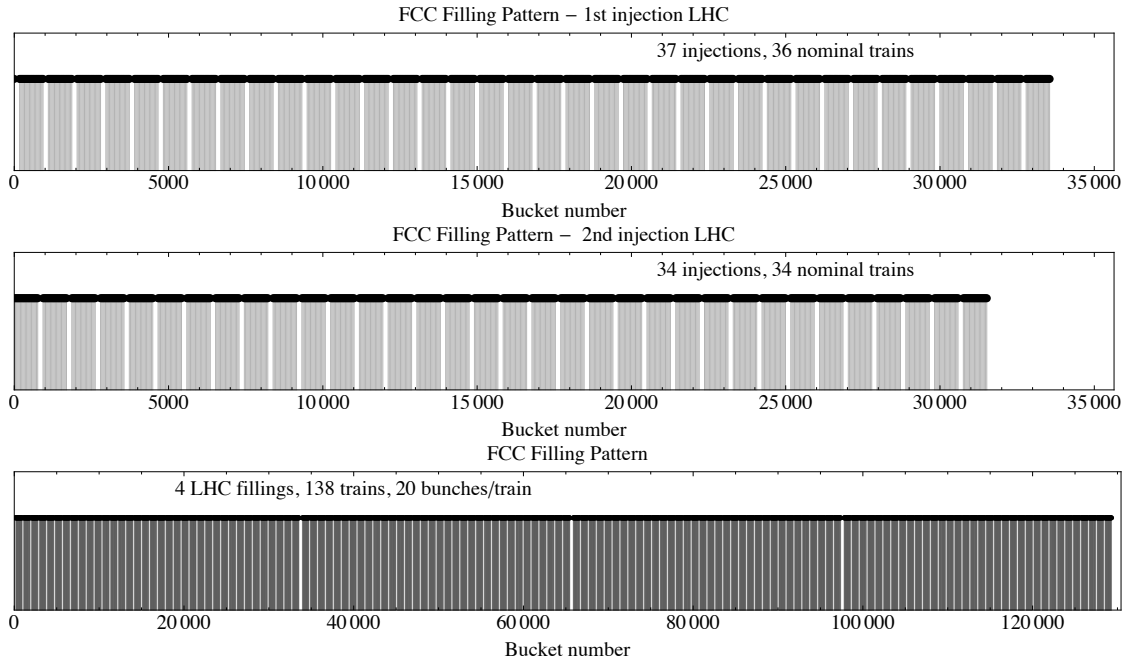


Figure 12.1: Example of the construction of an FCC filling scheme for ions in the baseline scenario. The top row shows the LHC-beam for the first injection into the FCC (including a pilot bunch to set-up the LHC for train injections from the SPS), the middle row shows the pattern for the following 3 injections to fill one FCC beam. The counter-rotating ring of the LHC can produce the counter-rotating beam for the FCC in parallel.

Filling time

The time required to inject all bunches into the FCC is limited by the cycle time of its injectors. Since no injector upgrades have been studied so far, the following estimates are based on the current LHC injector cycle times, with some small but reasonable improvements for the LHC [326], which could in principle be implemented today.

Because of the electron cooling in LEIR, its cycle takes at least 2.4 s⁶. The PS cycle is faster and thus does not add any extra time. A sketch of a potential SPS cycle is displayed in Fig. 12.2. The blue line indicates the evolution of the beam's momentum (equivalent to magnet current) and the red line the intensity evolution. Each step corresponds to an injection arriving from the PS every 2.4 s. In this version, two 20-bunch-trains are accumulated in the SPS before acceleration. This reduces the optimum FCC filling time by reducing the integrated SPS ramping time. Including preparation and ramping times, this SPS cycle has a total length of 32.4 s and for the scheme in Fig. 12.1 it has to be executed 138 times (without the pilot). Adopting a preparation time of about 7 min per LHC cycle⁷ from the proton study, plus 2 min extra for FCC setup with pilot beam, the first LHC filling takes 28.5 min, while the following three can be prepared in 25.4 min. Therefore the total time to prepare both FCC beams sums up to 105 min. In an ideal scenario the first LHC filling could be prepared in parallel to the FCC ramp down and injection preparation, such that the minimum time spent at FCC injection could be optimised to 76 min. The integrated luminosity projections presented in this chapter are based on this optimised injection scenario.

Nevertheless, the estimate of the injection time for p-p operation is still about a factor two smaller (see Chapter 10). For heavy-ion filling, twice as many SPS to LHC transfers are needed, while it takes about three times longer to prepare the ion beams up to the SPS. It would only be possible to obtain a theoretical filling time for ions of the order of the one estimated for proton operation, if the injectors could produce the ion beams twice as fast⁸. In that case the optimum time to produce all four FCC filling cycles reduces to 67 min. Producing the first LHC filling in parallel to FCC injection preparation, reduces the filling time to 49 min (= 3 × 16.2 min).

It should be noted that these numbers represent a theoretical minimum, achieved with an availability of 100% for all injectors.

⁶Currently 3.6 s

⁷Including the preparation of injection, magnet cycle, extraction

⁸LHC preparation time is assumed to be at the lower limit already.

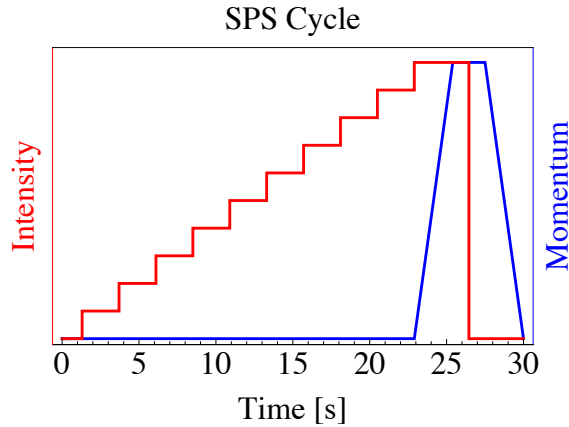


Figure 12.2: Example of a filling and acceleration cycle in the SPS.

Run schedule

The total FCC-hh time that will be dedicated to heavy-ion physics will depend on the physics priorities which have not yet been fixed. Nevertheless, a plausible approach is to follow a similar strategy as for the LHC. Since the beginning of the LHC heavy-ion programme, the scheduling strategy has been to place a one-month-long ion run just before the end-of-year technical stop in (almost⁹) every operational year. The total circulating beam current in heavy-ion runs is generally less than in proton runs. This reduces radiation levels in all machines and the heavy-ion runs provide an effective initial radiation cool-down period before the maintenance work during the subsequent shutdown. Additionally, throughout the LHC lifetime it has been very efficient in terms of luminosity production to distribute the total run time over many years, because many upgrades and improvements (partially considered for HL-LHC era) were implemented between runs. This led to a significant enhancement of the integrated luminosity from one run to the next. These advantages would be lost if the total run time were to be scheduled in a single block.

For an FCC lifetime of 25 years, split into runs of five years each, including around two years of long shutdown and two end-of-year technical stops distributed over an operational period of three years (see Chapter 2.5 in Ref. [1]), about 15 (3 years times 5 Runs) one-month heavy-ion runs would be expected.

12.1.2 Performance estimates

The performance estimates presented in this section are based on the time evolution of the beam parameters, intensity (N), transverse emittance (ε_{xy}) and bunch length (σ_s), obtained from the numerical solution of a system of four coupled differential equations, including luminosity burn-off, intrabeam scattering (IBS) and synchrotron radiation damping. For more information on the physical processes and computational technique see Ref. [319].

Lead-lead collisions

The FCC-hh enters a new, highly-efficient operating regime, in which a large fraction of the injected intensity can be converted to useful integrated luminosity. Figure 12.3 shows the luminosity and beam parameter evolution throughout the collision period during Pb–Pb operation. Thanks to strong synchrotron radiation damping, the beam emittances shrink rapidly and compensate the rapid decay of initial luminosity seen at lower-energy colliders. The luminosity may even increase during a fill until the beams are exhausted. Not only is this natural beam cooling twice as fast for lead ions as for protons, it can also be more fully exploited since the lower overall bunch charges do not, for example, lead to high beam-beam tune-shifts. In the beginning of the fill, when the emittances and bunch length are large, radiation damping clearly dominates IBS. Nevertheless, IBS becomes stronger as emittances decay, such that after about 1 hour at top energy, IBS is able to counteract the damping and to keep the emittances at a rather constant level. The remaining slow emittance decrease arises from the intensity burn-off, which weakens the IBS.

⁹In short years with an extended end-of-year shutdown, ion operation may not be scheduled to allow sufficient time for proton operation after the re-start.

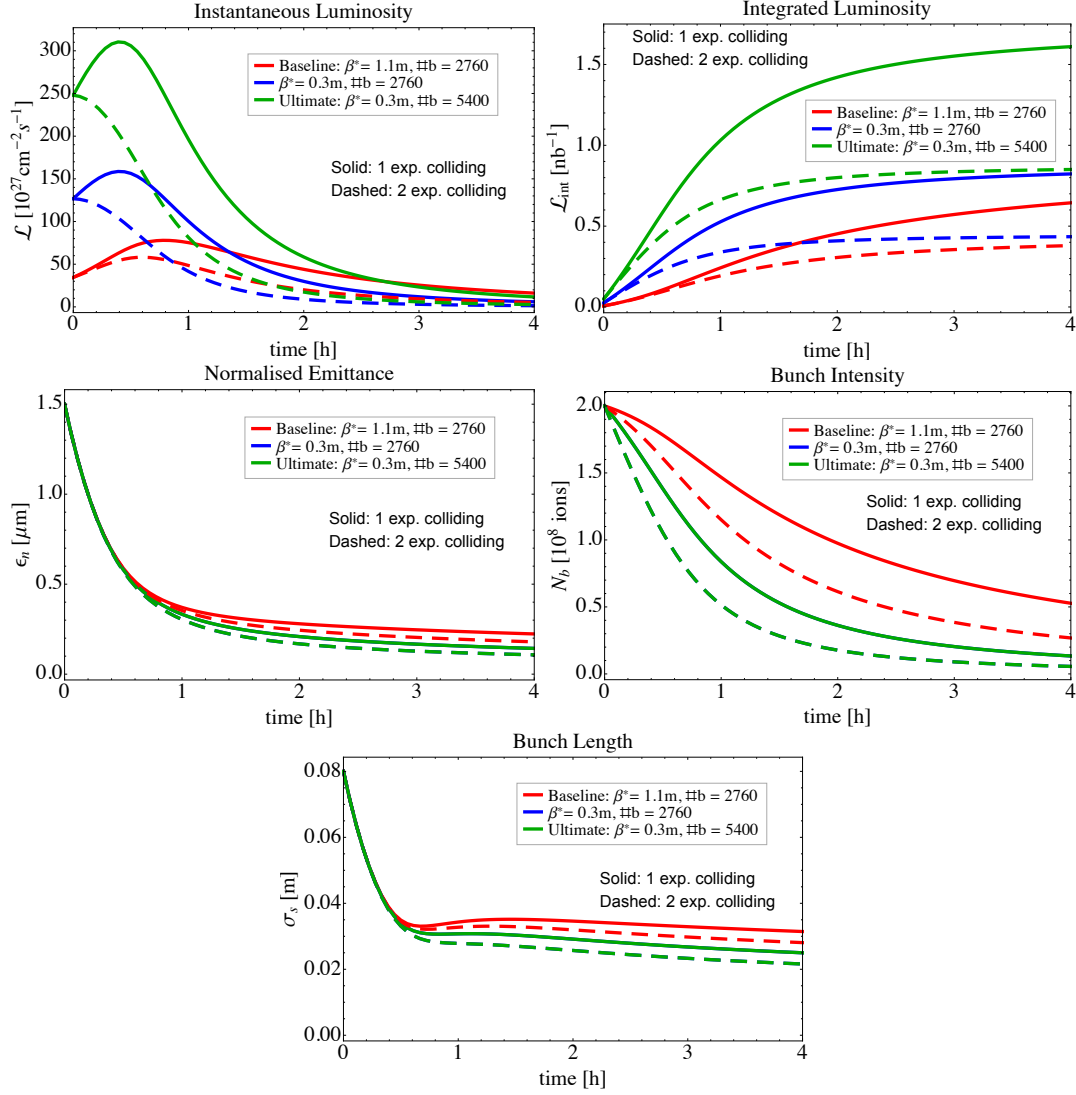


Figure 12.3: Pb–Pb beam and luminosity evolution. Top: instantaneous (left) and integrated (right) luminosity, middle: normalised emittance (left) and bunch intensity (right), bottom: bunch length. Two burn-off scenarios are shown: one (solid lines) and two (dashed lines) experiments with collisions. The baseline (red) and ultimate (green) beam parameter scenarios (see Table 12.1) are displayed. Blue indicates an intermediate scenario, with ultimate β^* , but baseline number of bunches (the blue lines are hidden behind the green for the bunch evolution plots, since the bunch parameters are the same as in the ultimate scenario).

The calculations shown assume full transverse IBS coupling, keeping the vertical transverse emittance from decaying to unrealistically small values¹⁰.

How much luminosity can be integrated over a run strongly depends on the turn-around time, i.e. the time required to come back into collisions after a beam dump. The time needed to inject all bunches into the accelerator is a major, and critical, component of the turn-around time since it is directly proportional to the cycle time and availability of the injectors. In 2016 the LHC achieved a minimum turn-around time of 2.5 hours [327]. Therefore any measures envisaged to shorten the LHC cycle (see Chapter 10) boost both peak and integrated luminosities.

The effect of this is shown Fig. 12.4, which illustrates the (average) luminosity that would be integrated in an ideal 30-day run at full performance with perfect efficiency (no down time or other interruptions) as a function of the LHC turn-around time. Particle losses on the FCC injection plateau due to IBS debunching are included.

¹⁰In LHC heavy-ion operation the coupling is generally well corrected so the vertical emittance growth from IBS is typically negligible and the emittance immediately starts to shrink because of radiation damping. An appropriate level of betatron coupling would have to be introduced in the FCC.

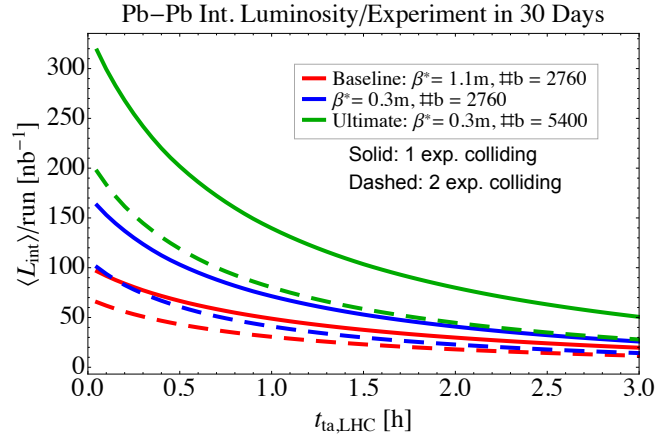


Figure 12.4: Pb–Pb optimal average integrated luminosity as a function of LHC turn-around time, assuming 100% efficiency and machine availability. In 2016 the LHC achieved an minimum turn-around time of 2.5 hours [327]. With a faster cycling LHC (see Chapter 10) the theoretical optimum of the LHC turn-around for an ion cycle could be around 26 minutes, depending on the filling scheme. Colour code and scenarios as in Fig. 12.3.

The solid lines show the projections for a single experiment taking data, the dashed lines assume two experiments with the same configuration. The integrated luminosity per experiment goes down, because the intensity burn-off becomes twice as strong and the total available luminosity has to be shared between the experiments. The estimates of the integrated luminosity are summarised in Table 12.1, where a 50% performance efficiency factor¹¹ was applied to give a realistic assessment of the potential performance.

Luminosity projections are made for experiments placed in the low- β^* regions. The case of a special heavy-ion experiment installed in the secondary IP has not been studied. The luminosity potential of such an experiment would be reduced, due to the larger β^* and potentially fewer colliding bunches.

Proton-lead collisions

The second major heavy-ion operation mode is proton-lead collisions. Performance projections are based on the calculation of the beam evolution during a fill, as shown in Fig. 12.5. These assume the same Pb beam as in Pb–Pb operation and a proton-beam with the same number of charges and geometrical emittances as the Pb beam. In this operation mode the luminosity lifetime is longer than for Pb–Pb because the bunches in the two beams have comparable charges, so there are about 82 times as many protons as Pb nuclei.

Thus, in every collision event, one Pb and one proton are burned-off but the fractional change in population (or the observable charge) for the Pb beam is larger. The proton beam intensity remains nearly constant for the duration of the fill, whilst the Pb intensity decays rapidly¹². Even though the initial beam sizes of the two species are assumed to be equal, the different radiation damping times lead to unequal beam sizes and bunch length. Figure 12.6 and Table 12.1 show a computation of the integrated luminosity for p–Pb, equivalent to the calculation for the Pb–Pb above.

This collision mode has potential for still higher luminosity. The proton beam intensity assumed is much lower compared to proton operation and by increasing it, the luminosity production could be enhanced. The LHC p–Pb run in 2016 [324] started to explore increased proton beam intensities and for the maximum of about 60% more proton charge, no beam-beam problems were found.

¹¹ Similar factors are used for HL-LHC projections.

¹² Because of the lower interaction cross-section in p–Pb compared to Pb–Pb collisions the Pb intensity decay is still slower than in Pb–Pb.

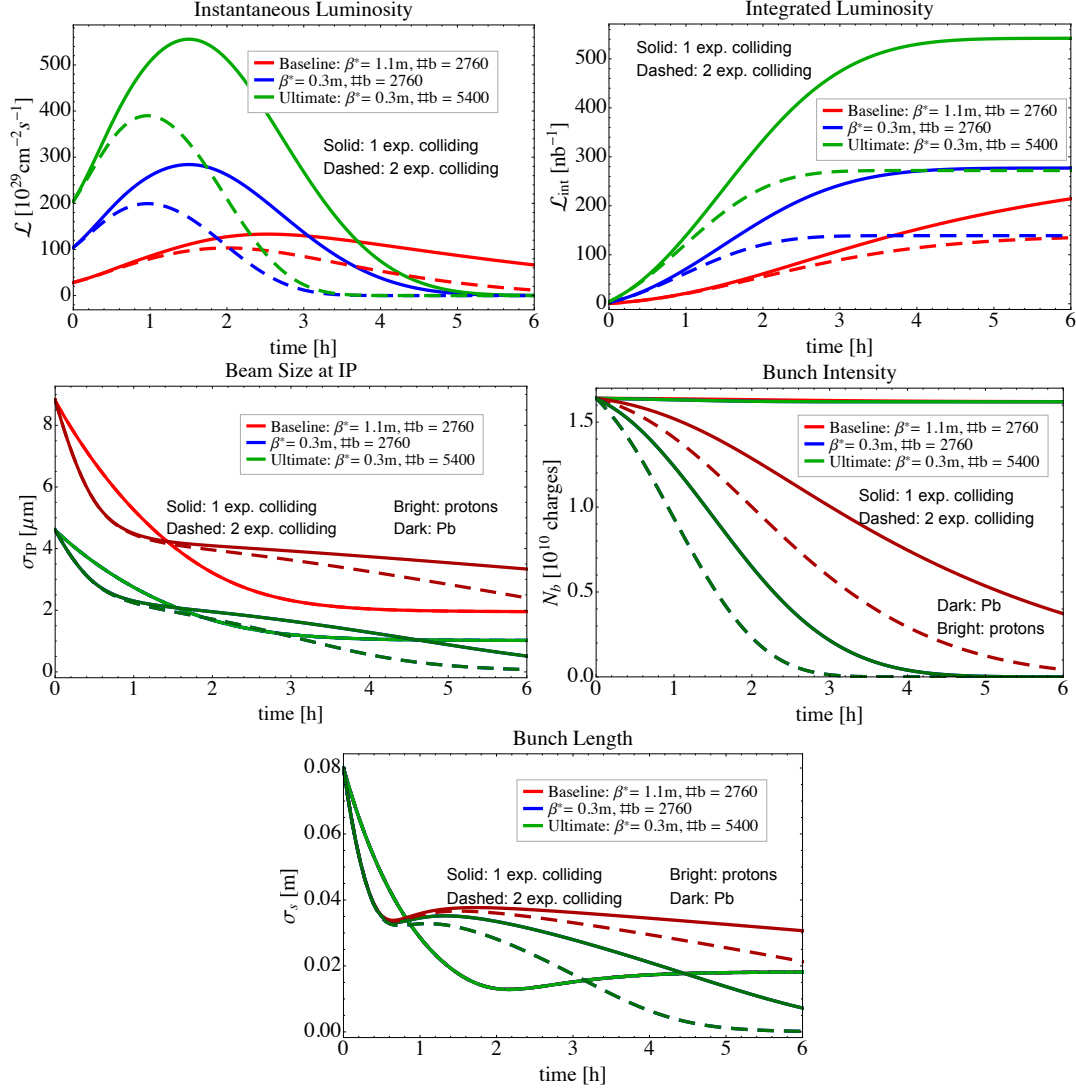
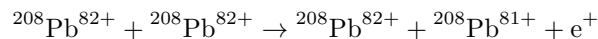


Figure 12.5: p–Pb beam and luminosity evolution. Top: instantaneous (left) and integrated (right) luminosity, middle: beam size at IP (left) and bunch intensity (right), bottom: bunch length. Proton (bright colours) and Pb (darker colours) beam evolution are indicated. Two burn-off scenarios are shown: one (solid lines) and two (dashed lines) experiments with collisions. The baseline (red) and ultimate (green) beam parameter scenarios (see Table 12.1) are displayed. Blue indicates an intermediate scenario, with ultimate β^* , but the baseline number of bunches (the blue lines are hidden behind the green for the bunch evolution plots since the bunch parameters are the same as in the ultimate scenario).

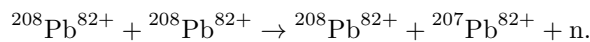
12.2 Key issues

12.2.1 Power deposition from secondary beams

Ultraperipheral electromagnetic interactions, where the two nuclei do not overlap, dominate the total event cross-section, $\sigma_{c,tot}$, during heavy-ion collisions and cause the initial intensity to decay rapidly [328]. The most important interactions in Pb–Pb collisions are bound-free pair production (BFPP)



and electromagnetic dissociation (EMD)



The processes above are only the first order reactions. In higher order reactions two or more electrons

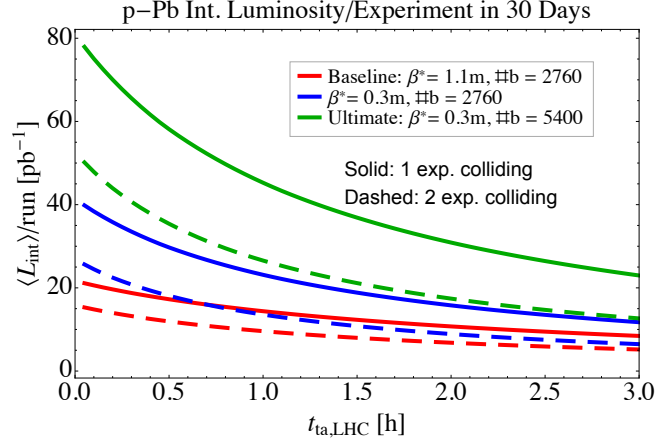


Figure 12.6: p–Pb optimal average integrated luminosity as a function of LHC turn-around time, assuming 100% efficiency and machine availability. In 2016 the LHC achieved an minimum turn-around time of 2.5 hours [327]. With a faster cycling LHC (see Chapter 10) the theoretical optimum of the LHC turn-around for an ion cycle could be around 26 minutes, depending on the filling scheme. Colour code and scenarios according to Fig. 12.5.

are captured or more nucleons are emitted, but the cross-sections are small compared to the first order process¹³. These interactions change the charge state or mass of one of the colliding ions, creating a secondary beam emerging from the collision point, as illustrated in Fig. 12.7. The resulting momentum deviation of the secondary beam lies outside the momentum acceptance of the ring, resulting in a localised impact on the beamscreen, (depending on the lattice) most probably around a superconducting magnet downstream from the IP. Such losses occur on each side of every IP where ions collide.

The total event cross-section is given by the sum over the cross-sections of all possible interactions removing particles from the beam in collision (burn-off). Apart from the inelastic hadronic interactions, the effects of BFPP and EMD are the main contributions in Pb-Pb collisions:

$$\begin{aligned}\sigma_{c,tot} &= \sigma_{c,BFPP} + \sigma_{c,EMD} + \sigma_{c,hadron} \\ &\approx 344 \text{ b} + 284.2 \text{ b} + 7.9 \text{ b} \simeq 636.1 \text{ b}.\end{aligned}$$

The numerical values are estimated for $E_b = 50Z \text{ TeV}$ in Ref. [329]. They agree within about 20% with the estimates made with the aid of Refs. [330, 331].

The production rate of these processes is proportional to the instantaneous luminosity and will thus change during the fill. Nevertheless, the magnets would suffer from a continuous high exposure. Under LHC conditions the risk of quenching a superconducting magnet due to these losses is already high [332]. In the FCC the peak luminosity could be two orders of magnitude higher, making operation without countermeasures impossible. The power, P , in these secondary beams can be calculated as the production rate times the particle energy:

$$P = \sigma_c \mathcal{L} E.$$

Figure 12.8 shows the power evolution of the BFPP1 beam ($^{208}\text{Pb}^{81+}$ ions, capture of one e^-), which has the highest cross-section and accordingly the highest intensity and damage potential.

For the computation of the beam power, the simulated luminosity from Fig. 12.3 was used. The maximum power goes up to (in the case of beams colliding in one experiment) $P \approx 18 \text{ kW}$ (baseline) and $P \approx 70 \text{ kW}$ (ultimate). Depending on the aperture and optics in the FCC, the EMD1 beam ($^{207}\text{Pb}^{82+}$ ions, emission of one neutron) might also hit the beamscreen, depositing additional energy. For comparison, the BFPP1 beam power in the HL-LHC is about 150 W, which could quench an LHC dipole and, possibly, inflict long-term damage. Countermeasures are definitely required to absorb these particles before they can hit the superconducting magnets.

Collimators in the dispersion suppressor (DS) around the IPs, called TCLDs¹⁴, are planned for FCC-hh proton operation (see Chapter 9). The optimised positions for p-p are marked with vertical black lines in Fig. 12.7. Since they are installed to absorb collision debris with large rigidity offsets, these locations also suit the heavy-ion

¹³For the purpose of estimating the upper limit, higher orders are ignored.

¹⁴As also discussed for HL-LHC heavy-ion operation [333, 334]

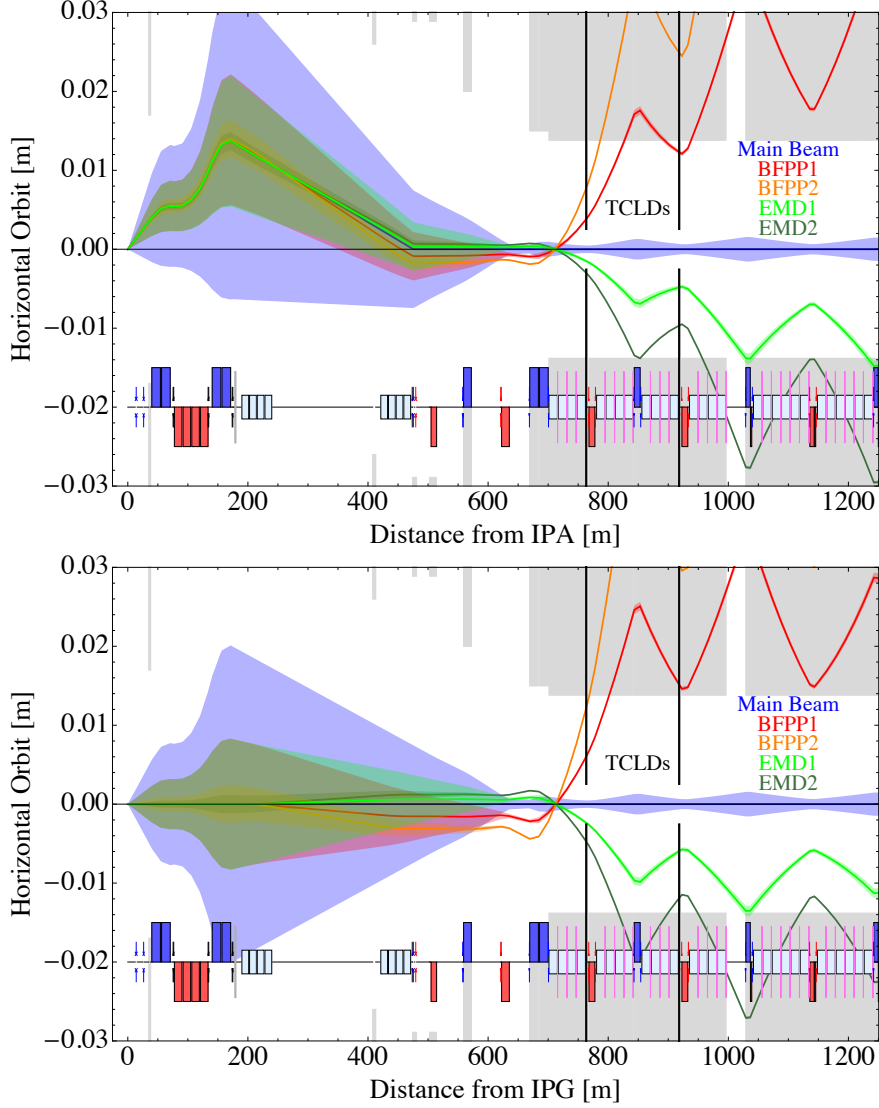


Figure 12.7: Beam envelopes of secondary beams emerging from IPA (top) and IPG (bottom) downstream to the end of the dispersion suppressor (DS). Blue: main $^{208}\text{Pb}^{82+}$ beam (10σ envelope), red: BFPP1 ($^{208}\text{Pb}^{81+}$), orange: BFPP2 ($^{208}\text{Pb}^{80+}$), light green: EMD1 ($^{207}\text{Pb}^{82+}$), dark green: EMD2 ($^{206}\text{Pb}^{82+}$, 1σ envelopes). The grey shaded area represents the aperture and the rectangles on the bottom are the beam line elements (light blue boxes are the main dipoles, red and dark blue boxes are the focusing and defocusing quadrupoles). The two black lines show DS collimator positions, installed in the lattice to absorb debris from p-p collisions.

requirements. Depending on the collimator opening, the first TCLD in cell 8 intercepts the BFPP1 beam, while the EMD1 beam is caught by the second TCLD in cell 10.

Further studies are needed to determine whether a synergistic collimator design would be sufficient to stop the beams produced in heavy-ion collisions at the highest energy of the FCC. Since heavy-ions have a high probability of fragmenting when passing through the collimator material, special attention should be given to particle showers exiting the collimators and being deposited in the downstream superconducting magnets.

12.2.2 Collimation performance

In general, the collimation system performance for ion beams is worse than for protons [335,336]. When ions of the beam halo are intercepted by the primary collimators they can undergo nuclear fragmentation and electromagnetic dissociation inside the jaws. These interactions can produce fragments with insufficient spatial offset to be captured by the secondary collimators but with a change in charge-to-mass ratio large enough to push their magnetic rigidity

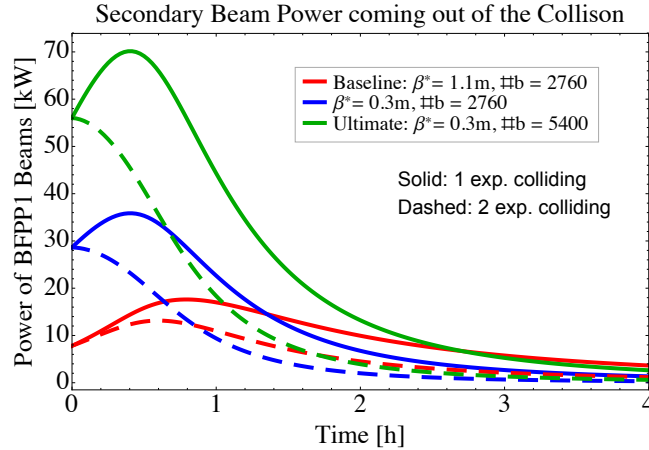


Figure 12.8: Power carried by secondary beams from the bound-free pair-production process. Colour code and scenarios according to Fig. 12.3.

outside the ring acceptance. Such fragments are lost on the cold aperture of the dispersion suppressor¹⁵ and cause localised energy deposition greater than in the case of protons. In the LHC, the loss rate in the DS limits the ion beam intensity. As a mitigation measure in HL-LHC, additional dispersion suppressor collimators (TCLDs) will be installed around the collimation insertion [27, 28, 337]. The same principle is planned to be used in FCC-hh.

The cleaning performance of the FCC collimation system, which was first designed and optimised for proton beams, has been studied for ion beams. Both betatron and momentum cleaning for lead-ions were fully evaluated at injection and collision energy, while only the most critical case (betatron cleaning at top energy and momentum cleaning at injection) is presented¹⁶. Loss maps and a comparison of the cold losses with the estimated 12-minute beam-lifetime quench limit are presented. Further analyses of the aperture losses investigated the ion species population and energy spectrum.

The studies use the SixTrack-FLUKA active coupling framework [249, 338]. In this framework, SixTrack [24, 45, 46, 252] is used to track the particles in the magnetic lattice, while FLUKA [62, 63] evaluates the interactions with the collimators. When particles arrive at a collimator in SixTrack, they are handed over to FLUKA, which executes a Monte Carlo simulation of the atomic and nuclear interactions in the collimator material and passes the surviving primary beam ions and fragmented secondary ions back to SixTrack for further tracking. This approach, based on a coupling between these two simulation codes, provides the best predictions yet for the collimation system performance with ions, because it is able to treat the strong dependence of the local cleaning inefficiency on the interactions inside the collimator material. This technique became available through the recent extension of SixTrack to include tracking of arbitrary ion species [339].

The quench limit estimate (see Chapter 9.4.2) is based on FLUKA simulations of proton losses in the DS (protons/m/s). In order to make it applicable for ions, this value is converted to the equivalent longitudinal power density (Energy/m/s). Under the assumptions of a 12-minute beam-lifetime and the total ion beam intensity for the baseline scenario (see Table 12.1), the cleaning inefficiency allowed for ions before quenching evaluates to $8 \times 10^{-6} \text{ m}^{-1}$. It is likely that the estimate is too pessimistic, but further input is needed from magnet and energy deposition studies to establish a new baseline. This limit is indicated on the loss maps in Figs. 12.9 and 12.10 as a red dashed horizontal line.

A summary of the essential collimator settings¹⁷ can be found in Table 12.2. The collimator layout and settings are adopted from the nominal proton case. This means that the physical collimator openings in millimetres are the same as in Chapter 9. Note that the reference σ used in Table 12.2 is based on the proton normalised emittance of $2.2 \mu\text{m}$, which corresponds to a smaller geometric beam size than assumed for the ion beams (Table 12.1), resulting in somewhat tighter collimators for ions relative to their beam size.

¹⁵ where the $\Delta p/p$ acceptance shrinks

¹⁶ For more details on the collimation system itself and how the most critical cases are defined see Chapter 9.

¹⁷ The full parameter list can be found in the collimation chapter 9, see Table 9.6.

Table 12.2: Table of parameters for collision optics.

| Parameter | Unit | Injection | Collision |
|--|----------------------------------|-------------------------|-----------|
| Energy per nucleon | [TeV] | 1.3 | 19.7 |
| β^* | [m] | 4.6 | 0.3 |
| Crossing angle | [μ rad] | 0 | 100 |
| Particle | - | $^{208}\text{Pb}^{82+}$ | |
| Proton equivalent normalised emittance | [$\mu\text{m}\cdot\text{rad}$] | 2.2^a | |
| TCP jaw length | [cm] | 30 | |
| TCP opening | [σ] | 7.57 | |
| Number of simulated primary particles | - | 1×10^6 | |
| Number of simulated turns | - | 700 | |

^a This corresponds to the design proton emittance, which is $\sim 40\%$ smaller than what is assumed in Table 12.1 for the ion beam parameters. The numeric value of the collimator opening in σ is based on this value.

Betatron cleaning at top energy

Betatron loss maps for Beam 1 horizontal at top energy with and without TCLDs are shown in Fig. 12.9 top and bottom, respectively. The corresponding zooms into the betatron cleaning insertion (IRJ) are displayed in Fig. 12.10. For the nominal collimation configuration (with TCLDs), most of the losses in the dispersion suppressor of IRJ, as well as all of the cold peaks observed in the rest of the ring, are comfortably below the quench limit. The removal of the TCLDs (see bottom plots of Figs. 12.9 and 12.10) brings up numerous cold loss peaks with a magnitude well above the quench limit, both in the IPJ dispersion suppressor and in the arcs. This demonstrates that TCLDs

- installed at the nominal locations, optimised for protons, are also effective in intercepting ion losses.
- are essential for operation at nominal ion beam intensity.

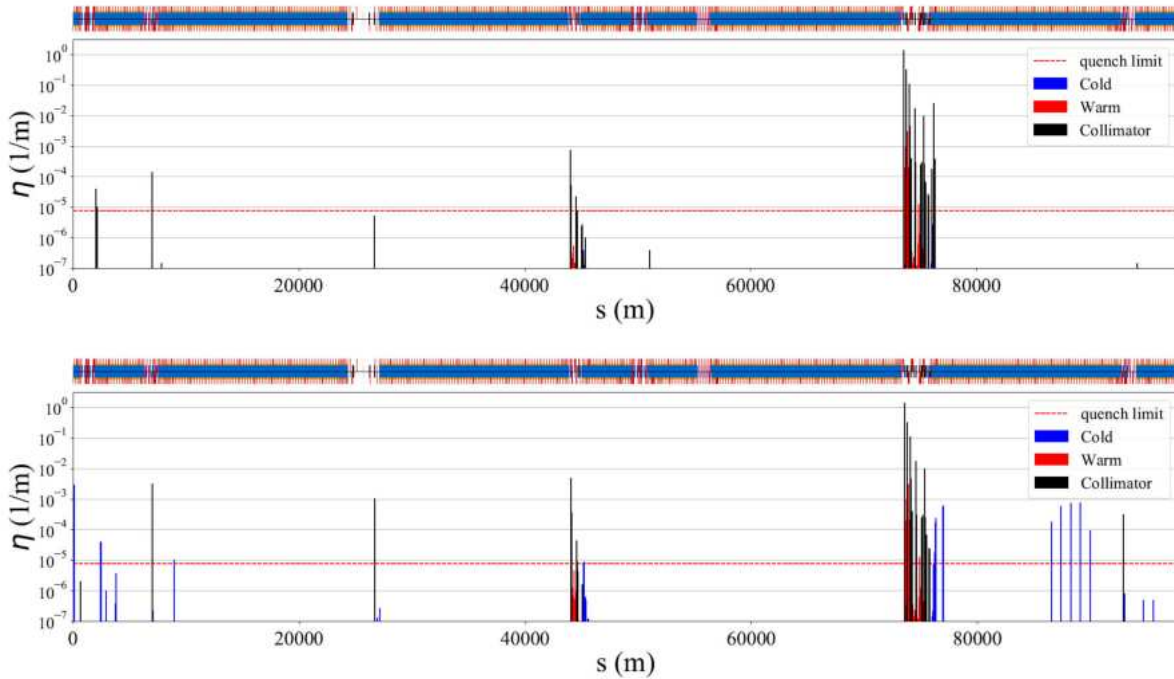


Figure 12.9: Full ring betatron loss map of Beam 1 horizontal at top energy for collision optics with nominal collimation settings (top) and TCLDs removed (bottom). The estimated quench limit is displayed as the red horizontal dashed line at $\eta = 8 \times 10^{-6} \text{ m}^{-1}$.

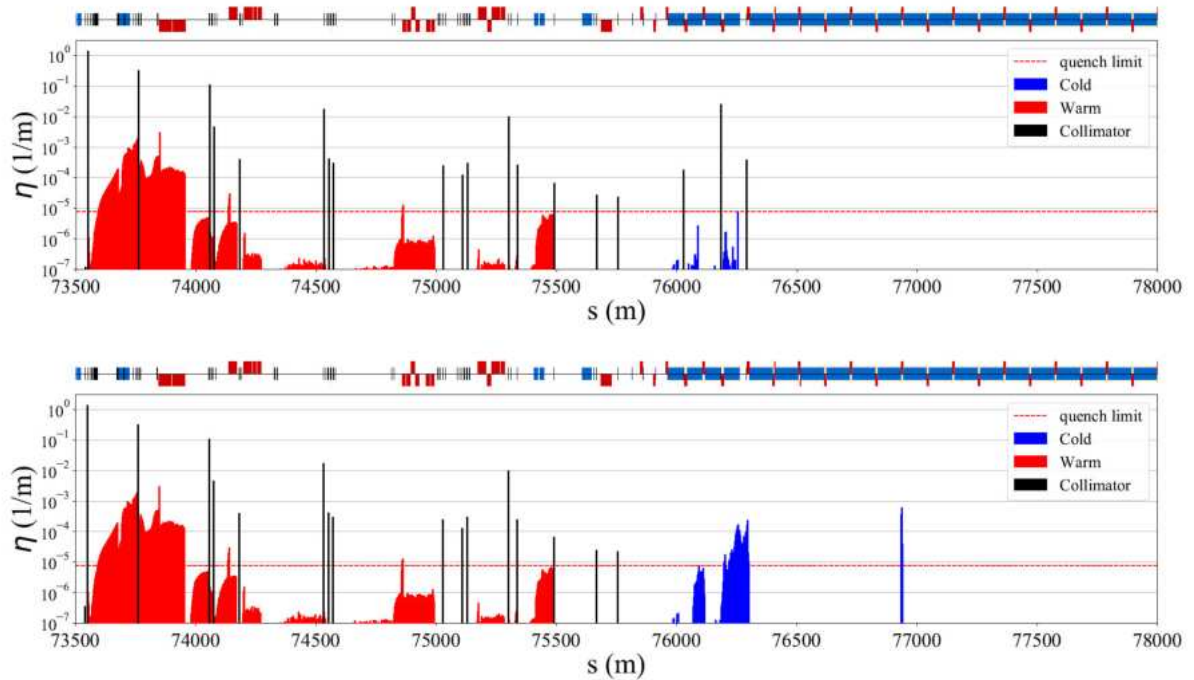


Figure 12.10: Enlarged view of the betatron cleaning insertion IRJ for betatron loss maps shown in Fig. 12.9. Top: collision optics with nominal collimation settings, bottom: TCLDs removed.

Detailed analysis of the cold aperture losses in the dispersion suppressor are presented in Fig. 12.11. The largest energetic fractions of these losses are generated by light ion fragments. No fragments with $A > 160$ are observed. The simulation results reveal that the TCLDs successfully intercept the heavy fragments coming from the warm section, but do not fully absorb the hadronic showers generated in the primary collimators. Some products still reach the cold aperture. Even though the tracking simulations indicate that the direct losses (from the primaries) are below the quench limit, the showers leaking out of the collimators impose a quench risk. It is therefore important to perform energy deposition studies to evaluate the power deposition in the coils of the most critical magnets and assess whether additional masks are required to protect them further.

Off-momentum cleaning at injection

The loss map for off-momentum cleaning at injection is shown in Fig. 12.12. As expected, the worst cold losses are observed in the DS after the off-momentum cleaning insertion. While the TCLDs absorb a significant fraction of the losses, three extensive cold-loss clusters are observed in the DS and one additional smaller cluster in the downstream arc. Further investigations of the quench limit at injection energy and the total rate of losses during the ramp are needed to determine whether additional mitigation measures are required.

The results presented show that, within the scope of this study, the collimation system designed and configured for proton beams is also adequate for ion operation. No show-stoppers were identified in the collimation system performance with ion beams with baseline parameters.

12.2.3 Ion injector chain

The injector chain is crucial for the performance of the collider. Most importantly the total beam intensity is determined by the capabilities of the pre-injectors. They define the maximum number of particles per bunch and the various bunch spacings within an injected train. The fast radiation damping in the energy regime of the FCC diminishes the importance of the emittance preservation in the injectors. All estimates made in this document rely on the assumption of having the same beam quality as can presently be achieved in the LHC. Many of the current injectors will be very old at the time FCC starts operation (e.g. the PS will be close to 100 years although it is refurbished regularly), with consequences for their availability and performance. If a new injector chain is to be

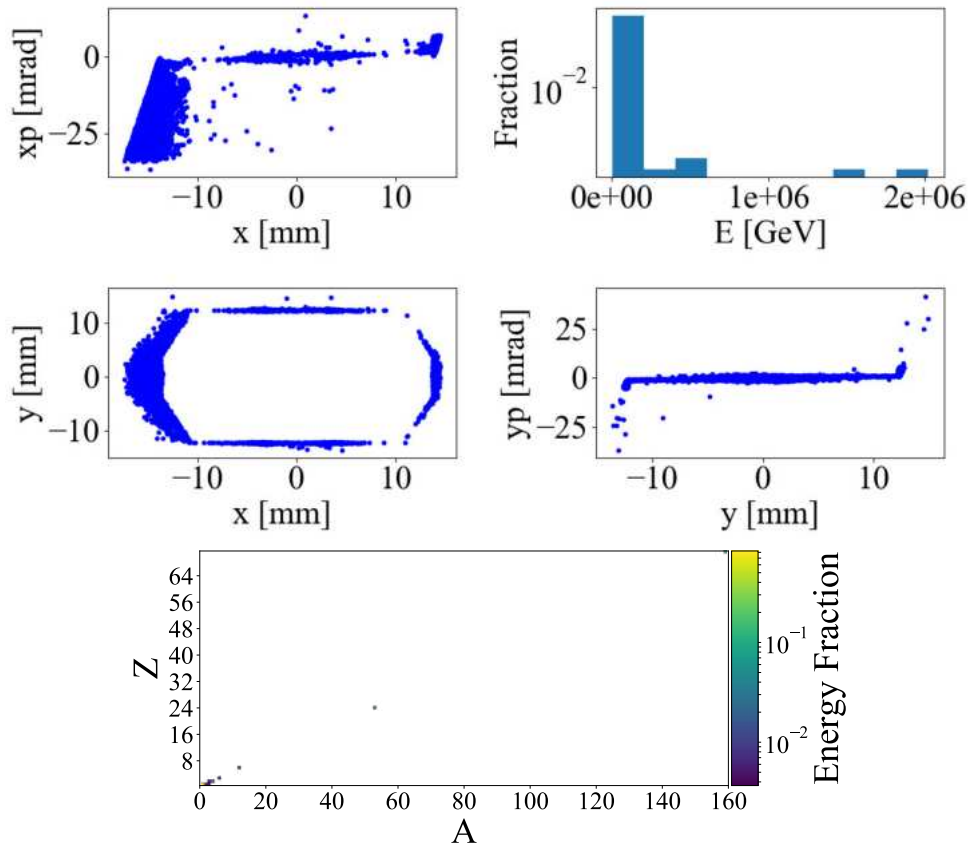


Figure 12.11: Aperture losses in the dispersion suppressor of IRJ for nominal collimation settings (incl. TCLDs). The transverse distributions of aperture impacts (4 plots on the top) show events collected over the range $S = 76000$ m to 77000 m, which includes the DS. The A-Z distribution of the aperture losses (bottom) is weighted by the energy of the lost particle normalised to the total energy lost in the DS. No ion species with $A > 160$ are found in the cold losses, demonstrating the effectiveness of the TCLDs in intercepting heavy-ion fragments coming from the primary collimator.

built for the FCC, then ions should be included in the design study from an early stage. In that case, the achievable parameters and luminosity performance might then be superior to those assumed here.

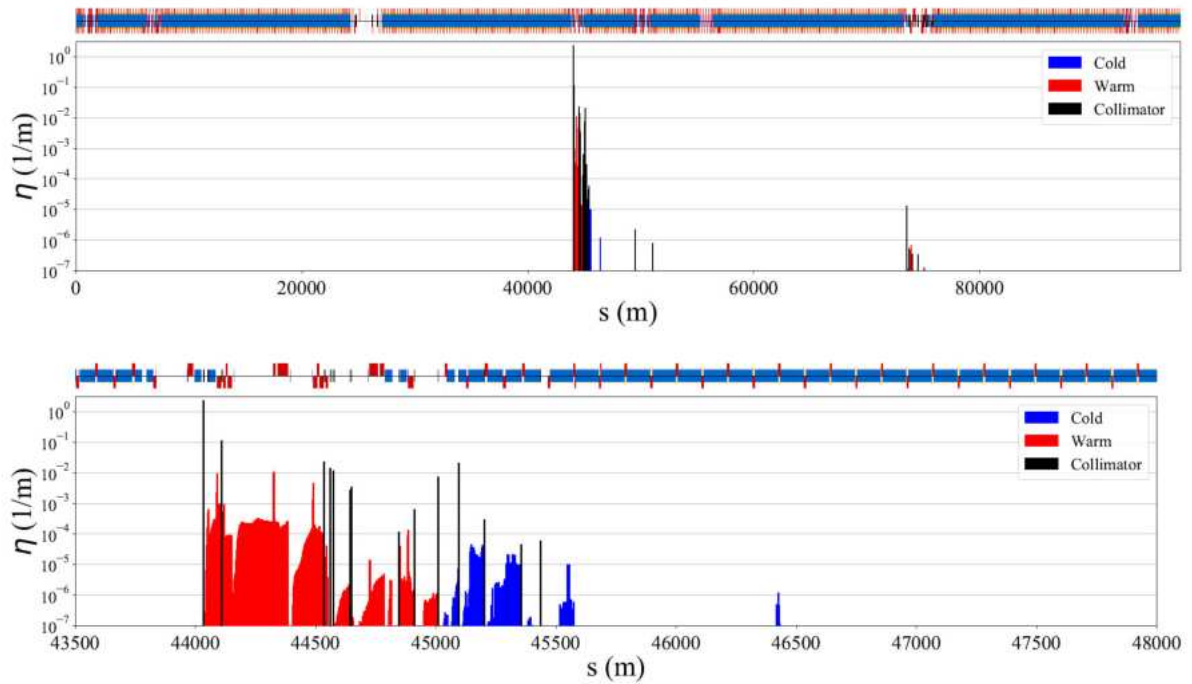


Figure 12.12: Off-momentum loss map of Beam 1 horizontal for injection optics with nominal collimation settings (top) and an enlarged view of the off-momentum collimation insertion (bottom).

12.3 Additional hardware specifications

12.3.1 Dispersion suppressor collimators

As discussed in detail in Section 12.2, special collimators need to be installed in the DS regions

- on the out-going beams of all interaction points in which ions collide, to absorb the secondary beams produced,
- downstream of the collimation insertions to absorb the fragmentation products from collimator–ion interactions.

Suitable locations for these collimators, which partially coincide with other collimator needs for proton operation, have been identified. A combined collimator design, covering the requirements of both operational modes, still remains to be studied. Because of the high and continuous power deposition from the secondary beams around the interaction points, these collimators have to be highly resistant and feature a special cooling system to extract the energy deposited.

12.3.2 RF system

The FCC RF system (see Chapter 3.4 of Ref. [1]) is similar to the LHC design. The possibility of individual, i.e. un-linked, RF systems for the two beams needs to be maintained for p–A operation. The RF frequency difference of protons and lead ions on the central orbit at 3.3 TeV is about $\Delta f_{RF} \simeq 90$ Hz. This would lead to an orbit separation of the two beams of about $\Delta x_c \simeq 7.2$ mm in the arcs for a maximum dispersion of $D_{x,max} = 3.5$ m. An off-momentum injection with this orbit offset for locked frequencies is unacceptable. For a superconducting SPS and a reduced injection energy of 1.2 TeV the off-momentum beam separation becomes $\Delta x_c \simeq 56$ mm ($\Delta f_{RF} \simeq 650$ Hz). Thus, as in the LHC for p–Pb operation, on-momentum injection with different RF frequencies of the two beams is necessary. After acceleration to 50 TeV the frequency difference becomes $\Delta f_{RF} \simeq 0.4$ Hz. At this energy the two RF systems can be locked and *cogging* can be performed to adjust the timing of the bunches for collisions in the IPs at a residual off-momentum orbit separation of $\Delta x_c \simeq 0.04$ mm.

12.3.3 Beam position monitors

The number of charges per bunch in p–Pb operation is very different for the two species. The intensity burn-off is much faster for the Pb beam compared to the proton beam and the initial proton bunch charge might be higher¹⁸. For this reason, the beam position monitor (BPM) system needs to be operated in different sensitivity ranges for the two species in the LHC. This is particularly problematic for the BPMs that see both beams in the common beam pipes around the IPs, as these can only see one beam, depending on their sensitivity setting.

The mitigation in the LHC uses the so-called *synchronous orbit*. For each common BPM a bunch with no long-range interaction is chosen such that at any time the selected bunch passes the BPM alone. This is done only for the common BPMs, because in this case the orbit measurement of the full beam is based on a single bunch, which would not be acceptable on the whole circumference. Moreover, due to the moving long-range encounters at injection and during the ramp before the RF systems are locked, this technique is not applicable because an individual signal can not be guaranteed. During these phases of the cycle the BPMs concerned are disabled and are not part of the feedback system. This effect should be kept in mind for the FCC BPM design so that either the sensitivity ranges could be optimised or a similar technique to the synchronous orbit could be applied.

A second issue, first observed in LHC p–Pb operation, concerning the interlock BPMs in the beam dump insertion, could limit the fill length in the FCC to below the optimum for p–Pb and Pb–Pb. These BPMs trigger a beam dump if the orbit at the extraction point is outside the limits for a clean and safe dump. This can be triggered by an orbit offset or certain bunches not being measured. Thanks to the strong radiation damping, the FCC will operate close to the ultimate limit of burning off all particles in the beam. Nevertheless, the interlock BPMs have a intensity limit, below which bunches are not detected. When the intensity of the first bunch falls below this limit a beam dump will be triggered – before the optimum fill length for luminosity production is reached. The FCC interlock BPM design should therefore aim for the lowest threshold possible, in order to optimise the ion fill lifetime.

12.4 Colliding other nuclei

Originally the choice to study collisions of lead ions was taken in analogy to LHC. The heavy-ion physics community has also studied the physics case for collisions of lower Z ions [340], which would also have advantages from the accelerator physics and design point of view.

The contributions of the ultraperipheral electromagnetic processes to the total cross-section is highly dependent on the charge number of the ions colliding:

$$\begin{aligned}\sigma_{c,\text{BFPP}} &\propto Z^7 \\ \sigma_{c,\text{EMD}} &\propto Z^4.\end{aligned}$$

This brings two advantages for lower Z :

- Reduced secondary beam power emerging from the collision point, because fewer electromagnetic interactions take place.
- Increased luminosity lifetime, because fewer particles are lost by electromagnetic interactions making more particles available for hadronic interactions.

The CERN accelerator chain is capable of producing many different ion species. In previous years the SPS provided argon and xenon for the fixed target physics programme [341]. By changing the main and support gas in the ion source, it would also be easy to produce certain other species [342]. The noble gases are especially favourable. From experience in the LHC and the SPS fixed target programme, the bunch intensity is expected to show a dependence on the particle charge. Since effects like space charge and intra-beam scattering become stronger with higher charge number, an increase in average bunch charge for lighter ions is observed [341]. Empirically, a highly simplified parametric (p) scaling law for the bunch intensity dependence on species charge has been postulated [340]:

$$N_b(Z, A) = N_b(82, 208) \left(\frac{Z}{82} \right)^{-p} \quad (12.1)$$

¹⁸The projections presented assume equal initial bunch charges, however LHC experience shows potential for higher luminosity by increasing the proton bunch charge until the beam-beam limit.

$$\text{where } p = \begin{cases} 1.9, & \text{fixed target experience} \\ 0.75, & \text{LHC: Xe run vs. best Pb} \end{cases}$$

This approximation assumes that other quantities like geometric beam size, filling scheme, other loss rates, etc., are equal. Nevertheless, it can be used to project luminosity performance as a function of p . The fixed target requirements on beam quality (e.g. emittance) are less stringent, therefore the estimates in this section use $p = 1.5$ as a reasonable value for LHC and thus FCC-hh.

The species argon (Ar), calcium (Ca), krypton (Kr), xenon (Xe) and lead (Pb), were chosen in collaboration with the heavy-ion physics community from among species that were or could easily be produced with the present CERN ion source. This list is not intended to be complete or to present the final choice, but rather give an overview of a representative set of possible Z values.

As an example, the choice of Xe in the SPS in 2017 was based on an experiment's request, but the final ^{129}Xe isotope was determined by constraints on the RF frequency in the PS and the cost of the pure isotope. This isotope was not well-studied in low-energy physics experiments, which complicated the analysis of the data taken in LHC collisions. An alternative species, in a similar mass range, would be indium (^{115}In). For this metal, nuclear density distributions could be easily measured in fixed target experiments with electron, neutron and proton scattering. Moreover, neutron emission cross-sections and charge-changing cross-sections measured in the SPS [343, 344] could be extrapolated to higher collision energies. This knowledge is of great value in the interpretation of data from a collider.

In order to quantify the gain in luminosity production in collisions of lighter- Z nuclei with respect to the baseline of Pb-Pb, one should consider the nucleon-nucleon luminosity presented in Fig. 12.13. The power carried by the BFPP and EMD beams is illustrated in Fig. 12.14. In the following, luminosity labelled with AA are nucleus-nucleus and NN are nucleon-nucleon values. Nucleus-nucleus values can be converted to nucleon-nucleon values by multiplying by A^2 .

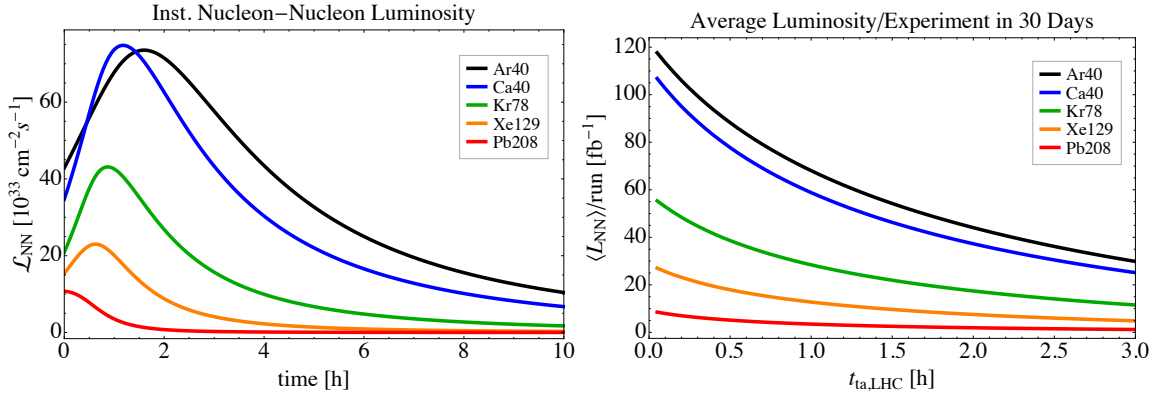


Figure 12.13: Nucleon-nucleon luminosity for a set of alternative ion species, calculated for the ultimate parameter scenario with 50 ns bunch spacing and two experiments in collisions. Left: Instantaneous evolution along a fill. Right: Average integrated luminosity for a 30 day run as a function of the LHC turnaround time. The red line is equivalent to the dashed green line in Fig. 12.4, which shows the nucleus-nucleus luminosity for the Pb-Pb scenarios considered.

The projections are based on the parameters summarised in Table 12.3 and the ultimate parameter scenario as described in Table 12.1 for beams colliding in two experiments. Bunch intensities are scaled from the assumed 2×10^8 Pb-ions per bunch using Eq. (12.1) and $p = 1.5$. The event cross-sections were estimated with RELDIS [345] and are taken from Ref. [329]. The estimated uncertainty¹⁹ on these cross-sections is about 5% for Pb and about 15% for less known nuclei like Kr [346].

The luminosity evolution in Fig. 12.13 clearly shows the expected longer lifetime and higher rates for decreasing Z thanks to the reduced cross-sections of ultraperipheral processes and higher bunch intensities. Applying the same criteria to estimate the integrated luminosity as discussed in Subsection 12.1.2, Table 12.3 gives predictions for Ar, Ca, Kr and Xe in a 30 day run. In the extreme case, the integrated nucleon-nucleon luminosity per run could be expected to be an order of magnitude larger for Ar than Pb. Investigating the power carried by

¹⁹Derived by comparison with other simulation codes and data

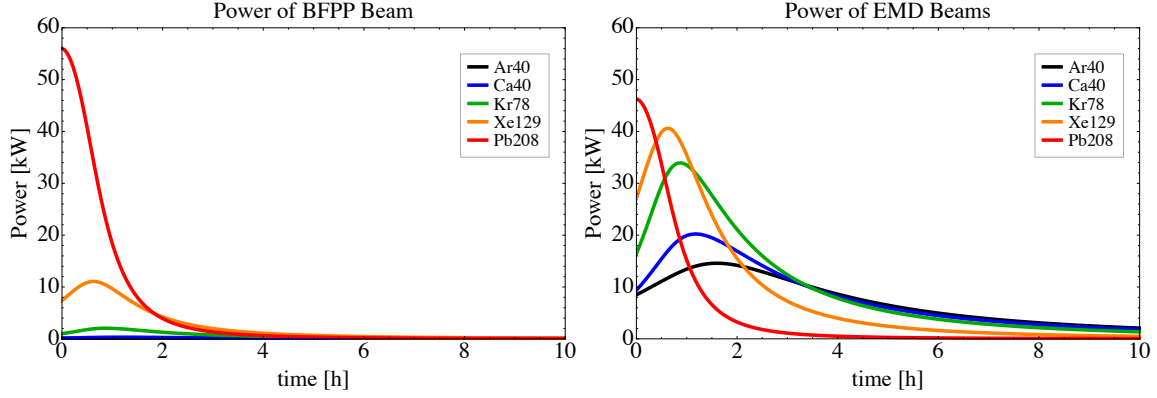


Figure 12.14: Total power carried by secondary beams produced by BFPP (left) and EMD (right) processes for a set of A-A collisions corresponding to the cases shown in Fig. 12.13.

the secondary beams more closely, as displayed in Fig. 12.14, it becomes evident that the reduction of the power deposited by BFPP products is already significant when going to Xe. However, the EMD cross-sections do not reduce as fast with the species charge, thus the power deposited by EMD products already exceeds that of BFPP for Xe. Note that the EMD power shown here uses the total EMD cross-section, therefore not all particles would be lost in the same place as they are split into EMD1 and EMD2 beams which are produced with a cross-section of comparable magnitude.

Table 12.3: Parameter projections for alternative nuclei. Luminosity labelled with AA are nucleus-nucleus and NN are nucleon-nucleon values. All calculations assume the ultimate parameter scenario and two experiments in collisions.

| Isotope | $^{40}\text{Ar}^{18+}$ | $^{40}\text{Ca}^{20+}$ | $^{78}\text{Kr}^{36+}$ | $^{129}\text{Xe}^{54+}$ | $^{208}\text{Pb}^{82+}$ |
|--|------------------------|------------------------|------------------------|-------------------------|-------------------------|
| Number of particles [10^8] | 19.4 | 16.6 | 6.9 | 3.7 | 2.0 |
| $\sigma_{\text{BFPP,tot}}^a$ [b] | ~ 0.02 | 0.042 | ~ 1 | ~ 18.5 | 344 |
| $\sigma_{\text{EMD,tot}}^a$ [b] | 2.2 | 2.7 | 16.6 | 67.9 | 284.2 |
| $\sigma_{\text{hadronic}}^a$ [b] | 2.764 | 2.767 | 4.29 | 5.89 | 7.9 |
| σ_{tot}^a [b] | 5 | 5.5 | 22 | 92.3 | 636 |
| Power carried by BFPP beams [kW] | 0.1 | 0.3 | 2.0 | 11.0 | 56.0 |
| Power carried by EMD beams [kW] | 14.6 | 20.2 | 33.9 | 40.6 | 46.3 |
| Optimum time in collisions [h] | 4.5 | 3.75 | 3.0 | 2.25 | 1.25 |
| Initial \mathcal{L}_{AA} [$10^{30}\text{cm}^{-2}\text{s}^{-1}$] | 26.8 | 21.7 | 3.4 | 0.92 | 0.25 |
| Initial \mathcal{L}_{NN} [$10^{30}\text{cm}^{-2}\text{s}^{-1}$] | 42855 | 34713 | 20893 | 15353 | 10729 |
| Peak \mathcal{L}_{AA} [$10^{30}\text{cm}^{-2}\text{s}^{-1}$] | 46.0 | 46.8 | 7.1 | 1.4 | 0.25 |
| Peak \mathcal{L}_{NN} [$10^{30}\text{cm}^{-2}\text{s}^{-1}$] | 73552 | 74805 | 43130 | 23017 | 10729 |
| Integrated \mathcal{L}_{AA} [$\text{nb}^{-1}/\text{run}$] | 28381 | 25074 | 3286 | 560 | 62 |
| Integrated \mathcal{L}_{NN} [$\text{fb}^{-1}/\text{run}$] | 45.4 | 40.1 | 20.0 | 9.3 | 2.7 |
| Rate of hadronic interactions [MHz] | 127.1 | 129.4 | 30.4 | 8.1 | 2.0 |
| Events per bunch crossing | 7.7 | 7.8 | 1.8 | 0.5 | 0.1 |

^a Taken from Ref. [329]

12.4.1 Lower injection energy

A scenario where the SPS is upgraded with superconducting magnets to replace the LHC as the final injector before the FCC is under consideration. In this case the ramping time of the superconducting magnets becomes a significant fraction of the SPS cycle length, as illustrated in Fig. 12.15. Figure 12.15 assumes the cycle times discussed in Subsection 12.1.1, except for the longer ramp in the SPS. The filling shown in Fig. 12.1 would take about 1.5 to

2 hours. Moreover the debunching losses and emittance growth²⁰ from IBS are enhanced at lower energy on the FCC injection plateau, whilst the dwell times are prolonged. Therefore, a reduction of the FCC injection energy by using a superconducting SPS would reduce the total intensity and with it, the overall performance of heavy-ion operation. If this option becomes preferred, more detailed studies are required to estimate the impact on luminosity for heavy ions.

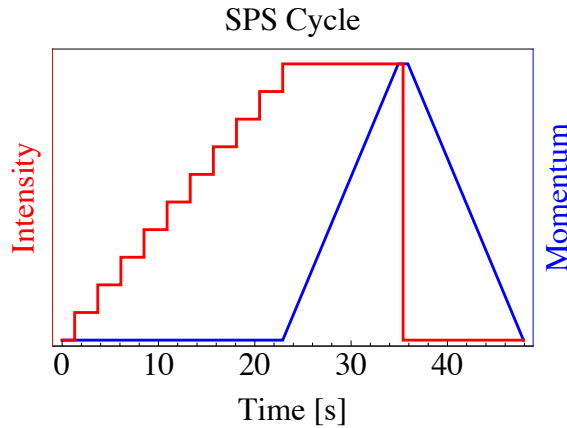


Figure 12.15: Example of a filling and acceleration cycle in the superconducting SPS.

12.5 Conclusion and outlook

Table 12.1 summarises key parameters for Pb–Pb and p–Pb operation at $E_b = 50Z$ TeV in the FCC-hh. For p–Pb operation, the Pb beam is assumed to be the same as for Pb–Pb. The calculated luminosity values assume an optimised theoretical turn-around time of around 26 min per LHC ion cycle and an additional preparation time in the FCC-hh of 1.2 h per FCC-hh filling, as quoted in Ref. [347]. It was assumed that the first LHC beam is prepared during preparation time of the FCC-hh, so that the total turn-around time sums up to about 150 minutes. This represents a theoretical minimum. In reality early beam aborts and other faults will increase this time and somewhat reduce the integrated luminosity.

The final values for the integrated luminosity in a typical annual one-month run quoted in Table 12.1 assume a ‘performance efficiency factor’ of 50% to allow for set-up time, down-time and other deviations from the idealised running described in Figs. 12.4 and 12.6 (a similar factor was observed during LHC operation [348] and applied in HL-LHC performance projections). For the moment, no studies of upgrades to the heavy-ion injectors (source, linac, accumulation ring, PS and SPS synchrotrons) have been performed. If upgrades to these machines can be envisaged by the time of FCC-hh operation, then even higher luminosities are likely to be available.

Heavy-ion operation imposes challenging specifications for the collimation system, including certain adaptations of the FCC-hh main ring, e.g. special absorbers in key locations for the high flux of modified ions from the bound-free pair-production process at the interaction point. The cross-sections of these processes are so high that the powers continuously deposited in a very localised spot exceed a few tens of kilowatts. These special absorbers need to be installed in the cold area of the dispersion suppressor on both sides of each interaction region where ions collide. They must not only ensure that the power deposited by the impacting ions is safely removed, but also that the fragmentation products produced do not escape to the subsequent superconducting magnet area. An absorber design still remains to be studied. Collimation of the heavy-ion beams will also be a difficult issue and require further absorbers or, possibly, the application of new collimation technologies such as bent crystals or electron lenses. The potential of these technologies is under study at the LHC.

If the demands on the collimation system are too extreme for lead ion operation, an ion species with a lower charge number (Z) could be used. The cross-sections of the ultra-peripheral electromagnetic processes are proportional to high powers of Z . Therefore the power of the secondary beams emerging from the collision point would be reduced, while providing a longer luminosity lifetime, since more particles are available for hadronic interactions. The physics case for lower- Z ion species is under study in the community.

²⁰This effect is less important than the particle losses, because the very fast radiation damping at FCC top energy will quickly reduce the emittances.

References

- [1] M. Benedikt, *et al.*, “Future Circular Collider Study. Volume 3: The Hadron Collider (FCC-hh) Conceptual Design Report,” Tech. Rep. CERN-ACC-2018-0058, CERN, Geneva, Dec 2018. *Published in Eur. Phys. J. Spec. Top.* 228 (2019) 755–1107. doi:10.1140/epjst/e2019-900087-0.
- [2] A. Abada, *et al.*, “Future Circular Collider Study. Volume 1: FCC Physics Opportunities Conceptual Design Report”, Tech. Rep. CERN-ACC-2018-0056, CERN, Geneva, Dec 2018. *Published in Eur. Phys. J. C* 79 (2019) 474. doi:10.1140/epjc/s10052-019-6904-3.
- [3] M. Mangano, ed., *Heavy ions at the Future Circular Collider, Chapter 4*, vol. Vol.3/2017 of *CERN Yellow Reports: Monographs*. CERN, Geneva, 2017. arXiv:1710.06353. doi:10.23731/CYRM-2017-003.
- [4] M. Benedikt, *et al.*, “Future Circular Collider Study. Volume 2: Accelerators, Technical Infrastructure and Safety Feasibility Study Report:”, Tech. Rep. CERN-FCC-ACC-2025-0004, CERN, Geneva, Mar 2025. arXiv:2505.00274. doi:10.17181/CERN.EBAY.7W4X.
- [5] S. Furuseth, “Head-On Beam-Beam Interactions in High-Energy Hadron Colliders. GPU-Powered Modelling of Nonlinear Effects,” Master’s thesis, NTNU, 2017. CERN-THESIS-2017-279 (2017).
- [6] S. Arsenyev and D. Schulte, “Broadband Impedance of Pumping Holes and Interconnects in the FCC-hh Beamscreen,” in *Proceedings, 9th International Particle Accelerator Conference (IPAC 2018): Vancouver, Canada*, April 29–May 4, 2018. doi:10.1088/1742-6596/1067/2/022003.
- [7] M. Benedikt, D. Schulte, and F. Zimmermann, “Optimizing integrated luminosity of future hadron colliders,” *Phys. Rev. Spec. Top. Accel. Beams*, vol. 18, no. 10, p. 101002, October, 2015. doi:10.1103/PhysRevSTAB.18.101002.
- [8] X. Buffat and D. Schulte, “Evolution of the Beam Parameters during Luminosity Production in the Future Circular Hadron Collider,” in *Proc. of International Particle Accelerator Conference (IPAC’16), Busan, Korea, May 8–13, 2016*, 7th International Particle Accelerator Conference, (Geneva, Switzerland), pp. 1426–1429, JACoW, June 2016. doi:10.18429/JACoW-IPAC2016-TUPMW008.
- [9] F. Antoniou *et al.*, “Can we predict luminosity?,” in *7th Evian Workshop on LHC beam operation, Evian-les-Bains*, (France), pp. 125–132, December 13–15 2016.
- [10] R. Alemany Fernandez, *et al.*, “FCC-hh turn-around cycle,” Tech. Rep. CERN-ACC-2016-0341, CERN, 2016.
- [11] M. Hofer, “Optics Design for the Low Luminosity Experiments in the FCC-hh,” Master’s thesis, Vienna University of Technology, November 28 2017. CERN-THESIS-2017-418.
- [12] W. Bartmann *et al.*, “Beam Transfer to the FCC-hh Collider from a 3.3 TeV Booster in the LHC Tunnel,” in *Proceedings of the IPAC’15, Richmond, VA, USA, May 3–8, 2015*, (Geneva, Switzerland), pp. 3901–3904, JACoW, June 2015. doi:10.18429/JACoW-IPAC2015-THPF089.
- [13] T. Kramer *et al.*, “Considerations for the Injection and Extraction Kicker Systems of a 100 TeV Centre-of-Mass FCC-hh Collider,” in *Proceedings of the IPAC’16, Busan, Korea*, (Geneva, Switzerland), pp. 3901–3904, JACoW, May 8–13 2016. doi:10.18429/JACoW-IPAC2016-THPOR049.
- [14] J. A. Uythoven *et al.*, “Injection Protection Upgrade for the HL-LHC,” in *Proceedings of the IPAC’15, Richmond, VA, USA, May 3–8, 2015*, (Geneva, Switzerland), pp. 2136–2139, JACoW, June 2015. doi:10.18429/JACoW-IPAC2015-TUPTY051.
- [15] W. Bartmann, *et al.*, “Dump system concepts for the Future Circular Collider,” *Phys. Rev. Accel. Beams*, vol. 20, p. 031001, Mar 2017. doi:10.1103/PhysRevAccelBeams.20.031001.
- [16] F. Burkart *et al.*, “Conceptual design considerations for the 50 TeV FCC beam dump insertion,” in *Proceedings of the IPAC’16, Busan, Korea, May 8–13, 2016*, (Geneva, Switzerland), pp. 1356–1359, JACoW, June 2016. doi:10.18429/JACoW-IPAC2016-TUPMR047.
- [17] O. S. Brüning *et al.* (editors), “LHC design report v.1 : The LHC main ring,” *CERN-2004-003-V1*, 2004. doi:10.5170/CERN-2004-003-V-1.
- [18] M. Fiassarri, *et al.*, “First Design of a Proton Collimation System for 50 TeV FCC-hh,” *Proceedings of the International Particle Accelerator Conference 2016, Busan, Korea*, p. 2425, 2016. doi:10.18429/JACoW-IPAC2016-WEPMW006.

- [19] M. Fiascaris, R. Bruce, and S. Redaelli, “A conceptual solution for a beam halo collimation system for the Future Circular hadron-hadron Collider (FCC-hh),” *Nucl. Instrum. and Methods Phys. Res., A*, vol. 894, pp. 96–106, 2018. doi:10.1016/j.nima.2018.03.042.
- [20] R.W. Assmann, “Collimators and Beam Absorbers for Cleaning and Machine Protection,” *Proceedings of the LHC Project Workshop - Chamonix XIV, Chamonix, France*, p. 261, 2005.
- [21] G. Robert-Demolaize, *Design and Performance Optimization of the LHC Collimation System*. PhD thesis, Université Joseph Fourier, Grenoble, 2006.
- [22] R.W. Assmann *et al.*, “The Final Collimation System for the LHC,” *Proc. of the European Particle Accelerator Conference 2006, Edinburgh, Scotland*, p. 986, 2006.
- [23] C. Bracco, *Commissioning Scenarios and Tests for the LHC Collimation System*. PhD thesis, EPFL Lausanne, 2008.
- [24] R. Bruce, *et al.*, “Simulations and measurements of beam loss patterns at the CERN Large Hadron Collider,” *Phys. Rev. Spec. Top. Accel. Beams*, vol. 17, p. 081004, Aug 2014. doi:10.1103/PhysRevSTAB.17.081004.
- [25] R. Bruce, *et al.*, “Reaching record-low β^* at the CERN Large Hadron Collider using a novel scheme of collimator settings and optics,” *Nucl. Instr. Meth. Phys. Res. A*, vol. 848, pp. 19–30, Jan 2017. doi:10.1016/j.nima.2016.12.039.
- [26] G. Apollinari, *et al.*, *High-Luminosity Large Hadron Collider (HL-LHC): Technical Design Report V. 0.1*. CERN Yellow Reports: Monographs. CERN-2017-007-M, Geneva: CERN, 2017. doi:10.23731/CYRM-2017-004.
- [27] R. Bruce, A. Marsili, and S. Redaelli, “Cleaning Performance with 11T Dipoles and Local Dispersion Suppressor Collimation at the LHC,” *Proceedings of the IPAC’14, Dresden, Germany*, p. 170, 2014. doi:10.18429/JACoW-IPAC2014-MOPRO042.
- [28] A. Lechner *et al.*, “Power Deposition in LHC Magnets With and Without Dispersion Suppressor Collimators Downstream of the Betatron Cleaning Insertion,” in *Proceedings of the International Particle Accelerator Conference 2014, Dresden, Germany*, 2014. doi:10.18429/JACoW-IPAC2014-MOPRO021.
- [29] J. Molson, *et al.*, “Status of the FCC-hh collimation system,” *Proceedings of the International Particle Accelerator Conference 2017, Copenhagen, Denmark*, p. 64, 2017. doi:10.18429/JACoW-IPAC2017-MOPAB001.
- [30] M. I. Besana, *et al.*, “Energy deposition in the betatron collimation insertion of the 100 TeV future circular collider,” *Proceedings of the International Particle Accelerator Conference 2017, Copenhagen, Denmark*, p. 68, 2017. doi:10.18429/JACoW-IPAC2017-MOPAB003.
- [31] A. Krainer, “Design and Simulation of new protection devices in the dispersion suppressor regions for the Future Circular Collider Project,” Master’s thesis, Graz University of Technology, Austria, 2019.
- [32] R. Bruce *et al.*, “Status of collimation system studies.” Fourth Annual Meeting of the Future Circular Collider study, Amsterdam, The Netherlands, April 2018.
- [33] R. Martin, *et al.*, “Interaction region design driven by energy deposition,” *Phys. Rev. Accel. Beams*, vol. 20, p. 081005, Aug 2017. doi:10.1103/PhysRevAccelBeams.20.081005.
- [34] S. Fartoukh, “Achromatic telescopic squeezing scheme and application to the LHC and its luminosity upgrade,” *Phys. Rev. Spec. Top. Accel. Beams*, vol. 16, p. 111002, Nov 2013. doi:10.1103/PhysRevSTAB.16.111002.
- [35] J. Barranco García, “Beam-beam studies for FCC-hh.” FCC week 2018, Amsterdam, April, 2018.
- [36] E. Cruz-Alaniz, *et al.*, “Design of the large hadron electron collider interaction region,” *Phys. Rev. Accel. Beams*, vol. 18, p. 111001, Nov 2015. doi:10.1103/PhysRevSTAB.18.111001.
- [37] R. de Maria, “Layout design for final focus systems and applications for the LHC interaction region upgrade.” CERN-LHC-PROJECT-REPORT-1051, 2007.
- [38] W. Herr, *et al.*, “Long Range Beam-beam Effects in the LHC,” in *Proceedings, ICFA Mini-Workshop on Beam-Beam Effects in Hadron Colliders (BB2013): CERN, Geneva, Switzerland, March 18–22 2013*, pp. 87–92, 2014. doi:10.5170/CERN-2014-004.87.
- [39] T. Pieloni *et al.*, “Two Beam Effects,” in *Proc. 2014 Evian Workshop on LHC Beam Operation*, (Geneva), pp. 69–79, CERN, 2014.

- [40] X. Buffat, *et al.*, “Long-range and head-on beam-beam: what are the limits?,” in *7th Evian workshop on LHC beam operation: Evian-les-Bains, France.*, (Geneva), pp. 133–140, CERN, 2017.
- [41] T. Pieloni, *A study of beam-beam effects in hadron colliders with a large number of bunches*. PhD thesis, Ecole Polytechnique Federale de Lausanne (EPFL), 2008.
- [42] W. Herr, *et al.*, “Observations of beam-beam effects at high intensities in the LHC,” in *Proc. of International Particle Accelerator Conference (IPAC’11), San Sebastian, Spain, September 4-9, 2011*, (Geneve), pp. 1936–1938, JACoW, Sep 2011.
- [43] W. Herr, “Features and implications of different LHC crossing schemes,” Tech. Rep. CERN-LHC-Project-Report-628, CERN, Geneva, Feb 2003.
- [44] J. Barranco García *et al.* EuroCirCol Meeting Oct 2017, Presentation at the LHC machine committee, October, 2017.
- [45] Sixtrack web site: <http://sixtrack.web.cern.ch/SixTrack/>.
- [46] F. Schmidt, “SixTrack User’s Reference Manual,” Tech. Rep. CERN/SL/94-56-AP, CERN, 1994.
- [47] W. Herr and T. Pieloni. http://cern.ch/lhc-beam-beam/combi_welcome.html.
- [48] T. Pieloni and W. Herr, “Coherent beam-beam modes in the CERN Large Hadron Collider (LHC) for multiple bunches, different collision schemes and machine symmetries,” in *Proceedings of 2005 Particle Accelerator Conference, Knoxville, Tennessee*, pp. 4030–4032, May 2005.
- [49] T. Pieloni and W. Herr, “Models to study multi bunch coupling through head-on and long-range beam-beam interactions,” CERN-LHC-Project-Report-937 and Proceedings of EPAC06, Edinburgh, United Kingdom, 2006, CERN, 2006.
- [50] M. Crouch, *Luminosity Performance Limitations due to the Beam-Beam Interaction in the Large Hadron Collider*. PhD thesis, Manchester University, 2017.
- [51] M. Giovannozzi, “Proposed scaling law for intensity evolution in hadron storage rings based on dynamic aperture variation with time,” *Phys. Rev. Spec. Top. Accel. Beams*, vol. 15, p. 024001, Feb 2012. doi:10.1103/PhysRevSTAB.15.024001.
- [52] X. Buffat, *et al.*, “Stability diagrams of colliding beams in the Large Hadron Collider,” *Phys. Rev. Spec. Top. Accel. Beams*, vol. 17, p. 111002, Nov 2014. doi:10.1103/PhysRevSTAB.17.111002.
- [53] H. Grote, F. Schmidt, and L. H. A. Leunissen, “LHC Dynamic Aperture at Collision,” Tech. Rep. LHC-PROJECT-NOTE-197, CERN, Geneva, Aug 1999.
- [54] Y. Luo and F. Schmidt, “Dynamic Aperture Studies for LHC Optics Version 6.2 at Collision,” Tech. Rep. LHC-PROJECT-NOTE-310, CERN, Geneva, Jan 2003.
- [55] M. Crouch *et al.*, “Dynamic aperture studies of long-range beam-beam interactions at the LHC,” in *Proceedings, 8th International Particle Accelerator Conference (IPAC 2017): Copenhagen, Denmark*, (Geneva, Switzerland), pp. 3840–3843, JACoW, May 2017. doi:10.18429/JACoW-IPAC2017-THPAB056.
- [56] J. Barranco García, *et al.*, “Beam-Beam Studies for FCC-hh,” in *Proc. of International Particle Accelerator Conference (IPAC’17), Copenhagen, Denmark, 14–19 May, 2017*, (Geneva, Switzerland), pp. 2109–2112, JACoW, May 2017. doi:10.18429/JACoW-IPAC2017-TUPVA026.
- [57] J. Gareyte, J. Koutchouk, and F. Ruggiero, “Landau damping, Dynamic Aperture and Octupoles in the LHC,” Tech. Rep. LHC-Project-Report-91, CERN, Geneva, Switzerland, 1997.
- [58] J. Shi, O. Kheawpum, and L. Jin, “Global Compensation of Long-range Beam-beam Interactions with Multipole Correctors,” in *Proc. of EPAC 2002, Paris, France*, pp. 1296–1298, EPS-IGA and CERN, June 2002.
- [59] T. Pieloni *et al.*, “Colliding High Brightness Beams in the LHC,” in *Proc. of HB2012, Beijing, China*, pp. 180–182, 2012.
- [60] X. Buffat, *et al.*, “Probing the behaviour of high brightness bunches in collision at 6.5 TeV and the interplay with an external source of noise (MD1433),” Apr 2017. CERN-ACC-NOTE-2017-0030.
- [61] S. V. Furusest and X. Buffat, “Modeling of nonlinear effects due to head-on beam-beam interactions,” *Phys. Rev. Accel. Beams*, vol. 21, p. 081002, Aug 2018. doi:10.1103/PhysRevAccelBeams.21.081002.
- [62] A. Ferrari, *et al.*, “FLUKA: a multi-particle transport code,” *CERN Report CERN-2005-10*, 2005. doi:10.5170/CERN-2005-010.
- [63] T. Böhlen, *et al.*, “The FLUKA Code: Developments and Challenges for High Energy and Medical Applications,” *Nuclear Data Sheets*, no. 120, pp. 211–214, 2014.

- [64] E. Skordis, *et al.*, “Impact of Beam Losses in the LHC Collimation Regions,” in *Proc. 6th International Particle Accelerator Conference (IPAC’15)*, Richmond, VA, USA, May 3-8, 2015, pp. 2116–2119, June 2015. doi:10.18429/JACoW-IPAC2015-TUPTY046.
- [65] F. Cerutti *et al.*, “Beam loss studies in IP.” talk at FCC week 2018, Amsterdam, Netherlands, April, 2018.
- [66] A. Infantino, B. Humann, and F. Cerutti, “Energy deposition from collision debris in FCC-hh EIR.” presented at the 4th EuroCirCol meeting, Oct 2018.
- [67] D. Schoerling, “Review of peak power limits for high-luminosity IR triplet magnets,” 2017.
- [68] L. Bottura, “11T Magnet Operating Margin.” Presented at the 8th HL-LHC Collaboration Meeting, Oct 2018.
- [69] R. Walker, “Synchrotron radiation,” in *CAS – CERN Accelerator School : 5th General Accelerator Physics Course*, vol. 1, pp. 437–454, Geneva, Switzerland: CERN, 1992. doi:10.5170/CERN-1994-001.437.
- [70] M. Boscolo and H. Burkhardt, “Tools for Flexible Optimisation of IR Designs with Application to FCC,” in *Proc. 6th International Particle Accelerator Conference (IPAC15)*, pp. 2072–2074, 2015. doi:10.18429/JACoW-IPAC2015-TUPTY031.
- [71] L. Deniau, *et al.*, *The MAD-X program: Methodical Accelerator Design User’s Reference Manual*. CERN, Geneva, Switzerland, Oct 2018.
- [72] A. Naumann, *et al.*, *ROOT: Data Analysis Framework User’s Guide*. CERN, Geneva, Switzerland, May 2018.
- [73] S. Agostinelli *et al.*, “Geant4—a simulation toolkit,” *Nucl. Instrum. Methods Phys. Res., A*, vol. 506, no. 3, pp. 250 – 303, 2003. doi:10.1016/S0168-9002(03)01368-8.
- [74] F. Collamati, *et al.*, “Synchrotron radiation backgrounds for the FCC-hh experiments,” *J. Phys.: Conf. Ser.*, vol. 874, no. 1, p. 012004, 2017. doi:10.1088/1742-6596/874/1/012004.
- [75] R. Kersevan, M. Ady, and J. Pons, *Molflow–SynRad: A Monte Carlo Simulator package developed at CERN*. CERN, Geneva, Switzerland.
- [76] J. Abelleira, L. van Riesen-Haupt, *et al.*, “An alternative final-focus system for the FCC-hh: triplet optimization with energy deposition studies,” *submitted for publication*, 2018.
- [77] L. van Riesen-Haupt, *et al.*, “A Code for Optimising Triplet Layout,” in *Proc. of International Particle Accelerator Conference (IPAC’17)*, Copenhagen, Denmark, 14–19 May, 2017, pp. 2163–2166, May 2017. doi:10.18429/JACoW-IPAC2017-TUPVA043.
- [78] J. Abelleira, *et al.*, “Energy Deposition Studies and Luminosity Evolution for the Alternative FCC-hh Triplet,” in *Proc. 9th International Particle Accelerator Conference (IPAC’18)*, Vancouver, BC, Canada, April 29–May 4, 2018, (Geneva, Switzerland), pp. 352–355, JACoW Publishing, June 2018. doi:10.18429/JACoW-IPAC2018-MOPMK003.
- [79] L. van Riesen-Haupt, *et al.*, “An Optimised Triplet for the Final Focus of the FCC-HH with a 40m Final Drift,” in *Proc. 9th International Particle Accelerator Conference (IPAC’18)*, Vancouver, BC, Canada, April 29–May 4, 2018, (Geneva, Switzerland), pp. 364–367, JACoW Publishing, June 2018. doi:10.18429/JACoW-IPAC2018-MOPMK007.
- [80] R. Tomás, *et al.*, “HL-LHC Alternative Scenarios,” in *Chamonix 2014: Workshop on LHC Performance*, pp. 217–224, 2015. doi:10.5170/CERN-2015-002.217.
- [81] Pieloni, T and others, “Beam-beam effects in the HE-LHC.” FCC week 2018, Amsterdam, Netherlands, April 2018.
- [82] A. Chancé *et al.*, “Status of the Beam Optics of the Future Hadron-Hadron Collider FCC-hh,” in *Proc. of 7th International Particle Accelerator Conference (IPAC’16)*, Busan, Korea, May 8-13, 2016, (Geneva, Switzerland), pp. 1470–1472, JACoW, June 2016. doi:10.18429/JACoW-IPAC2016-TUPMW020.
- [83] H. M. Durand *et al.*, “HL-LHC Alignment Requirements and Associated Solutions,” in *Proc. of 8th International Particle Accelerator Conference (IPAC’17)*, Copenhagen, Denmark, 14–19 May, 2017, (Geneva, Switzerland), pp. 1893–1896, JACoW, May 2017. doi:10.18429/JACoW-IPAC2017-TUPIK085.
- [84] D. Boussard and T. P. R. Linnecar, “The LHC Superconducting RF System,” Tech. Rep. CERN-LHC-Project-Report-316, CERN, Geneva, Dec 1999.
- [85] E. Shaposhnikova, “Longitudinal beam dynamics and RF requirements.” The third Annual Meeting of the Future Circular Collider Study, Berlin, 2017.

- [86] E. Shaposhnikova and I. Karpov, “Longitudinal beam dynamics and RF requirements.” The fourth Annual Meeting of the Future Circular Collider Study, Amsterdam, 2018.
- [87] A. Lechner, “Status of FCC-hh studies on injection/extraction protection devices and the dump.” Presented at FCC General Design Meeting, CERN, Geneva, December 2017.
- [88] A. Lechner, “FCC-hh protection absorbers and dumps.” Presented at FCC Week, Beurs van Berlage, Netherlands, April 2018.
- [89] E. Renner, “Machine Protection of the Future Circular Hadron Collider FCC-hh: Injection and Extraction,” Master’s thesis, Vienna, Tech. U., 2018. Presented 13 Aug 2018.
- [90] I. Lamas Garcia *et al.*, “HiRadMat TCDI / TDI material tests (3D Carbon/Carbon and graphic 75/50).” presented at 7th HL-LHC Collaboration Meeting, Madrid, Spain, November 2017.
- [91] V. Raginel *et al.*, “First Experimental Results on Damage Limits of Superconducting Accelerator Magnet Components Due to Instantaneous Beam Impact,” *IEEE Trans. Appl. Supercond.*, vol. 28, no. 4, p. 8800310, 2018. doi:10.1109/TASC.2018.2817346.
- [92] F. M. Velotti, *Higher brightness beams from the SPS for the HL-LHC era*. PhD thesis, EPFL, Lausanne, Switzerland, 2017. CERN-THESIS-2017-041.
- [93] R. Bruce, *et al.*, “Updated parameters for HL-LHC aperture calculations for proton beams,” Tech. Rep. CERN-ACC-2017-0051, CERN, Geneva, Jul 2017.
- [94] Y. Nie, *et al.*, “Numerical simulations of energy deposition caused by 50 MeV–50 TeV proton beams in copper and graphite targets,” *Phys. Rev. Accel. Beams*, vol. 20, no. 8, p. 081001, 2017. doi:10.1103/PhysRevAccelBeams.20.081001.
- [95] A. Chmielinska, *Optimization of the Beam Screen for the FCC Injection Kicker Magnets*. PhD thesis, Ecole Polytechnique, Lausanne, 2019. Presented 10 Dec 2019.
- [96] D. Woog, *et al.*, “Design of an Inductive Adder for the FCC injection kicker pulse generator,” *J. Phys. Conf. Ser.*, vol. 874, no. 1, p. 012096, 2017. doi:10.1088/1742-6596/874/1/012096.
- [97] M. J. Barnes, *et al.*, “Future circular collider injection and extraction kicker topologies and solid state generators,” *Phys. Rev. Accel. Beams*, vol. 22, no. 7, p. 071001. 12 p, 2019. doi:10.1103/PhysRevAccelBeams.22.071001.
- [98] D. Woog, *et al.*, “First Prototype Inductive Adder for the FCC Injection,” in *Proc. 9th International Particle Accelerator Conference (IPAC’18), Vancouver, BC, Canada, April 29–May 4, 2018*, (Geneva, Switzerland), pp. 2553–2556, JACoW Publishing, June 2018. doi:10.18429/JACoW-IPAC2018-WEPMF076.
- [99] D. Barna, “High field septum magnet using a superconducting shield for the Future Circular Collider,” *Phys. Rev. Accel. Beams*, vol. 20, no. 4, p. 041002, 2017. doi:10.1103/PhysRevAccelBeams.20.041002.
- [100] A. Sanz Ull, *Optimized design of magnetic septa for the Future Circular Collider*. PhD thesis, Eindhoven, Tech. U., 2019. Presented 14 Jun 2019.
- [101] V. Raginel, *et al.*, “First results from magnet component damage experiments due to beam heating.” Presentation at the 39th HL-LHC Technical Committee Meeting, 2017.
- [102] A. Will, *et al.*, “First results on superconducting magnet damage tests at 4K with beam.” Presentation at the 8th HL-LHC Collaboration Meeting, 2018.
- [103] N. Tahir, *et al.*, “Beam Induced Hydrodynamic Tunneling in the Future Circular Collider Components,” *Phys. Rev. Accel. Beams*, vol. 19, no. 8, p. 081002, 2016. doi:10.1103/PhysRevAccelBeams.19.081002.
- [104] M. Cauchi, *et al.*, “High energy beam impact tests on a LHC tertiary collimator at the CERN high-radiation to materials facility,” *Phys. Rev. Spec. Top. Accel. Beams*, vol. 17, p. 021004, Feb 2014. doi:10.1103/PhysRevSTAB.17.021004.
- [105] A. Fasso *et al.*, “The physics models of FLUKA: status and recent developments,” *Proc. of the Computing in High Energy and Nuclear Physics 2003 Conf., La Jolla*, 2003.
- [106] M. Atanasov *et al.*, “Upgrade of the TCDQ Diluters for the LHC Beam Dump System,” in *Proc. 6th International Particle Accelerator Conference (IPAC’15), Richmond, VA, USA, May 3–8, 2015*, (Geneva, Switzerland), pp. 3079–3082, JACoW, June 2015. doi:10.18429/JACoW-IPAC2015-WEPMN067.
- [107] J. Uythoven *et al.*, “Upgrades to the LHC Injection and Beam Dumping Systems for the HL-LHC Project,” in *Proc. 5th International Particle Accelerator Conference (IPAC’14), Dresden, Germany, June 15–20, 2014*, (Geneva, Switzerland), pp. 141–144, JACoW, July 2014. doi:10.18429/JACoW-IPAC2014-MOPRO032.

- [108] I. Efthymiopoulos, *et al.*, “HiRadMat: A New Irradiation Facility for Material Testing at CERN,” in *Proceedings of the 2nd International Particle Accelerator Conference, San Sebastian, Spain*, pp. 1665–1667, September 2011.
- [109] F. Nuiry *et al.*, “Low-Z material R&D application for Beam Intercepting Devices (BID) at CERN,” in *3rd International Workshop on Spallation Materials Technology, Chattanooga, TN, USA*, November 2016.
- [110] F. Carra *et al.*, “The MultiMat Experiment at CERN HiRadMat Facility: Advanced Testing of Novel Materials and Instrumentation for HL-LHC Collimators,” in *Proc. of International Particle Accelerator Conference (IPAC’17), Copenhagen, Denmark*, pp. 76–79, May 2017. doi:10.18429/JACoW-IPAC2017-MOPAB005.
- [111] O. Brüning, *et al.*, eds., *LHC Design Report Vol.1: The LHC Main Ring*, ch. Beam Dumping System. CERN, 2004. doi:10.5170/CERN-2004-003-V-1.
- [112] S. Péraire and P. Sala, “Beam dumps and beam stoppers for LHC and CNGS transfer lines,” Tech. Rep. LHC Project Report 465, CERN, 2001.
- [113] J. Kidd, *et al.*, “A High Intensity Beam Dump for the Tevatron Beam Abort System,” *IEEE Trans. Nucl. Sci.*, no. 28, pp. 2774–2776, 1981. doi:10.1109/TNS.1981.4331909.
- [114] B. Hanna and C. Crawford, “Construction of a new Tevatron Collider Beam Abort Dump,” in *Conference Record of the 1991 IEEE Particle Accelerator Conference*, pp. 970–972, 1991.
- [115] M. Schmitz, “Overview of the Beam Abort System for the 820GeV/c HERA Proton Ring,” in *Proceedings of the 3rd European Particle Accelerator Conference, Berlin, Germany*, pp. 1455–1456, 1992.
- [116] N. Tahir, *et al.*, “Hydrodynamic tunneling studies for a water beam dump,” in *Presentation at the FCC Week 2017, Berlin*, 2017.
- [117] F. Benedek, *et al.*, “Realization of the optimal beam dilution pattern of the FCC-hh ring using beating frequencies,” *FCC Week 2019*, 2019.
- [118] A. Chancé, *et al.*, “Updates on the Optics of the Future Hadron-Hadron Collider FCC-hh,” in *Proc. of 8th International Particle Accelerator Conference (IPAC’17), Copenhagen, Denmark, 14–19 May, 2017*, (Geneva, Switzerland), pp. 2023–2026, JACoW, May 2017. doi:10.18429/JACoW-IPAC2017-TUPVA002.
- [119] A. Chancé, *et al.*, “First results for a FCC-hh ring optics design,” Tech. Rep. CERN-ACC-2015-0035, CERN, Geneva, Apr 2015.
- [120] A. Chancé, *et al.*, “Overview of Arc Optics of FCC-hh,” in *Proc. 9th International Particle Accelerator Conference (IPAC’18), Vancouver, BC, Canada, April 29–May 4, 2018*, pp. 141–144, June 2018. doi:10.18429/JACoW-IPAC2018-MOPMF025.
- [121] C. Tambasco *et al.*, “Landau Damping Studies for the FCC: Octupole Magnets, Electron Lens and Beam-Beam Effects,” in *Proc. 9th International Particle Accelerator Conference (IPAC’18), Vancouver, BC, Canada, April 29–May 4, 2018*, pp. 3150–3153, June 2018. doi:10.18429/JACoW-IPAC2018-THPAF074.
- [122] L. Gonzalez *et al.*, “Results on the FCC-hh Beam Screen at the KIT Electron Storage Ring KARA,” in *Proc. 9th International Particle Accelerator Conference (IPAC’18), Vancouver, BC, Canada, April 29–May 4, 2018*, (Geneva, Switzerland), pp. 55–57, JACoW Publishing, June 2018. doi:10.18429/JACoW-IPAC2018-MOZGBE5.
- [123] D. Schoerling, “Magnet status towards the CDR.” FCC week 2017, Berlin, Germany, 2017.
- [124] C. Lorin, *et al.*, “Design of a Nb₃Sn 400 T/m Quadrupole for the Future Circular Collider,” *IEEE Trans. Appl. Supercond.*, vol. 28, no. 3, pp. 1–5, 2018. doi:10.1109/TASC.2018.2797945.
- [125] B. Dalena, *et al.*, “Advance on Dynamic Aperture at Injection for FCC-hh,” in *Proc. of 8th International Particle Accelerator Conference (IPAC’17), Copenhagen, Denmark*, (Geneva, Switzerland), pp. 2027–2030, JACoW, May 2017. doi:10.18429/JACoW-IPAC2017-TUPVA003.
- [126] B. Dalena *et al.*, “Dipole Field Quality and Dynamic Aperture for FCC-hh,” in *Proc. 9th International Particle Accelerator Conference (IPAC’18), Vancouver, BC, Canada, April 29–May 4, 2018*, (Geneva, Switzerland), pp. 137–140, JACoW Publishing, June 2018. doi:10.18429/JACoW-IPAC2018-MOPMF024.
- [127] O. S. Brüning and S. D. Fartoukh, “Field Quality Specification for the LHC Main Dipole Magnets,” Tech. Rep. LHC-Project-Report-501. CERN-LHC-Project-Report-501, CERN, Geneva, Oct 2001.
- [128] A. Chao and M. Tigner, *Handbook of Accelerator Physics and Engineering*. Handbook of Accelerator Physics and Engineering, World Scientific, 1999. doi:10.1142/8543.

- [129] Y. Nosochkov and D. M. Ritson, “The provision of IP crossing angles for the SSC,” in *Proceedings of International Conference on Particle Accelerators (PAC’93), Washington DC, USA*, pp. 125–127, May 1993.
- [130] P. Hagen, “Magnetic model of the normal-conducting magnets MBW, MBXW(H) and MCBW(H/V),” November 2009.
- [131] E. Todesco and G. Sabbi, “Requirements for Nb₃Sn inner triplet and comparison with present state of the art,” Tech. Rep. CERN-ACC-2013-001, HILUMILHC-MIL-MS-33, CERN, Nov 2012.
- [132] B. Dalena *et al.*, “First Evaluation of Dynamic Aperture at Injection for FCC-hh,” in *Proc. of 7th International Particle Accelerator Conference (IPAC’16), Busan, Korea, May 8–13, 2016*, (Geneva, Switzerland), pp. 1466–1469, JACoW, June 2016. doi:10.18429/JACoW-IPAC2016-TUPMW019.
- [133] A. Fedynitch, *Cascade Equations and Hadronic Interactions at Very High Energies*. PhD thesis, KIT, 2015. CERN-THESIS-2015-371.
- [134] P. K. Skowronski *et al.*, “Advances in MAD-X using PTC,” 2007. LHC-Project-Report-1016.
- [135] S. Tygier, *et al.*, “Recent Development and Results With the Merlin Tracking Code,” in *Proc. of 8th International Particle Accelerator Conference (IPAC’17), Copenhagen, Denmark, 14–19 May, 2017*, (Geneva, Switzerland), pp. 104–106, JACoW, May 2017. doi:10.18429/JACoW-IPAC2017-MOPAB013.
- [136] E. Todesco. Private Communication, 2017.
- [137] R. K. Adair and H. Kasha, “The Range of Muons in Rocks,” in *Proceedings, 13th International Conference on Cosmic Rays, Denver, Colorado*, pp. 1740–1745, January 1973.
- [138] Particle Data Group. *Passage of particles through matter*, 2005.
- [139] M. I. Besana, *et al.*, “Evaluation of the radiation field in the future circular collider detector,” *Phys. Rev. Accel. Beams*, vol. 19, p. 111004, Nov 2016. doi:10.1103/PhysRevAccelBeams.19.111004.
- [140] H. Rafique, *et al.*, “Proton Cross-Talk and Losses in the Dispersion Suppressor Regions at the FCC-hh,” in *Proc. of 8th International Particle Accelerator Conference (IPAC’17), Copenhagen, Denmark, 14–19 May, 2017*, (Geneva, Switzerland), pp. 1763–1765, JACoW, May 2017. doi:10.18429/JACoW-IPAC2017-TUPIK037.
- [141] J. Abelleira, *et al.*, “Cross-Talk Studies between FCC-hh Experimental Interaction Regions,” in *Proc. of 8th International Particle Accelerator Conference (IPAC’17), Copenhagen, Denmark, 14–19 May, 2017*, (Geneva, Switzerland), pp. 2136–2138, JACoW, May 2017. doi:10.18429/JACoW-IPAC2017-TUPVA036.
- [142] G. Iadarola, *Electron cloud studies for CERN particle accelerators and simulation code development*. PhD thesis, University of Naples, 2014. CERN-THESIS-2014-047. Presented 23 May 2014.
- [143] G. Iadarola, *et al.*, “Evolution of Python Tools for the Simulation of Electron Cloud Effects,” in *Proc. of 8th International Particle Accelerator Conference (IPAC’17), Copenhagen, Denmark, 14–19 May, 2017*, (Geneva, Switzerland), pp. 3803–3806, JACoW, May 2017. doi:10.18429/JACoW-IPAC2017-THPAB043.
- [144] M. A. Furman and M. T. F. Pivi, “Probabilistic model for the simulation of secondary electron emission,” *Phys. Rev. Spec. Top. Accel. Beams*, vol. 5, p. 124404, Dec 2002. doi:10.1103/PhysRevSTAB.5.124404.
- [145] R. Kirby and F. King, “Secondary electron emission yields from PEP-II accelerator materials,” *Nucl. Instrum. Methods Phys. Res., A*, vol. 469, no. 1, pp. 1–12, 2001. doi:10.1016/S0168-9002(01)00704-5.
- [146] R. Cimino, *et al.*, “Can low-energy electrons affect high-energy physics accelerators?,” *Phys. Rev. Lett.*, vol. 93, p. 014801, Jun 2004. doi:10.1103/PhysRevLett.93.014801.
- [147] V. Baglin, *et al.*, “A Summary of Main Experimental Results Concerning the Secondary Electron Emission of Copper,” Tech. Rep. LHC-Project-Report-472, CERN, Geneva, Aug 2001.
- [148] B. Henrist, *et al.*, “Secondary electron emission data for the simulation of electron cloud,” in *Proceedings of E-CLOUD’02*, 2002.
- [149] R. Cimino and I. Collins, “Vacuum chamber surface electronic properties influencing electron cloud phenomena,” *Applied Surface Science*, vol. 235, no. 1, pp. 231–235, 2004. doi:10.1016/j.apsusc.2004.05.270.
- [150] K. Ohmi and F. Zimmermann, “Head-Tail Instability Caused by Electron Clouds in Positron Storage Rings,” *Phys. Rev. Lett.*, vol. 85, pp. 3821–3824, Oct 2000. doi:10.1103/PhysRevLett.85.3821.
- [151] K. Ohmi, F. Zimmermann, and E. Perevedentsev, “Wake-field and fast head-tail instability caused by an electron cloud,” *Phys. Rev. E*, vol. 65, p. 016502, Dec 2001. doi:10.1103/PhysRevE.65.016502.

- [152] K. Ohmi, “[Electron cloud effect in damping rings of linear colliders](#),” in *Proceedings of ELOUD’04*, (Geneva), CERN, CERN, 2005.
- [153] K. Ohmi, *et al.*, “Study of Electron Cloud Instabilities in FCC-hh,” in *Proceedings, 6th International Particle Accelerator Conference (IPAC 2015): Richmond, Virginia, USA, May 3–8, 2015*, pp. 2007–2009, 2015. doi:10.18429/JACoW-IPAC2015-TUPTY006.
- [154] I. Bellafont, *et al.*, “Design of the future circular hadron collider beam vacuum chamber,” *Phys. Rev. Accel. and Beams*, vol. 23, p. 033201, Mar 2020. doi:10.1103/PhysRevAccelBeams.23.033201.
- [155] I. Bellafont, R. Kersevan, and L. Mether, “Summary of Modelling Studies on the Beam Induced Vacuum Effects in the FCC-hh,” in *Proc. 10th International Particle Accelerator Conference (IPAC’19), Melbourne, Australia, 19-24 May 2019*, no. 10 in International Particle Accelerator Conference, (Geneva, Switzerland), pp. 1331–1334, JACoW Publishing, Jun. 2019. doi:10.18429/JACoW-IPAC2019-TUPMP038.
- [156] A. Liedl, *et al.*, “Photo reflectivity and photo electron yield of technical surfaces,” in *Proc. of The Joint INFN-CERN-ARIES Workshop on Electron-Cloud Effects (ELOUD’18), La Biodola, Isola d’Elba, Italy*, June 2018. doi:10.23732/CYRCP-2020-007.125 .
- [157] R. Cimino, *et al.*, “Nature of the decrease of the secondary-electron yield by electron bombardment and its energy dependence,” *Phys. Rev. Lett.*, vol. 109, p. 064801, Aug 2012. doi:10.1103/PhysRevLett.109.064801.
- [158] V. Petit, *et al.*, “Role of the different chemical components in the conditioning process of air exposed copper surfaces,” *Phys. Rev. Accel. Beams*, vol. 22, p. 083101, Aug 2019. doi:10.1103/PhysRevAccelBeams.22.083101.
- [159] G. Iadarola, *et al.*, “[Analysis of the beam induced heat loads on the LHC arc beam screens during Run 2](#),” Tech. Rep. CERN-ACC-NOTE-2017-0066, CERN, Dec 2017.
- [160] G. Iadarola, *et al.*, “[Electron clouds and heat load in Run 2](#),” in *Proc. 9th LHC Operations Evian Workshop 30 Jan-1 Feb 2019, Evian, France, CERN, Geneva, Switzerland, 2019*.
- [161] C. Yin Vallgren, *et al.*, “Amorphous carbon coatings for the mitigation of electron cloud in the CERN Super Proton Synchrotron,” *Phys. Rev. Spec. Top. Accel. Beams*, vol. 14, p. 071001, Jul 2011. doi:10.1103/PhysRevSTAB.14.071001.
- [162] R. Valizadeh *et al.*, “Low Secondary Electron Yield of Laser Treated Surfaces of Copper, Aluminium and Stainless Steel,” in *Proc. of International Particle Accelerator Conference (IPAC’16), Busan, Korea*, pp. 1089–1092, May 2016. doi:10.18429/JACoW-IPAC2016-TUOCB02.
- [163] R. Valizadeh, *et al.*, “Reduction of secondary electron yield for e-cloud mitigation by laser ablation surface engineering,” *Appl. Surf. Sci.*, vol. 404, no. Supplement C, pp. 370–379, 2017. doi:10.1016/j.apsusc.2017.02.013.
- [164] N. Mounet, *The LHC Transverse Coupled-Bunch Instability*. PhD thesis, EPFL, 2012.
- [165] E. Metral, “Beam screen issues,” in *Proceedings, EuCARD-AccNet-EuroLumi Workshop: The High-Energy Large Hadron Collider (HE-LHC10): Villa Bighi, Malta, Republic of Malta, October 14-16, 2010*, 2011. doi:10.5170/CERN-2011-003.83.
- [166] N. Mounet, N. Biancacci, and D. Amorim, “[ImpedanceWake2D code](#).”
- [167] Code [CST PARTICLE STUDIO](#) - Wakefield Solver.
- [168] U. Niedermayer, O. Boine-Frankenheim, and H. D. Gersm, “Space charge and resistive wall impedance computation in the frequency domain using the finite element method,” *Phys. Rev. Spec. Top. Accel. Beams*, vol. 18, Mar 2015. doi:10.1103/physrevstab.18.032001.
- [169] D. Hynds, *et al.*, “Amorphous-carbon thin films for the mitigation of electron clouds in particle accelerators.” Final CARE-HHH Workshop on Scenarios for the LHC Upgrade and FAIR, CERN-2009-004, 2009. doi:10.5170/cern-2009-004.128.
- [170] P. C. Pinto. Private Communication, 2018.
- [171] B. Riemann, *et al.*, “Resistive-Wall Impedance of Insertions for FCC-hh,” in *Proc. 9th International Particle Accelerator Conference (IPAC’18), Vancouver, BC, Canada, April 29–May 4, 2018*, (Geneva, Switzerland), pp. 378–381, JACoW Publishing, June 2018. doi:10.18429/JACoW-IPAC2018-MOPMK014.
- [172] G. Stupakov, “Low frequency impedance of tapered transitions with arbitrary cross sections,” *Phys. Rev. Spec. Top. Accel. Beams*, vol. 10, p. 094401, 2007. doi:10.1103/PhysRevSTAB.10.094401.
- [173] D. Angal-Kalinin, “[Review of Coupled Bunch Instabilities in the LHC](#),” in *Proc. of EPAC 2002, Paris, France*, pp. 290–292, EPS-IGA and CERN, June 2002.

- [174] S. Arsenyev, O. Boine-Frankenheim, and D. Schulte, “FCC-hh transverse impedance budget,” in *Proc. 9th International Particle Accelerator Conference (IPAC’18), Vancouver, BC, Canada, April 29–May 4, 2018*, (Geneva, Switzerland), pp. 149–152, JACoW Publishing, June 2018. doi:10.18429/JACoW-IPAC2018-MOPMF029.
- [175] F. J. Sacherer, “A longitudinal stability criterion for bunched beams,” *IEEE Trans. Nucl. Sci.*, vol. 20, pp. 825–829, June 1973. doi:10.1109/TNS.1973.4327254.
- [176] V. I. Balbekov and S. V. Ivanov, “Thresholds of longitudinal instability of bunched beam in the presence of dominant inductive impedance,” 1991. IHEP-OUNK–91-14.
- [177] J. Esteban Müller, E. Shaposhnikova, and L. Rivkin, *Longitudinal intensity effects in the CERN Large Hadron Collider*. PhD thesis, Ecole Polytechnique, Lausanne, Apr 2016. Presented 28 June 2016.
- [178] E. Shaposhnikova, “Longitudinal beam parameters during acceleration in the LHC.,” Tech. Rep. LHC-PROJECT-NOTE-242, CERN, Geneva, Dec 2000.
- [179] E. Shaposhnikova, “Beam dynamics: RF requirements for the FCC-hh.” The second Annual Meeting of the Future Circular Collider Study, Rome, 2016.
- [180] S. Y. Lee, *Accelerator Physics*. World Scientific, 4th ed., 2019. doi:10.1142/11111.
- [181] D. Boussard, “RF power requirements for a high intensity proton collider ; parts 1 (chapters I, II, III) and 2 (chapters IV, V, VI),” Tech. Rep. CERN-SL-91-16-RFS, CERN, Geneva, May 1991.
- [182] T. Mastoridis, P. Baudrengnien, and J. Molendijk, “Cavity voltage phase modulation to reduce the high-luminosity Large Hadron Collider rf power requirements,” *Phys. Rev. Accel. Beams*, vol. 20, p. 101003, oct 2017. doi:10.1103/PhysRevAccelBeams.20.101003.
- [183] I. Karpov and P. Baudrengnien, “Transient beam loading and RF power evaluation for future circular colliders,” *Phys. Rev. Accel. Beams*, vol. 22, p. 081002, Aug 2019. doi:10.1103/PhysRevAccelBeams.22.081002.
- [184] E. Keil, W. Schnell, and P. Strolin, *Feedback damping of horizontal beam transfer errors*. CERN Yellow Reports: Monographs, Geneva: CERN, 1969. doi:10.5170/CERN-1969-027.
- [185] G. Rochepeau, *et al.*, “Damping of transverse oscillations in the ISR,” 1971. CERN-ISR-RF-71-42.
- [186] W. Höfle, “Progress In Transverse Feedbacks and Related Diagnostics for Hadron Machines,” May 2013. CERN-ACC-2013-0193.
- [187] K. Li *et al.*, “Code Development for Collective Effects,” in *Proc. of ICFA Advanced Beam Dynamics Workshop on High-Intensity and High-Brightness Hadron Beams (HB’16), Malmö, Sweden, July 3–8, 2016*, no. 57 in WEAM3X01, pp. 362–367, Aug. 2016. doi:10.18429/JACoW-HB2016-WEAM3X01.
- [188] J. Komppula, “Optimization Algorithms for PyHEADTAIL Multibunch Simulations.” PyHEADTAIL Meeting #18 – CERN 15 June, 2018.
- [189] J. Komppula, W. Höfle, and K. Li, “Simulation Tools for the Design and Performance Evaluation of Transverse Feedback Systems,” in *Proc. of International Particle Accelerator Conference (IPAC’17), Copenhagen, Denmark*, pp. 1912–1915, JACoW, May 2017. doi:10.18429/JACoW-IPAC2017-TUPIK091.
- [190] P. Baudrengnien *et al.*, “LHC Transverse Feedback System and its Hardware Commissioning,” *Proc. 11th European Particle Accelerator Conf. (EPAC’08)*, pp. 3266–3268, June 2008.
- [191] D. Valuch, “ADT operation. A cook book of black magic.” LBOC Meeting No 61 – CERN 24 May, 2016.
- [192] N. Klinkenberg, “Computational studies of collective effects in particle beams in the Future Circular Collider.” Westfälische Hochschule in cooperation with CERN, 2018. Bachelor thesis, CERN-THESIS-2018-168.
- [193] E. Koukovini-Platia, *et al.*, “Study of Single Bunch Instabilities with Transverse Feedback at Diamond,” in *Proc. of 8th International Particle Accelerator Conference (IPAC’17), Copenhagen, Denmark, 14–19 May, 2017*, (Geneva, Switzerland), pp. 4489–4492, JACoW, May 2017. doi:10.18429/JACoW-IPAC2017-THPVA029.
- [194] E. Métral, *et al.*, “Destabilising Effect of the LHC Transverse Damper,” in *Proc. 9th International Particle Accelerator Conference (IPAC’18), Vancouver, BC, Canada, April 29–May 4, 2018*, (Geneva, Switzerland), pp. 3076–3079, JACoW Publishing, June 2018. doi:10.18429/JACoW-IPAC2018-THPAF048.
- [195] S. Berg and R. D. Ruth, “Transverse Multibunch Instabilities for Non-Rigid Bunches,” in *Proceedings, Particle Accelerator Conference: Dallas, TX, USA*, pp. 3076–3078, May 1–5, 1995.

- [196] X. Buffat, *Transverse beams stability studies at the Large Hadron Collider*. PhD thesis, Ecole Polytechnique Federale de Lausanne (EPFL), 2015.
- [197] W. Herr, “Introduction to Landau Damping,” in *CAS—CERN Accelerator School : Advanced Accelerator Physics* (W. Herr, ed.), pp. 377–403, CERN, 2014. doi:10.5170/CERN-2014-009.377.
- [198] “DYNAP: Tunes, Tune Footprints, Smear and Lyapunov Exponent.” in *MAD-X User’s Guide*.
- [199] W. Herr, “Particle tracking with MAD-X including LHC beam-beam interactions,” LHC project note 344, CERN, 2004.
- [200] J. Barranco García and T. Pieloni, “Global compensation of long-range beam-beam effects with octupole magnets: dynamic aperture simulations for the HL-LHC case and possible usage in LHC and FCC.,” May 2017. CERN-ACC-NOTE-2017-0036.
- [201] X. Buffat *et al.*, “Our understanding of transverse instabilities and mitigation tools/strategy,” in *8th LHC Operations Evian Workshop 12–14 December 2017 Evian, France*, CERN, Geneva, Switzerland, 2017.
- [202] X. Buffat *et al.*, “MD 3288: Instability latency with controlled noise,” Mar 2019. CERN-ACC-NOTE-2019-0011.
- [203] C. Tambasco *et al.*, “Triggering of instabilities by BTF measurements.” LHC Beam Operation Committee (LBOC) 27 March, 2018.
- [204] E. Metral *et al.*, “Update of the HL-LHC operational scenarios for proton operation,” Jan 2018. CERN-ACC-NOTE-2018-0002.
- [205] V. Shiltsev, *et al.*, “Landau damping of beam instabilities by electron lenses,” *Phys. Rev. Lett.*, vol. 119, p. 134802, Sep 2017. doi:10.1103/PhysRevLett.119.134802.
- [206] W. Fischer, *et al.*, “Compensation of head-on beam-beam induced resonance driving terms and tune spread in the relativistic heavy ion collider,” *Phys. Rev. Accel. Beams*, vol. 20, p. 091001, Sep 2017. doi:10.1103/PhysRevAccelBeams.20.091001.
- [207] Y. Chin, “Landau damping of a multi-bunch instability due to bunch-to-bunch tune spread,” in *Proc. of 1987 IEEE Particle Accelerator Conference (PAC1987)*, Washington (DC), USA, pp. 1213–1215, IEEE, Mar 1987.
- [208] S. Sakanaka and T. Mitsuhashi, “Construction of an RF Quadrupole Magnet for Suppressing Transverse Coupled-Bunch Instabilities,” in *Proc. of 1991 IEEE Particle Accelerator Conference (PAC1991)*, San Francisco (CA), USA, pp. 1836–1838, IEEE, May 1991.
- [209] V. V. Danilov, “Increasing the transverse mode coupling instability threshold by RF quadrupole,” *Phys. Rev. Spec. Top. Accel. Beams*, vol. 1, p. 041301, Aug 1998. doi:10.1103/PhysRevSTAB.1.041301.
- [210] E. A. Perevedentsev and A. A. Valishev, “Synchrotron dynamics with a radio-frequency quadrupole,” in *Proc. of European Particle Accelerator Conference 2002 (EPAC’02)*, Paris, France, pp. 1574–1576, JACoW, Jun 2002.
- [211] L. D. Landau, “On the vibration of the electronic plasma,” *Zh. Eksp. Teor. Fiz.*, vol. 16, p. 574, 1946. doi:10.1016/B978-0-08-010586-4.50066-3.
- [212] A. W. Chao, *Physics of Collective Beam Instabilities in High Energy Accelerators*. Wiley Series in Beam Physics and Accelerator Technology, Wiley, 1993. ISBN: 978-0-47-155184-3.
- [213] A. Grudiev, “Radio frequency quadrupole for Landau damping in accelerators,” *Phys. Rev. Spec. Top. Accel. Beams*, vol. 17, p. 011001, Jan 2014. doi:10.1103/PhysRevSTAB.17.011001.
- [214] H. W. Pommerenke, *et al.*, “RF design studies on the 750 MHz radio frequency quadrupole linac for proton-induced x-ray emission analysis,” *Phys. Rev. Accel. Beams*, vol. 22, p. 052003, May 2019. doi:10.1103/PhysRevAccelBeams.22.052003.
- [215] M. Schenk, *et al.*, “Analysis of transverse beam stabilization with radio frequency quadrupoles,” *Phys. Rev. Accel. Beams*, vol. 20, p. 104402, Oct 2017. doi:10.1103/PhysRevAccelBeams.20.104402.
- [216] M. Schenk, *et al.*, “Vlasov description of the effects of nonlinear chromaticity on transverse coherent beam instabilities,” *Phys. Rev. Accel. Beams*, vol. 21, p. 084402, Aug 2018. doi:10.1103/PhysRevAccelBeams.21.084402.
- [217] M. Schenk, *et al.*, “Experimental stabilization of transverse collective instabilities in the LHC with second order chromaticity,” *Phys. Rev. Accel. Beams*, vol. 21, p. 084401, Aug 2018. doi:10.1103/PhysRevAccelBeams.21.084401.
- [218] K. Papke and A. Grudiev, “Design of an RF quadrupole for Landau damping,” *Phys. Rev. Accel. Beams*, vol. 20, p. 082001, Aug 2017. doi:10.1103/PhysRevAccelBeams.20.082001.

- [219] J. Scott Berg and F. Ruggiero, “Stability diagrams for Landau damping,” in *Proc. of Particle Accelerator Conference 1997 (PAC’97)*, Vancouver (British Columbia), Canada, pp. 1712–1714, May 1997. doi:10.1109/PAC.1997.750810.
- [220] E. Métral, *et al.*, “Beam Instabilities in Hadron Synchrotrons,” *IEEE Trans. Nucl. Sci.*, vol. 63, pp. 1001–1050, Apr 2016. doi:10.1109/TNS.2015.2513752.
- [221] S. Calatroni and R. Vaglio, “Surface resistance of superconductors in the presence of a dc magnetic field: frequency and field intensity limits,” *IEEE Trans. Appl. Supercond.*, vol. 27, p. 3500506, 2017.
- [222] S. Calatroni, *et al.*, “Thallium-based high-temperature superconductors for beam impedance mitigation in the Future Circular Collider,” *Supercond. Sci. Technol.*, vol. 30, p. 075002, 2017.
- [223] P. Krkotić, U. Niedermayer, and O. Boine-Frankenheim, “High-temperature superconductor coating for coupling impedance reduction in the fcc-hh beam screen,” *Nucl. Instrum. Methods Phys. Res., A*, vol. 895, pp. 56–61, Mar 2018. doi:10.1016/j.nima.2018.03.049.
- [224] J. Gutierrez, “HTS YBaCuO Coated Conductors for the FCC-hh beam screens.” Contribution to the FCC Week 2018, 2018.
- [225] S. Calatroni, “Proposals for impedance measurements at CERN.” FCC-hh impedance and beam screen workshop, Mar 2017.
- [226] S. Arsenyev and D. Schulte, “Modeling coupling impedance of a rough surface,” in *Proc. 9th International Particle Accelerator Conference (IPAC 2018): Vancouver, BC, Canada*, pp. 157–160, April 29–May 4, 2018. doi:10.18429/JACoW-IPAC2018-MOPMF031.
- [227] J. Fox *et al.*, “Control of Intra-Bunch Vertical Instabilities at the SPS - Measurements and Technology Demonstration,” in *Proc. of 8th International Particle Accelerator Conference (IPAC’17)*, Copenhagen, Denmark, 14–May, 2017, (Geneva, Switzerland), pp. 2005–2007, JACoW, May 2017. doi:10.18429/JACoW-IPAC2017-TUPIK119.
- [228] K. Li, W. Höfle, and G. Rumolo, “Modelling and Studies for a Wideband Feedback System for Mitigation of Transverse Single Bunch Instabilities,” in *Proc. of International Particle Accelerator Conference (IPAC’13)*, Shanghai, China, pp. 3019–3021, May 2013.
- [229] K. Li *et al.*, “Wideband feedback demonstrator system—selected results from 2017.” LIU MD Days—15.03.2018, CERN, 2018.
- [230] R. W. Assmann, “Preliminary Beam-based specifications for the LHC collimators,” Tech. Rep. LHC-PROJECT-NOTE-277, CERN, Geneva, Jan 2002.
- [231] J. B. Jeanneret, “Momentum losses in LHC : the special case of RF uncaptured protons,” *CERN SL-Note-92-56-EA*, 1992.
- [232] S. Wretborn, *et al.*, “Study of off-momentum losses at the start of the ramp in the Large Hadron Collider,” Tech. Rep. CERN-ACC-NOTE-2017-0065, CERN, Sep 2017.
- [233] R. Bruce, R. W. Assmann, and S. Redaelli, “Calculations of safe collimator settings and β^* at the CERN Large Hadron Collider,” *Phys. Rev. Spec. Top. Accel. Beams*, vol. 18, p. 061001, Jun 2015. doi:10.1103/PhysRevSTAB.18.061001.
- [234] A. Marsili, R. Bruce, and S. Redaelli, “Collimation Cleaning for HL-LHC Optics Scenarios with Error Models,” *Proceedings of the International Particle Accelerator Conference 2014, Dresden, Germany*, pp. 163–165, 2014. doi:10.18429/JACoW-IPAC2014-MOPRO040.
- [235] G. Valentino, *et al.*, “Successive approximation algorithm for beam-position-monitor-based LHC collimator alignment,” *Phys. Rev. Spec. Top. Accel. Beams*, vol. 17, p. 021005, 2014. doi:10.1103/PhysRevSTAB.17.021005.
- [236] R. Bruce, *et al.*, “Parameters for HL-LHC aperture calculations and comparison with aperture measurements,” Tech. Rep. CERN Report CERN-ACC-2014-0044, CERN, 2014.
- [237] R. Bruce, *et al.*, “Parameters for aperture calculations at injection for HL-LHC,” Tech. Rep. CERN-ACC-2016-0328, CERN, Geneva, Feb 2016.
- [238] C. Alabau Pons, *et al.*, “LHC aperture measurements,” *Proceedings of IPAC 10, Kyoto, Japan*, p. 477, 2010.
- [239] C. Alabau Pons, *et al.*, “IR1 and IR5 aperture at 3.5 TeV,” Tech. Rep. CERN-ATS-Note-2011-110 MD, CERN, Nov 2011.
- [240] R. Assmann, *et al.*, “Aperture Determination in the LHC Based on an Emittance Blowup Technique with Collimator Position Scan,” *Proceedings of IPAC11, San Sebastian, Spain*, p. 1810, 2011.

- [241] S. Redaelli, *et al.*, “Aperture measurements in the LHC interaction regions,” *Proceedings of IPAC12, New Orleans, Louisiana, USA*, p. 508, 2012.
- [242] C. Alabau Pons, *et al.*, “IR2 aperture measurements at 3.5 TeV,” Tech. Rep. CERN-ATS-Note-2012-017 MD, CERN, Feb 2012.
- [243] R. Bruce, *et al.*, “IR8 aperture measurements at injection energy,” Tech. Rep. CERN-ATS-Note-2013-026 MD, CERN, Geneva, Apr 2013.
- [244] R. Bruce, *et al.*, “IR2 aperture measurements at 4.0 TeV,” Tech. Rep. CERN-ACC-NOTE-2013-0011, CERN, Geneva, Aug 2013.
- [245] P. Hermes, *et al.*, “Improved Aperture Measurements at the LHC and Results from their Application in 2015,” *Proceedings of the International Particle Accelerator Conference 2016, Busan, Korea*, p. 1446, May 2016. doi:10.18429/JACoW-IPAC2016-TUPMW014.
- [246] N. Fuster-Martinez, R. Bruce, and S. Redaelli, “LHC β^* -reach MD: aperture measurements at small β^* ,” Tech. Rep. CERN-ACC-NOTE-2017-0064, CERN, Nov 2017.
- [247] N. Fuster-Martinez, *et al.*, “Aperture measurements with AC dipole,” Tech. Rep. CERN-ACC-NOTE-2018-0008, CERN, Feb 2018.
- [248] J.B. Jeanneret, “Geometrical tolerances for the qualification of LHC magnets,” Tech. Rep. CERN-LHC-Project-Report-1007, CERN, Dec 2006.
- [249] A. Mereghetti *et al.*, “Sixtrack-FLUKA active coupling for the upgrade of the SPS scrapers,” in *Proceedings of the International Particle Accelerator Conference 2013, Shanghai, China*, 2013. WEPEA064.
- [250] A. Mereghetti, *Performance Evaluation of the SPS Scraping System in View of the High Luminosity LHC*. PhD thesis, University of Manchester, 2015.
- [251] E. Skordis, *et al.*, “FLUKA coupling to Sixtrack,” *CERN-2018-011-CP, Proceedings of the ICFA Mini-Workshop on Tracking for Collimation, CERN, Geneva, Switzerland*, p. 17, 2018.
- [252] G. Robert-Demolaize, *et al.*, “A new version of SixTrack with collimation and aperture interface,” *Proc. of the Particle Accelerator Conf. 2005, Knoxville*, p. 4084, 2005.
- [253] G. Battistoni *et al.*, “Overview of the FLUKA code,” *Annals Nucl. Energy*, vol. 82, pp. 10–18, 2015. doi:10.1016/j.anucene.2014.11.007.
- [254] B. Auchmann, *et al.*, “Testing beam-induced quench levels of LHC superconducting magnets,” *Phys. Rev. Spec. Top. Accel. Beams*, vol. 18, p. 061002, 2015. doi:10.1103/PhysRevSTAB.18.061002.
- [255] J. Jeanneret *et al.*, “Quench levels and transient beam losses in LHC magnets,” Tech. Rep. CERN-LHC-Project-Report-44, CERN, May 1996.
- [256] L. Bottura *et al.*, “Expected performance of 11T and MB dipoles considering the cooling performance,” *Presentation at 8th HL-LHC collaboration meeting, CERN, Geneva Switzerland*, 2018.
- [257] M. Varasteh *et al.*, “Cold loss studies for the quench limit assessment,” in *4th EuroCirCol Meeting*, Oct 2018.
- [258] The CMS Collaboration, “Absolute Calibration of Luminosity Measurement at CMS: Summer 2011 Update,” Tech. Rep. CMS-PAS-EWK-11-001, CERN, Geneva, 2011.
- [259] R. Tomás, private communication.
- [260] J. Molson, *et al.*, “Simulating the LHC collimation system with the accelerator physics library MERLIN,” *Proceedings of ICAP12, Rostock-Warnemünde, Germany*, pp. 12–14, 2012.
- [261] M. Serluca, *et al.*, “Hi-Lumi LHC Collimation Studies with MERLIN Code,” in *Proc. 5th International Particle Accelerator Conference (IPAC’14), Dresden, Germany, June 15-20, 2014*, no. 5 in International Particle Accelerator Conference, (Geneva, Switzerland), pp. 784–787, JACoW, July 2014. doi:10.18429/JACoW-IPAC2014-MOPRI077.
- [262] D. Tommasini *et al.*, “Status of the 16 T Dipole Development Program for a Future Hadron Collider,” *IEEE Trans. Appl. Supercond.*, vol. 28, no. 3, p. 4001305. 5 p, 2018. doi:10.1109/TASC.2017.2780045.
- [263] A. Dallochio, *Study of thermomechanical effects induced in solids by high-energy particle beams: analytical and numerical methods*. PhD thesis, CERN-THESIS, 2008.
- [264] F. Carra, *et al.*, “New TCSM Design Outcome of HRMT-23: Robustness of HL-LHC jaws.” Special LHC Collimation Upgrade Specification Meeting: Material and design readiness for LS2 productions, CERN, 2017.

- [265] A. Bertarelli, *et al.*, “[HRMT-36 \(Multimat\) Experiment: Preliminary Results.](#)” LHC Collimation Upgrade Specification Meeting N° 96, CERN, 2017.
- [266] E. Quaranta, *et al.*, “[Towards optimum material choices for the HL-LHC collimator upgrade.](#)” IPAC16, Busan, Korea, 2016.
- [267] T. Furness, “[Design and integration of an active dynamic compensation for the collimator jaw in the Multimat experiment.](#)” Eucard2 WP11 topical meeting, CERN, 2017.
- [268] D. Mirarchi, *Crystal Collimation for LHC*. PhD thesis, Imperial College London, 2015.
- [269] D. Mirarchi, *et al.*, “Design and implementation of a crystal collimation test stand at the Large Hadron Collider,” *The European Physical Journal C*, vol. 77, p. 424, Jun 2017. doi:10.1140/epjc/s10052-017-4985-4.
- [270] W. Scandale, *et al.*, “Observation of channeling for 6500 GeV/c protons in the crystal assisted collimation setup for LHC,” *Phys. Lett. B*, vol. 758, pp. 129 – 133, 2016. doi:10.1016/j.physletb.2016.05.004.
- [271] R. Appleby *et al.*, “[Report from the Review Panel,](#)” *Review of the needs for a hollow electron lens for the HL-LHC*, CERN, Geneva, Switzerland, 2016.
- [272] F. Bordry, *et al.*, “[Machine Parameters and Projected Luminosity Performance of Proposed Future Colliders at CERN,](#)” Tech. Rep. CERN-ACC-2018-0037, CERN, Oct 2018. <https://arxiv.org/abs/1810.13022>.
- [273] M. Pojer, “[LHC Operation,](#)” in *8th LHC Operations Evian Workshop* (T. Argyropoulos, S. Dubourg, and G. Trad, eds.), pp. 47–50, CERN, 2019.
- [274] M. S. Camillocci, *et al.*, “Combined Ramp and Squeeze to 6.5 TeV in the LHC,” in *Proc. of 7th International Particle Accelerator Conference (IPAC’16), Busan, Korea, May 8–13, 2016*, (Geneva, Switzerland), pp. 1509–1512, JACoW, June 2016. doi:10.18429/JACoW-IPAC2016-TUPMW031.
- [275] D. Jacquet, “[Injection,](#)” in *Proc. 6th Evian Workshop on LHC beam operation* (B. Goddard and S. Dubourg, eds.), (Geneve), pp. 49–52, CERN, Oct. 2016.
- [276] M. Solfaroli Camillocci, “[Scope and results of hardware commissioning to 3.5 TeV and lessons learnt,](#)” in *Proceedings of the Chamonix 2010 workshop on LHC performance* (C. Carli, ed.), (Geneve), pp. 34–36, CERN, Apr. 2010.
- [277] V. Shiltsev, “On performance of high energy particle colliders and other complex scientific systems,” *Mod. Phys. Lett. A*, vol. 26, no. 11, pp. 761–772, 2011. doi:10.1142/S0217732311035699.
- [278] R. Steerenberg and J. Wenninger, “Operational challenges and performance of the LHC during run II,” in *Proceedings of the 61st ICFA Advanced Beam Dynamics Workshop on High-Intensity and High-Brightness Hadron Beams*, (Geneve), pp. 357–361, JACoW, 2018. doi:10.18429/JACoW-HB2018-THA2WD01.
- [279] F. Bertinelli, *et al.*, “[Towards a Consolidation of LHC Superconducting Splices for 7 TeV Operation,](#)” in *Proc. of International Particle Accelerator Conference (IPAC’10), Kyoto, Japan*, (Geneve), pp. 367–369, JACoW, 2010.
- [280] O. Brüning, *et al.*, “[LHC Full Energy Exploitation Study: Operation at 7 TeV,](#)” Tech. Rep. CERN-ACC-2017-0086, CERN, Sep 2017.
- [281] B. Todd, L. Ponce, and A. Apollonio, “[LHC Availability 2016: Proton Run,](#)” Tech. Rep. CERN-ACC-NOTE-2016-0067, CERN, Dec 2016.
- [282] B. Todd, *et al.*, “[LHC Availability 2017: Proton Run,](#)” Tech. Rep. CERN-ACC-NOTE-2017-0063, CERN, Dec 2017. <https://cds.cern.ch/record/2294852>.
- [283] A. Niemi, *Modeling Future Hadron Colliders’ Availability for Physics*. PhD thesis, Tampere University, Apr 2019.
- [284] A. Niemi, *et al.*, “Availability modeling approach for future circular colliders based on the LHC operation experience,” *Phys. Rev. Accel. Beams*, vol. 19, p. 121003, Dec. 2016. doi:10.1103/PhysRevAccelBeams.19.121003.
- [285] J. Penttinen, A. Niemi, and J. Gutleber, “[An Open Modelling Approach for Availability and Reliability of Systems - OpenMARS,](#)” Tech. Rep. CERN-ACC-2018-0006, CERN, Jan 2018.
- [286] J. Penttinen, *et al.*, “An open modelling approach for availability and reliability of systems,” *Reliab. Eng. Syst. Saf.*, vol. 183, pp. 387 – 399, 2019. doi:10.1016/j.ress.2018.11.026.
- [287] Schoerling, D. and Auchmann, B. and al., “The 16 T Dipole Development Program for FCC and HE-LHC,” *IEEE Trans. Appl. Supercond.*, vol. 29, no. 5, pp. 1–9, 2019. doi:10.1109/TASC.2019.2900556.

- [288] M. Benedikt and F. Zimmermann, “Future Circular Collider Study: Status and Plans,” in *FCC Week 2017, Berlin, Germany*, 2017.
- [289] D. Schulte, “FCC-hh Machine Layout and Optics,” in *FCC Week 2016, Roma, Italy*, 2016.
- [290] Y. Nie, *et al.*, “Numerical simulations of energy deposition caused by 50 MeV–50 TeV proton beams in copper and graphite targets,” *Phys. Rev. Accel. Beams*, vol. 20, no. 8, 2017. doi:10.1103/PhysRevAccelBeams.20.081001.
- [291] D. C. Wilson, *et al.*, “Hydrodynamic calculations of 20-TeV beam interactions with the SSC beam dump,” *Proceedings of the 15th Particle Accelerator Conference, Washington, DC*, p. 3090, May 1993.
- [292] N. A. Tahir, *et al.*, “The CERN Large Hadron Collider as a Tool to Study High-Energy Density Matter,” *Phys. Rev. Lett.*, vol. 94, p. 135004, Apr 2005. doi:10.1103/PhysRevLett.94.135004.
- [293] N. A. Tahir, *et al.*, “Large Hadron Collider at CERN: Beams generating high-energy-density matter,” *Phys. Rev. E*, vol. 79, p. 046410, Apr 2009. doi:10.1103/PhysRevE.79.046410.
- [294] N. A. Tahir, *et al.*, “Impact of high energy high intensity proton beams on targets: Case studies for Super Proton Synchrotron and Large Hadron Collider,” *Phys. Rev. Spec. Top. Accel. Beams*, vol. 15, p. 051003, May 2012. doi:10.1103/PhysRevSTAB.15.051003.
- [295] T. Baer, *Very Fast Losses of the Circulating LHC Beam, their Mitigation and Machine Protection*. PhD thesis, Universität Hamburg, Oct 2013. Presented 25 Nov 2013.
- [296] M. Werner, *et al.*, “A Fast Magnet Current Change Monitor for Machine Protection in HERA and the LHC,” in *Proc. of 10th Int. Conf. on Accelerator & Large Expt. Physics Control Systems (ICALEPCS’05), Geneva, Switzerland*, October 2005.
- [297] Y. Nie, M. Jonker, and R. Schmidt, “Beam Related Machine Protection of the Future Circular Collider,” in *Proceedings of International Particle Accelerator Conference (IPAC’17), Copenhagen, Denmark*, pp. 2063–2066, May 2017. doi:10.18429/JACoW-IPAC2017-TUPVA012.
- [298] R. Schmidt, “Concept and architecture of the machine protection systems for FCC,” in *FCC Week 2015, Washington DC, USA*, 2015.
- [299] F. Burkart, “Injection and extraction straight and dump lines,” in *FCC Week 2017, Berlin, Germany*, 2017.
- [300] T. Baer, *et al.*, “LHC machine protection against very fast crab cavity failures,” *Proceedings of IPAC2011, San Sebastián, Spain*, 2011.
- [301] A. Santamaría García, *Experiment and Machine Protection from Fast Losses caused by Crab Cavities in the High Luminosity LHC*. PhD thesis, Ecole Polytechnique, Lausanne, 2018. doi:10.5075/epfl-thesis-8533.
- [302] B. Lindstroem, *et al.*, “Fast Failures in the LHC and the future High Luminosity LHC,” *Arxiv*, 2020.
- [303] M. Valette, *et al.*, “CLIQ and Quench Heater firing: effect on the beam,” in *7th HL-LHC Annual Meeting, Madrid, 2017*, 2017.
- [304] E. Ravaoli, “Fast failure due to triplet event: update on the field simulations.” 169th SPS and LHC Machine Protection Panel Meeting, CERN, Geneva, 14.09.2018.
- [305] J. M. Jimenez *et al.*, “Observations, Analysis and Mitigation of Recurrent LHC Beam Dumps Caused by Fast Losses in Arc Half-Cell 16L2,” *Proc. 9th International Particle Accelerator Conference (IPAC’18), Vancouver, BC, Canada*, pp. 228–231, 2018. doi:10.18429/JACoW-IPAC2018-MOPMF053.
- [306] N. A. Tahir, “Feasibility studies of a water beam dump for 50 TeV FCC proton beam,” in *FCC Week 2017, Berlin, Germany*, 2017.
- [307] R. Schmidt, “Machine Protection and Interlock Systems for Circular Machines - Example for LHC,” *2014 Joint International Accelerator School: Beam Loss and Accelerator Protection, Newport Beach, CA, USA, 5–14 Nov 2014*, Aug 2016. doi:10.5170/CERN-2016-002.319.
- [308] Y. Nie, “Overall machine protection,” in *FCC Week 2018, Amsterdam, Netherlands*, 2018.
- [309] R. Schmidt, *et al.*, “Protection of the CERN Large Hadron Collider,” *New Journal of Physics*, vol. 8, no. 11, p. 290, 2006. doi:10.1088/1367-2630/8/11/290.
- [310] R. B. Appleby, *et al.*, “Beam-related machine protection for the cern large hadron collider experiments,” *Phys. Rev. Spec. Top. Accel. Beams*, vol. 13, p. 061002, 2010. doi:10.1103/PhysRevSTAB.13.061002.
- [311] M. Camillocci, “Update of procedure in case of a non-working beam dump.” 169th SPS and LHC Machine Protection Panel Meeting, CERN, Geneva, 14.09.2018.

- [312] S. Wagner, *et al.*, “Quantitative reliability analysis of interlock systems for particle Accelerators,” *Phys. Rev. Accel. Beams*, vol. 25, p. 073501, 2022. doi:10.1103/PhysRevAccelBeams.25.073501.
- [313] M. Fitterer *et al.*, “Hollow Electron Beam Collimation for HL-LHC - Effects on the Beam Core,” in *Proc. of International Particle Accelerator Conference (IPAC’17), Copenhagen, Denmark, 14–19 May, 2017*, 8th International Particle Accelerator Conference, (Geneva, Switzerland), pp. 2482–2485, JACoW, May 2017. doi:10.18429/JACoW-IPAC2017-WEOBA2.
- [314] G. Stancari, *et al.*, “Collimation with Hollow Electron Beams,” *Phys. Rev. Lett.*, vol. 107, p. 084802, Aug 2011. doi:10.1103/PhysRevLett.107.084802.
- [315] B. Dehning, *et al.*, “Diamond Detectors as Beam Monitors,” Tech. Rep. CERN-BE-2011-001, CERN, Geneva, May 2010.
- [316] E. Verbitskaya, *et al.*, “Development of silicon detectors for Beam Loss Monitoring at HL-LHC,” *JINST*, vol. 12, pp. C03036–C03036, Mar 2017. doi:10.1088/1748-0221/12/03/c03036.
- [317] J. W. van Hoorne, “Cherenkov Fibers for Beam Loss Monitoring at the CLIC Two Beam Module,” Master’s thesis, Technische Universität Wien, May 2012.
- [318] B. Goddard, “Addition of a Beam Loss Monitor Interlock with Direct Input to the LHC Beam Dump,” Tech. Rep. LHC-BLM-EC-0001, CERN, May 2006. EDMS Document No. 715795.
- [319] M. Schaumann, “Potential performance for Pb-Pb, p-Pb, and p-p collisions in a future circular collider,” *Phys. Rev. Spec. Top. Accel. Beams*, vol. 18, p. 091002, September 2015. doi:10.1103/PhysRevSTAB.18.091002.
- [320] M. Schaumann and J.M. Jowett, “A First Look at the Performance for Pb-Pb and p-Pb collisions in FCC-hh,” in *FCC Study Kickoff Meeting, Geneva, Switzerland, Feb 2014*.
- [321] J.M. Jowett *et al.*, “FCC-hh as a heavy-ion collider,” in *FCC week 2015, Washington DC, USA, 2015*.
- [322] A. Dainese *et al.*, “Heavy-ion physics studies for the Future Circular Collider,” in *FCC Week 2016, Rome, Italy, 2016*.
- [323] M. Schaumann *et al.*, “Heavy-ions at the FCC-hh,” in *FCC week 2017, Berlin, Germany, 2017*.
- [324] J.M. Jowett *et al.*, “The 2016 proton-nucleus run of the LHC,” in *Proc. of the International Particle Accelerator Conference, IPAC2017, Copenhagen, Denmark, 2017*. doi:10.18429/JACoW-IPAC2017-TUPVA014.
- [325] M. Schaumann, “Semi-Empirical Model for Optimising Future Heavy-Ion Luminosity of the LHC,” in *Proceedings of the International Particle Accelerator Conference, IPAC14, Dresden, Germany, 2014*. doi:10.18429/JACoW-IPAC2014-TUPRO014.
- [326] D. Manglunki. private communication.
- [327] K. Fuchsberger, “Turn-around - analysis and possible improvements,” in *Proceedings of the 7th Evian Workshop on LHC beam operation, 2016*. CERN-ACC-2017-094.
- [328] A.J. Baltz, M.J. Rhoades-Brown, and J. Weneser, “Heavy-ion partial beam lifetimes due to Coulomb induced processes,” *Phys. Rev. E*, vol. 54, p. 4233, 1996. doi:10.1103/PhysRevE.54.4233.
- [329] I.A. Pshenichnov and S. Gunin, “Electromagnetic interactions of nuclei at the FCC-hh,” in *Talk given at the XV International Seminar on Electromagnetic Interactions of Nuclei, Moscow, October 2018*.
- [330] H. Meier, *et al.*, “Bound-free electron-positron pair production in relativistic heavy-ion collisions,” *Phys. Rev. A*, vol. 63, p. 032713, 2001. doi:10.1103/PhysRevA.63.032713.
- [331] H.H. Braun, *et al.*, “Hadronic and electromagnetic fragmentation of ultrarelativistic heavy ions at LHC,” *Phys. Rev. Spec. Top. Accel. Beams*, vol. 17, p. 021006, 2014. doi:10.1103/PhysRevSTAB.17.021006.
- [332] R. Bruce, *et al.*, “Beam losses from ultraperipheral nuclear collisions between $^{208}\text{Pb}^{82+}$ ions in the Large Hadron Collider and their alleviation,” *Phys. Rev. Spec. Top. Accel. Beams*, vol. 12, p. 071002, 2009. doi:10.1103/PhysRevSTAB.12.071002.
- [333] J.M. Jowett, M. Schaumann, and R. Versteegen, “Heavy ion operation from Run 2 to HL-LHC,” in *Proceedings of RLIUP: Review of LHC and Injector Upgrade Plans, Archamps, France* (B. Goddard and F. Zimmermann, eds.), 2014. doi:10.5170/CERN-2014-006.167.
- [334] A. Zlobin *et al.*, “Status of 11T 2-in-1 Nb3Sn dipole development for LHC,” in *Proceedings of the 5th International Particle Accelerator Conference, IPAC-2014, Dresden, Germany, p. 2722, 2014*. doi:10.18429/JACoW-IPAC2014-WEPRI097.

- [335] P.D. Hermes *et al.*, “Measured and simulated heavy-ion beam loss patterns at the CERN Large Hadron Collider,” *Nucl. Instrum. Methods Phys. Res., A*, 2016. doi:10.1016/j.nima.2016.02.050.
- [336] H.H. Braun *et al.*, “Collimation of heavy ion beams in LHC,” in *EPAC '04, Lucerne, Switzerland*, July 2004. MOPLT010.
- [337] D. Mirarchi *et al.*, “Cleaning Performance of the Collimation System of the High Luminosity Large Hadron Collider,” in *Proceedings of the International Particle Accelerator Conference 2016, Busan, Korea*, 2016. doi:10.18429/JACoW-IPAC2016-WEPMW030.
- [338] P.D. Hermes *et al.*, “Simulation of heavy-ion beam losses with the SixTrack-FLUKA active coupling,” in *IPAC '16, Busan, Korea*, June 2016. doi:10.18429/JACoW-IPAC2016-WEPMW029.
- [339] P. Hermes, *Heavy-ion collimation at the Large Hadron Collider - simulations and measurements*. PhD thesis, Phys. Dept., Westfälischen Wilhelms-Universität Münster, 2016.
- [340] Z. Citron *et al.*, “Future physics opportunities for high-density QCD at the LHC with heavy-ion and proton beams,” *CERN Yellow Reports: Monographs*, no. 2019-007, pp. 1159–1410, 2019. doi:10.23731/CYRM-2019-007.1159.
- [341] D. Manglunki *et al.*, “CERN’s Fixed Target Primary Ion Programme,” in *Proceedings of the 7th International Particle Accelerator Conference, IPAC-2016, Busan, Korea*, 2016. doi:10.18429/JACoW-IPAC2016-TUPMR027.
- [342] D. Kuchler. private communication.
- [343] E.V. Karpechev *et al.*, “Emission of forward neutrons by 158A GeV indium nuclei in collisions with Al, Cu, Sn and Pb,” *Nuclear Physics A*, no. 921, pp. 60–84, 2014. doi:10.1016/j.nuclphysa.2013.11.003.
- [344] U.I. Uggerhoj *et al.*, “Charge-changing interactions of ultrarelativistic nuclei,” *Phys. Rev. C*, vol. 72, no. 057901, 2005. doi:10.1103/PhysRevC.72.057901.
- [345] I.A. Pshenichnov, “Electromagnetic excitation and fragmentation of ultrarelativistic nuclei,” *Phys. Part. Nuclei*, vol. 42, no. 2, pp. 215–250, 2011. doi:10.1134/S1063779611020067.
- [346] I.A. Pshenichnov. private communication.
- [347] R. Alemany Fernandez, “News and progress of turn-around time studies,” in *FCC-hh meeting on extraction, insertion and turn-around time studies*, March 2016.
- [348] B. Todd *et al.*, “LHC Availability 2017: Proton Physics - Setting the Scene,” in *8th Evian Workshop on LHC beam operation*, 2017.